

# **Elevation and Deformation Extraction from TomoSAR**

**Lang Feng**

**Thesis submitted for the degree of  
Doctor of Philosophy**



Mullard Space Science Laboratory  
Department of Space and Climate Physics  
University College London

2019

This page is intentionally left blank.

## **Author Declaration**

I, Lang Feng, confirm that the work presented in this thesis is my own. Where information has been derived from other sources, I confirm that this has been indicated in the thesis.

LANG FENG

2019-02-01

This page is intentionally left blank.



# Abstract

3D SAR tomography (TomoSAR) and 4D SAR differential tomography (Diff-TomoSAR) exploit multi-baseline SAR data stacks to provide an essential innovation of SAR Interferometry for many applications, sensing complex scenes with multiple scatterers mapped into the same SAR pixel cell. However, these are still influenced by DEM uncertainty, temporal decorrelation, orbital, tropospheric and ionospheric phase distortion and height blurring. In this thesis, these techniques are explored. As part of this exploration, the systematic procedures for DEM generation, DEM quality assessment, DEM quality improvement and DEM applications are first studied. Besides, this thesis focuses on the whole cycle of systematic methods for 3D & 4D TomoSAR imaging for height and deformation retrieval, from the problem formation phase, through the development of methods to testing on real SAR data.

After DEM generation introduction from spaceborne bistatic InSAR (TanDEM-X) and airborne photogrammetry (Bluesky), a new DEM co-registration method with line feature validation (river network line, ridgeline, valley line, crater boundary feature and so on) is developed and demonstrated to assist the study of a wide area DEM data quality. This DEM co-registration method aligns two DEMs irrespective of the linear distortion model, which improves the quality of DEM vertical comparison accuracy significantly and is suitable and helpful for DEM quality assessment.

A systematic TomoSAR algorithm and method have been established, tested, analysed and demonstrated for various applications (urban buildings, bridges, dams) to achieve better 3D & 4D tomographic SAR imaging results. These include applying Cosmo-Skymed X band single-polarisation data over the Zipingpu dam, Dujiangyan, Sichuan, China, to map topography; and using ALOS L band data in the San Francisco Bay region to map urban building and bridge.

A new ionospheric correction method based on the tile method employing IGS TEC data, a split-spectrum and an ionospheric model via least squares are developed to correct ionospheric distortion to improve the accuracy of 3D & 4D tomographic SAR imaging. Meanwhile, a pixel by pixel orbit baseline estimation method is developed to address the research gaps of baseline estimation for 3D & 4D spaceborne SAR tomography imaging. Moreover, a SAR tomography imaging algorithm and a differential

tomography four-dimensional SAR imaging algorithm based on compressive sensing, SAR interferometry phase (InSAR) calibration reference to DEM with DEM error correction, a new phase error calibration and compensation algorithm, based on PS, SVD, PGA, weighted least squares and minimum entropy, are developed to obtain accurate 3D & 4D tomographic SAR imaging results. The new baseline estimation method and consequent TomoSAR processing results showed that an accurate baseline estimation is essential to build up the TomoSAR model. After baseline estimation, phase calibration experiments (via FFT and Capon method) indicate that a phase calibration step is indispensable for TomoSAR imaging, which eventually influences the inversion results. A super-resolution reconstruction CS based study demonstrates X band data with the CS method does not fit for forest reconstruction but works for reconstruction of large civil engineering structures such as dams and urban buildings. Meanwhile, the L band data with FFT, Capon and the CS method are shown to work for the reconstruction of large manmade structures (such as bridges) and urban buildings.

# Impact Statement

A new DEM co-registration algorithm co-aligns two DEMs, which improves the quality of DEM relative accuracy significantly and is suitable and helpful for DEM quality assessment. This method can also be used for merging and fusing bathymetry (seafloor) with land DEM data at the coast region to generate a future global DEM. In addition, this algorithm works well for finding the correct landing site and precise and safe planetary rover landing, which can be used for future planetary rover landing missions. More specifically, the algorithm can be integrated with IMU and DEM-producing sensors in Guidance, Navigation and Control (GNC) system for navigation in different environments (sea, land, air, space and deep space) for different applications.

The DEM over the UK (in particular the TanDEM-X IDEM and the TanDEM-X DEM) quality report and statistical analysis results are useful for future DEM users and DEM makers.

A new ionospheric correction and mapping method not only addresses the SAR ionospheric accuracy degradation problem, its high-resolution TEC data can also be obtained after processing, which (TEC data) can be used in many other application fields, like communications, radio astronomy, as well as many other terrestrial planets and their satellites (moons), with the same earth-like environment, and so on.

The systematic TomoSAR and D-TomoSAR algorithm and methods to retrieve the 3D & 4D information can be potentially useful for many future applications (urban buildings, bridges, dams, forests, and icy regions on the Earth and the Moon) and missions.

This page is intentionally left blank.

# Acknowledgements

First and foremost, I would like to express my greatest thanks to my supervisors, Prof. Jan-Peter Muller and Dr Jonathan Rae. Individually, Peter, I thank you for your useful suggestions, excellent guidance, constant encouragement and generous support in my life and study throughout my PhD program in the UK and invaluable time during the writing up of this thesis. I also thank you for helping me to improve my English in each tutorial, all documents feedbacks, and supporting me to take English course to improve my English in Surrey University and UCL, and providing me with countless opportunities to take courses, training and conferences over the last four years. Jonny, I cannot thank you enough for your valuable advice, creative guidance, thought-provoking viewpoints, continuous support, constant encouragement and much of your time in tutorials and reading my thesis. I have been enormously fortunate to have you and Peter as my supervisors. In addition, I would like to express my greatest gratitude to my PhD panel chair, Dr Daisuke Kawata. I appreciate your continuous support, constant encouragement and invaluable advice provided throughout my PhD programme. I also thank you for being positive in my abilities and for being patient in listening and understanding me when I have most needed it. I am also grateful to my examiners, Prof. Shaun Quegan and Prof. Tim Wright, for constructive comments that improved this thesis. I would also like to thank the China Scholarships Council (CSC) and UCL MAPS Dean prize joint research scholarship for providing the financial support, allowing this work to be undertaken.

I owe special thanks to a few individuals whose contribution to this project was in some way immense. First, I would like to thank Terri Freemantle from Space Catapult, Harwell space campus for arranging the provision of CORSAIR011 data. Besides, I would like to thank Prof. Tim Wright and Prof. Andy Hooper from the University of Leeds for organising COMET InSAR training workshop 2017 and providing code and data in this workshop and Dr David Bekaert from JPL NASA for providing SAR code. Meanwhile, I would like to thank Prof. Zhenhong Li for his valuable advice, thought-provoking viewpoints and providing GACOS data. Moreover, I would like to thank Prof. Stefano Tebaldini from Politecnico di Milano, Prof. Laurent Ferro-Famil from the University of Rennes for providing data and code and ESA for providing data and

organising the ESA 4th advanced course on radar polarimetry. I am grateful to Prof. Jingfa Zhang, Dr Qisong Jiao and Dr Hongbo Jiang from the Institute of Crustal Dynamics, China Earthquake Administration for 2017 fieldwork and collaborations. Moreover, I am grateful to Amy from the University of Colorado and National Snow and Ice Data Center of USA for providing ICESat data and code. I also gratefully acknowledge Dr Randolph Kirk, Elpitha Howington-Kraus from USGS for providing DEM code.

Special mention and thanks must go to Prof. Shiyuan Hu, Prof. Miaozhong Xu, Prof. Haigang Sui and Prof. Kaiming Sun, my former supervisors at Wuhan University, for arousing my initial interest and guiding me into the space photogrammetry, remote sensing and GIS field back in 2005. I also would like to thank my former boss Prof. Yingcheng Li at the Chinese Academy of Surveying and Mapping for constant encouragement and generous support in my life and work from 2009 to 2014.

There are too many people at the MSSL, UCL that I would like to say thanks to. Edward Malina, thank you for being there whenever I need your advice, help and everyday lift to MSSL during the second year of my PhD. Jason Hunt, thank you for the kindest help provided during the second year of my PhD too. I am grateful to Denis Gonzalez Caniulef, Ravindra Desai, Zakari Tsiga, Jennifer Y H Chan and Georgina Graham for their friendship, support, help and enjoyable time at Ariel House MSSL the first year when I am in the UK. Moreover, I also like to thank our group members Panagiotis Sidiropoulos, Yu Tao, Said Kharbouche, Edward Malina, Alistair Francis and Divya Persaud, Siting Xiong, Alfiah Rizky Diana Putri, Jacqueline Campbell, George Cann, Daoxi Zhang, Luyi Sun, Josh Veitch-Michaelis, Wil Poole for their help, support, useful discussion and all the good times at MSSL in the last 4 years. I am additionally grateful to Edward Malina, Alistair Francis and Divya Persaud for their time spending on proofreading of several chapters of this thesis. I also like to thank Rosalind Medland, Libby Daghorn, Julia Wehrle, Suzanne Winter, Samantha Babister, Jane Salton, Philippa Elwell, Martin de la Nougerede, Craig Theobald, Roger Woodliffe, Paul Prior, Paul Lamb and all people of MSSL management team, general office, computer group and other research groups for their support and help at the MSSL.

Finally, I reserve my most heartfelt appreciation and thanks to my family. I am grateful to my parents and my sister for supporting my seemingly endless education and sharing in my struggles and successes.

# Table of Contents

<b>Title</b> .....	1
<b>Author Declaration</b> .....	3
<b>Abstract</b> .....	5
<b>Impact Statement</b> .....	7
<b>Acknowledgements</b> .....	9
<b>Table of Contents</b> .....	11
<b>List of Figures</b> .....	15
<b>List of Tables</b> .....	21
<b>List of Acronyms</b> .....	23
<b>List of Symbols</b> .....	27
<b>1 Introduction</b> .....	31
1.1 Thesis Introduction and Motivation .....	31
1.2 Thesis Aims, Research Questions and Objectives .....	35
1.3 Thesis Structure .....	37
<b>2 Literature Review</b> .....	39
2.1. Review of TomoSAR.....	39
2.1.1. Background .....	39
2.1.2. TomoSAR and D-TomoSAR Research Progress.....	44
2.1.3. TomoSAR Application .....	48
2.2. Digital Elevation Model (DEM) .....	55
2.2.1. DEM Acquisition Methods .....	56
2.2.2. DEM Products of Earth and Other Planets (Including the Moon) ..	56
2.2.3. DEM Accuracy Standard and Quality Assessment Method .....	59
2.3. DEM Generation from InSAR.....	70
2.3.1. Introduction and Background.....	70
2.3.2. Radar Equation.....	75
2.3.3. Synthetic Aperture Radar (SAR) .....	76
2.3.4. InSAR History and Current Research .....	77
2.3.5. InSAR Principles.....	77
2.3.6. InSAR for DEM Key Processing Technology .....	79
2.4. DEM Generation from Photogrammetry and Radargrammetry .....	85

2.4.1.	Photogrammetry for DEM .....	85
2.4.2.	DEM Generation from Radargrammetry .....	93
2.5.	LIDAR and Radar Altimeters (CryoSat-2) for DEMs.....	95
2.6.	Review of DEM for TomoSAR.....	96
2.7.	Review of Atmospheric and Ionospheric Correction .....	97
2.7.1.	Atmospheric and Ionospheric Correction .....	97
2.7.2.	Ionospheric Correction.....	101
2.8.	Summary.....	107
3	DEM Generation and DEM Quality Assessment .....	109
3.1	DEM Generation .....	109
3.1.1	DEM Generation from TanDEM-X.....	109
3.1.2	Reference Bluesky DTM Generation.....	111
3.2	Quality Assessment of TanDEM-X IDEM & Tandem-X DEM.....	112
3.2.1	Introduction.....	113
3.2.2	Test Area and Metadata Information .....	115
3.2.3	Absolute Accuracy Validation Method by KGPS .....	119
3.2.4	Absolute Vertical Accuracy Validation Method by ICESat .....	124
3.2.5	Vertical Comparison Accuracy Method .....	129
3.2.6	Experimental Results .....	137
3.2.7	Analysis and Discussion .....	154
3.2.8	Conclusions.....	162
3.3	DEM Quality Assessment and Improvement for TomoSAR.....	164
3.3.1	TanDEM-X 12 m DEM Data over Zipingpu Dam .....	164
3.3.2	TanDEM-X 12 m DEM Data Quality Assessment and Editing ....	165
3.4	Overall Conclusions .....	168
4	The Atmospheric and Ionospheric Correction Algorithm for TomoSAR ..	171
4.1	Atmospheric Correction .....	172
4.1.1	PS and ERA-I Model for Absolute Atmospheric Phase .....	173
4.1.2	GACOS for Absolute Atmospheric Phase .....	175
4.2	Ionospheric Correction Algorithm .....	176
4.2.1	Introduction and Basic Parameters .....	176
4.2.2	Split Spectrum.....	179
4.2.3	IGS TEC and International Reference Ionospheric Model.....	193
4.2.4	The Method for TEC Retrieval .....	195



4.2.5	Experiment, Results and Validation of the TEC Method .....	199
4.3	Conclusions .....	206
5	TomoSAR and Differential TomoSAR Algorithms .....	207
5.1	The Principles of SAR Tomography .....	208
5.1.1	SAR Tomography Three-dimensional Imaging Principle .....	208
5.1.2	SAR Tomography Workflow .....	219
5.2	SAR Differential Tomography Imaging Principle .....	223
5.2.1	SAR Differential Tomography Imaging Principle .....	224
5.2.2	SAR Differential Tomographic Imaging Process Workflow .....	225
5.3	SAR Tomographic Phase Error Compensation .....	228
5.3.1	Tomographic Phase Error Compensation based on PS-InSAR .....	228
5.3.2	The PGA Phase Error Compensation Algorithm .....	231
5.3.3	Combined Phase Error Compensation Algorithm .....	233
5.3.4	SAR Interferometry Phase Calibration with Dem Errors .....	238
5.4	SAR Tomography Three-dimensional High-resolution Imaging .....	241
5.4.1	Sparse Aperture for 3D Imaging .....	241
5.4.2	Basic Theory of Compressive Sensing .....	244
5.4.3	An Improved Compressive Sensing Method .....	249
5.5	SAR Differential Tomography 4D Imaging .....	251
5.5.1	D-TomoSAR Phase Error Compensation based on PS-InSAR .....	251
5.5.2	D-TomoSAR Imaging based on Compressive Sensing .....	255
5.6	Conclusions .....	257
6	Application of TomoSAR to X-band .....	259
6.1	Test Sites and COSMO-SkyMed Spaceborne SAR .....	260
6.2	Co-registration .....	265
6.3	Pixel-by-pixel Baseline estimation .....	270
6.4	Deramping Results .....	280
6.5	Phase Calibration .....	282
6.5.1	Atmospheric Correction and TomoSAR Results .....	282
6.5.2	DEM Error Estimation for Phase Compensation .....	285
6.5.3	PS-SVD-PGA-LS-ME Phase Calibration .....	288
6.6	Phase Calibration Results .....	289
6.6.1	DEM Error Compensation and Atmospheric Calibration .....	289
6.6.2	DEM Error, Atmospheric and PS-SVD-PGA-LS-ME Calibration .....	290
6.6.3	SAR Interferometry Phase Calibration Reference to DEM .....	291

6.7	TomoSAR Imaging Results.....	293
6.7.1	Compressive Sensing (CS).....	293
6.7.2	TomoSAR Results.....	301
6.7.3	Fieldwork in Zipingpu Dam for TomoSAR Result Validation.....	303
6.7.4	Discussion .....	306
6.8	D-TomoSAR based on Compressive Sensing Results .....	308
6.9	Discussion on Limitations and Advantages of X-band .....	312
6.10	Conclusions.....	313
7	Conclusions.....	315
7.1	Thesis Overview .....	315
7.1.1	DEM Validation .....	316
7.1.2	Atmospheric and Ionospheric Correction Algorithm.....	318
7.1.3	Orbit Baseline Estimation for 3D & 4D TomoSAR Imaging.....	319
7.1.4	TomoSAR and D-TomoSAR Algorithm and Experiments .....	320
7.2	Contributions.....	321
7.3	Publications .....	323
7.3.1	Peer Review Publications.....	323
7.3.2	Conference Publications & Presentations .....	324
7.3.3	Conference Posters.....	324
7.4	Future Work .....	325
	<b>Appendices.....</b>	<b>327</b>
	<b>A. KGPS tables.....</b>	<b>327</b>
	<b>B. Tables of the accuracy of DEM products .....</b>	<b>331</b>
	<b>C. The Global TEC map from IGS .....</b>	<b>339</b>
	<b>D. The original and new interpolated orbits.....</b>	<b>341</b>
	<b>E. The Application of TOMOSAR to ALOS L Band over San Francisco</b>	<b>345</b>
	<b>References .....</b>	<b>365</b>

# List of Figures

Figure 2.1 Global SAR research progress.....	43
Figure 2.2 TomoSAR, PolSAR, and PolInSAR principle.....	43
Figure 2.3 Radar penetration depth of pure ice (Gay and Ferro-Famil, 2016) .....	54
Figure 2.4 The lunar maps of the north (top) and south (bottom) pole.....	54
Figure 2.5 The reflectance of hydroxyl (OH) molecules .....	55
Figure 2.6 DSM and DTM.....	55
Figure 2.7 Canopy penetration varies with different wavelengths .....	57
Figure 2.8 Relative vertical accuracy (Maune 2007) .....	64
Figure 2.9 Airy 1830 ellipsoid and ODN height .....	65
Figure 2.10 Illustration of the Ordnance Survey National Grid.....	66
Figure 2.11 ODN datum distribution .....	67
Figure 2.12 Coordinate system conversion methods relationship .....	67
Figure 2.13 OSGM02/OSTN02 .....	67
Figure 2.14 Remote sensing image matching algorithms .....	68
Figure 2.15 The image matching principle .....	70
Figure 2.16 Electromagnetic spectrum and waves.....	72
Figure 2.17 Microwave bands in the electromagnetic spectrum .....	72
Figure 2.18 Atmospheric transmittance of the Earth to various wavelengths.....	73
Figure 2.19 C-band scattering path delay due to forward scattering in the rain .....	75
Figure 2.20 Radar equation principal.....	76
Figure 2.21 Flat Earth SAR imaging geometry .....	77
Figure 2.22 Typical geometry of InSAR (Bamler and Hartl, 1998) .....	78
Figure 2.23 The flowchart of DEM production by using InSAR .....	79
Figure 2.24 Simplified SAR processing chain. ....	80
Figure 2.25 SAR GEI coordinate system (Liu et al., 2006).....	82
Figure 2.26 Stereo and tri-stereo comparison .....	86
Figure 2.27 Optical satellite imaging geometry model (Wang, 2006).....	91
Figure 2.28 The 3D information extraction workflow from stereo imagery .....	93
Figure 2.29 Solar wind and Earth's magnetosphere.....	102

Figure 2.30 The Earth's upper atmosphere.....	102
Figure 2.31 Earth's atmosphere and ionosphere plasma density (Kelley, 2009)...	104
Figure 2.32 The composition of the Earth's atmosphere varies with altitude .....	105
Figure 2.33 The conceptual illustration showing the E-layer and F-layer.....	107
Figure 3.1 TanDEM-X DEM processing workflow.....	111
Figure 3.2 Study area (© Google 2015).....	115
Figure 3.3 DEM, ICESat and KGPS datasets used in the analysis.....	119
Figure 3.4 DEM matching windows .....	123
Figure 3.5 ICESat coordinate system and ICESat waveform .....	125
Figure 3.6 ICESat data footprints of the filtered results .....	128
Figure 3.7 The TanDEM-X IDEM statistical validation processing workflow ....	129
Figure 3.8 Vertical comparison accuracy assessment flowchart.....	130
Figure 3.9 OSGB1936 Airy 1830 ellipsoid and ODN height .....	131
Figure 3.10 Final DEM co-registration flowchart .....	133
Figure 3.11 Refine registration by using ICP.....	134
Figure 3.12 Co-registration results of IDEM 30 m.....	136
Figure 3.13 Correlation and histogram .....	140
Figure 3.14 Correlation and histogram .....	141
Figure 3.15 Correlation and histogram .....	142
Figure 3.16 Correlation and histogram .....	143
Figure 3.17 Correlation and histogram .....	144
Figure 3.18 Correlation and histogram .....	145
Figure 3.19 Correlation and histogram .....	146
Figure 3.20 Elevation residuals.....	158
Figure 3.21 RMSE of DEM data compared to GPS and Bluesky DTM .....	160
Figure 3.22 Standard deviation of the DEM height differences .....	162
Figure 3.23 Standard deviation of the DEM height differences .....	162
Figure 3.24 Location of the 12 m TanDEM-X DEM data .....	165
Figure 3.25 TanDEM-X 12 m DEM map .....	165
Figure 3.26 Elevation residuals.....	167
Figure 3.27 TanDEM-X 12 m DEM data after hole replacement.....	168
Figure 3.28 TanDEM-X 12 m DEM data after hole replacement.....	168
Figure 4.1 PS points in the test area.....	174
Figure 4.2 ERA-I model atmosphere total phase .....	174

Figure 4.3 ZTD of 20160603 .....	175
Figure 4.4 ZTD of 20160725 (the date of the master image, unit: metre) .....	175
Figure 4.5 Split range spectrum (Gomba et al., 2016) .....	180
Figure 4.6 Two test area in Tocopilla, Chile .....	182
Figure 4.7 The merged ALOS-1 SAR data .....	183
Figure 4.8 Ionosphere correction by the split spectrum method of test 1 .....	185
Figure 4.9 Ionosphere correction by the split spectrum method of test 1 .....	187
Figure 4.10 Ionosphere correction by the split spectrum method of test 2 .....	189
Figure 4.11 Ionosphere correction by the split spectrum method of test 2 .....	191
Figure 4.12 C-band InSAR result .....	192
Figure 4.13 IRI Electron density (Ne) map at (31N, 103.55E) on 2016-7-25 .....	194
Figure 4.14 Zoom in IRI Electron density (Ne) map at (31N, 103.55E) .....	194
Figure 4.15 IRI Electron density (Ne) hour map .....	195
Figure 4.16 The flowchart of the TEC method .....	197
Figure 4.17 The global TEC map of the closest time of the ALOS SAR .....	200
Figure 4.18 The TEC map of the closest time of ALOS SAR measure time .....	200
Figure 4.19 The small test area SAR image in San Francisco Bay, USA .....	201
Figure 4.20 The split-spectrum differential TEC result map of the ALOS SAR ..	202
Figure 4.21 High resolution (200 m) TEC map on 2009/02/01 .....	203
Figure 4.22 Electron density and IRI TEC map .....	204
Figure 4.23 The differential TEC map (High resolution TEC map - IRI TEC) ....	205
Figure 5.1 2D resolution element of a conventional SAR. ....	209
Figure 5.2 TomoSAR imaging geometry .....	210
Figure 5.3 3D resolution element of a tomographic SAR .....	210
Figure 5.4 Three-dimensional imaging .....	211
Figure 5.5 Multiple flights of a single radar system for SAR tomography .....	214
Figure 5.6 The geometric relationship between the master and slave image .....	216
Figure 5.7 SAR tomography workflow .....	219
Figure 5.8 The relationship of oblique slant point .....	220
Figure 5.9 SAR differential tomographic imaging process workflow .....	226
Figure 5.10 Synthetic aperture forms in SAR differential tomography .....	227
Figure 5.11 Compressed sensing of the measurement process .....	246
Figure 6.1 The test site in Sichuan China .....	262
Figure 6.2 A small test subarea at Zipingpu dam in Dujiangyan .....	262

Figure 6.3 The position and information of Test-A area .....	265
Figure 6.4 The DEM simulated radar image.....	267
Figure 6.5 Master image (20160725).....	267
Figure 6.6 The slave image (20160603) before co-registration.....	268
Figure 6.7 The slave image (20160603) after co-registration.....	268
Figure 6.8 The interferogram between 20160810 and master 20160725 SLC .....	269
Figure 6.9 The zoom-in map of the interferogram.....	269
Figure 6.10 Typical geometry of InSAR and the baseline .....	271
Figure 6.11 Pixel-by-pixel baselines estimation .....	271
Figure 6.12 The original and interpolated time in each pixel .....	274
Figure 6.13 The interpolated orbits.....	275
Figure 6.14 Perpendicular baseline estimation .....	277
Figure 6.15 Parallel baseline estimation .....	278
Figure 6.16 BioSAR 2008 L band data tomograms via the Capon method.....	280
Figure 6.17 Tomograms results via FFT and Capon in Test-A.....	282
Figure 6.18 PS point for phase calibration.....	283
Figure 6.19 Comparison between the ERA and GACOS .....	284
Figure 6.20 FFT and CAPON results.....	285
Figure 6.21 DEM error maps in the dam area.....	288
Figure 6.22 FFT and Capon results.....	290
Figure 6.23 FFT and Capon results.....	291
Figure 6.24 FFT and Capon results.....	292
Figure 6.25 Acquisition geometry of the simulation.....	294
Figure 6.26 Topography and targets in the ground coordinate system .....	295
Figure 6.27 The position of the SAR sensors of the 14 measurements .....	295
Figure 6.28 The SAR measurement signal with random noise.....	296
Figure 6.29 The SAR measurement signal with added white Gaussian noise.....	297
Figure 6.30 TomoSAR results of Test-A.....	298
Figure 6.31 Tomograms via CS in Test-A.....	299
Figure 6.32 Tomograms via CS .....	299
Figure 6.33 Tomograms via CS in Test-A after error elimination .....	300
Figure 6.34 CS results in Test-A referenced to DEM elevation.....	301
Figure 6.35 TomoSAR results of the sub-test area at Zipingpu dam .....	302
Figure 6.36 Fieldwork at Zipingpu dam in Duijiangyan Sichuan China .....	304

Figure 6.37 Difference map .....	305
Figure 6.38 TomoSAR results shown in Google Earth.....	306
Figure 6.39 D-TomoSAR results in the sub-test area of Figure 6.2.....	309
Figure 6.40 Mean velocity map of PS points.....	310
Figure 6.41 D-TomoSAR results at the position of the PS points .....	311
Figure 6.42 D-TomoSAR velocity results validation.....	312
 Figure C. 1 The global TEC map of the closest time of the ALOS SAR.....	 340
 Figure E. 1 The small test area in San Francisco Bay, USA.....	 347
Figure E. 2 The position and information of Test-A area.....	348
Figure E. 3 The position and information of Test-B area.....	349
Figure E. 4 Ionospheric correction via split spectrum .....	351
Figure E. 5 TomoSAR results via FFT in Test-A area .....	352
Figure E. 6 TomoSAR results via Capon in Test-A area.....	353
Figure E. 7 TomoSAR results via FFT in Test-A area .....	355
Figure E. 8 TomoSAR results via Capon in Test-A area.....	355
Figure E. 9 TomoSAR results referenced to SRTM via FFT in Test-A area.....	357
Figure E. 10 TomoSAR results via FFT in Test-B area .....	358
Figure E. 11 TomoSAR results referenced to SRTM via FFT in Test-A area.....	359
Figure E. 12 TomoSAR results via Capon in Test-B area.....	360
Figure E. 13 TomoSAR results via CS in Test-A and Test-B area .....	361
Figure E. 14 The height, depth, and length of the Golden gate bridge .....	363

This page is intentionally left blank.



## List of Tables

Table 2.1 Classification of time series InSAR methods (Hanssen, 2001) .....	41
Table 2.2 SAR data application in the disaster field .....	50
Table 2.3 Horizontal elevation accuracy comparison (Maune, 2007) .....	62
Table 2.4 Vertical elevation accuracy comparison .....	63
Table 2.5 Typical microwave wavelength and frequency (Collin, 2007) .....	73
Table 2.6 Current satellite SAR sensor (CRCSI, 2015; Rincon et al., 2019).....	74
Table 2.7 Optical mapping satellites all over the world.....	87
Table 2.8 American geolocation standard in satellite mapping (Wang, 2006).....	90
Table 2.9 Comparisons of InSAR atmospheric correction methods .....	100
Table 3.1 Experiment DEM input datasets .....	115
Table 3.2 Window size test statistics.....	123
Table 3.3 The internal quality flags of ICESat GLAH14 data .....	126
Table 3.4 Accuracy parameters for the TanDEM-X IDEM validation .....	128
Table 3.5 WGS84 to Osgb36 Helmert transformation.....	131
Table 3.6 Difference statistics based on matchups of KGPS and Bluesky .....	147
Table 3.7 The accuracy of the EO DEM products over the UK (against KGPS) .	148
Table 3.8 Height difference statistics over the UK .....	149
Table 3.9 Height difference statistics over the UK against the ICESat GLAS14.	149
Table 3.10 The accuracy of the DEM products of the UK.....	150
Table 3.11 Height differences of the 12 m DEM data.....	152
Table 3.12 Height differences of 30 m DEM data .....	152
Table 3.13 Height differences of 90 m DEM data .....	153
Table 3.14 The accuracy of the EO DEM products over the UK.....	154
Table 3.15 12 m DEM data height differences before and after co-registration...	167
Table 3.16 Difference statistics of 12 m DEM in Dujiangyan against ICESat .....	167
Table 4.1 Estimated ionospheric effects for one-way radio traversal .....	177
Table 4.2 The two TEC value of the closest time of ALOS SAR measure time...	200
Table 5.1 Summary of the spectral estimation methods .....	243

Table 6.1 Ascending COSMO-SkyMed spotlight data stacks .....	263
Table 6.2 Simulation parameters.....	294
Table 6.3 Ascending COSMO-SkyMed spotlight data stacks .....	305
Table A. 1 12 m DEM difference statistics based on KGPS .....	327
Table A. 2 Difference statistics based on KGPS and Bluesky matching .....	328
Table A. 3 Difference statistics based on KGPS and Bluesky matching .....	328
Table A. 4 Difference statistics based on KGPS and Bluesky matching .....	329
Table A. 5 Difference statistics based on KGPS and Bluesky matching .....	329
Table A. 6 Difference statistics based on KGPS and Bluesky matching .....	330
Table A. 7 Difference statistics based on KGPS and Bluesky matching .....	330
Table B. 1 DEM products (12 m) control point data RMSE statistics in England	331
Table B. 2 DEM products (12 m) accuracy (90% means 1.6* RMSE) .....	331
Table B. 3 DEM products (12 m) RMSE statistics in Scotland.....	332
Table B. 4 DEM products (12 m) accuracy (90% means 1.6* RMSE) .....	332
Table B. 5 DEM products (30 m) RMSE statistics in WALES and England.....	332
Table B. 6 DEM products (30 m) accuracy (90% means 1.6* RMSE) .....	333
Table B. 7 DEM products (30 m) RMSE statistics in Scotland.....	333
Table B. 8 DEM products (30 m) accuracy (90% means 1.6* RMSE) .....	333
Table B. 9 DEM products (30 m) RMSE statistics in UK .....	334
Table B. 10 DEM products (30 m) accuracy (90% means 1.6* RMSE) in UK....	335
Table B. 11 DEM products (90 m) RMSE statistics in WALES and England.....	335
Table B. 12 DEM products (90 m) accuracy (90% means 1.6* RMSE) .....	336
Table B. 13 DEM products (90 m) RMSE statistics in Scotland.....	336
Table B. 14 DEM products (90 m) accuracy (90% means 1.6* RMSE) .....	336
Table B. 15 DEM products (90 m) RMSE statistics in UK .....	337
Table B. 16 DEM products (90 m) accuracy (90% means 1.6* RMSE) in UK....	338
Table D. 1 The original orbit information based on time.....	341
Table D. 2 The new interpolated orbits based on time.....	342
Table E. 1 ALOS data metadata .....	346
Table E. 2 Characteristics of ALOS PALSAR sensor .....	350

# List of Acronyms

3D	3 Dimension x, y, z
4D	4 Dimension x, y, z and time
ALMA	Atacama Large Millimeter/submillimeter Array
ASTER	Advanced Spaceborne Thermal Emission and Reflection Radiometer
BA	Bundle Adjustment
BF	Beamforming
CMB	Cosmic Microwave Background
CT	Coherence Target/Coherence point Target
DEM	Digital Elevation Model
Diff-PolTomoSAR	Polarimetric Differential-TomoSAR
Diff-TomoSAR	Differential-TomoSAR
D-InSAR	Interferometric Synthetic Aperture Radar
DLR	The German Aerospace Centre (German: Deutsches Zentrum für Luft- und Raumfahrt e.V.), abbreviated DLR
DORIS	Doppler Orbitography and Radiopositioning Integrated by Satellite
DSM	Digital Surface Model
DTM	Digital Terrain Model
D-TomoSAR	Differential-TomoSAR
E-M	Electromagnetic
EMR	Electromagnetic radiation
ESA	European Space Agency
ESE	Environmental Science and Engineering
ETRF	European Terrestrial Reference Frame
ETRF	European Terrestrial Reference Frame
FAST	The Five-hundred-metre Aperture Spherical Radio Telescope
FFT	Fast Fourier Transform

FPGA	Field-Programmable Gate Array
GMTED2010	Global Multi-resolution Terrain Elevation Data 2010
GNSS	Global Navigation Satellite System
GPS	Global Positioning System
GsTL	Geostatistics Template Library
HRTI/DTED	High Resolution Terrain Information/Digital Terrain Elevation Data
IC	Integrated Circuit
InSAR	Interferometric Synthetic Aperture Radar
ISAR	Inverse Synthetic Aperture Radar
ITRF	International Terrestrial Reference Frame
ITRF	International Terrestrial Reference Frame
KGPS	Kinematic GPS
KML	Keyhole Markup Language
LAS	LIDAR Standard Data Format
LLR	Lunar Laser Ranging
LLR	Lunar Laser Ranging
LOFAR	Low Frequency Array
LOLA	Lunar Orbiter Laser Altimeter
LPC	LIDAR Point Cloud
LS	Least Squares
LUMV	Linear Unbiased Minimum-Variance
MAI	Multi aperture Interferometric Synthetic Aperture Radar
ME	Minimum Entropy
MEGDR	The Mission Experiment Gridded Data Record
MLE	Maximum Likelihood Estimation
MMIC	Monolithic Microwave Integrated Circuit
M-RELAX	Multilook Relax algorithm
MSSL	Mullard Space Science Laboratory
MTI	Multi-time Interferometric Synthetic Aperture Radar (MTI, e.g. StaMPS/MTI)
MUSIC	Multiple Signal Classification
NASA	The National Aeronautics and Space Administration

NLS	Nonlinear Least Squares
NMAS	National Map Accuracy Standards
NSR	Normal-Slant-Range direction (NSR direction)
NSSDA	National Standard for Spatial Data Accuracy
OSGM02	Ordnance Survey Geoid model
OSTN02	The Ordnance Survey National Grid Transformation
PGA	Phase gradient autofocus
PolInSAR	Polarimetric Synthetic Aperture Radar Interferometry
PolSAR	Polarimetric Synthetic Aperture Radar
Pol-TomoSAR	Polarimetric-TomoSAR
PS	Persistent Scatterer
PSI	Persistent Scatterer InSAR
QI	Quality Insurance
RD	Range Doppler
RFM	Rational Function Model
RPC	Rational Polynomial Coefficients
SAR	Synthetic Aperture Radar
SBAS	Small Baseline Subset algorithm
SGM	Semi-Global Matching
SKA	Square Kilometre Array
SLC	Single Look Complex
SLR	Satellite Laser Ranging
SVD	Singular value decomposition
TCP	Temporal Coherence Point
TEC	Vertical Total Electron Content
TECU	Total Electron Content Unit
THZ	Terahertz
TIN	Triangular Irregular Network
TomoSAR	Tomography Synthetic Aperture Radar or SAR tomography
USGS	The United States Geological Survey
USGS	United States Geological Survey
UTM	Universal Transverse Mercator
VLBI	Very Long Baseline Interferometry

VTEC	VTEC Vertical Total Electron Content
WGS84	World Geodetic System 1984
ZHD	ZHD Zenith Hydrostatic Delay
ZPDDM	Zenith-Path-Delay Difference Map
ZTD	ZTD Zenith Total Delay
ZWD	ZWD Zenith Wet Delay

# List of Symbols

$\emptyset_{simu\_m}$	simulation phase
$\Delta b_{\perp}$	the vertical baseline sampling interval
$\varepsilon_0$	free space permittivity
$g_m$	the average tropospheric gravitational acceleration
$A_r$	the effective area of the receive antenna
$B_{\parallel}$	the parallel baseline
$B_{\perp}$	the perpendicular baseline
$G_t$	transmit antenna gain
$P_r$	received signal power
$P_t$	peak transmit power
$f_0$	centre frequency
$f_{dr}$	azimuth FM rate
$k_2$	TEC second derivative with time
$\Delta_G$	the correction value of tile points coordinates
$\Delta_O$	the correction value of orientation parameters
$\Phi_K$	the phase of the special pixel (PS point)
$\theta_B$	the direction of propagation of the wave and the angle of the earth's magnetic field.
$\mu_0$	vacuum permeability
$\xi_m$	wave number
$\rho_r$	range resolution
$\rho_s$	elevation resolution
$\rho_x$	azimuth resolution
$\sigma_c^2$	variance of the clutter noise
$\sigma_{zK}^2$	the variance of the difference of modulation phase caused by clutter in the kth significant cell point
$\tau_{ref}$	reference delay
$\varphi_{atmo}$	the phase error caused by atmospheric disturbance
$\varphi_{defo}$	the phase error caused by the terrain deformation

$\varphi_e$	phase error
$\omega_s$	the angular frequency of the elevation direction
$\omega_x$	the angular frequency of the azimuth direction
$\omega_y$	the angular frequency of the range direction
$\phi_{nonl}$	the phase of nonlinear deformation
$\phi_{tropo}$	the tropospheric phase delay
$\otimes$	the Kronecker symbol
$\emptyset$	phase
$\mu m$	micrometre, electromagnetic spectrum wavelength unit
$e$	electronic power
$\mathbf{g}(m)$	the $m^{\text{th}}$ data after deramping of SLC image
$h$	the height of SAR above a reference plane
$\Delta b$	the elevation aperture size
$\Phi$	the measurement matrix.
$\Psi$	the matrix composed of many basis functions
$B$	baseline vector
$Q(m)$	the $m^{\text{th}}$ SLC image
$R$	radar to object range
$T$	temperature
$W$	the bandwidth of the chirp
$c$	light speed
$dp$	disparity distance
$e$	the water vapour pressure
$exp$	exponential function
$f$	frequency
$m$	electronic mass
$r$	range direction
$s$	elevation or cross range
$\nu$	electronic effective collision frequency
$\nu(s)$	the deformation rate of LOS
$x$	azimuth direction
$z$	topography elevation



$\Delta\Phi_K$	the differential phase of the special pixel (PS point)
$\Delta\varphi$	differential phase
$\theta$	the sensing matrix (or compressive sensing information operator)
$\alpha$	baseline angle
$\gamma(s)$	complex scattering coefficient
$\delta\rho$	range difference
$\theta$	look angle
$\lambda$	wavelength
$\rho$	antenna efficiency
$\sigma$	target radar cross-section
$\omega$	free space wave frequency

This page is intentionally left blank.

# Chapter 1

## Introduction

### 1.1 Thesis Introduction and Motivation

As is well known, if there is a changing electric field anywhere in space, it will excite a magnetic field around it; likewise, a changing magnetic field can also excite an electric field in its surrounding space. This electric field energy and magnetic field energy continue to interact with each other to form an alternating electromagnetic (E-M) field changing over time. These E-M fields propagate in space in the form of wave fluctuations, which are called electromagnetic waves. In the 1860s, Maxwell studied these electromagnetic fields and wave theories and created the famous Maxwell's equations based on previous research by many scientists (Maxwell, 1861; Maxwell, 1864; Maxwell, 1873). Based on these theories, the phenomenon that electromagnetic waves are synchronised oscillations of electric and magnetic fields that propagate with a different speed through vacuum and media is called electromagnetic radiation (EMR) (Simpson, 1997). This electromagnetic radiation is photon-based waves of the electromagnetic field, propagating (radiating) through the time and space domain, carrying electromagnetic energy. According to the range and scope of frequencies (wavelengths) of electromagnetic radiation and their photon energies, scientists have constructed an electromagnetic spectrum theory, which includes gamma rays, X-rays, ultraviolet, visible light, infrared, microwaves and radio waves (Purcell and Morin, 2013; Fornaro and Serafino, 2004).

## Chapter 1. Introduction

With advances in materials science, energy science, mechanical manufacturing, automatic control engineering, artificial intelligence, machine (deep) learning, electronics industry and technology development, the radio, microwave and radar (radio detection and ranging) techniques were studied and developed by several nations all over the world, and these techniques can be used in astrogeodesy, planetary observation, earth observation and military and civilian applications. Nowadays, radio astronomy and radar (radio detection and ranging) science studies are currently two of the important research areas for helping human beings explore and detect possible organics and life in our solar system, galaxy and Universe, which may also help humankind to achieve and succeed in Earth-like exoplanet search, planetary landing, planetary sample return, planetary resource extraction, interstellar space city construction, space travel and tourism, interplanetary infrastructure construction, planetary and eventually interstellar migration.

The research in radio astronomy provide us infinite opportunities to access the largest scales of the sky to test general relativity (Rovelli, 2017), the physics of inflation (Borde et al., 2003; Komatsu and Spergel, 2002) and fundamental assumptions about the isotropy of the Universe (Thorne, 1967), map dark matter and hunt for dark energy (Newburgh et al., 2016); moreover, it can generate the fully three-dimensional maps of our Universe (Newburgh et al., 2016) and exhibit the galaxy formation processes across cosmic time (Smolcic et al., 2015; De Zotti et al., 2018), which nowadays has identified a number of different sources of radio emission (Kraus et al., 1986; Torson, 1980) including stars, galaxies and entirely new classes of objects (pulsars, quasars, masers, radio galaxies, microwave background radiation, the Sun, the solar activity, and so on) (Kraus et al., 1986; Martin and Irvine, 1983; Thompson et al., 1986; Kellermann et al., 2004; Greisen, 2003; Kramer et al., 2006; Torson, 1980). Many radio astronomy facilities have been built all over the world, like many countries' very long baseline interferometry (VLBI) space and deep space network, ALMA, LOFAR, SKA, Chinese FAST, and so on (Sutinjo et al., 2017; Kelley and Quinn, 2017; Chengalur, 2017; Wild, 2017; Kraus, 1966; Kundu, 1965; Rohlfs and Wilson, 2013).

Research in radar astronomy now is also very popular in astronomy, Earth and planets observation, as well as their satellites (moons), even asteroids and comets. COBE (1989), WMAP (2001) and Planck (2009) spacecraft have been launched by NASA and ESA to map the cosmic microwave background (CMB) at microwave frequencies, which utilises a radiometer. The ESA Herschel spacecraft (55-671  $\mu\text{m}$ ) was launched on 2009 by ESA to observe (active between 2009-2013) the cool, dusty and distant Universe,

while APEX for submillimetre astronomy was built in Chile's Atacama high desert region to perform a similar job based on earth. Actually, planetary radar astronomy observations have primarily used the Earth-based radar telescopes, but lately, it utilises the spaceborne transmitter or receiver in satellites (Ostro, 1993). Planetary radars, which is sensitive to ice or metal, can penetrate clouds and cometary comae to explore the near-surface planetary structure, roughness, dielectric properties, scattering characteristics and density (Ostro, 1993). Up to now, planetary radar astronomy experiments not only have provided a huge amount of important knowledge on the dynamical and geological characteristics of inner planets, their moons (natural satellites), comets and asteroids, but they also have helped to establish the scale of the solar system, have contributed to precise planetary ephemerides and gravitation theories significantly (Ostro, 1993). Many radar satellites have also been or are about to be launched, such as Magellan (1994) radar for Venus, Cassini (1997) RADAR instrument for Saturn and its satellites (moons), Mars Reconnaissance Orbiter (2005) Shallow Radar (SHARAD) sounder and Mars Express (2005) Mars Advanced Radar for Subsurface and Ionosphere Sounding (MARSIS) for Mars, Lunar Reconnaissance Orbiter (LRO 2009) Miniature Radio Frequency (Mini-RF) for the Earth's moon (Carter et al., 2017; Patterson et al., 2017; Mitchell et al., 2017) and in the near future the JUICE mission (RIME-Radar for Icy Moons Exploration, SWI - Sub-millimetre Wave Instrument, RPWI-Radio & Plasma Wave Investigation, 3GM radio science package-Gravity & Geophysics of Jupiter and Galilean Moons) for Jupiter and its satellites (moons) (Titov et al., 2014). The Magellan multimode S-band radar had three modes: SAR, altimetry, and passive radiometry to map almost all the Venusian surface, while the Cassini RADAR instrument transmits and receives Ku-band signal, which has four modes: passive radiometry, altimetry, SAR imaging, and scatterometry (Evans and Hagfors, 1968; Ostro et al., 2002; Hagfors and Evans, 1968; Bondarenko et al., 2017; Verma et al., 2017; Madanayake et al., 2017; Torson, 1980). Besides, the lunar penetrating radar in Chinese Chang'E-3 lander was used in the Chinese lunar exploration mission (Yuan et al., 2017). What is more, the Arecibo Planetary Radar and the Goldstone Solar System Radar are also in regular use for planetary research (Lawrence et al., 2018).

Nowadays, based on MMIC, IC, FPGA and antenna techniques, there are a lot of radar systems, including continuous wave radars, mono-pulse radars, edge-sweep tracking radars, pulsed Doppler radars, phased array radars, digital array radars, pulse compression radars, space-based surveillance radars, synthetic aperture radars (SAR), bistatic radars, ultra-wideband radars, millimetre-wave radars, THZ radars, and so on,

## Chapter 1. Introduction

which are applied to applications such as mobile phones, gesture sensing control applications, space exploration, automated cars, railway, UAV, aircraft, commercial plane landing, ship, submarine, robotics, smart city, smart home and all kinds of civilian and military applications. Besides, satellite radar technology is developing very fast for radio communications, satellite communications, weather forecasting, broadcasting, observation, mapping, and so on. Meanwhile, in various domains, geodetic space technology, which uses radar techniques, like global navigation satellite system (GNSS: GPS, Chinese Beidou, GLONASS and Galileo), VLBI, DORIS, are also very crucial for spacecraft telemetry, spacecraft remote control, satellite communication and satellite navigation. Moreover, satellite gravimetry of space geodesy also relies on radar techniques. CHAMP (2000 by DLR) use GPS receivers to measure the accurate high (GPS satellite) and low (CHAMP) orbit and achieve gravity measurements. GRACE (NASA and DLR 2002) has K Band inter-satellite ranging equipment and GPS, which are crucial for the satellite to satellite tracking gravity measurements. GOCE (2009 by ESA) used radar-based GPS-GLONASS and sensitive gravity gradiometer to measure gravitational gradients along three orthogonal axes for gravity measurements (Xu et al., 2017; Ince and Pagiatakis, 2017; Zahzam et al., 2017). Furthermore, radargrammetry and radar (microwave) remote sensing is more popular in radio and radar research field, which commonly has five categories: microwave radiometer, satellite radar altimeter, scatterometer, sounding radar, Synthetic Aperture Radar (SAR) (Young et al., 2017; Fitch, 2012). Nowadays, except airborne radar, there are many spaceborne radar programs and missions (see Table 2.6). In these spaceborne radar missions, L, S, C, X, Ku, K and Ka bands are used on different satellites. In the future, the P band satellite will be launched in the ESA BIOMASS Earth explorer programme (Saatchi et al., 2012). However, on many terrestrial planets and their satellites (moons) with a magnetosphere and atmosphere, solar wind and EUV radiation create ions in the upper atmosphere as a plasma ionosphere, which dramatically decreases the accuracy of these observations (like SAR and other radio and radar observation).

3D SAR tomography (TomoSAR) (Reigber and Moreira, 2000; Fornaro et al., 2003; Nannini et al., 2008; Lombardini et al., 2013a) and 4D SAR differential tomography (Diff-TomoSAR) (Lombardini and Cai, 2012; Lombardini, 2005a; Xiang and Bamler, 2010; Lombardini and Pardini, 2012; Lombardini et al., 2013b; Tebaldini and Rocca, 2012; Huang et al., 2012) exploit multi-baseline SAR data stacks to make an essential innovation of SAR Interferometry, to sense complex scenes with multiple

scatterers mapped into the same SAR pixel cell (Feng and Muller, 2017). In addition to the 3D shape reconstruction and deformation solution in complex urban and infrastructure areas (Fornaro et al., 2003; Lombardini et al., 2013a), and recent cryosphere ice investigations (Ferro-Famil et al., 2012), promising tomographic forest applications (Nannini et al., 2008; Lombardini and Cai, 2008; Pardini and Papathanassiou, 2011; Lombardini and Viviani, 2015), e.g. tree height estimation, biomass estimation, sub-canopy topographic imaging, and even search, rescue, tracking and surveillance under tree and forest (Lombardini and Viviani, 2015). However, these scenes are characterized and influenced by DEM uncertainty, temporal decorrelation of scatterers, orbital, tropospheric and ionospheric phase distortion and a continuing open issue regarding possible height blurring and accuracy losses for TomoSAR applications, particularly in densely vegetated mountainous rural areas (Feng and Muller, 2017) and the polar ice regions of Earth, the polar regions of many planets (Venus, Mars, Saturn and Jupiter) and their icy satellites (moons), like Io, Europa, Ganymede, Callisto and so on. Thus, it is urgently needed to study DEM uncertainty, temporal decorrelation, orbital, tropospheric, ionospheric phase distortion for 3D & 4D tomographic SAR imaging.

This thesis intends to create an automatic DEM generation and validation method by photogrammetry & bistatic InSAR and an ionosphere & atmosphere correction and mapping method for TomoSAR imaging. By research on 3D & 4D tomographic SAR imaging algorithm, a better systematic tomography SAR (TomoSAR) method will be constructed. Furthermore, 3D & 4D tomographic SAR imaging will be studied using Cosmo-Skymed X band data in Zipingpu dam, Dujiangyan, Sichuan, China, and using ALOS L band data in San Francisco Bay (urban building and bridge), USA and in the future by using the MiniSAR and MiniRF data over the north and south polar ice regions of the Earth's moon (where water is hypothesized as existing). Such research results could be beneficial for future Earth and planetary observation as well as radio and radar astronomy.

## 1.2 Thesis Aims, Research Questions and Objectives

The primary aims of this thesis are to assess uncertainties in the retrieval of topographic elevation (DEM, DSM, DTM) from different spaceborne sources (stereo-optical, LIDAR, InSAR, stereo-SAR, radar altimetric data). In addition, new ionospheric

## Chapter 1. Introduction

& atmospheric correction and mapping methods are studied and applied to try to provide better 3D & 4D tomographic SAR accuracy. Furthermore, with research on new 3D & 4D tomographic SAR imaging algorithms, a better systematic tomography SAR (TomoSAR) method will be built and tested in the densely vegetated mountainous rural areas (dam) of China and urban areas (building and bridge) of San Francisco Bay, USA. Based on the aims of the thesis, the following research questions will be addressed:

- How to validate the TanDEM-X IDEM and TanDEM-X DEM data over the UK, and what does this suggest about the accuracy and utility of this new data source?
- How to achieve better 3D & 4D tomographic SAR imaging accuracy with the help of ionospheric & atmospheric correction and mapping methods?
- How to obtain 3D tomographic SAR imaging and accurate 3D point cloud deformation by using SAR tomography and differential SAR tomography in densely vegetated mountainous rural and urban areas with the slow motion, ionospheric and atmosphere influence?
- How to test and improve the accuracy of 3D & 4D tomographic SAR imaging in the densely vegetated mountainous rural areas of China, urban areas (building and bridge) of San Francisco Bay, USA.

To answer the research questions above, several objectives have been set:

- Develop an automatic DEM quality assessment method to process big TanDEM-X IDEM data (12 m, 30 m, 90 m) and TanDEM-X DEM data (90 m) of the UK.
- Investigate a systematic method of DEM generation, quality assessment, DEM quality improvement (filter, fusion, editing, and so on) and eventually DEM application (like DEM for TomoSAR).
- Develop a new ionospheric and atmospheric correction method based on the research of previous scientists
- Develop a new algorithm to exploit the potential of the new class of high resolution space-borne SAR systems for tomographic reconstruction (TomoSAR), i.e. 3D and 4D SAR imaging, in mountainous rural and urban environment.
- Compare, test, validate, fuse and improve the 3D & 4D tomographic SAR imaging results using Cosmo-Skymed X band data in Zipingpu dam, Dujiangyan, Sichuan,



China, as well as using ALOS L band data in San Francisco Bay (urban building and bridge), USA.

After this research, the systematic procedures of photogrammetry and bistatic InSAR for DEM generation, DEM quality assessment, DEM quality improvement and DEM applications will be established, which may be used in future DEM generation and DEM data applications for Earth observation and deep space exploration. Meanwhile, the systematic methods for 3D & 4D TomoSAR imaging for height and deformation retrieval will also be established, which can be potentially useful for many future applications (urban buildings, bridges, dams, forests, icy regions on the Earth and the Moon) and missions.

### 1.3 Thesis Structure

Based on the research aims, questions and objectives, this thesis has the following structure: a literature review of the present state of knowledge in the context of the aims and objectives of my research is provided in Chapter 2, which includes a review of DEM and DEM quality assessment, a review of DEM generation from SAR, a review of DEM generation from photogrammetry, a review of DEM generation from radargrammetry, a review of DEM for TomoSAR, a review of ionospheric and atmospheric correction for TomoSAR and a review of TomoSAR algorithms and applications. In Chapter 3, an introduction of DEM generation by using spaceborne bistatic InSAR (TanDEM-X) and airborne photogrammetry (Bluesky) is first given, then quality assessment methods and the results of TanDEM-X IDEM & TanDEM-X DEM data of UK & TanDEM-X DEM data of China is presented. Lastly, high resolution TanDEM-X DEM with quality improvement post-processing method is studied. In Chapter 4, a new ionospheric and atmospheric correction method is developed to try to achieve higher 3D & 4D tomographic SAR imaging accuracy; the 3D TomoSAR imaging method using ALOS L band data in San Francisco Bay (urban building and bridge), USA, based on the ionospheric and atmospheric correction results, is tested and studied in Appendix E. Based on mathematical derivation, a new TomoSAR and differential TomoSAR algorithm and systematic TomoSAR method are developed in Chapter 5 to try to obtain high accuracy 3D & 4D tomographic SAR imaging results. In Chapter 6, a systematic

## **Chapter 1. Introduction**

TomoSAR algorithm and methods are simulated, demonstrated, tested in various application areas (urban, bridge, dam) to try to achieve better 3D & 4D tomographic SAR imaging results, which including using Cosmo-Skymed X band data in Zipingpu dam, Dujiangyan, Sichuan, China. Finally, in Chapter 7, the results of this thesis study are summarised, and the novelty and the contributions of the research work are discussed alongside outlining future work.

# **Chapter 2**

## **Literature Review**

In this chapter, a comprehensive review of the topic area is undertaken in the context of the aims and objectives of my PhD research. This chapter is divided into seven sections; the first section is a review of TomoSAR, which includes its background, research progress, and applications. As a digital elevation model (DEM) is essential for TomoSAR processing, the second section focuses on introducing DEM, which includes DEM accuracy standards, current DEM quality assessment methods, and current DEM products on Earth and other planets. The third section introduces the InSAR DEM acquisition method and goes on to describe it in more detail. The fourth section discusses the DEM generation by photogrammetry and radargrammetry. The fifth section introduces the DEM generation by LIDAR and radar altimeters. The sixth section discusses a review of DEM for TomoSAR. The final section focuses on the review of atmospheric and ionospheric corrections for TomoSAR.

### **2.1. Review of TomoSAR**

#### **2.1.1. Background**

Currently, SAR is broadly applied in many fields: geology, glacier motion, seismology (earthquakes), terrain deformation, landslide movement, land subsidence, land uplift, volcanoes, glacier flow, glacier post-rebound, urban and building health monitoring, canopy (forest) height, biomass estimation, and so on (Kumar et al., 2011). With the development of increasingly complex technologies and big SAR data, SAR has

## Chapter 2. Literature review

evolved into many advanced modes, which include InSAR (single platform - dual antenna or repeat-pass mode), D-InSAR, Bistatic InSAR, Time series InSAR, PolSAR, PolInsar, Tomography SAR (TomoSAR), Diff-TomoSAR, Pol-TomoSAR, and Diff-PolTomoSAR (repeat-pass mode is required for data stacks).

Generally, InSAR is based on a phase difference (the phase equation is shown below) (Zebker et al., 1997; Hanssen, 2001). In Equation (2.1),  $\Delta\varphi_{int}$  is InSAR phase,  $\Delta\varphi_{flat}$  is the flat ground phase,  $\Delta\varphi_{topo}$  is the topography or elevation phase,  $\Delta\varphi_{geomorbit}$  is the orbit phase error based on the baseline,  $\Delta\varphi_{atm}$  is the atmosphere phase,  $\Delta\varphi_{noise}$  is the noise phase caused by noises in the system (thermal effects, quantization, other nonlinearities), and  $\Delta\varphi_{deformation}$  is the deformation phase.

$$\Delta\varphi_{int} = \Delta\varphi_{flat} + \Delta\varphi_{topo} + \Delta\varphi_{geomorbit} + \Delta\varphi_{atm} + \Delta\varphi_{noise} + \Delta\varphi_{deformation} \quad (2.1)$$

More specifically, these phases are caused by many factors:

- 1) One of the biggest sources of the InSAR phase comes from the ground surface and changes in the line of sight direction
- 2) Incoherent: leafy trees, water, large baselines
- 3) Unwrapping errors: discontinuities
- 4)  $\Delta\varphi_{deformation}$ : deformation phase in the line of sight direction
- 5)  $\Delta\varphi_{atm}$ : wet (water vapour), hydrostatic, and liquid components, clouds in atmospheric effect and Total Electron Content (TEC) in ionospheric effect

InSAR can be used to monitor deformation based on Equation (2.1). However, time series InSAR technology has become increasingly popular as it can generate higher accuracy surface deformation map and generates more information than InSAR. Time series InSAR technologies include stacking, persistent or permanent scatterers (PS), least squares (LS), small baseline subset algorithm (SBAS), coherence target/coherence point target (CT), temporal coherence point (TCP), multitemporal InSAR (MTI), and multiscale InSAR time series (MInTS) (Hanssen, 2001; Ferretti et al., 2000; Ferretti et al., 2001b; Usai et al., 2000; Zhang et al., 2011; Berardino et al., 2002; Mora et al., 2003). Of these, SBAS and PS-InSAR are the most popular techniques. The classification is summarised in Table 2.1 below. These methods can be applied to realise highly accurate surface deformation information.

Table 2.1 Classification of time series InSAR methods (Hanssen, 2001)

Items	Single master image	Multi-master image				
	PSInSAR (PSI)	Stacking	Generalised SBAS			
			LS	SBAS	CT	TCP
Main algorithm origin	Ferretti et al., 2000; Hooper et al., 2004; 2007; Kampes, 2006; Shanker et al., 2007	Sandwell et al.,2000; Strozzi et al.,2001	Usai et al.,1997; 1999; 2000; 2002; 2003	Berardino et al., 2001; 2002; Lanari et al., 2004; 2007; Hetland et al., 2012	Mora et al., 2001; 2003; Blanco et al., 2006; 2007; 2008; Duque et al., 2007; Zhang Hong et al.,2009	Zhang et al., 2011; 2012
Baseline requirements	Baseline requirements are lower; long Baseline is available	Does not exceed the critical baseline	Small baseline	Small baseline	Small baseline	Small baseline
Interferogram generation	Full resolution (no multi-view)	multi-view	multi-view	multi-view	multi-view	multi-view
Pixel selection	Based on the amplitude or phase deviations residuals	All public pixels in Interferogram	Based on Coherence	Based on Coherence	Based on Coherence	Based on Coherence
Scattering mechanism	Best dominant scatterers pixels	Random scattering pixels	Random scattering pixels	Random scattering pixels	Random scattering pixels	Random scattering pixels
Filtering	Butterworth filter	no	no	Gaussian	Gaussian	no

Items	Single master image	Multi-master image				
	PSInSAR (PSI)	Stacking	Generalised SBAS			
			LS	SBAS	CT	TCP
Phase unwrapping	Stepwise_3D(Hooper et al., 2007)	Cut branches or Snaphu	Cut branches or Snaphu	Cut branches or Snaphu	Cut branches or Snaphu	Cut branches or Snaphu
Atmosphere suppression	Band-pass filter for a removable estimate	Average weakening phase	Average weakening phase	Temporal low pass filter attenuates (or external data correction)	Temporal low pass filter attenuates (or external data correction)	Average weakening phase
Parameter estimation	Deformation, rail, air, DEM error	Linear deformation rate	Linear deformation rate	DEM error, deformation rate, APs	DEM error, deformation rate, APs	DEM error, the linear deformation rate
Interferogram numbers	Numerous (typically 20 or more) (McCormack et al., 2011)	Numerous (typically 20 or more)	Numerous (typically 20 or more)	Numerous (typically 20 or more)	Small number (the number of interferograms is depended on the threshold of coherence, e.g. 10 interferograms, the threshold is about 0.9 (Liao et al., 2006))	Small number (2 or more)

Due to the development of increasingly complex and capable technologies, advanced interferometric SAR techniques allow for 2.5D, 3D, 4D or even higher dimensional SAR imaging (see Figure 2.1 for the development of SAR techniques) (Bamler et al., 2009). After Time series InSAR technology, tomography SAR (TomoSAR) (shown in Figure 2.2), Diff-TomoSAR, Pol-TomoSAR and Diff-PolTomoSAR have become popular; this has opened the door to SAR pixel extracting joint 3D vertical height and dynamical information of superimposed moving scatterers in the same SAR cell. In the processing flow of 3D tomography SAR and 4D SAR differential tomography (Diff-TomoSAR), a high-quality reference DEM is essential to help achieve 3D tomograms and derive reliable deformation measurements. More details about TomoSAR and DEM are presented below.

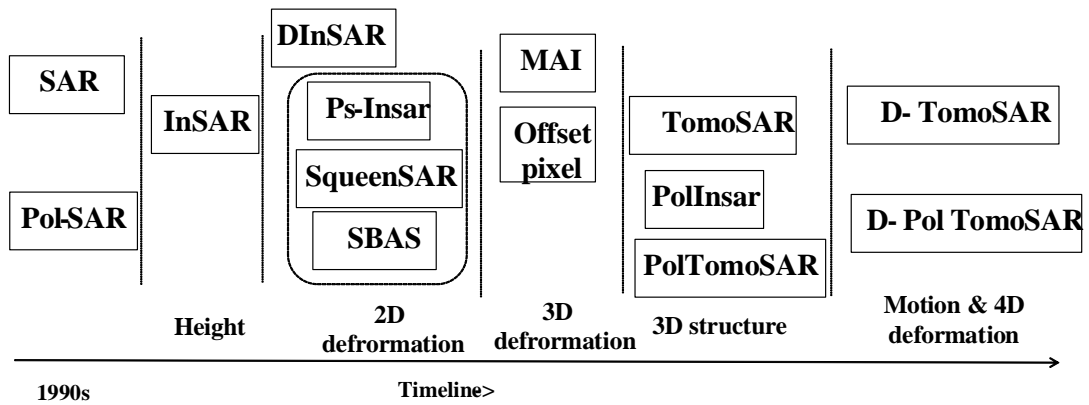


Figure 2.1 Global SAR research progress, (note that 3D deformation, 3D structure, motion and 4D deformation (4D means 3D plus time dimension) are particularly popular applications)

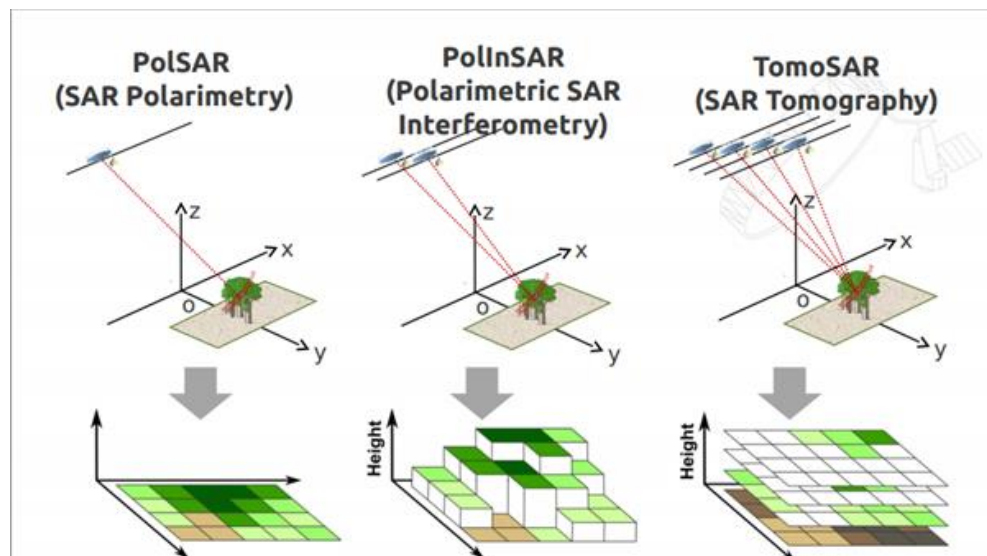


Figure 2.2 TomoSAR, PolSAR, and PolInSAR principle; TomoSAR can measure 3D points and 3D structures (Quegan, 2017)

### 2.1.2. TomoSAR and D-TomoSAR Research Progress

Advanced interferometric SAR techniques enable 2.5D, 3D, 4D (x, y, z and time) or higher dimensional SAR imaging (Bamler et al., 2009). This allows for 3D shape and deformation or subsidence of individual buildings to be retrieved. With only two acquisitions, multiple scatterers along elevations within one pixel cannot be separated in InSAR. Moreover, the accuracy of InSAR and D-InSAR is restricted by electromagnetic path delay variations in the troposphere and by temporal decorrelation of the surface (Hanssen, 2001). These distortions can be mitigated by temporal averaging of multiple interferograms which in turn reduce the temporal resolution. Persistent scatterer interferometry (PSI) was introduced in 1999 (Ferretti et al., 2000; Ferretti et al., 2001a; Ferretti et al., 2001b) as a method for the long-term monitoring of subsidence, particularly in urban environments. Generally, 20-100 single look complex (SLC) SAR data are used for interferogram and PSI analysis. Each pixel in each interferogram is characterised by its range and azimuth coordinates, as well as by the temporal and the spatial baseline of the interferogram. PSI theoretically assumes the presence of only one single scatterer in the pixel; however, in a high-rise urban environment, it is likely that multiple scatterers occur in one pixel.

3D SAR tomography (TomoSAR) (Reigber and Moreira, 2000; Fornaro et al., 2003; Nannini et al., 2008; Lombardini et al., 2013a) and 4D SAR differential tomography (Diff-TomoSAR) (Lombardini and Cai, 2012; Lombardini, 2005a; Lombardini and Pardini, 2012; Lombardini et al., 2013b; Xiang and Bamler, 2010; Tebaldini and Rocca, 2012; Huang et al., 2012) exploit multi-baseline SAR data stacks to create an essential innovation of SAR Interferometry: to sense complex scenes with multiple scatterers mapped into the same SAR cell (pixel). Aside from 3D shape reconstruction and deformation solutions in complex urban/infrastructure areas (Fornaro et al., 2003; Lombardini et al., 2013a), and recent cryosphere ice investigations (Ferro-Famil et al., 2012), emerging tomographic remote sensing applications include many forest scenarios (Nannini et al., 2008; Lombardini and Cai, 2008; Pardini and Papathanassiou, 2011); for example tree height and biomass estimation (Minh et al., 2016; Martín del Campo et al., 2018; Minh et al., 2015), sub-canopy topographic mapping, and even search, rescue, and surveillance operations under tree cover and in forests (Feng and Muller, 2017).



The idea of tomographic imaging was first introduced to the field of SAR research in the 1990s (Piau, 1994; Jakowatz and Thompson, 1995; Homer et al., 2002) in order to overcome the limitations (like 3D information extraction) of 2D SAR imaging. The initial experiment was carried out in a laboratory under ideal experimental conditions (Pasquali et al., 1995), and subsequently by using airborne systems (Reigber and Moreira, 2000). Over the last nineteen years, the 3D and 4D SAR tomographic imaging technology have been rapidly developing. The most salient points and achievements are as follows.

From 1999 to 2000, Reigber and Moreira processed 13 frames of the same track L-band polarimetric tomography data obtained by the ESAR airborne system. This was the first time that the concept of the tomographic (vertical distance) synthetic aperture was proposed, which considered the ambiguous problem caused by the small amount of same flight data, large tomographic aperture, and irregular tomographic dimension space sampling. The tomographic dimension (height) to the fuzzy suppression method was analysed, and the final airborne tomography three-dimensional imaging results were obtained (Reigber and Moreira, 2000).

From 2000 to 2002, Stebler et al processed multiple baseline airborne polarimetric interference data measurements to study the tree scattering theory and its properties for scattering centres, and used simulation methods to evaluate polarisation interference coherent scattering model (Stebler et al., 2000; Stebler et al., 2001; Stebler et al., 2002).

In 2003, Lombardini and Gini used multi-baseline SAR data to effectively separate the scattering unit echoes at different altitudes and demonstrated such research is of great significance for the monitoring application in complex target environments such as urban architecture (Lombardini et al., 2003; Lombardini and Gini, 2003). Luckman also fully exploited the advantages of multi-baseline SAR interferometry and studied the method of scattering intensity to separate scattering centres along the vertical direction of scattering particles (Luckman and Grey, 2003). In the same year, Lombardini first proposed the concept of differential tomographic SAR, combining elevation resolution, velocity resolution, the differential working mode and tomography SAR, to construct a two-dimensional baseline and time spectrum analysis processing framework. Based on this, a data-driven two-dimensional baseline and time spectral estimator was also proposed to allow for the joint processing of tomographic SAR data (Lombardini, 2005a).

In 2005, Reigber obtained the vertical structure scattering characteristics of the natural scene by using the 3D imaging results of the full polarimetric SAR data with the

## Chapter 2. Literature review

high-resolution tomography SAR method. The results of the three-dimensional imaging of Polarimetric SAR were used for the parameter estimation and application performance analysis of the Polarimetric SAR interferometer estimation inversion method. The results showed that the three-dimensional imaging results of the polarimetric SAR are helpful to evaluate the performance and accuracy of the vegetation parameter inversion algorithm (Reigber et al., 2005).

In 2006, Nannini proposed a tomographic baseline correction method for SAR tomography. At the same time, he presented the results of time-domain beamforming in tomography and compared it to the spectral estimation method to validate the effectiveness of time-domain beamforming for tomographic focusing (Nannini and Scheiber, 2006).

In 2007, Chen and Kasilingam presented a super-resolution processing framework for tomographic SAR imaging to separate the various scattering targets in the vertical range and analysed the possibility of this multi-baseline polarisation interferometric SAR tomography method (Chen and Kasilingam, 2007). Nannini proposed a tomographic dimension data processing method: the tomographic SAR image registration is completed under the radar geometry corresponding to different focusing elevations, and the tomographic dimension focusing process is subsequently completed. This method can correct data registration errors at different focusing depths caused by radar geometric changes (Nannini and Scheiber, 2007).

In 2009, Tebaldini studied the three-dimensional information acquisition technology of natural scenes, based on the measured data of airborne multi-baseline polarisation interferometry SAR acquired by the European Space Agency's BioSAR missions (Tebaldini, 2009a; Tebaldini, 2009b).

In 2009, Nannini analysed and estimated the minimum amount of data required for tomographic SAR imaging and investigated the minimum dimensions needed to separate two diffusive particles with a certain elevation difference. On this basis, a 3D tomographic imaging method with self-adaptive motion compensation based on different focused reference elevations was presented (Nannini and Scheiber, 2007; Nannini et al., 2009). Meanwhile, Lombardini proposed a differential full-resolution tomography SAR processing method by improving the original algorithm based on the differential tomography SAR concept (Lombardini, 2009).

In 2010, researchers such as Zhu and Bamler of the DLR Laboratory in Germany used a tomographic SAR inversion method based on L1 norm compression sensing to

separate scattering particles distributed along the vertical dimension within the same cell. Subsequently, this method has been applied to 3D ultra-high-resolution tomographic SAR imaging in complex urban environments, while the compressive sensing method based on the L1 norm has also been applied to differential tomography SAR (Zhu and Bamler, 2010c; Zhu and Bamler, 2010b; Xiang and Bamler, 2010).

In the same year, Fornaro used 43-frame data of the ERS system from 1995 to 2000 to measure the deformation field in the urban portions of Rome, Italy (Fornaro et al., 2010). In 2011, Reale et al. used 25-frame TerraSAR-X data from 2008 to 2009 to conduct a SAR tomographic four-dimensional imaging experiment at the Mirage Hotel in Las Vegas, USA (Reale et al., 2011), fully demonstrating the high resolution of the TerraSAR-X system.

In 2011, Huang, Ferro-Famil and Reigber developed a tomographic SAR imaging technique to retrieve concealed targets under vegetation cover, based on E-SAR's airborne L-band Polarimetric SAR data in the Dornstetten region. They then proposed a new polarisation analysis method, which can effectively improve the artificial target response and the natural environment clutter separation ability (Huang et al., 2012; Huang et al., 2013).

In 2012, full-polarised tomography (SAR) technology was first used to reconstruct three-dimensional images for leaf covered hidden target detection and parameters by Nannini and Scheiber (Nannini et al., 2012). At the same time, Min studied tomographic SAR 3D imaging based on the Bayesian sparse reconstruction method (Min et al., 2012). Pauciullo also studied the detection and extraction method of secondary scattering mechanisms based on the three-dimensional tomographic SAR imaging results. The experimental results showed that the results of this study could be effectively applied to the parameter extraction (position, deformation, seasonal thermal change, and so on) of complex urban buildings (Pauciullo et al., 2012).

In 2013, researchers such as Aguilera, Nannini, and Reigber presented a Wavelet-based Compressed Sensing (WCS) method to obtain 3D tomographic SAR imaging by using 21 frames of E-SAR's L-band fully polarimetric SAR tomographic data (Aguilera et al., 2013).

In 2014, Zhu and Bamler of DLR Laboratory in Germany used a compressive sensing method (super-resolution SAR tomography for multidimensional imaging) to reconstruct individual buildings (shape and motion) over a city (Zhu and Bamler, 2014).

## **Chapter 2. Literature review**

In 2015, Stefano Tebaldini presented tomographic analysis results for L-Band SAR data over the Mittelbergferner glacier in the Austrian Alps, during the ESA AlpTomoSAR campaign (February/March 2014), which showed the complexity of the sub-surface glacier scattering (Tebaldini et al., 2015).

In 2016, Irena Hajnsek and Matteo Pardini presented the results of P and L-Band 3D SAR imaging of the AfriSAR Campaign in African forests (Hajnsek et al., 2016).

In 2017, Alessandra Budillon studied the fast super-resolution localisation and detection method to locate multiple scatterers in synthetic aperture radar tomography (Budillon et al., 2017).

In conclusion, TomoSAR is a method for 3D SAR imaging in the elevation direction, in which a two-dimensional synthetic aperture is formed in the elevation direction with the help of the high-resolution range direction imaging stacks for TomoSAR reconstruction (see Figure 2.2 above) (Bamler et al., 2009). From this reconstructed elevation profile, multiple targets are detected, and the 3D distribution of the targets can be obtained (Zhu and Bamler, 2012). In this way, classical 2D InSAR can be considered as a simple parametric case of 3D TomoSAR (Zhu and Bamler, 2012). D-TomoSAR (4D SAR imaging) (Lombardini, 2005b; Fornaro et al., 2009; Zhu and Bamler, 2010a), exploits the strengths of both TomoSAR and PSI, which inverts the motion of the scatterers with 3D TomoSAR reconstruction (Zhu and Bamler, 2010a). It can retrieve motion and elevation information of multiple scatterers in a SAR pixel cell using a spectral analysis method (Zhu and Bamler, 2012). However, research on SAR tomography using spaceborne systems still has many issues related to real data processing, which need to be further investigated and addressed.

### **2.1.3. TomoSAR Application**

The TomoSAR technique is one of the advanced techniques of InSAR. InSAR has many applications such as topographic mapping, global environmental changes (glacier melting, permafrost degradation, glacial drift, polar ice changes, etc.), monitoring and evaluation of disasters (seismic crustal deformation, volcanic activities, landslides, regional land subsidence, etc.), energy resource exploration (oil and gas field exploitation, mineral resources exploitation, groundwater extraction, etc.) and so forth. The application of InSAR Data for disasters is summarised in Table 2.2 below (Wang et al., 2010; Xuedong et al., 2011; Tantiaparp et al., 2012; Qin et al., 2013; Ferretti et al., 2007b;

Ge et al., 2009; Xiong et al., 2014), which shows that the TomoSAR technique can be used in many ways: landslide applications, earthquakes, snow density and snowmelt glacier ice flow, vegetation biomass information extraction, marine disasters in sea ice, oil spill monitoring, geological disaster damage assessment, and so on.

Theoretically, since D-InSAR has been introduced to monitor the slow motion of landslides (Akbarimehr et al., 2013), the D-InSAR method has become popular and applied to many landslides; a sub-pixel offset technique was first introduced to monitor the Shuping landslide in China with TerraSAR-X spotlight SAR data (XiaoFan et al., 2011), which has already produced promising results. Moreover, D-TomoSAR can be used to monitor landslides because of its motion detection capabilities.

In addition to landslides, tomographic SAR technology has also been applied to research focused on the estimation of biomass, the 3D mapping of complex buildings in cities, the vertical structure scattering features of penetrable objects (ice, snow, vegetation and canopy, etc.), temporal decorrelation of scatterer analysis, partially coherent object detection, and scatterers cloud (SC), to name but a few (Fornaro et al., 2014; Lombardini and Cai, 2014; Morrison and Bennett, 2014; Pauciullo et al., 2014; Wang et al., 2014), with more promising applications to be studied in the future.

Table 2.2 SAR data application in the disaster field

Items	Disaster type	Single polarisation	Full or multi-polarisation	InSAR	PolInSAR and TomoSAR/PolTomoSAR
Pre-disaster warning	Drought warning	√	√		√
	Land use classification		√	√	√
	Snow density and snowmelt flood forecasting		√		√
	High-precision digital elevation			√	√
	Earthquakes, landslides, mudslides and <u>other geological disaster warnings</u>			√	√
	Glacier ice flow movement monitoring and early warning			√	√
	Vegetation biomass abnormal information extraction			√	√
	Flood extent and secondary disaster monitoring	√	√	√	√

Items	Disaster type	Single polarisation	Full or multi-polarisation	InSAR	PolInSAR and TomoSAR/PolTomoSAR
Monitoring when a disaster is occurring	Earthquake and secondary disaster monitoring	√	√	√	√
	Landslides, mudslides, and secondary disaster monitoring	√	√	√	√
	Continuous monitoring of drought	√	√	√	√
	Marine disasters in sea ice, oil spill monitoring	√	√	√	√
	Ice monitoring	√	√	√	√
	Snow level monitoring	√	√	√	√
	Crop area and growth monitoring	√	√		√
	Snow cover depth and density monitoring		√		√
	Loss of vegetation monitoring				√

Items	Disaster type	Single polarisation	Full or multi-polarisation	InSAR	PolInSAR and TomoSAR/PolTomoSAR
Post-disaster assessment	The assessment of flood disaster losses	√	√	√	√
	Drought damage assessment	√	√		√
	Crop yield loss assessment		√		√
	Snow scope of the assessment	√	√	√	√
	Standing building evaluation following an earthquake		√		√
	Seismic deformation field to assess the extent of earthquake damage			√	√
	Geological disaster damage assessment earthquakes, landslides, mudslides, and others			√	√
	Vegetation damage assessment				√



Based on SAR penetration in icy regions (Gay and Ferro-Famil, 2016) (shown in Figure 2.3), icy TomoSAR imaging research has been conducted on the Earth, other planets, and even some icy moons. Lunar Reconnaissance Orbiter (LRO 2009) Miniature Radio Frequency (Mini-RF S band and X band raw data, Bistatic radar data, Level 1 SAR, Level 1 interferometry, Level 2 SAR, Level 3 SAR mosaics, and Level 3 Sandia SAR stereo data) will greatly advance our understanding of our own moon, giving us the first glimpses inside the Moon's coldest, permanently shadowed polar craters of water ice (Cahill et al., 2014; Mitchell et al., 2017; Djachkova et al., 2017). In recent work, Mini-RF provided the radar view of the physical properties of the lunar surface and subsurface for the first time, particularly in the permanently shadowed area, shown in Figure 2.4 (Elphic et al., 2007; Spudis et al., 2013; Vondrak et al., 2010b). For ice detection on the Moon, methods, like spectrometry (around  $3\mu\text{m}$ , shown in Figure 2.5), modes of Lunar prospector neutron spectrometer (LEND) data (Sanin et al., 2012), and the circular polarization ratio (CPR) of Mini-RF data have been recently used (Mandt et al., 2016; Cahill et al., 2014; Vondrak et al., 2010a). Currently, scientists use the high Mini-RF CPR levels inside the crater to indicate the presence of ice on the moon. It might be the case that ice formed in the permanently shadowed area because the sun's light never touches and heats the surface in the dark areas of the crater. In the experiment's image analysis (NASA, 2017), high CPR occurs inside the craters. These high CPR values suggest that the crater floor is rougher inside than outside (terrain) and something else (possibly ice) could be causing the high CPR value, as opposed to the blocky terrain. When passing through ice, the radar signal keeps the original polarisation of the radar wave, resulting in the high circular polarisation ratios (CPR) (Cahill et al., 2012; Nozette et al., 2010; Thomson et al., 2012; Patterson et al., 2012; McKerracher et al., 2010). On that basis, scientists point to a high CPR value to indicate the presence of ice in the Moon's craters. However, the emerging icy TomoSAR imaging can detect the depth of ice, make 3D tomographic imaging tomograms and reconstruct the ice structure, which will be another method for ice retrievals, inter-comparison and inter-calibration of lunar ice in the future.

## Chapter 2. Literature review

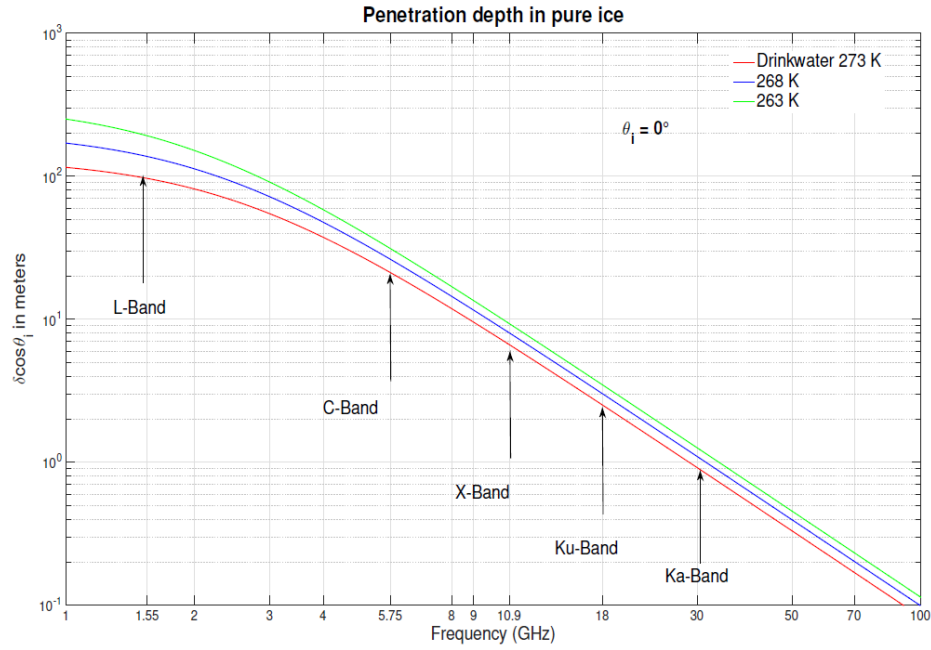


Figure 2.3 Radar penetration depth of pure ice (Gay and Ferro-Famil, 2016)

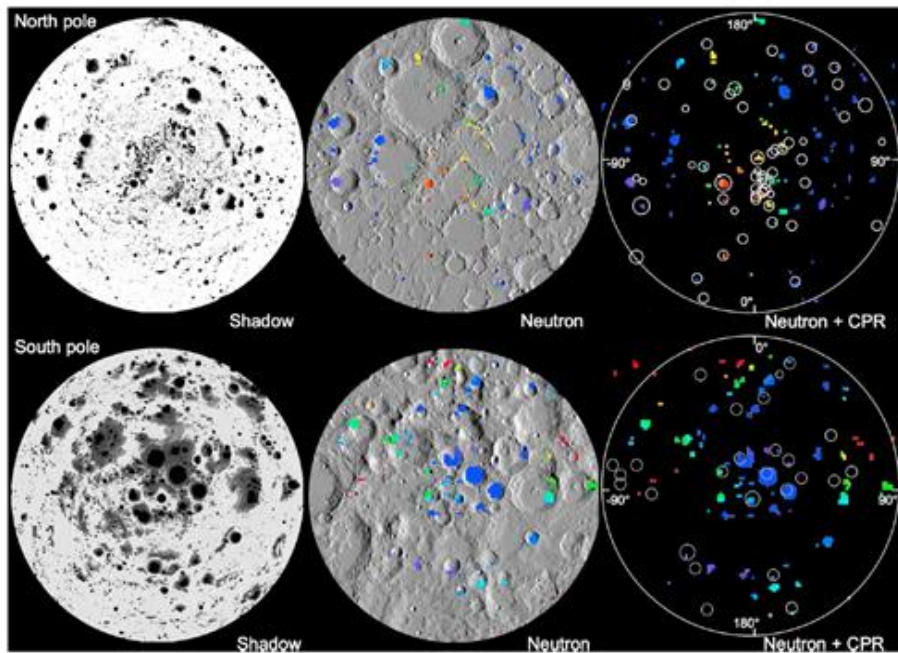


Figure 2.4 The lunar maps of the north (top) and south (bottom) pole (Spudis et al., 2013), (left) permanently shadowed areas (black areas), (middle) neutron spectrometer data (red means high water equivalent hydrogen, purple and blue represents lower water equivalent hydrogen) (Elphic et al., 2007), and (right) CPR anomalous craters interpreted from Mini-RF data (white circles might contain ice)

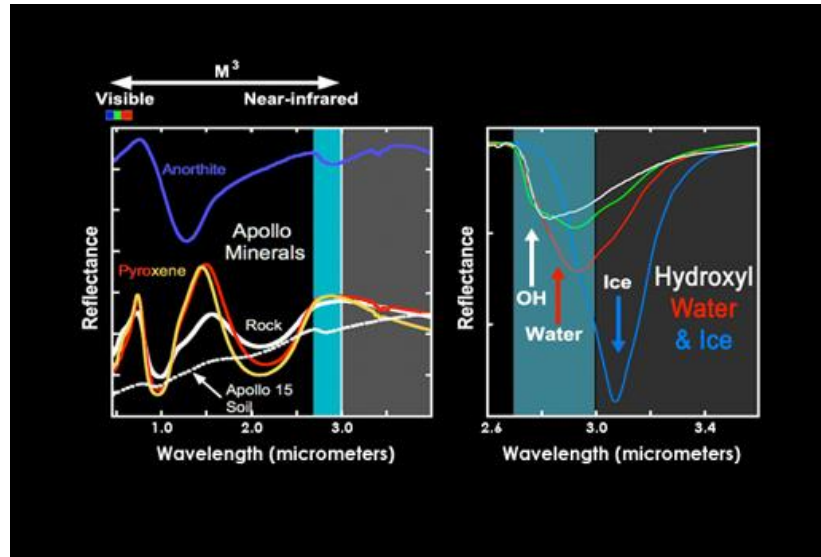


Figure 2.5 The reflectance of hydroxyl (OH) molecules, water and ice on the Moon  
(Credit: ISRO/NASA/JPL-Caltech/Brown Univ)

## 2.2. Digital Elevation Model (DEM)

A digital elevation model (DEM) is defined as continuous elevation values (regular grid array of z-values) referenced to a datum (datum of the geographic coordinate system) (Lieu and Sorby, 2008) for a terrain surface, such as planets (Earth, Mars etc.), moons, or asteroids (Mayhew, 2015), which includes both a digital surface model (DSM) and a digital terrain model (DTM). Theoretically, the digital surface model (DSM) symbolises the terrain's surface including all objects on it (buildings, structures, trees etc.), while the digital terrain model (DTM) presents the bare ground surface without any objects (see Figure 2.6) on it.

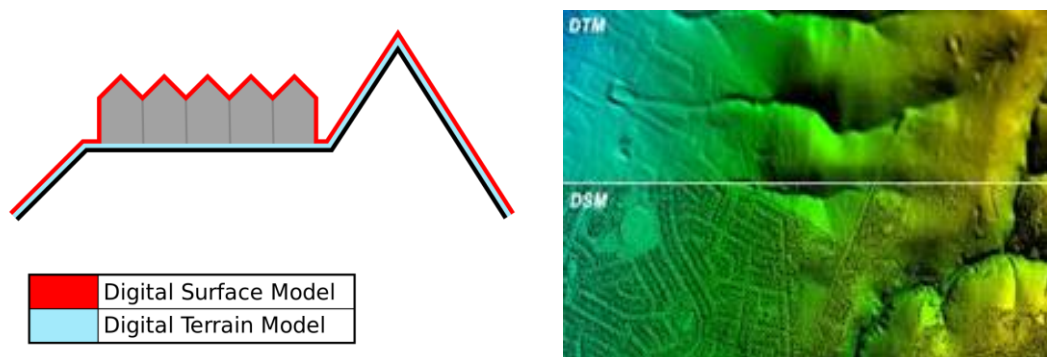


Figure 2.6 DSM and DTM (Wikipedia, 2016a), digital surface model (DSM) symbolises the terrain's surface including all objects on it (buildings, structures, trees etc.), while the digital terrain model (DTM) presents the bare ground surface without any objects

## **Chapter 2. Literature review**

Generally, DEM data can be a raster (a grid of squares), contour line models, and vector-based triangular irregular networks (TIN) (Maune, 2007). They can be converted from one data format to another. The DEM quality is a measurement, which represents how the elevation differs from the 'true elevation' (absolute accuracy) and how accurate the elevation is for the point-to-point accuracy (relative accuracy) at each pixel. Several factors influence the quality of DEM products: terrain roughness, grid (pixel) resolution, sampling density, elevation (height) resolution, terrain analysis method, interpolation method, and so on (Maune, 2007).

### **2.2.1. DEM Acquisition Methods**

There are many methods for obtaining elevation data (DEMs): surveying and mapping by drones (unmanned aerial vehicles (UAV)), airborne photogrammetry, spaceborne photogrammetry, LIDAR, Interferometry Synthetic Aperture Radar (InSAR), radar altimeters, Kinematic GPS (KGPS), theodolite or total station, inertial surveying and mapping and range imaging (Maune, 2007). Some of these methods will be described in more detail below.

### **2.2.2. DEM Products of Earth and Other Planets (Including the Moon)**

#### **2.2.2.1. *Earth***

Much of Earth's DEM data is free to the public. A DEM called GTOPO30 (30 arcseconds resolution, about 1000 m, in the whole world) is free (Denker, 2005; Miliarexis and Argialas, 1999), with poor quality in some areas. A much higher quality and higher resolution (30 m) DEM from the ASTER is also free, which covers 99% of the Earth's area (Hirano et al., 2003; Fujisada et al., 2005). A similarly high resolution (30 metres) is now free to public users from the Shuttle Radar Topography Mission (SRTM). Besides, SRTM and GTOPO30 cover continental land only, and SRTM (Argyriou and Teeuw, 2013; Breit and Bamler, 1998; Gao et al., 2012; Hofton et al., 2006; Li et al., 2013; Rodriguez et al., 2006; Shih, 2014; Solberg et al., 2013) does not possess data for the polar regions. The SRTM data does not represent the top of the canopy, as it (C band) penetrates a short distance into the canopy (the penetration capabilities of different band radar is shown in Figure 2.7). Antarctic 500 m DEM and Greenland 1 km DEM by ICESat are also available from the National Snow and Ice Data

Center of NASA (Brenner et al., 2007; Schutz et al., 2005). Besides, a new digital elevation model (1, 2, and 5 km grid cells) of the Antarctic ice sheet and ice shelves was generated by the CryoSat-2 satellite radar altimeter data between July 2010 and July 2016 (Minh et al., 2015), which can be used for terrain correction of gravity measurements (Álvarez et al., 2012). Seafloor elevation data (bathymetry) is typically obtained using depth sounding (sonar) equipment mounted on a ship. The SRTM30Plus (Paskevich, 2005) dataset is a global elevation model which combines bathymetric data, GTOPO30 and SRTM together. Furthermore, there is another global data called GMTED2010 (Danielson and Gesch, 2011b), which is 225 m resolution based on SRTM data and other data. A new 12 m global non-free DEM with a higher accuracy ( $< 2$  m) has been produced by the TerraSAR-X and TanDEM-X satellite missions (Werninghaus, 2004), which is now available (after 2018); but the quality assessment is still ongoing (Wessel et al., 2018).

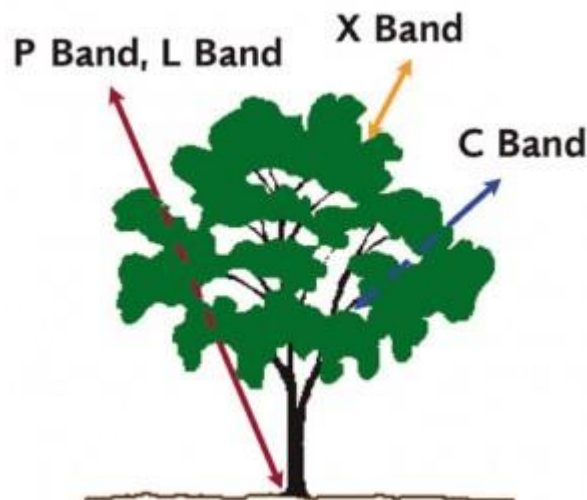


Figure 2.7 Canopy penetration varies with different wavelengths (Parker, 2018)

### 2.2.2.2. *The Moon and Mars*

There is a wealth of DEM data relating to the Moon from lunar exploration missions conducted by different countries over the past 60 years. Following the Luna 3 probe launched by the Soviet Union in October 1959, America sent out several lunar missions: the Ranger Series from 1962 to 1965, the Lunar Orbiter series from 1966 to 1967, the Surveyor series from 1966 to 1968, the Clementine spacecraft in 1994, and the Lunar Prospector in 1999 (Cai et al., 2010). Recent decades have enjoyed an upsurge in lunar exploration 50 years after the Americans first landed on the moon (Cai et al., 2010). In recent years, following the success of ESA's Smart-1 mission, Japan sent the Kaguya

## Chapter 2. Literature review

explorer (2007), India sent the Chandrayaan-1 (2008), America sent the Lunar Reconnaissance Orbiter (2009), and China launched Chang'E-1, Chang'E-2, Chang'E-3, Chang'E-4 and Chang'E5-T1 (Cai et al., 2010).

The Lunar Orbiter Laser Altimeter (LOLA) (Cai et al., 2010), is an instrument on the Lunar Reconnaissance Orbiter (LRO) (Chin et al., 2007), which provides both lunar surface topography measurements as well as ancillary data about surface slopes, roughness and 1064 nm reflectance. LOLA (Cai et al., 2010) is a multi-beam laser altimeter (wavelength is 1064.4 nm with a pulse repetition rate of 28Hz). A diffractive optical element is used to split a single laser beam into five output beams (28HZ, five beams means 140 measurements/second), with each beam having a 100  $\mu$ rad divergence, and the mapping spot is 5 m in diameter. The 5 spot pattern signal of the backscattered pulses is transferred onto separate optical fibres and detected by the receiver (a silicon avalanche photodiode detector) (Cai et al., 2010).

Chang'E-1, successfully launched on October 24, 2007, at the Xichang Satellite Launch Centre in China and was the first lunar exploration mission by the People's Republic of China. Moreover, it was adjusted into a circular lunar polar orbit on November 7, 2007, to complete its mission (Cai et al., 2010). Furthermore, a global lunar DEM was obtained from Chang'E-1 mission (Cai et al., 2010).

Currently, popular moon DEMs include ULCN2005<sup>1</sup>, CLTMs01<sup>2</sup>, and Kaguya models<sup>3</sup> (Cai et al., 2010). Chang'E Satellite orbit technologies are GPS, LLR, SLR, VLBI, DORIS (Cai et al., 2010). Three methods were used to obtain DEM: LIDAR plus precise orbit; photogrammetry without control points plus precise orbit; photogrammetry with LIDAR, but without control points and precise orbit (China 3 Line Array CCD + LIDAR). In relation to the last method, the laser height data is combined with CCD image data to create lunar surface controlling points. EO (exterior orientation elements) of the CCD image is calculated successfully by LIDAR control points of the lunar surface without precise orbit information.

For Mars, DEMs are also free and available to the public from MOLA data (MEGDR), generated by the Mars Orbiter Laser Altimeter (MOLA) instrument on the Mars Global Surveyor (MGS) as well as from the Mars Digital Terrain Model (DTM) from the Mars Reconnaissance Orbiter HiRISE on Mars Reconnaissance Orbiter (MRO)

---

<sup>1</sup> The Unified Lunar Control Network 2005

<sup>2</sup> Lunar topographic model CLTM-s01 from Chang'E-1 laser altimeter

<sup>3</sup> SELENE/Kaguya laser altimeter DEMs

and so on (Bradley et al., 2002). The DEMs from High-Resolution Stereo Camera (HRSC) (Gwinner et al., 2016) on ESA's Mars Express, the DEMs from Context Camera (CTX) (Tao et al., 2018; Tao and Muller, 2018) on MRO and the DEMs from HiRISE (Tao et al., 2018; Mattson et al., 2009; Kirk et al., 2008) are also generated by many research groups around the world.

### 2.2.3. DEM Accuracy Standard and Quality Assessment Method

Up to now, DEM has involved a certain level of uncertainty, and this uncertainty is not systematically applied and corrected to DEM data when using it in many applications (Wechsler, 1999). What causes DEM uncertainty? The uncertainty stems from DEM data, which is likely to contain errors. Therefore, it is necessary to check and assess the quality of the data when using it, and there is much research that has been conducted about DEM quality assessment. Many research papers use “ground truth” elevations (GPS, LIDAR, radar altimetry, stereo-photogrammetric data) with statistical methods, GIS visualisation methods and GIS analysis methods to obtain absolute/relative horizontal accuracy results (relative horizontal accuracy is the departure from a true relationship between two points. Thus, true data are selected first; the difference of the delta horizontal distance between two points is calculated to obtain the relative horizontal accuracy), absolute/relative vertical accuracy results (relative vertical accuracy is the difference of the delta elevation between two points), statistical tables, and quality maps.

Theoretically, DEM quality is a measurement, which represents how the elevation is different from the ‘true elevation’ (absolute accuracy) and how accurate the elevation is for the point-to-point accuracy (relative accuracy). Several factors, detailed below, influence the quality of DEM products (Greenwalt and Shultz, 1962; Caruso, 1987b).

- (1) Terrain roughness
- (2) Grid resolution or pixel size
- (3) Sampling density (elevation data collection method)
- (4) Vertical resolution
- (5) Interpolation algorithm
- (6) Noise and errors
- (7) Terrain analysis algorithm (Caruso, 1987b)

## Chapter 2. Literature review

### 2.2.3.1. DEM errors

DEM data contains three types of errors: random errors, systematic errors, and blunders (Feng and Muller, 2016). Although all three types may be minimised by refining techniques, they cannot be completely eliminated (Greenwalt and Shultz, 1962; Caruso, 1987b; Feng and Muller, 2016).

#### 1. Blunders

A blunder (error) for DEM data is a vertical error which exceeds 3 sigmas of the error, and it is easily identifiable (Caruso, 1987b).

#### 2. Systematic Errors

Systematic errors for DEM data follow some fixed pattern including vertical elevation shifts, which can be eliminated when detected (Caruso, 1987b).

#### 3. Random Errors

Random errors for DEM data are those residual errors after systematic errors and blunders have been removed, which are random and therefore beyond the user's control. (Caruso, 1987b).

### 2.2.3.2. Root-Mean-Square Error

RMSE is used in many fields of surveying. The vertical root-mean-square error (RMSE) (Greenwalt and Shultz, 1962; Caruso, 1987b) statistic, shown in Equation (2.2) is employed to quantify the vertical accuracy of a DEM data, covering both systematic errors and random errors. The RMSE is defined as:

$$RMSE = \sqrt{\frac{\sum (Z_i - Z_t)^2}{n}} \quad (2.2)$$

where:

$Z_i$  = interpolated DEM elevation of a test point

$Z_t$  = true elevation of a test point

$n$  = number of test points

For  $Z_t$ , the true elevation refers to the most probable elevation, because values are generally taken from good quality data. Available field control points are suggested to be used for calculation (Greenwalt and Shultz, 1962; Caruso, 1987b; Maune, 2007). A lower RMSE represents higher accuracy and vice versa.



### 2.2.3.3. Accuracy

DEM accuracy includes absolute and relative accuracy in horizontal and vertical dimensions (Greenwalt and Shultz, 1962; Caruso, 1987b). Generally, DEM elevation accuracy can be calculated according to the two rules shown below (Maune, 2007):

- 1) 90% confidence level accuracy = 1.6\*RMSE
- 2) 95% confidence level accuracy = 1.96\*RMSE

The error distributions of the point pixels are assumed to have a normal distribution (Maune, 2007; González and Bräutigam, 2015).

#### 2.2.3.3.1. Horizontal Accuracy

The horizontal accuracy is determined from the RMSE, a mathematical and statistical distance value from the x-y shift between the DEM pixel positions and the position of checkpoints ('real position') (Maune, 2007). Moreover, in order to measure the accuracy, the vertical component of the features (checkpoints) (i.e. crossing lines, road signs, etc.) must be clearly identified to measure the horizontal error in the DEM (Greenwalt and Shultz, 1962; Caruso, 1987b). Generally, DEM elevation horizontal accuracy can be calculated according to Equation (2.3), (2.4) and (2.5) shown below (Maune, 2007). In relation to the practical applications, there are many DEM accuracy standards for users to utilise, for example, NMAS and NSSDA horizontal accuracy standards of the USA are shown in Table 2.3.

$$RMSE_x = \sqrt{\sum (x_{data,i} - x_{check,i})^2 / n} \quad (2.3)$$

$$RMSE_y = \sqrt{\sum (y_{data,i} - y_{check,i})^2 / n} \quad (2.4)$$

$$\begin{aligned} RMSE_r &= \sqrt{\sum ((x_{data,i} - x_{check,i})^2 + (y_{data,i} - y_{check,i})^2) / n} \\ &= \sqrt{RMSE_x^2 + RMSE_y^2} \end{aligned} \quad (2.5)$$

where:

$x_{data,i}, y_{data,i}$  are the coordinates of the  $i^{th}$  checkpoint in the dataset

$x_{check,i}, y_{check,i}$  are the coordinates of the  $i^{th}$  checkpoint in the independent source of higher accuracy

$n$  is the number of checkpoints tested

$i$  is an integer ranging from 1 to  $n$

## Chapter 2. Literature review

Table 2.3 Horizontal elevation accuracy comparison (Maune, 2007)

NMAS Map scale	NMAS CMAS 90% confidence level Maximum error tolerance	NSSDA RMSE	NSSDA Accuracy of 95% confidence level
Equation	$1.015 * \frac{1/12000}{Map\ scale} m$	$67.0 * \frac{1/12000}{Map\ scale}$ cm	$1.159 * \frac{1/12000}{Map\ scale} m$
1" = 100' or 1:1,200	3.33 ft or 1.015 m	2.20 ft or 67.0 cm	3.80 ft or 1.159 m
1" = 200' or 1:2,400	6.67 ft or 2.033 m	4.39 ft or 1.339 m	7.60 ft or 2.318 m
1" = 400' or 1:4,800	13.33 ft or 4.063 m	8.79 ft or 2.678 m	15.21 ft or 4.635 m
1" = 500' or 1:6,000	16.67 ft or 5.081 m	10.98 ft or 3.348 m	19.01 ft or 5.794 m
1" = 1000' or 1:12,000	33.33 ft or 10.159 m	21.97 ft or 6.695 m	38.02 ft or 11.588 m
1" = 2000' or 1:24,000	40.00 ft or 12.192 m	26.36 ft or 8.035 m	45.62 ft or 13.906 m

### 2.2.3.3.2. Vertical Accuracy

DEM vertical accuracy is tested and assigned a vertical RMSE (the accuracy of Z), and Equation (2.6) is shown below (Maune, 2007). Like the horizontal accuracy standards detailed above, NMAS (National Map Accuracy Standards of USA) and NSSDA (National Standard for Spatial Data Accuracy of USA) vertical accuracy standards are shown in Table 2.4.

$$RMSE = \sqrt{\frac{\sum (Z_i - Z_t)^2}{n}} \quad (2.6)$$

Table 2.4 Vertical elevation accuracy comparison

Equivalent contour interval (ft or m)	NMAS VMAS 90% confidence level Maximum error tolerance	NSSDA RMSE	NSSDA The accuracy of 95% confidence level
Equation	$15.24 \times \frac{\text{contour interval}}{0.3048}$ cm	$9.25 \times \frac{\text{contour interval}}{0.3048}$ cm	$18.2 \times \frac{\text{contour interval}}{0.3048}$ cm
1 ft or 0.3048 m	0.5 ft or 15.24 cm	0.30 ft or 9.25 cm	0.60 ft or 18.2 cm
2 ft or 0.6096 m	1 ft or 30.48 cm	0.61 ft or 18.5 cm	1.19 ft or 36.3 cm
4 ft or 1.219 m	2 ft or 60.96 cm	1.22 ft or 37.0 cm	2.38 ft or 72.6 cm
5 ft or 1.524 m	2.5 ft or 76.2 cm	1.52 ft or 46.3 cm	2.98 ft or 90.8 cm
10 ft or 3.048 m	5 ft or 152.4 cm	3.04 ft or 92.7 cm	5.96 ft or 181.6 cm
20 ft or 6.096 m	10 ft or 304.8 cm	6.08 ft or 185.3 cm	11.92 ft or 363.2 cm
40 ft or 12.192 m	20 ft or 609.6 cm	12.16 ft or 370.6 cm	23.83 ft or 726.4 cm
80 ft or 24.384 m	40 ft or 1219.2 cm	24.32 ft or 741.2 cm	47.66 ft or 1452.8 cm

#### 2.2.3.3.3. Relative Vertical Accuracy

Accuracy measurements not only refer to absolute vertical accuracy, but they also include relative vertical accuracy (Maune, 2007; González and Bräutigam, 2015). Relative accuracy (point-to-point accuracy) is the departure from a true relationship between two points, the difference of the delta elevation (the delta elevation is the elevation difference between two points, then two delta elevations are differentiated). Generally, reference points should be selected at the top and bottom of uniform slopes as a very dense set of reference points to calculate relative vertical accuracy (Greenwalt and Shultz, 1962; Caruso, 1987b) shown in Figure 2.8. In many cases of DEM, relative vertical accuracy is much better (Maune, 2007) than the absolute vertical accuracy.

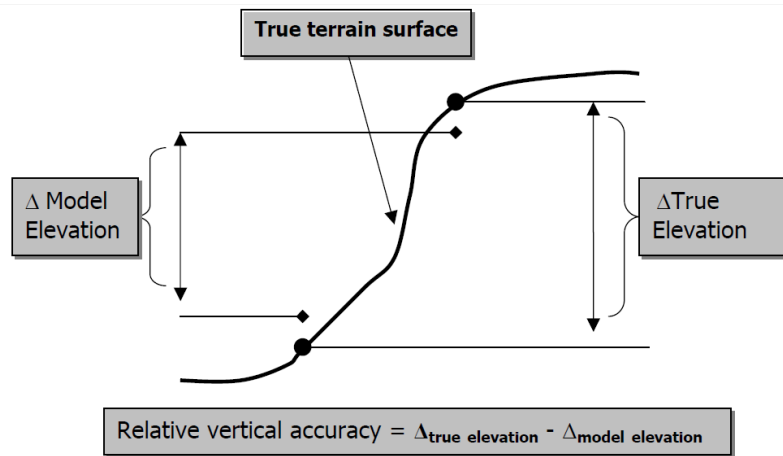


Figure 2.8 Relative vertical accuracy (Maune 2007)

### 2.2.3.4. DEM quality assessment methods

According to the accuracy standards and confidence percentages, QA/QC is used to guarantee the quality of DEMs. The quality control/quality assurance (QA/QC) (Hunter and Goodchild, 1997) process for DEM work may be divided into two categories: process quality control (QC) and product quality assurance (QA) (Maune, 2007). According to DEM accuracy specifications (Maune, 2007), the process QC should control the quality by taking part in the QC reviews of flight alignments, photographic quality, aerial triangulation, stereo compilation and completeness of supporting data DEM RMSE, data processing methods. Product quality assurance means it should be assured by the test group using a variety of inspection and testing techniques on the final deliverables to ensure the accuracy and format of the DEM according to the DEM accuracy specification (Maune, 2007).

Currently, people use “ground truth” elevations (GPS, LIDAR, radar altimetry, stereo-photogrammetric data) with statistical methods, GIS visualisation methods, and GIS analysis methods to obtain absolute/relative horizontal and vertical accuracy results, including statistical tables and quality maps. Statistical methods include derived topographic parameters (Bias, Relative Bias, Average Relative Absolute Difference (ARAD), Relative Root Mean Square Error (R-RMSE), Root Mean Square Error (RMSE), Log Root Mean Square Error (L-RMSE), Average and Standard Deviation of N Simulations, Maximum and Minimum of N Residuals, R-Squared statistic, t-test, and P-value) (Wechsler, 1999; Feng and Muller, 2016). Of these DEM quality assessment methods, DEM coordinate system conversion and DEM registration are the key initial steps. In the next section, these key steps will be described in more detail.

### 2.2.3.4.1. DEM coordinate system and conversion

A coordinate system is a system that is used to define the coordinate position of any object in a space, like Euclidean space (Iliffe, 2000). In the Cartesian coordinate system, the position is described in terms of  $x$ ,  $y$ ,  $z$ , while the position is represented by longitude, latitude, and height in geodetic coordinates. Normally, a coordinate system is based on an earth reference ellipsoid and datum. The ellipsoid is represented by the flattening coefficient  $f$  and the sphere's semi-major axis length  $a$  (loc.cit.). A Geodetic datum is a coordinate benchmark (a set of reference points) which is used to locate the vertical positions on the planets.

#### 2.2.3.4.1.1. OSGB1936 & ODN and conversion

In the UK, the Ordnance Survey National Grid reference system (OSGB1936) (Ordnance-Survey, 2015) was created after retriangulation using survey data generated between the years 1936 and 1962, which is based on the Airy 1830 ellipsoid (loc.cit.). The ODN (Ordnance Datum Newlyn) is the UK's national coordinate benchmark for orthometric heights above mean sea level, which was created based on tide gauge data at Newlyn, Cornwall (loc.cit.). The OSGB1936 grid is based on the OSGB36 datum, shown in Figure 2.9 and Figure 2.10.

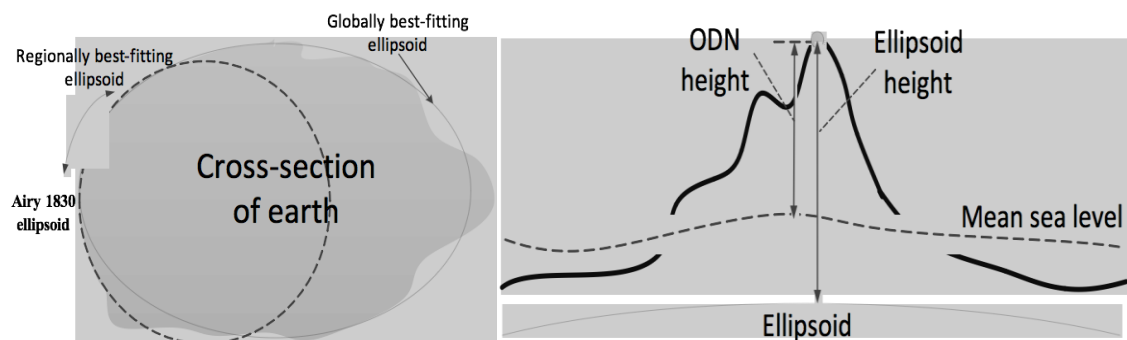


Figure 2.9 Airy 1830 ellipsoid and ODN height (Ordnance-Survey, 2015), Ordnance Survey Great Britain 1936, based on the Airy 1830 ellipsoid and the ODN height based on mean sea level

Different applications require different coordinate reference systems (datums) for geodesists, surveyors, and engineers. Generally, the coordinate systems used in the UK are ETRS89, OSGB36, ODN (loc.cit.). ODN uses a different benchmark for some areas of the UK, see Figure 2.11 below. Furthermore, ETRS89 (European Terrestrial Reference System 1989) is the coordinate system for GPS (WGS84) throughout Europe and the UK,

## Chapter 2. Literature review

based on ITRF89<sup>4</sup>/ETRF89<sup>5</sup>. In addition, there are the seven parameters method, the national geoid model OSGM02<sup>6</sup>/OSTN02<sup>7</sup> to convert WGS84 to OSGB36 ODN, and vice versa (Iliffe, 2000; Iliffe et al., 2003), as shown in Figure 2.12 and Figure 2.13 below. The OSGM02/OSTN02 transformation accuracy is about  $\pm 3.5$  metres (95%) either vertically or horizontally (Haklay, 2010; Iliffe et al., 2003).

The WGS84-ETRS89 (European Terrestrial Reference System of 1989), based on ITRF89 or ITRF89, and WGS84 (G1150) is connected to ITRF2000. When we convert IDEM from WGS84 (G1150) to OSGB36 ODN, we need to convert ITRF2000 to ITRFS89 with the 7-parameter Helmert transformation provided by ITRT/ETRF firstly to WGS84 (ETRS89) and then use OSTN02 & OSGM02 to convert WGS84 (ETRS89) to OSGB36 ODN.

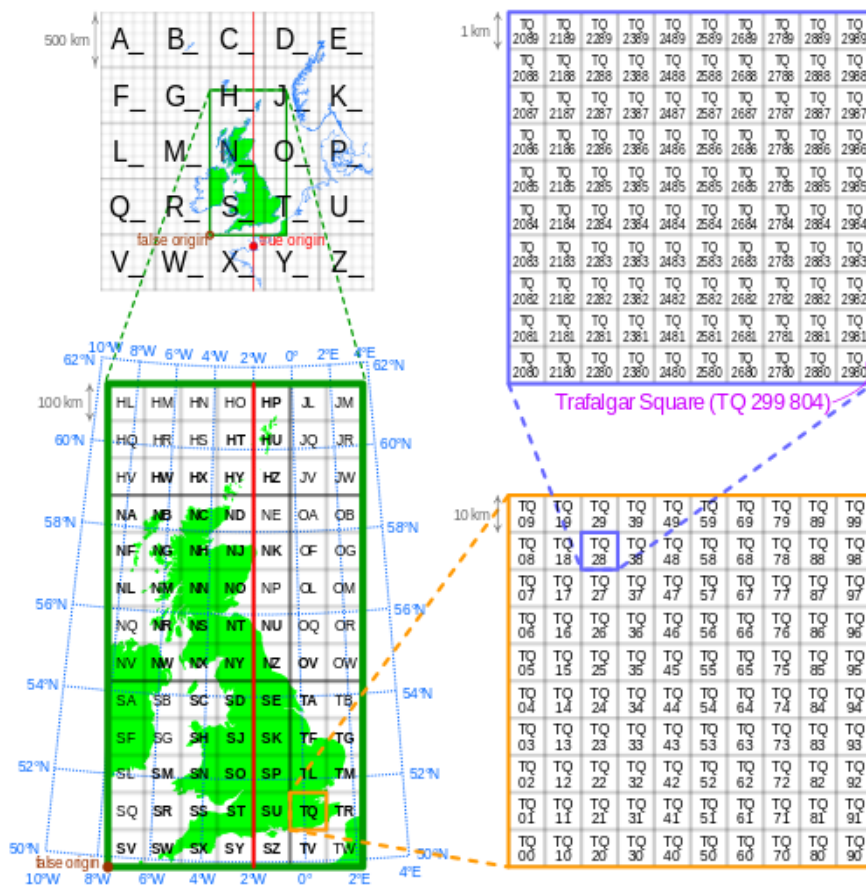


Figure 2.10 Illustration of the Ordnance Survey National Grid coordinate system and numbering rules  
(Ordnance-Survey, 2015)

<sup>4</sup> ITRF: International Terrestrial Reference Frame

<sup>5</sup> ETRF: European Terrestrial Reference Frame

<sup>6</sup> OSGM02: Ordnance Survey Geoid model

<sup>7</sup> OSTN02: The Ordnance Survey National Grid Transformation

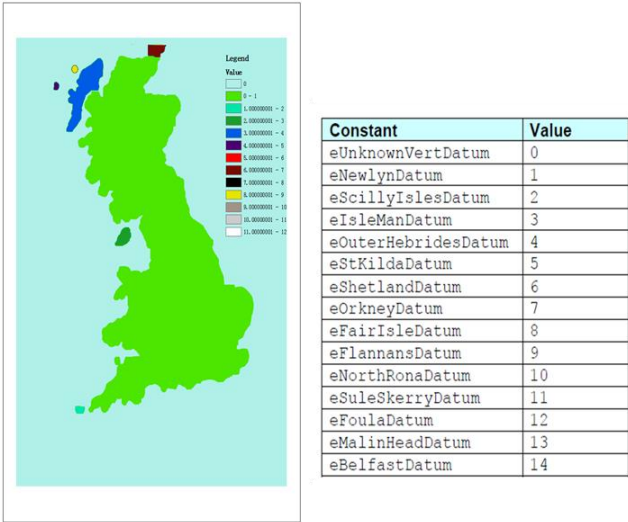


Figure 2.11 ODN datum distribution, different colours represent different datums

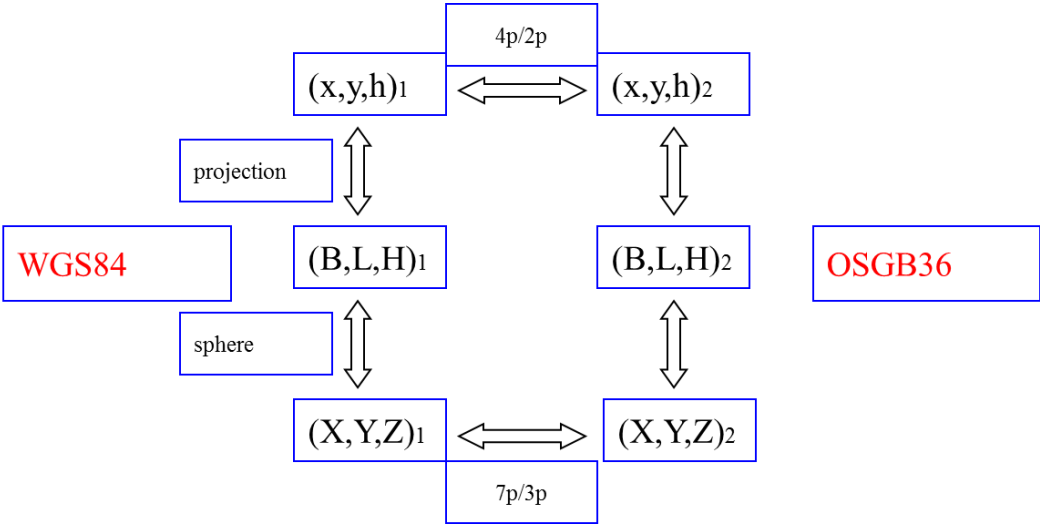


Figure 2.12 Coordinate system conversion methods relationship; (X, Y, Z) are Cartesian coordinates, (x, y, h) are projection coordinates; p is parameters. Thus, 7p is seven parameters method

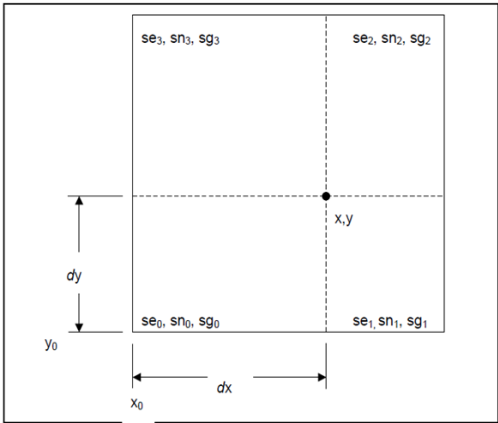


Figure 2.13 OSGM02/OSTN02 (Iliffe, 2000; Iliffe et al., 2003) method for transferring WGS84 to OSGB36 ODN

### 2.2.3.4.2. DEM Registration

Image matching approaches have been widely used in many applications, like photogrammetry, radargrammetry, remote sensing, GIS, computer vision, robotics, and so on. Image matching methods include local matching (like pixel-by-pixel matching), 2D global spatial coherence, and 1D semi-global spatial coherence along multiple paths (like SGM). Some popular image matching open sources in the field of photogrammetry are CMVS, PMVS and MicMac. The image matching principle is shown below in Figure 2.15, alongside the remote sensing image matching algorithms in Figure 2.14 (Brown, 1992; Zitova and Flusser, 2003).

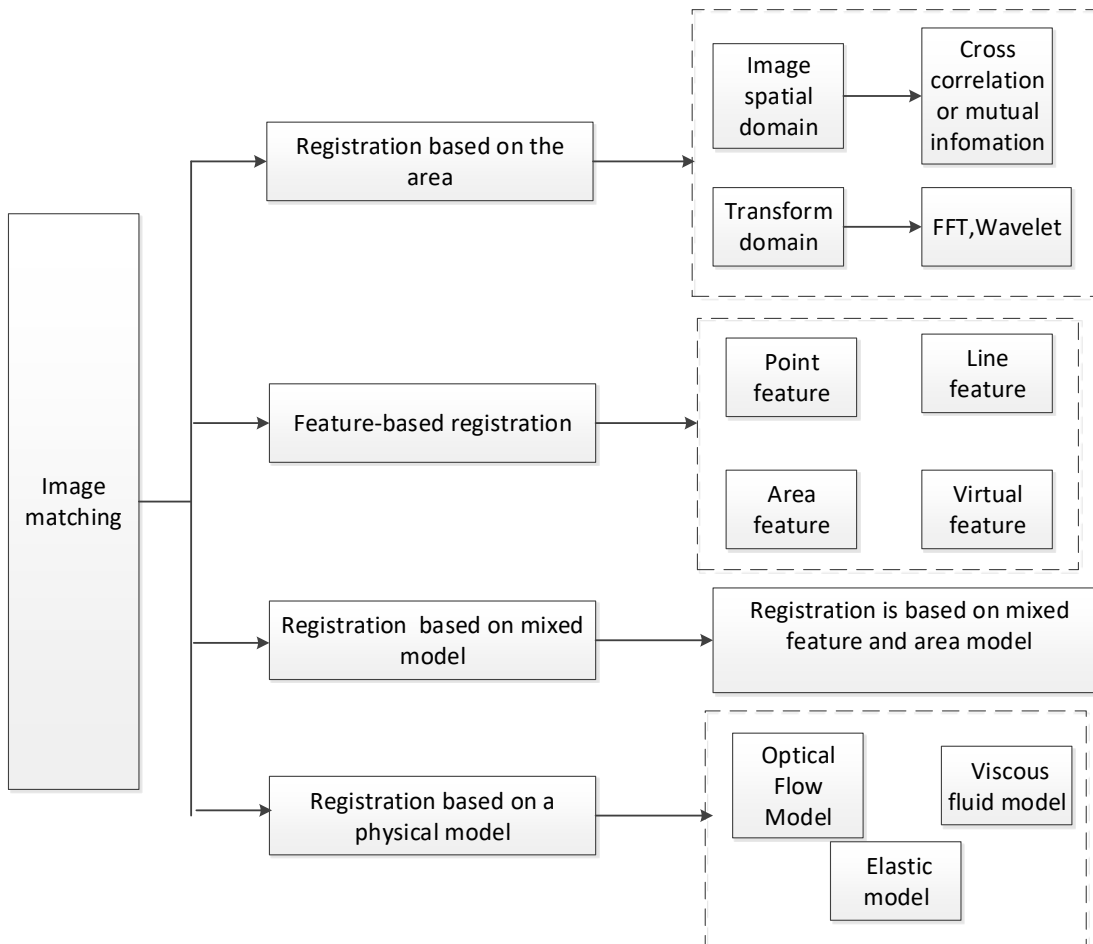


Figure 2.14 Remote sensing image matching algorithms (Brown, 1992; Zitova and Flusser, 2003)

DEM registration based on imaging matching is another crucial step as it can be used to seamlessly integrate different sources of DEMs in different resolutions in the same area (Fusion) or different areas (Merge). DEM-to-DEM registration has difficulties in finding feature points required for matching evaluation and error analysis. Although



Adaptive Least Square Correlation (ALSC) (Otto and Chau, 1989; André et al., 2008; Shin and Muller, 2012) can solve this problem, the ALSC process is relatively slow. Meanwhile, DEM-to-DEM registration always needs to solve horizontal shifts, vertical shifts and tilts between overlapping DEMs.

Bambang Trisakti and Ita Carolita (Trisakti and Carolita, 2010), used Ground Control Points by combining X-Y coordinate points and elevation (Z) points for DEM co-registration between ASTER Stereo Data and SRTM DEMs. Simultaneously, the accuracy was evaluated by comparing the height distribution of each profile along the vertical and horizontal transect lines of both DEM data. Tony Li and James Bethel (Li and Bethel, 2007) employed a two-step process for DEM alignments: an initial alignment step (vertical and horizontal) before a fine least squares matching method for DEM registration.

Hosford (Hosford et al., 2003) investigated the fusion method of a radargrammetric DEM with an airborne laser DEM. Howard Schultz (Schultz et al., 1999) proposed a DEM-to-DEM registration method for detecting changes in the vertical height dimension. Permanent Scatterers were also used by Alessandro Ferretti (Ferretti et al., 1998) to help DEMs fusion.

DEM validation for systematic error estimation was studied by B. Wessel (Wessel et al., 2008a), using the least squares adjustment method with reference data, GCPs and tie points. All in all, DEM co-registration methods can address both horizontal and vertical offsets separately or simultaneously. These methods can be divided into two categories. The first is 2.5D (separately, including seven parameters, contour-based 3D matching method, 3D least squares matching, ICP, LZD, and so on), another is 3D (separately, including cross-correlation method, mutual information method, gradient-based mutual information, and so on). In modern practice, the iterative closest point (ICP) (more details are in (2) of Section 3.2.5.2) and least z-difference (LZD) are popular methods for DEM co-registration.

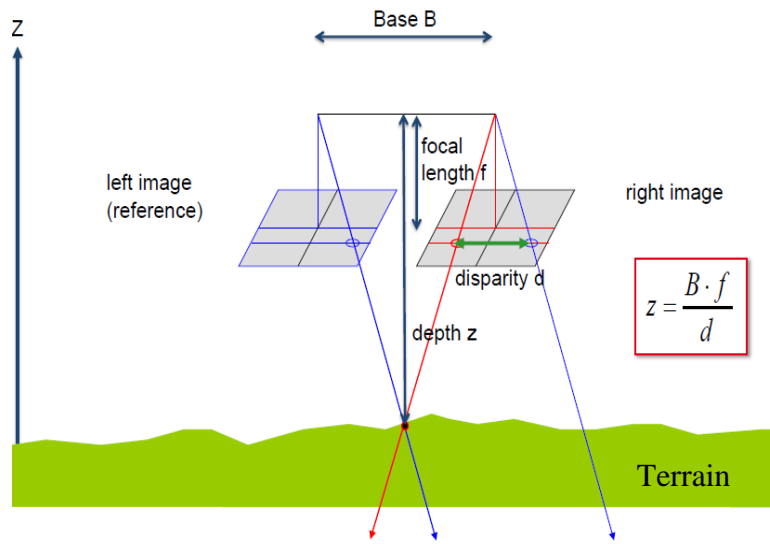


Figure 2.15 The image matching principle<sup>8</sup>, the disparity  $d$  can be obtained by calculating the differences of corresponding matching points

## 2.3.DEM Generation from InSAR

### 2.3.1. Introduction and Background

In 1951, Wiley (Budge and German, 2015) invented the synthetic aperture radar (SAR) concept. Following this innovation, the concept of SAR technology developed rapidly, such as motion-compensated, self-focusing, multiple beams, multi-look processing, inverse SAR (ISAR) and interference techniques, which greatly expanded the scope of SAR applications. SAR has now begun to experience single-band to multi-bands, unipolar to multipolar, fixed angle of incidence angles to variable angles of incidence, single mode to multiple modes of progressive development. Moreover, the antenna has also included a fixed beam antenna, a mechanical scanning antenna, a one-dimensional and a two-dimensional electronically scanned phased array (Freeman, 1992; Freeman, 2004; Bamler and Hanssen, 1997; Hanssen, 2001; Fuhrmann et al., 2015; Gong et al., 2015; Mahapatra et al., 2015). The Synthetic Aperture Radar (SAR) has both cloud-penetrating, and day/night operational capabilities. Moreover, because of Doppler and coherent scattering characteristics, Interferometric SAR (InSAR) can measure the travel path and phase with a high degree of accuracy to generate the interferometric phase. D-

---

<sup>8</sup> Source: Leica document – ‘Dense image matching and surface reconstruction when photogrammetry meets computational geometry’

InSAR uses differential interferometric phase as a new way to measure centimetric surface deformations of the terrain (Ferretti et al., 2007a).

Nowadays, there are many kinds of radar systems, including InSAR, ISAR, meteor SAR, BiSAR, MiniSAR, Bi/multi-static SAR, etc., and these systems are becoming increasingly popular and utilised in all manner of applications. In contrast, ISAR technology utilises the movement of the target and static emitter. MiniSAR is small and typically stationed inside the drone (UAV) or deep space exploration spacecraft (like the LRO Mini-RF for the Moon), while meteor SAR is used to monitor meteoroids (Jones et al., 2005). Bistatic radar is a system where the transmitter and receiver are placed in different places with a distance. Multi-static SAR is made up of at least three components (for example, one transmitter and two receivers, two transmitters and one receiver, or multiple transmitters and multiple receivers) (Nezlin et al., 2007; Fang and Xiang, 2010). Moreover, a radar system in which one or more geographically separated transmitters transmit radar signal to one or more receivers has become a common (new generalisation) bi/multi-static radar system configuration (Nezlin et al., 2007; Fang and Xiang, 2010). However, due to technological advances, many other radar systems are currently being studied and produced by scientists and companies around the world.

To acquire the information of a given target through remote sensing, it is essential that the target's reflectance and scattering information can be recorded by the remote sensor. This communication of information is usually achieved through the propagation of electromagnetic waves (see Figure 2.16) (Benson, 1999) which encompass the very short wavelengths of gamma rays (typically one picometre) to the very long wavelengths of radio waves (typically the scale of kilometres). The frequency of given electromagnetic radiation is inversely correlated with its wavelength. Theoretically, microwave remote sensing systems (passive and active mode radar systems) will utilise microwave bands, typically including Ka, Ku, X, C, S, L, P band (Elachi, 1988). The microwave is a subset of electromagnetic radiation, and microwave bands are shown in Figure 2.17 and Table 2.5 below. Radar systems use these bands because these are within atmospheric windows that do not get absorbed by oxygen or water vapour. Although electromagnetic radiation has the ability to convey information to remote sensors, the Earth's atmosphere severely constrains the electromagnetic propagation process. It filters out most electromagnetic radiation of very short and long wavelengths and only allows the radiation within certain wavebands to pass through. As shown in Figure 2.18, microwave bands have low atmospheric absorption. Therefore, they are best for radar systems, which is the reason

## Chapter 2. Literature review

why radar systems have atmosphere/cloud-penetrating capabilities. However, scattering delays of radar can be induced by atmospheric conditions, clouds and rain; for rain, the magnitude is decided by rain density and the wavelength (shown in Figure 2.19) used by the radar (Li, 2005).

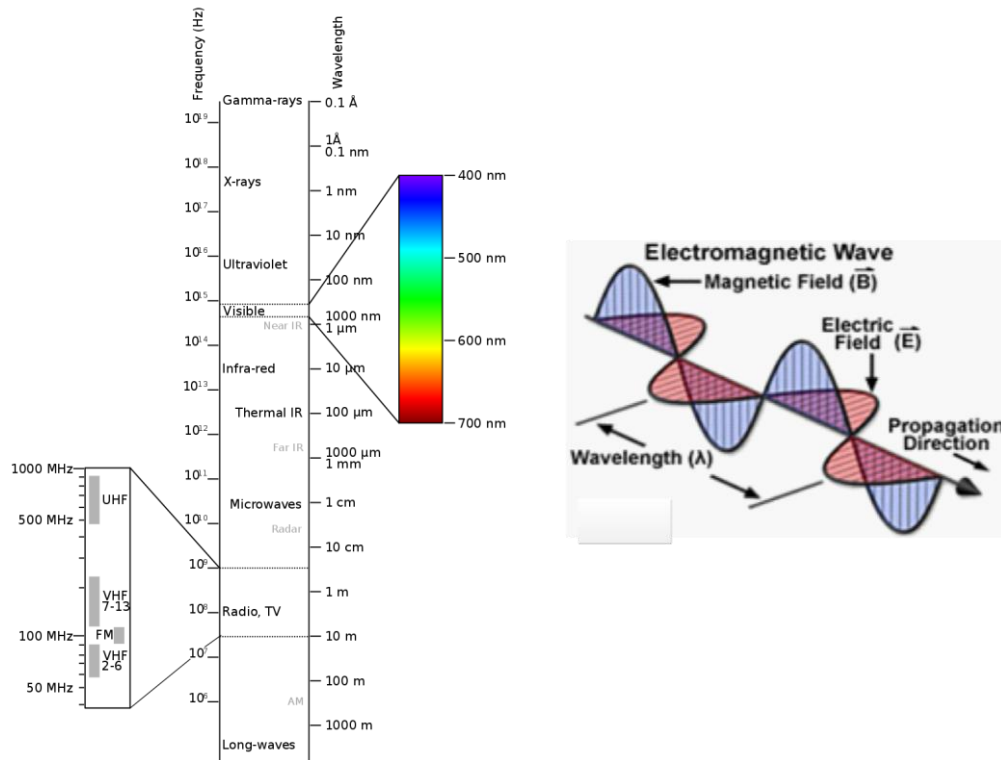


Figure 2.16 Electromagnetic spectrum and waves (Wikipedia, 2016b), the magnetic field is perpendicular to the electric field



### Radar System

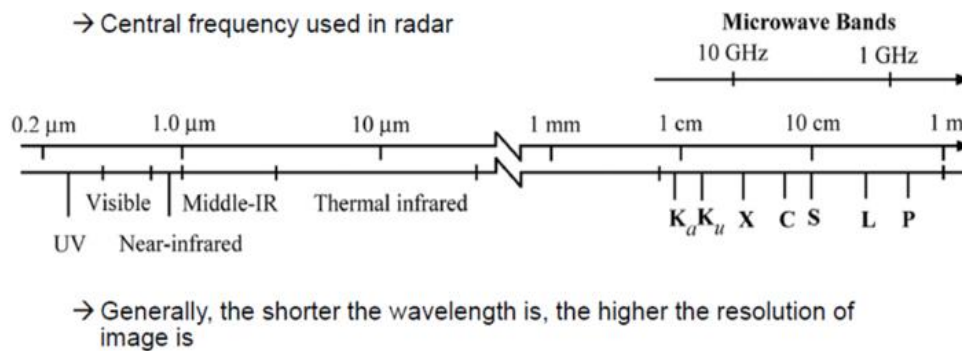


Figure 2.17 Microwave bands in the electromagnetic spectrum, microwave bands are between 1 mm and 1 m (USGS)

Table 2.5 Typical microwave wavelength and frequency (Collin, 2007)

Band	Frequency range (GHz)	Wavelength range	Typical SAR wavelengths
P	0.3-1	100-30 cm	66.7 cm
L	1-2	30-15 cm	23.5 cm
S	2-4	15-7.5 cm	12.0 cm
C	4-8	7.5-3.75 cm	5.7 cm
X	8-12.5	3.75-2.4 cm	3.1 cm
Ku	12.5-18	24-16.7 mm	22.09 mm
K	18-26.5	16.7-11 mm	16.7-11 mm
Ka	26.5-40	11-7.5 mm	11-7.5 mm

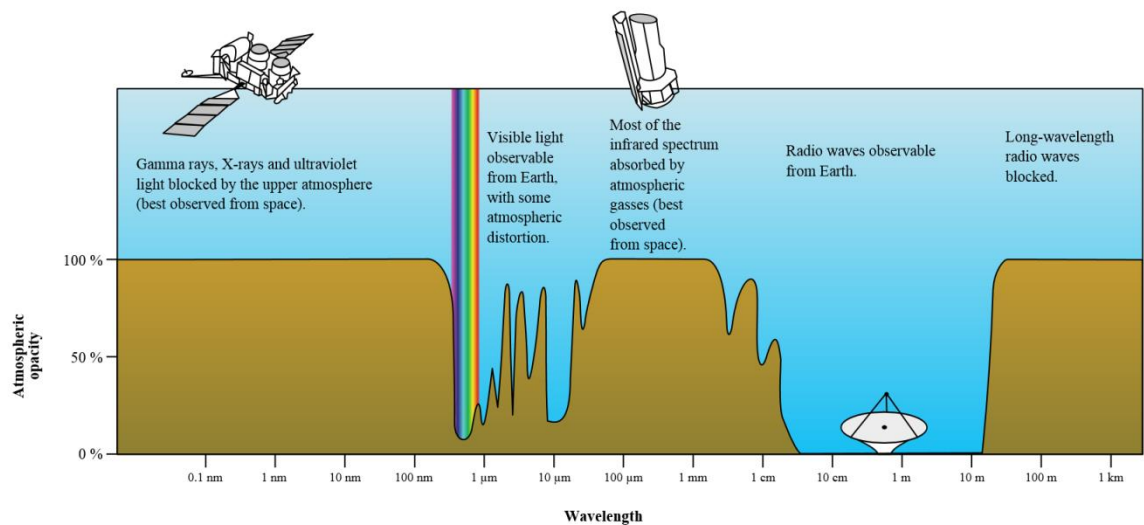


Figure 2.18 Atmospheric transmittance of the Earth to various wavelengths(Wikipedia, 2016b),  
microwave bands (1 mm to 1 m) have low atmospheric absorption

In modern times, there are many radar programmes and missions. In the document ‘Satellite and Airborne SAR Sensor Specifications’ (CRCSI, 2015), most of the current operational satellites, project plans, and airborne SAR sensors (public) in the world are presented in detail respectively. The current operational spaceborne SAR and the wavebands are shown in Table 2.6. Within these airborne SAR systems, L, S, C and X bands are used by many different satellites. In the future, a P band satellite will be

## Chapter 2. Literature review

launched as part of the ESA BIOMASS earth exploration programme. In contrast to other satellites, TerraSAR-X and TanDEM-X can generate high-resolution DEM.

Table 2.6 Current satellite SAR sensor (CRCSI, 2015; Rincon et al., 2019)

Satellite	Country	time	End of mission	altitude (Km)	View angle (Deg)	wavelength (cm)	Resolution (m)	Scan width (km)	Revisited period (day)	Critical baseline (km)
Seasat	USA	1978	1978	800	20-26	23.5 (L)	25	100	---	4.5
ERS-1	ESA	1991	2000	782-785	21-26	5.6 (C)	30	102.5	35	1.1
JERS-1	Japan	1992	1998	568	38	23.5 (L)	18	75	44	4.5
ERS-2	ESA	1995	2011	782-785	21-26	5.6 (C)	30	102.5	35	1.1
Radarsat	Canada	1995	2013	793-821	20-50	5.6 (C)	9-25	50-500	24	1.1
ALOS-1	Japan	2006	2011	628	8-60	L	10-100	30-350	46	N/A
Radarsat-2	Canada	2007		798	18-50	5.6 (C)	3-100	18-500	24	N/A
TerraSAR-X	Germany	2007		514	35	3.1 (X)	1, 1	150	11	N/A
TanDEM-X	Germany	2009		514	35	X	1, 1	150	11	N/A
HJ-1C	China	2012		500	31-44.5	S	5, 20	100	31	N/A
Sentinel-1	ESA	2014		693	20-45	5.6 (C)	5x20 20x40 5x5	N/A	12	N/A
ALOS-2	Japan	2014		628	8-70	L	3-100	25-490	14	N/A
GF3	China	2016		755	17-60	C	1-500	10-650	29	N/A

Satellite	Country	time	End of mission	altitude (Km)	View angle (Deg)	wavelength (cm)	Resolution (m)	Scan width (km)	Revisited period (day)	Critical baseline (km)
SAOCOM	Argentina	2016		620	20-50	L	10-100	30-350	16	N/A
NovaSAR-S 1	UK	2018		574-592	14-57.3	9.4 (S)	6-30	13-400	14	N/A

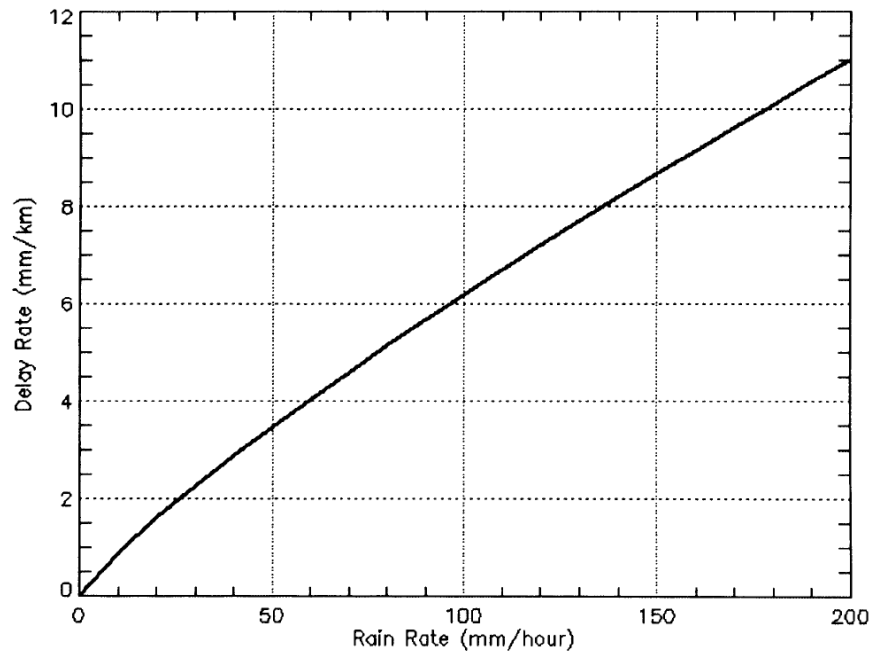


Figure 2.19 C-band scattering path delay due to forward scattering in the rain (Li, 2005)

### 2.3.2. Radar Equation

Radar equation is defined by the principle of power transformation from the transmitter (or back) to the receiver (wave propagation). The receiving power ( $P_r$ ) is determined by the reflection characteristics of the target (radar cross-section  $\sigma$ ), the slant range ( $R$ ), and the transmitted power ( $P_t$ ) (Stiglitz and Resnick, 1989; Levanon, 1988), as shown in Figure 2.20. The radar equation is the foundation of all radar technology, which is shown in Equation (2.7) below.

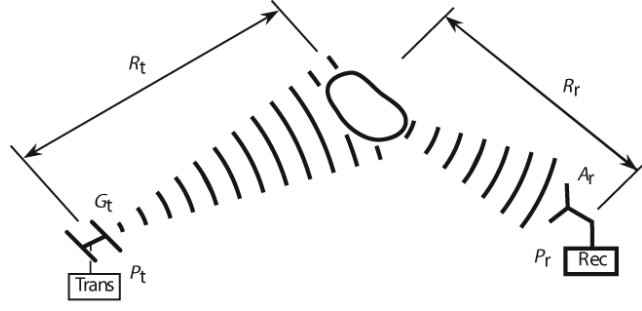


Figure 2.20 Radar equation principal (Stiglitz and Resnick, 1989; Levanon, 1988), the left antenna is a transmitter, and the right one is a receiver

$$P_r = \frac{P_t}{4\pi R_t^2} \times G_t \times \sigma \times \frac{1}{4\pi R_r^2} \times A_r \quad (2.7)$$

where:

$P_t$  = peak transmit power (watts)

$G_t$  = transmit antenna gain (no units)

$R_t$  = radar transmit antenna to object range (metres)

$R_r$  = radar receive antenna to object range (metres)

$\sigma$  = target radar cross-section (square metres)

$P_r$  = received signal power (watts)

$A_r$  = the effective area of the receive antenna, square metres  $A_r = \rho A$

$\rho$  = antenna efficiency,  $0 < \rho < 1$  (no units)

$A$  = physical area of the antenna (square metres)

### 2.3.3. Synthetic Aperture Radar (SAR)

SAR is an advanced form of radar that exploits the motion of the sensor platform to achieve high-resolution microwave imaging (Ulaby et al., 2014). A simplified example of the geometry for a typical side-looking SAR system is illustrated in Figure 2.21. The antenna is mounted on a satellite or aircraft, which travels in the azimuth direction and views targets at different ranges (the range is the distance between the target and the phase centre of the antenna). The combination of range and azimuth characterises the native coordinates of SAR imagery and denotes points in the slant-plane. The main lobe of the radar antenna illuminates a finite area on the ground, and within this region, across-track components define the swath (Wortham, 2014). The far-field approximation defines the angular beam pattern as the Fourier Transform of the physical antenna aperture. Thus, the



shape of the antenna determines the swath and the azimuthal widths of the antenna footprint. For SAR imaging, the antenna is usually rectangular, and a two-dimensional sinc function approximates the transmit beam pattern, which is inversely proportional to the aperture size (Bracewell, 2003).

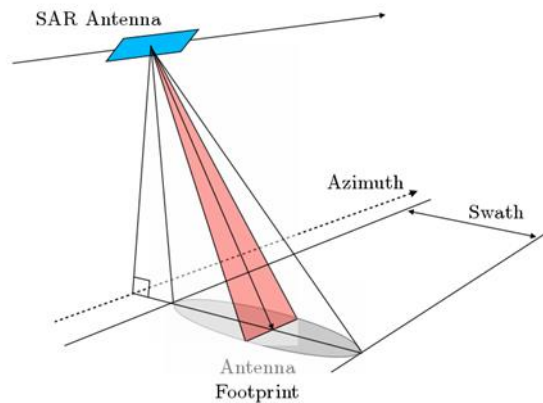


Figure 2.21 Flat Earth SAR imaging geometry (Wortham 2014), the satellite travels in the azimuth direction and views targets at a range

### 2.3.4. InSAR History and Current Research

In 1969, Rogers (Rogers and Ingalls, 1969) first reported an interferometry radar (with its base antenna station on Earth) application to map the planet, Venus. Zisk (Zisk, 1972) used the same method to achieve a measure of lunar surface topography. Graham (Graham, 1974) first introduced interferometric measurement technology into SAR signal processing in airborne InSAR systematic observations to measure changes in topography. The advances in InSAR technology developed in recent years include time series InSAR, aperture InSAR technology - multi-aperture InSAR (MAI), PolInSAR, SAR tomography, Multi-time InSAR (MTI, e.g. StaMPS/MTI) and SqueeSAR (squeeze SAR) technology (Kuzuoka et al., 2013; Herrera et al., 2007). However, to make the technology more useful, more research needs to be carried out to make it more robust, accurate and reliable.

### 2.3.5. InSAR Principles

Spaceborne InSAR, which uses the interferometric phase, is a well-developed technique for DEM production (Feng et al., 2015). The typical InSAR geometry (Bamler and Hartl, 1998) is shown in Figure 2.22 below.

## Chapter 2. Literature review

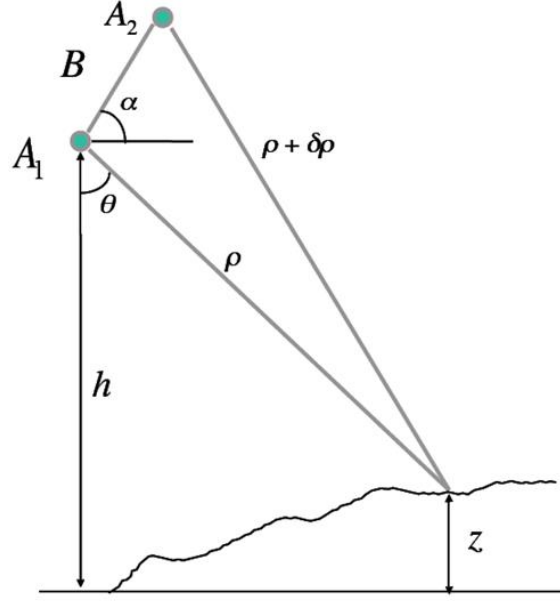


Figure 2.22 Typical geometry of InSAR (Bamler and Hartl, 1998),  $B$  is the baseline vector,  $\rho$  is the range,  $\delta_\rho$  is the range difference,  $h$  is the height of SAR above a reference plane,  $z$  is the topography elevation,  $\theta$  is the look angle,  $\alpha$  is the baseline angle

$$\varphi = -\frac{4\pi}{\lambda} \delta_\rho \quad (2.8)$$

$$\sin(\theta - \alpha) = \frac{(\rho + \delta_\rho) - \rho^2 - B^2}{2\rho B} \quad (2.9)$$

$$z = h - \rho \cos\theta \quad (2.10)$$

In Figure 2.22, Equation (2.8), (2.9), and (2.10),  $B$  is the baseline vector,  $\rho$  is the range,  $\delta_\rho$  is the range difference,  $h$  is the height of SAR,  $z$  is the topography elevation,  $\theta$  is the look angle,  $\alpha$  is the baseline angle,  $\varphi$  is InSAR phase,  $\pi$  is 3.14. According to the equations<sup>9</sup> above, if we want to learn DEM height, we need to know an extreme accurate baseline ( $B$ ,  $\alpha$ ) and total differential phase, both of which are easy to obtain from InSAR processing (Bamler and Hartl, 1998). The basic premise of InSAR is that by taking the phase (range phase and scattering phase) difference of two SAR scenes, the scattering phase components in the same pixel position can be assumed as the same (when they are differential in InSAR, it becomes 0), and the obtained phase is proportional to the differences in range. Firstly, raw data with satellite calibration information must be

<sup>9</sup> Source:2012 USGS & CASM training lecture note--Radar signal processing and InSAR processing

focused to a single look complex (SLC) image by using an imaging algorithm. After focusing, the next critical steps include atmospheric and ionospheric correction and co-registration; then conjugate multiplication is used to calculate the phase difference pixel-by-pixel between the master and slave SLC (interferogram calculation) (Bamler and Hartl, 1998). Following the interferogram calculation, baseline estimation, removal of flat earth phase, phase unwrapping, baseline refinement, height calculation and geocoding are executed to obtain a DEM. The flowchart of DEM production is shown in Figure 2.23 below. These key technologies will be described in detail in the following section.

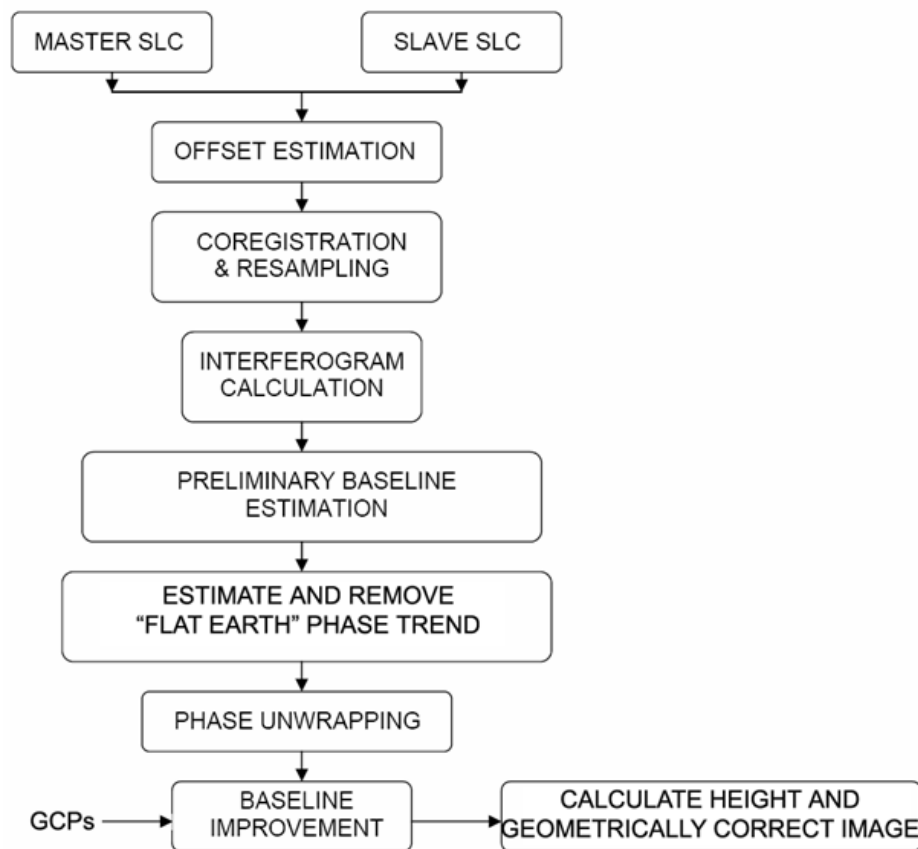


Figure 2.23 The flowchart of DEM production<sup>10</sup> by using InSAR

### 2.3.6. InSAR for DEM Key Processing Technology

The flowchart of DEM generation technologies is shown above, and here follows a brief description.

<sup>10</sup> Source: 2012 USGS & CASM training lecture note - Radar signal processing and InSAR processing

## Chapter 2. Literature review

### 2.3.6.1. SAR calibration

SAR calibration includes internal calibration (antenna pattern, gain drift, noise equivalent sigma zero, total zero Doppler steered), stable orbit calibration, absolute radiometric calibration, polarimetric calibration and geometric calibration, etc. (Jackson and Woode, 1992; Lancashire, 1987; Meadows, 1992; Freeman, 1992; Schwerdt et al., 2010). In addition to pre-flight calibration, the antenna pattern measurement of in-flight calibration also matters for spaceborne SAR. The in-flight measurements of spaceborne SAR antenna patterns are needed by SAR calibration through the use of corner reflectors, ground receivers, ground transmitters, external characteristic factor method, natural objects (like the Amazon Rainforest) and model measurement methods (Ji, 2012).

### 2.3.6.2. SAR Imaging

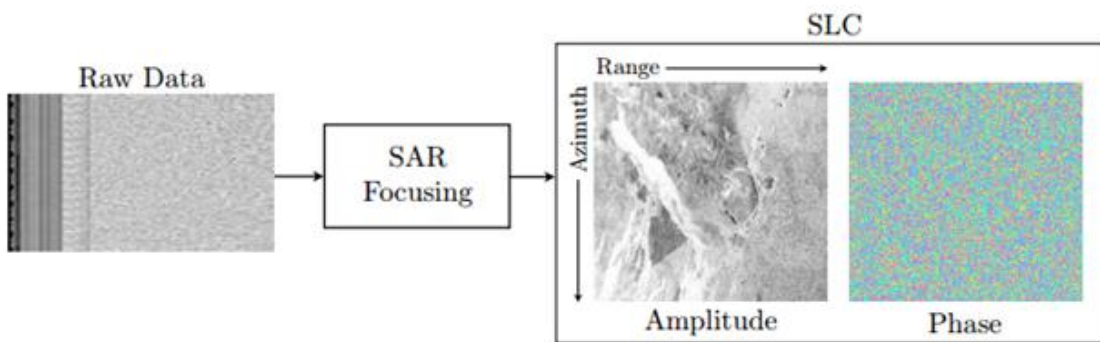


Figure 2.24 Simplified SAR processing chain. Raw data are received as I and Q samples. After focusing, the SLC is a two-dimensional complex image, with the amplitude representing the ground reflectivity and random phase between each pixel (Wortham 2014)

After raw satellite data is obtained, the raw data is focused into a single look complex image (SLC), with pixels denoting complex reflectivities in the slant-plane and accurate geolocation. It is known that the amplitude of a SLC image can be displayed as an image (shown in Figure 2.24) on the basis of the geometric and physical properties of electromagnetic scattering.

### 2.3.6.3. Imaging algorithms

SAR imaging algorithms include Back Projection (BP), SPECAN, Range Doppler (RD), Chirp Scaling (CS), Frequency Scaling (FS), W-K algorithm, Chirp-Z-Transform (CZT), Polar Format (PF) and the algorithms based on compressive sensing theory and new image modes (Wong et al., 2008; Comblet et al., 2006; Zhang et al., 2007; Ulander et al., 2010). Speckle suppression is one of the critical steps in the interpretation

and application of SAR image interpretability, and multi-look, spatial filtering method and transform filtering (FFT & wavelet) method are used to process the SAR data too (Wong et al., 2008). The SAR image compression techniques in the world have been widely discussed and can be summarised into four categories: (1) vector quantisation, (2) wavelet transformation, (3) content-based coding, and (4) compressed sensing (Costa et al., 2015; Donoho, 2006b).

Amongst all these algorithms, the range-Doppler (RD) algorithm is an effective and common one for SAR imaging. More specifically, the range-Doppler algorithm is an accurate approximation for SAR imaging processing for typical spaceborne imaging geometries, and it is computationally efficient. Meanwhile, the algorithm forming Single Look Complex (SLC) images is a phase-preserving method, which most fits burst data, and can be used to process full azimuth bandwidth (Bamler, 1992; Lord and Inggs, 1999; Neo et al., 2008; Wong et al., 1997). Recently, the SAR imaging algorithms based on compressive sensing are also promising because these algorithms are the most congruent ones for high resolution SAR imaging reconstruction based on sparse SAR raw data.

#### ***2.3.6.4. Space-Borne SAR Image Geolocation Algorithm***

The process of spaceborne SAR image pixel location is called geolocation, which relies on the geolocation model to geolocate each pixel accurately, ranging from image coordinates to real geographical coordinates in the Cartesian coordinate system ( $x, y, z$ ) or the geodetic coordinate system (longitude, latitude and height). Up to now, these geolocation models mainly include polynomial models, Leberl, Konecny, and RD (range-Doppler) model (Curlander, 1982). Figure 2.25 shows the SAR geolocation model in the Geocentric Equatorial Inertial (GEI) coordinate system, in which the earth centre is defined as the origin, the x-axis points toward the vernal equinox, the y-axis is defined to build a right-handed coordinate system, whereas the z-axis points to the North Pole (Liu et al., 2006). Based on the RD geolocation theory, three equations (shown below) are set up for a fixed target  $R_t(x_t, y_t, z_t)$  on the ground, which includes range, Doppler and Earth model equation (Liu et al., 2006).

## Chapter 2. Literature review

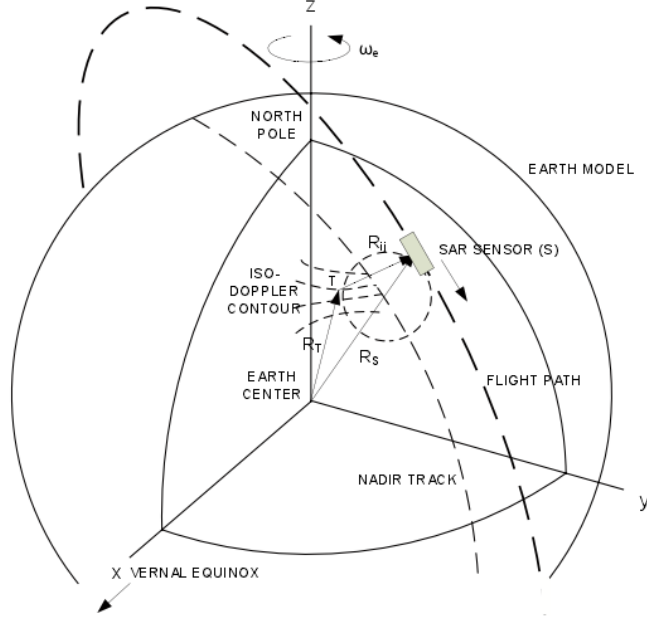


Figure 2.25 SAR GEI coordinate system (Liu et al., 2006), the black dot line is flight orbit around the earth with the target on earth

According to Figure 2.25, the first equation is the range equation,

$$R = |R_s - R_t| \quad (2.11)$$

where  $R_s$  is the sensor position vectors,  $R_t$  is the target position vectors, and  $R$  represents the distance between the target and the sensor, (Liu et al., 2006).

The second equation is the Doppler equation,

$$f_d = -\frac{2}{\lambda} \frac{(R_s - R_t)(V_s - V_t)}{|R_s - R_t|} \quad (2.12)$$

where  $V_s$  is the sensor velocity vector,  $V_t$  is the target velocity vectors,  $\lambda$  is the radar wavelength, and  $f_d$  is the Doppler frequency (Liu et al., 2006).

The third equation for RD mode is the Earth model equation,

$$\frac{x_t^2 + y_t^2}{(R_e + h)^2} + \frac{z_t^2}{R_p^2} = 1 \quad (2.13)$$

where  $h$  is the target elevation relative to the ellipsoid model,  $R_e$  is the equator radius, and  $R_p$  is the polar radius (Liu et al., 2006). Besides, the equation of  $R_p$  is defined as below, and  $f$  is the ellipsoid flattening factor.

$$R_p = (1 - f)(R_e + h) \quad (2.14)$$

Finally, the three unknown target geolocation parameters  $R_t(x_t, y_t, z_t)$ , can be obtained by the simultaneous solution of range equation (2.11), Doppler equation (2.12) and Earth model equation (2.13), which are illustrated in Figure 2.25.

### 2.3.6.5. *Baseline estimation*

Interferometric phase, which includes ground phase, terrain phase, deformation phase (linear and non-linear), atmospheric phase and other phases, is the key to InSAR data processing. Moreover, during processing, baseline estimation is the core parameter to measure the ground phase, given that the accuracy of the baseline estimation has a direct impact on the final relative and absolute height accuracy in InSAR processing. Basically, to obtain an accurate DEM by InSAR at the metre level, a minimum of the cm-level baseline estimate accuracy is required (Feng et al., 2015).

Baseline estimation methods (Bamler and Hartl, 1998; Ren Kun, 2003) can be classified into the following categories: 1) baseline estimation through the Doppler equation, the range distance equation and the Earth ellipsoid equation; 2) based on ground control points or a DEM; 3) the use of a precise orbit or registration rule; 4) assessment of the frequency of interference fringes in the ground plane. Previous studies have shown that baseline estimation based on the frequency of interference fringes requires the least information with compromising accuracy. Baseline estimation based on a precise orbit is completely dependent on the orbit, but the availability of precise orbit is low. Control points based baseline estimation method requires many control points to guarantee the high accuracy of baseline estimation. Similar to the control points method, the DEM based method is the best choice to achieve a higher-level accuracy of baseline estimation, mainly because many global DEMs have been produced from spaceborne EO sensors, such as from InSAR (SRTM, TerraSAR-X, TanDEM-X), stereo-photogrammetric (ASTER, SPOT, PRISM and IRS-3P) and LIDAR (ICESat) (Feng et al., 2015).

### 2.3.6.6. *Co-registration*

Accurate co-registration is crucial for InSAR (Scheiber et al., 1999). It is reported that 0.05-pixel misregistration error in azimuth direction results in a 15 m elevation error for SRTM DEM generation by InSAR (Bamler and Hartl, 1998; Holzner et al., 2001). Thus, an exact fine co-registration in azimuth direction is required for InSAR especially in rugged terrain. By contrast, the coherence drops only 0.003 through the previously mentioned misregistration (0.05 pixel) in the range direction (Just and Bamler, 1994). Generally, 0.01 pixel error (azimuth and range) is the common threshold for the co-

## Chapter 2. Literature review

registration step of InSAR processing (Just and Bamler, 1994). A typical SAR co-registration procedure is from coarse in terms of pixel level accuracy to fine subpixel accuracy (Li and Bethel, 2008). Moreover, Gabriel (Gabriel and Goldstein, 1988) discussed a sub-pixel registration method and an implementation method was proposed based on the correlation coefficient of two complex images, as well as the phase difference signal to noise ratio for two complex images; and recently this sub-pixel registration method has been widely used and is likely to be further developed in the future. Ferretti (Ferretti et al., 2011) proposed a function of the phase difference according to the mean disturbing image of two complex images to analyse the quality indicators and registration control point displacement vector, which focuses on phase noise and needs to depend on the range offsets, azimuth offsets, and the scaling factor in the range direction. Scheiber (Scheiber and Moreira, 2000) proposed that the interferometric SAR image spectral difference can be used for complex image co-registration, which neither needs any interpolation nor cross-correlation procedures and also no coherence or fringe optimisation is a necessity. Almost all of these co-registration methods have good registration results, but their efficiency is not high enough. Therefore, the study on co-registration is needed, given its direct influences on the results of interferometry.

### 2.3.6.7. *Phase unwrapping*

Phase unwrapping is the next critical step in InSAR data processing, and the unwrapping phase affects the outcome of the quality of DEM directly. Therefore, how to select the optimal phase unwrapping approach has been a focus among scholars, and many algorithms have been proposed by researchers. So far, phase unwrapping methods include path tracking, least squares, and optimal estimation algorithm. Goldstein (Goldstein et al., 1988) proposed a branch cut method interferometric phase unwrapping, which is widely used in the InSAR data processing. In Ghiglia's paper (Ghiglia and Romero, 1994), a two-dimensional phase-weighted least squares criterion was given as a solution to the unwrapping phase. The non-weighted least squares phase unwrapping method is equivalent to Poisson's equation of the second boundary conditions, using a fast-discrete cosine transform, while the weighted least squares phase unwrapping method is an iterative method. Fornaro (Fornaro et al., 1996a) proposed the least squares equation and unwrapping consistency method theoretically, and following that, Fornaro (Fornaro et al., 1996b) tested a multi-grid technology method for phase unwrapping, which is much better. Costantini (Costantini, 1998) discussed a fast phase-based network



solution to phase unwrapping, and Xu (Xu and Cumming, 1999) proposed a region growing phase unwrapping method. Chen and Zebker (Chen and Zebker, 2000) proposed an implementation of the Statistical-cost, Network-flow Algorithm for Phase Unwrapping (SNAPHU), which regards the phase unwrapping as a maximum posteriori probability estimation issue and uses three different built-in statistical models to solve it. Moreover, network-flow techniques have been used to solve the posed optimisation problem (Chen and Zebker, 2000). Yong and Wang Chao (Yong et al., 2002) proposed a phase unwrapping method named as ‘irregular network flow algorithm’, which can avoid noise error and guarantee the phase unwrapping in the high-quality regions, and then acquire good results. Based on many research and inter-comparisons (Chen and Zebker, 2000; Chen and Zebker, 2001; Zappa and Busca, 2008), the Goldstein approach (used in ROI\_PAC<sup>11</sup>) is widely used in InSAR data processing (Buckley et al., 2000); as well as SNAPHU which formulates comparable unwrapped solutions, and, in many tests (Chen and Zebker, 2000; Chen and Zebker, 2001; Chen and Zebker, 2002), the accuracy of SNAPHU is comparable with or better than that of other available algorithms.

## 2.4.DEM Generation from Photogrammetry and Radargrammetry

### 2.4.1. Photogrammetry for DEM

#### 2.4.1.1. Background

Nowadays, many countries have launched high resolution mapping satellites. Many satellite imaging corporations and agencies can provide users with  $\leq 1\text{ m} - 5\text{ m}$  DSMs, DTMs, and an orthorectified satellite image mosaic at  $\leq 1\text{ m}$  resolution. In the past, no satellite data is available in some remote areas, but at present, DEMs can be generated from stereo imagery from a variety of satellites (IKONOS, Pleiades-1, SPOT-5, SPOT-6, SPOT-7, GeoEye-1, WorldView-1, WorldView-2, and so on). The Triscopic-Stereo acquisition mode, unlike the three array sensor (PRISM) on ALOS and some other satellites, but similar with programmed 3D acquisition operations of Pleiades-1A and Pleiades-1B Satellites and other satellites, can obtain elevation that is hidden in urban

---

<sup>11</sup> ROI\_PAC (Repeat Orbit Interferometry Package) is a powerful open source software package for processing diverse satellite interferometric synthetic aperture radar (InSAR) data.

## Chapter 2. Literature review

canyons in densely built-up areas or steep terrain and mountains (Satimagingcorp, 2015), which is shown in Figure 2.26 below. Furthermore, current optical mapping satellites in the world are shown in Table 2.7. As it is shown in Table 2.7, in the future, thanks to the high precision, high-stability, high-dexterity platform technology and high-precision load technology, the mapping satellite will be developed from a multi-line array to a single line array detection & surveying and mapping satellite, this phenomenon will also happen in deep space exploration (including the planetary exploration) field.

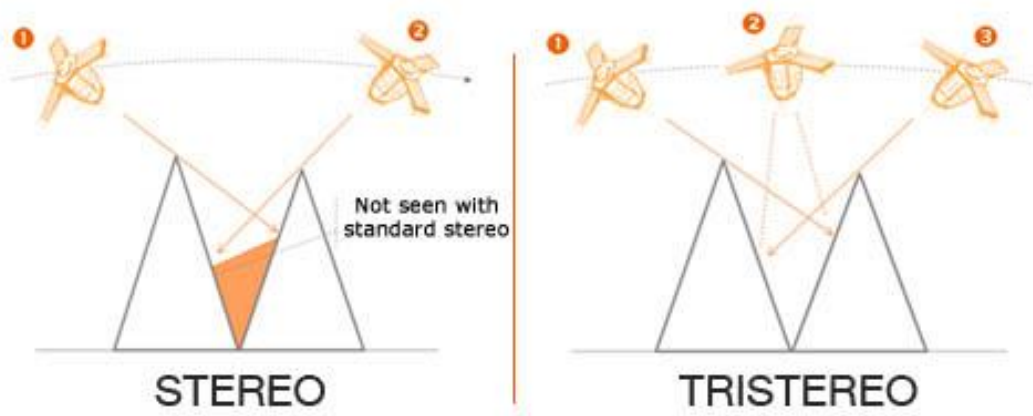


Figure 2.26 Stereo and tri-stereo comparison(Satimagingcorp, 2015), note the Tri-Stereo cameras can obtain elevation that is hidden in steep terrain or urban canyons in densely built-up areas

Table 2.7 Optical mapping satellites all over the world<sup>12</sup>

Satellite	country	Launch date	Sensor	Type	Number of Bands	Resolution	Revisited Period	Scan Bandwidth	Field of application
						(m)	(day)	(km)	
NEMO	USA	2000	AVIRIS	high	210	30	7	30	Coastal Zone Resources
			PIC	Panchromatic	1	5			
Rapid-Eye	Germany	2008	CCD	Multi-spectral	5	5.8/6.5	1/5.5	77	Mapping, Note: 90Resources and Environment (5 satellites)
MOMS	Germany	1999	MOMS	Panchromatic	3	4.5		37	Mapping, Resources and Environment
			CCD	Multi-spectral	4	13.5			
Sentinel-2B	Europe	2013		Panchromatic	5				Land, forestry, fishing
				Multi-spectral	10				
SPOT-5	France	2002	HRG	Panchromatic	1	2.5	26	60	Mapping, Resources and Environment
				Multi-spectral	4	10			
			HRS	Panchromatic	1	5,10			
CARTOSAT	India	2005	CCD	Panchromatic	2 Line Array	2.5	5	30	Mapping, Resources and Environment
ALOS	japan	2006	PRISM	Panchromatic	3 Line Array	2.5	46	70/35	Mapping, Resources and Environment
			AVNIR-2	Multi-spectral	4	10			

<sup>12</sup> Source: Photogrammetry lecture note of Wuhan University.

Satellite	country	Launch date	Sensor	Type	Number of Bands	Resolution	Revisited Period	Scan Bandwidth	Field of application
						(m)	(day)	(km)	
RazakSAT	Malaysia	2009	CCD	Panchromatic, Multi-spectral	1	2.5 5	1	20	LAND, Forest, Fishing industry
THEOS	Thailand	2008	CCD	Panchromatic	1	2	26	22	Mapping, land, agriculture, forestry, flood
				Multi-spectral	4	15		90	
EROS-1A	Israel	2000	CCD	Panchromatic	1	1.8	2.5	14	Resources and Environment
							10.5		
KOMPSAT-2	Korea	2006	CCD	Panchromatic	1	1		15	Topography, resource survey
				Multi-spectral	4	4			
IKONOS-2	The USA GeoEye	1999	IKONOS2	Panchromatic	1	1	2.9	11	Mapping, Resources and Environment
				Multi-spectral	4	4	1.6		
OrbView-3	The USA GeoEye	2003	OrbView-3	Panchromatic	1	1	3	8	Mapping, Resources and Environment
				Multi-spectral	4	4			
QuickBird-2	USA Digital Globe	2001	QuickBird2	Panchromatic	1	0.61	<6	16.5	Mapping, Resources and Environment
				Multi-spectral	4	2.44			

Satellite	country	Launch date	Sensor	Type	Number of Bands	Resolution	Revisited Period	Scan Bandwidth	Field of application
						(m)	(day)	(km)	
WorldView-2	USA Digital Globe	2008	WorldView-2	Panchromatic	1	0.46	1.1	16.4	Mapping, ocean, archaeology
				Multi-spectral	8	1.84	3.7		
GeoEye-1	The USA GeoEye	2008		Panchromatic	1	0.41	3	15.2	Mapping, Resources and Environment
				Multi-spectral	4	1.65			
Pleiades HR-1A 1B	France	2010	CCD	Panchromatic	1	0.7	13	20	Mapping, Resources and Environment
		2011		Multi-spectral	4	2.8			

## Chapter 2. Literature review

For remote sensing mapping satellites, the stereo mapping accuracy without the use of ground control points is an important indicator of the satellite's performance. Many factors affect the accuracy of satellite mapping, according to the principles of photogrammetry, including camera baseline errors, attitude errors, image point measurement errors and the camera's internal parameters such as the focal length and distortion. Except for the sensor itself, these error factors also involve the GPS satellite positioning system, the attitude measurement and control system and camera payload system (Wang, 2006). It is said that sensor development and design attitude measurement precision, precise orbit, radiometric calibration, geometric calibration and three-dimensional mapping are the key technologies of spaceborne photogrammetry (Wang, 2006). Regarding practical spaceborne mapping satellite design and DEM generation, we need to establish some standards to guarantee our accuracy, for example, the American geolocation standards for satellite survey mapping are shown in Table 2.8 below (Wang, 2006).

Table 2.8 American geolocation standard in satellite mapping (Wang, 2006)

<b>Scale Denominator</b>	<b>Ground pixel (m)</b>	<b>Contour line spacing CI (m)</b>	<b>Elevation error (m, 1<math>\sigma</math>)</b>	<b>Plane error (m, 1<math>\sigma</math>)</b>
50 000	5	20	6	15
25 000	2.5	10	3	7.5
Note: 90% (1.64* $\sigma$ ) error < control accuracy				

### 2.4.1.2. Spaceborne push broom optical imaging geometry model

Optical satellite imaging geometry models are an attempt to model the physical geometry (Rigorous model). One of the optical satellite imaging geometry models is shown in Figure 2.27 below, which shows the relationship between the satellite and ground targets. (Wang, 2006)

The calculation formula of the optical satellite imaging geometry model is shown in Equation (2.15) below. This model is widely used along with various satellite orbital models (Low-order Polynomial Model, Piecewise Polynomial Model, Orientation Interpolation Model) within DEM generation. It is also used in satellite calibration frequently with an additional interior calibration parameter model (Zhang, 2000) and other satellite orbital models (Chen, 2008).

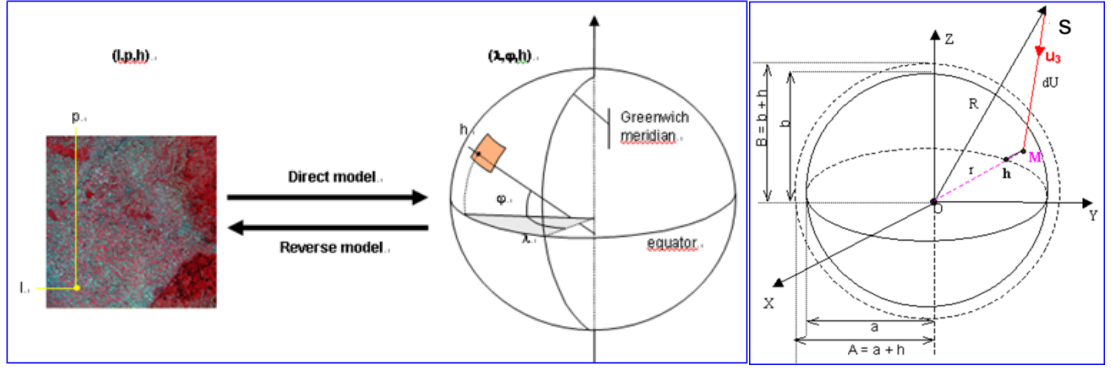


Figure 2.27 Optical satellite imaging geometry model (Wang, 2006), showing the relationship between satellite and targets

$$\begin{bmatrix} X \\ Y \\ Z \end{bmatrix}_{WGS84} = \begin{bmatrix} X_{GPS} \\ Y_{GPS} \\ Z_{GPS} \end{bmatrix} + R_{J2000}^{WGS84} R_{star}^{J2000} (R_{star}^{body})^T \quad (2.15)$$

$$\begin{bmatrix} D_x \\ D_y \\ D_z \end{bmatrix} + \begin{bmatrix} d_x \\ d_y \\ d_z \end{bmatrix} + R_{camera}^{body} \begin{pmatrix} -\tan(\psi_y) \\ \tan(\psi_x) \\ 1 \end{pmatrix} * f$$

where:

- 1)  $X, Y, Z$  refer to the ground point coordinate values of the coordinate system
- 2)  $WGS84$  and  $J2000$  are coordinate systems (Wang, 2006)
- 3)  $X_{GPS}, Y_{GPS}, Z_{GPS}$  are the satellite coordinate values in the coordinate system
- 4)  $x, y$  are coordinates of the image, like a point in the coordinate system of the image
- 5)  $f$  is the focal length of the camera
- 6)  $R$  is the coordinate system conversion matrix

The satellite orbital models (like second-order polynomials) (Chen, 2008), which are used to calculate the satellite coordinate values and the coordinate system conversion matrix of the above Equation (2.15), are shown in the equation below.

$$\begin{aligned} X_i^c &= a_0 + a_1 t + a_2 t^2 & \omega_i^c &= d_0 + d_1 t + d_2 t^2 \\ Y_i^c &= b_0 + b_1 t + b_2 t^2 & \varphi_i^c &= e_0 + e_1 t + e_2 t^2 \\ Z_i^c &= c_0 + c_1 t + c_2 t^2 & \kappa_i^c &= f_0 + f_1 t + f_2 t^2 \end{aligned} \quad (2.16)$$

where  $\omega_i^c, \varphi_i^c, \kappa_i^c$  are the pointing angles of the  $i$ th point or image row;  $X_i^c, Y_i^c, Z_i^c$  represent the perspective centre position of the sensor of the  $i$ th point or image row;  $a_0,$

## Chapter 2. Literature review

$b_0 \dots f_2$  are the polynomial coefficients and  $t$  refers to the time. In this way, the 36 polynomial coefficients in the stereo pair can be adjusted in bundle adjustment calculation to obtain the refined Exterior Orientation (EO) parameters (Chen, 2008).

### 2.4.1.3. Rational Function Model ---- RPC

Another option of sensor modelling in DEM production is the Rational Function Model (RFM) based on Rational Polynomial Coefficients (RPC), which is frequently used by many companies and institutes. Besides, the Open Geospatial Consortium (OGC) adopted RFM as the standard image transfer format (OGC, 1999). Compared with the rigorous sensor model (shown above in Section 2.4.1.2), the RFM establishes a geometric relationship between the ground coordinates of the objects and corresponding image coordinates, which is simple and easy to be understood and efficient for high resolution satellite mapping (Liu et al., 2006; Yu et al., 2017a). More importantly, it does not need to provide precise orbit information for users. The RPC model (Wang, 2006) equation is shown below (Equation (2.17) and (2.18)):

$$x = \frac{a_0 + a_1X + a_2Y + a_3Z + a_4X^2 + a_5XY + a_6Y^2 + \dots}{1 + b_1X + b_2Y + b_3Z + b_4X^2 + b_5XY + b_6Y^2 + \dots} \quad (2.17)$$

$$y = \frac{c_0 + c_1X + c_2Y + c_3Z + c_4X^2 + c_5XY + c_6Y^2 + \dots}{1 + d_1X + d_2Y + d_3Z + d_4X^2 + d_5XY + d_6Y^2 + \dots} \quad (2.18)$$

where:

- 1)  $X, Y, Z$  are ground point coordinate values of the coordinate system
- 2)  $x, y$  coordinates of the image
- 3)  $a_i, b_i, c_i, d_i$  are rational polynomial coefficients

### 2.4.1.4. DEM generation from photogrammetry

In principle, a photogrammetric DEM can be generated based on the collinearity equation, which is a physical model (Rigorous model) establishing the geometric relationship between ground coordinates of the objects and the corresponding image coordinates (Xu et al., 2010). However, another alternative Sensor Model called Rational Function Model (RFM), based on Rational Polynomial Coefficients (RPC), is also popularly used in practical production.

The classical photogrammetric workflow for DSM generation via stereo images is shown in Figure 2.28 below. In the orientation step, the RPC model or a rigorous model is utilised. With the images imported along with RPC and metadata parameters, image pyramids are generated. Then tie points in two or more images are extracted and control



points (i.e. street furniture, crossing roads, etc.) are measured for matching to calculate the relative and absolute orientation of image pairs (tie points are auto-measured or artificial assisted) (Poli and Caravaggi, 2012). After automatic tie point detection and photogrammetric bundle adjustment, interior and exterior orientation parameters are obtained. Then, the DSM (3D coordinates in object space) is generated with dense stereo image matching between stereo images. In the final step, the mask operations (rivers, oceans, lakes ...) and the additional manual editing (like blunder filtering or tree and building removal) are applied to improve the DSM quality (Poli and Caravaggi, 2012).

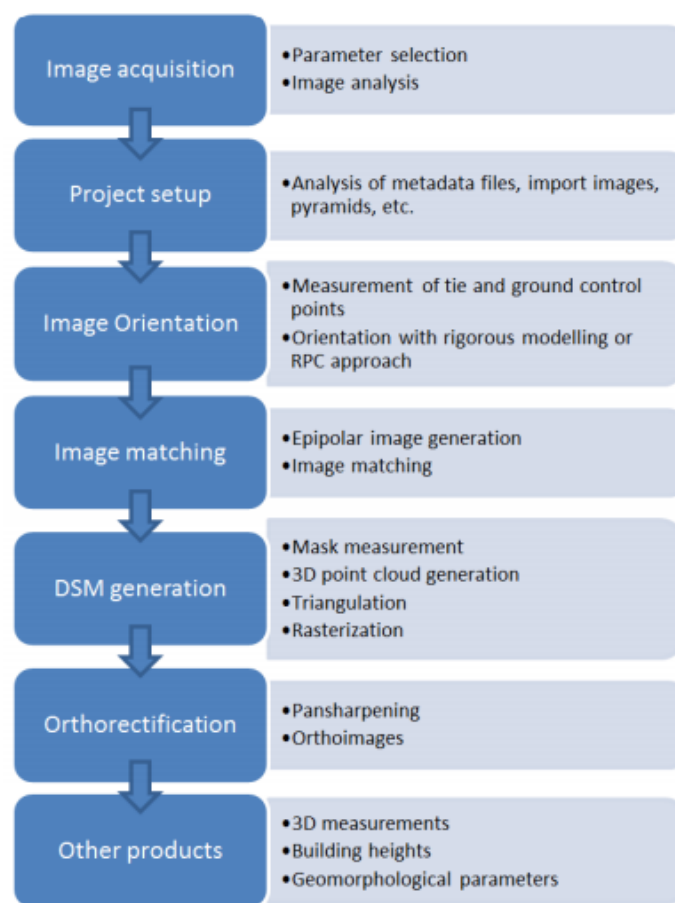


Figure 2.28 The 3D information extraction workflow from stereo imagery via a rigorous model or RPC model (Poli and Caravaggi, 2012)

### 2.4.2. DEM Generation from Radargrammetry

Digital surface models (DEMs) can be generated by Synthetic Aperture Radar (SAR) images using radargrammetry techniques. Radargrammetry using magnitude (intensity) is less affected by atmospheric influence when compared to TomoSAR using

## Chapter 2. Literature review

phase. Theoretically, the radargrammetric procedure includes three main stages: an accurate geometric correspondence between image space and object space must be established firstly; then, it is needed to solve the inverse trisection problem and the coordinates  $(X, Y, Z)$  of each terrain point, whose image coordinates  $(x_{col1}, y_{line1})$  and  $(x_{col2}, y_{line2})$  are found via a matching process, are obtained. The huge number of points obtained are introduced into a finite-element block bundle adjustment where the whole DEM area is divided into blocks & tiles, and continuity constraints between tiles are imposed. Consequently, the final raster DEM (regular grid) is obtained by dense matching after blunders and wrong matches are eliminated (Crosetto and Aragues, 1999). Matching and bundle adjustment are the key steps for radargrammetry. In the process of bundle adjustment, the range-Doppler (RD) model (introduced previously in Section 2.3.6.4) with non-attitude-sensitive orbit model is used.

Radargrammetry is a classic method to generate relatively high-quality DEMs using SAR images based on stereogrammetry. (Paillou and Gelautz, 1999). Compared to Interferometric Synthetic Aperture Radar (InSAR), radargrammetry is less likely to be influenced by the atmosphere, due to the fact that there are very weak atmospheric effects on the SAR image intensity for radargrammetry (Yu et al., 2010), especially for longer radar wavelengths. More specifically, InSAR uses the phase of the SAR image, while radargrammetry uses the magnitude (intensity or amplitude) value of the SAR image. Although the ionosphere causes spatially and temporally varying shifts, the intensity of the SAR image is less contaminated than the phase by atmospheric heterogeneity (Yu et al., 2010). Besides, the atmospheric disturbance is not the main issue in radargrammetry processing (Massonnet and Souyris, 2008). Generally, the radargrammetry technique for terrain elevation extraction based on stereoscopic pairs acquires at different incidence angles, which requires the incidence angle of the observation with about 10 to 20 degrees difference between two input image pairs over the same area (Mercer, 1995; Paillou and Gelautz, 1999). Spaceborne SAR stereogrammetry can be categorised into two types, namely, the same side stereogrammetry and opposite side stereogrammetry. The former one is relatively easy with the same image storage order, but the intersection angle is small, and the theoretical intersection accuracy is low. The stereoscopic angle of the opposite side stereogrammetry fits stereogrammetry better, but the descending and ascending image storage order is completely different, while it is relatively difficult to conduct the image matching and stereoscopic observation (Yu et al., 2010). Therefore, the SAR imaging collection plan of descending and ascending mode data, and the proper

selection of intersection angles for more accurate DEM products is needed. Moreover, the matching method and bundle adjustment range-Doppler (RD) model are critical to process large area data in radargrammetric applications.

### **2.5.LIDAR and Radar Altimeters (CryoSat-2) for DEMs**

Airborne LIDAR utilises a laser instrument mounted on an aircraft to measure the distance between the aircraft and objects based on the travel time of the laser light. Airborne LIDAR Bathymetry (ALB) systems can be used to measure a certain distance (depth) beneath the water surface; however, their effectiveness depends entirely on the transparency of the water. LIDAR systems have no cloud penetration capabilities if cloud optical depth  $\gg 3$ , but it can be operated during day and night (NASA, 2010). The LIDAR Point Cloud (LPC) of the USA provided by the United States Geological Survey (USGS) are available for the public. These points are stored as LIDAR Standard Data Format (LAS) with geo-referenced  $x, y, z$  (elevation) coordinates and other attributes. Besides, there are ground-based three-dimensional (3D) terrestrial laser scanner (TLS) for LIDAR data acquisition, for example, the RIEGL VZ-1000, which uses a narrow infrared laser beam and a fast scanning mechanism (based on a fast rotating multi-facet polygonal mirror) with echo digitisation and online waveform processing for LIDAR data collection.

The GLAS (the Geoscience Laser Altimeter System) on ICESat (Ice, Cloud, and land Elevation Satellite) was the first spaceborne LIDAR instrument for global Earth observations (NASA, 2010), which is a laser system used to measure distance, on the basis of the precise orbit and attitude information from a Global Positioning System (GPS) receiver and a star-tracker attitude determination system (Feng and Muller, 2016). The laser transmitted short pulses (4 nanoseconds) of visible green light (532 nanometres) and near-infrared light (1064 nanometres wavelength) (Feng and Muller, 2016). Laser pulses were emitted at 40HZ to shine 70 metres (diameter) spots with 170 metres interval spacing (NASA, 2010). Moreover, the full global data on waveform LIDAR from 2003 to 2009 was collected (Feng and Muller, 2016), whose elevation product has high vertical accuracy ( $\leq 1$  m) and could be used to evaluate the quality of other DEMs (Feng and Muller, 2016). It is well known that SRTM C data is validated by ICESat data because

## Chapter 2. Literature review

LIDAR has high vertical accuracy (Carabajal and Harding, 2005). Furthermore, the Mercury Laser Altimeter (MLA), the Mars Orbiter Laser Altimeter (MOLA) and the Lunar Orbiter Laser Altimeter (LOLA) also provide a precise topographic model and geodetic grid for planetary exploration (Anthony et al., 2010).

CryoSat-2 was launched on April 8<sup>th</sup>, 2010, and the interferometric radar altimeter with twin antennas is the main instrument to measure the distance between open water and floating ice (Helm et al., 2014; Labroue et al., 2012; Sandwell et al., 2013). CryoSat-2 can precisely monitor changes in the thickness of floating ice in the polar sea and those of ice sheets in Greenland and Antarctica. Moreover, DEMs can be generated in these areas using CryoSat-2 data. It is well known that SEASAT, GEOSAT, ERS-1, TOPEX/POSEIDON, ERS-2, GFO, Jason-1, Envisat-1, Jason-2 and Jason-3 (launched in 2016) all mount radar altimeters which can be used to make DEM or for DEM quality assessment (Sandwell et al., 2013; Helm et al., 2014).

## 2.6. Review of DEM for TomoSAR

In the processing of 3D TomoSAR imaging and 4D SAR differential tomography (Diff-TomoSAR), a high-quality reference DEM is essential for the derivation of reliable deformation measurements. Nowadays, an external DEM is necessary for ensuring the reliability of results by using it for co-registration, subtraction of topographic relief distortion effects, topographic compensation, height reference control points and georeferencing. A high-quality reference DEM is required by most SAR data processing (eg. InSAR, TomoSAR, PolInSAR, D-TomoSAR) to generate accurate results in various applications, such as monitoring earthquakes, volcanic activities, mining deformations, glacier movement, subsidence and landslides (Gabriel et al., 1989; Goldstein et al., 1993; Massonnet et al., 1993; Zebker et al., 1994; Tomas et al., 2010).

In TomoSAR processing, the shifts between a master and slave images result from a change in radar acquisition geometry, which depends on the orbit, topography and slope. Accurate (sub-pixel) image co-registration is the first processing step, an essential step as well, to avoid low phase coherence, since the conventional co-registration procedure based on an approximate polynomial warp function becomes inaccurate when dealing with rough topography, long interferometric baselines and especially high-resolution SAR imagery (Nitti et al., 2011).

In TomoSAR processing, a reference DEM is required for flattening the topographic phase, compensating the backscattered power measurements and geocoding the TomoSAR products. Firstly, to perform terrain topography correction, phase correction is needed to remove the ground phases from the original SLC data stack. After baseline interpolation and phase calibration steps, tomographic imaging algorithm (like Fourier transform, Capon<sup>13</sup>, and so on) is executed with the multi-baseline SLC stacks at every azimuth and slant range pixel location (D. Ho Tong Minh et al., 2016). Subsequently, a multilayer complex data result is obtained with a fixed height interval above the terrain (DEM). Finally, the terrain (DEM) is used to map the multilayer data stack onto the ground geometry (georeferencing step) with high resolution as well as high vertical and planimetric accuracy (D. Ho Tong Minh et al., 2016).

## 2.7. Review of Atmospheric and Ionospheric Correction

Atmospheric delay of SAR mainly includes ionospheric delay and tropospheric delay. Thus both corrections need to be addressed for different microwave wavelengths involved.

### 2.7.1. Atmospheric and Ionospheric Correction

#### 2.7.1.1. General maths principle and methods of atmospheric correction

The phase ( $\varphi_1$  and  $\varphi_2$ ) in a SAR image is shown in Equation (2.19) and (2.20) below (Ding et al., 2008; Zebker et al., 1997). In Equation (2.19) and (2.20),  $R_1$  and  $R_2$  are slant (oblique) ranges from the SAR system to the ground;  $\Delta R_1$  and  $\Delta R_2$  are radar signal delays when passing through the atmosphere due to pressure, atmospheric temperature, water vapour, etc.;  $\lambda$  is the radar wavelength.

$$\varphi_1 = -\frac{4\pi}{\lambda} (R_1 + \Delta R_1) \quad (2.19)$$

$$\varphi_2 = -\frac{4\pi}{\lambda} (R_2 + \Delta R_2) \quad (2.20)$$

---

<sup>13</sup> The Capon is an adaptive beamforming Capon spectrum method, which uses the inverse of the covariance matrix, in order to weight the individual elevations adaptively according to their estimated power. J. Capon proposed the Capon spectrum estimation method in his paper “High-resolution frequency-wavenumber spectrum analysis”

## Chapter 2. Literature review

The interferometric phase is shown in Equation (2.21) below,

$$\varphi = \varphi_1 - \varphi_2 = -\frac{4\pi}{\lambda}(R_1 - R_2) \pm -\frac{4\pi}{\lambda}(\Delta R_1 - \Delta R_2) \quad (2.21)$$

where  $-\frac{4\pi}{\lambda}(\Delta R_1 - \Delta R_2)$  is the atmospheric delay phase that needs to be corrected in processing,  $\Delta R_1$  and  $\Delta R_2$  are atmospheric propagation delays in the LOS (line of sight) direction, which is computed from the integral between the top of the troposphere and the surface elevation  $z_0$  (Baby et al., 1988).

$$\begin{aligned} \Delta R &= 10^{-6} \int_{z_0}^{\infty} N dz \\ &= 10^{-6} \left[ \frac{k_1 R_d}{g_m} P(z_0) + \int_{z_0}^{\infty} \left( k_2 \frac{e}{T} + k_3 \frac{e}{T^2} \right) dz \right] M_e \end{aligned} \quad (2.22)$$

In the above expression,

$P(z_0)$  is the pressure of the surface (Pa);

$N$  is the refractive index;

$e$  is the water vapour pressure (Pa);

$g_m$  is the average tropospheric gravitational acceleration ( $\text{m/s}^2$ );

$T$  is the temperature (K);

$M_e$  is the transform parameter, which projects zenith total delay (ZTD) to slant range direction calculated using elevation angles;

Other parameters are constant parameters, generally,  $R_d = 287.05 \text{ J K}^{-1} \text{ kg}^{-1}$ ,  $k_3 = 3.75 \times 10^3 \text{ K Pa}^{-1}$ ,  $k_2 = 0.233 \text{ K Pa}^{-1}$ ,  $k_1 = 0.776 \text{ K Pa}^{-1}$  (Yu et al., 2018).

ZTD consists of two parts, zenith wet delay (ZWD) and the hydrostatic part (ZHD, zenith hydrostatic delay). The physical parameter of water vapour is generally precipitable water vapour (PWV) in the atmosphere, and zenith wet delay (ZWD) has the following relationship to PWV.

$$\begin{aligned} \text{ZWD} &= \left[ 10^{-6} \rho_w \cdot \left( k' + \frac{k}{T_M} \right) \cdot R_v \right] \cdot \text{PWV} \\ &= \Pi \cdot \text{PWV} \end{aligned} \quad (2.23)$$

$k'$  and  $k$  are refractive constants,  $\rho_w$  is liquid density,  $T_M$  is the weighted average temperature of the troposphere, and  $R_v$  is the specific atmospheric constant.  $\Pi$  is a dimensionless scale factor (usually 6.0 - 6.5), 6.2 can be used in common cases (Ding et al., 2008; Zebker et al., 1997). Meanwhile, in Equation (2.24), (2.25) and (2.26) below,  $\delta_\varphi$  is atmospheric delay phase calculated by using ZWD;  $\delta_h$  is the height (elevation,

DEM) error caused by atmospheric delay; and  $\delta_{\Delta\rho}$  is the deformation error caused by atmospheric delay. On top of that,  $B_{\perp}$  is perpendicular baseline vector;  $R$  is range;  $\delta_{\varphi}$  is range difference;  $\theta$  is look angle. By using GPS, MODIS, MERIS, FY data with all the equations, it is easy to get PWV and to perform atmospheric correction (Li et al., 2005).

$$\delta_{\varphi} = \frac{4\sqrt{2}\pi}{\pi} \frac{1}{\cos \theta} \delta_{ZWD} \quad (2.24)$$

$$\delta_h = \frac{\lambda}{4\pi} \frac{R \sin \theta}{B_{\perp}} \delta_{\varphi} = \frac{\sqrt{2}R \tan \theta}{B_{\perp}} \delta_{ZWD} \quad (2.25)$$

$$\delta_{\Delta\rho} = \frac{\sqrt{2}}{\cos \theta} \delta_{ZWD} \quad (2.26)$$

#### 2.7.1.2. Research progress of atmospheric correction

Existing atmospheric correction methods mainly employ the correction methods which only use SAR images (e.g. PS), a numerical atmospheric model and correction methods which employ external water vapour sources (e. g. surface meteorological data plus operational weather models, MERIS, MODIS, GPS and an atmospheric numerical model). The propagation delay (Li et al., 2005) through the neutral atmosphere is a major error of InSAR. Massonnet et al. (Massonnet et al., 1994) conducted an InSAR experiment on the Landers earthquake of 1992 and first discovered the atmospheric influence in InSAR. Zebker et al. (Zebker et al., 1997) reported that a 10 - 14 cm error in deformation retrievals could be caused by 20% of spatial or temporal changes from relative humidity, and possibly 80 - 290 m of error in DEM generation with poor baseline estimation. Many techniques have been proposed and studied for atmospheric effect mitigation in interferograms, including stacking and calibration. Calibration methods involve spatial reduction of path delays using independent data, such as continuous GNSS networks (Bock and Williams, 1997; Williams et al., 1998), while lamination methods (stacking) can mitigate  $1/N^{1/2}$  of the temporally uncorrelated noise using temporal averaging of N-independent interferograms (Zebker et al., 1997). Up to now, the estimation approaches of the tropospheric signal in InSAR data include weather models (ERA-I (ECWF), MERRA, MERRA2, WRF) (Pinel et al., 2011; Wadge et al., 2002; Walters et al., 2013; Walters et al., 2014), GNSS data (Williams et al., 1998), spectrometer measurements (MERIS (Envisat), MODIS (AQUA and TERRA)) (Li et al., 2006), or the combination of spectrometer data with weather models (Walters et al., 2013) or the combination of spectrometer measurements with GNSS (Puysségur et al., 2007; Li

## Chapter 2. Literature review

et al., 2009), statistical DEM based methods (Bekaert et al., 2015), GACOS (GPS + DEM + ECWF high resolution) (Yu et al., 2017b) and PS methods (Ferretti et al., 2000; Hooper et al., 2004; Hooper et al., 2007). In our tomography processing, we will use some of these methods. The comparison of the InSAR atmospheric correction methods in terms of their advantages and disadvantages based on previous research is shown in Table 2.9 below.

Many high-resolution radar satellites like COSMO-SkyMed, TerraSAR-X, RADARSAT-2 and HJ-C have already been launched, and some high-resolution radar satellites will be launched in the near future. How to effectively remove the impact of the atmosphere on SAR data and how to calculate and improve the accuracy of atmospheric phase delay with the removal of atmospheric effects remain major challenges.

Table 2.9 Comparisons of InSAR atmospheric correction methods

Methods	SAR image data frame numbers	Other required data	Advantages	Disadvantages	Universality	Fields of application
By-pair analysis	At least 3	None	Qualitative judgments, recognition of the phase stripe atmosphere	Difficult to quantify	Medium	Deformation monitoring
Lamination (Zebker et al., 1997)	Many (N)	None	Assumed atmospheric effects as the main source of noise	The number of images needs more	Medium	Topography
Permanent scatterers method (Ferretti et al., 2000; Hooper et al., 2004; Hooper et al., 2007)	20 to 30	None	Solving deformation while removes the atmospheric phase	It requires a sufficient number of PS points. It cannot be used for fast deformation, vegetated areas and continuous surfaces.	Good	Point of land subsidence
Correction method based on meteorological information modelling (Pinel et al., 2011; Wadge et al., 2002; Walters et al., 2013; Walters et al.,	Unlimited	Meteorological data	No cloud restrictions	Lower accuracy, and the ground station sparse	Medium	Deformation monitoring



Methods	SAR image data frame numbers	Other required data	Advantages	Disadvantages	Universality	Fields of application
2014; Li et al., 2008; Baby et al., 1988)						
Correction method based on GPS data (Williams et al., 1998)	Unlimited	GPS data	High precision, without cloud limit, interval minutes	GPS site sparse, spacing a few to several hundred km	Good	Deformation monitoring
Space radiometer measurements (Li et al., 2006)	Unlimited	MERIS, MODIS, FY and other data	High spatial resolution of km stage in which up to 300m MERIS	Limited by cloud	Very good	Deformation monitoring
Atmospheric correction method based on a numerical atmospheric model (Wadge et al., 2002; Jolivet et al., 2014; Gong et al., 2010)	Unlimited	Numerical simulation of atmospheric models and parameters data	Higher spatial resolution, km level, time and time closer to the SAR data, without cloud limit,	Stability needs to be improved	Good	Deformation monitoring

### 2.7.2. Ionospheric Correction

The ionosphere is an ever-changing and complex open system, which constitutes a day-to-night system that influences radio signal propagation and enables radio communications. There is a strong coupling interaction between the ionosphere and other regions of the Sun-Earth system, including the mesosphere, the thermosphere, the magnetosphere, interplanetary medium and the Sun, shown in Figure 2.29 and Figure 2.30. Radio signals traversing through the ionosphere exhibit refraction delays, reflections, Faraday rotation, absorption, dispersion, depolarisation, scintillation and other effects (Hunsucker, 2013; Goodman, 2006). These effects have direct impacts on satellite navigation, satellite communications, SAR and radar, which reflect the error rate of the electronic information system, communication quality, positioning accuracy, distance, ranging accuracy and other performance indicators. Due to the disturbance of the earth's space environment caused by solar activities, ionospheric disturbance and ionospheric heterogeneity can even cause serious consequences such as the interruption

## Chapter 2. Literature review

of satellite communication & satellite navigation, the inability of SAR radar imaging, and the loss of targeting of space-based surveillance radar (Budden, 2009).

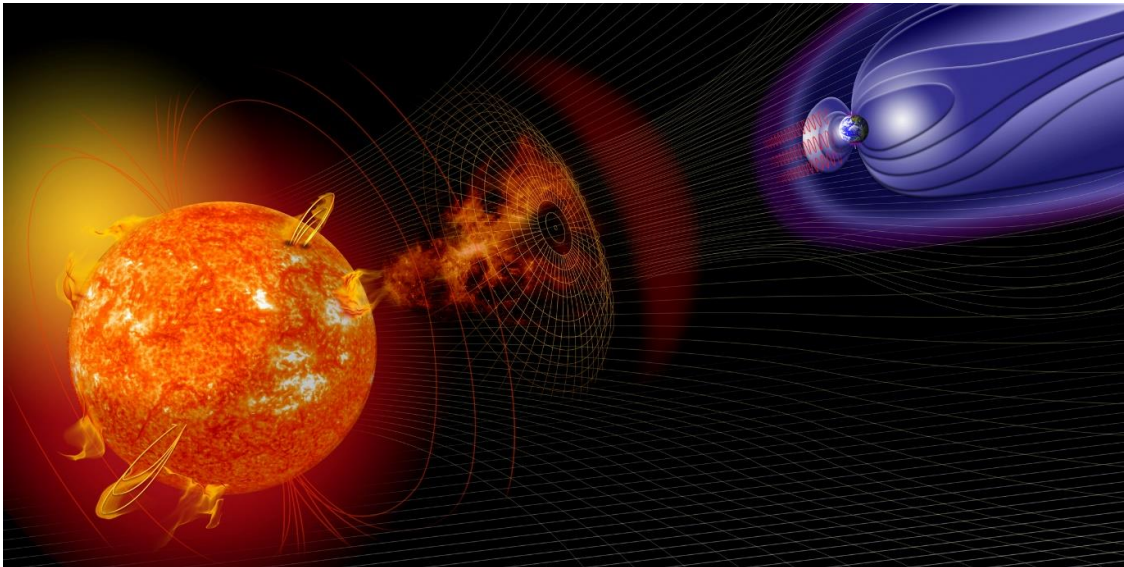


Figure 2.29 Solar wind and Earth's magnetosphere (NASA, 2016)

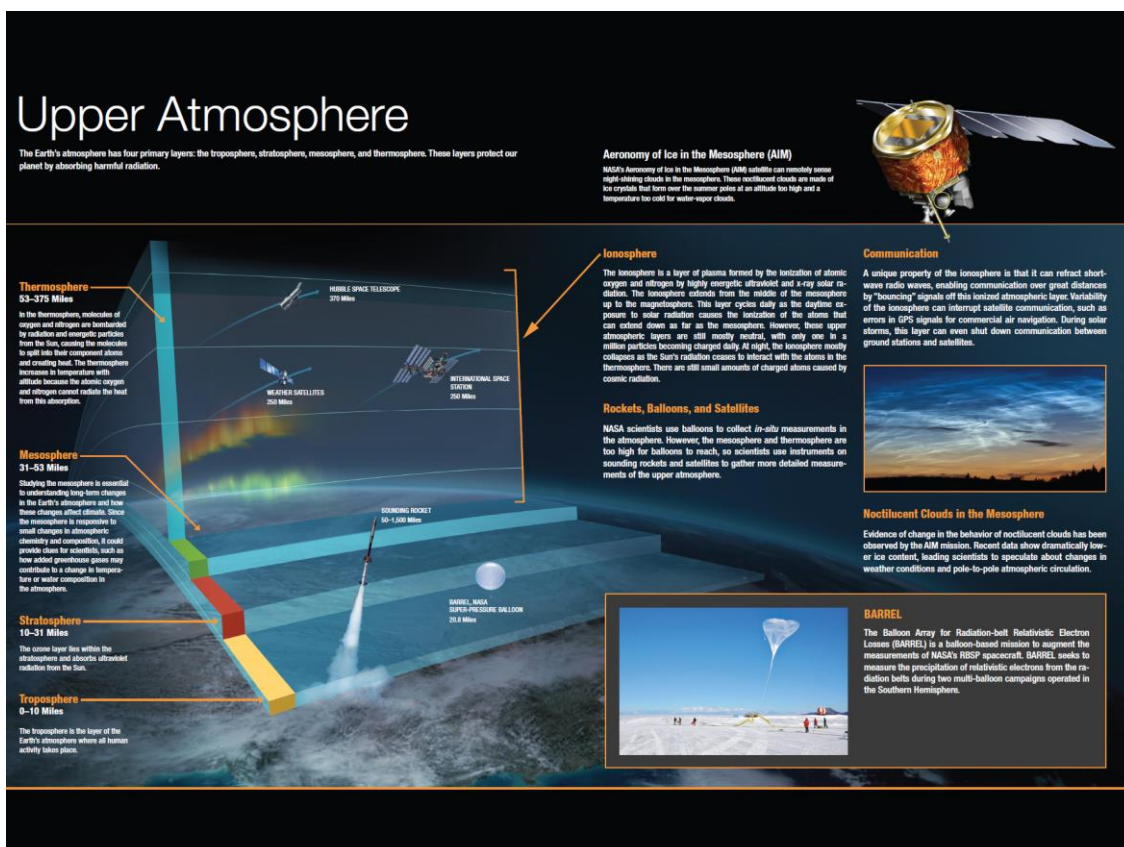


Figure 2.30 The Earth's upper atmosphere (NASA, 2015)

The ionisation of the upper-most part of the atmosphere by ultraviolet (or shorter) solar radiation or cosmic radiation produces a partial plasma of electrons and electrically

charged atoms and molecules (Kim, 2013). The process of controlling the ionosphere can be generally divided into two categories: one is known as "photochemical process", which leads to the generation and disappearance of the ionosphere; the other is termed the "transport process", which causes the diffusion and drift movement of the ionosphere. The relative importance of these two types of processes varies with height, and photochemical processes play a dominant role in the low ionosphere (D, E, F1 zones), whereas the F2 transport over the F1 zone gradually dominates (Kelley, 2009), as shown below in Figure 2.31 and Figure 2.32.

The purpose of ionospheric detection is to obtain information on the physical parameters of the ionosphere, such as ionospheric electron content, ion temperature, ion density, electron temperature, electron density, and their temporal/spatial variation and characteristics, including diurnal variation, seasonal variations, solar cycle change and global distribution, regional distribution, vertical profile and drift movement and other information. Through the study of these survey and detection results, physical and kinetic mechanisms such as ionospheric formation processes, morphology mode, ionisation transport, thermal energy transport and thermal equilibrium are revealed. The development of ionospheric research is a process of mutual promotion of testing and theory, including ground-based ionospheric detection and space-based ionospheric exploration. With the continuous development of ionospheric detection technology, many ground detection methods such as inclinometer, VLF radar, backscatter detector, incoherent scatter radar and ground-based airglow imager have emerged. The advantages of ground-based ionosphere detection lie in the fact that long-term continuous observation of the ionospheric environment in a selected area can be carried out by ground ionospheric detection equipment. Its disadvantage is that the distribution station is limited by the geographical environment. For example, it is not easy to carry out long-term foundation observation in marine areas (Sharp et al., 1977). Space-based ionosphere detection techniques can be divided into three categories: radio detection, optical remote sensing and in situ detection. For space-based ionosphere, radio detection mainly uses the ionosphere to extract ionospheric information from dispersion effects such as Doppler dispersion, time delay and Faraday rotation of satellite-loaded radio signals. For optical remote sensing, the Earth's ionosphere with the species of O, N<sub>2</sub>, O<sub>2</sub> and O<sup>+</sup> and other particles (electrons and ions, shown in Figure 2.31) releases extreme ultraviolet airglow light; observations can be analysed to understand the above content of particles, and then inverse temperature, density and other environmental parameters. The main load includes

## Chapter 2. Literature review

extreme UV imager, edge airglow imager, photometer, spectrometer, and so on. For in situ detection, instruments and equipment are carried on satellites or rockets for the local ionospheric physical parameters measurement, such as Langmuir probes, plasma analysers, magnetometers, electric field metres, neutral wind metres and spectrum analysers, to obtain ionospheric composition, electron temperature and density, electric field strength, magnetic field strength, neutral wind field, plasma spectroscopy and other information (Evans, 1974; Hayakawa, 2007; Melbourne et al., 1994; Benson, 2010; Pi et al., 2011; Zheng et al., 2009; Ouzounov et al., 2011).

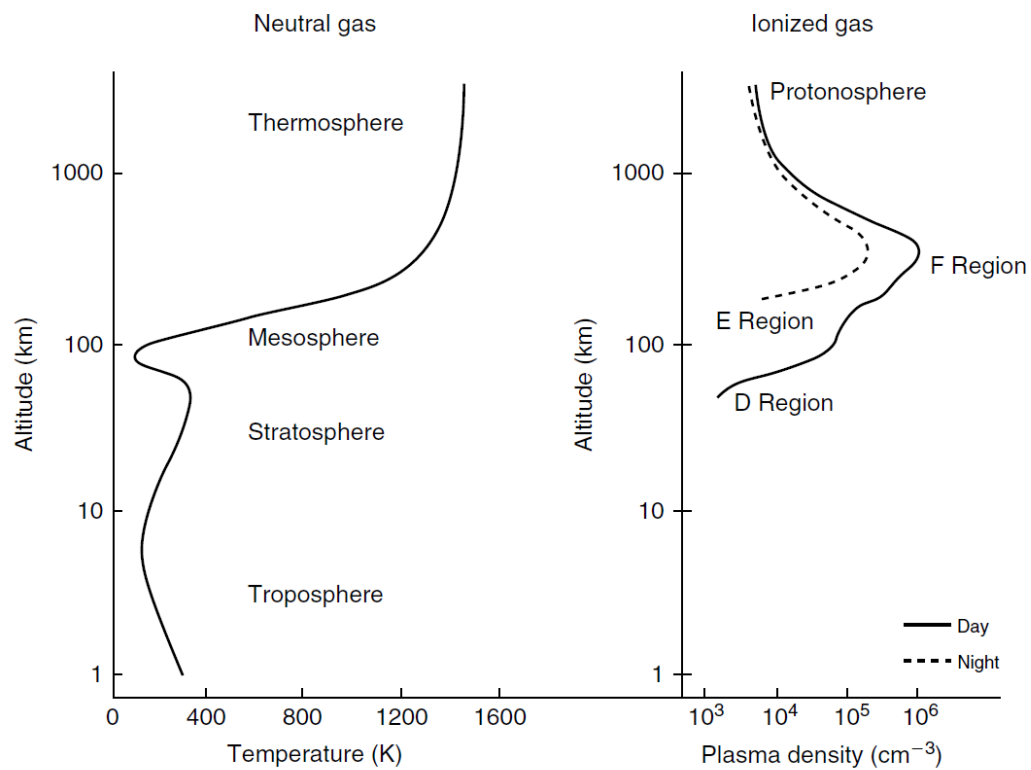


Figure 2.31 Earth's atmosphere and ionosphere plasma density (Kelley, 2009)

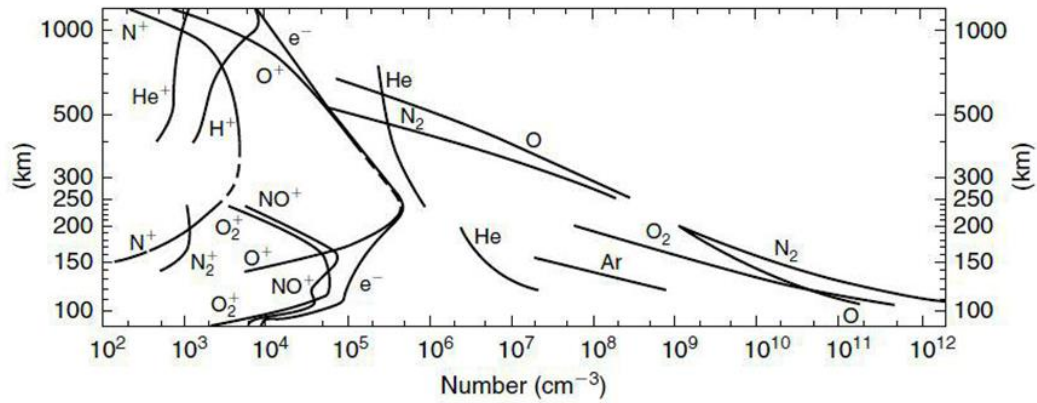


Figure 2.32 The composition of the Earth's atmosphere varies with altitude (Kelley, 2009)

The ionosphere refracts the EM waves that travel through it (Kim, 2013), which affects the propagation of EM waves at radio frequencies because of the ion and free electron contents in it (based on magnetoionic theory, particles and waves interact with each other). The free electrons and ions are formed by cosmic radiation or high-energy short-wavelength (mainly ultraviolet) solar radiation. The density number of free electrons increases with altitude and reaches its peak at approximately 250-400 km, while it decreases after this peak as the atmosphere becomes thinner (Kim, 2013). The ionosphere is often highly dynamic (spatial and temporal behaviour of the ionosphere), often coupled with both the Earth's atmosphere and the charged interplanetary media, because it is confined in the magnetic fields of both the Sun and the Earth (Kim, 2013). Large and small scale irregularities in the concentrations of electrons in the ionosphere are caused by the ionospheric instabilities. Moreover, unpredictable and abrupt solar activities precipitate charged particles into the ionosphere, which perturbs the spatial distribution of free electrons in the ionosphere. Such dynamic irregularities mostly occur in auroral and post-sunset equatorial zones (Belcher, 2008; Wright et al., 2003; Liu et al., 2003; Antennas and Committee, 1977; Aarons, 1982; Kelley, 2009). Therefore, some scientist split the ionosphere phenomenon into ionosphere background and scintillation. For ionosphere background, many models are studied, like GPS-based IGS TEC (Feltens and Schaer, 1998), while for scintillation, which can be described with the power-law scale size spectrum equation (Kim, 2013), the WBMOD (Secan et al., 1987) ionospheric scintillation mode is commonly used.

The accuracy of the TomoSAR and DInSAR techniques is greatly influenced by residual DEM error, orbital error, ionospheric and tropospheric phase delays, etc. In addition, for the ionospheric delay in InSAR and TomoSAR, compared to the influence

## Chapter 2. Literature review

of the ionosphere on all spatial scales, the small-scale ionospheric disturbances (scintillation) influence InSAR and TomoSAR significantly (Chapin et al., 2006). More specifically, the ionospheric phase artefacts particularly occur in long-wave SAR systems such as P-band and L-band SAR, for example, ALOS L band PALSAR (see the relative altitudes between ALOS PALSAR and the E-layer & F-layer of the ionosphere in Figure 2.33). Generally, phase distortion similar to orbital errors (for long wavelength), severe phase screens, azimuth streaking and decorrelation can be caused by the ionosphere (Kim, 2013). However, azimuth shifts (associated interferometric decorrelation), polarimetric distortion (Faraday rotation) and (differential) interferometric phase screens induced by the ionosphere can be corrected (Chen, 2013; Kim, 2013).

Phase artefacts in SAR images can be attributed to ionospheric delays in addition to neutral tropospheric delays. Ionospheric path delay  $R_{path\ delay}$  is in the simplified Equation (2.27).

$$R_{path\ delay} = \frac{40.28}{f^2} \Delta TEC \quad (2.27)$$

In Equation (2.27),  $f$  is frequency, and  $\Delta TEC$  is the differential TEC in the master and slave time. The quadratic frequency term in the equation suggests that increasingly significant path delays occur at lower frequencies, which means that the X-band is less influenced than the C-band and L-band. The azimuth shift caused by the ionosphere in interferograms results in azimuth streaks in SAR images (Chen, 2013). Gray et al. (Gray et al., 2000), Wegmuller et al. (Wegmuller et al., 2006), as well as Strozzi et al. (Strozzi et al., 2008) discovered and studied such azimuth streaks in L-band interferograms, and Meyer and Nicoll (Meyer and Nicoll, 2008a) investigated the theoretical background of this ionospheric influence. Pi et al. (Pi et al., 1997) proposed a technique to image the ionospheric inhomogeneities using spaceborne polarimetric SAR data and global GPS ionospheric TEC maps. By contrast, Jingyi Chen (Chen, 2013) directly obtained the azimuth mis-registration in radar interferograms by interpreting and using ionospheric TEC from independent GPS measurements simultaneously (Pi et al., 1997; Zebker et al., 1997). In addition, Gomba (Gomba et al., 2014; Gomba et al., 2016), used the range split-spectrum method to split the frequency bandwidth into two range subbands (lower subband and higher subband) and computed interferograms and ionospheric differential phase to correct the ionospheric influence for InSAR and compensate the ionospheric phase screen for the Sentinel-1 TOPS and ALOS-2 ScanSAR Modes data (Gomba et al., 2017). Fattahi et al. (Fattahi et al., 2017) extended the split range-spectrum technique to

correct the ionospheric influence for multitemporal InSAR (InSAR time-series analysis). Hu et al. (Hu et al., 2017) integrated the temporal-variant background ionosphere and the geosynchronous SAR (GEO SAR) long integration time model to obtain the 3D computerised ionospheric tomography imaging for GEO SAR. Moreover, the correction of the azimuth and range shifts and the Faraday rotation has been researched in several works in these references (Wegmuller et al., 2006; Chen and Zebker, 2012; Rignot, 2000; Wright et al., 2003; Freeman, 2004; Kimura, 2009; Meyer and Nicoll, 2008b; Gomba et al., 2016; Hu et al., 2017; Fattahi et al., 2017).

Overall, although many types of research have been carried out, the ionospheric correction accuracy still needs to be improved, and the effective detection and correction of ionospheric phase distortion from SAR images are necessary to be measured and addressed.

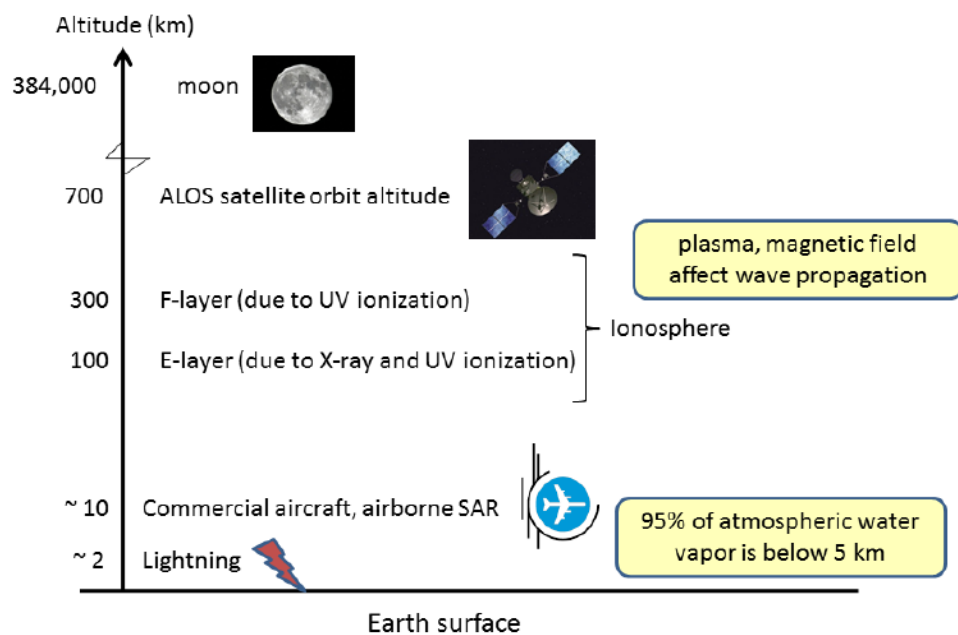


Figure 2.33 The conceptual illustration showing the E-layer and F-layer of the ionosphere and the relative altitudes of ALOS PALSAR. Note that the atmospheric water vapour that contributes to atmosphere noise is much closer to the ground than the ionosphere (Chen, 2013)

## 2.8. Summary

DEMs are important for 3D SAR tomography and 4D differential SAR tomography processing. Currently, spaceborne methods, including InSAR, photogrammetry, radargrammetry, LIDAR and radar altimeters are mainly used to

## **Chapter 2. Literature review**

generate DEM. With the development of these space-based methods, many global DEMs of Earth and other planets are being produced from spaceborne sensors now. DEM data, like other spatial datasets, has errors (random errors, systematic errors and blunders) because of many factors (atmosphere, complex terrain, satellites noise, processing methods, etc.). Therefore, how to generate DEM and use a reliable and validated DEM for 3D SAR tomography and 4D differential SAR tomography (Feng and Muller, 2017) needs to be studied.

Moreover, 3D SAR tomography and 4D differential SAR tomography are still influenced by temporal decorrelation, orbital, tropospheric and ionospheric phase distortion and height ambiguity. Therefore, how to explore the limits of 3D SAR tomography and 4D differential SAR tomography algorithms with a lot of ionospheric and atmospheric influences is still a problem remaining to be studied.



# **Chapter 3**

## **DEM Generation and DEM Quality Assessment**

In this chapter, a description of the DEM generation from TanDEM-X via the bistatic InSAR technique is first given, then the Bluesky DTM generation by using aerial photogrammetry from the stereo-optical data is introduced with an uncertainty discussion. Moreover, the quality assessment methods and the results of the validation of the TanDEM-X IDEM 12 m, 30 m and 90 m data of the UK, the SRTM 30 m data of the UK, the ASTER G-DEM 30 m data of the UK and the TanDEM-X DEM 90 m data of the UK using Bluesky DTM, KGPS (Kinematic GPS) and ICESAT ‘truth’ data are presented. What is important is that a new DEM co-registration (surface matching) method with line feature validation (river network line, ridgeline, valley line, crater boundary feature, and so on) is proposed, tested and demonstrated to assist the quality assessment of DEM datasets. Lastly, the high-resolution TanDEM-X 12 m DEM data in China with quality assessment using the SRTM DEM and ICESAT ‘truth’ data and its quality improved post-processing method for better TomoSAR accuracy is analysed and presented.

### **3.1 DEM Generation**

#### **3.1.1 DEM Generation from TanDEM-X**

### Chapter 3. DEM Generation and DEM Quality Assessment

TanDEM-X (TerraSAR-X add-on for Digital Elevation Measurements) opens up a new era in spaceborne radar remote sensing. TanDEM-X is a special spaceborne SAR mission (bistatic InSAR stripmap mode for DEM) that is formed by adding a second almost identical spacecraft instrument to TerraSAR-X and operating the two satellites in a closely controlled formation flight with typical inter-spacecraft distances between 250 and 500 m (Moreira et al., 2004; Zink et al., 2008). The TerraSAR-X and TanDEM-X fly in a helix constellation, which forms a high-precision radar interferometer formation in space. In this way, it enables the acquisition of highly accurate cross-track and along-track interferograms without the inherent accuracy limitations imposed by repeat-pass interferometry, like atmospheric disturbances and temporal decorrelation (Krieger et al., 2007).

Both X-band SAR satellites are based on active phased array technology, which includes Spotlight, Stripmap, and ScanSAR modes with full polarization capability. The centre frequency is 9.65 GHz, and the chirp bandwidth can be selected up to 300 MHz. The aperture size of the array antenna is about  $4.8 \text{ m} \times 0.7 \text{ m}$ , mounted on the spacecraft body with 12 panels and 32 waveguide subarrays for both H and V polarisations, which enables flexible beam shaping and agile beam pointing (Krieger et al., 2007).

The primary objective of the TanDEM-X mission is the generation of a worldwide, consistent, timely, and high-precision DEM based on the accuracy requirements (absolute vertical/horizontal accuracy  $< 10 \text{ m}$ , relative horizontal accuracy  $< 3 \text{ m}$ , relative vertical accuracy (slope  $\leq 20\%$ )  $< 2 \text{ m}$ , relative vertical accuracy (slope  $> 20\%$ )  $< 2 \text{ m}$ ) (Krieger et al., 2007). Data were acquired covering all landmasses at least twice (small and large baselines) for the generation of a global digital elevation model (DEM) from 2010 until 2014. Difficult terrain (mountains with radar shadowing and layover effects, forests and deserts) is covered at least four times (Böer et al., 2016).

The workflow of the TanDEM-X DEM generation (Gonzalez et al., 2009) is shown in Figure 3.1. The process for producing the final DEM products includes two steps: the Integrated TanDEM-X Processing (ITP) (Fritz et al., 2012) and the Mosaicking and Calibration Processing (MCP) (Wessel et al., 2008b). The DEM generation ingested the incoming acquisitions, focusing the individual complex images, forming the filtered interferogram, executing the phase unwrapping, performing height pre-calibration for accurate phase-to-height conversion and finally generating geocoded raw DEMs (Zink et al., 2014). Following this, the raw DEM tilts were calibrated against ICESat data. Finally,

## Chapter 3. DEM Generation and DEM Quality Assessment

all elevation data were mosaicked with the help of calibration corrections and fusion weights, and the DEM data were split into output DEM tiles ( $1^\circ$  by  $1^\circ$ ). The DEM products also include a relative height accuracy map, a water indication mask, flag masks and additional quality control and system calibration data (Böer et al., 2016).

From this fantastic mission (bistatic X-Band interferometric SAR), the 12 m, 30 m, 90 m TanDEM-X IDEM data and the 12 m, 90 m TanDEM-X DEM data based on the WGS84-G1150 geographic coordinate system are available (Feng and Muller, 2016). However, the data are influenced by the baseline determination errors, the phase errors of the radar instruments, the interferometric phase errors, random errors and other errors, which need validation.

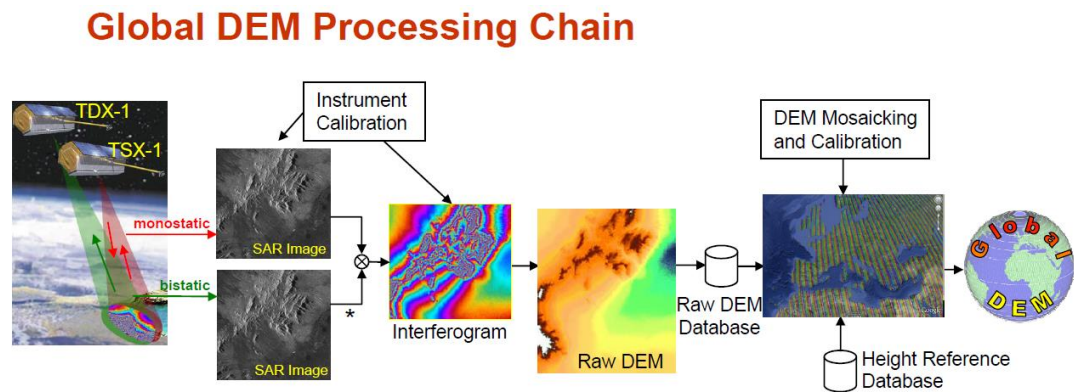


Figure 3.1 TanDEM-X DEM processing workflow (Gonzalez et al., 2009)

### 3.1.2 Reference Bluesky DTM Generation

Bluesky DTM, based on the OSGB36 and ODN projection coordinate system, is a commercial 5 m DTM from Bluesky Limited, which is made available for us through the UK academic community from the LANDMAP project (Muller et al., 2001). Bluesky data is from Bluesky Ltd. based on aerial photogrammetry (Landmap, 2014). The data were photogrammetrically interpolated from the stereoscopic aerial photography collected between 1999 and 2008; a photogrammetric DSM was generated first, then it was processed into DTM (a bare earth model).

The photogrammetric DSM can be generated based on the collinearity equation (a rigorous physical model). The classical photogrammetric workflow for DTM generation via stereo images is shown in Figure 2.28 in Chapter 2. For Bluesky DTM/DTM generation, in the orientation step, the rigorous model was utilised. With the images imported along with metadata parameters, image pyramids were generated. Then

### Chapter 3. DEM Generation and DEM Quality Assessment

the tie points in two or more images were extracted, and the control points (i.e. street furniture, crossing roads, etc.) were measured for matching in order to calculate the relative and absolute orientation of image pairs (tie points are auto-measured or artificial assisted) (Poli and Caravaggi, 2012). After the automatic tie point detection and photogrammetric bundle adjustment, the interior and exterior orientation parameters were obtained. Then, the DSM (3D coordinates in object space) was generated with dense stereo image matching between the stereo images. In the final step, the mask operations (rivers, oceans, lakes ...) and additional manual editing (such as blunder filtering or tree and building removal) were applied to generate the DTM/DEM (Poli and Caravaggi, 2012).

The Bluesky DTM (5 m and 10 m) has uncertainties. The accuracy of the Bluesky DTM is calculated based on the Kinematic GPS (KGPS) and ICESat data. Because the Kinematic GPS from the LANDMAP project (Muller et al., 2001) and the ICESat lidar data have high accuracy (shown in Table 3.1), they can be used as control point data for DEM accuracy assessment. Therefore, the vertical RMSE accuracy of the Bluesky DTM is 4.21 m when compared with the KGPS data over the UK in the experiment. The vertical RMSE accuracy of the Bluesky DTM is 5 m when compared with the ICESat lidar data over the UK. In addition, in the LANDMAP project, the accuracy (RMSE) of the Bluesky DTM is 1 m in X, Y and 1.5 m in Z respectively in England and Wales (Landmap, 2014). For Scotland, the accuracy is lower due to its more rugged terrain, but it is also around 1 m in X, Y respectively (Bluesky, 2018); against the Kinematic GPS, the vertical RMSE accuracy (in Z) of the Bluesky DTM is 5.6 m; against the ICESat lidar data, the vertical RMSE accuracy of the Bluesky DTM is 6 m. Overall, the accuracy of the Bluesky DTM data is relatively high (as it meets the HRTI/DTED-3<sup>14</sup> absolute vertical accuracy standard (Krieger et al., 2005b): 12 m resolution,  $LE90 \leq 10$  m absolute accuracy) and the advantage of the Bluesky DTM data is that it covers the whole area of the UK. Therefore, Bluesky DTM can be used as the ‘truth’ data for other DEM data validation in the UK.

## 3.2 Quality Assessment of TanDEM-X IDEM & Tandem-X DEM

---

<sup>14</sup> HRTI/DTED is high resolution terrain information/digital terrain elevation data

### 3.2.1 Introduction

For the Earth's land surface, the downstream processing of Earth Observation (EO) data over land and some coastal areas for applications in land or atmospheric retrieval require corrections for topographic relief and/or slope and aspect (Feng and Muller, 2016). Moreover, for traditional mapping applications, this also requires a Digital Elevation Model (DEM) of the "bare earth" land surface (Feng and Muller, 2016). As the spatial resolution of the SAR/IR/VIS images increases, so does the need to improve the DEM spatial resolution and accuracy. Now, such global DEMs are being produced from spaceborne EO sensors, such as from SAR (SRTM, TerraSAR-X and TanDEM-X), stereophotogrammetric (ASTER, SPOT, PRISM and IRS-3P), radar altimeters (CryoSat-2) and LIDAR (ICESat) (Wang et al., 2011; Fujisada et al., 2012; Farr et al., 2007; Feng and Muller, 2016). EO-DEM usually measure the observable canopy elevation that can vary from the top-of-canopy to the bare earth depending on the technique and wavelength employed. Each EO DEM comes with limited validation, and in some cases, they use different coordinate systems, datums and spheroids.

Spatial data error sources have been summarised as measurement errors, processing errors and data errors (Pike, 2002; Wechsler, 2007), and DEM data, like all other spatial data sets, has errors. More specifically, DEM data contain three types of errors: systematic errors, random errors and blunders. Although all three types of errors may be reduced in magnitude by refinements in technique and precision, they cannot be completely eliminated (Brown and Bara, 1994; Caruso, 1987b). In addition, these DEM errors are elusive and constitute uncertainty (Wechsler, 2007), and the effects of these errors in a DEM are often not noticed by DEM users. Furthermore, current methods and techniques to quantify DEM uncertainty are not readily available, nor are they systematically applied to the DEM data application. Therefore it is critical to validate DEM products for public users (Danielson and Gesch, 2011a; Gesch, 1994). So far, many studies have been conducted by scientists from all over the world. GPS is the typical way to validate the absolute accuracy of DEM products, which has been applied in SRTM and ASTER G-DEM accuracy validation (Reuter et al., 2009; Tachikawa et al., 2011; Team, 2009; Rodriguez et al., 2005; Goncalves and Oliveira, 2004; Fujisada et al., 2012; Eckert et al., 2005; Rodriguez et al., 2006; Li et al., 2013). Meanwhile, external DEM like stereophotogrammetric data, LIDAR and radar altimetry have also been introduced to

### Chapter 3. DEM Generation and DEM Quality Assessment

assess the quality of DEMs. For example, the terrain elevation derived from ICESat/GLAS and satellite radar altimetry data from ERS-1/2 or airborne LIDAR is usually applied in many DEM validation and quality accuracy assessments (Berry et al., 2007; Enßle et al., 2014; Carabajal and Harding, 2005). However, the primary challenge in validating the quality of a digital elevation model is obtaining a useful reference data set that is accurate enough and has suitable coverage to encompass the entire area of interest. Fortunately, NASA's Ice, Cloud and land Elevation Satellite (ICESat) using the Geoscience Laser Altimeter System (GLAS) has collected a unique set of full-waveform Light Detection And Ranging (LiDAR) data with global coverage from 2003 to 2009 (Feng and Muller, 2016). The vertical accuracy of this elevation dataset (GCP from the GLAS LiDAR point) is  $\leq 1$  m which is suitable for evaluating large area DEMs around the world (Feng and Muller, 2016).

Recently, the United States released one arc-second gap-filled version of the SRTM DEM dataset without any specification reporting its accuracy. Moreover, it is demonstrated that the continuing lack of any useful quality indicator (QI) for ASTER will make it difficult to employ this global DEM source, which highlights that this gap needs to be filled. Through a data grant (IDEM\_CALVAL0207) from DLR, an intermediate first-pass only TanDEM-X DEM (called IDEM) was available at three different spatial resolutions of 1/3rd arc-second ( $\approx 12.5$  m), one arc-second ( $\approx 30$  m), three arc-seconds ( $\approx 90$  m) over the UK along with limited areas around the world. The objective of this study is to assess the accuracy of TanDEM-X in comparison to a national DEM (Bluesky DTM), SRTM 1, ASTER G-DEM, ICESat and KGPS data over the UK in order to extrapolate these results across the globe. Generally, high accuracy points are selected as the control points for the absolute vertical accuracy of the DEM data. According to Table 3.1, the ICESat data have the highest vertical accuracy, and the Bluesky data have the second highest vertical accuracy in England, KGPS ranks the third. The ICESat and KGPS data have higher accuracy than the Bluesky data in Scotland, due to Scotland's more rugged terrain. In our experiment, the ICESat data and KGPS data are deemed to be the 'truth' data, so the absolute accuracy is assessed by the ICESat and KGPS data, while the DEM to 'truth' data vertical comparison<sup>15</sup> accuracy is assessed by other DEM 'truth' data, like Bluesky.

---

<sup>15</sup> The difference between each DEM and the 'truth' height data

### 3.2.2 Test Area and Metadata Information

The UK area is selected as the study site (Figure 3.2 from Google), which lies on the European continental shelf, as part of the Eurasian Plate. The UK is located off the north-west coast of continental Europe, and it stretches over about ten degrees of latitude on its longer, north-south axis and occupies an area of 209,331 km<sup>2</sup> excluding its smaller surrounding islands (Rose, 1982; Thrift and Walling, 2000; Feng and Muller, 2016). The metadata information of the data in this quality assessment study is shown in Table 3.1 below. What should be paid attention to is that the coordinate system of different DEMs data is different. Maps of the DEM datasets (TanDEM-X IDEM, TanDEM-X DEM, SRTM, ASTER G-DEM, Bluesky DTM, all based on OSGB36 ODN), the KGPS (Kinematic GPS) data footprint and the ICESat data footprint used in this study are shown in Figure 3.3 below.



Figure 3.2 Study area (© Google 2015)

Table 3.1 Experiment DEM input datasets

<b>Data Set</b>	<b>SRTM</b>	<b>Aster GDEM</b>	<b>TanDEM- X IDEM</b>	<b>Bluesky</b>	<b>ICESat GIAS 14</b>	<b>KGPS</b>
<b>Coverage</b>	GLOBAL	GLOBAL	UK & worldwide (3'')	UK, Ireland	UK	UK

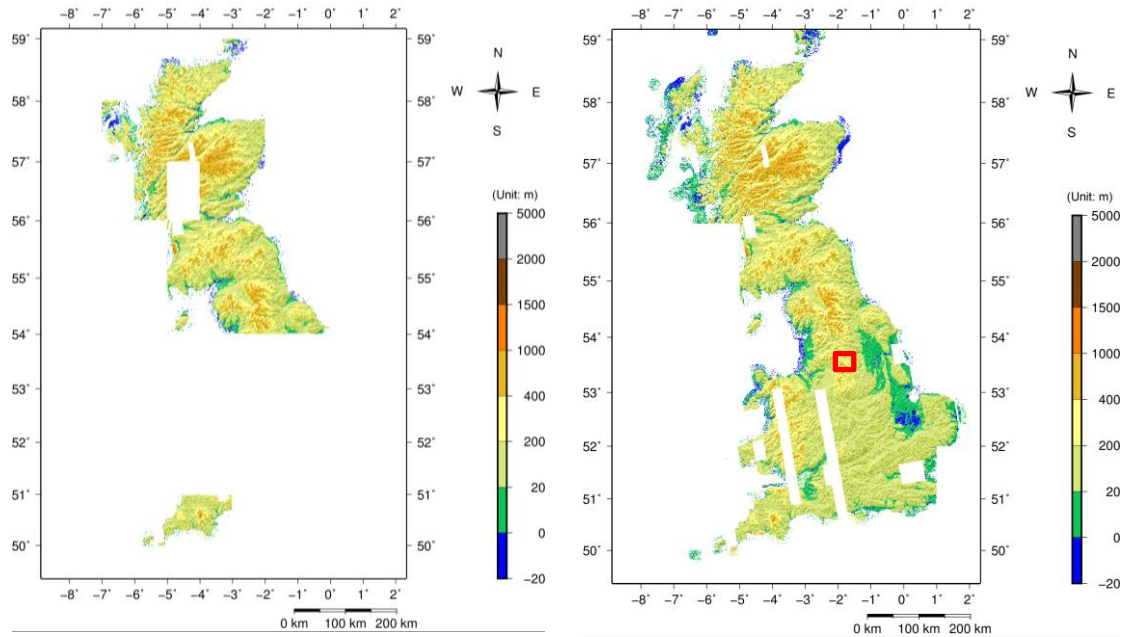
### Chapter 3. DEM Generation and DEM Quality Assessment

Data Set	SRTM	Aster GDEM	TanDEM- X IDEM	Bluesky	ICESat GIAS 14	KGPS
<b>Source</b>	NASA JPL/USGS	USGS	DLR- TerraSAR- X	Bluesky Ltd. based on aerial photogrammetr y (Landmap, 2014)	National Snow and Ice Data Centre, NASA	Landmap Project (Landmap, 2014)
<b>Resolution</b>	1 arc- second	1 arc- seconds	0.4" ( $\approx$ 12 m) 1" ( $\approx$ 30 m) 3" ( $\approx$ 90 m)	10 m or 5 m	172 m spacing.	Approximatel y 20 m spacing.
<b>Accuracy</b>	Accuracy of 20 m in X, Y and 16 m in Z, the relative accuracy of 15 m in X, Y and 10 m in Z (Rodrigue z et al., 2006)	Accuracy of 20 m in X, Y and 30 m in Z (Fujisada et al., 2005)	Accuracy of 10 m in X, Y and Z, relative accuracy of 2 m (slope<20% ) and 4 m (slope>20% ) in Z (Krieger et al., 2005a)	Accuracy of 1 m in X, Y and 1.5 m in Z <sup>16</sup>	Horizontal accuracy < 5 m, Vertical accuracy < 1 m (sub- metre)	Accuracy of about 2.5 m in X, Y and Z
<b>Ellipsoid</b>	WGS84	WGS84	WGS84- G1150	OSGB36	TOPEX Poseidon- Jason Ellipsoid	OSGB36
<b>Vertical Datum</b>	EGM96	EGM96	WGS84- G1150	ODN	TOPEX Poseidon- Jason Ellipsoid	ODN
<b>Projection</b>	Geographi c Lat/Lon	Geographi c Lat/Lon	Geographic Lat/Lon	Transverse Mercator projection	Geographi c Lat/Lon	Transverse Mercator projection
<b>Acquisitio n Date</b>	February 2000	February 2000	2011-2013	1999-2008	2004-2008	2000

<sup>16</sup> This accuracy is for the data in England and Wales (Landmap, 2014). For Scotland, the accuracy is larger due to its more rugged terrain.

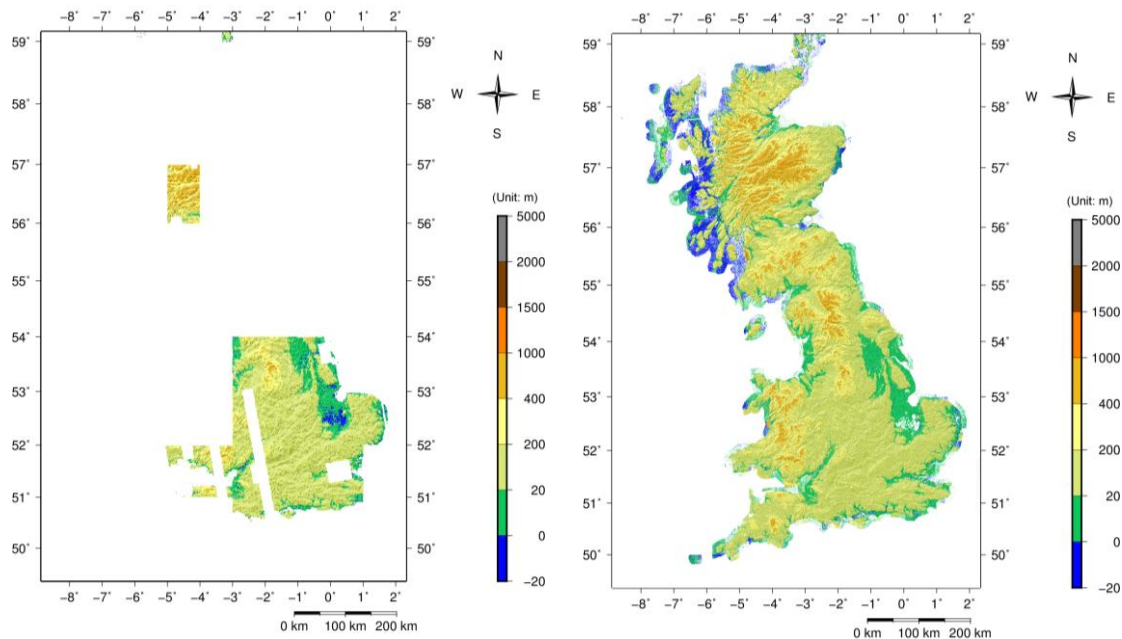


### Chapter 3. DEM Generation and DEM Quality Assessment



(a)

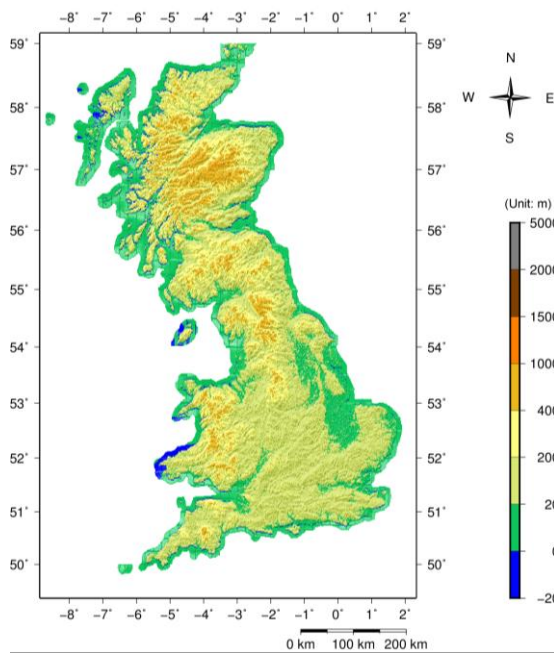
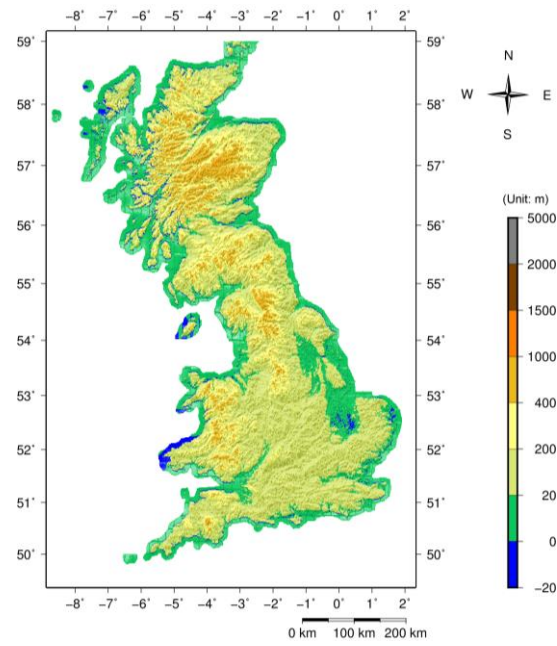
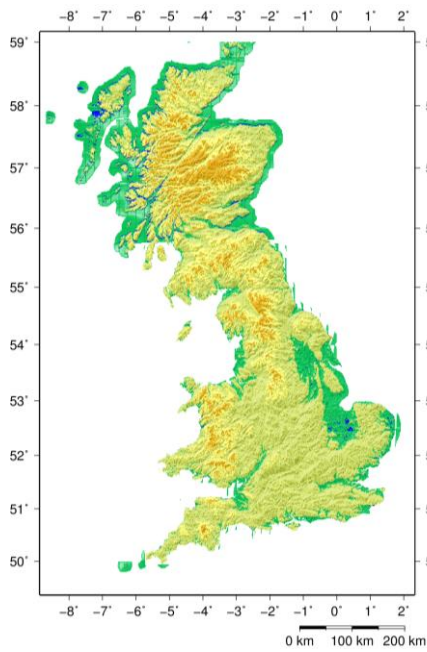
(b)



(c)

(d)

### Chapter 3. DEM Generation and DEM Quality Assessment



## Chapter 3. DEM Generation and DEM Quality Assessment

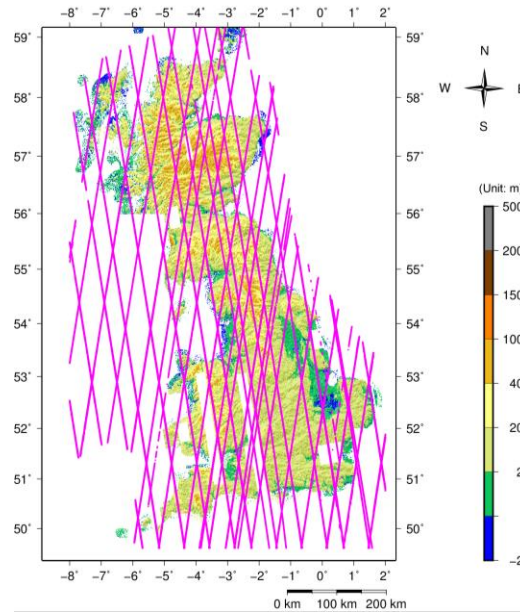


Figure 3.3 DEM, ICESat and KGPS datasets used in the analysis, all data are based on the OSGB36 ODN vertical datum: (a) TanDEM-X IDEM 30 m; (b) TanDEM-X IDEM 90 m; (c) TanDEM-X IDEM 12 m; (d) TanDEM-X DEM 90 m; (e) Bluesky DTM 30 m<sup>17</sup>; (f) SRTM DEM 30 m; (g) Aster GDEM 30 m; (h) Kinematic - GPS data in the UK<sup>18</sup> (Landmap, 2014; Muller et al., 2001). The black line is KGPS points which are plotted in a small-scale map; (i) ICESat GIA14 raw data from 2014 to 2018 in the UK, and the red line is the footprint of ICESat data (Feng and Muller, 2016)

The quality assessment includes planimetric and vertical accuracy. The statistical analysis usually employs vertical root-mean-square error (RMSE), which is used in many fields for assessing survey accuracy. The RMSE (Caruso, 1987a; CARTER, 1992; Pfeifle and Seidel, 1996) is used to quantify the vertical accuracy of a DEM for both random and systematic errors. Another important method for DEM vertical accuracy assessment is mean error, or bias, which implies that whether a DEM has an overall vertical offset (either positive or negative) from the true ground level (Gesch et al., 2016). Also, the accuracy measurement not only refers to the absolute vertical accuracy; but it also includes the vertical comparison accuracy.

### 3.2.3 Absolute Accuracy Validation Method by KGPS

The validation of the Digital Elevation Models (DEMs) is very important when the data is to be used by users. Generally, checkpoints are needed to validate the DEM,

<sup>17</sup> the Bluesky DTM under license from Dr Kamie Kitmitto at MIMAS.

<sup>18</sup> The K-GPS data is from Landmap Project.

### Chapter 3. DEM Generation and DEM Quality Assessment

but the manual selection of checkpoints is prone to error and time-consuming. Moreover, the big DEM data and the difficulty in identifying ground control points are common in many applications, which indicates that automatic methods are urgently needed (Muller et al., 2001). Currently, GPS plus image to image registration or image to map registration (finding identifiable visible features) are used to validate the accuracy of DEMs in automatic processes (Maune, 2007; Dowman et al., 2000b), but sometimes high accuracy (geolocation accuracy) maps or images (optical or SAR amplitude images) can't be obtained. Moreover, SAR image to optical image registration could be used to find the x, y, z coordinate of GPS in an un-validated DEM; but continuous lines are not shown in SAR image for linear features, and it is usually not possible to determine the centre of a road intersection at a SAR pixel correctly (Dowman et al., 2000a). In this DEM validation case, the LANDMAP project produced Kinematic GPS with accuracy approximately 2.5 m in X, Y, and Z and with 20 m spacing along roads (obtained by car) in the UK (Muller et al., 2001), but no amplitude images are provided for TanDEM-X so GPS plus image to image registration or image to map registration method could not be applied (if small image tile at GPS point is available, image matching or feature matching with GPS coordinates can be used to obtain the planimetric accuracy). However, SRTM 1, ASTER G-DEM, TanDEM-X IDEM, TanDEM-X DEM and Bluesky-DEM height value of the road area is almost the same, because the optical and radar penetration ability is weak over the road area, and the planimetric accuracy of the Bluesky DTM and the accuracy (X, Y, and Z) of the KGPS data are very high. Moreover, the Bluesky DTM data and the KGPS data match-up very well in any 3D (horizontal and vertical) visual interpretation experiment, as they are all in the same coordinate system and have high accuracy. More specifically, The accuracy in X and Y of the Bluesky DTM is 1 m, of the KGPS data is 2.5 (Landmap, 2014), and the worst matching accuracy in X and Y is 3.5 m for the Bluesky DTM and KGPS data, while the resolution of the un-validated DEM data (SRTM 1, ASTER G-DEM, TanDEM-X IDEM and TanDEM-X DEM data) is more than 12 m. Therefore, DEM to DEM (Bluesky DTM to un-validated DEM) registration is useful to find the correct X, Y coordinates of KGPS in an un-validated DEM; then, KGPS data are used to quantify the absolute vertical quality of the un-validated DEM data.

Meanwhile, GPS data may have errors, which also need to be eliminated when carrying out DEM validation. This chapter proposed the automatic validation of the DEM's absolute accuracy by using the existing Bluesky DTM and GPS data. It is known

### Chapter 3. DEM Generation and DEM Quality Assessment

that the absolute vertical quality of the DEM data is influenced by the planimetric quality; the higher planimetric shift can significantly contribute to higher vertical discrepancies (Maune, 2007). Vertical accuracy cannot be validated by GPS directly, the GPS planimetric position should be found correctly at first. Thus, this chapter proposed GPS plus DEM registration to find the GPS position on the un-validated DEMs and to validate the absolute planimetric accuracy of the un-validated DEMs using the existing Bluesky DTM and then used matched GPS data to validate the absolute vertical accuracy of the un-validated DEMs (Feng and Muller, 2016).

The automatic method is as follows. Firstly, all DEM data are converted into the same coordinate system (OSGB36 & ODN) (Iliffe, 2000), then, the GPS points are selected, the height differences between Bluesky data and the GPS points are calculated, and, where the differences are very large ( $> 60$  m), the GPS data are eliminated because of the gross errors in GPS data. Following that, the GPS x and y coordinates are used as the central pixels to determine an appropriate oversampling (three times) of the window size of the un-validated DEM and the Bluesky DTM data (template). Next, the cross-correlation method is used to match the DEM to find an accurate and correctly matched GPS planimetric coordinate in the un-validated DEM (sub-pixel accuracy). Moreover, the RANSAC (random sample consensus) algorithm for outlier elimination is used to improve the DEM matching accuracy, x and y and the height of z in the un-validated DEM are recorded. Finally, the absolute planimetric and vertical DEM accuracy are calculated by using the KGPS data (x, y, z) and matched points (x, y, z) in the un-validated DEM data.

#### ***3.2.3.1 GPS and DEM Template Matching by Cross-Correlation***

##### **(1) Normalised cross-correlation**

Remote sensing image matching is a popular method to solve some matching problems, but DEM registration is also beneficial for the seamless fusion of different sources of DEMs at the same place in different resolutions. DEM-to-DEM registration has difficulties in finding the feature points required for matching evaluation and error analysis. Meanwhile, DEM-to-DEM registration always needs to solve horizontal shifts, vertical shifts and tilts between overlapping DEMs. However, in our case, GPS data give us the initial position of the pixel point. Thus DEM-to-DEM registration only needs to achieve pixel or subpixel accuracy and cross-correlation can attain this accuracy. The correlation coefficient of cross-correlation quantifies the correlation and dependence of the measures, which indicates the statistical relationships between two or more observed

### Chapter 3. DEM Generation and DEM Quality Assessment

data or random variable values (Yoo and Han, 2009). The score values range from 1 to -1, 1 represents a good match and -1 symbolises a completely anti-correlated relationship (Yoo and Han, 2009; Zhao et al., 2006). The formula for correlation coefficient  $r$  is shown in Equation (3.1) below, where the dataset  $(x_1, \dots, x_n)$  is the  $x$  values with  $n$  times observations and another dataset  $(y_1, \dots, y_n)$  is the  $y$  values with  $n$  times observations.

$$r = r_{xy} = \frac{\sum_{i=1}^n (x_i - \bar{x})(y_i - \bar{y})}{\sqrt{\sum_{i=1}^n (x_i - \bar{x})^2} \sqrt{\sum_{i=1}^n (y_i - \bar{y})^2}} \quad (3.1)$$

where:

$n, x_i, y_i$  are defined as above,

$\bar{x}$  is the sample mean value, and analogously for  $\bar{y}$ .

#### (2) Parameters

The difficult issues of this algorithm are how to find the best parameters like matching window size, template window size and the threshold of the correlation coefficient. Normally, different data have their own parameters, and sometimes the same remote sensing data with the same parameters in some areas may not fit in other areas (Kanade and Okutomi, 1994).

Although the search window size, the template window size of the Bluesky DTM and the correlation coefficient threshold are measure-independent and small-changing (similar) parameters (all parameters are independent and the results are sensitive to a small change in each parameter, which means the value of each parameter is similar), they may still affect the final matching results. Therefore, we did many experiments and tested the search window size, template window size and correlation coefficient threshold (the window samples are shown in Figure 3.4). The following template window sizes 3\*3, 5\*5, 7\*7, 9\*9, 11\*11, 13\*13, 15\*15 are tested. Because the Bluesky DTM has a high resolution and in order to obtain high sub-pixel matching accuracy, the DEM data are oversampled three times. Thus, all of the test window sizes are three times the designed window sizes (9\*9, 15\*15, 21\*21, 27\*27, 33\*33, 39\*39, 45\*45). The tested search window sizes are 1, 2, 3 pixels larger than template window size in four directions. From Table 3.2, the larger the template window size is, the bigger the matched point number is; when the template window size is 33\*33, the vertical and planimetric accuracy tends to be stable (33\*33 is used, as a bigger window means a larger memory and a larger matching time, which will cost a lot of energy). Therefore, according to the RMSE, the matching correct rate and matching point number, through many experiments, 33\*33 is

## Chapter 3. DEM Generation and DEM Quality Assessment

the best template window size, 35\*35 is the best search window size, and 0.8 is the best correlation coefficient threshold. The statistical test data is shown in Table 3.2 below.

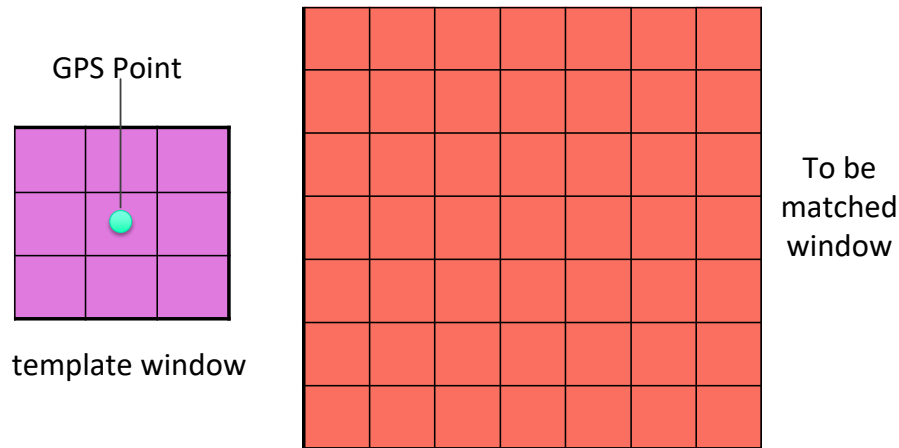


Figure 3.4 DEM matching windows, the left is the template window, and the right window is to be the matched window

Table 3.2 Window size test statistics (UK TanDEM-X IDEM 30m data; the total GPS points are 302805 and the correlation coefficient threshold is 0.8)

Template Window size	9*9	15*15	21*21	27*27	33*33	39*39	45*45
Matched points	48537	71066	89974	105655	116778	126982	136240
Matched height RMSE (m)	7.4	6.5	6.1	5.9	5.3	5.3	5.3
Matched XY RMSE (m)	13.3	13.4	13.5	13.5	13.6	13.6	13.6

### 3.2.3.2 RANSAC Algorithm and affine transformation model

The random sample consensus (RANSAC) algorithm (Fischler and Bolles, 1981) is a conventional parameter estimation approach used to select a significant proportion of consensus data from the input data. Fischler and Bolles (Fischler and Bolles, 1981) pointed out in their paper, that these conventional sampling techniques usually use as much of the data as possible to obtain an initial solution before proceeding to eliminate outliers, while the RANSAC algorithm initially uses the smallest possible set of data before proceeding to enlarge the data set with consistent data points (Fischler and Bolles, 1981). In our case, after matching, there are errors in the matching pairs, which need to be eliminated. Thus, the RANSAC algorithm is used to complete this work (eliminating

### Chapter 3. DEM Generation and DEM Quality Assessment

outlier) and a 2D affine transformation is used as the model in the RANSAC algorithm for this study. The 2D affine transformation is shown in Equation (3.2) below. In the equation, the dataset  $x_i$  is the position value of the  $i^{th}$  KGPS point in the  $x$  direction (axis), and the dataset  $y_i$  is the position values of the  $i^{th}$  KGPS point in the  $y$  direction (axis).  $x'_i$  and  $y'_i$  are the  $x$  and  $y$  values of the DEM data. Besides, these parameters  $a$ ,  $b$ ,  $c$ ,  $d$ ,  $e$ ,  $f$  are the 2D affine transformation coefficients.

$$\begin{aligned} ax_i + by_i + c &= x'_i \\ dx_i + ey_i + f &= y'_i \end{aligned} \quad (3.2)$$

The affine transformation model RANSAC algorithm is summarised as follows:

(1) select three points randomly to calculate the model parameters; (2) calculate to obtain the parameters of the affine transformation model; (3) set the error distance threshold  $r$  and calculate how many points from the set of points that fit with the affine transformation model; (4) if the percentage of selected points set over the total number of points exceeds a predefined threshold  $\sigma$ , re-estimate the model parameters using all identified points and terminate; (5) otherwise, repeat steps 1 through 4, but if repeating times are longer than iterations  $N$ , then stop and break out (Wasnik, 2014). In this algorithm, the number of iterations  $N$ , is usually set high enough to ensure that the point consensus set is large enough (usually set to 90% of the total number of points). After the RANSAC algorithm, the best matching GPS points can be achieved for absolute accuracy validation.

#### 3.2.4 Absolute Vertical Accuracy Validation Method by ICESat

The Geoscience Laser Altimeter System (GLAS) onboard the NASA ICESat satellite is made up of a laser system, a Global Positioning System (GPS) receiver, and a star-tracker attitude determination system, which collected data from February 2003 to October 2009. The laser transmits short pulses (4 nanoseconds) of visible green light (532 nanometers) and infrared light (1064 nanometres wavelength) (Feng and Muller, 2016). Photons are reflected back to the spacecraft from the surface of the Earth and the atmosphere, including from the inside of clouds, which are collected in a 1 metre diameter telescope and the illuminated spots (footprints) are 70 metres in diameter, spaced at 170-metres intervals along the Earth's surface (Schutz et al., 2005). The spacecraft's position and laser pointing are combined to obtain the precise location of the footprint on the surface to a few metres' accuracies (Schutz et al., 2005; Zwally et al., 2002). The elevation



### Chapter 3. DEM Generation and DEM Quality Assessment

of the surface for each laser footprint is calculated by minusing the measured distance to the surface from the height of the spacecraft. For land elevations, the centroid of the received pulse between the signal start and end is used for DEM validation (Feng and Muller, 2016), shown in Figure 3.5. Three lasers are mounted on the spacecraft and used sequentially during the mission. However, only the data (GLAH14 product) acquired by Laser 3 were used for TanDEM-X IDEM validation, from October 2004 to October 2008 (Feng and Muller, 2016).

The first step is pre-processing the data (converting all data to the same coordinate system and datum) (Feng and Muller, 2016). The ICESat GLA14 land elevations data is based on the TOPEX/Poseidon-Jason ellipsoid (Bhang et al., 2007), while the coordinate system of TanDEM-X IDEM is already WGS84-G1150 for validation. The offset via the empirically derived formula provided by NSIDC (Fabian et al., 2000) is obtained for ICESat GLA14 data and the National Grid Transformation OSTN02 and the National Geoid Model OSGM02 (OSTN02 & OSGM02) was used to convert the Bluesky DTM from OSGB36 ODN to the WGS84 coordinate system (Feng and Muller, 2016). The transformation accuracy is about  $\pm 3.5$  metres (95% of confidence, assumed as a Gaussian distribution) either vertically or horizontally (Haklay, 2010; Iliffe et al., 2003).

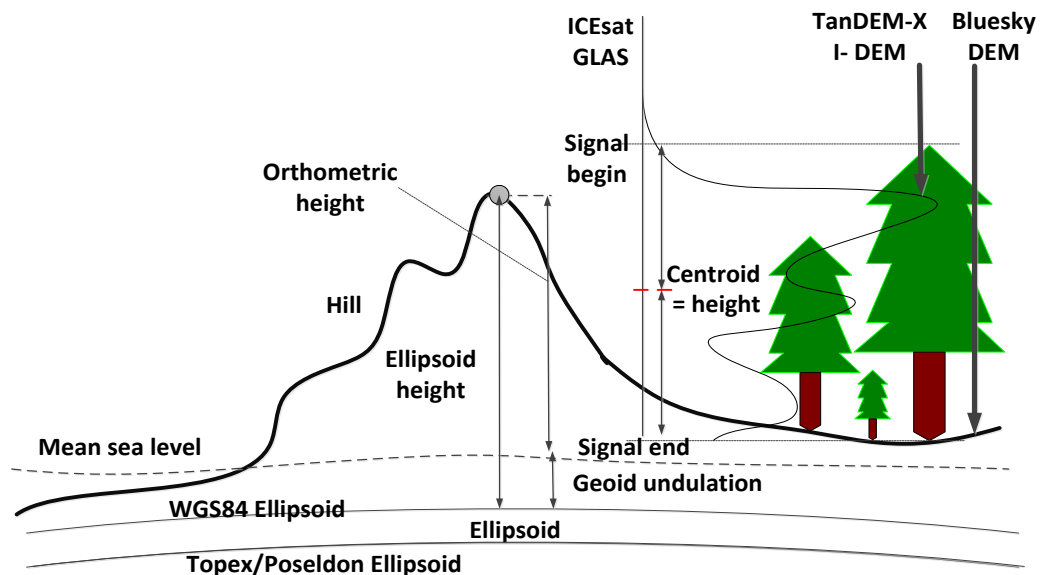


Figure 3.5 ICESat coordinate system and ICESat waveform. The ICESat coordinate system and ICESat waveform (Bhang et al., 2007; DHI, 2014) over forest canopy relative to the wavelength signal from TanDEM-X and Bluesky DTM; the elevation measurements used in this DEM validation have been calculated from the centroid of the received pulse between signal start and end, defined for alternate parameterisation (Feng and Muller, 2016), the height is different via different instruments

### Chapter 3. DEM Generation and DEM Quality Assessment

The second step is data filtering (Fabian et al., 2000; Feng and Muller, 2016). First, using the internal quality flags shown in Table 3.3 below as criteria in the ICESat GLAH14 data files, the ICESat GLAH14 data is filtered initially (Feng and Muller, 2016). The filtered results are obtained, as shown in Figure 3.6 (b) and (c). It is easy to see from these figures that a single year of ICESat data is insufficient for TanDEM-X IDEM validation; therefore, ICESat data from 2004 to 2008 are utilised for validation. In addition, ICESat locations with elevations deviating more than 60 metres (ICESat and Bluesky DTM elevation difference) are excluded to obtain refined ICESat elevation without extreme outliers (Feng and Muller, 2016).

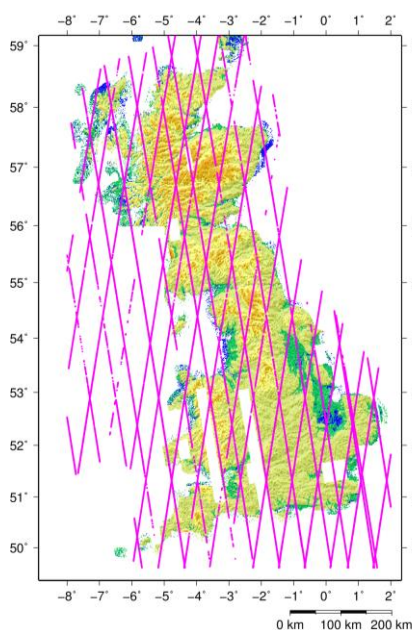
The third step is that the IDEM values are subtracted from the corresponding ICESat elevations. Finally, the data comparison and statistical validation of the IDEM vertical accuracies are executed according to some standards and statistical methods (Maune, 2007). The statistic equations used for representing TanDEM-X IDEM vertical accuracy are summarised in Table 3.4 below. With millions of potential ICESat reference points (10/2004 – 10/2008) across the whole UK, the TanDEM-X IDEM statistical validation has therefore been processed automatically following the proposed processing workflow (Feng and Muller, 2016), shown in Figure 3.7 below. All code is written by me, except for the ICESAT import code, which is obtained from the University of Colorado and National Snow and Ice Data Centre of the United States of America.

Table 3.3 The internal quality flags of ICESat GLAH14 data  
(DHI, 2014; Fabian et al., 2000)

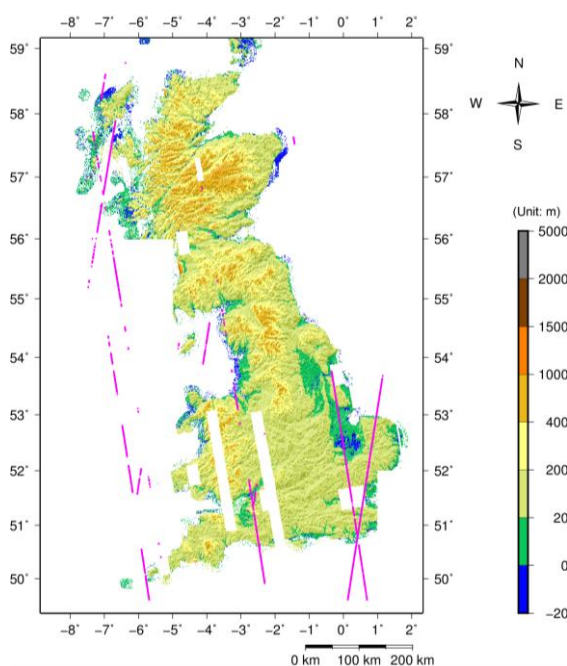
Attribute	Group	Description	Flag values and meanings
i_ElvuseFlg	Data_40HZ/Quality	Flag indicating whether the elevations on this record should be used.	0 (valid) 1 (not valid)
i_satCorrFlg	Data_40HZ/Quality and Elevation Corrections	Saturation Correction Flag; indicates if the returns are saturated or not and correction to elevation for saturated waveforms.	0 (not saturated) 1 (inconsequential) 2 (applicable) 3 (not computed) 4 (not applicable)

### Chapter 3. DEM Generation and DEM Quality Assessment

Attribute	Group	Description	Flag values and meanings
i_rng_UQF	Data_40HZ/Quality	Range offset quality flags	0 (valid) 1 (not valid)
i_FRir_qaFlag	Data_40HZ/Elevation Flags	Cloud contamination; indicates probable cloud contamination	15 (no cloud) Other number (not good for elevation control point)
i_AttFlg1	Data_40HZ/Quality	Denotes off-nadir angle (first bit flag)	0 (off-nadir angle within limits) 1 (large off-nadir angle)
i_DEM_hires_elv	Data_40HZ/Quality	Difference of GLAS height to high resolution DEM values from the SRTM source	< 100 m (good) >100 m (not good)



(a)



(b)

### Chapter 3. DEM Generation and DEM Quality Assessment

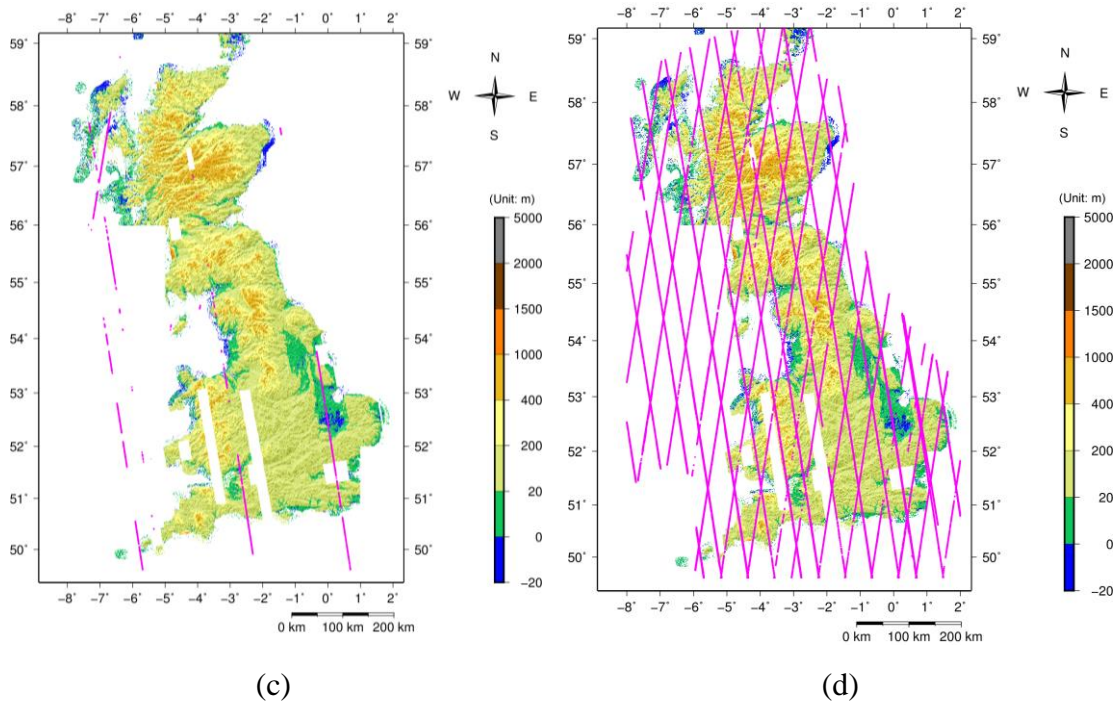


Figure 3.6 ICESat data footprints of the filtered results in 2006 and ICESat data footprints of the filtered results from 2004 to 2008, all DEM data are based on the OSGB36 ODN vertical datum (Feng and Muller, 2016): (a) All ICESat data footprints in 2006; (b) ICESat data footprints after filtering in 2006 (with large off-nadir angle data); (c) ICESat data footprints of the filtered results in 2006<sup>19</sup> (without large off-nadir angle data; (d) ICESat data footprint of the filtered results from 2004 to 2008 (without large off-nadir angle data) (Feng and Muller, 2016)

Table 3.4 Accuracy parameters for the TanDEM-X IDEM validation, where  $h_{IDem}$  is the IDEM elevation and  $h_{ICESat}$  is the ICESat elevation (Feng and Muller, 2016)

Number of checkpoints	n
Vertical error	$\Delta h = h_{IDem} - h_{ICESat}$
Root mean square error	$RMSE = \sqrt{\frac{\sum (h_{IDem} - h_{ICESat})^2}{n}}$
Mean error (or bias)	$\Delta \bar{h} = \frac{\sum (h_{IDem} - h_{ICESat})}{n}$
Standard deviation	$\sigma = \sqrt{\frac{\sum (\Delta h - \Delta \bar{h})^2}{n - 1}}$

<sup>19</sup> One-year data (2006) is selected as it is easy to see the filtering results. All year data (2004-2008) are too many and it is not easy to see whether the filter method works or not if they are plotted on the map.

<b>Linear error at 90% confidence level</b> (means 90% of the data value is smaller than $1.6 * RMSE$ )	$LE90 = 1.6 * RMSE$
<b>Threshold for outliers</b>	$ \Delta h  > 3 * RMSE$

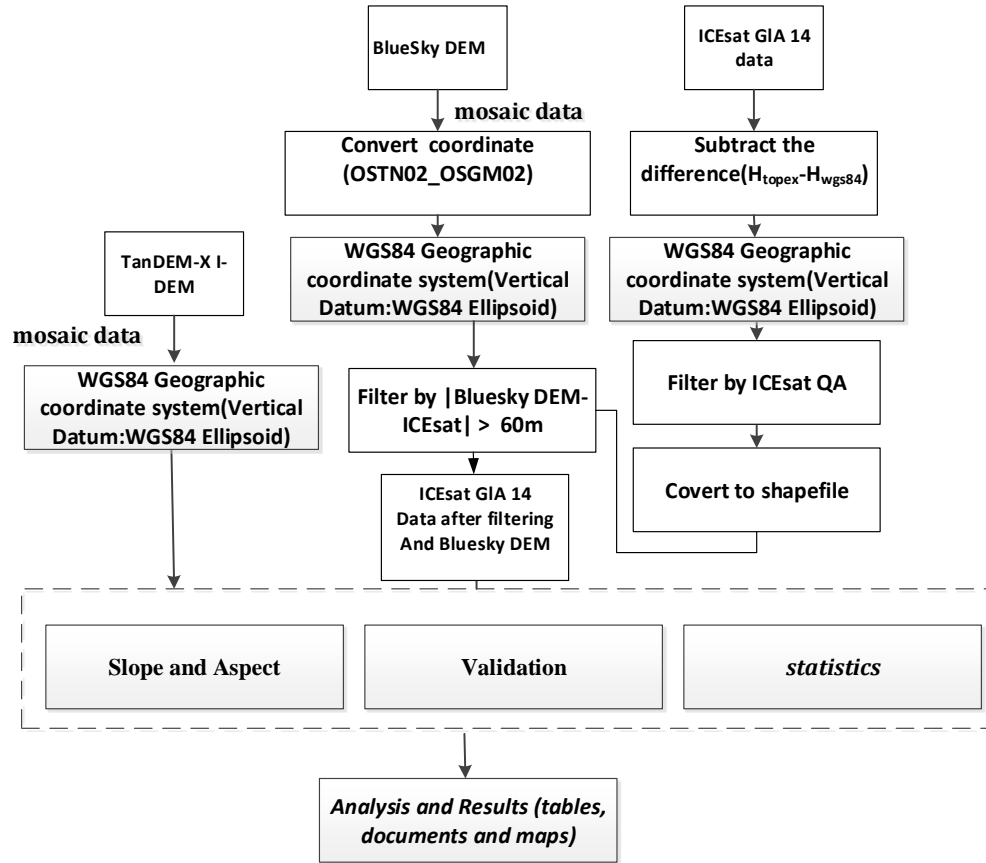


Figure 3.7 The TanDEM-X IDEM statistical validation processing workflow using the ICESat data (Feng and Muller, 2016)

### 3.2.5 Vertical Comparison<sup>20</sup> Accuracy Method

To obtain the vertical comparison accuracy of the DEM data, all DEM data need to be converted into the same coordinate system, because of the different coordinate systems of each DEM. A commercial 5 m and 10 m DTM from Bluesky limited corporation is used as the “ground-truth” reference data. A 7-parameter model and the OSTN02 & OSGM02 datum are used to project TanDEM-X IDEM, ASTER G-DEM and SRTM 1 from the WGS84 ellipsoid datum onto the same OSGB36 ODN datum. Then,

<sup>20</sup> The height difference between each DEM and the ‘truth’ DEM

## Chapter 3. DEM Generation and DEM Quality Assessment

several different COTS-based DEM co-registration techniques: (1) feature-based (Moravec, Harris & Foerstner) + least squares matching; (2) surface matching method; (3) SIFT + least squares matching were tested and the control co-registration accuracy (RMSE) are all smaller than 0.5 pixels to attain high sub-pixel accuracy. Lastly, surface matching is introduced to obtain vertical comparison accuracy of the DEMs. The flowchart is shown in Figure 3.8 below. All code is written by me, the OSTN02 & OSGM02 library is developed by the Ordnance Survey and it is used for coordinate transformation. The development of surface matching is introduced below. Besides, software, like ENVI, Erdas and ArcGIS, are used for statistics, analysis and mapping.

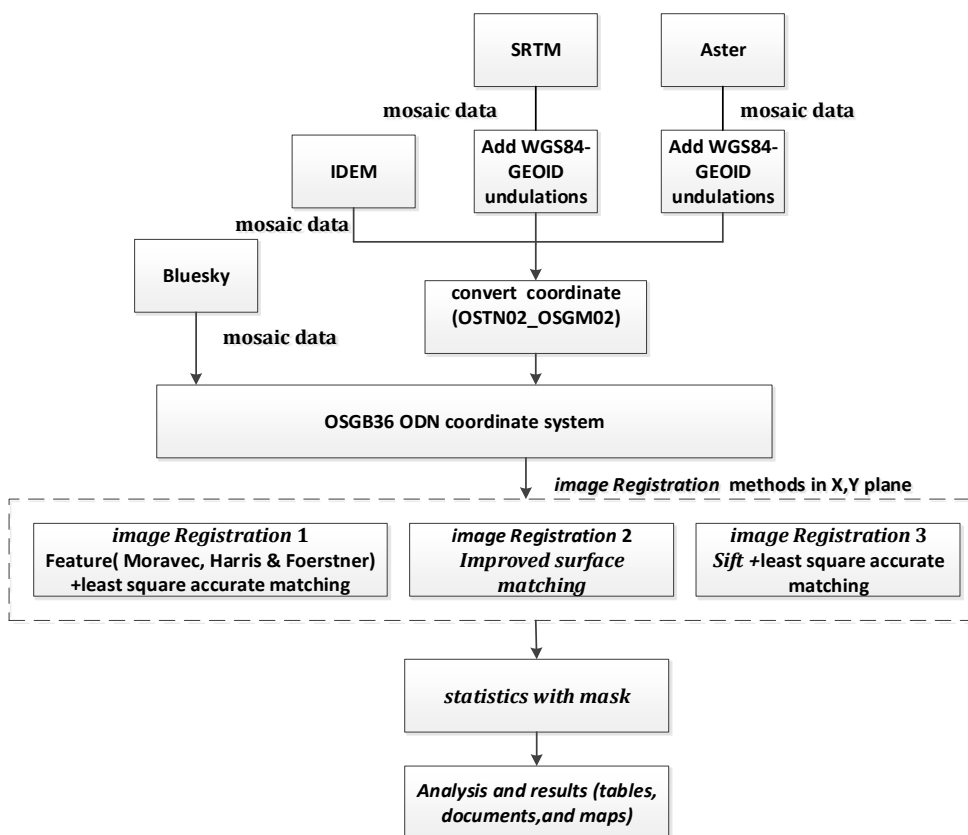


Figure 3.8 Vertical comparison accuracy assessment flowchart

### 3.2.5.1 OSGB1936 & ODN

The Ordnance Survey National Grid reference system (OSGB1936) (Ordnance-Survey, 2015) is based on the Airy 1830 ellipsoid and was created after the retriangulation of 1936-1962 (Figure 3.9) (Iliffe, 2000). The OSGB1936 Airy 1830 ellipsoid is a reference ellipsoid (the reference centre is selected as the best fit for the UK region terrain, semi-major axis  $a = 6377563.396$  m, semi-minor axis  $b = 6356256.909$  m, inverse

### Chapter 3. DEM Generation and DEM Quality Assessment

flattening  $1/f = 299.3249646$ , prime meridian longitude is the zero Greenwich meridian) defined in 1936, which is the best fit to the UK regional terrain, shown in Figure 3.9. Ordnance Datum Newlyn (ODN) is the UK's national coordinate system for heights referring to the mean sea level (orthometric heights) (Map projection: Transverse Mercator projection using the Redfearn series (the eighth order series of the transformation equation between latitude & longitude and the projection coordinates of  $x$  &  $y$ ) (Redfearn, 1948); True Origin:  $49^{\circ}\text{N}$ ,  $2^{\circ}\text{W}$ ; False Origin: 400 km west, 100 km north of True Origin; Scale Factor: 0.9996012717), shown in Figure 3.9, which was originally based on the tide gauge readings at Newlyn, Cornwall (Iliffe, 2000). ODN has a different benchmark for some areas in the UK (Fell and Tanenbaum, 2002). Theoretically, the Ordnance Datum Newlyn (ODN) means the mean sea level, which is the surface with the same gravity field value, whereas the Ordnance Survey National Grid reference system is based on the Airy 1830 ellipsoid, which is the best fit for the terrain of the UK. It is easy to use seven parameters (shown in Table 3.5 below), the National Grid Transformation OSTN02 and the National Geoid Model OSGM02 (OSTN02 & OSGM02) to convert WGS84 to OSGB36 ODN and vice versa (Iliffe, 2000; Feng and Muller, 2016).

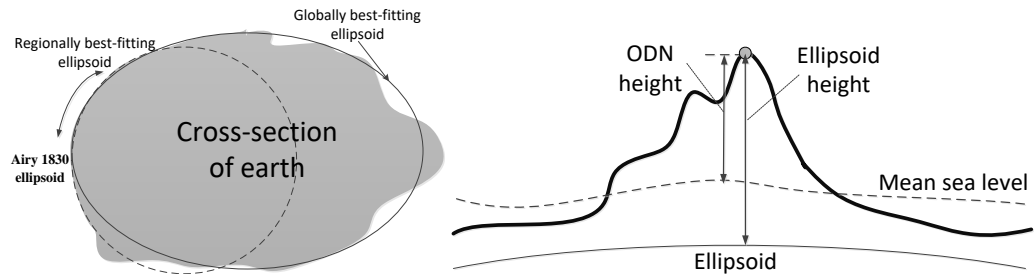


Figure 3.9 OSGB1936 Airy 1830 ellipsoid and ODN height (Ordnance-Survey, 2015)

Table 3.5 WGS84 to Osgb36 Helmert transformation (Haklay, 2010; Iliffe et al., 2003)

<b>Tx (m)</b>	<b>Ty (m)</b>	<b>Tz (m)</b>	<b>S (ppm)</b>	<b>Rx (sec)</b>	<b>Ry (sec)</b>	<b>Rz (sec)</b>
-446.448	125.157	-542.060	20.4894	- 0.1502	- 0.2470	- 0.8421

#### 3.2.5.2 DEM co-registration (surface matching) method

DEM co-registration (surface matching) aligns two DEM datasets, which can attain high vertical comparison accuracy. The least squares (LS) iterative method can be used to minimise the differences between a matching surface and a reference (Lin et al., 2010), but this LS method is time-consuming with small tile processing. Therefore, a new

### Chapter 3. DEM Generation and DEM Quality Assessment

surface matching method is proposed. In this new method, tile processing, edge-merging tips and indirect sampling are employed to automatically process large areas in the UK. However, the method is still based on 3D conformal transformation. Basically, the following equation (shown in Equation (3.3)) is a 3D conformal transformation model.

$$X_0 = sM^T X_i + T \quad (3.3)$$

In Equation (3.3),  $X_i$  is the 3D coordinate of a point in the un-co-registered DEM coordinate space.  $X_0$  is the transformed 3D coordinates of DEM data,  $s$  is the scale parameter (usually is 1),  $T$  is a matrix of the translation vector ( $T_x$ ,  $T_y$  and  $T_z$ ) and  $M$  is the rotation matrix (three rotations  $\omega$ ,  $\varphi$  and  $\kappa$ ). After the execution of this transformation model, the transformed 3D coordinates of DEM data are obtained (Lin et al., 2010). In this experiment, the Bluesky DTM data is used as the reference data.

#### (1) Sparse registration

DEM co-registration techniques were proposed to process the gridded DEMs to minimise shifts. These DEMs are tiled according to a 2D grid (e.g. 512 x 512) in the whole UK. For the two resolutions of the IDEM data (30 m, 90 m), they are oversampled four times (7.5 m, 22.5 m) and the Bluesky DTM data is sampled to the same resolution. If the data have a large shift (e.g.  $> 15$  pixels), the first coarse horizontal shift and vertical shift estimation can be achieved using cross-correlation. First of all, the edge images can be extracted from these DEMs (or hillshade DEM map) using any edge detector, such as the Sobel algorithm or canny algorithm (Vincent and Folorunso, 2009; Singh and Datar, 2013; Grossmann, 1988; Green, 2002). Then the initial alignment is executed to find out the initial shifts horizontally and vertically ( $x, y, z$ ), which is obtained by cross-correlating the edge images. Generally, a unique cross-correlation peak can be found with the initial horizontal shift. Vertical shifts can be obtained by cross-correlating the height histogram of the DEMs in the height fields (Wang and Zhu, 2015). Though the results are sparse, it is usually sufficient for the next coarse estimation. Moreover, as previous coarse matching has accuracy problems with large differences between  $x$ ,  $y$  and  $z$ , thus, the OSGB36+ODN system DEM data value is shifted into data based on the centre of the block/tile (centre value as zero points) first. Then, sparse initial registration via a pyramidal method (Harris3d/sift3d + KEYPOINT-BASED 4-POINTS CONGRUENT SETS (K4PC)) is introduced to obtain initial coarse matching matrix results (Ahuja and Waslander, 2014; Rusu and Cousins, 2011; Theiler et al., 2014). Furthermore, refined co-registration using the Iterative Closest Point (ICP) was utilised to get highly accurate



### Chapter 3. DEM Generation and DEM Quality Assessment

matching matrices. Moreover, the global optimisation of each tile using Gaussian weights was executed. Finally, data post-processing like Offset data to the original value was performed to obtain the final co-registration results (show in Figure 3.10). All the code is written by me. Many libraries are used. The Point Cloud Library (PCL) library is used for data filtering and sparse initial registration (K4PC algorithm). The ICP algorithm is based on the libpointmatcher library from the Swiss Federal Institute of Technology Zurich (ETH).

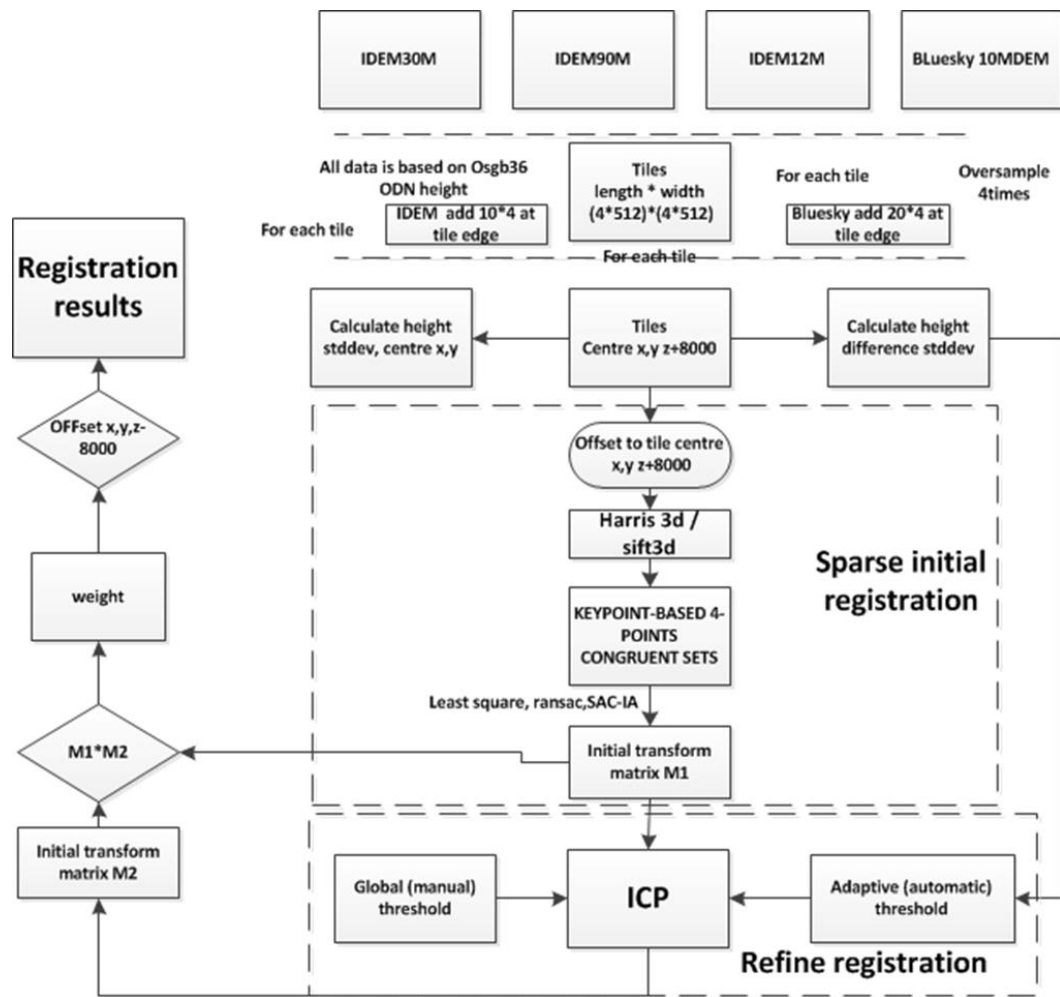


Figure 3.10 Final DEM co-registration flowchart

#### (2) Refine registration by using ICP

For fine-tuning the registration, many computational solutions exist, which are mostly variants of the standard principle to minimise the Euclidean distances between the nearby points. These methods are 1) ICP (Besl and McKay, 1992); 2) Least Z-Difference, LZD (Tonggang et al., 2005) ; 3) Least Squares 3D matching, LS3D (Gruen and Akca, 2005). The most popular approach is the Iterative Closest Point (ICP) algorithm (Besl and

### Chapter 3. DEM Generation and DEM Quality Assessment

McKay, 1992), which includes point to plane and point to point modes. The advantages of ICP is that it is good at 3D matching and has high accuracy. On the other hand, ICP is also known for its susceptibility to the problem of local minima (Sharp et al., 2002), due to the non-convexity of the problem as well as the local iterative procedure it adopts. Being an iterative method, ICP requires a good initialisation, without which the algorithm may easily become trapped in a local minimum. If this occurs, the solution may be far from the true (optimal) solution, resulting in an erroneous estimation. To deal with the issue, coarse initial alignment is needed first, like global optimality, through feature matching.

In our case, the data is first oversampled four times at the real resolution, and the data are split into small tiles (tile size is 512\*512), meanwhile overlapped edge pixels are introduced to maintain the good mosaic relationship between each tile (shown in Figure 3.11). Furthermore, a transformation matrix is calculated for every tile by the ICP method. Finally, a threshold is used via an adaptive (automatic) threshold by minimising the standard deviation to gain the best ICP matching matrix score. Finally, after co-registration, the IDEM, SRTM and Aster GDEM data are all well co-registered with the Bluesky data. Here, the high accuracy water feature is used to check the co-registration results visually, see the IDEM30M co-registration example in Figure 3.12 below.

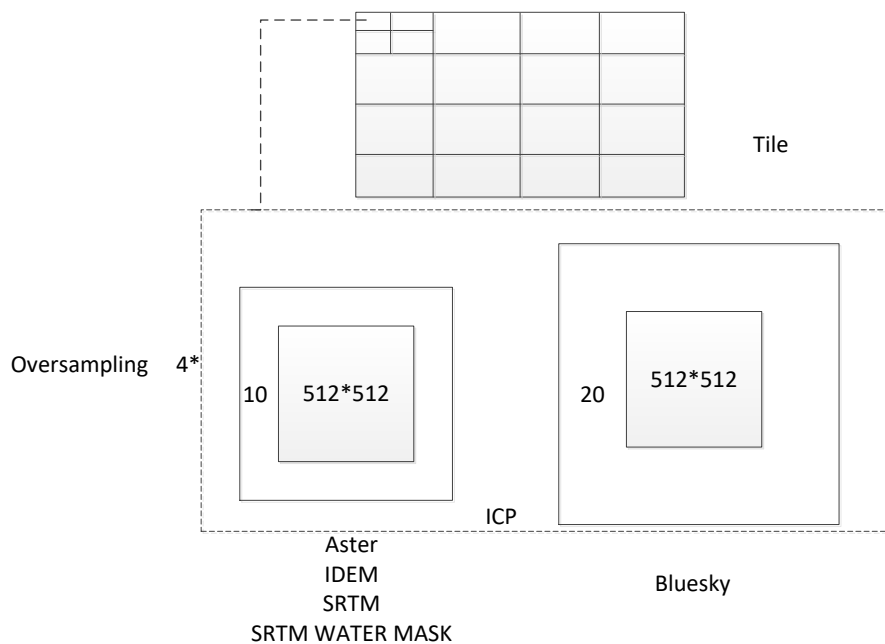
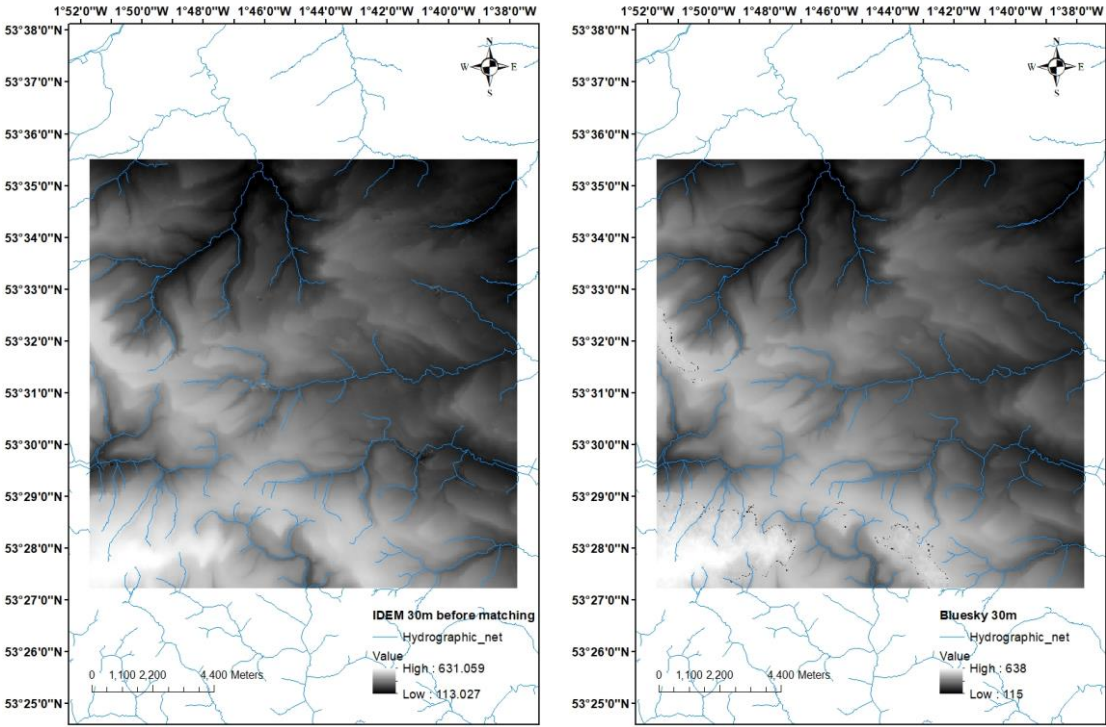


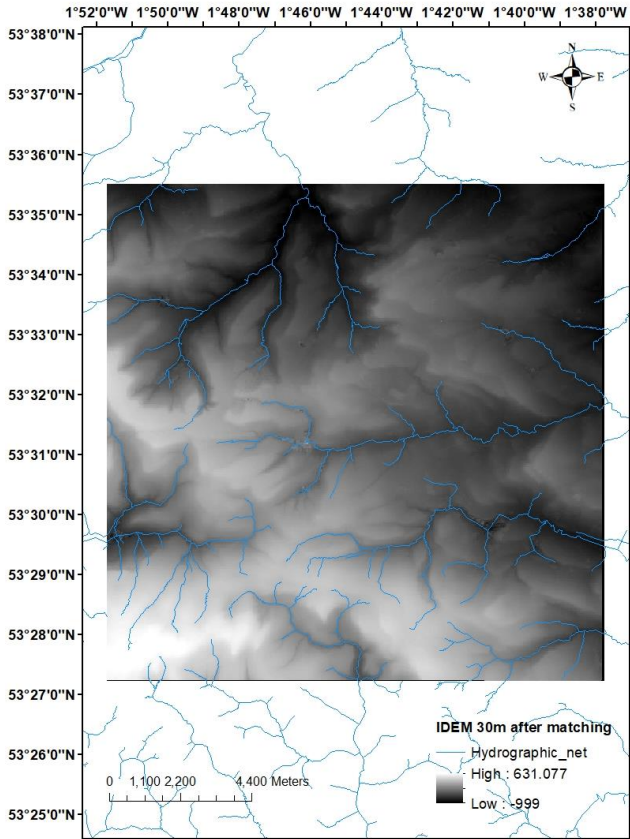
Figure 3.11 Refine registration by using ICP, the up figure is the tiles, the lower-left figure is the size of the un-co-registered data tile, the lower-right window is the size of the reference data tile

Chapter 3. DEM Generation and DEM Quality Assessment

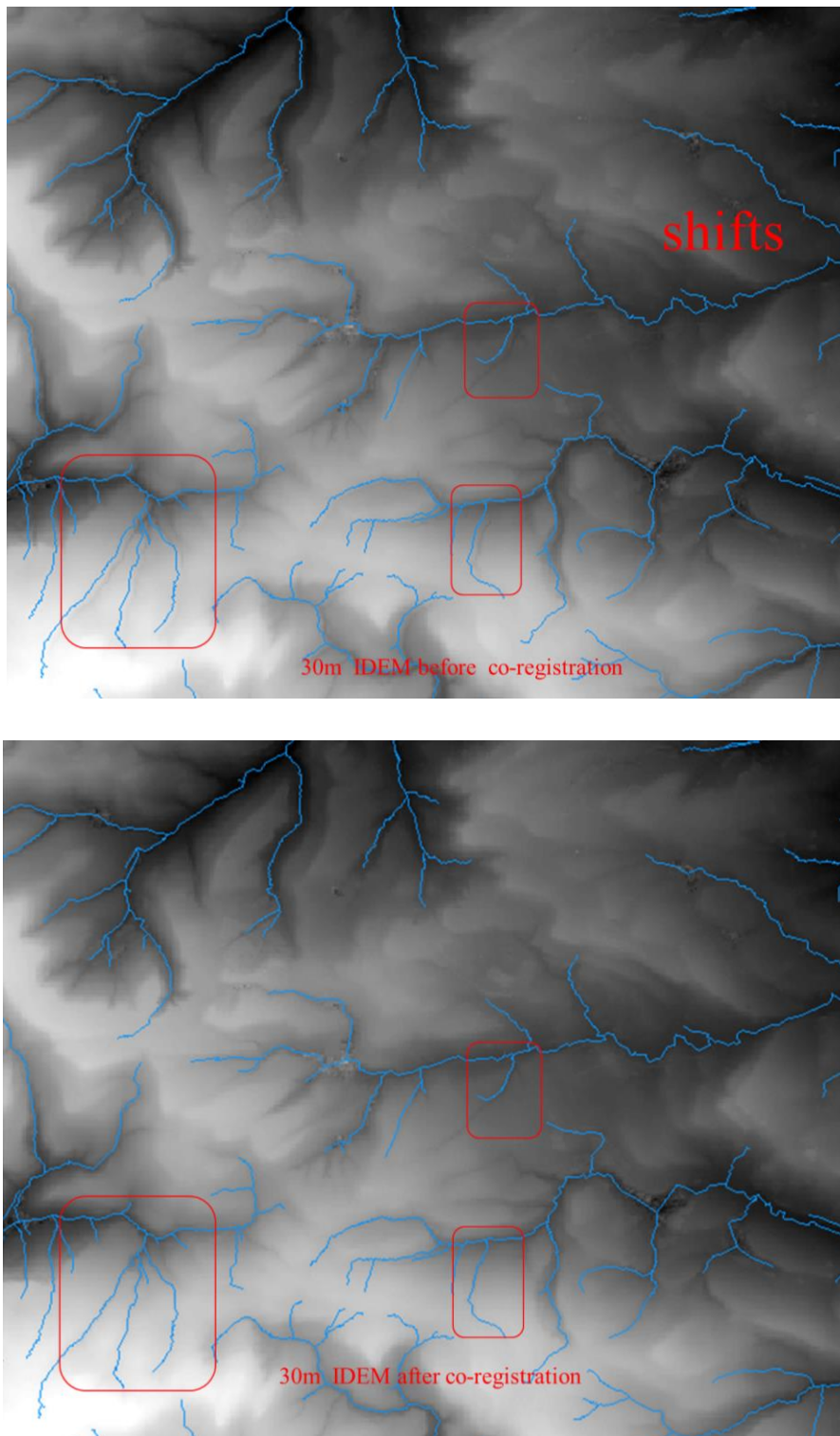


(a)

(b)



(c)



(d)

Figure 3.12 Co-registration results of IDEM 30 m in a tile area: (a) IDEM 30 m before co-registration; (b) 30 m Bluesky reference data; (c) IDEM 30 m after co-registration with Bluesky reference data; (d) Comparison results of the zoom-in area, the top picture has shifted (where the river network is not well-matched with the DEM image in the red box), while the bottom picture shows the well-matched result after matching (where the river network is well matched with the DEM image in the red box)

### ***3.2.5.3 Apply the UK River Mask with a buffer to eliminate elevations contaminated by water***

DEM data, like other geospatial datasets, contain errors. More specifically, DEM data contain three types of errors: blunders, systematic errors and random errors (Feng and Muller, 2016). Although all these errors can be minimised by refinement techniques, they cannot be completely removed (Feng and Muller, 2016). It is known that water areas, including ponds, rivers, lakes and seas, have a weak backscatter radar signal, which causes blunders in the DEM data. So, these blunders need to be eliminated from the DEM data.

As we do not have access to the raw radar image from TanDEM-X, it is hard to extract the boundaries of the water features. Fortunately, the SRTM project has produced SRTM Water Body Data (SWBD) - the water feature product, which represents all large area water features (Slater et al., 2006). However, the product only covers pixels where the water area is  $> 1 \text{ km}^2$  (Lakes greater than 600-metres in length and 183-metres in width) (Yamazaki et al., 2014), so, it is inadequate to eliminate all of the water-related blunders. For the UK, an open source dataset of water features was obtained from the UK Ordnance Survey. This data can be exploited within a GIS to build a buffer and eliminate some small blunder areas. However, the data sometimes still do not cover some of the smallest river features. So, in this case, a hydrological network is introduced using the hydrology spatial analysis tool of ArcGIS to extract the water features from the DEM data and a buffer is applied to associate these with the water feature extraction. After these steps, we fuse all three datasets together to cover the largest, median and small water areas. Lastly, all these water "blunder areas" are masked from the DEM data, which are then ready for the next quality assessment statistical steps.

## **3.2.6 Experimental Results**

The vertical RMSE accuracy of the Bluesky DTM is 4.21 m when compared with the KGPS data directly, and the vertical RMSE accuracy of the Bluesky DTM is 5 m when compared with the ICESat data over the UK.

### ***3.2.6.1 Absolute accuracy test results by KGPS***

The test results confirm the lack of any significant differences between the GPS data and the DEMs in the UK. The linear regression analysis reveals a strong correlation

### Chapter 3. DEM Generation and DEM Quality Assessment

between the DEMs and GPS data for the 12 m, 30 m, 90 m resolution DEMs data in the UK (Figure 3.13, Figure 3.14, Figure 3.15, Figure 3.16, Figure 3.17, Figure 3.18 and Figure 3.19). The analysis of variance (ANOVA) tests of the linear regression data, showed that this correlation is highly significant in the UK (as  $p < 0.0001$  in all tests); and the constant item in the line equation in these figures indicates that the systematic error is large (around 2 m) for all of the DEM data except for the TanDEM-X 90 m data (0.2445 m).

According to the standard deviation and the RMSE of the difference between the two data sets in the results, the standard deviation for ASTER data is very large, which is about 11.5 metres. In addition, the difference between GPS and ASTER G-DEM 30 m in the UK is larger than the other differences in these figures below, and the histogram below also shows the discrete Gaussian distribution. This bigger error might be because the Aster DEM is generated by optical stereo matching and there are a lot of inaccurate matches in this process.

From the results, there is a bigger error (the difference between the elevation models) at low elevation than at high elevation. These bigger errors might be caused by KGPS. As is shown in Figure 3.3 (h), the KGPS data is acquired by a moving car on the roads of the UK. Some roads of the UK with low elevation are close to coastal areas, rivers and lakes, the KGPS might not be accurate because of the multi-pass phenomenon of the GPS signal by the waterside. In addition, the GPS is L band, the trees, buildings and mountains surrounding the road would also cause the multi-pass effect to the GPS signal. Another cause might be the random errors in the DEM data. For the photogrammetry-based DEM, there are some inaccurate matching of the roads because there is not an obvious feature on the road for matching and wrong matches might be caused by trees, buildings, mountains and shadows by the roadside. Besides, there are some holes in the data in low elevation areas of the roads, because sometimes the baseline is not small enough to acquire data from the deep and low elevation areas. These are shown in the results in Figure 3.17, where the difference between GPS and ASTER G-DEM 30 m in the UK is larger than the other differences. For the InSAR-based DEM, there are some holes in the low elevations of the road area because of low coherence, or due to the influence of a nearby river, lake or coastal water area. What is more, there are also hole errors which might be caused by shadows in the SAR data. Furthermore, this

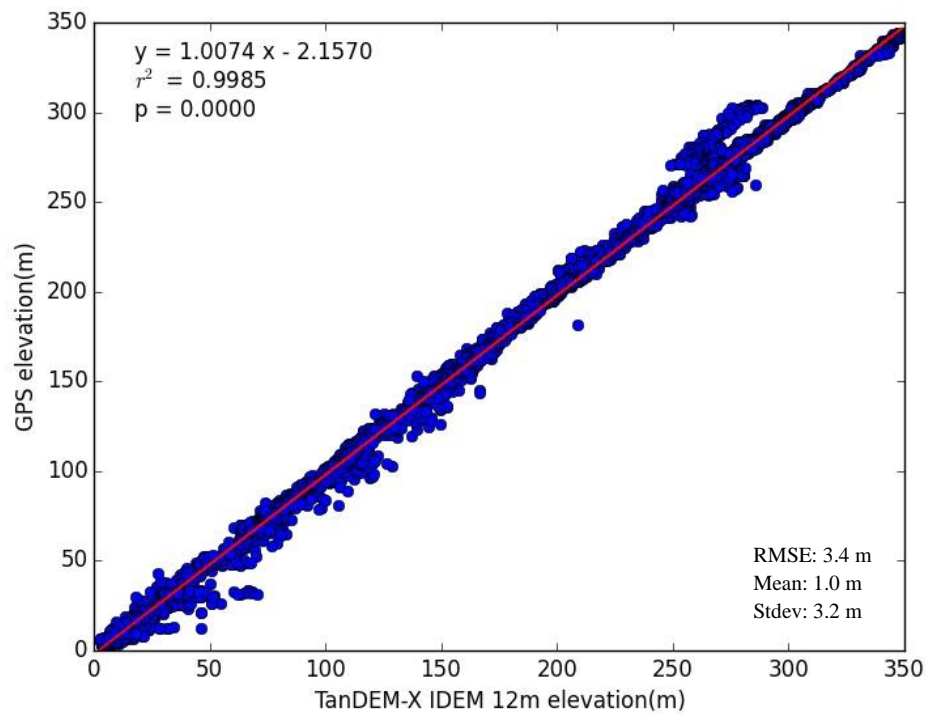
### Chapter 3. DEM Generation and DEM Quality Assessment

might be caused by low planimetric accuracy on some roads, which means the KGPS does not match very well with the DEM data in the X and Y plane over these roads.

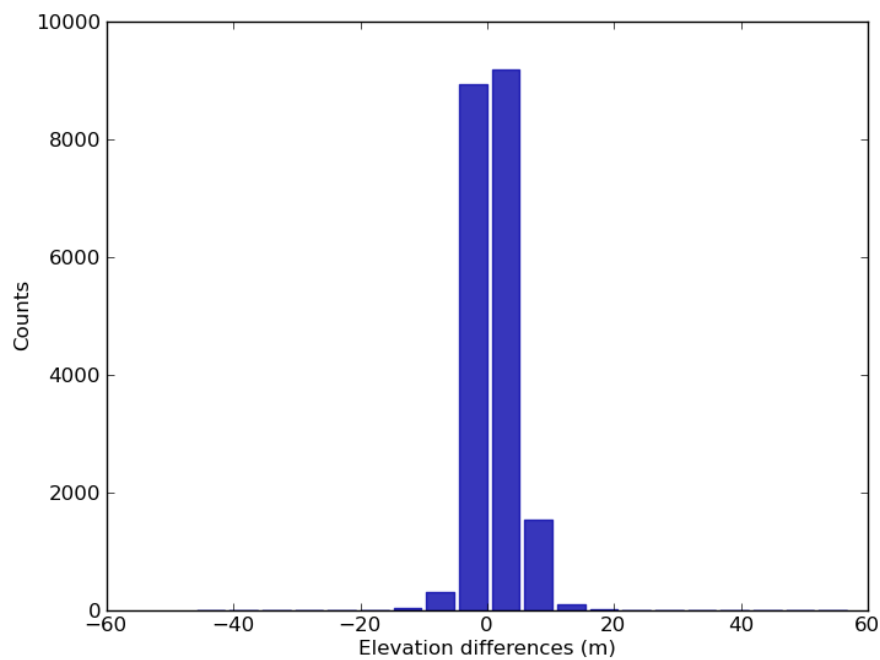
Compared to the TanDEM-X IDEM 90 m data, the TanDEM-X DEM 90 m data appear to have smaller systematic errors, which means the TanDEM-X DEM data have been post-processed and generated by resampling from high resolution to 90 m resolution using angular degree grids rather than metric grids, but the large standard deviation and RMSE hint that the TanDEM-X DEM 90 m data still have random errors.

The absolute vertical accuracy results of the test data are shown in Table 3.6 and Table 3.7 below. More statistical tables are shown in Appendix A. These tables summarise the vertical discrepancies between DEMs and GPS. In the UK, against the kinematic GPS tracks, TanDEM-X IDEM has  $1.0 \pm 3.2$  m in England & Wales, and  $0.8 \pm 5.6$  m in Scotland for 12 m and the corresponding values are  $1.3 \pm 5.2$  m for 30 m and  $1.5 \pm 6.5$  m for 90 m; SRTM has  $1.7 \pm 5.2$  m for 30 m, and  $1.7 \pm 5.1$  m for 90 m; ASTER GDEM has  $-1.6 \pm 11.5$  m for 30 m, and  $-1.7 \pm 11.7$  m for 90 m; TanDEM-X DEM has  $0.08 \pm 6.7$  m for 90 m.

### Chapter 3. DEM Generation and DEM Quality Assessment



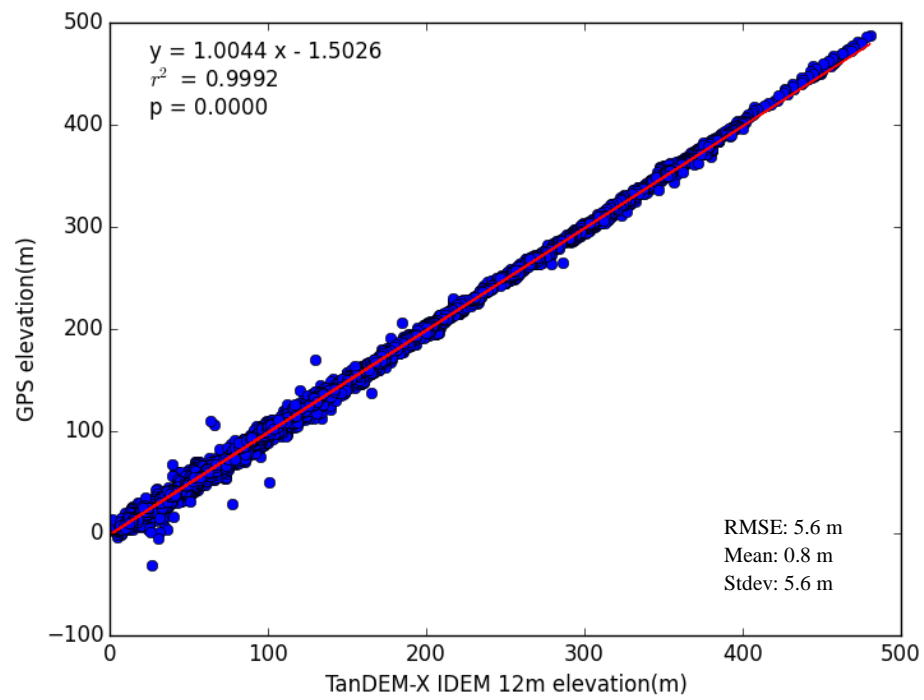
(a)



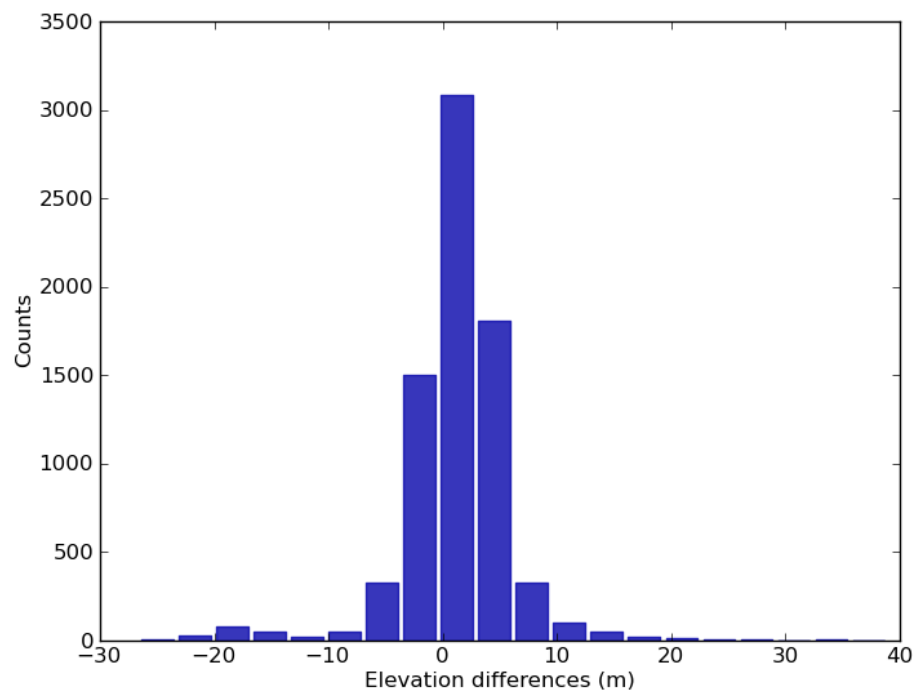
(b)

Figure 3.13 Correlation and histogram: (a) Correlation between GPS and IDEM 12 m in Scotland, the systematic error is very large (-2.1570), the correlation of the two datasets is highly significant (0.9985); (b) Histogram of the elevation differences between IDEM 12 m in Scotland and GPS





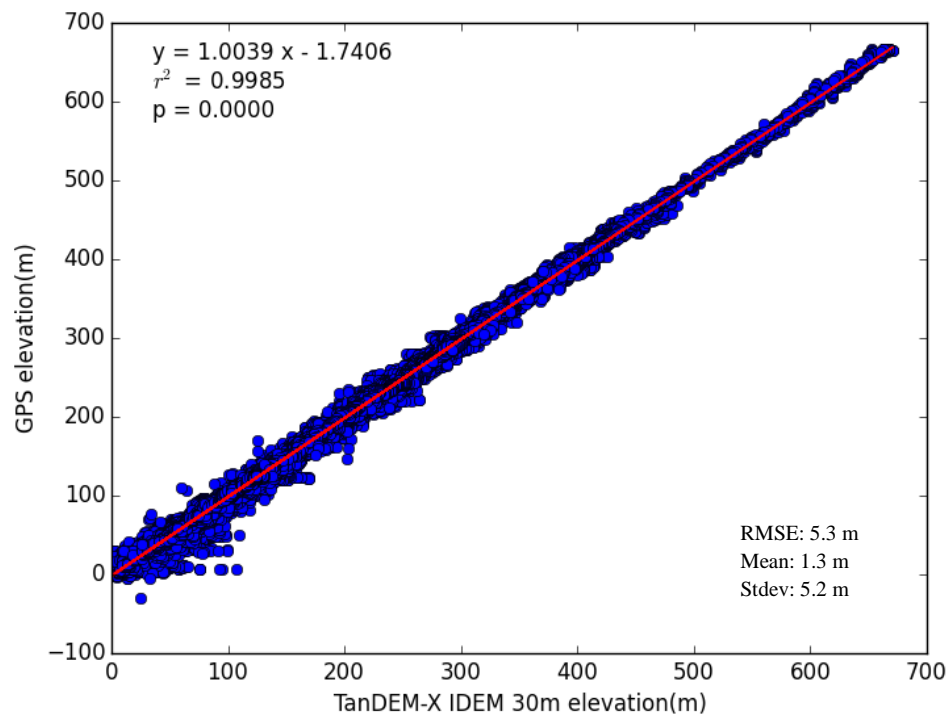
(a)



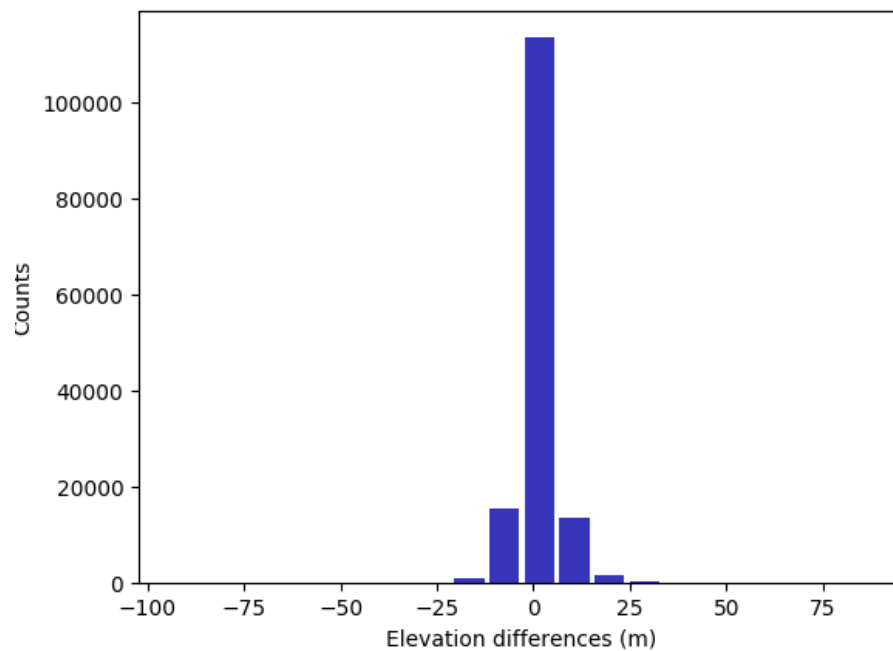
(b)

Figure 3.14 Correlation and histogram: (a) Correlation between GPS and IDEM 12 m in England, the systematic error is very large (-1.5026), the correlation of the two datasets is highly significant (0.9992); (b) Histogram of the elevation differences between IDEM 12 m in England and GPS

### Chapter 3. DEM Generation and DEM Quality Assessment

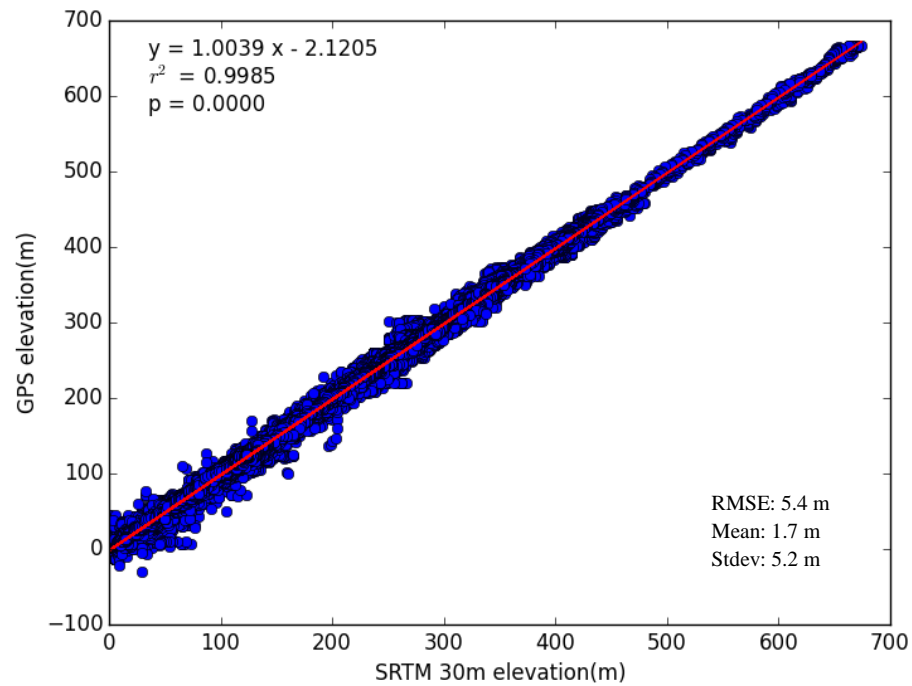


(a)

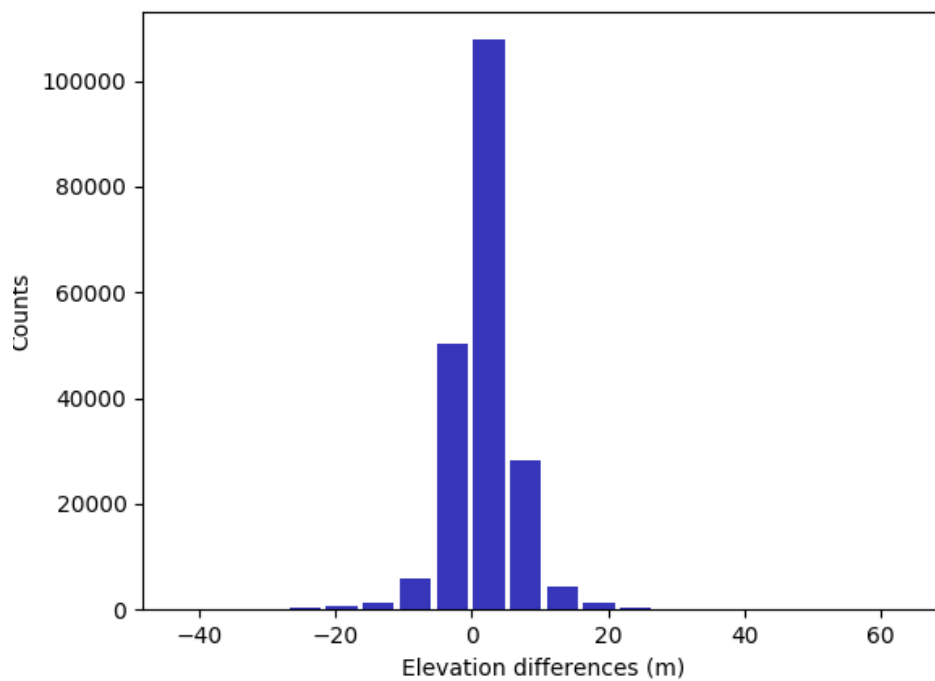


(b)

Figure 3.15 Correlation and histogram: (a) Correlation between GPS and IDEM 30 m in the UK, the systematic error is very large (-1.7406), the correlation of the two datasets is highly significant (0.9985); (b) Histogram of the elevation differences between IDEM 30 m in the UK and GPS



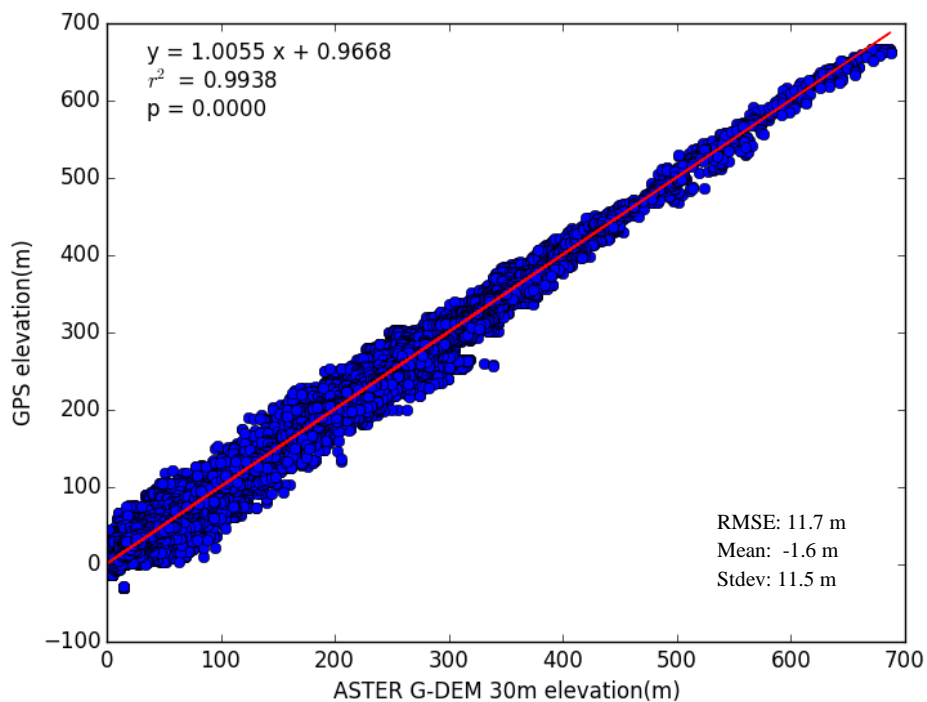
(a)



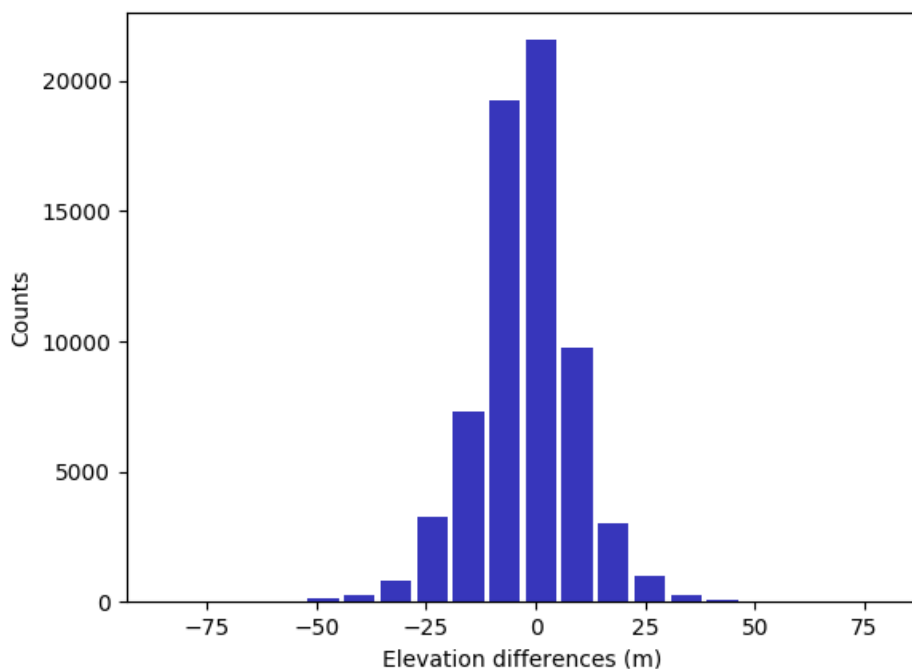
(b)

Figure 3.16 Correlation and histogram: (a) Correlation between GPS and SRTM 30 m in the UK, the systematic error is very large (-2.1205), the correlation of the two datasets is highly significant (0.9985); (b) Histogram of the elevation differences between SRTM 30 m in the UK and GPS

### Chapter 3. DEM Generation and DEM Quality Assessment

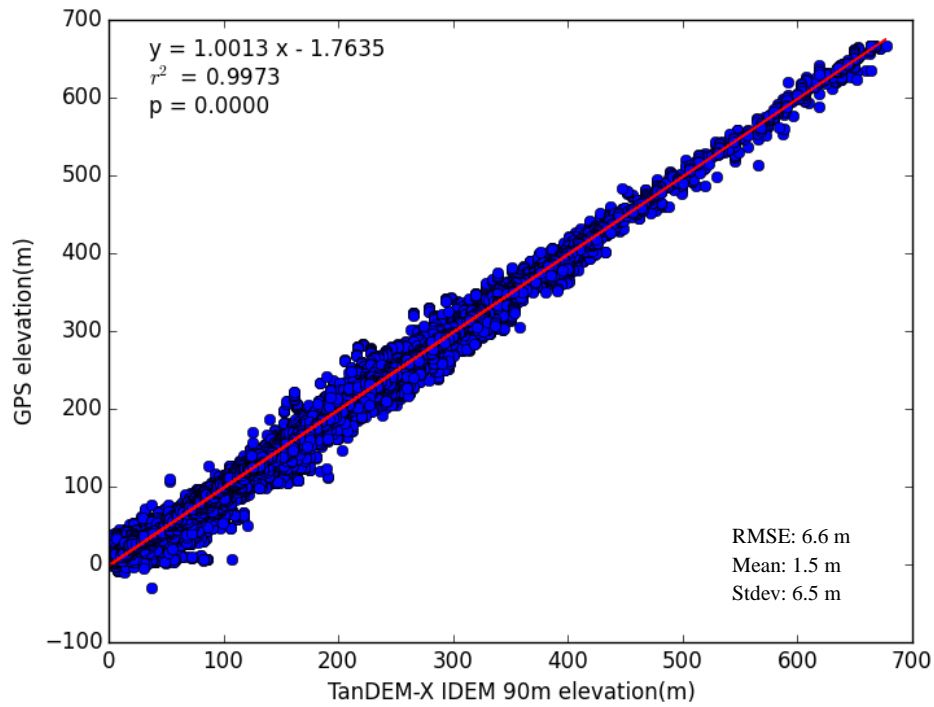


(a)

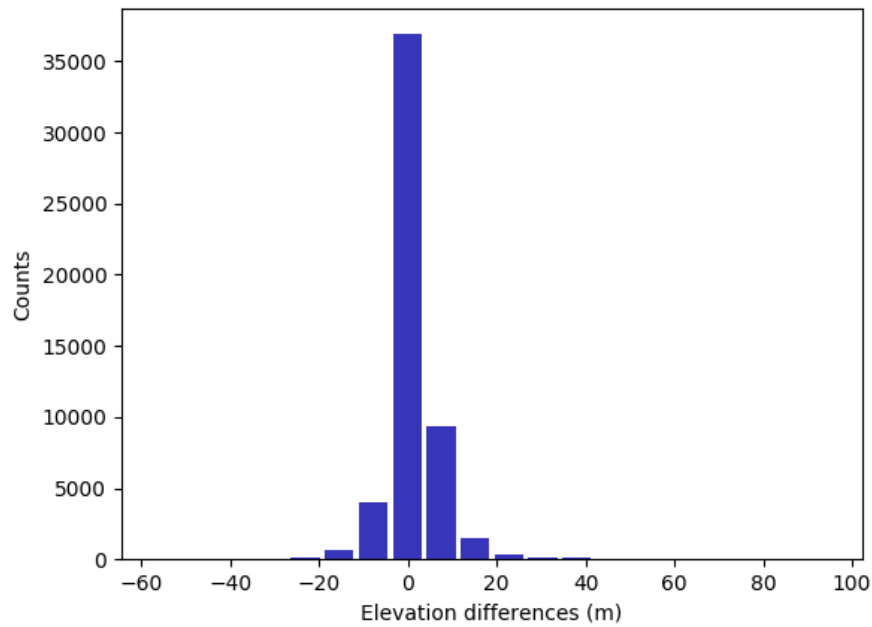


(b)

Figure 3.17 Correlation and histogram: (a) Correlation between GPS and ASTER G-DEM 30 m in the UK, the systematic error is very large (0.9668), the correlation of the two datasets is highly significant (0.9938); (b) Histogram of the elevation differences between ASTER G-DEM 30 m in the UK and GPS



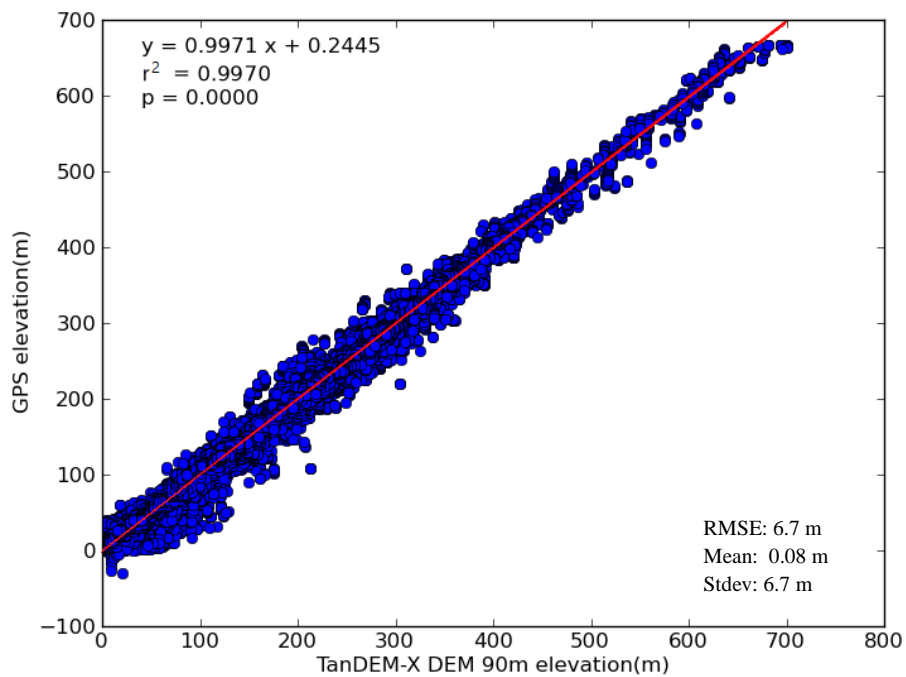
(a)



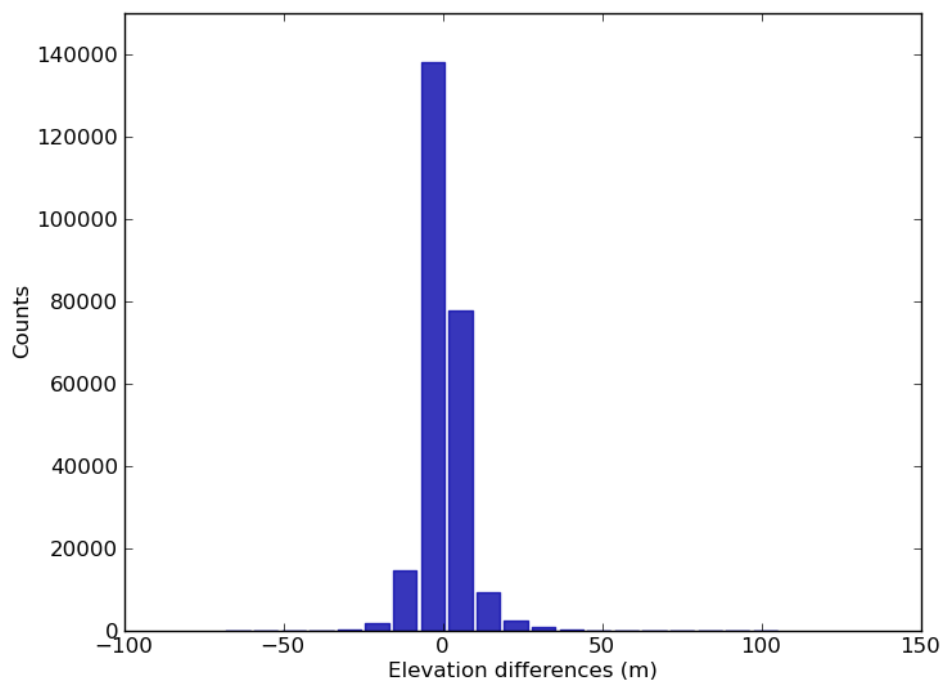
(b)

Figure 3.18 Correlation and histogram: (a) Correlation between GPS and IDEM 90 m in the UK, the systematic error is very large (-1.7635), the correlation of the two datasets is highly significant (0.9973); (b) Histogram of the elevation differences between IDEM 90 m in the UK and GPS

### Chapter 3. DEM Generation and DEM Quality Assessment



(a)



(b)

Figure 3.19 Correlation and histogram: (a) Correlation between GPS and TanDEM-X DEM 90 m in the UK, the systematic error is very small (0.2445), the correlation of the two datasets is highly significant (0.9970); (b) Histogram of the elevation differences between TanDEM-X DEM 90 m in the UK and GPS

Table 3.6 Difference statistics based on matchups of KGPS and Bluesky over the UK (after the elimination of GPS errors), unit: metres.

DATA	REGION	Resolution	xMin	xMax	xMean	xStdev $\sigma$	xRMSE	yMin	yMax	yMean	yStdev $\sigma$	yRMSE	RMSEXY	hMin	hMax	hMean	hStdev $\sigma$	Height RMSE
IDEM	England	12	-6.0	6.0	-1.3	3.6	3.8	-6.0	6.0	0.8	3.6	3.7	5.4	-46.1	57.1	1.0	3.2	3.4
	Scotland	12	-6.0	6.0	-1.9	3.9	3.9	-6.0	6.0	-5.0	3.7	3.7	5.4	-26.6	38.9	0.8	5.6	5.6
	UK	30	-15.0	15.0	-5.7	8.0	9.8	-15.0	15.0	1.3	9.3	9.4	13.6	-94.0	88.0	1.3	5.2	5.3
	UK	90	-45.0	40.3	-16.2	19.1	25.0	-45	45.0	-11.6	23.8	26.4	36.4	-51.2	78.0	1.5	6.5	6.6
TanDEM-X DEM	UK	90	-45.0	45.0	7.2	17.3	18.8	-21.7	33.1	0.3	21.9	22.5	29.4	-68.6	105.5	0.08	6.7	6.7
ASTER	UK	30	-15.0	15.0	-4.4	6.5	7.8	-15.0	15.1	3.4	7.2	8.0	11.1	-79.8	85.7	-1.6	11.5	11.7
SRTM	UK	30	-15.0	15.0	-6.4	7.4	9.7	-15.0	15.0	3.3	8.9	9.6	13.6	-43.4	64.6	1.7	5.2	5.4

## Chapter 3. DEM Generation and DEM Quality Assessment

Table 3.7 The accuracy of the EO DEM products over the UK (against KGPS)

DEM Product	Resolution	REGION	Absolute Horizontal RMSE(m)	Absolute Vertical RMSE (m)	Control point data	vertical RMSE difference between the DEM and the Bluesky DTM (m)	Control point data
<b>TanDEM-X IDEM</b>	12 m	England	5.4	3.4	KGPS	1.9	Bluesky
	12 m	Scotland	5.4	5.6	KGPS	4.1	Bluesky
	30 m	UK	13.6	5.3	KGPS	3.7	Bluesky
	90 m	UK	36.4	6.6	KGPS	4.4	Bluesky
<b>TanDEM-X DEM</b>	90 m	UK	29.4	6.7	KGPS	5.2	Bluesky
<b>SRTM 1</b>	30 m	UK	13.6	5.4	KGPS	4.1	Bluesky
<b>ASTER G-DEM</b>	30 m	UK	11.1	11.7	KGPS	4.5	Bluesky

### 3.2.6.2 Absolute accuracy test results by ICESAT

The accuracy results (aspect relationship, slope relationship and accuracy) are shown in Table 3.8, Table 3.9 and Table 3.10 below. The vertical discrepancies between the TanDEM-X IDEM data and ICESat GLAS14 data are summarised in these tables. In the UK, against the ICESat GLAS14 elevation data, the TanDEM-X IDEM data has the vertical accuracy of  $-0.03 \pm 3.7$  m over England and Wales and  $0.3 \pm 5.3$  m over Scotland for 12 m,  $-0.07 \pm 6.6$  m for 30 m, and  $0.02 \pm 9.3$  m for 90 m; the TanDEM-X DEM 90 m data has the accuracy of  $0.2 \pm 10.1$  m over the UK. In addition, 90% of all TanDEM-X IDEM data (LE90: the 90<sup>th</sup> percentile linear error<sup>21</sup>, meaning that a minimum of 90 percent of vertical errors fall within the stated LE90 value (Maune, 2007; Di et al., 2000)) are below 16.2 m (Feng and Muller, 2016), and 90% of all TanDEM-X DEM data (LE90) are below 18.4 m.

<sup>21</sup> Linear error (LE) means the maximum deviation value to the linear fitting line of the entire error data (Maune, 2007; Di et al., 2000)



### Chapter 3. DEM Generation and DEM Quality Assessment

Table 3.8 Height difference statistics over the UK (30 m IDEM-ICESat) (Feng and Muller, 2016)

Statistics		Point number	Mean (m)	Stdev $\sigma$	RMSE (m)
Slope classes	Slope < 5°	51317	-0.1	5.2	5.2
	5° ≤ Slope < 10°	6098	1.2	10.4	10.5
	10° ≤ Slope < 20°	1810	0.5	15.3	15.3
	Slope > 20°	156	5.2	20.0	20.6
Aspect regions	N (0°)	7797	1.9	6.9	7.1
	NE (45°)	7490	0.6	5.9	5.9
	E (90°)	8009	-0.5	5.8	5.8
	SE (135°)	7852	-1.4	6.6	6.8
	S (180°)	8055	-1.6	6.5	6.7
	SW (225°)	6730	-0.6	5.9	5.9
	W (270°)	6571	0.7	6.8	6.8
	NW (315°)	6751	1.8	7.1	7.3
	Flat (none)	126	0.3	14.3	14.3
England and Wales		40633	-0.1	5.4	5.4
Scotland		18748	0.1	8.6	8.6
UK		59381	-0.1	6.6	6.6

Table 3.9 Height difference statistics over the UK against the ICESat GLAS14 elevation data (Feng and Muller, 2016)

Point number	Mean (m)	Stdev $\sigma$ (m)
TanDEM-X IDEM England and Wales 12 m	-0.03	3.7
TanDEM-X IDEM Scotland 12 m	0.3	5.3
TanDEM-X IDEM UK 30 m	-0.07	6.6
TanDEM-X IDEM UK 90 m	0.02	9.3
TanDEM-X DEM UK 90 m	0.2	10.1

## Chapter 3. DEM Generation and DEM Quality Assessment

Table 3.10 The accuracy of the DEM products of the UK (control point data: ICESAT GLA14) (Feng and Muller, 2016)

DEM Product	Independent Pixel Spacing	Absolute Vertical Accuracy, (90% Confidence level) LE90 ( $\leq 1.6 \cdot \text{RMSE}$ ) (m)	Coverage
TanDEM-X IDEM	12 m	$\leq 7.4$	England
TanDEM-X IDEM	12 m	$\leq 8.5$	Scotland
TanDEM-X IDEM	30 m	$\leq 8.7$	WALES and England
TanDEM-X IDEM	30 m	$\leq 13.7$	Scotland
TanDEM-X IDEM	30 m	$\leq 10.5$	UK
TanDEM-X IDEM	90 m	$\leq 14.0$	WALES and England
TanDEM-X IDEM	90 m	$\leq 16.1$	Scotland
TanDEM-X IDEM	90 m	$\leq 14.8$	UK
TanDEM-X DEM	90 m	$\leq 14.7$	WALES and England
TanDEM-X DEM	90 m	$\leq 18.4$	Scotland
TanDEM-X DEM	90 m	$\leq 16.2$	UK

### 3.2.6.3 Vertical comparison<sup>22</sup> accuracy results

The vertical comparison accuracy results are summarised in the following tables. These tables summarise the discrepancies between DEMs and Bluesky. Over the UK, before DEM co-registration, against the Bluesky DTM, the height differences of the TanDEM-X IDEM at 12m grid-spacing are  $1.2 \pm 4.4$  m over England and Wales, and

---

<sup>22</sup> The height difference between each DEM and the ‘truth’ DEM

1.7±9.4 m over Scotland; 2.1±17.5 m for 30 m, and 2.1±18.7 m for 90 m over the UK; the differences of SRTM are  $2.2 \pm 8.1$  m for 30 m and  $2.1 \pm 9.5$  m for 90 m in the UK; the differences of ASTER GDEM are  $0.2 \pm 15.2$  m for 30 m grid-spacing, and  $0.2 \pm 15.6$  m for 90 m grid-spacing in the UK; TanDEM-X DEM 90 m has differences of  $0.5 \pm 11.1$  m over the UK. After DEM co-registration, compared to the Bluesky DTM, the 12m TanDEM-X IDEM has differences of  $0.4 \pm 2.3$  m for England & Wales and  $0.5 \pm 4.2$  m for Scotland; with corresponding values of  $0.1 \pm 3.9$  m at 30 m and  $0.01 \pm 4.5$  m at 90 m; SRTM has differences of  $0.5 \pm 4.0$  m for 30 m, and  $0.05 \pm 4.2$  m for 90 m; ASTER GDEM has differences of  $0.2 \pm 4.0$  m for 30 m, and  $0.05 \pm 4.6$  m for 90 m; TanDEM-X DEM 90 m show differences of  $0.2 \pm 5.4$  m over the UK.

In the UK, against Bluesky, the TanDEM-X IDEM 12 m data in England and Wales show an improvement in the standard deviations of the height differences from 13.2 m to 6.9 m ( $3\sigma$ ) after co-registration, the TanDEM-X IDEM 12 m data in Scotland shows an improvement in the standard deviations of the height differences from 27.3 m to 12.6 m ( $3\sigma$ ) after co-registration; the TanDEM-X IDEM 30 m data indicates that the standard deviations of the height differences increase from 52.5 m to 11.7 m ( $3\sigma$ ); according to the TanDEM-X IDEM 90 m data, the standard deviations of the height differences have been improved from 56.1 m to 13.5 m ( $3\sigma$ ); the 30 m SRTM data shows an improvement in the standard deviations of the height differences from 24.3 m to 12 m ( $3\sigma$ ) after co-registration; the 30 m ASTER GDEM data shows an improvement in the standard deviations of the height differences from 45.6 m to 12.3 m ( $3\sigma$ ) after co-registration; the TanDEM-X DEM 90 m data indicates that co-registration enhances the standard deviations of the height differences from 33.3 m to 16.2 m ( $3\sigma$ ).

According to the TanDEM-X IDEM 12 m data in England and Wales, the bias has been improved from 1.2 m to 0.4 m after co-registration against Bluesky in the UK. The TanDEM-X IDEM 12 m data in Scotland demonstrates that the co-registration bias has been improved from 1.7 m to 0.5 m; the TanDEM-X IDEM 30 m data show that bias has been improved from 2.1 m to 0.1 m because of co-registration; based on the TanDEM-X IDEM 90 m data, bias has been improved from 2.1 m to 0.01 m; the SRTM 30 m data indicates that co-registration has improved bias from 2.2 m to 0.5 m; before and after co-registration, the bias value of the ASTER GDEM 30 m data is the same at 0.2 m; the bias of the TanDEM-X DEM 90 m data has been improved from 0.5 m to 0.2 m after co-registration. All these results show that registration with the ‘truth’ DEM data can improve the accuracy of the DEM data by minimising the systematic errors. Compared

### Chapter 3. DEM Generation and DEM Quality Assessment

to the TanDEM-X IDEM 90 m data, the shift of TanDEM-X DEM 90 m data is smaller, which hints that the TanDEM-X DEM 90 m data have been generated by resampling from high resolution to 90 m resolution using angular degree grids rather than metric grids (as the shift is to do with the sampling theory).

Table 3.11 Height differences of the 12 m DEM data before and after co-registration to Bluesky DTM

Basic Stats	Matching status	Number of points	Min ( $3\sigma$ )	Max ( $3\sigma$ )	Mean (m)	Stdev $\sigma$
IDEM 12 m- Bluesky 12 m (England)	before	1770530784	-91.5	83.5	1.2	4.4
	after	1770530784	-58.0	62.0	0.4	2.3
IDEM 12 m- Bluesky 12 m (Scotland)	before	51864675	-60.4	82.0	1.7	9.1
	after	51864675	-60.0	65.6	0.5	4.2

Table 3.12 Height differences of 30 m DEM data before and after the co-registration to Bluesky DTM

Basic Stats	Matching status	Number of points	Min ( $3\sigma$ )	Max ( $3\sigma$ )	Mean (m)	Stdev $\sigma$
IDEM 30 m- Bluesky 30 m	before	1326641940	-78.4	89.7	2.1	17.5
	after	1326641940	-59.7	59.9	0.1	3.9
SRTM 30 m- Bluesky 30 m	before	1326641940	-44.0	36.4	2.2	8.1
	after	1326641940	-61	60.0	0.5	4.0
Aster 30 m-Bluesky 30 m	before	1326641940	-80.0	73.6	0.2	15.2
	after	1326641940	-60.0	60.0	0.2	4.1
IDEM 30 m-Aster 30 m	before	1326641940	-51.2	77.7	1.9	14.4
	after	1326641940	-90.0	90.0	0.1	4.9
SRTM 30 m Aster 30 m	before	1326641940	-74.2	73.5	2.0	14.8
	after	1326641940	-90.0	90.0	0.4	5.2
IDEM 30 m-SRTM 30 m	before	1326641940	-74.3	86.1	-0.1	15.9
	after	1326641940	-90.0	90	-0.3	3.0

Table 3.13 Height differences of 90 m DEM data before and after co-registration to Bluesky DTM

Basic Stats	Matching status	Number of points	Min ( $3\sigma$ )	Max ( $3\sigma$ )	Mean (m)	Stdev $\sigma$
IDEM 90 m- Bluesky 90 m	before	82981888	-92.8	93.9	2.1	18.7
	after	82981888	-60.0	60.0	0.01	4.5
TanDEM-X DEM 90 m-Bluesky 90 m	before	111887674	-93.2	92.8	0.5	11.1
	after	111887674	-60.0	60.0	0.2	5.4
SRTM 90 m- Bluesky 90 m	before	82981888	-50.6	43.7	2.1	9.5
	after	82981888	-60.0	60.0	0.05	4.2
Aster 90 m- Bluesky 90 m	before	82981888	-80.1	74.7	0.2	15.6
	after	82981888	-60.0	60.0	0.05	4.6
IDEM 90 m-Aster 90 m	before	82981888	-56.9	87.9	1.9	15.0
	after	82981888	-60.0	60.0	-0.03	5.2
SRTM 90 m Aster 90 m	before	82981888	-80.7	77.9	1.9	15.9
	after	82981888	-62.1	59.8	0.01	5.9
IDEM 90 m- SRTM 90 m	before	82981888	-90.4	92.6	0.03	17.6
	after	82981888	-60.0	60.0	0.002	4.4

#### 3.2.6.4 The accuracy of the DEM products

According to the equation (90% confidence level accuracy =  $1.6 \times \text{RMSE}$ ) in Chapter 2, the elevation accuracy of the DEM products (90% of the data difference is smaller than the product accuracy) are calculated. The calculation results are shown in the statistical tables in Appendix B and the accuracy of the DEM products of the UK is summarised in Table 3.14 below. The reference data for the vertical comparison accuracy validation is Bluesky, while the reference data for the vertical and horizontal accuracy validation is KGPS. In the UK, for the 90% confidence level, against KGPS, TanDEM-X IDEM has the absolute vertical accuracy of 5.5 m in England and Wales and 9.0 m in Scotland for 12 m, 8.5 m for 30 m, and 10.6 m for 90 m; SRTM has 8.7 m for 30 m; ASTER GDEM has 18.8 m for 30 m, and TanDEM-X DEM 90 m has the absolute vertical accuracy of 10.7 m in the UK. After DEM co-registration, against Bluesky, 90% of all TanDEM-X IDEM data (linear error at 90% confidence level) are below 7.1 m; 90% of all TanDEM-X DEM data (linear error at 90% confidence level) are below 8.4 m; 90% of all SRTM DEM data (linear error at 90% confidence level) are below 6.6 m and 90%

### Chapter 3. DEM Generation and DEM Quality Assessment

of all TanDEM-X DEM data (linear error at 90% confidence level) are below 7.2 m. Therefore, the TanDEM-X DEM and TanDEM-X DEM data over the UK all meet the HRTI/DTED-3 (Krieger et al., 2005b) absolute vertical accuracy standard (12 m resolution,  $LE_{90} \leq 10$  m absolute accuracy).

Table 3.14 The accuracy of the EO DEM products over the UK (against KGPS and Bluesky DTM), ( $LE_{90}$  means 90%,  $LE_{90} \leq 1.6 \cdot RMSE$ )

DEM Product	Resolution	REGION	Absolute Horizontal Accuracy $LE_{90}$ (m)	Absolute Vertical Accuracy $LE_{90}$ (m)	Control Point Data	Vertical Comparison Accuracy $LE_{90}$ (m)	Control Point Data
TanDEM-X IDEM	12 m	England	$\leq 8.7$	$\leq 5.5$	KGPS	$\leq 3.1$	Bluesky
	12 m	Scotland	$\leq 8.7$	$\leq 9.0$	KGPS	$\leq 6.6$	Bluesky
	30 m	UK	$\leq 21.8$	$\leq 8.5$	KGPS	$\leq 6.0$	Bluesky
	90 m	UK	$\leq 58.3$	$\leq 10.6$	KGPS	$\leq 7.1$	Bluesky
TanDEM-X DEM	90 m	UK	$\leq 47.0$	$\leq 10.7$	KGPS	$\leq 8.4$	Bluesky
SRTM 1	30 m	UK	$\leq 21.8$	$\leq 8.7$	KGPS	$\leq 6.6$	Bluesky
ASTER G-DEM	30 m	UK	$\leq 17.8$	$\leq 18.8$	KGPS	$\leq 7.2$	Bluesky

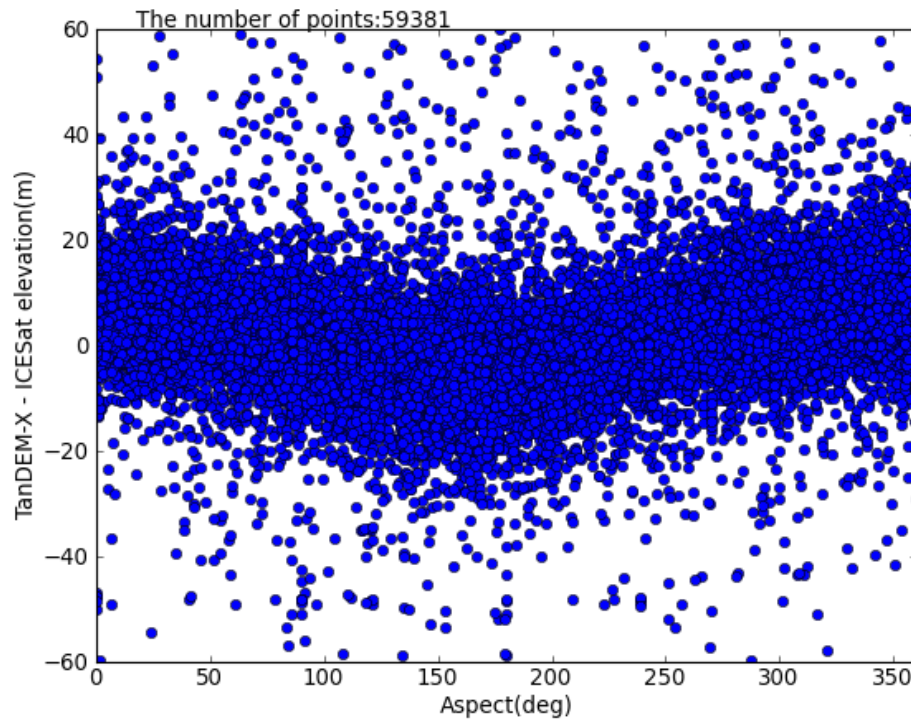
### 3.2.7 Analysis and Discussion

#### 3.2.7.1 TanDEM-X IDEM error analysis using topographic attributes

In this experiment, both the standard deviations and RMSE (see 3.2.6) of the DEM height differences are calculated in order to assess the accuracy of the DEM products. The effect of topography on the spatial distribution of the vertical errors is studied by analysing the residuals in several terrain attributes (like slope, aspect and elevation) (Feng and Muller, 2016).

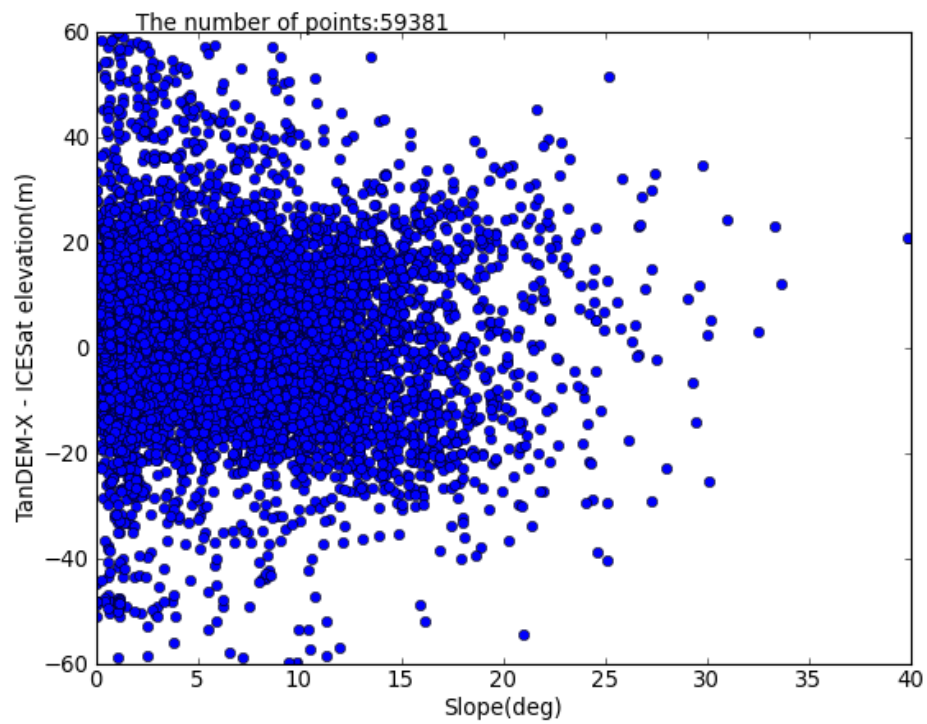
Over the UK (based on Table 3.8), there are some relationships between the differences (30 m IDEM data) and slopes or aspects of the terrain (Figure 3.20 a and b), the differences are distributed evenly in different aspects, and they are mostly between -20 m and 20 m; the large differences occur below elevations of 150 m (Figure 3.20 c). The systematic error is very small, and a strong correlation between ICESAT GLA14

data and TanDEM-X IDEM 30 m data can be seen from the linear regression analysis (Figure 3.20 d). The statistical value of the probability distribution (PDF means probability distribution function) of the positive, negative and total difference value in the different slope categories are shown in Figure 3.20 e. The density of the differences becomes progressively smaller with the increasing slope (Figure 3.20 b and e), and the biggest probability distribution is in the category of the slope that is smaller than  $5^\circ$ , so is the positive, negative probability distribution. The total probability density of the eight aspects (based on Table 3.8) is almost the same (Figure 3.20 a and f). There is a line in Figure 3.20 c, which implies that large errors occur in the low elevation area; besides, the error might have a linear relationship with the elevation below 100 m; or this line might exist because there are not enough ICESat points for validation, which cause the anomalous distribution. Besides, TanDEM-X IDEM 12 m and 90 m have the same pattern as TanDEM-X IDEM 30 m in the UK (Feng and Muller, 2016).

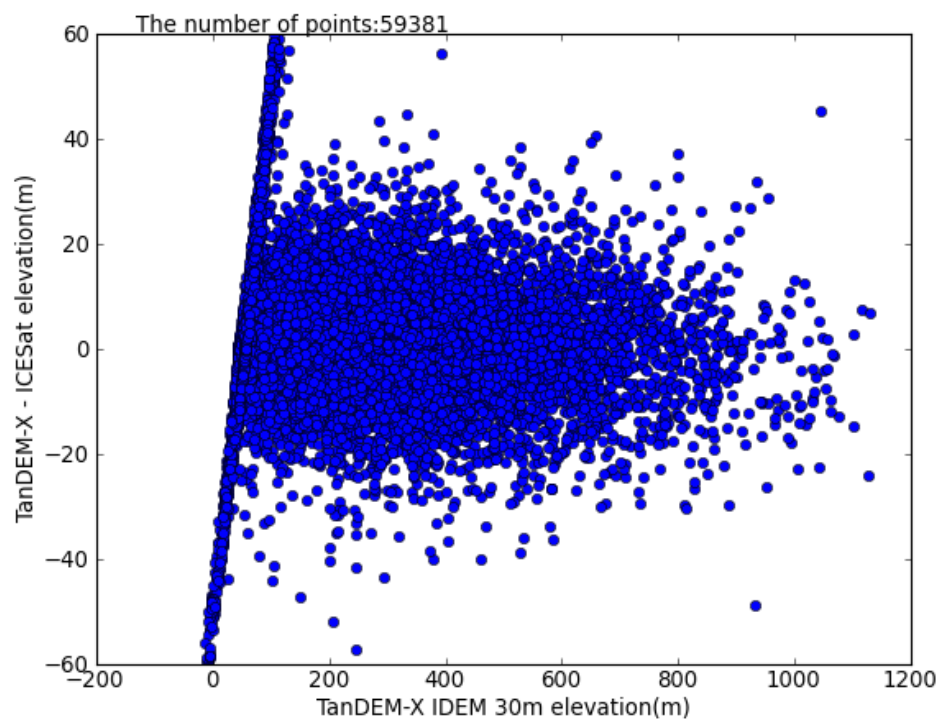


(a)

### Chapter 3. DEM Generation and DEM Quality Assessment

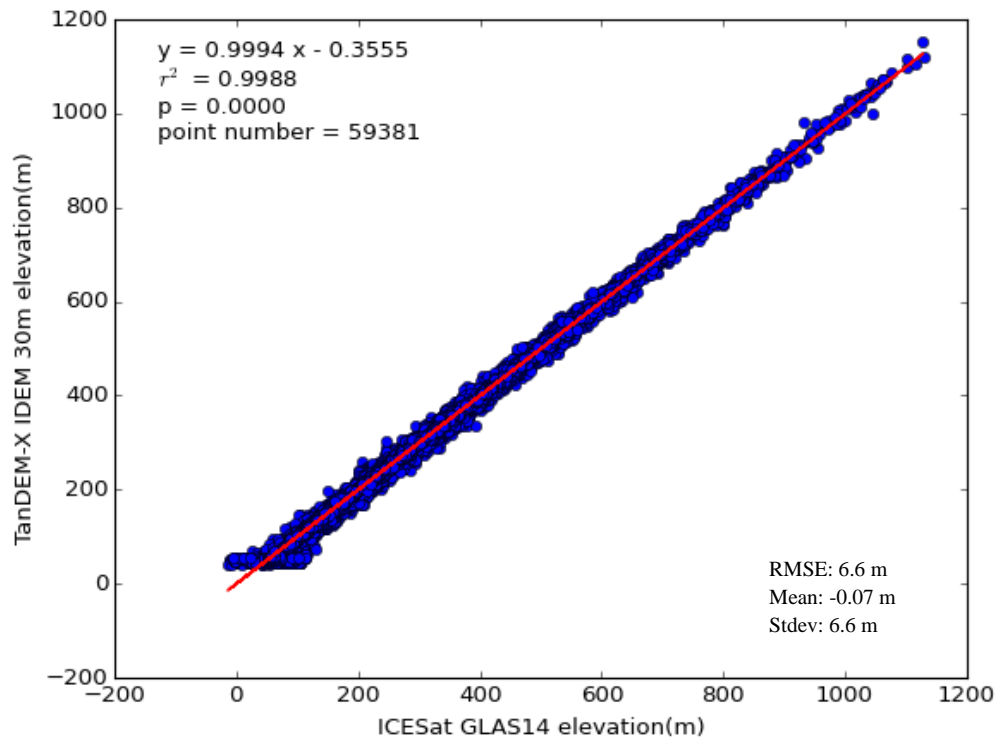


(b)

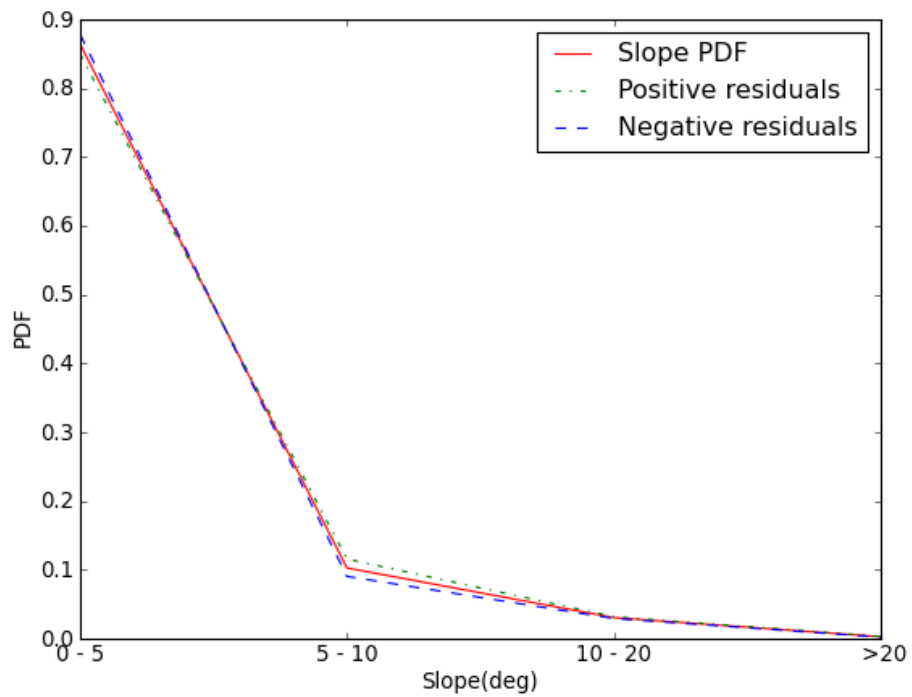


(c)

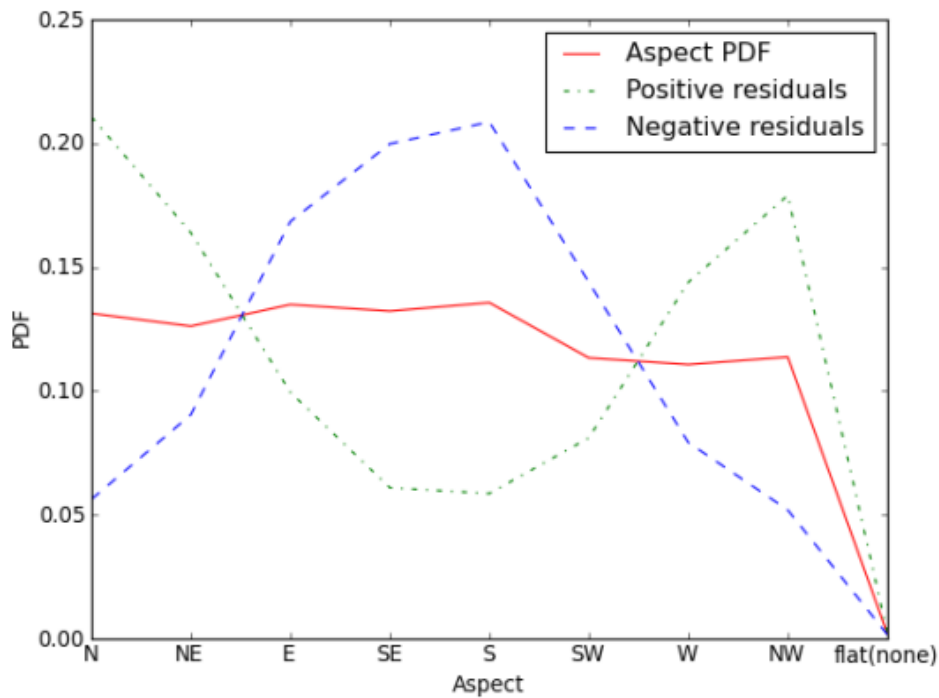




(d)



(e)



(f)

Figure 3.20 Elevation residuals between the TanDEM-X IDEM data and ICESAT GLA14 elevation data in the UK (30 m IDEM): (a) The elevation difference with aspect; (b) The elevation difference with slope; (c) The elevation difference with elevation derived from the TanDEM-X IDEM data; (d) Correlation between ICESAT GLA14 and IDEM data; (e) Probability density functions (PDFs) of slope for positive and negative residuals and of overall slope; (f) Probability density functions (PDFs) of aspect measured at locations with positive and negative residuals and PDFs of the overall aspect, North means aspect 0 degrees, East means aspect 90 degrees, South means aspect 180 degrees, and West means aspect 270 degrees (shown in Table 3.8) (Feng and Muller, 2016)

### 3.2.7.2 Analysis and discussion of TanDEM-X IDEM

In this analysis, both the standard deviation and RMSE (see 3.2.6 and Appendix B) of the DEM height difference reflect the absolute and vertical comparison accuracy of the DEM products.

(1) Using the ICESat GLA14 data to validate TanDEM-X IDEM, it is necessary to filter the data errors, outliers, cloud contamination and so on; besides, the coordinate system of these two data sets should be converted into the same reference ellipsoid (Feng and Muller, 2016).

(2) From Table 3.7 and Table 3.10 (see the data in the Independent Pixel Spacing column and Absolute Vertical Accuracy column) and Table 3.14 above, the accuracy (the standard deviation and RMSE) of all DEM products decreases typically when the

resolution (pixel spacing) increases. This might be because the grid resolution, sampling method or pixel size and interpolation algorithm influence the DEM accuracy, and the random error accumulation and the bigger horizontal shift cause different height errors. Besides, the footprint of the ICESat GLA14 data is 70 m (the centroid height of the raw waveform data is used for validation, shown in Figure 3.5), which might introduce uncertainty with the different resolution when compared to the 12 m, 30 m and 90 m TanDEM DEM data because the horizontal position uncertainty might cause height differences, so the elevation values in 70 m grid area (match-up the ICESat footprint) of the high resolution DEMs (12 m and 30 m, higher than 70 m) are extracted to calculate the median value for the quality assessment (Feng and Muller, 2016).

(3) From Table 3.8 and other resolution results, the accuracy of all DEM products varies a little with different aspects, but it decreases when the slopes increase, which hints that the slope has a strong effect on the vertical accuracy of the TanDEM-X IDEMs. In the small slope site, errors are smaller, while in the larger slope terrain, large errors and data voids are more frequent, and their location is strongly influenced by the topography (Feng and Muller, 2016).

(4) Within the absolute accuracy validation process, a good performance is shown using the GPS and corresponding DEM template matching through cross-correlation with RANSAC method. However, critical parameters like matching window size, template window size and the correlation coefficient threshold need to be selected carefully.

(5) For the vertical comparison accuracy validation process, the DEM to DEM co-registration accuracy is subpixel ( $RMSE < 0.5$  pixel) and it was demonstrated that surface matching could also improve this vertical comparison accuracy.

(6) For the UK, from these statistical tables above, with respect to the IDEM products, elevation differences change from one region to another. These variations may be due to voids, missing coastal areas and misidentified water features. This could also be caused by the acquisition geometry, signal noise, or reduced interferometric coherence and phase unwrapping errors.

(7) In the UK, against the kinematic GPS tracks, the 12 m TanDEM-X IDEM has  $1.005 \pm 3.2$  m in England & Wales, and  $0.808 \pm 5.558$  m in Scotland. Against the ICESat GLAS14 elevation data, compared the accuracy of  $-0.03 \pm 3.7$  m over England and Wales to the accuracy of  $0.3 \pm 5.3$  m over Scotland for the 12 m IDEM data, the standard deviation of the DEM height difference is larger in Scotland than in England. It is well known that the terrain height is more rugged and more complex over Scotland

### Chapter 3. DEM Generation and DEM Quality Assessment

than in England and Wales. Thus, this observation appears to reflect that the vertical accuracy is influenced by how rugged the terrain is. The vertical accuracy is lower in complex terrain areas than in plain areas.

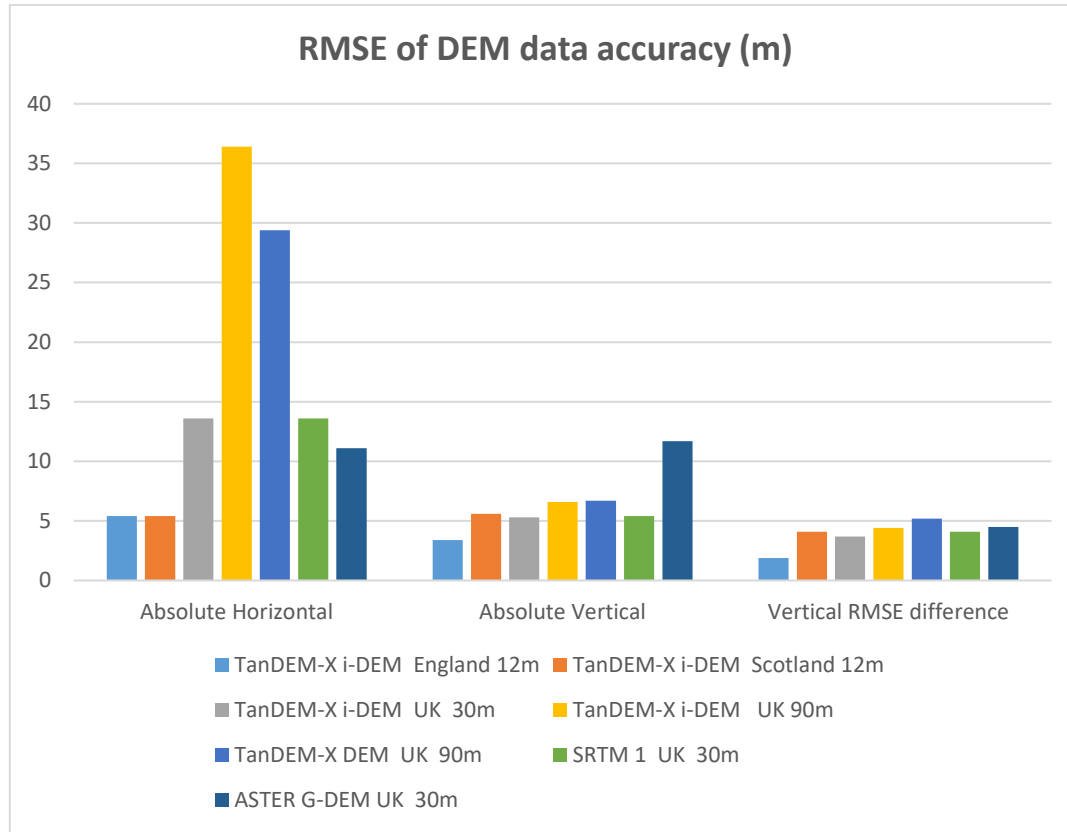


Figure 3.21 RMSE of DEM data compared to GPS and Bluesky DTM

(8) As is shown in Figure 3.21 above, over the UK, via KGPS, the planimetric accuracy of ASTER appears to be better than SRTM or IDEM. The reason is that different sensors have their own advantages and disadvantages. Stereo- optical sensors may have better plane positional accuracy than radar sensors (it is easy to find and locate control points in optical data, while it is not easy to locate the natural corner reflector precisely in SAR data), but relatively poorer vertical accuracy than a radar sensor. Meanwhile, via KGPS, the ASTER GDEM has the worst absolute vertical accuracy in all resolutions (12 m, 30 m and 90 m), while the IDEM appears to show the best absolute vertical accuracy in the 30 m resolution, but it ranks second at the 90 m resolution, compared to SRTM having the best absolute vertical accuracy at the 90 m resolution which ranks second at the 30 m resolution. This implies that the IDEM only has a higher absolute vertical accuracy than SRTM when the DEM data resolution is very high, while it is not the case

when the DEM data resolution is not very high. This may be caused by the DEM resampling and postprocessing methods.

(9) From all of the tables of statistics, in addition to Figure 3.22 and Figure 3.23 below, after matching, the TanDEM-X IDEM appears to show the highest vertical comparison accuracy over the whole UK when compared with Bluesky. SRTM is the second best in the UK, while ASTER GDEM is the lowest ranked over the UK. This implies that the vertical comparison accuracy of the IDEM is better than the ASTER GDEM in the UK areas after surface matching (DEM to DEM co-registration) processing.

(10) From the map of TanDEM-X DEM 90 m in Figure 3.3 (d) in page 119, the errors (there are many discrete points along the coastal areas in the UK, but there are not many islands along the coastal areas in the UK) can be seen in coastal areas. Compared to the TanDEM-X IDEM 90 m data, the TanDEM-X DEM 90 m data, appears to have better accuracy after surface matching and water mask, which hints the TanDEM-X DEM data have been post-processed (with the systematic errors, and so on) and generated by resampling from high resolution to 90 m resolution using angular degree grids rather than metric grids, but after surface matching and water mask, TanDEM-X DEM 90 m is not better than TanDEM-X IDEM 90 m, this might because the TanDEM-X DEM 90 m has more data with errors (coast and son on) than TanDEM-X IDEM 90 m, shown in Figure 3.3 (b) and (d). In addition, the small mean value (see Table 3.6, Table 3.9, Table 3.13 in Section 3.2.6) of the TanDEM-X DEM 90 m height difference reflects that the TanDEM-X DEM 90 m product does not appear to have any systematic vertical errors (shift). However, compared to other DEM data in Figure 3.22 and Figure 3.23 (and the statistical data, like Table 3.6, Table 3.7, Table 3.9, Table 3.13 in Section 3.2.6), the large standard deviation and RMSE still suggest that the 90 m TanDEM-X DEM has large random errors, which might be able to be improved in the future.

## Chapter 3. DEM Generation and DEM Quality Assessment

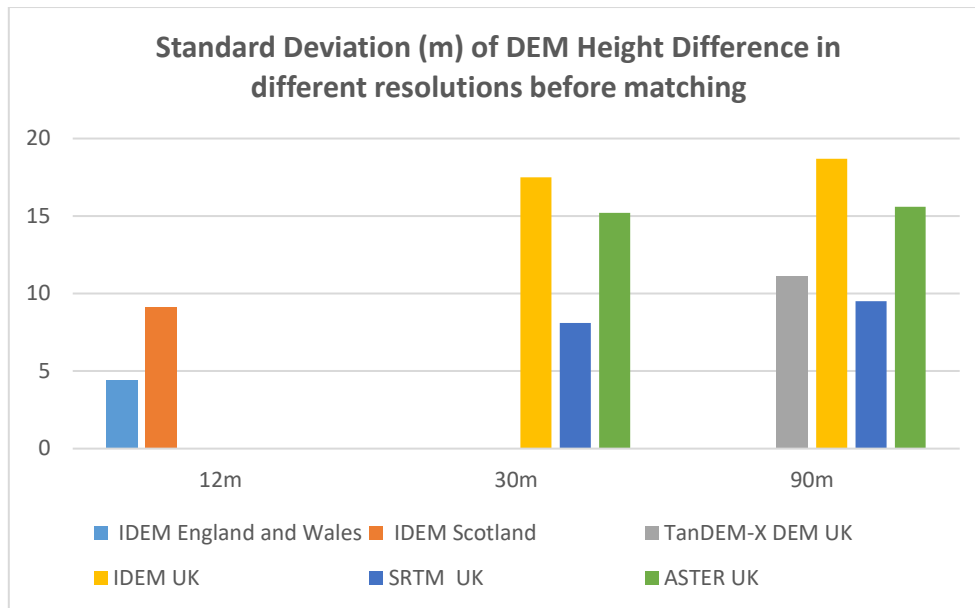


Figure 3.22 Standard deviation of the DEM height differences before surface matching

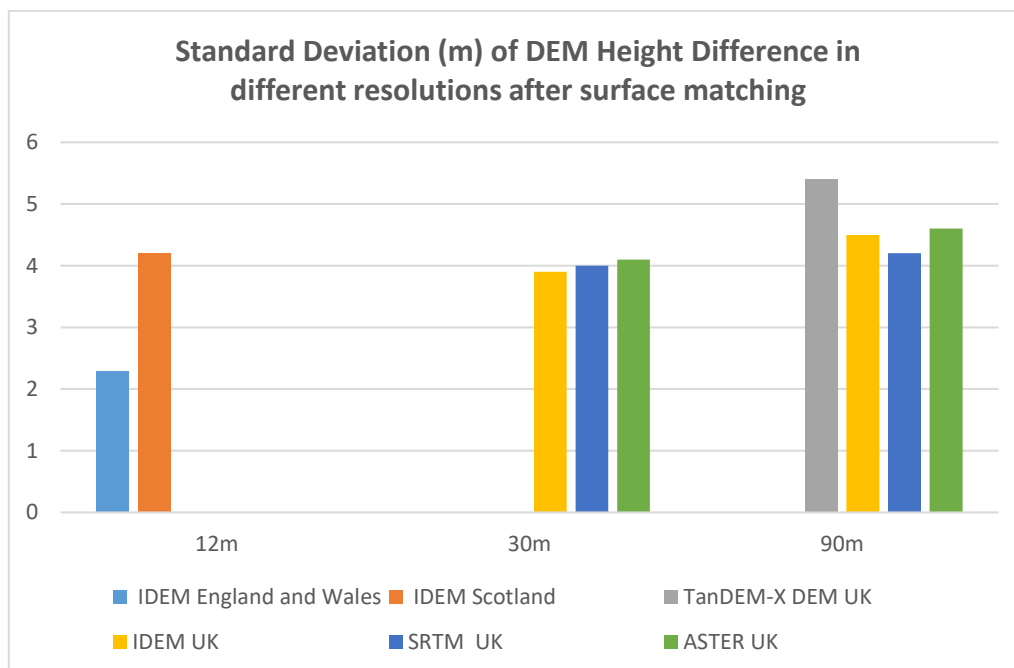


Figure 3.23 Standard deviation of the DEM height differences after surface matching

### 3.2.8 Conclusions

Through this quality assessment study, the accuracy of TanDEM-X IDEM in the UK is summarised as below: against the ICESat GLAS14 elevation data, the TanDEM-X IDEM data has the accuracy of  $-0.03 \pm 3.7$  m in England and Wales and  $0.4 \pm 5.3$  m over Scotland for 12 m,  $-0.07 \pm 6.6$  m for 30 m in the UK, and  $0.02 \pm 9.3$  m at 90 m in the UK; TanDEM-X DEM 90 m data has the accuracy of  $0.2 \pm 10.1$  m over the UK. In addition,

### Chapter 3. DEM Generation and DEM Quality Assessment

90% of all TanDEM-X IDEM data (linear error at 90% confidence level) are below 16.2 m (Feng and Muller, 2016), and 90% of all TanDEM-X DEM data (linear error at 90% confidence level) are below 18.4 m. This implies that the Digital Elevation Model (DEM) from the TanDEM-X mission (bistatic X-Band interferometric SAR) is better than many other products available now. The results also show that the topographic parameters (slope, aspect and relief) have a strong impact on the vertical accuracy of the TanDEM-X IDEMs. In high-relief and large slope terrains, large errors and data voids occur frequently, and their location is strongly influenced by topography, while in low to medium relief and low slope sites, the errors are smaller (Feng and Muller, 2016).

The TanDEM-X mission aims to generate a Digital Elevation Model (DEM) globally which is likely to be available from 2018, but its accuracy has not yet been validated completely. This chapter focuses on an assessment of the accuracy of a TanDEM-X intermediate DEM (IDEM) and a TanDEM-X DEM (in comparison to KGPS, “ground truth” from a national supplier (Bluesky) and SRTM 1 and ASTER G-DEM) over the UK in order to extrapolate these results in the global area. Through this research, the accuracy of TanDEM-X IDEM and DEM in the UK is summarised as: against kinematic GPS tracks, TanDEM-X IDEM has the accuracy of  $1.0 \pm 3.2$  m in England & Wales, and  $0.8 \pm 5.6$  m in Scotland for 12 m and the corresponding values are  $1.3 \pm 5.2$  m for 30 m and  $1.5 \pm 6.5$  m for 90 m; against kinematic GPS tracks, TanDEM-X DEM has the accuracy of  $0.08 \pm 6.7$  m for 90 m; against Bluesky, after DEM co-registration, TanDEM-X IDEM has differences of  $0.4 \pm 2.3$  m for England & Wales  $0.5 \pm 4.2$  m at 12 m; the corresponding values are  $0.1 \pm 3.9$  m at 30 m and  $0.01 \pm 4.5$  m at 90 m; TanDEM-X DEM 90 m has differences of  $0.2 \pm 5.4$  m in the UK.

DEM co-registration is a key step to assess the accuracy of DEM products in the UK. The absolute vertical accuracy of the IDEM product is better than the SRTM and ASTER GDEM products at a high and medium resolution (12 m, 30 m), while the vertical comparison accuracy of the IDEM product is worse (because of some errors) than the accuracy of the SRTM and ASTER GDEM products before the water mask. Compared to the TanDEM-X IDEM 90 m data, the TanDEM-X DEM 90 m data, appears to have better accuracy after the water mask and surface matching, which hints the TanDEM-X DEM data have been post-processed (with the shift, and so on) and generated by resampling from high resolution to 90 m resolution using angular degree grids rather than metric grids. After surface matching and the water mask, the vertical comparison accuracy of the IDEM product is better at 30 m than the SRTM and ASTER GDEM

## **Chapter 3. DEM Generation and DEM Quality Assessment**

products. However, the vertical comparison accuracy of the IDEM 90 m data still worse than other data. Moreover, though TanDEM-X DEM 90 m and TanDEM-X IDEM 90 m is better than the ASTER GDEM 90 m data (Figure 3.23), they are still not better than the SRTM data (this might be because SRTM is edited data, while TanDEM-X IDEM and TanDEM-X DEM 90 m still have many errors). Therefore, the accuracy of TanDEM-X IDEM (12 m, 30 m and 90 m) and TanDEM-X DEM 90 m needs to be improved in the future.

### **3.3 DEM Quality Assessment and Improvement for TomoSAR**

This thesis aims to utilise the TanDEM-X DEM data in 3D TomoSAR imaging and 4D SAR differential tomography (Diff-TomoSAR). Before using the 12 m TanDEM-X DEM as a reference, an initial validation is required. A novel automated co-registration technique called surface matching is employed to co-register the elevation data based on different vertical datums with offsets due to resampling errors. The use of surface matching techniques complements the defects of traditional co-registration methods using Ground Control Points (GCPs) especially when the datums are unknown. (Lin et al., 2010). After that, 12 m TanDEM-X DEM is edited to increase the accuracy and the new improved 12 m TanDEM-X DEM is employed as a reference DEM for the 3D TomoSAR imaging and 4D SAR differential tomography study, with the higher resolution DEM assisting TomoSAR co-registration, subtraction of topography, topographic compensation and georeferencing to dramatically improve the accuracy of the 3D TomoSAR imaging and 4D SAR deformation extraction.

#### **3.3.1 TanDEM-X 12 m DEM Data over Zipingpu Dam**

The 12 m TanDEM-X DEM data was obtained from DLR for 3D TomoSAR imaging and 4D SAR differential tomography (Diff-TomoSAR) in Zipingpu dam, Dujiangyan, Sichuan province, China (103.574284°E, 31.035097°N), shown in Figure 3.24. Moreover, the hill shade map is shown in Figure 3.25.



## Chapter 3. DEM Generation and DEM Quality Assessment

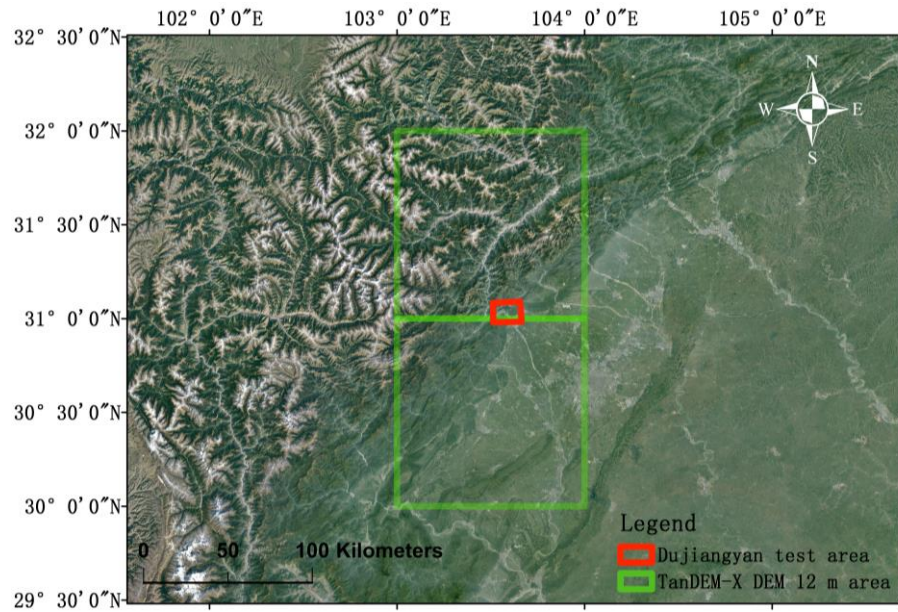


Figure 3.24 Location of the 12 m TanDEM-X DEM data, the red box area is the Dujiangyan TomoSAR test area using TanDEM-X DEM, the two green boxes are the two 12 m TanDEM-X DEM tiles, the 12 m DEM map of the two tiles are shown in Figure 3.25, the background image is the Google Earth image (image source: Landsat image/Copernicus)

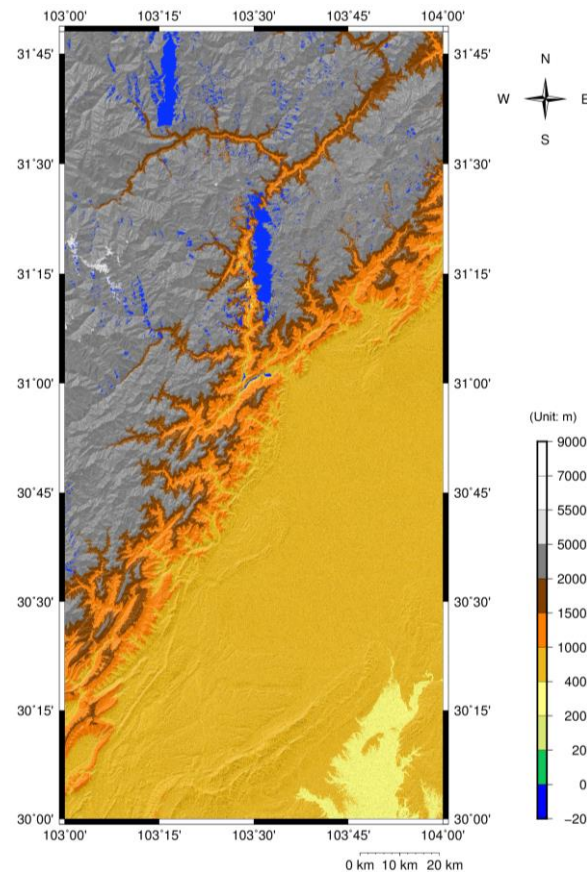


Figure 3.25 TanDEM-X 12 m DEM map of the two 12 m TanDEM-X DEM tiles in Figure 3.24, the blue areas are holes caused by low coherence or shadow

### 3.3.2 TanDEM-X 12 m DEM Data Quality Assessment and Editing

### Chapter 3. DEM Generation and DEM Quality Assessment

A high quality reference DEM is required by most SAR data processing (e.g. InSAR, TomoSAR, PolInSAR, TomoSAR, D-TomoSAR) to derive accurate results in various applications, such as monitoring earthquakes, volcanic activities, glacial movement, mining deformations, subsidence and landslides (Sun and Muller, 2016). Therefore, before using the DEM data, the DEM quality assessment is needed for tomography application.

According to the methods, discussed above, we use SRTM 30 m and ICESAT GLA14 data to validate the DEM before using them in the TomoSAR study. Through this study, the accuracy of the TanDEM-X 12 m DEM data in Dujiangyan is summarized as follows: against the ICESat GLA14 elevation data, TanDEM-X 12 m DEM has an accuracy of  $0.647 \pm 16.108$  m, against the SRTM 30 m data, TanDEM-X 12 m DEM has an accuracy of  $-0.355 \pm 15.945$  m, as shown in Table 3.15 and Table 3.16.

The effect of topography on the spatial distribution of vertical errors was studied by analysing the elevation differences in several terrain attributes (aspect, slope and elevation) again. The analysis results demonstrate the lack of significant differences between the DEMs and ICESAT data in Dujiangyan. The linear regression analysis suggests a strong correlation between the ICESAT GLA14 data and the TanDEM-X DEM 12 m DEMs data in Dujiangyan, shown in Figure 3.26 (a) below. The results of the analysis of variance (ANOVA) on the linear regression data show this correlation is highly significant in Dujiangyan ( $p < 0.0001$  in the test in Figure 3.26 (a)); and the systematic error is very small (the mean value of the difference in Table 3.15 and Table 3.16 is small). In Dujiangyan, comparisons of the differences (12 m TanDEM-X DEM data - between ICESAT GLA14 data) with the slopes and aspects show that the differences are mainly distributed around zero in Figure 3.26 (b) in all aspects and mainly distributed below the 50 degrees slope in Figure 3.26 (d). However, there are big differences scattered in Figure 3.26 (b) and (d). Besides, the standard deviation of the difference between the 12 m TanDEM-X DEM data and SRTM data is a little bit larger in Table 3.15, this might be because the 12 m TanDEM-X DEM data has errors, noise and a lot of changes (like new bridges, new dam, earthquake deformation, landslide deformation and so on in this area) after 2000 (the SRTM data were collected in 2000). Moreover, big differences occur over almost all elevations (Figure 3.20 (c)), so, the 12 m TanDEM-X DEM data have random errors (mainly from high frequency noise), which need filtering before using it.

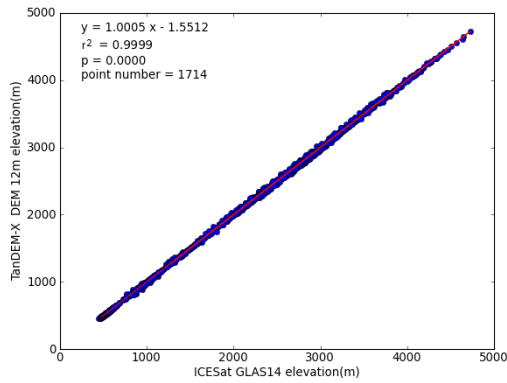
### Chapter 3. DEM Generation and DEM Quality Assessment

Table 3.15 12 m DEM data height differences before and after co-registration to SRTM

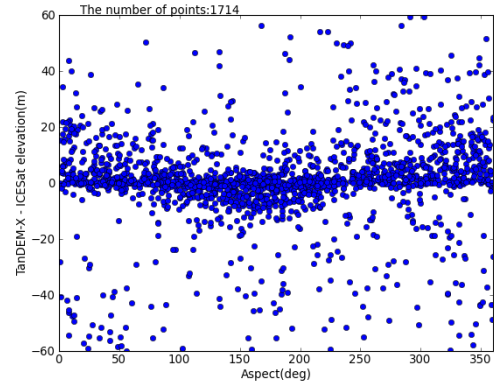
Basic Stats	Matching status	Min (3 $\sigma$ )	Max (3 $\sigma$ )	Mean (m)	Stdev $\sigma$
TanDEM-X 12 m DEM-SRTM 30 m	before	-60.5	60.5	-0.4	16.0
	after	-58.0	62.0	-0.4	15.9

Table 3.16 Difference statistics of 12 m DEM in Dujiangyan against ICESat (total points: 1714)

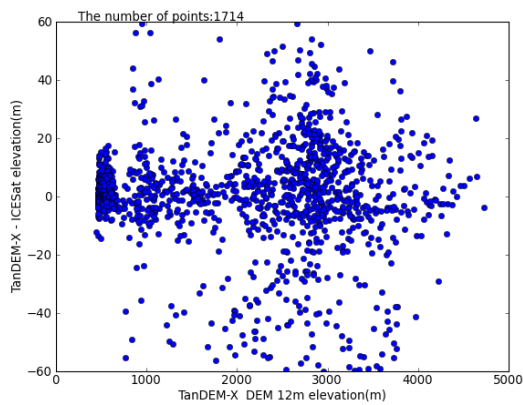
Basic Stats	Min (3 $\sigma$ )	Max (3 $\sigma$ )	Mean (m)	Stdev $\sigma$
TanDEM-X 12 m DEM 12 m-ICESat	-59.9	59.4	0.6	16.1



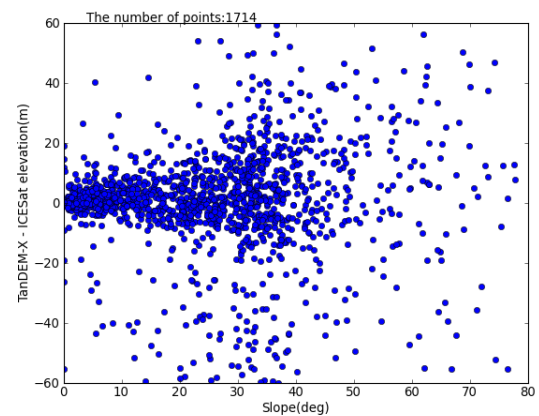
(a)



(b)



(c)



(d)

Figure 3.26 Elevation residuals between the TanDEM-X 12 m DEM and ICESAT GLA14 elevation data in China: (a) Correlation between ICESAT GLA14 and DEM data; (b) The elevation difference with the aspect; (c) The elevation difference with elevation derived from the TanDEM-X DEM data; (d) The elevation difference with the slope

## Chapter 3. DEM Generation and DEM Quality Assessment

As the TanDEM-X 12 m DEM has holes (caused by low coherence or shadows in the SAR data, the blue areas, shown in Figure 3.25), the SRTM 30 m data is used to replace the holes using Equation (3.4) in the Environment for Visualising Images (ENVI). Where  $| |$  is the symbol of absolute value,  $b1$  is SRTM data,  $b2$  is TanDEM-X 12 m DEM, and 5000 is used to detect the holes (very large negative value in the data) of TanDEM-X 12 m DEM. After that, the DEM data is edited using the Noise Removal and Smooth tool in ENVI. The new improved TanDEM-X 12 m DEM will be used in Chapter 6 for TomoSAR and D-TomoSAR imaging.

$$(|b1 - b2| > 5000) * b1 + (|b1 - b2| < 5000) * b2 \quad (3.4)$$

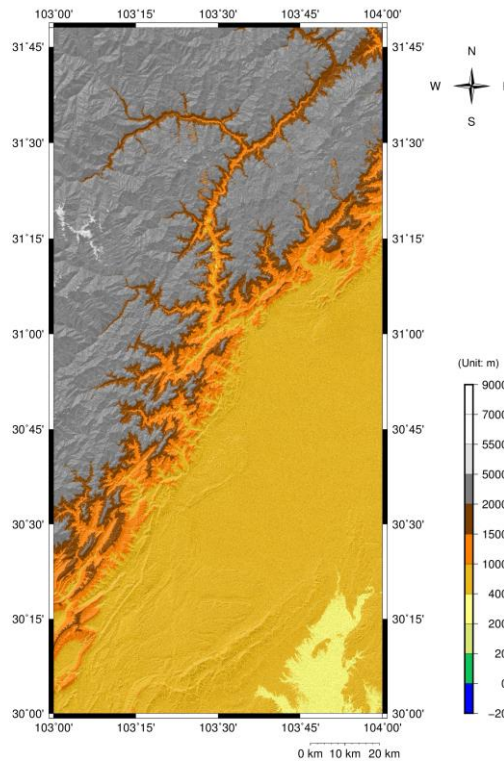


Figure 3.27 TanDEM-X 12 m DEM data after hole replacement using SRTM 30 m

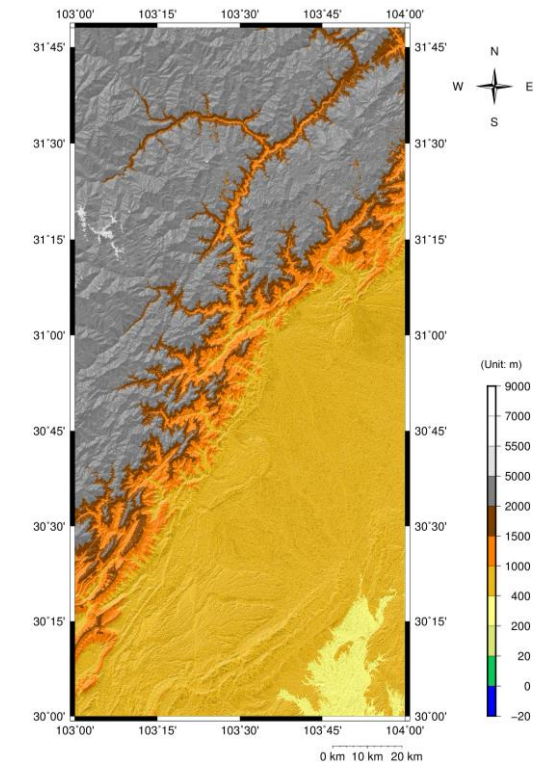


Figure 3.28 TanDEM-X 12 m DEM data after hole replacement, noise removal and smooth filtering

## 3.4 Overall Conclusions

This chapter investigated a systematic method of DEM quality assessment and DEM quality improvement (filter, fusion, editing, and so on). The DEM generation from TanDEM-X via the bistatic InSAR technique is first introduced, then Bluesky DTM

generation by using aerial photogrammetry from stereo-optical data is presented along with the discussion of DEM uncertainty. Moreover, the quality assessment methods and the results of the TanDEM-X IDEM 12 m, 30 m and 90 m data of the UK, the SRTM 30 m data of the UK, the ASTER G-DEM 30 m of the UK and the TanDEM-X DEM 90 m data of the UK using the Bluesky DTM, KGPS and ICESAT ‘truth’ data are presented. Following that, high resolution TanDEM-X 12 m DEM data in China with quality assessment using the SRTM DEM and ICESAT ‘truth’ data and quality improvement post-processing method for better TomoSAR accuracy is studied. Finally how to use the TanDEM-X DEM 12 m data in TomoSAR is studied.

Both the TanDEM-X IDEM and TanDEM-X DEM data are influenced by baseline determination errors, phase errors of the radar instruments, interferometric phase errors, random errors and other errors, which need accuracy validation. The Bluesky data, KGPS and ICESAT data all have high accuracy, which can be used for DEM validation. Through this quality assessment study, the DEM co-registration method (surface matching) is very important for evaluating the accuracy (horizontal and vertical offsets) of DEM products in the UK. Furthermore, the absolute vertical accuracy of the IDEM product is better than the SRTM and ASTER GDEM products at a high and medium resolution (12 m, 30 m), while the vertical comparison accuracy of the IDEM product is worse (because of some errors) than the accuracy of the SRTM and ASTER GDEM product before the water mask. Compared to the TanDEM-X IDEM 90 m data, the TanDEM-X DEM 90 m data, appears to have better accuracy after the water mask and DEM co-registration, which hints the TanDEM-X DEM data have been post-processed (with the bias, and so on) and generated by resampling from high resolution to 90 m resolution using angular degree grids rather than metric grids. After DEM co-registration and the water mask, the vertical comparison accuracy of IDEM product is the best at 30 m, but SRTM still has the best accuracy at 90 m, this might be because SRTM is edited data, while TanDEM-X IDEM and TanDEM-X DEM 90 m still have many errors. Therefore, the accuracy of the TanDEM-X IDEM (12 m, 30 m and 90 m) and TanDEM-X DEM 90 m needs to be improved in the future.

For the 12 m TanDEM-X DEM data used for the 3D TomoSAR imaging and 4D SAR differential tomography (Diff-TomoSAR) in Zipingpu dam, Dujiangyan, China, the quality of the 12 m TanDEM-X DEM data is evaluated first. Though the systematic error of the TanDEM-X 12 m DEM data is very small, the data have some holes, and the random errors (big differences occur over almost all elevations) are very large when

### **Chapter 3. DEM Generation and DEM Quality Assessment**

compared with SRTM and ICESAT data. Thus, the data is fused with SRTM in the hole areas and post-processed using noise removal and smooth tool. The final edited TanDEM-X 12 m data applied in 3D TomoSAR imaging will be studied for better TomoSAR results in Chapter 6. Overall, the systematic method of DEM quality assessment and DEM quality improvement (filter, fusion, editing and so on) is established in this chapter.

# **Chapter 4**

## **The Atmospheric and Ionospheric Correction Algorithm for TomoSAR**

For spaceborne SAR satellites, the ionosphere and atmosphere degrade the quality of SAR images, resulting in phase distortion, phase screens, azimuth streaking and decorrelation in the SAR images and during SAR processing. Therefore, it is critical to correct these problems in SAR and TomoSAR processing. In this chapter, the principles of the atmospheric and ionospheric correction algorithm for TomoSAR are first introduced. Then, the PS and ERA-I model for the absolute atmospheric phase and the GACOS model for the absolute atmospheric phase are presented. In addition, the ionospheric correction algorithms - split spectrum and differential TEC estimation are introduced in detail. Two experiments are studied over Tocopilla, Chile, to validate this split spectrum method, which provides the differential TEC data for our absolute TEC estimation method and our TomoSAR application. In addition, the IGS IONOX format TEC and International Reference Ionospheric Model are introduced. Finally, a proposed ionospheric correction method using IGS TEC data with the split-spectrum differential TEC data and the least squares model to obtain the absolute TEC for TomoSAR with experiment and validation work is executed.



## 4.1 Atmospheric Correction

According to the literature review in Section 2.7, we know that there are phase delays or advances (positive or negative phase value) phenomena when radar signals are propagating through the atmosphere medium, which will cause errors in SAR tomography imaging. The phase delay, which includes ionospheric (shown in Section 4.2), wet, hydrostatic, and liquid components (shown in Equation (4.1) and Equation (4.2)), through the atmospheric environment, is caused by the refractivity of radar signals (Smith and Weintraub, 1953; Davis et al., 1985). Different pressure, temperature, and the relative humidity of the troposphere result in different tropospheric phase delay spatially. Moreover, it is known that the liquid component is usually very small and it will cause a significant influence only in a saturated atmosphere (Bekaert et al., 2015; Hanssen, 2001). Therefore, the liquid component is usually ignored.

$$N = \left(k_1 \frac{P}{T}\right)_{\text{hydr}} + \left(k_2' \frac{e}{T} + k_3 \frac{e}{T^3}\right)_{\text{wet}} = N_{\text{hydr}} + N_{\text{wet}} \quad (4.1)$$

$$\phi_{\text{tropo}} = \frac{-4\pi}{\lambda} \frac{10^{-6}}{\cos \theta} \int_{h_1}^{h_{\text{top}}} (N_{\text{hydr}} + N_{\text{wet}}) dh \quad (4.2)$$

where  $P$  is total atmospheric pressure,  $N$  is the refractive index,

$T$  is the temperature,

$e$  is the partial pressure of water vapour,

$k_1 = 77.6 \text{ K hPa}^{-1}$ ,  $k_2' = 23.3 \text{ K hPa}^{-1}$ , and  $k_3 = 3.75 \cdot 10^5 \text{ K}^2 \text{ hPa}^{-1}$ ,

$\phi_{\text{tropo}}$  is the tropospheric phase delay (two-way), along with the radar line of sight between the top of the troposphere  $h_{\text{top}}$  and the height  $h_1$  (Bekaert et al., 2015; Hanssen, 2001).

Now, there are many approaches to estimate and correct the influence of tropospheric delay for the InSAR application, which includes the weather model method (ERA-I (ECWF), MERRA, MERRA2, WRF) (Pinel et al., 2011; Wadge et al., 2002; Walters et al., 2013; Walters et al., 2014), the method using GNSS data (Williams et al., 1998), the method using spectrometer measurements (MERIS (Envisat), the method using MODIS (AQUA and TERRA)) (Li et al., 2006), the method using spectrometer data and weather models (Walters et al., 2013), the method using spectrometer measurements and GNSS (Puysségur et al., 2007; Li et al., 2009), statistical DEM based



methods (Bekaert et al., 2015), GACOS (GPS + DEM + ECWF high resolution) (Yu et al., 2017b) and the persistent scatterer (PS) methods (Ferretti et al., 2000; Hooper et al., 2004; Hooper et al., 2007). In my tomography processing, some of these methods, like GACOS and ERA will be used. The comparison results and the analysis of the GACOS and ERA-I atmospheric correction are shown in Section 6.5.1.

### 4.1.1 PS and ERA-I Model for Absolute Atmospheric Phase

We first used the PS method to find the PS points (shown in Figure 4.1) and to obtain the initial atmospheric errors. After obtaining the linear deformation and the DEM error at each PS point, the residual phase can be obtained by subtracting them (DEM and deformation) from the initial differential interferogram, and the residual phase is mainly composed of an atmospheric phase, a nonlinear deformation phase and a noise phase (Ferretti et al., 2001b). This residual phase includes the influence of the nonlinear deformation phase and atmospheric delay, but the two phases show different characteristics in the time and spatial domain of the interferogram. In the spatial domain, the atmospheric delay phase is a low-frequency signal, but in the time domain, the atmospheric delay phase is a high-frequency random signal. The nonlinear deformation is a low-frequency signal with a strong correlation in the spatial range of the PS model (Ferretti et al., 2000). It also appears as a low-frequency signal with a strong correlation in the time domain (most of the time this is correct, but it is not always like this; thus, some earthquakes and manmade structures cannot be detected precisely and errors exist in these detections). The phase of the noise is not related to both the time and the spatial domain, which has high-frequency characteristics. Therefore, the atmospheric delay phase and nonlinear deformation can be obtained by the temporal domain filtering method and the spatial domain filtering method (Li and Wu, 2018; Ferretti et al., 2001b). By using high-pass filtering in the time domain of the phase residual of each PS point, the atmospheric delay phase and the noise phase can be obtained. Besides, the atmospheric delay is strongly spatially correlated, and the correlated noise is weakly spatially correlated. After low-pass filtering in the space domain, the phase of atmospheric delay at each PS point in each differential interferogram can be obtained (Ferretti et al., 2001b; Ferretti et al., 2000).

As the PS method based on linear atmospheric phase ramps and simple data analysis is not accurate, we switched to the ERA method based on StaMPS and TRAIN

## Chapter 4. The atmospheric and ionospheric correction algorithm for TomoSAR

open source. Firstly, we set the UTC time (when the satellite passes over my study area) in processing, then accessed the ERA-I model (<https://apps.ecmwf.int/auth/login/>) after downloading the weather model data. Finally, the zenith total delays (zenith tropospheric wet and dry delays) were obtained for each of the SAR dates. The tropospheric phase of the PS points is shown in Figure 4.2.

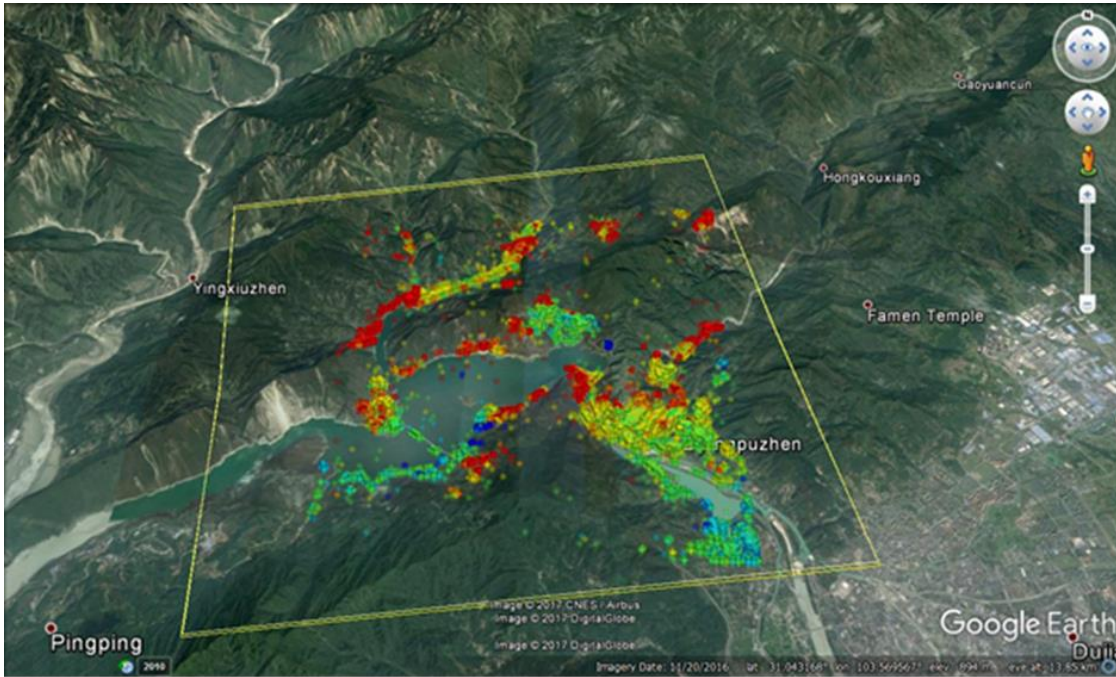


Figure 4.1 PS points in the test area, the background image is Google Earth image

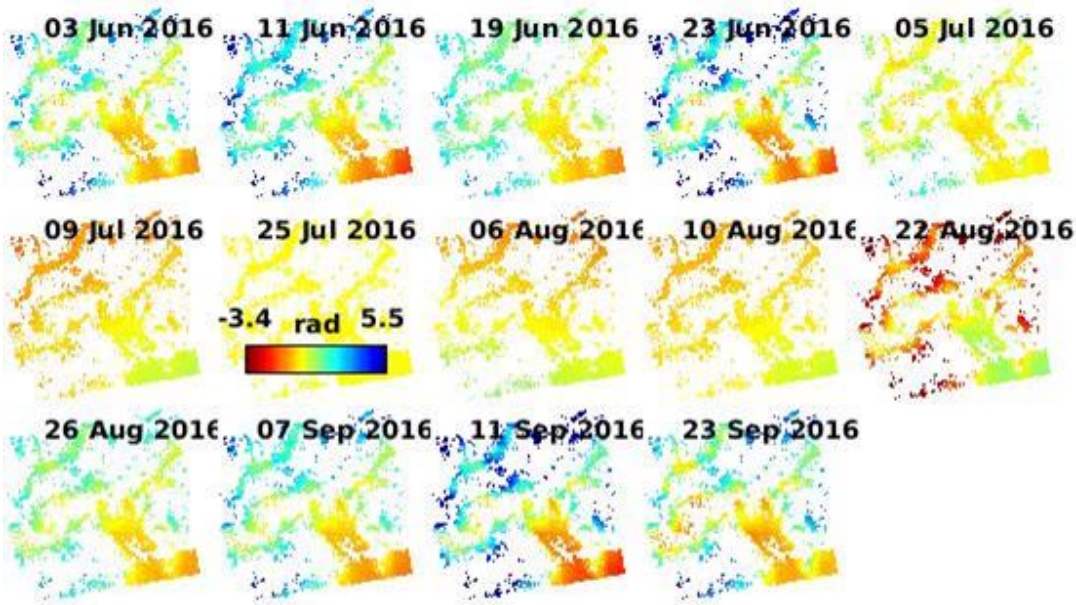


Figure 4.2 ERA-I model atmosphere total phase related to the master total phase (hydrostatic and wet delay, the colour bar is in the middle picture of 25 Jul 2016, the master date is 25 Jul 2016)

### 4.1.2 GACOS for Absolute Atmospheric Phase

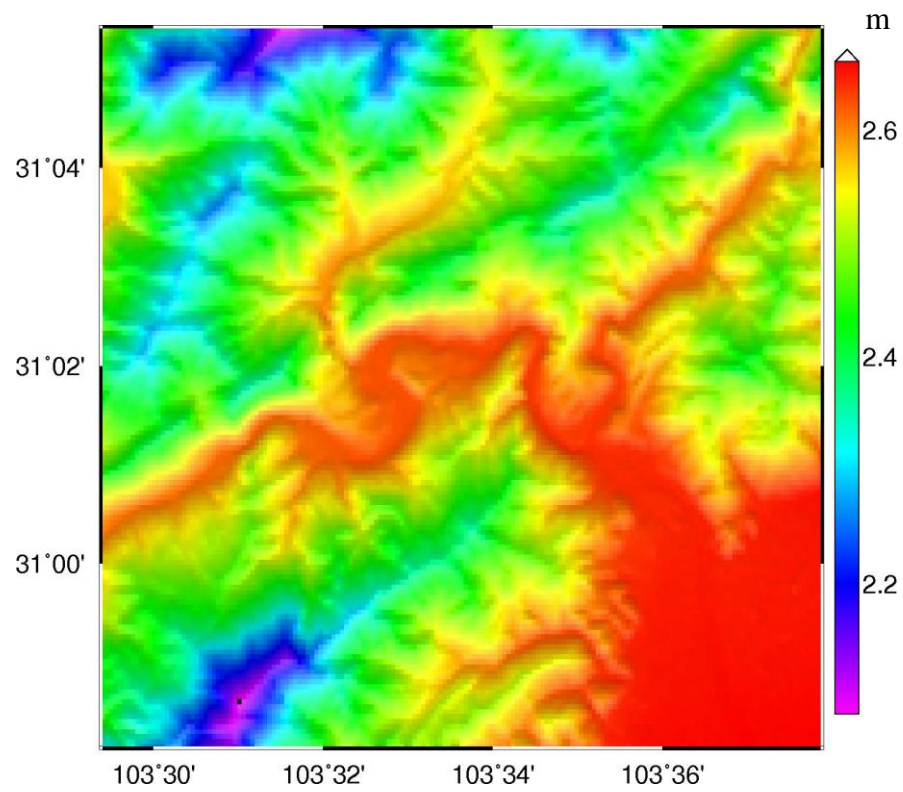


Figure 4.3 ZTD of 20160603 (unit: metre)

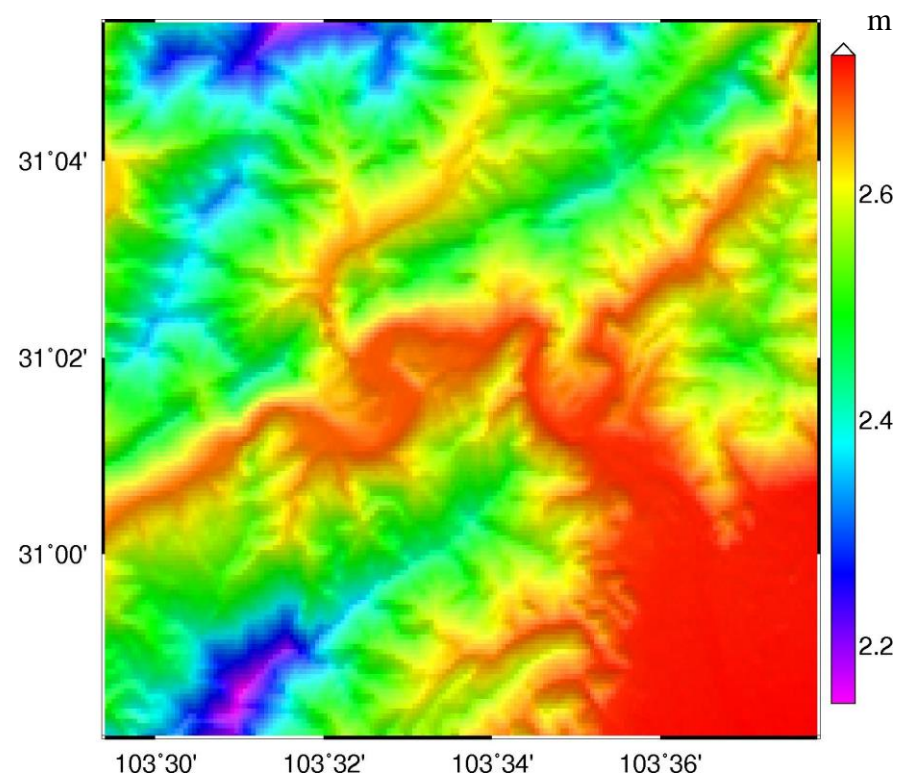


Figure 4.4 ZTD of 20160725 (the date of the master image, unit: metre)

Like the ERA-I model, we can download the tropospheric zenith delay based on the time and geocoordinates in the GACOS (Yu et al., 2017b) website (<http://ceg-research.ncl.ac.uk/v2/gacos/>). The data resolution is 90 metres. This tropospheric zenith delay (shown in Figure 4.3 and Figure 4.4) will be transferred to the phase of each SAR date, which will be used in the TomoSAR process.

## 4.2 Ionospheric Correction Algorithm

### 4.2.1 Introduction and Basic Parameters

With the advent of the information age, satellite navigation, spaceborne radar, satellite communications and ground-based radio and radar telescope have been widely used in various aspects of civilian and military applications. The ionospheric impact on these spatial information systems is mainly reflected in the propagation effect of the radio signals on the satellite link, which may lead to a weakening of the radio signals, degraded imaging quality of Synthetic Aperture Radar (SAR), InSAR generated digital elevation models (DEMs) with reduced precision and degraded navigation positioning accuracy. Thus, the impact on remote sensing, navigation, and other mapping fields cannot be ignored.

The ionospheric impact on the spatial information radio traversal (link) (also see in Table 4.1) is mainly as follows (Aarons, 1982).

- 1) The ionosphere causes dispersion, absorption, Faraday rotation, ionospheric delay, and changes to the radio signal in the apparent arrival direction due to refraction.
- 2) Random polarisation rotation and ionospheric delay are caused by various irregular body structures.
- 3) The Doppler effect due to the nonlinear relationship between the Faraday rotation, time delay, the frequency and the relative motion of the ionospheric irregularity of the ray link.
- 4) Ionospheric irregularities cause flickering of the electrical signal, causing random fluctuations in the signal amplitude, signal phase, polarisation, and arrival angle.



Table 4.1 Estimated<sup>23</sup> ionospheric effects for one-way radio traversal<sup>24</sup> (elevation angles is about 30° ) (from Recommendation ITU-R P.531) (Aarons, 1982)

Effect	Frequency dependence	0.1 GHz	0.25 GHz	0.5 GHz	1 GHz	3 GHz	10 GHz
Propagation delay	$1/f^2$	25 $\mu$ s	4 $\mu$ s	1 $\mu$ s	0.25 $\mu$ s	0.028 $\mu$ s	0.0025 $\mu$ s
Faraday rotation	$1/f^2$	30 rotations	4.8 rotations	1.2 rotations	108°	12°	1.1°
Refraction	$1/f^2$	< 1°	< 0.16°	< 2.4'	< 0.6'	< 4.2"	< 0.36"
Variation in the direction of arrival (r.m.s.)	$1/f^2$	20'	3.2'	48"	12"	1.32"	0.12"
Absorption (mid-latitude)	$1/f^2$	< 1 dB	< 0.16 dB	< 0.04 dB	< 0.01 dB	< 0.001 dB	< 1 * 10 <sup>-4</sup> dB
Absorption (auroral and/or polar cap)	$1/f^2$	5 dB	0.8 dB	0.2 dB	0.05 dB	6 * 10 <sup>-3</sup> dB	5 * 10 <sup>-4</sup> dB
Dispersion	$1/f^3$	0.4 ps/Hz	0.026 ps/Hz	0.0032 ps/Hz	0.0004 ps/Hz	1.5 * 10 <sup>-5</sup> ps/Hz	4 * 10 <sup>-7</sup> ps/Hz
Scintillation <sup>25</sup>	See Rec. ITU-R P.531(Aarons, 1982)	See Rec. ITU-R P.531	See Rec. ITU-R P.531	See Rec. ITU-R P.531	> 20 dB peak-to-peak	≈10 dB peak-to-peak	≈4 dB peak-to-peak

#### (1) TEC

The spatial distribution of electron density is one of the main parameters in the study of ionospheric propagation. However, we almost do not care about the rate of change of the radio wave at a certain point in the ionosphere, but we are more concerned with the overall change of the signal along the propagation path in the ionosphere. The total number of electrons integrated between two points (like a GPS transmitter and ground receiver) along a tube of one metre squared cross section is called the integral electron content (or Total Electron Content: TEC) (Mannucci et al., 1998; Sardon et al., 1994). The TEC represents the total number of electrons contained in a column per unit area of a signal in its propagation path. The unit is TECU,  $\text{TECU} = 1 \times 10^{16} \text{el}/\text{m}^2$  and  $\text{el}/\text{m}^2$  means electrons per square metre.  $N_e$  is Electron density.

<sup>23</sup> TEC is  $10^{18}$  electrons/ $\text{m}^2$ , low latitudes in daytime and high solar activity (Aarons, 1982).

<sup>24</sup> Ionospheric effects above 10 GHz are negligible. X band is 8 GHz-12 GHz, and it is normally around 9.6 GHz for many X band satellites

<sup>25</sup> Values are observed under conditions of a high sunspot number near the geomagnetic equator during the early local night-time hours at the equinox (Aarons, 1982).

#### Chapter 4. The atmospheric and ionospheric correction algorithm for TomoSAR

$$\text{TEC} = \int_{\text{path}} N_e(s) ds \quad (4.3)$$

(2) Refractive index

The ionospheric refractive index (Thayer, 1974; Jones and Stephenson, 1975; Ponomarenko et al., 2009) is also one of the most important parameters in ionospheric propagation research. The phase refractive index expression (Lawrence et al., 1964; Budden, 1988) is

$$n_p^2 = 1 - \frac{X}{1 - jZ - \frac{Y_T^2}{2(1 - X - jZ)} \pm \left[ \frac{Y_T^4}{4(1 - X - jZ)^2} + Y_L^2 \right]^{1/2}} \quad (4.4)$$

where

$$X = \frac{\omega_p^2}{\omega^2}, \quad Y = \frac{\omega_H}{\omega}, \quad Z = \frac{\nu}{\omega}, \quad Y_L = \frac{\omega_L}{\omega}, \quad Y_T = \frac{\omega_T}{\omega}$$

$$\omega_p = \sqrt{\frac{N_e e^2}{\epsilon_0 m}} : \text{Plasma angular frequency}$$

$$\omega_H = \frac{\mu_0 H e}{m} : \text{Electronic magnetic rotation frequency, where } H e \text{ refers to } H * e$$

$$H = B/\mu_0 : \text{Geomagnetic field intensity}$$

$$B : \text{Magnetic induction intensity}$$

$$\omega_L = \omega_H \cos \theta_B, \quad \omega_T = \omega_H \sin \theta_B$$

$$N_e : \text{Electron density}$$

$$\omega : \text{Free space wave angle frequency of the signal}$$

$$m : \text{Electronic mass } (9.109 \times 10^{-31} \text{ kg})$$

$$\nu : \text{Electronic effective collision frequency}$$

$$e : \text{Electronic power } (1.602 \times 10^{-19} \text{ C})$$

$$\epsilon_0 : \text{Free space permittivity } (8.854 \times 10^{-12} \text{ F/m})$$

$$\mu_0 : \text{Vacuum permeability}$$

$\theta_B$  : The angle between the direction of the propagation wave and the direction of the earth's magnetic field.

Assuming no consideration of magnetic ion ray fission (which means isotropic, the approximate ray theory can be used, and the propagation direction of a wave is considered as a quasi-longitudinal propagation. Based on the magnetoionic theory, the plasma in the ionosphere is an anisotropic dispersion medium, but as the SAR frequency is higher, the effect of ion motion can be omitted  $\nu=0$ , electronic magnetic rotation frequency  $\omega_H$  is small), the equation can be simplified as:

$$n_p \approx 1 - \frac{\omega_p^2}{2\omega^2} \quad (4.5)$$

The phase refractive index and the group refractive index has a derivative relationship (based on the frequency of the signal) (Rogers and Hopler, 1988). Therefore, the group refractive index is:

$$n_g \approx 1 + \frac{\omega_p^2}{2\omega^2} \quad (4.6)$$

### (3) The Scintillation Index

Ionospheric scintillation, reflected by the random fluctuation of the refractive index (Whitney and Malik, 1968; Shaft, 1974; Yeh and Liu, 1982; Hunsucker and Hargreaves, 2002), and due to the inhomogeneous distribution of electron density in the ionosphere, further causes severe random fluctuations in the signal amplitude (Belcher and Cannon, 2014), signal phase, polarisation, and arrival angle.

$$S_4^2 = \frac{\langle I^2 \rangle - \langle I \rangle^2}{\langle I \rangle^2} \quad (4.7)$$

where  $I$ , in the equation above, represents the strength of the signal,  $\langle \rangle$  means mathematical expectation. When the amplitude scintillation index  $S_4$  is equal to 1, the scintillation reaches a saturation state. Sometimes, if the amplitude scintillation index value of  $S_4$  is greater than 1, the ionospheric scintillation phenomenon occurs. Phase scintillation index is expressed as the standard deviation of the carrier phase (Whitney and Malik, 1968; Shaft, 1974; Yeh and Liu, 1982; Hunsucker and Hargreaves, 2002). The standard deviation of the carrier phase  $\sigma_\phi$  is

$$\sigma_\phi = \sqrt{\langle \phi^2 \rangle - \langle \phi \rangle^2} \quad (4.8)$$

where  $\phi$  is the carrier phase,  $\langle \rangle$  means mathematical expectation. When  $S_4$  is less than 0.5, the amplitude scintillation index  $S_4$  and the phase scintillation index  $\sigma_\phi$  have a linear relationship and are approximately equal, but if the scintillation index is greater than 0.5, there is no obvious linear relationship between the two indexes (Whitney and Malik, 1968; Shaft, 1974; Yeh and Liu, 1982; Hunsucker and Hargreaves, 2002).

## 4.2.2 Split Spectrum

The range split-spectrum method splits the frequency bandwidth into two range subbands, where each band has the centre frequencies of  $f_L$  and  $f_H$  ( $L$  represents the

## Chapter 4. The atmospheric and ionospheric correction algorithm for TomoSAR

lower subband, and  $H$  represents the higher subband) (Gomba et al., 2014; Gomba et al., 2016), shown in Figure 4.5. Then, the interferograms are computed for each subband (Gomba et al., 2014; Kim and Papathanassiou, 2014), which generates the InSAR phase of  $\Delta\phi_L$  and  $\Delta\phi_H$  (Gomba et al., 2016).

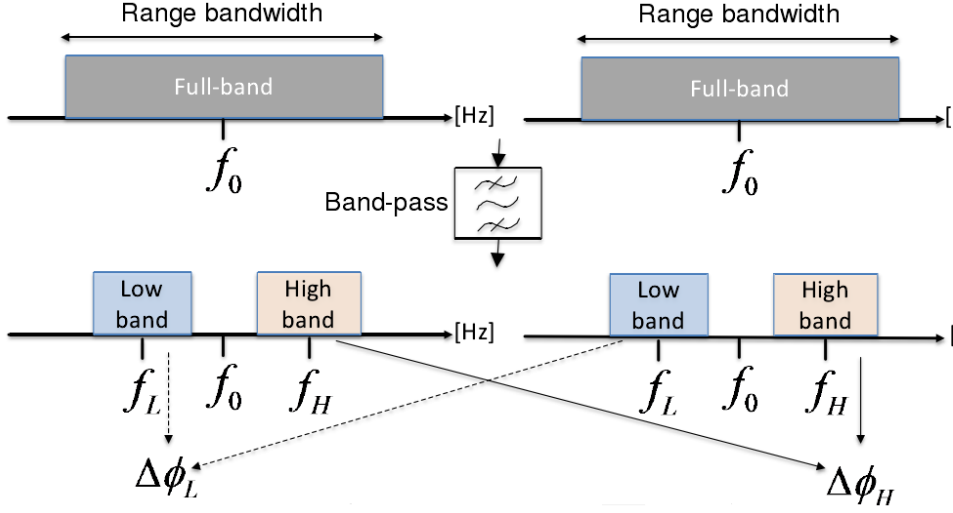


Figure 4.5 Split range spectrum (Gomba et al., 2016)

$$\Delta\phi_L = \Delta\phi_{\text{non-disp}} \frac{f_L}{f_0} + \Delta\phi_{\text{iono}} \frac{f_0}{f_L} \quad (4.9)$$

$$\Delta\phi_H = \Delta\phi_{\text{non-disp}} \frac{f_H}{f_0} + \Delta\phi_{\text{iono}} \frac{f_0}{f_H} \quad (4.10)$$

From these equations above, the dispersive  $\Delta\phi_{\text{iono}}$  and nondispersive  $\Delta\phi_{\text{non-disp}}$  components of the phase delay can be calculated and obtained.

$$\Delta\phi_{\text{iono}} = \frac{f_L f_H}{f_0 (f_H^2 - f_L^2)} (\Delta\phi_L f_H - \Delta\phi_H f_L) \quad (4.11)$$

$$\Delta\phi_{\text{non-disp}} = \frac{f_0}{(f_H^2 - f_L^2)} (\Delta\phi_H f_H - \Delta\phi_L f_L) \quad (4.12)$$

Alternatively, the equation can be changed into phase and  $\Delta\text{TEC}$  ( $\Delta T_c$ ) mode (Rosen et al., 2010). Then, the differential TEC (Gomba et al., 2016; Rosen et al., 2010) can be obtained by using the equation below.

$$\begin{cases} \Delta\phi_L = \frac{4\pi}{\lambda_L} \sigma r_{nd} + 4\pi \frac{K}{c^2} \lambda_L \Delta T_c \\ \Delta\phi_H = \frac{4\pi}{\lambda_H} \sigma r_{nd} + 4\pi \frac{K}{c^2} \lambda_H \Delta T_c \end{cases} \quad (4.13)$$



$$\Delta T_c = \frac{\Delta\phi_H - \frac{\lambda_L}{\lambda_H} \Delta\phi_L}{\frac{4\pi K}{\lambda_H} \frac{1}{c^2} (\lambda_H^2 - \lambda_L^2)} \quad (4.14)$$

In the equation,  $\Delta T_c$  is the differential total electron content  $\Delta TEC$ ,  $\lambda$  is the wavelength,  $\Delta\phi$  is the differential phase, the subscript  $L$  represents the lower subband and the subscript  $H$  represents the higher subband,  $\sigma r_{nd}$  is the non-dispersive range term (topography, deformation and tropospheric path delay),  $c$  is light speed,  $K = 40.28 \text{ m}^3 \text{ s}^{-2}$ .

Two tests were studied in Tocopilla, Chile, shown in Figure 4.6. On 14 November 2007, the Tocopilla subduction thrust earthquake (Mw 7.7) occurred in the coastal region of northern Chile (Tocopilla) (Bejar Pizarro et al., 2010; Schurr et al., 2012). The ALOS-1 SAR data around the earthquake were used in these tests. The resolution of the SAR SLC data is about 4.45 metres in azimuth and 9.52 metres in range. The size of one frame SLC data is 27648 pixels in azimuth and 4762 pixels in range. Three frames are merged to process in the first test, shown by the blue rectangle in Figure 4.6; two frames are merged to process in the second test, shown by the red rectangle in Figure 4.6, and the merged ALOS-1 SAR data are shown in Figure 4.7. The ALOS-1 SAR images are upside down as all image data used in the test are in ascending mode.

The ALOS-1 SAR data are downsampled to 14 MHz bandwidth (as fine beam dual polarisation (FBD) and fine beam single polarisation (FBS) with bandwidths of 14 and 28 MHz). Then the data of the range-spectrum is split at 1/3 and 2/3 of 14 MHz as the low frequency and high frequency with the sub-band bandwidth of 6 MHz. After that, the split spectrum method is used to estimate the ionospheric (dispersive) and nondispersive components (Gomba et al., 2016). Invalid regions of the dispersive and nondispersive phase components are masked first, and the 2D Gaussian filter with a kernel size of 100 pixels in both range and azimuth directions is used to low-pass filter the estimated ionospheric and nondispersive phase components with the iterative filtering-interpolation approach (Fattahi et al., 2017) to get the ionosphere phase. Finally, the ionosphere phase is used to correct the InSAR interferogram phase and it can also be transformed to  $\Delta TEC$  for other applications, like TomoSAR.

The results are shown below. In the first example of the first test, the master date is 2007-11-29 after the earthquake, and the slave date is 2008-04-15 after the earthquake. In Figure 4.8 (a) and (b), after filtering, the differential ionospheric phase is clearer. In Figure 4.8 (c), the interferogram phase is strongly influenced by the ionospheric phase

## Chapter 4. The atmospheric and ionospheric correction algorithm for TomoSAR

screen. In Figure 4.8 (d), after compensation for the ionospheric delay, there are no stripes in the interferogram, which means the ionosphere phase is eliminated properly after ionospheric correction, but there are still some small residual phases which might be caused by the atmosphere. In the second example of the first test, and the master date is 2007-10-14 before the earthquake, the slave date is 2007-11-29 after the earthquake. In Figure 4.9 (a) and (b), after filtering, the differential ionospheric phase is also clearer. In Figure 4.9 (c), the interferogram phase is influenced by the ionospheric phase screen. In Figure 4.9 (d), after compensation for the ionospheric delay, there are still stripes (shown in the light blue rectangle box) in the interferogram, which is coseismic ground displacement caused by the 2007 -11-14 Tocopilla earthquake (Mw 7.7) (shown in Figure 4.6).

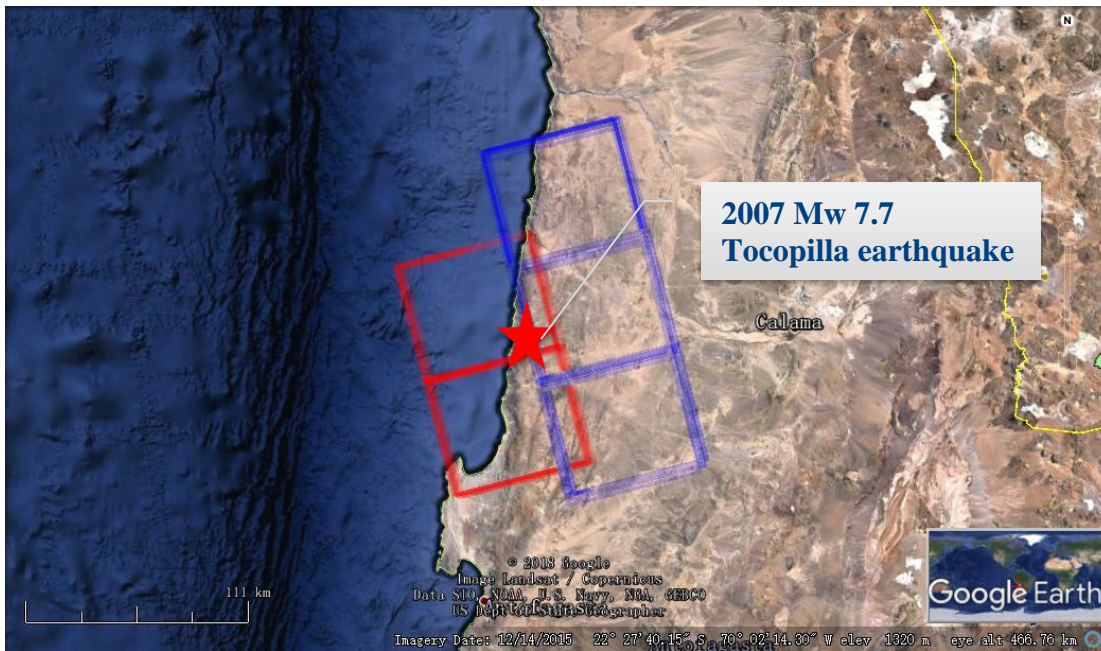


Figure 4.6 Two test area in Tocopilla, Chile, the blue rectangle is the footprint of ALOS-1 SAR in the first test, the red rectangle is the footprint of ALOS-1 SAR in the second test



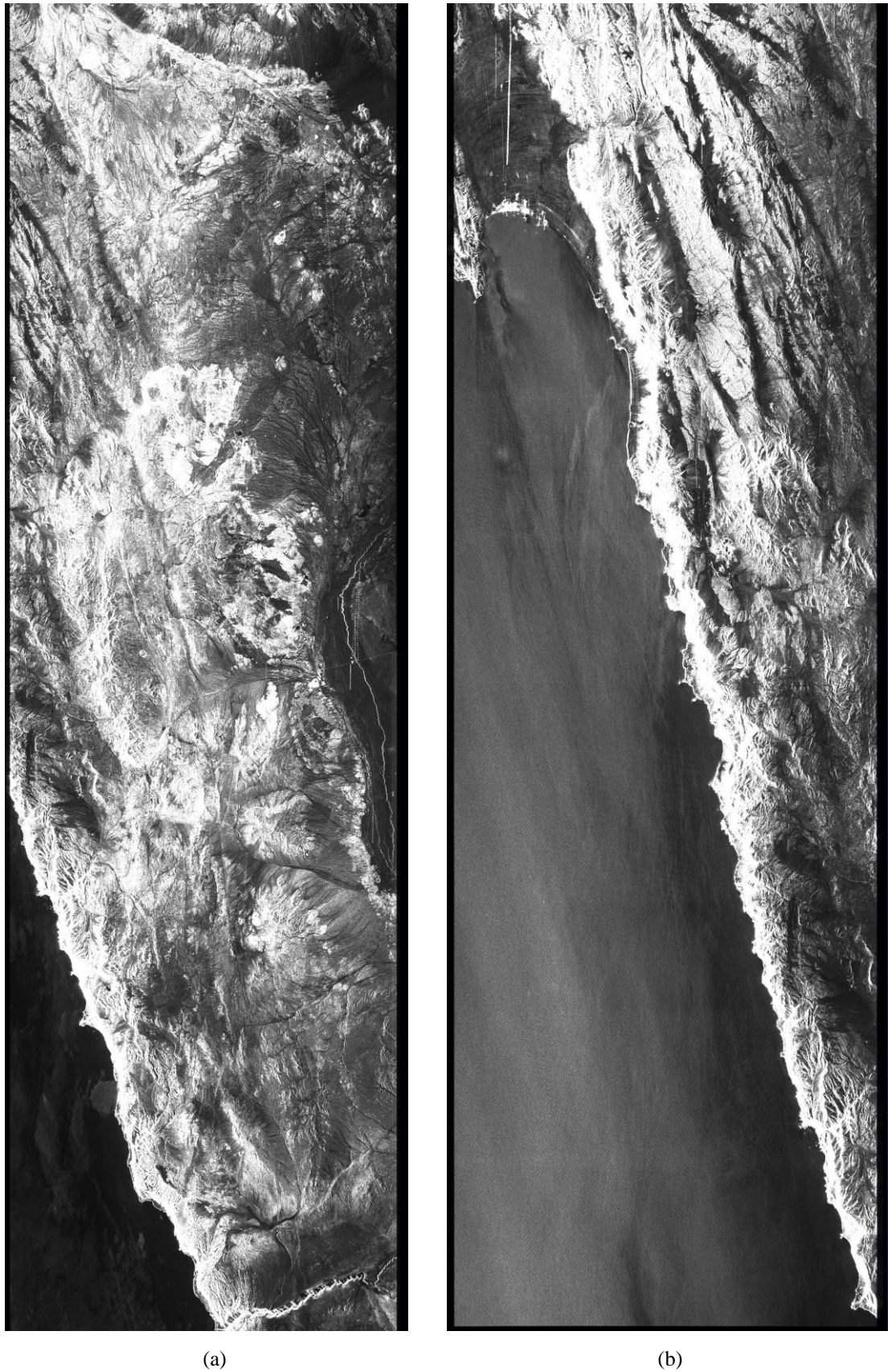
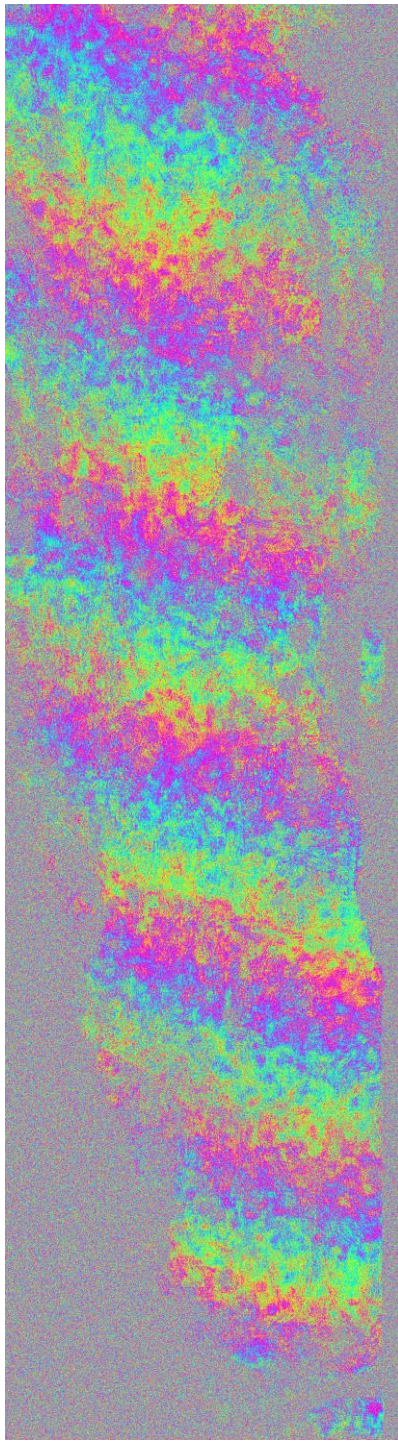


Figure 4.7 The merged ALOS-1 SAR data: (a) Merged ALOS-1 SAR data in the first test on 2007-11-29 after the earthquake; (b) Merged ALOS-1 SAR data in the second test on 2008-01-31 after the earthquake





(a)



(b)

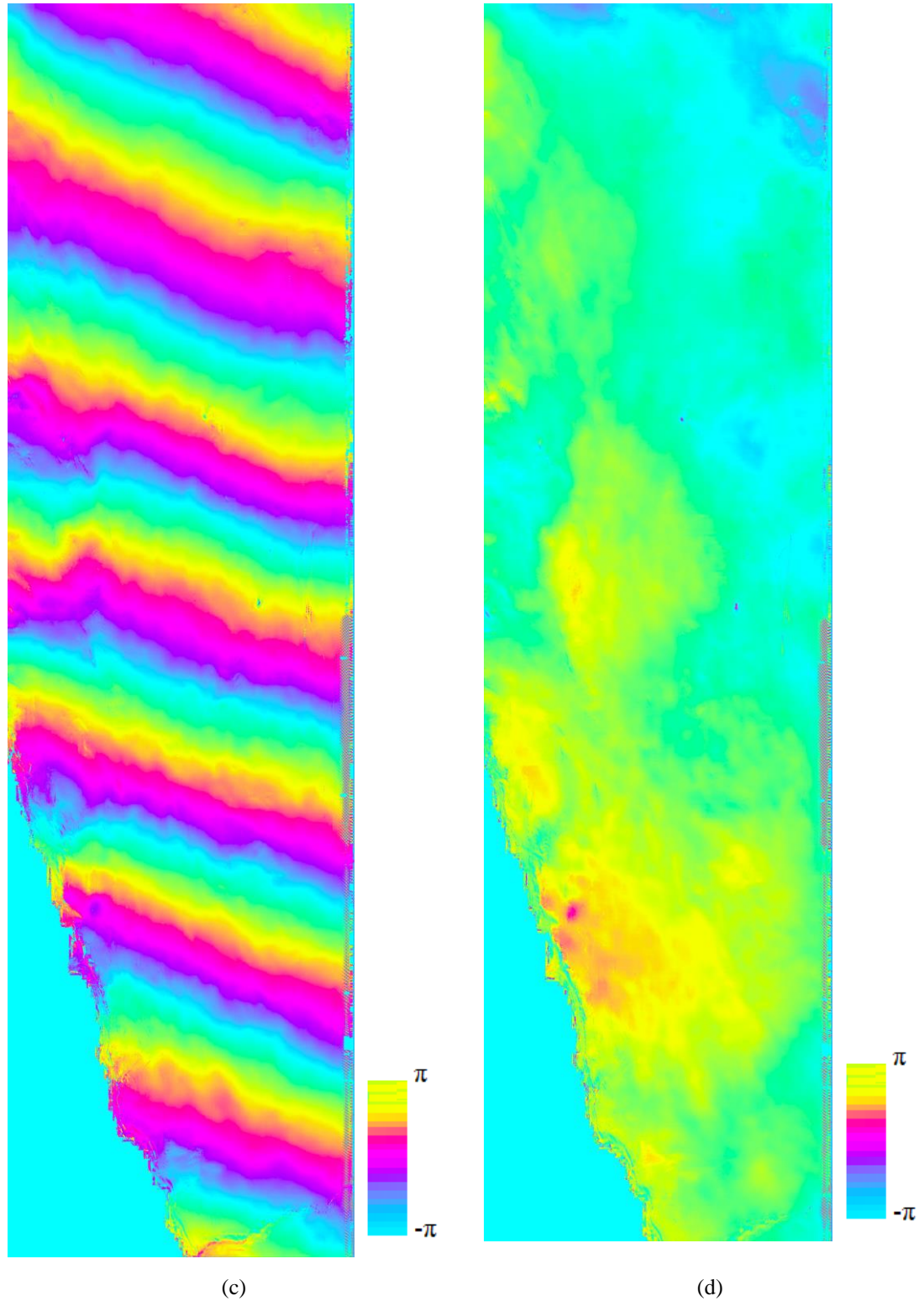
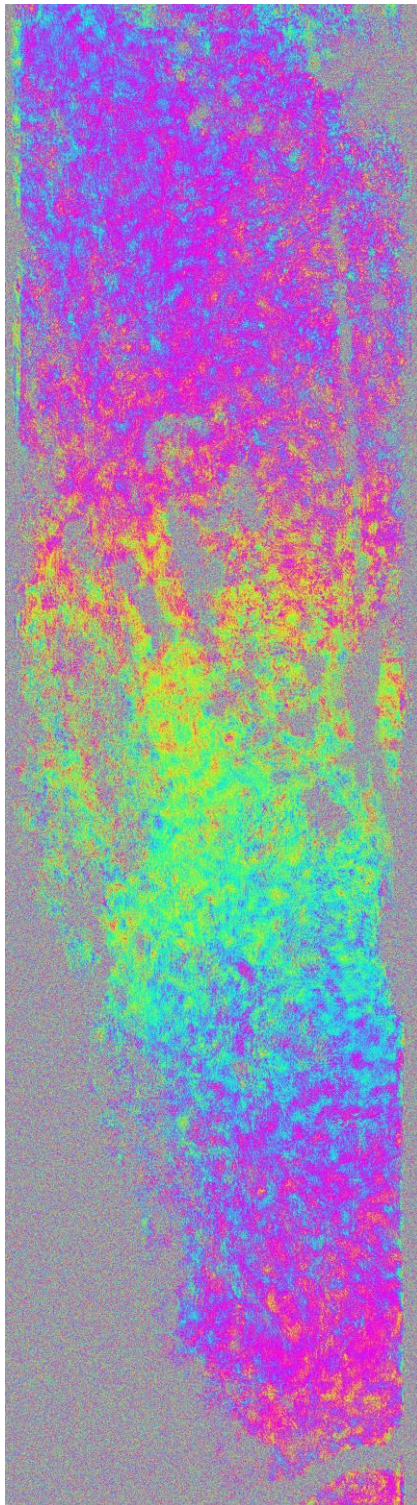
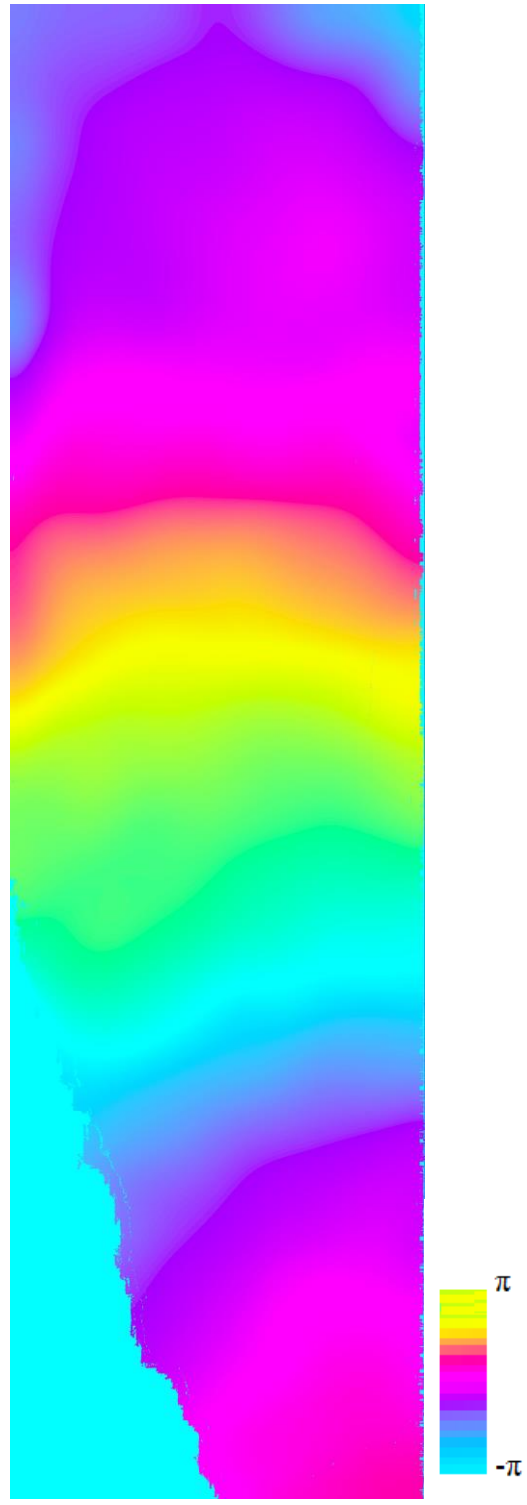


Figure 4.8 Ionosphere correction by the split spectrum method of test 1 in Tocopilla, Chile, the master date is 2007-11-29 after the earthquake, the slave date is 2008-04-15 after the earthquake: (a) Ionospheric phase before the filter; (b) Ionospheric phase after the filter; (c) InSAR phase before correction; (d) InSAR phase after ionospheric correction





(a)



(b)

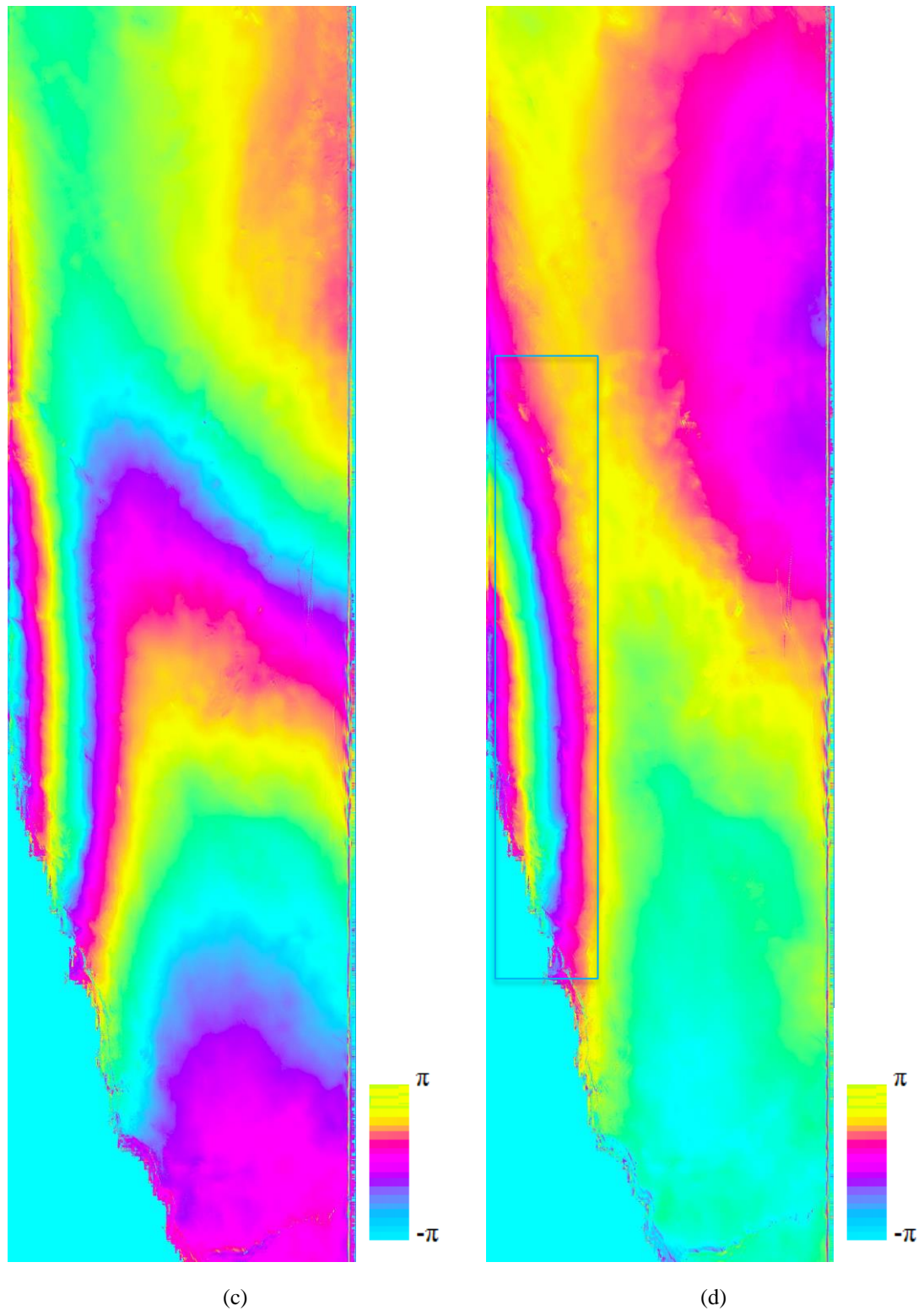
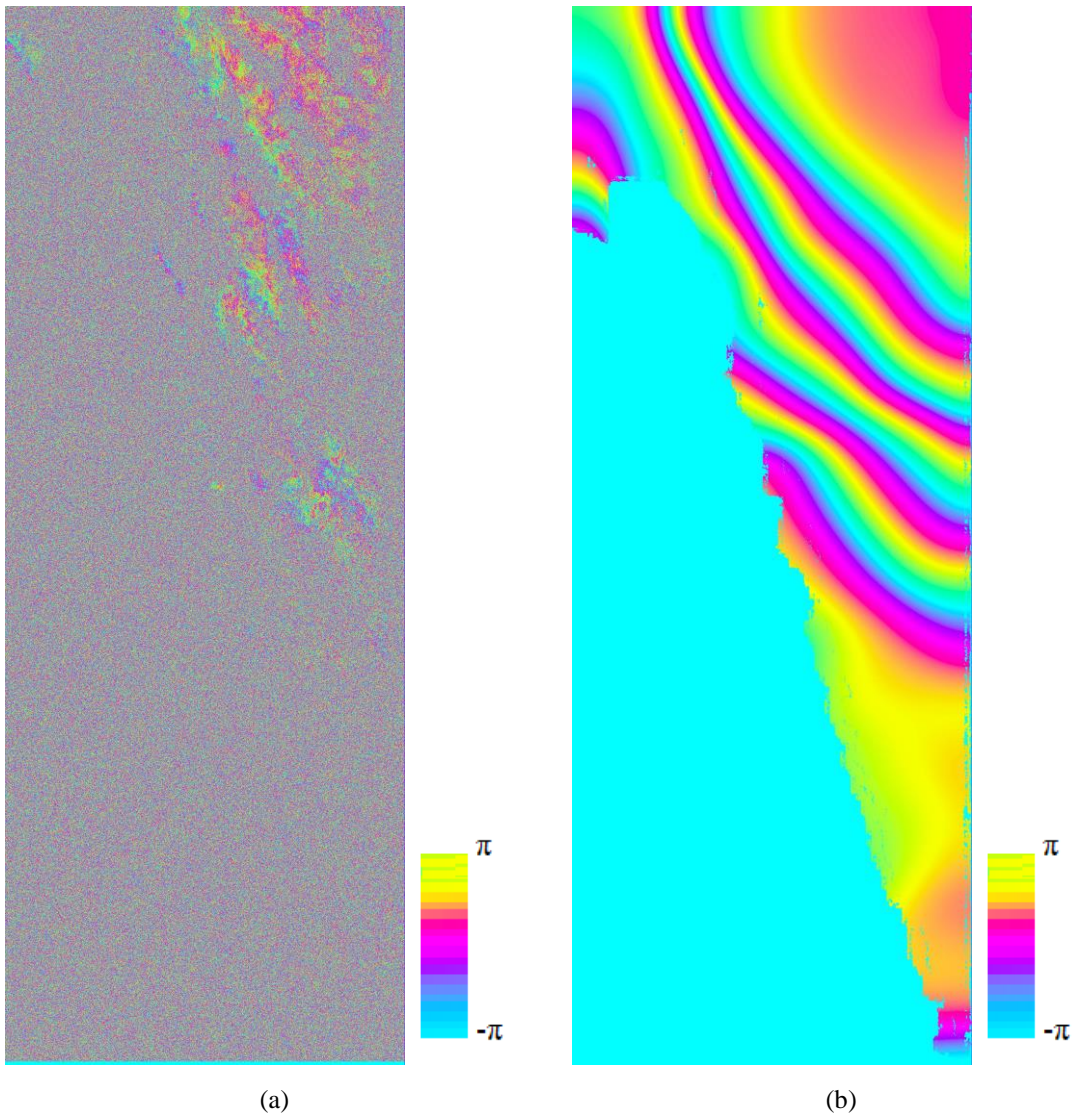


Figure 4.9 Ionosphere correction by the split spectrum method of test 1 in Tocopilla, Chile, the master date is 2007-10-14 before the earthquake, the slave date is 2007-11-29 after the earthquake: (a) Ionospheric phase before the filter; (b) Ionospheric phase after the filter; (c) Phase before ionospheric correction; (d) Phase after ionospheric correction, the interferogram stripes in the light blue rectangle box show that there is coseismic ground displacement caused by the 2007 -11-14 Tocopilla earthquake (Mw 7.7)







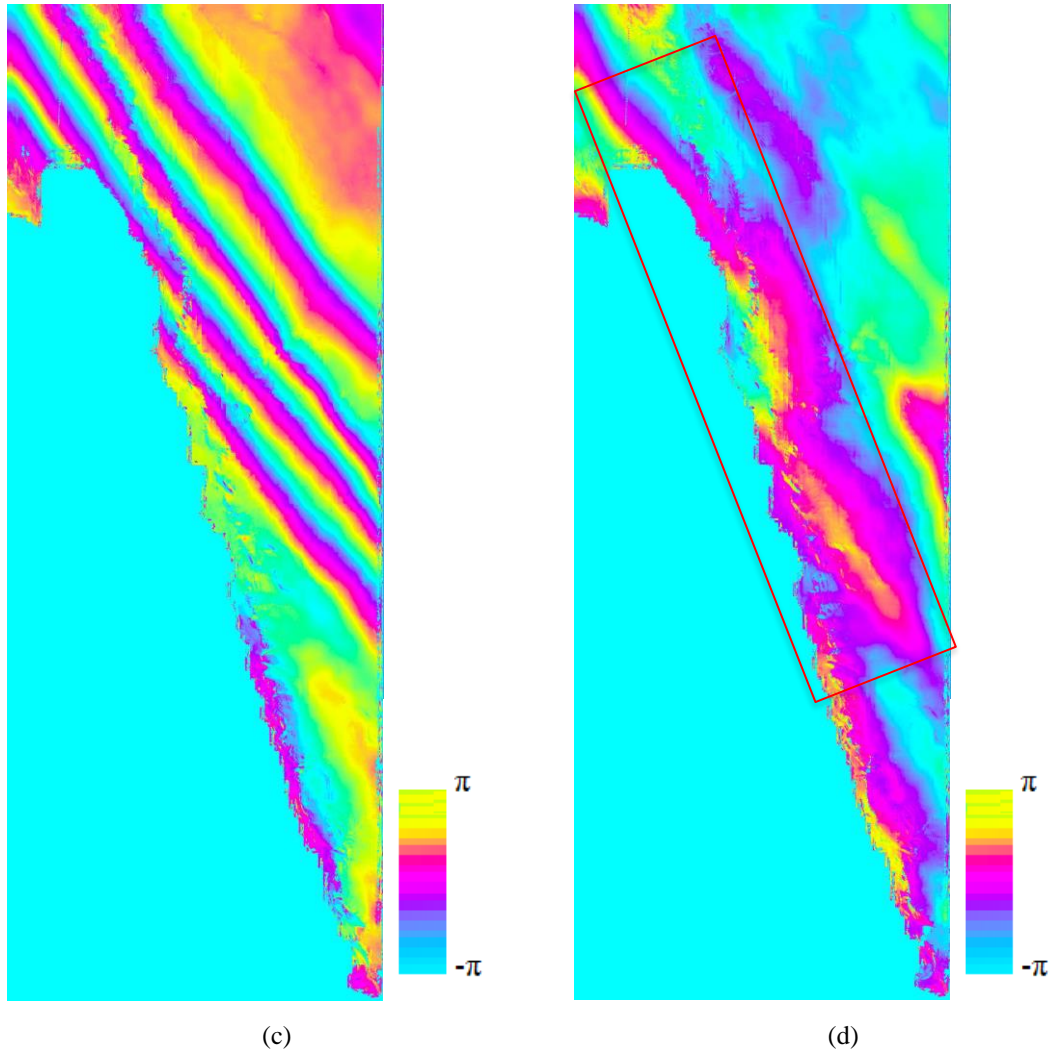
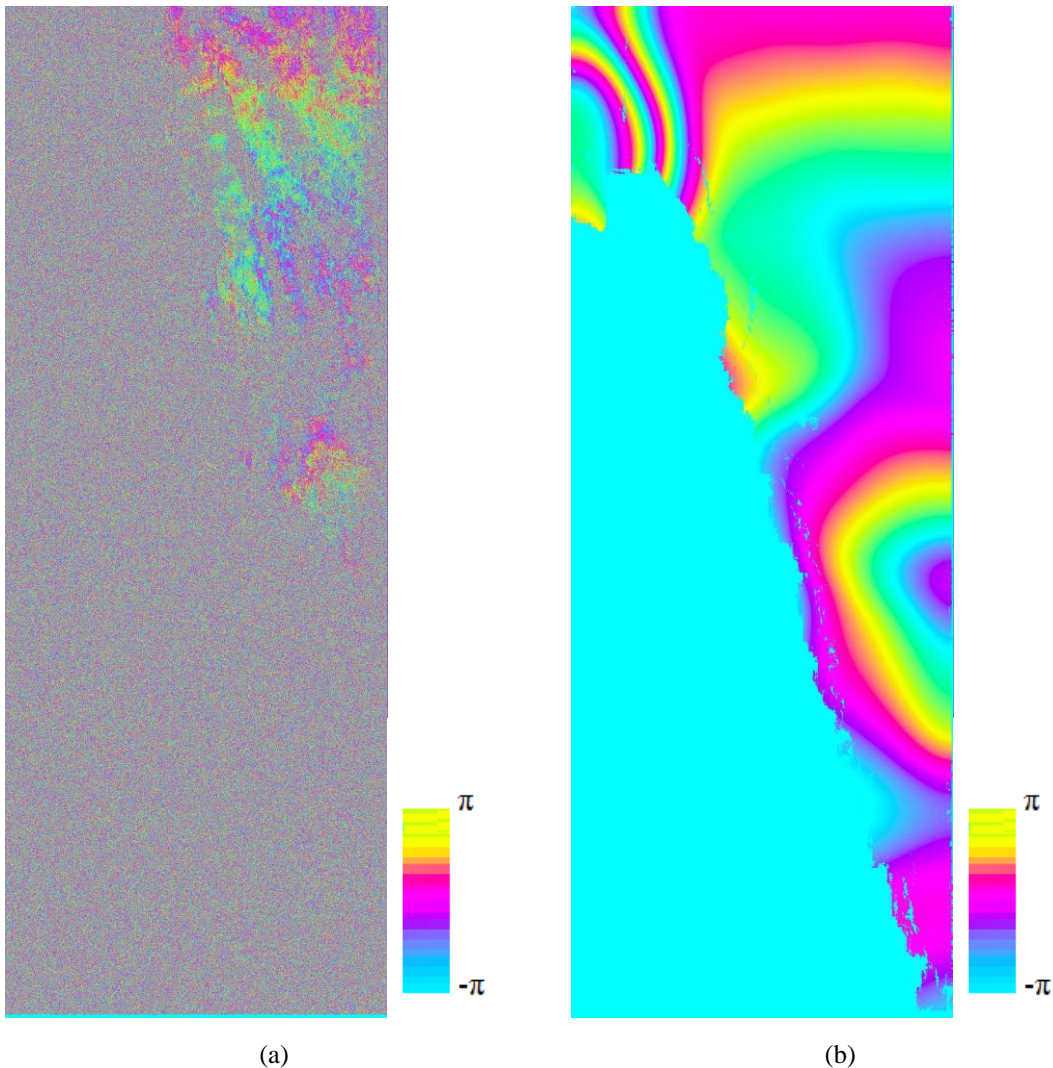


Figure 4.10 Ionosphere correction by the split spectrum method of test 2 in Tocopilla, Chile, the master date is 2008-01-31 after the earthquake, and the slave date is 2008-03-17 after the earthquake: (a) Ionospheric phase before the filter; (b) Ionospheric phase after the filter; (c) Phase before correction; (d) Phase after ionospheric correction, the stripes in the red rectangle box show that there are still some residuals after ionospheric correction especially along the coast, which might be caused by atmospheric and DEM errors

In the first example of the second test, the master date is 2008-01-31 after the earthquake, and the slave date is 2008-03-17 after the earthquake. In Figure 4.10 (a) and (b), after filtering, the differential ionospheric phase is clearer. In Figure 4.10 (c), it can be seen that the interferogram phase is strongly influenced by the ionospheric phase screen. In Figure 4.10 (d), after compensation for the ionospheric delay, there are some residuals (shown in the red rectangle box) especially along the coast, which might be caused by atmospheric and DEM errors. In the second example of the second test, the master date is 2007-09-15 before the earthquake, and the slave date is 2008-01-31 after the earthquake. In Figure 4.11 (a) and (b), after filtering, the differential ionospheric phase

#### Chapter 4. The atmospheric and ionospheric correction algorithm for TomoSAR

is also clearer. In Figure 4.11 (c), the interferogram phase is influenced by the ionospheric phase screen. In Figure 4.11 (d), after compensation for the ionospheric delay, there are many stripes in the interferogram, which show the coseismic ground displacement caused by the 2007 -11-14 Tocopilla earthquake (Mw 7.7) (shown in Figure 4.6 and Figure 4.11). The result shown in Figure 4.11 (d) (ascending, in the radar coordinate system) is similar to the C-band InSAR results (geocoded in the geographic coordinate system) using the ESA Envisat SAR data in Motagh's paper (Motagh et al., 2010) (shown in Figure 4.12). Besides, the deformation is about 35 cm ( $\approx 3$  fringes, one fringe referring to a half wavelength, if the zero benchmark is selected in the top-right pixel) in Figure 4.11 (d), which is similar to the 29 cm deformation in Motagh's paper (Motagh et al., 2010). The deformation difference might be caused by atmospheric influence (no atmospheric correction for L-band InSAR) and the different data acquisition times (the deformation increased to 40 cm in Motagh's paper shown in Figure 4.12).



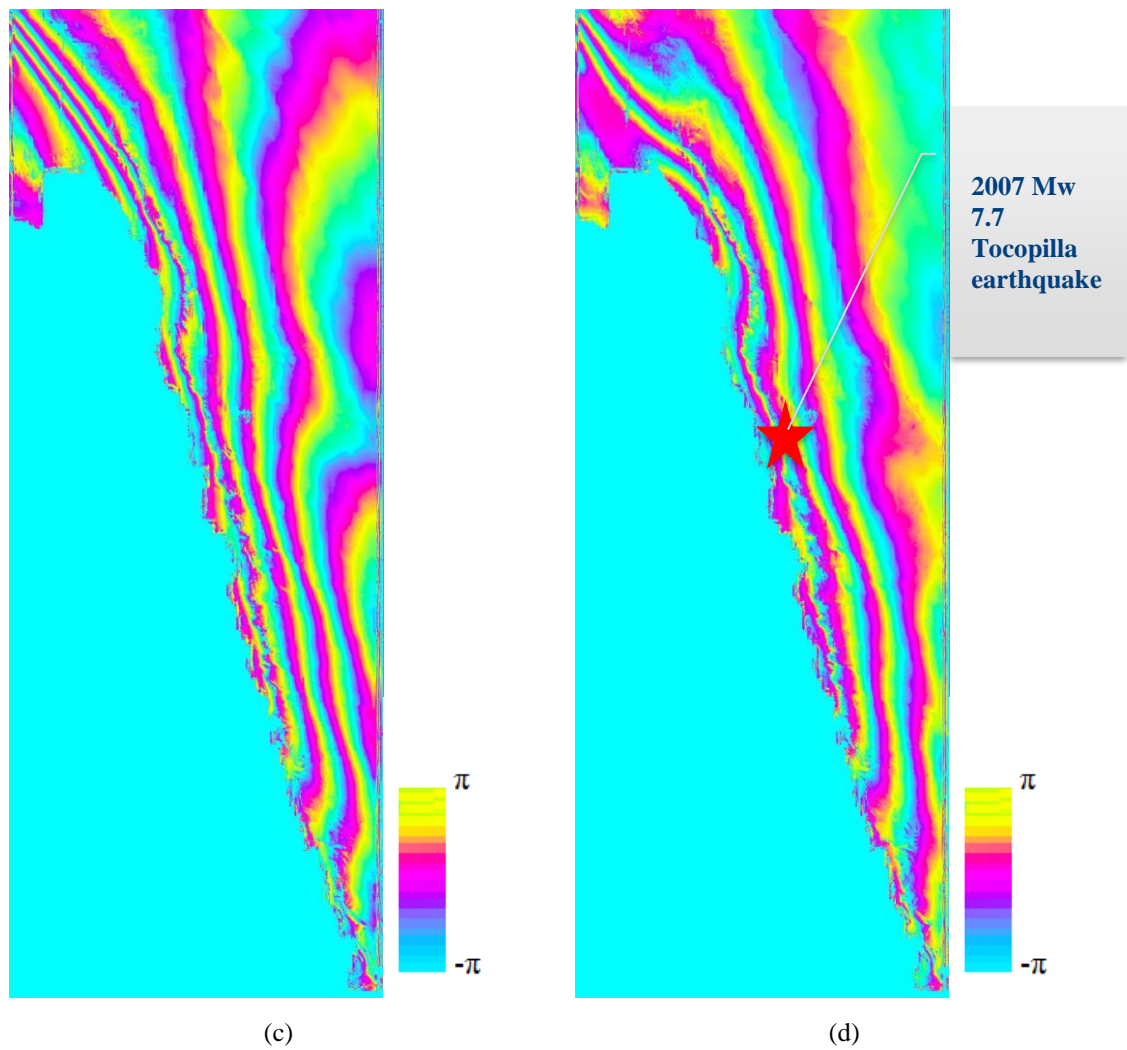
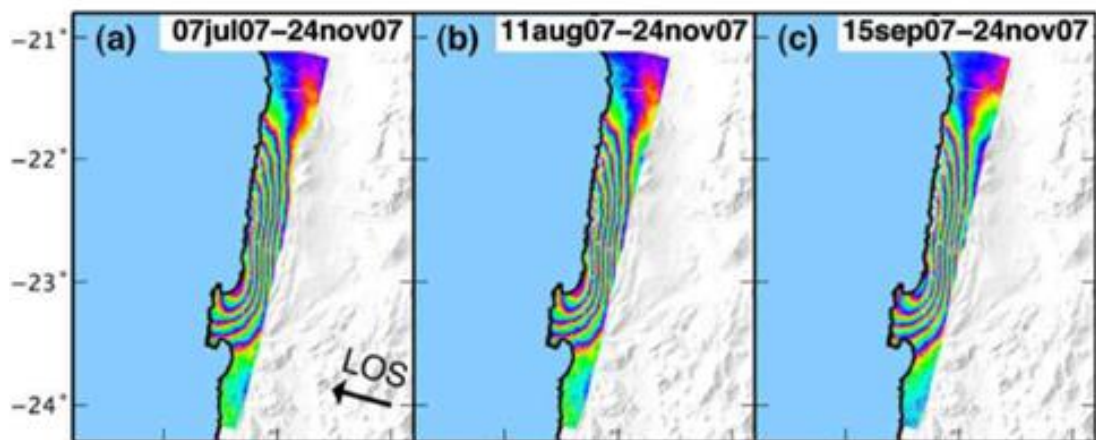


Figure 4.11 Ionosphere correction by the split spectrum method of test 2 in Tocopilla, Chile, the master date is 2007-09-15 before the earthquake, the slave date is 2008-01-31 after the earthquake: (a) Ionospheric phase before the filter; (b) Ionospheric phase after the filter; (c) Phase before correction; (d) Phase after ionospheric correction





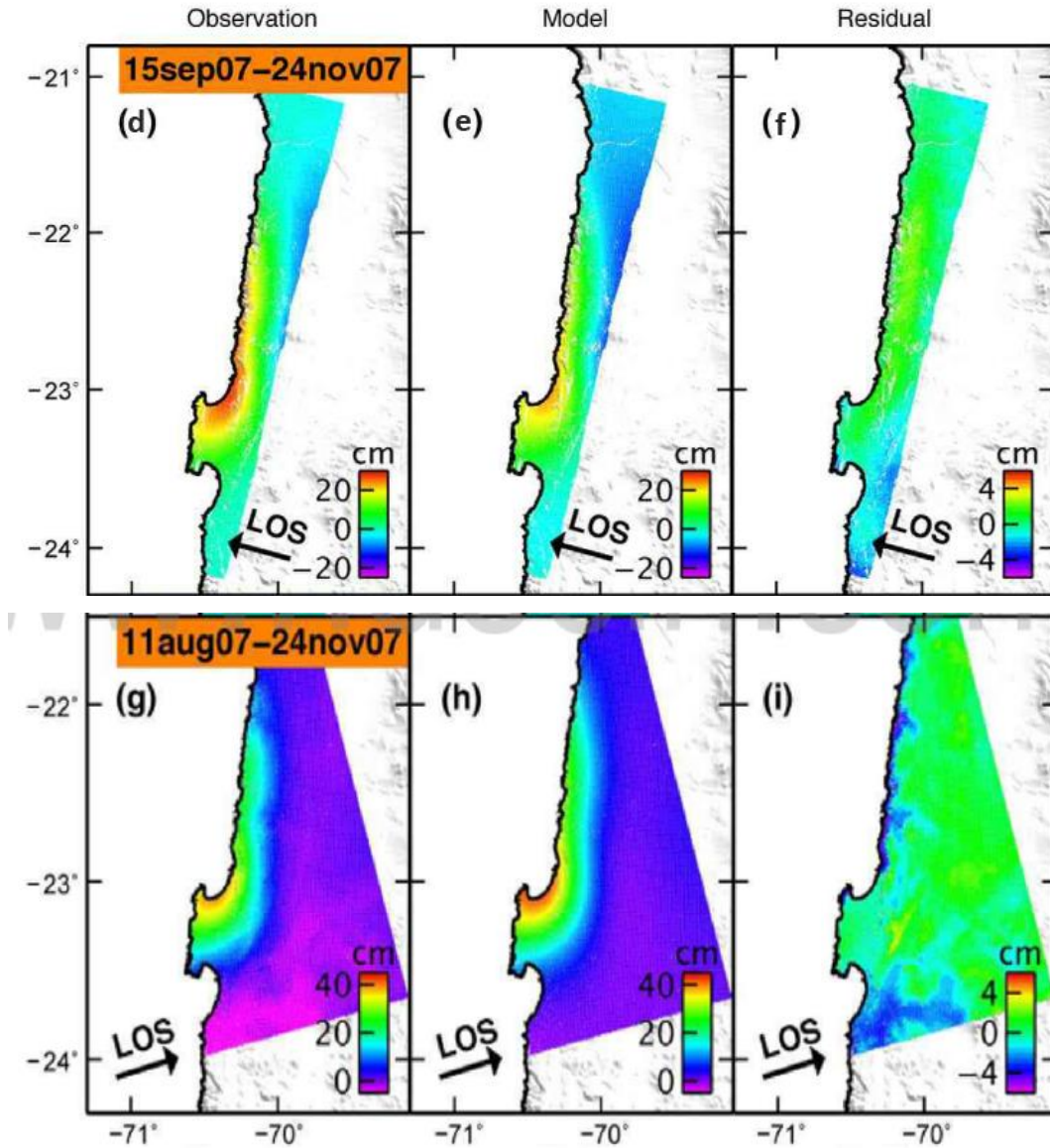


Figure 4.12 C-band InSAR result using ESA Envisat Image Mode data in Tocopilla, Chile. The top three figures are C-band InSAR interferogram results. The deformation is about 29 cm shown in the middle three figures, and the deformation is about 40 cm shown in the bottom three figures (Motagh et al., 2010)

These experiments reveal that the filtering method works satisfactorily and the ionospheric correction works reasonably as well. The ionospheric maximum delay shown in Figure 4.8 (b) is about 41.3 cm ( $2\pi$  means 11.8 cm for L band, seven fringes are 82.6 cm, SAR is a double way), which means that occasionally the ionospheric phase delay is very large for L-band InSAR, which requires correction in the InSAR processing. After ionospheric compensation, except for the coseismic ground displacement, there are still residuals, which implies that the residuals might be caused by ionospheric scintillation originating from the ionospheric irregularities, tropospheric delays, and DEM errors.

### 4.2.3 IGS TEC and International Reference Ionospheric Model

The VTEC grid data can be directly downloaded from the official website of the International GPS Service Centre (IGS) (<ftp://cddis.gsfc.nasa.gov/gnss/products/ionex/>). The file format is IONOX (Liu et al., 2005; Schaer et al., 1998). There are two kinds of data provided: rapid processing on the day and after a number of days for high-precision processing. The data provided by IGS have a spatial resolution of  $5^0$  in longitude,  $2.5^0$  in latitude, a time resolution of 2 hours, a longitude range of  $\pm 180^0$ , and a latitude range from  $-87.5^0$  to  $87.5^0$ . Due to multiple observation sites and the large data coverage, the use of these data to handle single-frequency observations of ionospheric delay correction has strong advantages. However, the resolution is very low, so it is best used for validation and initial data of some TEC methods.

In order to study the characteristics of the ionosphere, some international research institutes have established mature ionospheric models, including empirical models (based upon observations and statistics), physics-based models and data assimilation models (Nava et al., 2008; Béniguel, 2011; Secan, 2007; Bilitza et al., 2012; Kumar et al., 2014; Secan et al., 1987). For example, the International Reference Ionosphere (IRI) model (GSFC, 2012) and the NeQuick model (an ionospheric electron density model) are empirical models, which provide good mean performances and relationships between the model variables, but they are simple extrapolations in non-observation areas. The Thermosphere Ionosphere Exosphere - General Circulation Model (TIE-GCM) is a three-dimensional physics-based ionosphere model, which can provide real-time services and ionospheric forecasts, but its accuracy is influenced by the initialisation and boundary conditions (Shim et al., 2012; Elvidge, 2014). Except for the mature ionospheric models, there are also ionospheric scintillation models for highly variable and dynamic ionosphere in both time and space, which include the Global Ionospheric Scintillation Model (GISM), and the WBMOD (WideBand MOdel) Ionospheric Scintillation Model (Priyadarshi, 2015; Secan, 2007). As the IRI model can obtain the spatial distribution of the electron concentration easily when it is compared to other models, it will be used as validation data in this thesis's test. IRI as an empirical model was built using most of the available ground and space measurements, which represent monthly averages of electron and ion densities and temperatures from 50 km to 2000 km (Bilitza et al., 2017). The limitation of the IRI model is that it is sparse globally as it is based on available ground and space measurements with simple extrapolation in no observation areas. The IRI model provides

## Chapter 4. The atmospheric and ionospheric correction algorithm for TomoSAR

the TEC from 65 km to 2000 km (examples of the IRI Electron density ( $N_e$ ) map are shown in Figure 4.13, Figure 4.14 and Figure 4.15), so the TEC based on height processing (80 km to 760 km for ALOS L band) should be applied when used in validation.

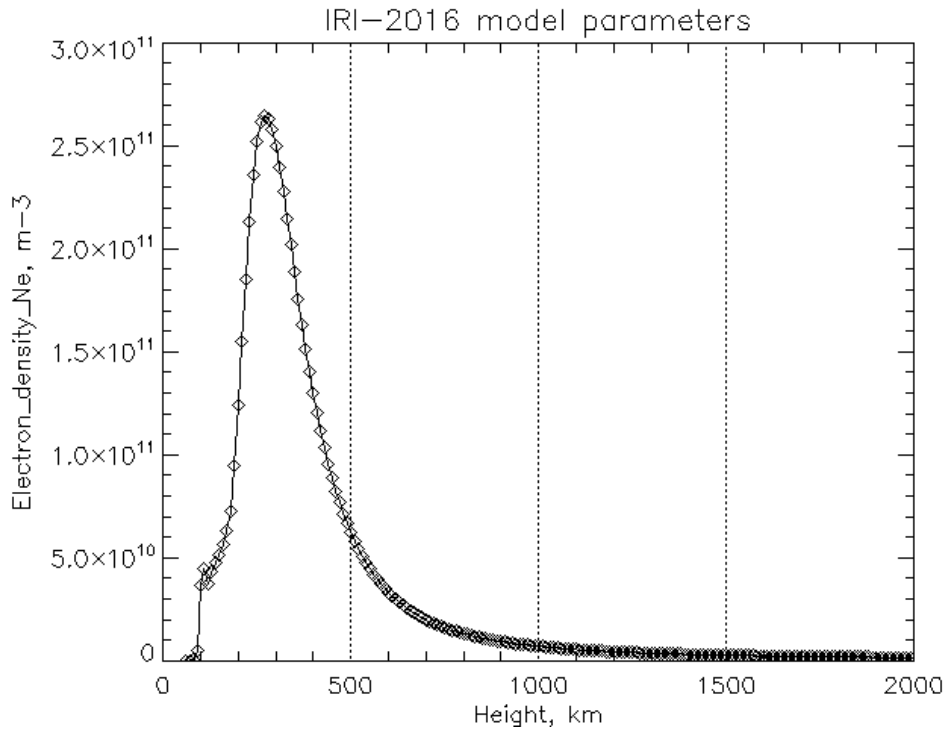


Figure 4.13 IRI Electron density ( $N_e$ ) map at (31N, 103.55E) on 2016-7-25

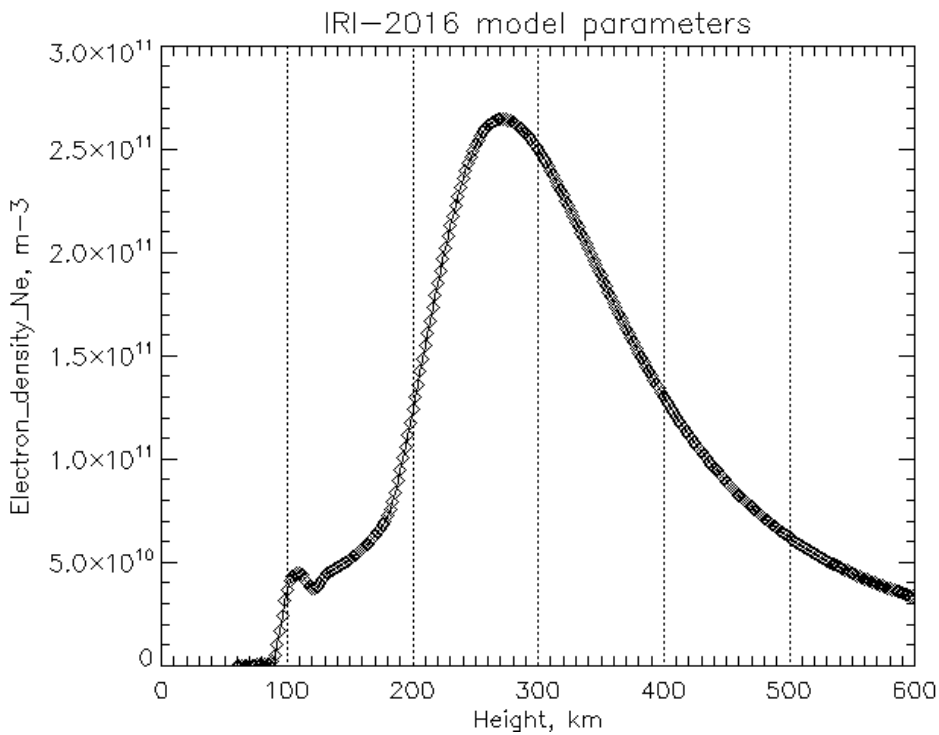


Figure 4.14 Zoom in IRI Electron density ( $N_e$ ) map at (31N, 103.55E) on 2016-7-25

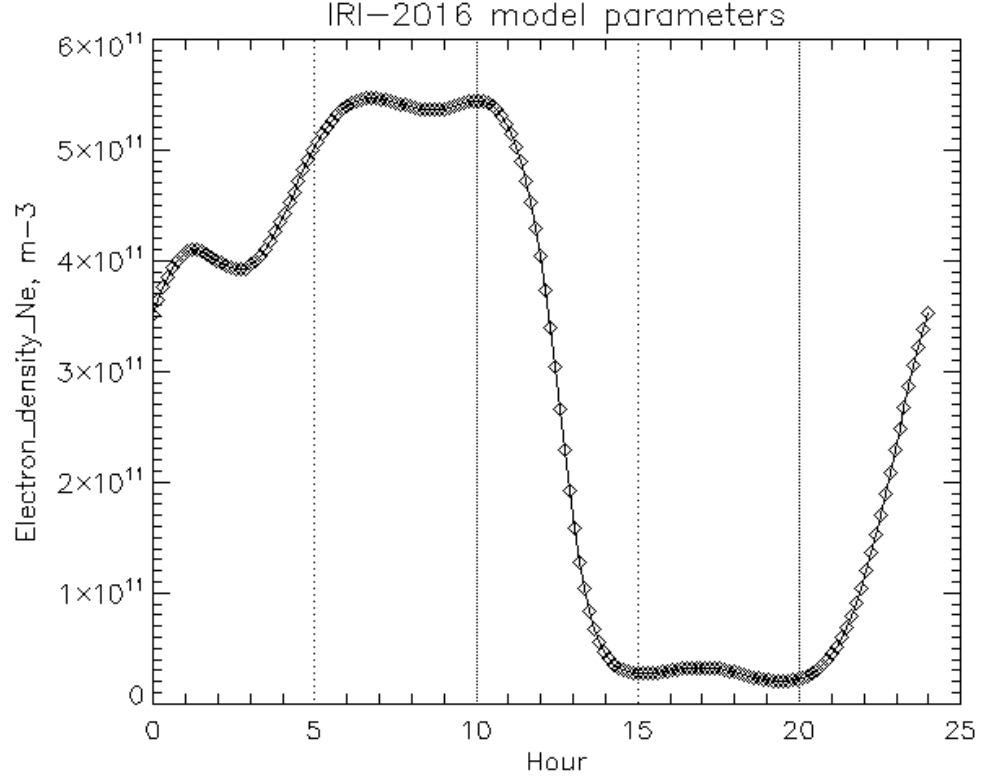


Figure 4.15 IRI Electron density (Ne) hour map (Year= 2016, Month= 07, Day= 25, Coordinate type = Geographic Latitude= 31, Longitude= 103.55, Time type = Universal, Height= 240km; parameters: Start time= 0, Stop time= 24, Step= 25 minutes)

#### 4.2.4 The Method for TEC Retrieval

As 3D SAR tomography imaging needs absolute TEC to calculate the unwrapped phase difference to make the ionospheric correction, a new method is proposed based on the IGS TEC data, split-spectrum and the ionospheric model.

When considering the temporal variance of the ionosphere (Hu et al., 2017), the TEC can be written as

$$\text{TEC} = \text{TEC}_0 + \Delta\text{TEC} \quad (4.15)$$

where  $\text{TEC}_0$  is the constant part of the variable TEC, which is the TEC value at a specific (setting) time and  $\Delta\text{TEC}$  is the varying part of the TEC, which changes with time.

$\Delta\text{TEC}$  is based on slow time  $t_a$ , so  $\Delta\text{TEC}$  can be written as below using a high-order polynomial approximation. In our new method, we define 20 parameters from  $k_1$  to  $k_{20}$

#### Chapter 4. The atmospheric and ionospheric correction algorithm for TomoSAR

$$\Delta\text{TEC} = k_1 \cdot t_a + k_2 \cdot k_a^2 + k_3 \cdot t_a^3 + \dots \quad (4.16)$$

After doing interferometry and using the split-spectrum method based on 4.2.2, the differential TEC ( $\Delta\text{TEC}_{\text{master-slave}}$ ) of two times can be calculated.

$$\Delta\text{TEC}_{\text{master-slave}} = \text{TEC}_{\text{master}} - \text{TEC}_{\text{slave}} \quad (4.17)$$

As we have IGS TEC data, we can sort out the nearest time (for example, data at 6 pm) of the TEC, we define the IGS TEC data as the constant background part ( $\text{TEC}_0 = \text{TEC}_{\text{IGS}}$ ) and calculate the slow time  $t_a$  (the difference between the background TEC time and the SAR acquisition time). Because GPS and SAR are at different altitudes, there is a constant TEC value between the TEC at different altitudes and we define it as  $\text{TEC}_{\text{shift}}$ .

$$\text{TEC}_{\text{SAR}} = \text{TEC}_{\text{IGS}} + \text{TEC}_{\text{shift}} \quad (4.18)$$

In this way, Equation (4.15) can be written as

$$\text{TEC}_i = \text{TEC}_{\text{SAR}_i} = \text{TEC}_{\text{IGS}_i} + \text{TEC}_{\text{shift}_i} + \Delta\text{TEC}_i \quad (4.19)$$

where  $i$  represents the different SAR data acquisition time of the different SAR data,  $\text{TEC}_i$  is the TEC value from 80 km to the SAR satellite. When we difference the master and the slave TEC, the differential TEC ( $\Delta\text{TEC}_{\text{master-slave}}$ ) can be obtained.  $\Delta\text{TEC}_{\text{master-slave}}$  is the differential TEC obtained in split-spectrum processing using the split-spectrum method in 4.2.2.

$$\begin{aligned} & \text{TEC}_{\text{master-slave}} \\ &= \text{TEC}_{\text{IGS\_master}} - \text{TEC}_{\text{IGS\_slave}} + \text{TEC}_{\text{shift\_master}} \\ & - \text{TEC}_{\text{shift\_slave}} + \Delta\text{TEC}_{\text{master}} - \Delta\text{TEC}_{\text{slave}} \end{aligned} \quad (4.20)$$

From the above equation, each pixel has an observation equation. Moreover, we can see that we have 42 unknown parameters (20 parameters  $k_1, k_2 \dots k_{20}$  of the slave, 20 parameters  $k_1, k_2 \dots k_{20}$  of the master,  $\text{TEC}_{\text{shift\_master}}$  and  $\text{TEC}_{\text{shift\_slave}}$ ). Because we know the differential TEC:  $\Delta\text{TEC}_{\text{master-slave}}$  from split-spectrum processing and  $\text{TEC}_{\text{IGS\_master}}$ ,  $\text{TEC}_{\text{IGS\_slave}}$  from IGS TEC data, we can use the least squares method to obtain the 42 parameters using the least squares equation (4.21).

$$A X + B = C \quad (4.21)$$

Equation (4.21) is detailed in Equation (4.22), which is the least squares model equation. After the least square calculation, we can get the absolute TEC based on the parameter results and Equation (4.19).



## Chapter 4. The atmospheric and ionospheric correction algorithm for TomoSAR

In more detail, our core concept is to achieve high resolution TEC, which could be used in many applications; our first application is TomoSAR. The data was split into small tiles for processing, like  $20 \times 20$ , and the resolution of IGS TEC is 5 degree, and our split TEC data resolution is 10 m. If we use  $20 \times 20$  for the tile, our resolution is 200 m, and although the tile size could be lower for a high resolution, the minimum is  $7 \times 7$  as we have 42 parameters (needs 42 equation  $< 49 = 7 \times 7$ ) to be calculated by least squares, meaning that the high theoretical resolution could be achieved up to 70 metres. As we are more concerned with the speed of the algorithm and the accuracy, we selected the tile size to be  $20 \times 20$ . In each tile, the equation for the least-squares model is constructed as below, in this least-squares model, the 21 parameters (the shift constant parameter and the 20 parameters are  $k_{10}, k_{11}, k_{12}, k_{13} \dots k_{110}, k_{111} \dots k_{120}$ ) of the master image data can be achieved using a matrix calculation (Equation (4.22)). Then the master TEC can be calculated using Equation (4.19). As we have differential split-spectrum TEC data, all TECs can be calculated based on the simple plus/minus method or by using the model parameters (Equation (4.22)) that are obtained in the least-squares model.

Each row of the matrix below (Equation (4.22)) has 400 ( $20 \times 20$  one tile) equations, which means the total equation of one tile is  $400 \times (n-1)$  ( $n$  is the number of measures). After the matrix calculation, the parameters and high-resolution TEC can be obtained. The flowchart is shown in Figure 4.16 below.

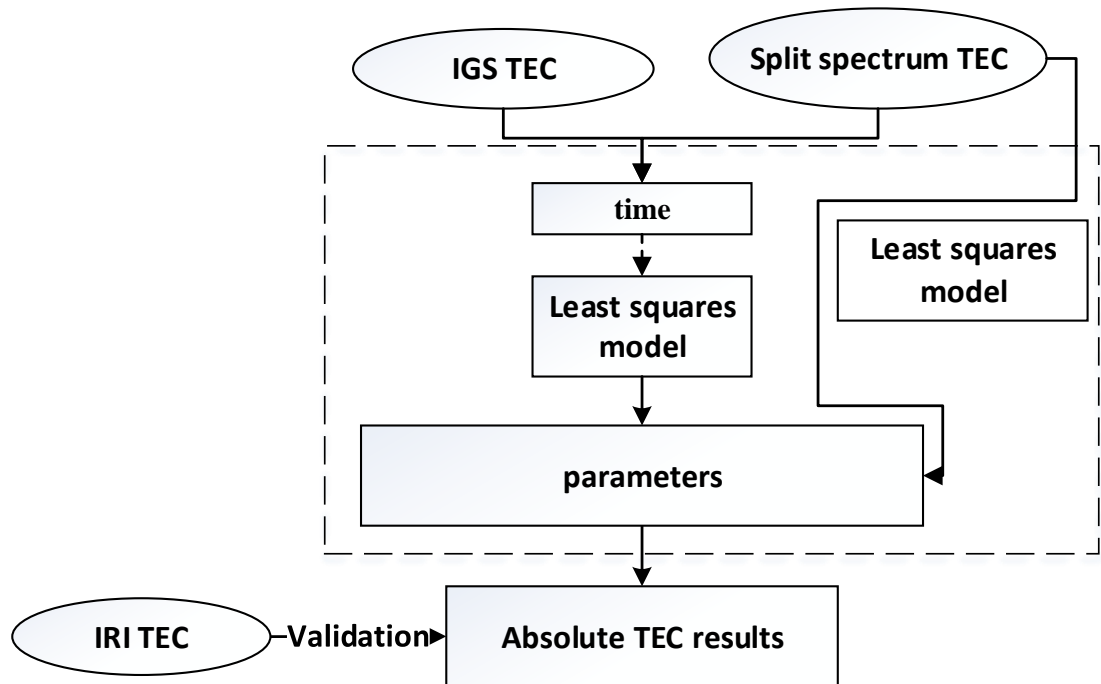


Figure 4.16 The flowchart of the TEC method

$$\begin{aligned}
 & \left[ \begin{array}{cccccccccccccccccccc}
 1 & t_1 & t_1^2 & t_1^3 & \dots & -1 & -t_2 & -t_2^2 & 0 & 0 & 0 & 0 & 0 & 0 & 0 & 0 & 0 & \dots \\
 1 & t_1 & t_1^2 & t_1^3 & & & 0 & & \dots & -1 & t_3 & t_3^2 & \dots & 0 & 0 & 0 & 0 & 0 \dots \\
 1 & t_1 & t_1^2 & t_1^3 & & & 0 & & & & & & & -1 & t_4 & t_4^2 & \dots & 0 \dots \\
 & \vdots & & & & & & \ddots & & & & & & & & \vdots & & \\
 & & & & & & & \dots & & & & & & & & & & \dots
 \end{array} \right] \\
 & * \begin{bmatrix} k_{10} \\ k_{11} \\ k_{12} \\ k_{13} \\ \dots \\ k_{20} \\ k_{21} \\ k_{22} \\ \dots \\ k_{30} \\ k_{31} \\ k_{32} \\ \dots \\ k_{40} \\ k_{41} \\ k_{42} \\ \dots \end{bmatrix} = \begin{bmatrix} \Delta \text{TEC}_{\text{split}} - (\text{TEC}_{\text{IGS\_master}} - \text{TEC}_{\text{IGS\_slave}}) \end{bmatrix} \quad (4.22)
 \end{aligned}$$

### 4.2.5 Experiment, Results and Validation of the TEC Method

The experiment was performed in San Francisco Bay, USA using the Advanced Land Observing Satellite (ALOS) data as one step of the TomoSAR experiment (shown in Figure 4.19), which is described in Appendix E. The Global IGS TEC raw maps of the closest time of the ALOS SAR acquisition time are shown in Figure 4.17 and Appendix C. One of the IGS TEC interpolation maps of the closest time of ALOS SAR measurement time used in the test (the subarea of San Francisco Bay, USA) is shown in Figure 4.18. The maps in the test are interpolated from the IGS TEC raw data using the nearest neighbour sampling method. The resolution of the IGS TEC data is  $5^\circ$  in longitude,  $2.5^\circ$  in latitude with fixed grid tiles, and the resolution of these interpolation maps is about 4.45 metres in azimuth and 9.52 metres in range (ALOS-1 SAR data resolution). Figure 4.18 shows that the image is on the boundary of 2 IGS cells, the two cell value (TEC value) of the different SAR acquisition date (used in the test) are shown in Table 4.2, and Figure 4.18 is the plot of two numbers with a sharp line presented. Besides, the separating line in the picture is irregular because this is the ascending SAR image in the radar coordinate system (the ALOS-1 satellite looking down-right flies from left to right in Figure 4.19) and the orbit inclination angle is  $98.16^\circ$ , the Earth is not a perfect sphere and the separating line is along the latitude (see Figure 4.18 and Figure 4.19). In Table 4.2, the TEC value is different at different time, and the TEC value of 2009/02/01 (the top is smaller than the bottom) is different from the others (the top is bigger than the bottom) in terms of spatial distribution, which means that the TEC distribution is variable at different positions and different times.

The split-spectrum differential TEC maps (obtained in the split-spectrum processing using the split-spectrum method discussed in Section 4.2.2) of the ALOS SAR at the slave measurement time in the small sub-test area of San Francisco Bay, USA, are shown in Figure 4.20. The master date is 2009-02-01, and others are the slave dates. The differential TEC (unit: TECU,  $\text{TECU} = 1 \times 10^{16} \text{el}/m^2$ ) represents the TEC value at the master SAR data acquisition time (20090201) minus the TEC value at the slave SAR data acquisition time.

## Chapter 4. The atmospheric and ionospheric correction algorithm for TomoSAR

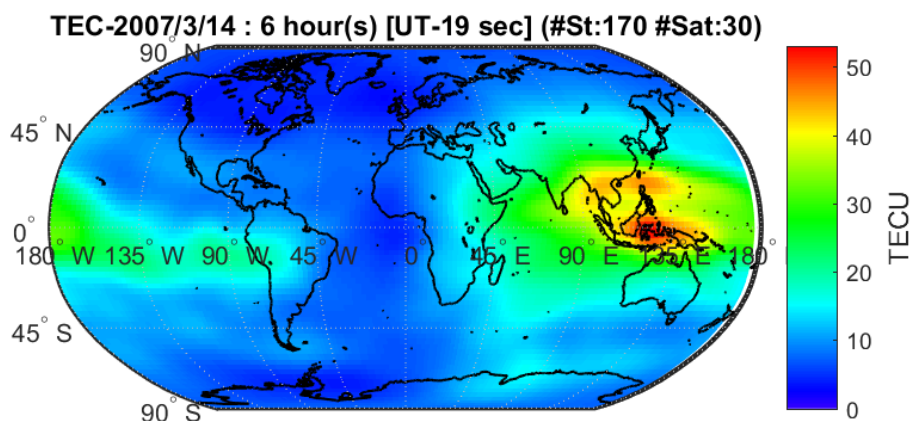


Figure 4.17 The global TEC map of the closest time of the ALOS SAR measurement time (19 s means the difference between UT (TAI) and GPS time, St is the station number used and Sat is the satellite number used for generating the map)

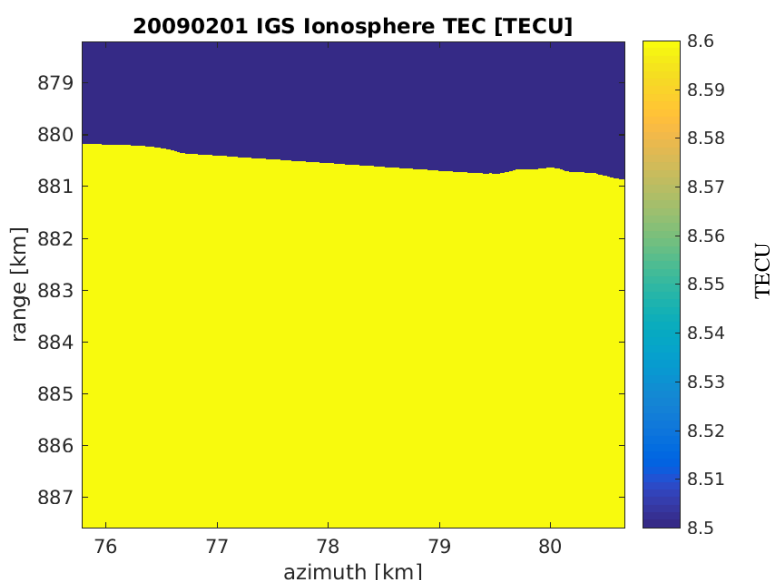


Figure 4.18 The TEC map of the closest time of ALOS SAR measure time in a small sub-test area of San Francisco Bay, USA (unit: TECU)

Table 4.2 The two TEC value of the closest time of ALOS SAR measurement time in a small sub-test area of San Francisco Bay, USA (unit: TECU), these two TEC values are effective from the TEC in two “squares” of size roughly 275 x 275 km centred 125 km N and S of the scene location

Date	2007 /03/14	2007 /04/29	2007 /07/30	2008 /01/30	2008 /11/01	2009 /02/01	2009 /03/19	2009 /122/0	2010 /03/22	2010 /12/23	2011 /03/25
Up TEC	11.4	7.4	6.4	9.3	11.6	8.5	7.7	13.3	9.9	14.4	14.9
Down TEC	11.3	7.1	6.2	8.8	11.4	8.6	7.2	12.9	9	14.1	14.1

## Chapter 4. The atmospheric and ionospheric correction algorithm for TomoSAR

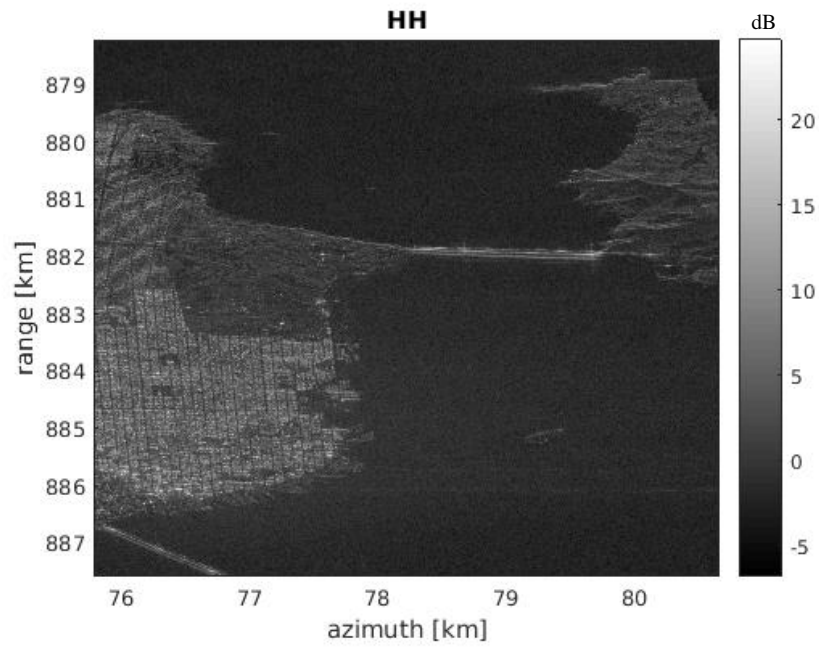
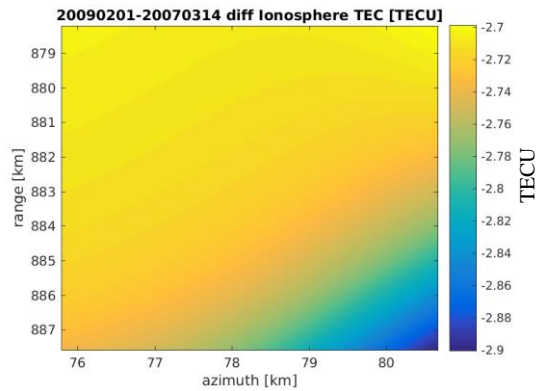
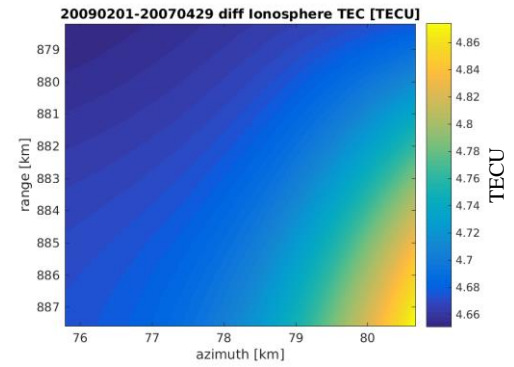


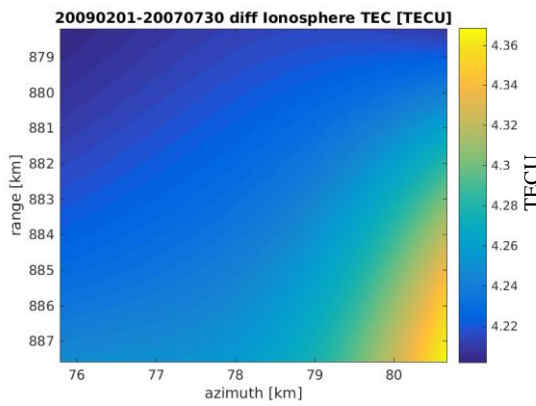
Figure 4.19 The small test area SAR image in San Francisco Bay, USA



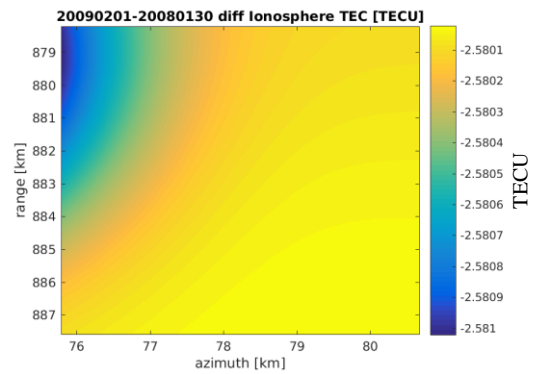
(a)



(b)



(c)



(d)

## Chapter 4. The atmospheric and ionospheric correction algorithm for TomoSAR

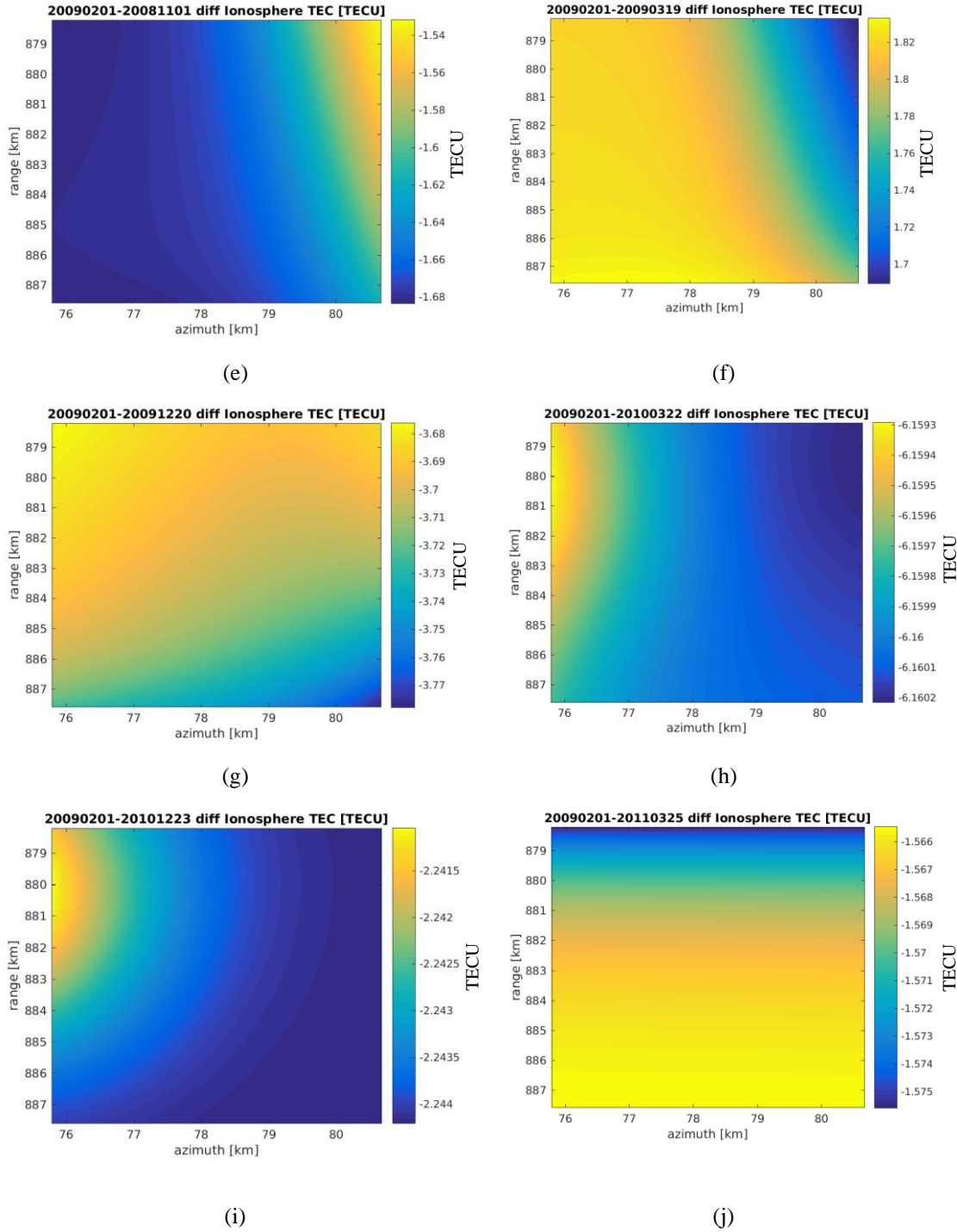


Figure 4.20 The split-spectrum differential TEC result map of the ALOS SAR of different slave measure time in a small sub-test area of San Francisco Bay, USA, the master date is 2009-02-01 (unit: TECU)

According to our proposed TEC method (the flowchart is shown in Figure 4.16), the TEC results were obtained and a TEC map of 2009/02/01 is shown in Figure 4.21. The size of the TEC map is 2001 by 2001 pixels and the size of a pixel is the same as an ALOS SAR image pixel about 4.45 metres in azimuth and 9.52 metres in range, which is interpolated from the 200 m resolution TEC results. Firstly, the absolute master TEC

( $TEC_{master}$ ) is obtained. The absolute master TEC map ( $TEC_{master}$ ) and the absolute slave TEC map are the TEC maps that we need in TomoSAR. As we have differential split-spectrum TEC data, all slave TEC data can be calculated based on the simple minus differential split-spectrum TEC from master SLC (as  $TEC_{split} = TEC_{master} - TEC_{slave}$ , so,  $TEC_{slave} = TEC_{master} - TEC_{split}$ ) or the least-squares model (the  $k$  parameters, like the 21 parameters ( $k_{10}, k_{11}, k_{12}, k_{13}, k_{14} \dots$ ) of the master and slave image data are obtained and then the TEC can be obtained using the least-squares model in 4.2.4).

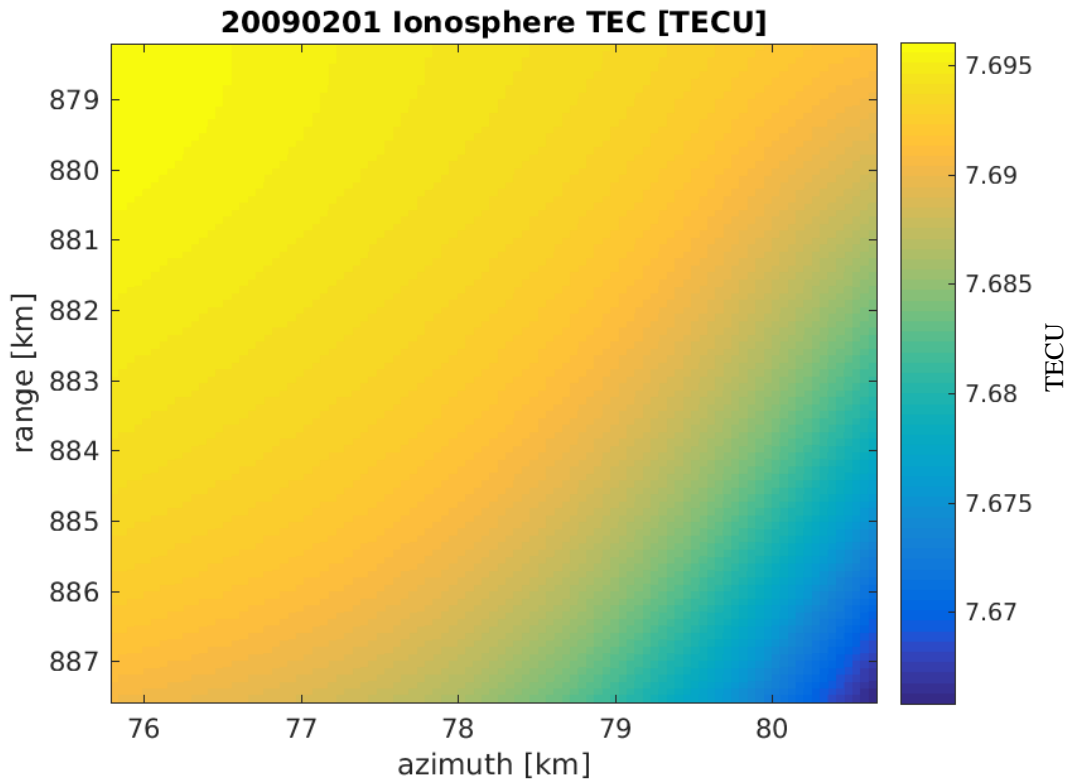


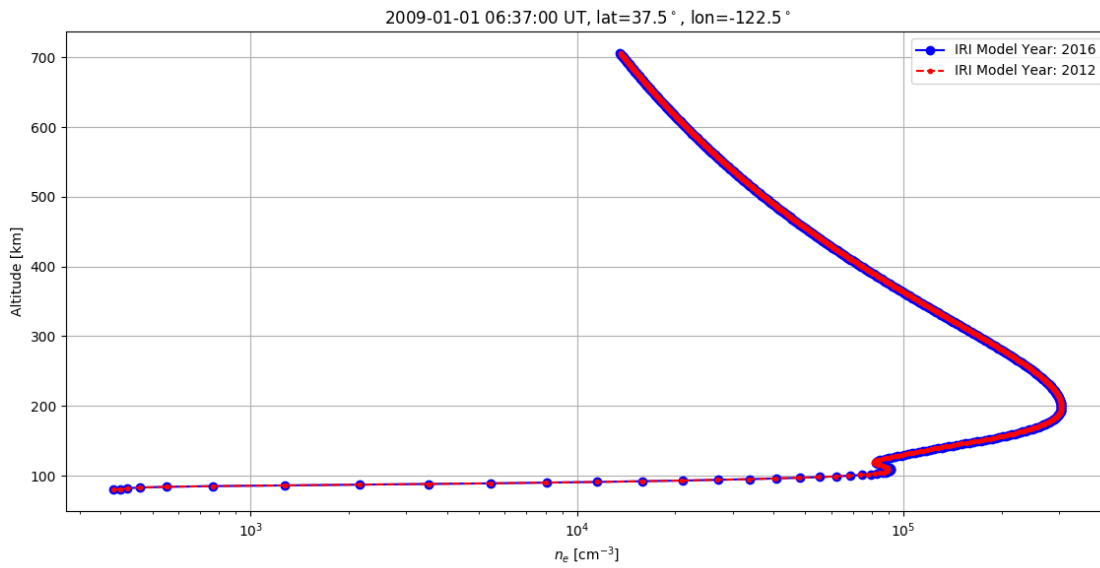
Figure 4.21 High resolution (200 m) TEC map on 2009/02/01

The IRI model TEC was used for validation. The electron density in the daytime is from 65 km to 2000 km and during the night, it is from 80 km to 2000 km. The ALOS satellite is at 706 km and the acquired time is at UTC 06: 37 (the local time is 22.37 at night). Thus, the IRI TEC must be calculated from 80 km to 706 km via the TEC definition and IRI density. Based on NASA's IRI model online service<sup>26</sup>, Figure 4.22 (a) shows the electron density from the ground to the ALOS satellite height of 706 km. According to the IRI electron density, the IRI TEC map is obtained via the TEC definition

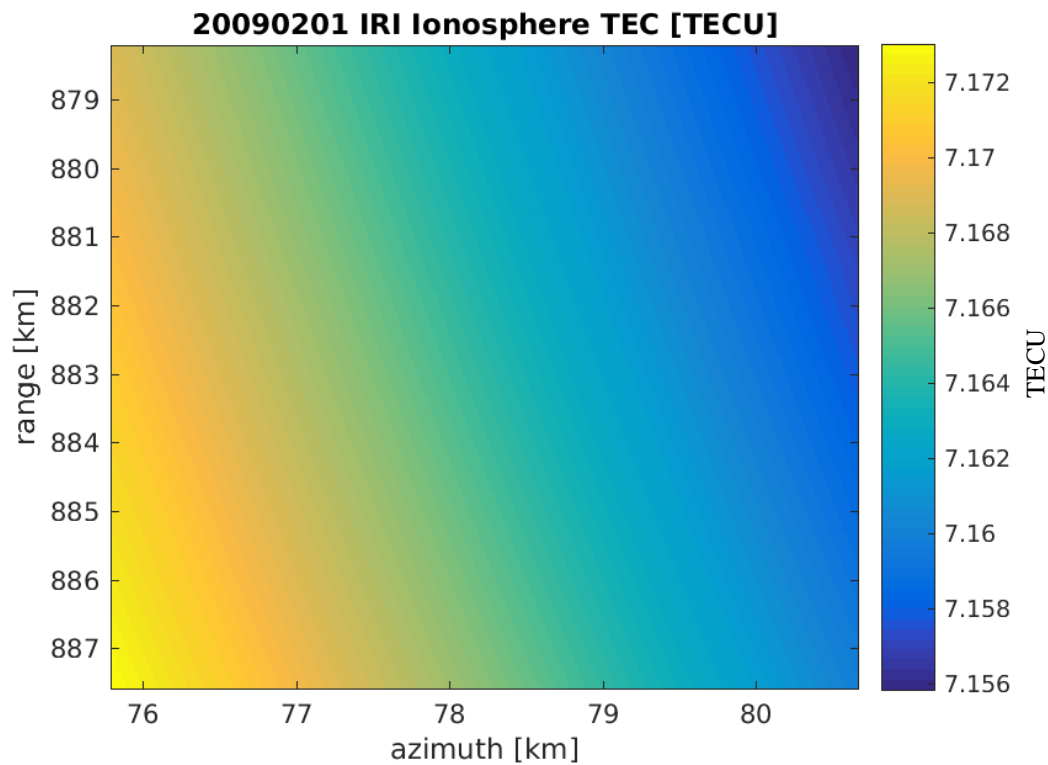
<sup>26</sup> [https://ccmc.gsfc.nasa.gov/modelweb/models/iri2016\\_vitmo.php](https://ccmc.gsfc.nasa.gov/modelweb/models/iri2016_vitmo.php)

## Chapter 4. The atmospheric and ionospheric correction algorithm for TomoSAR

(Equation (4.3)), IRI model and our Matlab code. The IRI TEC MAP from 80 km to 706 km is shown in Figure 4.22 (b), which is used for validation.



(a)



(b)

Figure 4.22 Electron density and IRI TEC map: (a) Electron density from the ground to ALOS satellite height 706 km; (b) IRI TEC MAP for validation (80-706 km)



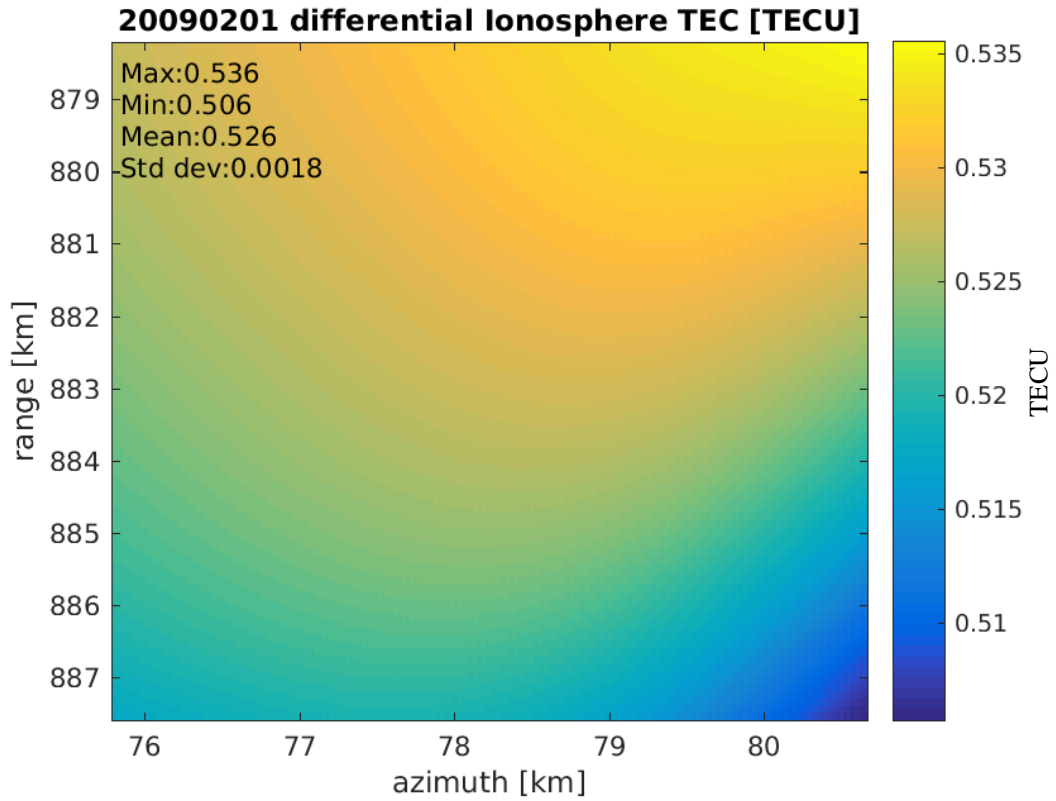


Figure 4.23 The differential TEC map (High resolution TEC map - IRI TEC)

The High TEC map was validated using the IRI TEC data. The maximum difference is 0.536 TECU, the minimum difference is 0.506 TECU, the mean difference is 0.526 TECU, and the standard deviation of difference is 0.0018 TECU. The uncertainty is about  $0.526 \pm 0.0018$  TECU, and the differential map is shown in Figure 4.23. There are small systematic errors; the mean 0.526 TECU difference might be because the high TEC map is calculated based on the IGS TEC data and there is a 1.34 TECU difference value between IGS data and IRI data (IGS TEC based on GPS is around 8.5 TECU shown in Figure 4.18, and IRI calculated based on SAR satellite height (ALOS-1 altitude is 706 km, from 80-706 km) is around 7.16 TECU). The uncertainty ( $0.526 \pm 0.0018$  TECU) is small, which demonstrates that the high-resolution TEC estimation method works. In this least-squares method, the absolute master TEC is obtained, and then other slave absolute TEC data can be obtained by minusing the split spectrum differential data. Moreover, as there is no truth data for validation, the validation was executed via current available IRI TEC data. There might be errors and uncertainties in the split spectrum results, but the errors will be compensated by phase calibration. In addition, there might be errors and uncertainties in the master absolute TEC results, but when we use this in TomoSAR, it is just the base TEC input value, which will cause a group phase shift to the TomoSAR, but

it has no influence on the TomoSAR structure. This shift can be corrected using the control point in TomoSAR processing.

### 4.3 Conclusions

In this chapter, the principles of the atmospheric and ionospheric correction algorithm for TomoSAR 3D SAR tomography imaging are first introduced. In addition, the PS and ERA-I model for the absolute atmospheric phase and the GACOS model for the absolute atmospheric phase are presented, and the ionospheric correction split spectrum algorithm for InSAR and differential TEC estimation are introduced. Two test areas were studied in Tocopilla, Chile, using this split spectrum method. These two experiments reveal that the filtering method works very well and that ionospheric correction works adequately. Furthermore, these two experiments also reveal that sometimes the ionospheric phase delay is very large for L-band InSAR, which needs to be corrected in the InSAR processing. After ionosphere compensation, apart from the coseismic ground displacement, there are still residuals, which might be caused by the ionospheric scintillation originating from ionospheric irregularities, tropospheric delays and DEM errors. Following this, the IGS IONOX format TEC and International Reference Ionospheric Model are introduced. Finally, my new TomoSAR ionospheric correction algorithm method is proposed for TEC estimation by using the IGS TEC data with the split-spectrum differential TEC data and least squares model. The experiment and validation of the TEC method were executed lastly for absolute TEC results. As there is no ‘truth’ data for validation, the validation was executed via the available IRI TEC data. Compared to the IRI TEC, the uncertainty of the TEC at the master date is about  $0.526 \pm 0.0018$  TECU. The systematic error is small. In addition, the TEC results are sufficient for our TomoSAR application as it has a relatively high resolution by using the IGS data, the split-spectrum data and the least squares model. The TomoSAR results with ionospheric corrections using these TEC results and split-spectrum data will be shown in Appendix E.

# **Chapter 5**

## **TomoSAR and Differential TomoSAR Algorithms**

Currently, there are many methods that can be used to obtain 3D information from SAR imaging data, such as PS InSAR and TomoSAR imaging. In this chapter, the systematic mathematical derivation for the workflow of TomoSAR and differential TomoSAR imaging are presented in detail. Firstly, the basic principles of 3D SAR tomography imaging and four-dimensional differential tomographic SAR imaging are introduced. Next, the SAR tomography workflow and four-dimensional differential tomography workflow are presented. Then, the PS-InSAR phase error compensation algorithm, PGA (phase gradient autofocus) phase error compensation algorithm, our SAR tomography imaging algorithm and our phase error compensation algorithm based on PS, SVD, PGA, weighted least squares and minimum entropy are also studied in detail; the SAR interferometry phase (InSAR) calibration with a DEM error correction method is also proposed and demonstrated in detail. Moreover, the sparse aperture for 3D imaging and the basic theory of compressive sensing are introduced. In addition, three-dimensional high-resolution tomography SAR imaging and four-dimensional differential tomography SAR imaging based on compressive sensing are studied with the mathematical formula derivation and the programming workflow introduction. Finally, conclusions are drawn at the end of the chapter.

### 5.1 The Principles of SAR Tomography

The main difference between SAR and other radars is that the synthetic aperture technique combines a small physical aperture with a large virtual aperture using the signal processing method, because two-dimensional SAR imaging forms a synthetic aperture only in the azimuth direction. The two-dimensional SAR image is actually the projection of the three-dimensional scene into the two-dimensional azimuth-range plane, but it cannot reflect the target height information (Tebaldini, 2010). Thus, the issue is how to extend two-dimensional SAR imaging to three-dimensional SAR tomography imaging from a two-dimensional aperture synthesis perspective. This section of this chapter will introduce this issue.

#### 5.1.1 SAR Tomography Three-dimensional Imaging Principle

A normal monostatic imaging SAR system consists of a side-looking transmitter and receiver mounted on a moving platform, such as an aeroplane or satellite. The native 3D reference frame of a SAR sensor that maps the parameters in the three directions are defined as below, the 2D resolution element of a conventional SAR is shown in Figure 5.1, and the TomoSAR imaging geometry is shown in Figure 5.2. TomoSAR uses a stack of complex SAR datasets taken at slightly different orbit positions and different times for the same area in order to build up a synthetic elevation aperture for 3D imaging (Tebaldini, 2010) (see Figure 5.2). Similar to the azimuth direction resolution in Figure 5.1, if the elevation aperture is sufficient, then the expected elevation resolution  $\rho_s$  (Tebaldini, 2010), based on the elevation aperture size  $\Delta b$ , is given by the equation below (see Figure 5.3):

$$\rho_s = \frac{\lambda r}{2\Delta b} \quad (5.1)$$

where  $\lambda$  is the wavelength,  $r$  is the range,  $\Delta b$  is the elevation aperture size.

The parameters in the 3D SAR maps (Figure 5.1 and Figure 5.3) are defined (Zhu, 2011) as below:

$x$ : azimuth, the flight direction of the sensor, is also called the along-track direction;

$r$ : range, line-of-sight (LOS) direction of the antenna, is also referred to as slant range;

$\Theta$  or  $\theta$ : elevation angle, the angle is between the slant range and the azimuth-ground range plane.

Elevation  $s$ : SAR does not provide imaging in this direction (perpendicular to the azimuth-range plane), and different elevation targets in the same azimuth-range ( $x-r$ ) coordinates cannot be distinguished in 2D SAR, but they can be detected in TomoSAR. Due to the large range distance in the order of hundreds of kilometres and the small angular divergence, this can be assumed to be a straight line. It is often called cross range  $s$  or elevation  $s$ .

Normal-slant-range direction (NSR direction): the NSR direction is the elevation ( $s$ ) direction, which is perpendicular to the azimuth-slant range plane.

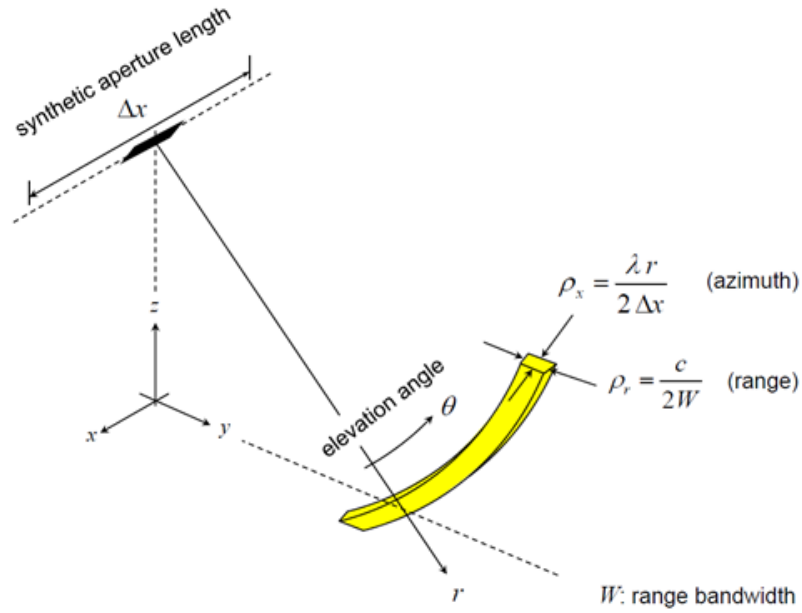


Figure 5.1 2D resolution element of a conventional SAR. The azimuth resolution  $\rho_x$  is determined by the azimuth synthetic aperture length  $\Delta x$  while the range resolution  $\rho_r$  is calculated by the bandwidth  $W$  of the chirp emitted by the antenna (Zhu, 2011)

In the analysis of the two-dimensional imaging principle of SAR (Lee and Pottier, 2009; Oliver and Quegan, 2004; Lazarov and Kostadinov, 2013; Soumekh, 1999; Mahafza, 2005; Richards, 2005), the actual targets exist in the three-dimensional space, while the two-dimensional SAR imaging result is the projection of the three-dimensional structure and targets into a two-dimensional plane. The three-dimensional space is divided into a series of equidistant cylindrical surfaces along the azimuth axis (Figure

## Chapter 5. TomoSAR and differential TomoSAR algorithms

5.3), but SAR does not have the ability to distinguish the targets on the same cylindrical surface, because these targets are compressed into the same distance in the same pixel. This is the cylindrical symmetric ambiguity problem in SAR two-dimensional imaging.

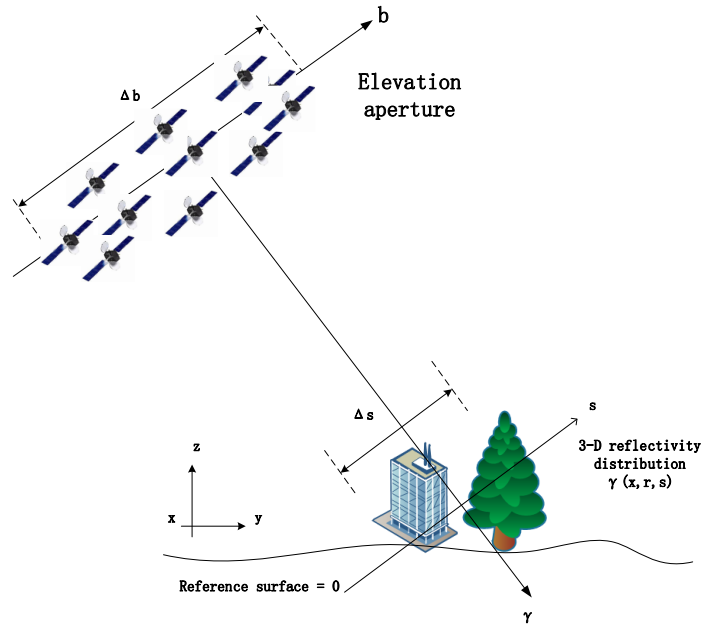


Figure 5.2 TomoSAR imaging geometry

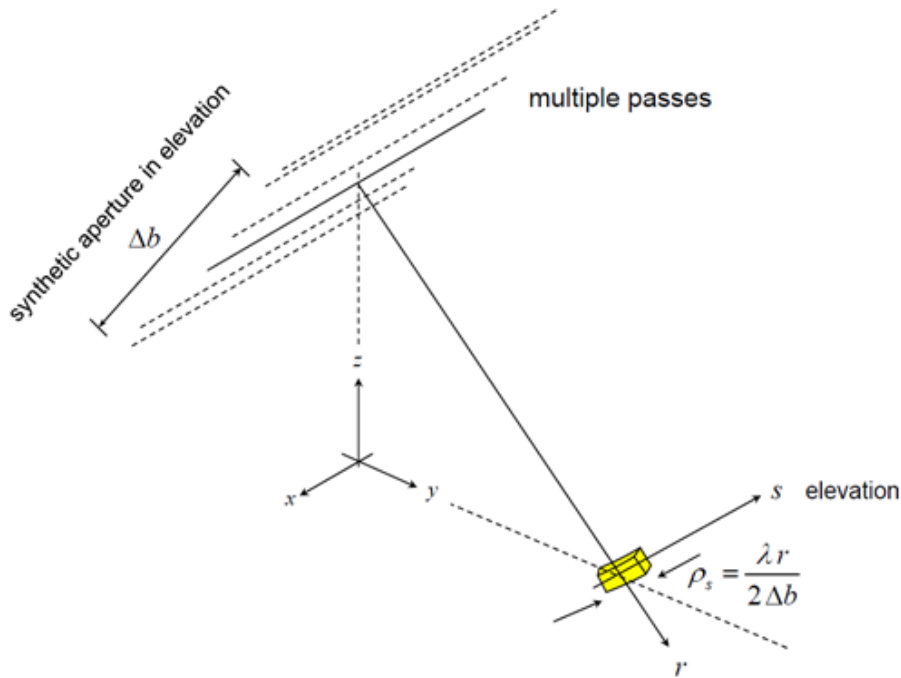


Figure 5.3 3D resolution element of a tomographic SAR, like the azimuth direction, the elevation resolution  $\rho_s$  is determined by the elevation aperture size  $\Delta b$  (Zhu, 2011)

Since the high azimuth resolution imaging can be obtained by the synthesis aperture method using a small size radar antenna, two-dimensional high-resolution imaging in the elevation plane can be realised if a two-dimensional synthetic aperture is formed in the elevation direction with the help of the high-resolution range direction imaging to achieve a true three-dimensional radar imaging. This is the basic idea of three-dimensional SAR imaging, as shown below.

Considering that the scene is a true three-dimensional scene, a cartesian coordinate system is established with the scene centre as the origin (Figure 5.4). The X-axis is parallel to the trajectory of the radar (velocity direction, when the radar point to the scene centre) and points to the radar movement side (the radar satellite doesn't manoeuvre in a straight line, it will vary little by little when flying around the Earth). The Y-axis distance points to the radar (slant range direction) and the S-axis is determined by the right-hand rule. The S direction is referred to as the normal-slant-range direction (called NSR direction or s elevation direction).

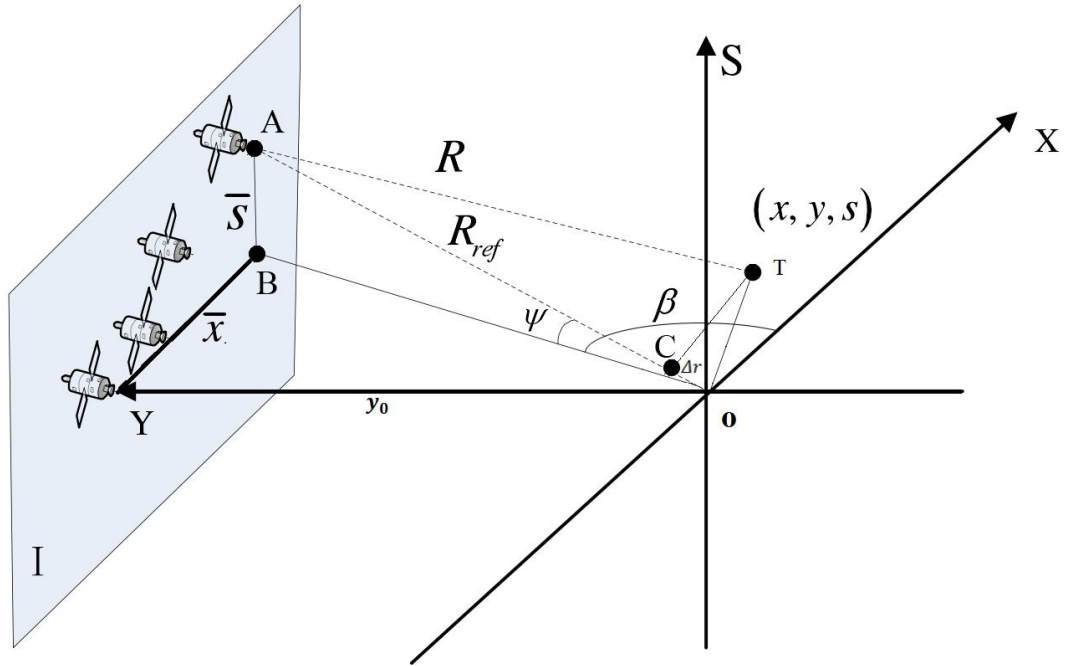


Figure 5.4 Three-dimensional imaging using a two-dimensional synthesis aperture (Xilong et al., 2012; Tebaldini, 2010)

Assuming that the radar is at a distance  $y_0$  from the X-S plane and it transmits a chirp signal in the plane I (Figure 5.4); meanwhile, considering that the complex

## Chapter 5. TomoSAR and differential TomoSAR algorithms

scattering coefficient of point  $(x, y, s)$  is  $\gamma(x, y, s)$  at the spatial location, when the radar is at  $(\bar{x}, y_0, \bar{s})$ , the received echo signal from the target  $(x, y, s)$  is

$$p_{rev}(\bar{x}, t, \bar{s}) = \gamma(x, y, s) \exp \left( j2\pi \left[ f_0(t - \tau) + \frac{1}{2}k_a(t - \tau)^2 \right] \right) \quad (5.2)$$

in which the two-way echo delay  $\tau$  is

$$\tau = \frac{2R(\bar{x}, y_0, \bar{s}, x, y, s)}{c} = \frac{2}{c} \sqrt{(x - \bar{x})^2 + (y - y_0)^2 + (s - \bar{s})^2} \quad (5.3)$$

where  $k_a$  is linear frequency modulation,  $f_0$  is the carrier frequency,  $c$  is optical velocity,  $R$  is slant range. The echo at the scene centre  $(0,0,0)$  is used as the reference signal  $p_{ref}(\bar{x}, t, \bar{s})$  for the de-chirp processing (Lee and Pottier, 2009; Oliver and Quegan, 2004; Lazarov and Kostadinov, 2013; Soumekh, 1999; Mahafza, 2005; Richards, 2005; Tebaldini, 2010; Xilong et al., 2012),

$$p_{ref}(\bar{x}, t, \bar{s}) = \exp \left( j2\pi \left[ f_0(t - \tau_{ref}) + \frac{1}{2}k_a(t - \tau_{ref})^2 \right] \right) \quad (5.4)$$

among them, the reference delay  $\tau_{ref}$  is calculated according to Equation (5.5).

$$\tau_{ref} = \frac{2R_{ref}(\bar{x}, y_0, \bar{s})}{c} = \frac{2}{c} \sqrt{\bar{x}^2 + y_0^2 + \bar{s}^2} \quad (5.5)$$

Like the two-dimensional SAR imaging (Lee and Pottier, 2009; Oliver and Quegan, 2004; Lazarov and Kostadinov, 2013; Soumekh, 1999; Mahafza, 2005; Richards, 2005), since the distance between the radar and the scene is much larger than the scene size, the slant distance  $R$  can be approximated as the value from the phase centre of the radar antenna to the target. In Figure 5.4, AT is slant distance  $R$ ; if  $AC=AT$ , as slant distance  $R$  is very large, then TC is assumed to be perpendicular to OA. In Figure 5.4, based on the trigonometric calculation, the following approximate relationship exists,

$$R(\bar{x}, y_0, \bar{s}, x, y, s) \approx R_{ref}(\bar{x}, y_0, \bar{s}) - \Delta r \quad (5.6)$$

$$\Delta r = x \cos\beta \cos\psi + y \sin\beta \cos\psi + s \sin\psi \quad (5.7)$$

where  $\Delta r$  is the distance of OC,  $\beta$  is the angle between OA and X axis,  $\psi$  is the angle  $\angle AOB$ .

According to a similar derivation process as in 2D imaging (de-chirp) (Lee and Pottier, 2009; Oliver and Quegan, 2004; Lazarov and Kostadinov, 2013; Soumekh, 1999; Mahafza, 2005; Richards, 2005) for the echo signal  $p_{rev}(\bar{x}, t, \bar{s})$ , by using the reference signal  $p_{ref}(\bar{x}, t, \bar{s})$  with the echo signal  $p_{rev}(\bar{x}, t, \bar{s})$ , the mixing result of  $q(\bar{x}, t, \bar{s})$  is

$$q(\bar{x}, t, \bar{s}) = p_{rev}(\bar{x}, t, \bar{s}) \cdot (p_{ref}(\bar{x}, t, \bar{s}))^* \quad (5.8)$$



$$= \gamma(x, y, s) \exp(j\omega_x x + j\omega_y y + j\omega_s s) \exp\left(j \frac{4\pi}{c^2} k_a \Delta r^2\right)$$

where  $(p_{ref}(\bar{x}, t, \bar{s}))^*$  is the conjugated form of  $p_{ref}(\bar{x}, t, \bar{s})$ . In which

$$\omega_x = \frac{4\pi}{c} (f_0 + k_a t') \cos\beta \cos\psi \quad (5.9)$$

$$\omega_y = \frac{4\pi}{c} (f_0 + k_a t') \sin\beta \cos\psi \quad (5.10)$$

$$\omega_s = \frac{4\pi}{c} (f_0 + k_a t') \sin\psi \quad (5.11)$$

$$t' = t - \tau_{ref} \quad (5.12)$$

If we ignore the residual phase  $\exp\left(j \frac{4\pi}{c^2} k_a \Delta r^2\right)$  caused by the mixing operation, then the equation changes to:

$$q(\bar{x}, t, \bar{s}) = \gamma(x, y, s) \exp(j\omega_x x + j\omega_y y + j\omega_s s) \quad (5.13)$$

where  $\omega_x$ ,  $\omega_y$ ,  $\omega_s$  are the angular frequencies of the azimuth, range and elevation direction. Since the radar receives the echo of all superpositions in the target area, the actual signal is in three-dimensional integral form as below:

$$q(\omega_x, \omega_y, \omega_s) = \iiint \gamma(x, y, s) \exp(j\omega_x x + j\omega_y y + j\omega_s s) dx dy ds \quad (5.14)$$

The above equation has the same form of the signal model in 2D imaging except that the currently observed data is a three-dimensional spectral sample of  $\gamma(x, y, s)$  (Xilong et al., 2012; Tebaldini, 2010). According to Equation (5.14), the three-dimensional feature target representation function  $\gamma(x, y, s)$  in three-dimensional SAR imaging can be obtained by the following process. First, the spectral data in the three-dimensional spherical coordinate system shown in Equation (5.9) - (5.11) is interpolated to the three-dimensional orthogonal coordinate system, and then the three-dimensional target information is obtained using the interpolated data through a three-dimensional Fourier transformation.

Now, multiple flights of the single radar system are the main data acquisition method used in SAR tomography with a different angle between the coordinate system  $X'-Y'-S'$  and the coordinate system  $X-Y-S$  rotated along the  $X$ -axis angle (Xilong et al., 2012; Tebaldini, 2010), as shown in Figure 5.5. In  $X-Y-S$ , the actual signal frequency spectrum is  $q(\omega_x, \omega_y, \omega_s)$ . In  $X'-Y'-S'$ ,  $\omega_{s'}$  is zero, the actual signal frequency spectrum  $q'(\omega_{x'}, \omega_{y'}, \omega_{s'})$  is  $q'(\omega_{x'}, \omega_{y'}, 0)$ , as shown in Equation (5.17), which is projected into the azimuth-range plane.

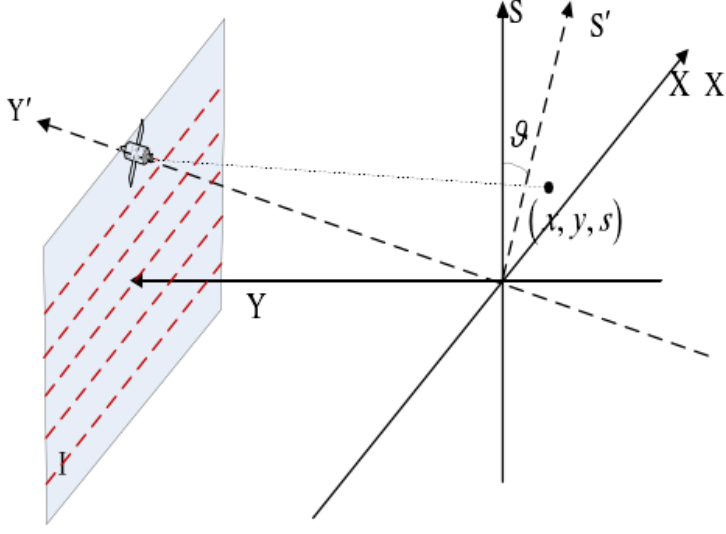


Figure 5.5 Multiple flights of a single radar system for SAR tomography (Xilong et al., 2012; Tebaldini, 2010)

$$\begin{bmatrix} \omega_x \\ \omega_y \\ \omega_s \end{bmatrix} = \begin{bmatrix} 1 & 0 & 0 \\ 0 & \cos\vartheta & -\sin\vartheta \\ 0 & \sin\vartheta & \cos\vartheta \end{bmatrix} \begin{bmatrix} \omega_{x'} \\ \omega_{y'} \\ \omega_{s'} \end{bmatrix} \quad (5.15)$$

$$\omega_x = \omega_{x'}, \quad \omega_y = \omega_{y'} \cos\vartheta, \quad \omega_s = \omega_{y'} \sin\vartheta \quad (5.16)$$

$$q'(\omega_{x'}, \omega_{y'}, 0) = q(\omega_x, \omega_y, \omega_s) = q(\omega_{x'}, \omega_{y'} \cos\vartheta, \omega_{y'} \sin\vartheta) \quad (5.17)$$

According to the above analysis, the synthetic aperture of NSR in SAR tomography imaging is obtained by synthesising the SAR SLC images after focusing on the azimuth-range plane. Given this, the characteristics of SLC SAR images are first analysed. SAR achieves a high range-resolution by transmitting a wide-band signal and a large synthetic aperture in the azimuth through the relative movement between the radar platform and the target, thereby obtaining a high azimuth resolution (Lee and Pottier, 2009; Oliver and Quegan, 2004; Lazarov and Kostadinov, 2013; Soumekh, 1999; Mahafza, 2005; Richards, 2005). In the Born approximation theory (according to the theory of quantum mechanics and electromagnetic fields, the electromagnetic wave scattering model satisfies the nonlinear integral equation, but the nonlinear integral equation is complicated to process. For the sake of simplicity (geometrical optics after the Born approximation can be used), the wave function of the Born approximation is used to describe the statistical distribution of electromagnetic waves, and the nonlinear integral equation is reduced to the linear integral equation for calculation) (Horsley et al.,

2015; Gilman and Tsynkov, 2015; Cheney, 2001), the complex value of the pixels indexed at  $(x, y)$  in the azimuth-distance direction is  $Q(x, y)$ .

$$Q(x, y) = \int_{x-\frac{\rho_x}{2}}^{x+\frac{\rho_x}{2}} \int_{y-\frac{\rho_y}{2}}^{y+\frac{\rho_y}{2}} PSF(x'' - x, y'' - y) \left[ \int_{s_{min}}^{s_{max}} \gamma(x'', y'', s) \exp\left(-j \frac{4\pi f_0}{c} R(x'', y'', s)\right) ds \right] dx'' dy'' \quad (5.18)$$

Among them,  $[s_{min}, s_{max}]$  is the target span range of NSR height;  $\gamma(x, y, s)$  is the three-dimensional distribution function of the complex scattering coefficient of the scene;  $R(x'', y'', s)$  is the slant range of  $(x'', y'', s)$  in pixel  $(x, y, s)$ ;  $\rho_x$  and  $\rho_y$  are the azimuth and range resolution, respectively;  $PSF(x, y)$  is the point spread function (PSF) after azimuth-range focusing, and the specific form is related to the window function used in SAR imaging (Lee and Pottier, 2009; Oliver and Quegan, 2004; Lazarov and Kostadinov, 2013; Soumekh, 1999; Mahafza, 2005; Richards, 2005). If windowing processing is not used during SAR imaging,  $PSF(x, y)$  can be written as below, shown in equation (5.19).

$$PSF(x, y) = \text{sinc}\left(\frac{\pi x}{\rho_x}\right) \text{sinc}\left(\frac{\pi y}{\rho_y}\right) \quad (5.19)$$

For the sake of simplicity, we assume that the azimuth-range is the ideal SAR focusing for any pixel (the bandwidth is ideally infinite) (Fornaro et al., 2005), the two-dimensional point spread function is a two-dimensional Dirac function (this function is equal to zero everywhere except for zero and whose integral over the entire real line is equal to one) (Lee and Pottier, 2009; Oliver and Quegan, 2004; Lazarov and Kostadinov, 2013; Soumekh, 1999; Mahafza, 2005; Richards, 2005), shown in the equation below.

$$PSF(x, y) = \delta(x)\delta(y) \quad (5.20)$$

Then the Equation (5.18) is simplified as

$$Q(x, y) = \int_{s_{min}}^{s_{max}} \gamma(x, y, s) \exp\left(-j \frac{4\pi f_0}{c} R(x, y, s)\right) ds \quad (5.21)$$

If one image is selected as the master image, the other images (referred to as slave images) are registered to this master image. After co-registration, the azimuth-range images correspond to the same feature within the same pixel indexed by  $(x, y)$ , and its complex value  $Q(x, y)$  can be expressed as

$$Q(m) = \int_{s_{min}}^{s_{max}} \gamma(s) \exp\left(-j \frac{4\pi f_0}{c} R_m(s)\right) ds, \quad m = 1, 2, \dots, M \quad (5.22)$$

## Chapter 5. TomoSAR and differential TomoSAR algorithms

where  $M$  is the total number of SLC data,  $m$  is the  $m^{th}$  measurement SLC data in this chapter, and  $R_m(s)$  is the  $m^{th}$  slant range  $R(x, y, s)$  at pixel  $(x, y, s)$ . In the previous analysis, it is assumed that the radar will fly in parallel along the X-S plane. Due to the constraints of the radar platform orbit design, it is very difficult to realise in actual flight, and the actual orbit of the radar needs to be projected into the X-S plane. In addition, in order to facilitate a high degree of focusing, it is necessary to correct the angular frequency in the support region in the NSR around zero Doppler frequency. Both requirements can be achieved by removing the phase terms caused by the slant reference distance in single look complex image sequences; this process is called deramping. The reference slant range used in deramping can be the centre distance of each image or the distance between the radar antenna phase centre of each image and a reference terrain (e.g. known DEM data). Although the removal of the slant range to the phase centre using the radar-recorded electromagnetic propagation delay is the most direct deramping method, the use of its deramping introduces additional atmospheric phase errors due to the echo delay being affected by atmospheric disturbances, which also needs to use the coregistration offset interpolation method to calculate the reference slant range. In fact, using a reference terrain is employed more commonly because it is only based on calculating a reference slant range based on the radar position and the terrain (Fornaro and Serafino, 2004; Fornaro et al., 2005). It should be noted that there is no essential difference between these two methods; the only difference is the zero-point benchmark.

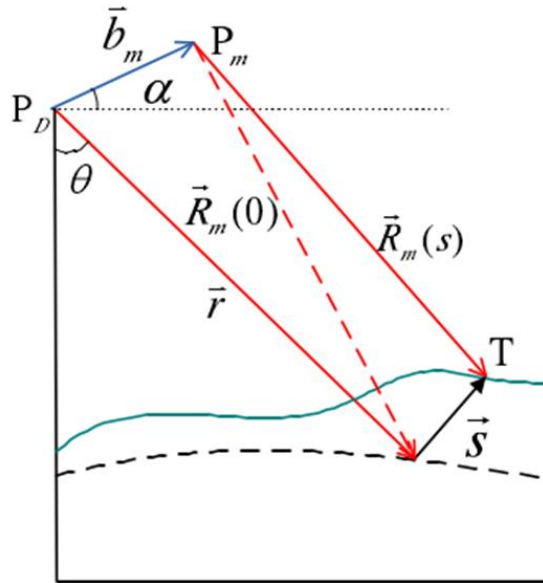


Figure 5.6 The geometric relationship between the master and slave image (Lu and Dzurisin, 2014; Parker, 2016; Ketelaar, 2009)

For example, we used a terrain DEM as the reference. Figure 5.6 shows the imaging relationship between the master and slave images (Lu and Dzurisin, 2014; Parker, 2016; Ketelaar, 2009). In the figure,  $P_D$  and  $P_m$  respectively represent the phase centre positions of the two primary and secondary SAR antennas, and the baseline  $b_m$  is the distance between  $P_D$  and  $P_m$ ;  $\alpha$  is the angle between the baseline and the horizontal plane;  $\theta$  is the incidence angle of the master image. After removing the phase term caused by the reference slant range  $R_m(0)$ , the  $m^{th}$  image can be written (Fornaro et al., 2003; Fornaro et al., 2005) as  $\mathbf{g}(m)$ .

$$\begin{aligned}\mathbf{g}(m) &= \exp\left(j\frac{4\pi f_0}{c}R_m(0)\right) \cdot Q(m) \\ &= \exp\left(j\frac{4\pi f_0}{c}R_m(0)\right) \cdot \int_{s_{min}}^{s_{max}} \gamma(s) \exp\left(-j\frac{4\pi f_0}{c}R_m(s)\right) ds \\ &= \int_{s_{min}}^{s_{max}} \gamma(s) \exp\left(-j\frac{4\pi f_0}{c}[R_m(s) - R_m(0)]\right) ds\end{aligned}\quad (5.23)$$

In Figure 5.6, it is easy to see the relationship:

$$\vec{R}_m(s) = \vec{r} + \vec{s} - \vec{b}_m \quad (5.24)$$

$$\vec{R}_m(0) = \vec{r} - \vec{b}_m$$

where  $\vec{r}$  is the vector of  $r$ ,  $r$  is the distance between the centre of the radar antenna and the zero height reference point;  $\vec{R}_m(s)$  is the vector form of  $R_m(s)$ ,  $\vec{R}_m(0)$  is the vector form of  $R_m(0)$ ,  $\vec{b}_m$  is the vector form of  $b_m$ ,  $\vec{s}$  is the vector form of  $s$ . From Equation (5.24), we can see that  $R_m(s) - R_m(0)$  is

$$\begin{aligned}R_m(s) - R_m(0) &= \langle \vec{R}_m(s), \vec{R}_m(s) \rangle^{1/2} - \langle \vec{R}_m(0), \vec{R}_m(0) \rangle^{1/2} \\ &= \sqrt{r^2 + s^2 + b_m^2 - 2rb_{\parallel m} - 2sb_{\perp m}} - \sqrt{r^2 + b_m^2 - 2rb_{\parallel m}}\end{aligned}\quad (5.25)$$

where  $b_{\parallel m} = b_m \sin(\theta - \alpha)$ ;  $b_{\perp m} = b_m \cos(\theta - \alpha)$ ;  $b_{\parallel m}$ ,  $b_{\perp m}$  are the parallel baseline and perpendicular baseline respectively.

Since the slant range  $r$  is much larger than the target NSR height  $s$  and the baseline length, Equation (5.25) is expanded in the Taylor format (Fornaro et al., 2003; Fornaro et al., 2005; Tebaldini, 2010; Xilong et al., 2012) and only the first-order term is retained, Equation (5.25) becomes

$$\begin{aligned}
 & R_m(s) - R_m(0) \\
 &= \sqrt{r^2 + s^2 + b_m^2 - 2rb_{\parallel m} - 2sb_{\perp m}} - \sqrt{r^2 + b_m^2 - 2rb_{\parallel m}} \\
 &\approx r \left[ 1 + \frac{s^2 + b_m^2 - 2rb_{\parallel m} - 2sb_{\perp m}}{2r^2} - \left( 1 + \frac{b_m^2 - 2rb_{\parallel m}}{2r^2} \right) \right] \\
 &= \frac{s^2}{2r} - \frac{sb_{\perp m}}{r}
 \end{aligned} \tag{5.26}$$

Substituting (5.26) into (5.23), we get  $\mathbf{g}(m)$ :

$$\begin{aligned}
 \mathbf{g}(m) &= \int_{s_{\min}}^{s_{\max}} \gamma(s) \exp \left( -j \frac{4\pi f_0}{c} \left( \frac{s^2}{2r} - \frac{sb_{\perp m}}{r} \right) \right) ds \\
 &= \int_{s_{\min}}^{s_{\max}} \gamma(s) \exp \left( j2\pi \frac{2b_{\perp m}f_0}{cr} s \right) \exp \left( -j \frac{2\pi f_0}{cr} s^2 \right) ds \\
 &= \int_{s_{\min}}^{s_{\max}} \gamma(s) \exp \left( j2\pi \frac{2b_{\perp m}}{\lambda r} s \right) \exp \left( -j \frac{2\pi}{\lambda r} s^2 \right) ds
 \end{aligned} \tag{5.27}$$

where  $\lambda = c / f_0$  is the radar wavelength. The phase term related to the square of  $s$  in the above equation corresponds to a quadratic term neglected in the far-field plane wave assumption. In SAR tomography, we are mostly concerned with the magnitude (intensity or amplitude) of the complex scattering coefficient  $\gamma(s)$ , that is to say, there is no requirement for the preservability of the image phase, so the quadratic phase term is negligible (or it can be said to be attributed to  $\gamma(s)$ ). Therefore, the  $m^{\text{th}}$  image can be rewritten in the following form (Fornaro et al., 2003; Fornaro et al., 2005; Tebaldini, 2010; Xilong et al., 2012).

$$\mathbf{g}(m) = \int_{s_{\min}}^{s_{\max}} \gamma(s) \exp(j2\pi\xi_m s) ds \tag{5.28}$$

$$\xi_m = \frac{2b_{\perp m}}{\lambda r} \tag{5.29}$$

The  $\xi_m$  is the spatial frequency spectrum corresponding to the height  $s$  in NSR direction, and the relationship between the spatial angular frequency is  $\xi_m = \omega_s / 2\pi$ . From Equation (5.29), it can be seen that the complex values  $\mathbf{g}(m)$ ,  $m = 1, 2, \dots, M$  is the target discrete cell samples of electromagnetic scattering characteristics  $\gamma(s)$  along the NSR direction of  $\xi_m$  after SLC image deramping. Therefore, the SAR tomographic imaging is essentially the use of spectral discrete sampling of the frequency spectrum to reconstruct the original signal.

### 5.1.2 SAR Tomography Workflow

According to the analysis in the previous section, the workflow of SAR tomography is shown in Figure 5.7. Firstly, all of the complex images are co-registered into SAR data stacks. Then the atmospheric and ionospheric correction is executed. Thereafter, the deramping and phase error compensation (as shown in the equation below) are applied. Finally, after height imaging and post-processing, the results (3D imaging and point cloud) can be obtained.

#### 1) Deramping

As evidenced by the analysis in the last section, the deramping operation plays an important role in SAR tomography. It is precise because of the removal of the centre slant phase that the intrinsic relationship between the observed data and the target NSR information established. The reference slant range used in the deramping step can be obtained in two ways (Fornaro et al., 2003, Fornaro et al., 2005, Tebaldini, 2010, Xilong et al., 2012): (1) by calculating the reference slant range using the radar transmission centre time delay and velocity recorded by the radar; (2) calculating the reference slant range based on the reference topography and the radar position (Sun et al., 2011).

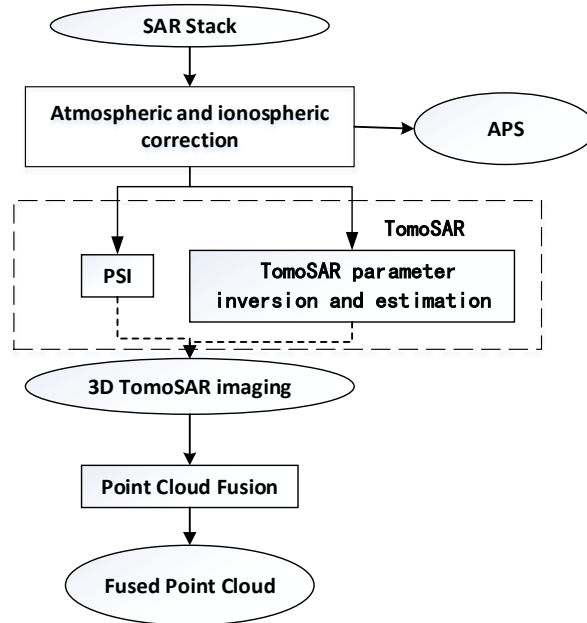


Figure 5.7 SAR tomography workflow, APS in the figure is atmospheric phase screen, PSI is persistent scatterer InSAR, Point Cloud Fusion here refers to the fusion of the 3D point clouds line by line as the processing is based on the azimuth line, and Fused Point Cloud is the final 3D imaging results of the point cloud

## Chapter 5. TomoSAR and differential TomoSAR algorithms

In Figure 5.8 below,  $P_D$  is the antenna phase centre position of the SAR satellite for the master SAR image,  $P_m$  is the antenna phase centre position of the SAR satellite for the  $m^{th}$  slave SAR image;  $r$  and  $r_m$  are the slant range of the master and slave image from the antenna phase centre position to the ground point  $T$ ,  $r'$  and  $r'_m$  are the slant range of the master and slave image from the antenna phase centre position to the ground point  $T'$ .  $H_{refe}$  is the elevation of the reference terrain, and  $H$  is the elevation difference between  $T$  and  $T'$ , which is called the elevation correction value relative to the reference terrain of the pixel point.

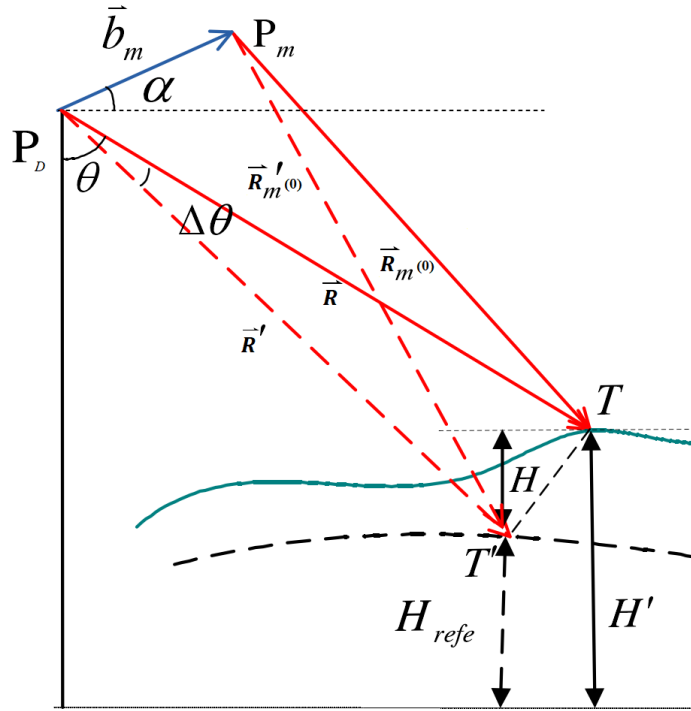


Figure 5.8 The relationship of oblique slant point in the true terrain and reference terrain (Lu and Dzurisin, 2014; Parker, 2016; Ketelaar, 2009; Xilong et al., 2012; Xilong et al., 2011)

How to use the DEM simulation phase for deramping is critical to TomoSAR imaging. This block below will describe this deramping based on a mathematical derivation. If Equation (5.28) is multiplied by  $\exp\left(-j\frac{4\pi}{\lambda}R\right)$ , and  $R$  is the central phase slant range of the master image, the equation becomes

$$\begin{aligned} p(\xi_m) &= \exp\left(-j\frac{4\pi}{\lambda}R\right) \mathbf{g}(m) \\ &= \int_{s_{min}}^{s_{max}} \exp\left(-j\frac{4\pi}{\lambda}R\right) \gamma(s) \exp(j2\pi\xi_m s) ds \end{aligned} \quad (5.30)$$



$$\xi_m = 2b_{\perp m}/\lambda r \quad (5.31)$$

$$\gamma'(s) = \exp\left(-j \frac{4\pi}{\lambda} R\right) \gamma(s) \quad (5.32)$$

$$p(\xi_m) = \int_{s_{min}}^{s_{max}} \gamma'(s) \exp(j2\pi\xi_m s) ds \quad (5.33)$$

Because the  $\mathbf{g}(m)$  has the following form,

$$\mathbf{g}(m) = \exp\left(j \frac{4\pi f_0}{c} R_m(0)\right) \cdot Q(m) = \exp\left(j \frac{4\pi}{\lambda} R_m(0)\right) \cdot Q(m) \quad (5.34)$$

where  $R_m(0)$  is the central reference slant range of each image (slave image), Equation (5.30) becomes

$$p(\xi_m) = \exp(j \cdot \varphi_m) \cdot Q(m) = \int_{s_{min}}^{s_{max}} \gamma'(s) \exp(j2\pi\xi_m s) ds \quad (5.35)$$

$$\varphi_m = -\frac{4\pi}{\lambda} [R - R_m(0)] \quad (5.36)$$

where  $Q(m)$  is the  $m^{\text{th}}$  SLC data (shown in the Equation (5.22)) and  $\varphi_m$  in Equation (5.35) and (5.36) is the interferometry phase, which can be obtained using the DEM simulation method. The simulation phase  $\varphi_{simu\_m}$  based on the master-slave relationship is obtained using the external DEM (shown in Figure 5.8), which is:

$$\varphi_{simu\_m} = -\frac{4\pi}{\lambda} b_{\parallel m} = -\frac{4\pi}{\lambda} b_m \sin(\theta - \Delta\theta - \alpha) \quad (5.37)$$

$$\varphi_m = \varphi_{simu\_m} \quad (5.38)$$

Therefore, a coarse DEM will be used following Equation (5.38) for deramping (the DEM can then be used to simulate the interferometry phase and replace  $\varphi_m$  in Equation (5.35) to finish the deramping step). For scenes with small flat relief, the ameliorated ellipsoid model can be employed according to the average elevation of the scene (using the same elevation value as the DEM).

As in InSAR (Lu and Dzurisin, 2014; Parker, 2016; Ketelaar, 2009), the InSAR calculation method is shown in Equation (5.39). In this way, we define that SLC data is flattened following Equation (5.40); this is the common operation of the flattening step in the code in many InSAR software.  $I_{mast}$  is the master SLC data,  $I_{slave}$  is the slave SLC data,  $()^*$  is the conjugated function,  $I_{flattening}$  is the flattening of the SLC data.

$$\begin{aligned} [I_{mast} \cdot (I_{slave})^*]_{flattening} &= I_{mast} \cdot (I_{slave})^* \cdot \exp(-j \cdot \varphi_{simu\_m}) \\ &= I_{mast} \cdot [I_{slave} \cdot \exp(j \cdot \varphi_{simu\_m})]^* \end{aligned} \quad (5.39)$$

## Chapter 5. TomoSAR and differential TomoSAR algorithms

$$(I_{slave})_{flattening} = I_{slave} \cdot \exp(j \cdot \varphi_{simu\_m}) \quad (5.40)$$

Fortunately, Equation (5.41) is the same as Equation (5.40) because  $Q(m)$  is the  $m^{\text{th}}$  SLC data. Equation (5.30) becomes Equation (5.41). Therefore, the flattening SLC data ( $I_{flattening}$ ) can be used in TomoSAR processing directly, followed by the core Equation (5.41), (5.42), (5.43), (5.44) and (5.45).

$$\begin{aligned} I_{flattening}(m) &= \exp(j \cdot \varphi_{simu\_m}) \cdot Q(m) \\ &= \int_{s_{min}}^{s_{max}} \exp\left(-j \frac{4\pi}{\lambda} R\right) \gamma(s) \exp(j2\pi\xi_m s) ds \end{aligned} \quad (5.41)$$

$$\gamma'(s) = \exp\left(-j \frac{4\pi}{\lambda} R\right) \gamma(s) \quad (5.42)$$

$$p(\xi_m) = \int_{s_{min}}^{s_{max}} \gamma'(s) \exp(j2\pi\xi_m s) ds \quad (5.43)$$

$$I_{flattening}(m) = p(\xi_m) = \int_{s_{min}}^{s_{max}} \gamma'(s) \exp(j2\pi\xi_m s) ds \quad (5.44)$$

$$\xi_m = 2b_{\perp m}/\lambda r \quad (5.45)$$

In addition, if the InSAR interferogram is used instead of the flattened SLC data, then the TomoSAR equations become as follows.

$$I_{master} = \gamma(s) \exp\left(-j \frac{4\pi}{\lambda} R_{master}\right) \quad (5.46)$$

$$I_{slave} = \gamma(s) \exp\left(-j \frac{4\pi}{\lambda} R_{slave}\right) \quad (5.47)$$

$$\begin{aligned} [I_{mast} \cdot (I_{slave})^*]_{flattening} &= I_{mast} \cdot (I_{slave})^* \cdot \exp(-j \cdot \varphi_{simu\_m}) \\ &= I_{mast} \cdot [I_{slave} \cdot \exp(j \cdot \varphi_{simu\_m})]^* \\ &= \int_{s_{min}}^{s_{max}} [\gamma(s)]^2 \cdot \exp(j2\pi\xi_m s) ds \end{aligned} \quad (5.48)$$

$$\xi_m = 2b_{\perp m}/\lambda r \quad (5.49)$$

### 2) Phase error compensation

Equation (5.28) and (5.44) are the SAR tomographic signal model without errors. In practice, however, there are usually many different kinds of errors. It is known that observational data are acquired by repeat passes on the spaceborne SAR platform. Not only is a good baseline for the tomography (perpendicular baseline) necessary, but a time baseline between the SLC image stacks is also needed to be considered in a tomography mission, and the time baseline can usually be one to several years in spaceborne

situations. Due to the existence of time baselines, there are phase errors caused by atmospheric disturbances and possible topographic deformation in the actual observed data (Fornaro et al., 2003; Fornaro et al., 2005; Tebaldini, 2010; Xilong et al., 2012). In this case, Equation (5.28) becomes:

$$\mathbf{g}(m) = \int_{s_{min}}^{s_{max}} \gamma(s) \exp(j2\pi\xi_m s) \exp(j[\varphi_{atm_o}(m) + \varphi_{def_o}(m)]) ds \quad (5.50)$$

$$m = 1, 2, \dots, M$$

$\varphi_{atm_o}(m)$  is the phase error caused by the atmospheric disturbance which includes atmospheric and ionospheric influences;  $\varphi_{def_o}(m)$  is the phase error caused by the terrain deformation. These two phase errors seriously affect the imaging performance of SAR tomography. Moreover,  $\varphi_{atm_o}(m)$  is one of the main factors restricting the practicality of SAR tomography. In order to improve the quality of SAR tomography, the phase errors must be corrected, see Section 5.3.

### 3) Real height

Through the above process, we get the NSR height instead of the height perpendicular to the horizontal plane. Thus, NSR to height conversion needs to be performed. The height (Fornaro et al., 2003; Fornaro et al., 2005; Tebaldini, 2010; Xilong et al., 2012) is

$$h = s \cdot \sin\theta \quad (5.51)$$

where  $h$  is the height perpendicular to the horizontal plane and  $\theta$  is the local incidence angle.

## 5.2 SAR Differential Tomography Imaging Principle

SAR differential tomography (D-TOMOSAR) technology is an extension of SAR tomography technology, which uses different spatial and temporal locations of multiple SAR images with different perspectives. When maintaining the azimuth-height to the two-dimensional synthetic aperture at the same time, the synthesis aperture is formed in the time-dimension, so as to achieve the azimuth-range-height-time four-dimensional imaging for the target (Fornaro et al., 2003; Fornaro et al., 2005; Tebaldini, 2010; Xilong et al., 2012; Lombardini, 2005a). The technology has broad prospects for development in disaster monitoring, resource census, military reconnaissance and other fields, which

have received wide attention from numerous research institutes and researchers from all over the world.

### 5.2.1 SAR Differential Tomography Imaging Principle

In SAR differential tomography, we focus not only on the three-dimensional information of the target but also on the deformation information of the target. At this time, Equation (5.28) is revised to the following form (Lombardini and Cai, 2012; Lombardini, 2005a; Xiang and Bamler, 2010; Lombardini and Pardini, 2012; Lombardini et al., 2013b; Tebaldini and Rocca, 2012; Huang et al., 2012),

$$\mathbf{g}(m) = \int_{s_{min}}^{s_{max}} \gamma(s) \exp(j2\pi\xi_m s) \exp(j\varphi_{defo}(m)) ds \quad (5.52)$$

$$m = 1, 2, \dots, M$$

where  $\xi_m = 2b_{m\perp} / \lambda r$ ;  $b_{m\perp}$  is the perpendicular baseline;  $\varphi_{defo}(m)$  is the phase term caused by the target deformation. In SAR tomography, the phase term  $\varphi_{defo}(m)$  is regarded as phase error, which needs to be removed by phase error compensation. However, in SAR differential tomography, this phase is the main source of information for deformation information extraction. It should be noted that the phase error due to atmospheric disturbance is not considered in Equation (5.52), which needs phase error compensation in terms of its practical processing (see Section 5.5.1 and Equation (5.161)).

In a linear deformation model, the deformation phase,  $\varphi_{defo}(m)$ , is given by:

$$\varphi_{defo}(m) = -\frac{4\pi}{\lambda} v(s) \cdot t_m \quad (5.53)$$

where  $v(s)$  is the deformation rate of LOS and  $t_m$  is the time base. Substituting the above formula into Equation (5.52), we get:

$$\mathbf{g}(m) = \int_{s_{min}}^{s_{max}} \gamma(s) \exp(j2\pi\xi_m s) \exp\left(-j\frac{4\pi}{\lambda} v(s) \cdot t_m\right) ds \quad (5.54)$$

$$m = 1, 2, \dots, M$$

If

$$f(s, v) = \gamma(s) \delta[v - v(s)] \quad (5.55)$$

the above formula can be written as follows (Lombardini and Cai, 2012; Lombardini, 2005a; Xiang and Bamler, 2010; Lombardini and Pardini, 2012; Lombardini et al., 2013b; Tebaldini and Rocca, 2012; Huang et al., 2012; Xilong et al., 2011):

$$\mathbf{g}(m) = \int_{s_{min}}^{s_{max}} \int_{v_{min}}^{v_{max}} f(s, v) \exp(j2\pi\xi_m s) \exp(j2\pi\eta_m v) ds dv \quad (5.56)$$

$$m = 1, 2, \dots, M$$

where  $[v_{min}, v_{max}]$  is the range of the deformation rate in the LOS direction and  $\eta_m$  is defined as follows:

$$\eta_m = -\frac{2t_m}{\lambda} \quad (5.57)$$

It can be seen from the above equation that the observed data in the SAR differential tomography is the two-dimensional joint spectrum of the target's radar scattering characteristic function in the NSR direction and the deformation rate dimension, which is equivalent to forming a two-dimensional synthetic aperture in the height and time direction. The synthetic aperture of NSR and the deformation rate dimension is determined by the vertical baseline and time baseline, respectively, and the Rayleigh resolution corresponding to the equivalent synthetic aperture is

$$\rho_s = \frac{\lambda r}{2B_{\perp}} \quad (5.58)$$

$$\rho_v = \frac{\lambda}{2T} \quad (5.59)$$

where  $T$  is the time baseline, and  $B_{\perp}$  is the perpendicular baseline.

### 5.2.2 SAR Differential Tomographic Imaging Process Workflow

Figure 5.9 shows the SAR differential tomography process workflow (Lombardini and Cai, 2012; Lombardini, 2005a; Xiang and Bamler, 2010; Lombardini and Pardini, 2012; Lombardini et al., 2013b; Tebaldini and Rocca, 2012; Huang et al., 2012; Xilong et al., 2011). The main difference between the SAR differential tomography and the SAR tomography is the phase error compensation and the two-dimensional imaging of the height-deformation rate, which are described below respectively:

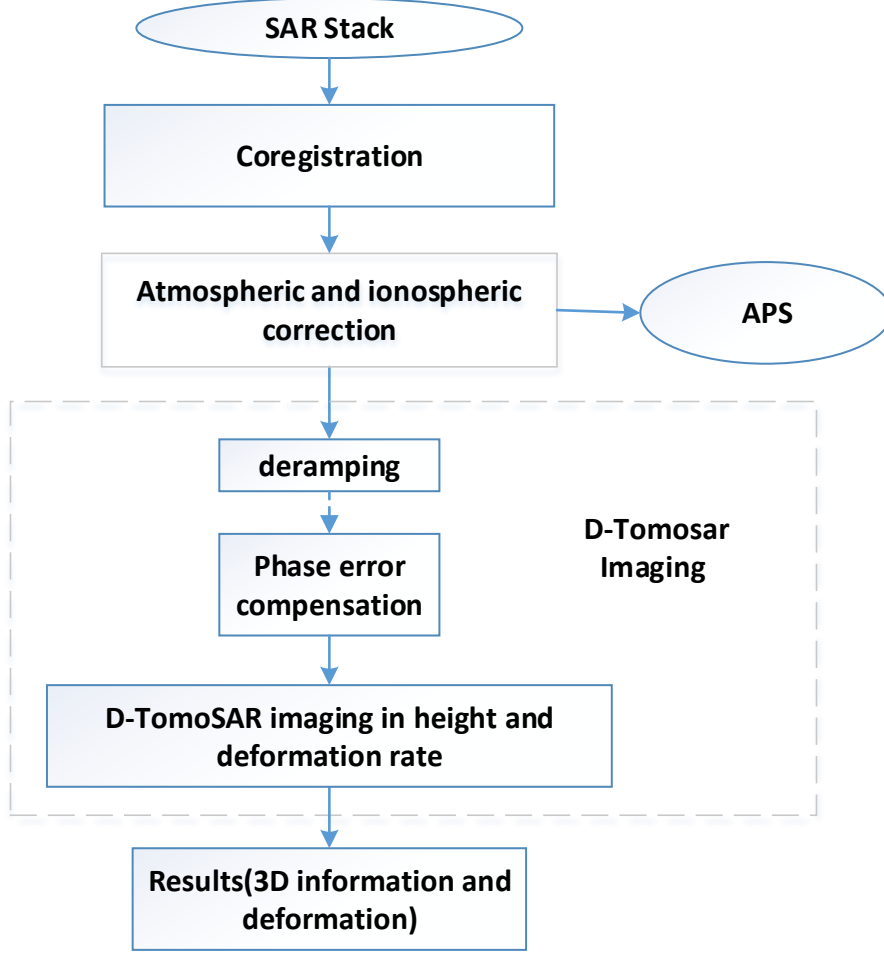


Figure 5.9 SAR differential tomographic imaging process workflow, APS is the atmospheric phase screen

1) Phase error compensation

In SAR differential tomography, the time baselines are needed to obtain the deformation information of the target. Due to the existence of time baselines, there are phase errors caused by atmospheric disturbances in the actual observed data. At this time, the observation data is expressed as follows.

$$\mathbf{g}(m) = \int_{s_{min}}^{s_{max}} \int_{v_{min}}^{v_{max}} f(s, v) \exp(j2\pi\xi_m s) \exp(j2\pi\eta_m v) \exp(j\varphi_e(m)) ds dv$$

$$m = 1, 2, \dots, M \quad (5.60)$$

In the equation,  $\varphi_e(m)$  is the phase error, mainly caused by atmospheric disturbance. In addition, except for the linear deformation of the target, the phase term caused by the non-linear deformation of the target should also be included. Any phase error that seriously affects the imaging performance of SAR differential tomography must be compensated in the inversion of the two-dimensional imaging of the height-

deformation rate. In Section 5.3, an in-depth study of this issue is carried out and a robust and efficient SAR differential tomography phase error compensation method is proposed.

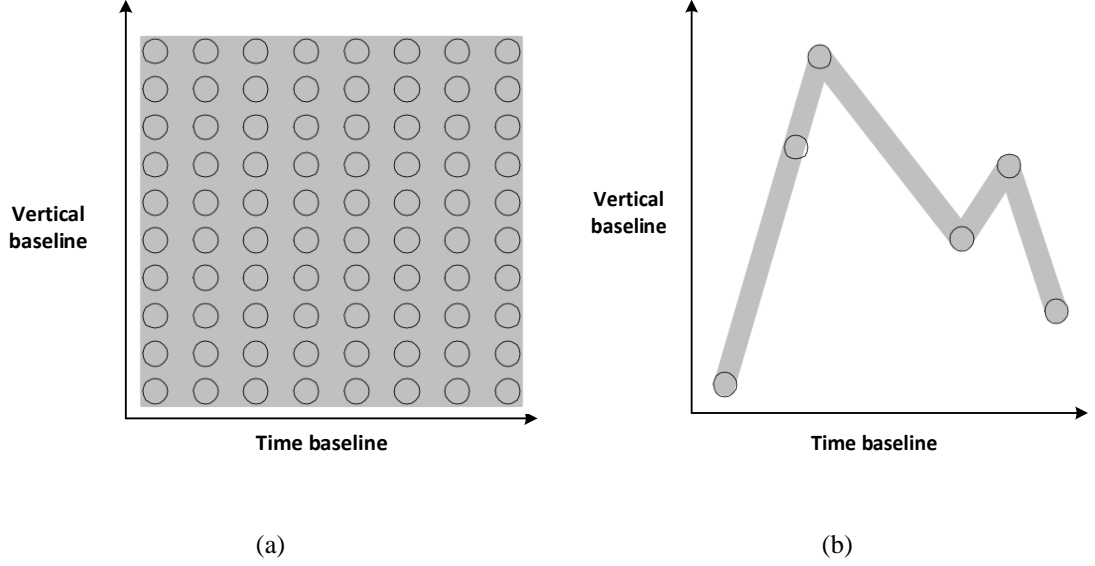


Figure 5.10 Synthetic aperture forms in SAR differential tomography (Zhu, 2011): (a) Two-dimensional full aperture; (b) The actual sparse aperture mode in practical cases

### 2) Two-dimensional height-deformation rate imaging

The 2D synthetic aperture form in SAR differential tomography is shown in Figure 5.10. Figure 5.10 (a) represents the ideal two-dimensional full aperture mode (Zhu, 2011). The observation data is filled in a two-dimensional aperture plane, and the vertical baseline and the time baseline are sampled at equal intervals. At this point, the two-dimensional Fourier transformation of the observed data can achieve better height-deformation rate imaging results. However, in practice, the data used for the SAR differential tomography are the same as the data used in SAR tomography and are usually obtained from multiple-passes of the same area by a radar satellite; so in practice, the data can only be collected, as shown in Figure 5.10 (b), in a two-dimensional sparse aperture mode. How to use the two-dimensional sparse synthetic aperture data to realise high-resolution imaging of the height-deformation rate and to maintain the azimuth-to-range resolution is an important challenge for SAR differential tomography (Fornaro et al., 2003; Fornaro et al., 2005; Tebaldini, 2010; Xilong et al., 2012). The next section will address this problem.

## 5.3 SAR Tomographic Phase Error Compensation

The phase errors from SAR satellite noise, atmospheric disturbances (atmospheric and ionospheric influences) and deformation (including linear deformation and nonlinear deformation) will cause severe problems (blur, false target, ambiguity, and so on) in 3D tomography and 4D differential tomography imaging, which need to be eliminated (Pardini et al., 2012; Tebaldini et al., 2016; Gocho et al., 2016; Pardini and Papathanassiou, 2014; Pardini et al., 2014).

### 5.3.1 Tomographic Phase Error Compensation based on PS-InSAR

Since the PS-InSAR technique can estimate the deformation information of the surface as well as the atmospheric phase, this technique can be used as a phase error compensation method for SAR tomography (Tebaldini and Guarnieri, 2010). The SLC image value at any pixel  $(x, y)$  is  $\mathbf{g}(\xi_m, x, y)$ ,

$$\begin{aligned} \mathbf{g}(\xi_m, x, y) = & \int_{-s_{max}}^{s_{max}} \exp(j\varphi_{atmo}(D, x, y)) \gamma(x, y, s) \exp(j2\pi\xi_m s) \exp(j[\varphi_e(m, x, y) \\ & - \varphi_{atmo}(D, x, y)]) ds + n_e(m, x, y) \\ & m = 1, 2, \dots, M \end{aligned} \quad (5.61)$$

where  $n_e(m, x, y)$  is noise.

$$\varphi_e(m, x, y) = \varphi_{atmo}(m, x, y) - \varphi_{nonl}(m, x, y) - \frac{4\pi}{\lambda} t_m v(x, y) \quad (5.62)$$

The results of PS-InSAR include the atmospheric phase of each image and the deformation information relative to the main image (including linear deformation and nonlinear deformation). By combining these results, an estimate of the phase error can be obtained.

$$\hat{\varphi}_e(m, x, y) = \hat{\varphi}_{atmo}(m, x, y) - \hat{\varphi}_{nonl}(m, x, y) - \frac{4\pi}{\lambda} \hat{v}(x, y) t_m \quad (5.63)$$

This estimated phase error is removed from  $\mathbf{g}(\xi_m, x, y)$  to compensate for the phase error,

$$\begin{aligned} \mathbf{g}'(\xi_m, x, y) &= \mathbf{g}(\xi_m, x, y) \exp(-j\hat{\varphi}_e(m, x, y)) \\ &= \int_{-s_{max}}^{s_{max}} \gamma(x, y, s) \exp(j2\pi\xi_m s) ds + n'_e(m, x, y) \end{aligned} \quad (5.64)$$



where  $m = 1, 2, \dots, M$ ;  $n'_e(m, x, y) = n_e(m, x, y) \exp(-j\hat{\phi}_e(m, x, y))$ .

Since PS-InSAR is only an estimation of the phase error at the PS point, the phase error estimated at any point  $(x, y)$  needs to be obtained by some mean methods or interpolation. In PS-InSAR processing, an interpolation method is usually used to interpolate the processing result at the PS point to the entire scene. The Kriging algorithm is the most widely used interpolation algorithm, and this can be done using open source GSTL (<http://gstl.sourceforge.net/>). We will discuss how to do this practically below.

If we define  $\varphi_{atmo}(D, x, y)$  as the atmospheric phase of the main image, then

$$\begin{aligned}
 & \varphi_e(m, x, y) - \varphi_{atmo}(D, x, y) \\
 &= \varphi_{atmo}(m, x, y) + \varphi_{defo}(m, x, y) - \varphi_{atmo}(D, x, y) \\
 &= -[\varphi_{atmo}(D, x, y) - \varphi_{defo}(m, x, y)] + \varphi_{defo}(m, x, y) \\
 &= -[\varphi_{atmo}(m, x, y) + \varphi_{defo}(m, x, y)] \\
 &= -\left[\varphi_{atmo}(m, x, y) + \varphi_{monl}(m, x, y) + \frac{4\pi}{\lambda} t_m v(x, y)\right]
 \end{aligned} \tag{5.65}$$

where the item  $\varphi_{atmo}(m, x, y) + \varphi_{monl}(m, x, y)$  is the residual phase in the differential interference phase at  $(x, y)$ .

$$\begin{aligned}
 \mathbf{g}(\xi_m, x, y) &= \int_{-s_{max}}^{s_{max}} \exp(j\varphi_{atmo}(D, x, y)) \gamma(x, y, s) \exp(j2\pi\xi_m s) \\
 &\quad \exp(j[\varphi_e(m, x, y) - \varphi_{atmo}(D, x, y)]) ds + n_e(m, x, y) \\
 &\quad m = 1, 2, \dots, M
 \end{aligned} \tag{5.66}$$

If we define

$$\gamma'(x, y, s) = \exp(j\varphi_{atmo}(D, x, y)) \gamma(x, y, s) \tag{5.67}$$

then

$$\begin{aligned}
 \mathbf{g}(\xi_m, x, y) &= \\
 &\int_{-s_{max}}^{s_{max}} \gamma'(x, y, s) \exp(j2\pi\xi_m s) \exp(-j\phi_{resi}(m, x, y)) \exp\left(-j\frac{4\pi}{\lambda} t_m v(x, y)\right) ds \\
 &\quad + n_e(m, x, y) \\
 &\quad m = 1, 2, \dots, M
 \end{aligned} \tag{5.68}$$

where  $n_e(m, x, y)$  is noise. In the tomographic process, we are interested in the magnitude  $\gamma(x, y, s)$  of the complex scattering coefficient. Since  $|\gamma'(x, y, s)| = |\gamma(x, y, s)|$ , so  $|\gamma'(x, y, s)|$  is also a function that reflects the height of the target. In the above equation, the phase error is the residual phase and linear deformation phase, so the

## Chapter 5. TomoSAR and differential TomoSAR algorithms

residual phase value and the linear deformation phase can be directly used to compensate  $\mathbf{g}(\xi_m, x, y)$  and the imaging results can still reflect the target along the elevation direction.

In PS-InSAR processing, after obtaining the results of the estimation of the elevation correction value and the deformation rate, if the unwrapping value of the differential phase is known, then an estimated value of the residual phase can be obtained by the equation below.

$$\hat{\phi}_{resi}(m, x, y) = \phi_{diff}(m, x, y) - (c_1 b_{\perp m} \hat{H} + c_2 t_m \hat{v}) \quad (5.69)$$

Since the direct observation is a wrapped phase, the residual phase cannot be obtained directly. However, the wrapped residual phase value is

$$\begin{aligned} W[\phi_{resi}(m, x, y)] &= W[\phi_{diff}(m, x, y) - (c_1 b_{\perp m} \hat{H} + c_2 t_m \hat{v})] \\ &= W[W[\phi_{diff}(m, x, y)] - (c_1 b_{\perp m} \hat{H} + c_2 t_m \hat{v})] \\ &= W[\phi_{wdiff}(m, x, y) - (c_1 b_{\perp m} \hat{H} + c_2 t_m \hat{v})] \end{aligned} \quad (5.70)$$

and

$$\exp(jW[\phi_{resi}(m, x, y)]) = \exp(j\phi_{resi}(m, x, y)) \quad (5.71)$$

Therefore,  $\mathbf{g}(\xi_m, x, y)$  can be compensated using the wrapped value of the residual phase.

Finally, as we only need the wrapped value of the residual phase and the linear deformation phase at the point  $(x, y)$ , the deformation rate at the PS point is interpolated to get the linear deformation rate field of the whole scene. For the residual phase wrapped value, we first need to get the wrapped value of the residual phase at the PS point estimated by the PS method. Because of the strong spatial correlation (the spatio-temporal characteristics of the residual phase in a small window; the spatio-temporal filtering can be used to obtain the atmospheric phase, the nonlinear deformation phase, the thermal noise phase in the PS method based on this) of the residual phase in a small window, a certain window range can be selected based on the point  $(x, y)$ , and then all of the PS points in the window range are averaged to obtain an estimation of the wrapped value of the residual phase at any point  $(x, y)$  for the whole image (Xilong et al., 2012; Tebaldini and Guarnieri, 2010).

From the previous analysis, it is not necessary to process the SAR SLC image to compensate for the phase error of the SAR tomography using the final PS-InSAR outputs. It is only needed to use (the PS-InSAR intermediate outputs) the wrapped residual phase value and the linear deformation phase for phase compensation. The height-direction imaging  $\gamma'(x, y, s)$  obtained by this method is different from  $\gamma(x, y, s)$ , because it has the

atmospheric phase error of the master SAR SLC image, but its amplitude can still reflect the height-direction characteristic (amplitude value character) of the target ( $|\gamma'(x, y, s)| = |\gamma(x, y, s)|$ ). Compared with the phase error compensation method based on the final output, the phase error compensation method based on the intermediate output avoids residual phase unwrapping, residual phase separation and atmospheric phase estimation. Residual phase error unwrapping is a complex process that requires the inversion of large sparse matrices, high computational time consumption, and high memory requirements on the hardware platform; while the phase error compensation method based on the intermediate output can greatly reduce computational complexity by avoiding this process. In addition, the residual phase separation and atmospheric phase estimation is only a rough estimation method using spatio-temporal filtering, and the low accuracy of the error processing can be avoided by using the intermediate output to compensate for the phase error (Xilong et al., 2012; Tebaldini and Guarnieri, 2010).

### 5.3.2 The PGA Phase Error Compensation Algorithm

In a simple way, we suppose that the resolution cell at  $(x_0, y_0)$  in the target range contains only a single strong scatterer at height 0 along the NSR direction and the size of the strong scatterer is much smaller than the size of the azimuth-range resolution cell. The scattering characteristic function  $\gamma(s)$  at the NSR direction can be approximated as the ideal impulse signal (this function is equal to zero everywhere except for  $s$  and whose integral over the entire real line is equal to one). Thus, the amplitude in different measures (SAR SLC data) at this cell is constant or it changes very little when errors exist (this will be used as the selected criteria for the special explicit elements (PS points)). When there are multiple strong scattering elements in the cell or noise effects, the amplitude in different measures (SAR SLC data) will no longer be a constant, and a certain fluctuation characteristic will be displayed.

$$\gamma(s) = \gamma \cdot \delta(s) \quad (5.72)$$

$$\gamma = A \exp(j\varphi_0) \quad (5.73)$$

$$\mathbf{g}(\xi) = \gamma \cdot \exp(j\varphi_e(\xi)) \quad (5.74)$$

$\gamma$  is the complex scattering coefficient of the strong scatterer pixel,  $A$  is the magnitude of  $\gamma$ ,  $\varphi_0$  is the phase of  $\gamma$ ,  $\varphi_e(\xi)$  is the phase error and  $\gamma(s)$  is the complex

## Chapter 5. TomoSAR and differential TomoSAR algorithms

scattering coefficient at  $s$  height point in NSR direction. By re-arranging the above formula  $\mathbf{g}(\xi)$  and derivation of  $\mathbf{g}(\xi)$ , we get

$$\mathbf{g}'(\xi) = \gamma \cdot \exp(j\varphi_e(\xi)) \cdot j\varphi'_e(\xi) = \mathbf{g}(\xi) \cdot j\varphi'_e(\xi) \quad (5.75)$$

where

$$\varphi'_e(\xi) = -j \frac{\mathbf{g}'(\xi)}{\mathbf{g}(\xi)} \quad (5.76)$$

When we get the derivative of the phase error, integrating it to get the phase error  $\varphi_e(\xi)$ ,

$$\varphi_e(\xi) = \int \varphi'_e(\xi) d\xi = -j \int \frac{\mathbf{g}'(\xi)}{\mathbf{g}(\xi)} d\xi \quad (5.77)$$

the above analysis assumes that  $\mathbf{g}(\xi)$  is a continuous signal and the position of strong scatterers is at zero in the NSR direction. In general, the discrete samples  $\mathbf{g}(\xi_m)$ ,  $m = 1, 2, \dots, M$ , of the continuous observed measure are obtained and the position of the strong scatterers in the NSR direction is not zero. If the position of the strong scatterers is  $s_0$ , after the removal of linear phase  $2\pi\xi_m s_0$ , the position of strong scatterers is at zero in the NSR direction and the equations become as follows:

$$\gamma(s) = \gamma\delta(s - s_0) = A \exp(j\varphi_0) \delta(s - s_0) \quad (5.78)$$

$$\mathbf{g}(\xi_m) = A \exp(j[\varphi_0 + \varphi_e(\xi_m) + 2\pi\xi_m s_0]), \quad m = 1, 2, \dots, M \quad (5.79)$$

$$F(\xi_m) = \exp(-j2\pi\xi_m s_0) \cdot \mathbf{g}(\xi_m) \quad (5.80)$$

$$= A \exp(j[\varphi_0 + \varphi_e(\xi_m)]), \quad m = 1, 2, \dots, M$$

As in the case of continuous signals, the difference between two adjacent samples after the removal of the linear phase  $2\pi\xi_m s_0$  is

$$F(\xi_m) - F(\xi_{m-1}) = F(\xi_m) \cdot \left[ 1 - \frac{F(\xi_{m-1})}{F(\xi_m)} \right] \quad (5.81)$$

$$F(\xi_m) \cdot \{1 - \exp(j[\varphi_e(\xi_{m-1}) - \varphi_e(\xi_m)])\}, \quad m = 2, 3, \dots, M \quad (5.82)$$

$$\Delta F(\xi_m) = F(\xi_m) - F(\xi_{m-1}) \quad (5.83)$$

$$\Delta\varphi_e(\xi_m) = \varphi_e(\xi_m) - \varphi_e(\xi_{m-1}) \quad (5.84)$$

$$\Delta F(\xi_m) = F(\xi_m) \cdot \{1 - \exp(-j\Delta\varphi_e(\xi_m))\}, \quad m = 2, 3, \dots, M \quad (5.85)$$

Expanding  $\exp(-j\Delta\varphi_e(\xi_m))$  into the Taylor model (Taylor function) (Fitzpatrick, 2009) and keeping the first order term

$$\exp(-j\Delta\varphi_e(\xi_m)) \approx 1 - j\Delta\varphi_e(\xi_m) \quad (5.86)$$

$$\Delta F(\xi_m) \approx F(\xi_m) \cdot j\Delta\varphi_e(\xi_m), \quad m = 2, 3, \dots, M \quad (5.87)$$

When we get the derivative of the phase error, we can integrate it to get the phase error  $\hat{\varphi}_e(\xi_m)$ .

$$\Delta\varphi_e(\xi_m) \approx -j \frac{\Delta F(\xi_m)}{F(\xi_m)}, \quad m = 2, 3, \dots, M \quad (5.88)$$

$$\hat{\varphi}_e(\xi_m) = \begin{cases} 0, & m = 1 \\ \sum_{i=2}^m \Delta\varphi_e(\xi_i), & m = 2, 3, \dots, M \end{cases} \quad (5.89)$$

Then after eliminating the errors, the measured signal becomes the signal shown in the equation below, where  $n_e(m, x, y)$  is noise. This method is called Phase-Gradient-Autofocus (PGA) phase error compensation (Wahl et al., 1994; Thompson et al., 1999; Li et al., 2018).

$$\begin{aligned} \mathbf{g}'(\xi_m, x, y) &= \exp(-j\hat{\varphi}_e(m)) \cdot \mathbf{g}(\xi_m, x, y) \\ &= \int_{-s_{max}}^{s_{max}} \gamma(x, y, s) \exp(j2\pi\xi_m s) ds + n_e(m, x, y) \\ &\quad m = 1, 2, \dots, M \end{aligned} \quad (5.90)$$

In SAR tomography, except for the dominant strong scattering in the SAR image, there are usually some weak scattering effects, such as the volume scattering of vegetation or the diffuse scattering of the ground. These weak scatterers are called clutter. If the SNR of a special dominant cell (PS) is not high, the phase error estimated by a single dominant cell deviates significantly. If there are multiple explicit elements within a certain window area, these special explicit elements (PS) can usually be combined to improve the estimation accuracy of the phase error (Wahl et al., 1994; Thompson et al., 1999; Li et al., 2018; Xilong et al., 2012). In synthesis processing using multiple special explicit elements (the special explicit elements are usually PS points, and these PS points should be selected firstly using PS-InSAR based on the amplitude dispersion index; the special explicit element only has one single strong scatterer with small change in amplitude, which means that the amplitude is constant in different SAR measures or it changes very little when errors exist), the emphasis is on the estimation of the phase error differences. Linear unbiased minimum-variance (LUMV) (Wang et al., 2018; Eichel and Jakowatz, 1989) and maximum likelihood estimation (MLE) (Jakowatz and Wahl, 1993) are the two major phase error difference estimators.

### 5.3.3 Combined Phase Error Compensation Algorithm

## Chapter 5. TomoSAR and differential TomoSAR algorithms

As LUMV and MLE (Jakowatz and Wahl, 1993; Eichel and Jakowatz, 1989) are the two-major phase error difference estimators for PGA, the kernel of LUMV is a linear unbiased minimum variance estimation of the phase error difference, while the kernel of the MLE is a maximum likelihood estimation of the phase error difference, but they all have drawbacks based on the ideal signal model. In the PGA algorithm, all of them are based on the premise that the clutter of all of the distinctive units obeys the independent and identically distributed complex Gaussian white noise assumption (the variance is the same in all PS points). When the actual situation can meet the above assumptions, both estimation methods can get good estimation accuracy. However, for two-dimensional SAR images, the clutter energy in the different special explicit elements (each PS pixel) is usually not the same (based on the energy, the variance is not the same for all PS points, as the dielectric constant and roughness of the material around the PS point are different. The atmosphere and thermal noise are also different. The incident angle of the satellite and the slant range is different), so it does not satisfy the above assumptions. At this point, the estimated performance of LUMV and MLE will be affected, resulting in a larger residual phase error (Xilong et al., 2012; Eichel and Jakowatz, 1989). Combined with minimum entropy, weighted Least-Squares method, singular value decomposition (SVD), and a PS method, we propose an improved PGA phase error compensation method based on many of the previous phase calibration research studies (Pardini et al., 2012; Tebaldini et al., 2016; Gocho et al., 2016; Pardini and Papathanassiou, 2014; Pardini et al., 2014; Xilong et al., 2012; Xilong et al., 2011; Tebaldini and Guarnieri, 2010). This method does not make any restrictive assumptions about the clutter variance but it instead estimates the variance of the modulation phase gradient caused by the clutter according to the characteristics of the data to achieve the least squares phase error estimation. More specifically, we selected strong scatterer points based on PS (Since the SLC observation signal is the spectrum of a single impulse function, its amplitude is constant. When there are multiple strong scatterers or noise effects, the SLC observation signal will no longer be constant and it will exhibit some undulation characteristics. The normalised amplitude variance and amplitude dispersion index (the ratio of standard deviation to the mean value of the amplitude, this is sometimes called the coefficient of variation of the amplitude) can be used as a criterion to select the resolution unit with a small amplitude fluctuation as the significant element); then we estimated the reference height based on SVD (the matrix in Equation (5.151) is decomposed to the singular value decomposition from and the complex scattering coefficient matrix  $\gamma$  is calculated, then the reference height  $s$  is

obtained where  $\gamma(s)$  is the maximum value of  $\gamma$  matrix) (Zhu and Bamler, 2010c); finally, we used Weighted Least-Squares with the PGA method and minimum entropy method to achieve the phase error estimation.

In both the LUMV and MLE estimation kernels, it is assumed that the clutter between the explicit elements are independent of each other, subject to a complex Gaussian distribution with a mean of 0 and a variance of  $\sigma_c^2$ . In this case, it is still assumed that the clutter of the special dominant unit (a PS pixel only has one strong single strong scatterer) obeys the zero-mean complex Gaussian distribution, and the clutter of the special unit (this special PS pixel is selected by amplitude dispersion index (the ratio of standard deviation to mean value of amplitude) and it is not based on the strength of coherence; it only has one single strong scatterer) is independent of each other. However, it is not required that the clutter of each significant unit (PS pixel) has the same variance. Thus, the variance of the clutter in the  $k^{th}$  significant unit is supposed as  $\sigma_{ck}^2$  (the clutter is complex, the real part and the imaginary part, which have a Gaussian distribution with a mean of 0 and a variance of  $\sigma_{ck}^2/2$ , are independent of each other). After estimating and removing the linear phase term caused by the position of the strong scattering element in each distinct unit via the SVD method, the phase of the special pixel (PS point) can be written as follows.

$$\Phi_k(\xi_m) = \varphi_e(\xi_m) + \varphi_{0k} + \varphi_{ck}, \quad k = 1, 2, \dots, K \quad (5.91)$$

$\varphi_{0k}$  is the initial phase of the single strong scatter (the PGA difference can eliminate this item in processing),  $\varphi_e$  is the phase error (which needs to be estimated),  $k$  is the  $k^{th}$  PS point and  $\varphi_{ck}$  is the modulation phase caused by clutter.

The PGA method in the same pixel is shown in the equations below, where  $\Delta\Phi_k(\xi_m)$  is a real number and the function  $Im()$  means taking the imaginary part of the complex number.

$$\Delta\Phi_k(\xi_m) = Im\left(\frac{[\Delta F_k(\xi_m) \cdot F_k^*(\xi_m)]}{|F_k(\xi_m)|^2}\right) = \Delta\varphi_e(\xi_m) + \Delta\varphi_{ck}(\xi_m) \quad (5.92)$$

$$k = 1, 2, \dots, K \quad m = 2, \dots, M$$

$$y = H \cdot \Delta\varphi_e(\xi_m) + z \quad (5.93)$$

$$y = [\Delta\Phi_1(\xi_m), \Delta\Phi_2(\xi_m), \dots, \Delta\Phi_k(\xi_m)]^T \quad (5.94)$$

$$H = [1, 1, \dots, 1]^T \quad (5.95)$$

$$z = [\Delta\Phi_{c1}(\xi_m), \Delta\Phi_{c2}(\xi_m), \dots, \Delta\Phi_{ck}(\xi_m)]^T \quad (5.96)$$

## Chapter 5. TomoSAR and differential TomoSAR algorithms

Because the points selected by PS are independent of each other, the modulation phase difference is also independent of each other. Then

$$E[\Delta\varphi_{ck1}(\xi_m)\Delta\varphi_{ck2}(\xi_m)] = E[\Delta\varphi_{ck1}(\xi_m)]E[\Delta\varphi_{ck2}(\xi_m)] = 0 \quad (5.97)$$

Therefore, the covariance matrix  $C_z$  of  $z$  has the following form

$$C_z = \text{diag}[\sigma_{c1}^2, \sigma_{c2}^2, \dots, \sigma_{ck}^2] \quad (5.98)$$

where  $\sigma_{ck}^2$  is the variance of the different modulation phases caused by clutter in the  $k^{\text{th}}$  significant cell point (PS). If we know the variances (these will be calculated in Equation (5.108) below)  $\sigma_{ck}^2$ ,  $ck = 1, 2, \dots, K$  of the modulation phase differences in all the special points, then the weighted least squares estimation of the phase error difference can be obtained by the following equation:

$$\Delta\hat{\varphi}_e^{wls}(\xi_m) = (H^T C_z^{-1} H)^{-1} H^T C_z^{-1} y \quad (5.99)$$

This is the basic idea of the improved PGA algorithm. It can be seen from the above analysis that the most important factor in this method is the determination of the weighted coefficients in the least squares estimation. From Equation (5.98), the weighted coefficient is determined by the variance of the modulation phase difference, so the determination of the weighted coefficient is actually the determination of the variance  $\sigma_{ck}^2$ ,  $ck = 1, 2, \dots, K$  of the modulation phase difference. The following will give a weighted coefficient estimation method.

Considering the  $k^{\text{th}}$  special explicit element, if the phase  $\varphi_{0k}$  of the complex scattering coefficient  $\gamma_k$  of the strong scattering element is zero (if it is not, then the PGA difference can eliminate this item in processing), and there is no phase error.

$$\begin{aligned} F_k(\xi_m) &= A_k + A_{ck} \exp(j\varphi_{ck}) \\ &= A_k + A_{ck} [\cos(\varphi_{ck}) + j\sin(\varphi_{ck})] = A_k + R_{ck}(\xi_m) + jI_{ck}(\xi_m) \\ m &= 1, 2, \dots, M \\ A_{ck} &\ll A_k \end{aligned} \quad (5.100)$$

$A_k$  is the magnitude of the complex scattering coefficient of the strong scatterer in the pixel.  $A_{ck}$  is the amplitude of the clutter noise for the point ( $A_{ck} \ll A_k$ , as this pixel has a strong scatterer),  $\varphi_{ck}$  is the phase of the clutter noise for the point,  $R_{ck}(\xi_m)$  and  $I_{ck}(\xi_m)$  are the real and imaginary parts of the clutter noise for the point. The clutter is complex; the real part and the imaginary part are independent of each other, subject to a Gaussian distribution with a mean of 0 and a variance of  $\sigma_{ck}^2/2$ . At this time, the phase of  $F_k(\xi_m)$  only contains the modulation phase caused by the clutter, shown in the equation below.



$$\varphi_{ck}(\xi_m) = \arctan\left(\frac{b_k(\xi_m)}{1 + a_k(\xi_m)}\right) \quad (5.101)$$

$$a_k(\xi_m) = \frac{R_{ck}(\xi_m)}{A_k}, \quad b_k(\xi_m) = \frac{I_{ck}(\xi_m)}{A_k} \quad (5.102)$$

$$1 + a_k(\xi_m) = 1 + \frac{A_{ck}}{A_k} \cos(\varphi_{ck}) > 0 \quad (5.103)$$

$a_k$  and  $b_k$  are independent of each other, subject to a Gaussian distribution with a mean of 0 and a variance of  $\frac{1}{2 \cdot SCR_k}$ ,

$$a_k(\xi_m) \sim N\left(0, \frac{1}{2 \cdot SCR_k}\right), \quad b_k(\xi_m) \sim N\left(0, \frac{1}{2 \cdot SCR_k}\right) \quad (5.104)$$

$$E[a_k(\xi_m)b_k(\xi_m)] = 0 \quad (5.105)$$

where  $SCR_k = \frac{A_k^2}{\sigma_{ck}^2}$  is the signal to clutter noise ratio of this special point (PS). We made a Taylor expansion for Equation (5.101) and just left the third-order approximation. Then, the variance and mean of the modulation phase of the point are shown below (Ye et al., 1999), respectively

$$E[\varphi_{ck}(\xi_m)] = 0 \quad (5.106)$$

$$\varphi_{ck}(\xi_m) \approx b_k(\xi_m) - b_k(\xi_m)a_k(\xi_m) + b_k(\xi_m)[a_k(\xi_m)]^2 - \frac{[b_k(\xi_m)]^3}{3} \quad (5.107)$$

$$\begin{aligned} \sigma_{ck}^2 &= E\{\{\varphi_{ck}(\xi_m) - E[\varphi_{ck}(\xi_m)]\}^2\} = E\{[\varphi_{ck}(\xi_m)]^2\} \\ &= E\left\{\left(b_k(\xi_m) - b_k(\xi_m)a_k(\xi_m) + b_k(\xi_m)[a_k(\xi_m)]^2 - \frac{[b_k(\xi_m)]^3}{3}\right)^2\right\} \\ &\approx \frac{1}{2 \cdot SCR_k} + \frac{5}{24 \cdot SCR_k^2} \end{aligned} \quad (5.108)$$

The above equations give the mean and variance of the modulation phase. Since the phase error in the SAR tomogram is a random error, the mean and variance of the modulation phase differences are (according to the sum and difference formula of variance  $Var[\varphi_{ck} - \varphi_{c(k-1)}] = Var(\varphi_{ck}) + Var[\varphi_{c(k-1)}]$ ).

$$E[\Delta\varphi_{ck}(\xi_m)] = 0 \quad (5.109)$$

$$\sigma_{ck}^2 = \frac{1}{SCR_k} + \frac{5}{12 \cdot SCR_k^2} \quad (5.110)$$

The above equation shows that the variance of the modulation phase difference can be calculated by the signal to clutter noise ratio (SCR). If the signal to clutter noise ratio SCR is obtained, then the variance of the modulation phase can be calculated. When

## Chapter 5. TomoSAR and differential TomoSAR algorithms

the SAR data is affected by the phase error, the amplitude characteristics can reflect the strength of  $SCR$  (Ye et al., 1999); then the  $SCR_k$  can be estimated through the modulation characteristics of the clutter's signal amplitude.

$$\begin{cases} c = \frac{1}{M} \sum_{m=1}^M |g_k(\xi_m)| \\ d = \frac{1}{M} \sum_{m=1}^M |g_k(\xi_m)|^2 \end{cases} \quad (5.111)$$

$$\begin{cases} c \approx A_k \left( 1 + \frac{1}{4 \cdot SCR_k} \right) \\ d \approx A_k^2 \left( 1 + \frac{1}{SCR_k} \right) \end{cases} \quad (5.112)$$

The  $SCR_k$  can be solved using the equations above. Finally, the  $SCR_k$  is

$$SCR_k \approx \frac{d}{4(2c^2 - d) - 4c\sqrt{4c^2 - 3d}} \quad (5.113)$$

Now, with the  $SCR$  of each PS point, we can obtain a weighted coefficient, and then use the weighted least squares estimation to obtain the SAR phase error of each tile using selected PS points.

As the PGA method is based on the strong spatial correlation and PS points in a tile (such as  $512 \times 512$ ), the phase correction results are the same in each tile of each data (SLC), which means that the coarse phase correction (tile correction) is achieved after this correction (PS, SVD, PGA and least squares). Then, the minimum entropy is used to refine the phase correction at the pixel level. The minimum entropy method (Pardini et al., 2014; Pardini et al., 2012) is based on that the entropy of the elevation profile (the Capon method is used to obtain the profile) is minimum when the data has no phase error contamination, which uses phase-error search methods to calculate the phase errors using the minimum criteria in each pixel of the SAR stacks (pixel by pixel processing). After the minimum entropy method, the refined estimated SAR phase error at each point  $(x, y)$  for the whole image can be obtained. Then the SLC data is corrected using the phase error results. Therefore, my combined phase calibration method is called the PS-SVD-PGA-LS-ME (PS, SVD, PGA, weighted least squares and minimum entropy) method.

### 5.3.4 SAR Interferometry Phase Calibration with Dem Errors

Another method to correct the phase is using the SAR interferometry phase. As the DEM simulation phase is used, Equation (5.38) changes to Equation (5.114). As the simulation phase by DEM is based on the external DEM data and DEM data has errors, the DEM error phase  $\varphi_{DEMerror}$  must be taken into consideration in TomoSAR processing.

$$\varphi_m = -\frac{4\pi}{\lambda}[R - R_m(0)] = \varphi_{simu\_m} + \varphi_{DEMerror} \quad (5.114)$$

As it is well known, the SLC complex data has errors, which include atmospheric error (atmosphere and ionosphere), orbit error, deformation (linear and nonlinear) and noises. The real complex data can be written as an ideal complex data plus all phase errors  $\varphi_e$ ,  $\varphi_{e\_master}$  is the phase error of the master data and  $\varphi_{e\_slave}$  is the phase error of the slave data. In this way, the interferometry phase in Equation (5.114) becomes Equation (5.116). Based on Equation (5.30), (5.35) and (5.36), Equation (5.30) becomes Equation (5.117). Besides, the real flattening complex data is shown in Equation (5.115), then Equation (5.117) becomes Equation (5.118). It is known that  $\varphi_{InSAR} = \varphi_{DEMerror} + \varphi_{e\_master} - \varphi_{e\_slave}$  is the interferometry phase after flattening by DEM, shown in Equation (5.119), because the DEM error phase plus master error phase minus slave error phase is InSAR phase after flattening. Therefore, based on Equation (5.115) and Equation (5.119), the TomoSAR processing equation (5.118) becomes Equation (5.120). It can be seen from the equations that the InSAR phase can be used for phase calibration. With phase errors and DEM error phase, the TomoSAR processing should use Equation (5.120) as below. In Equation (5.120),  $I_{flattening\_real}(m)$  is the flattening complex data using external DEM,  $\varphi_{InSAR}$  is the interferometry phase after flattening by DEM.  $\gamma'(s)$ , shown in Equation (5.32), is the inversion results of TomoSAR processing along the  $s$  direction.  $\xi_m$ , shown in Equation (5.29)), is the spatial frequency corresponding to the height  $s$  from normal-slant-range direction ( $s$  elevation direction).

$$I_{flattening\_real}(m) = \exp(j \cdot \varphi_{simu\_m}) \cdot Q(m) \quad (5.115)$$

$$\varphi_m = -\frac{4\pi}{\lambda}[R - R_m(0)] = \varphi_{simu\_m} + \varphi_{DEMerror} + \varphi_{e\_master} - \varphi_{e\_slave} \quad (5.116)$$

$$\begin{aligned} p(\xi_m) &= \exp(j \cdot \varphi_m) \cdot Q(m) = \exp(j \cdot \varphi_{simu\_m} + j \cdot \varphi_{DEMerror} \\ &\quad + j \cdot \varphi_{e\_master} - j \cdot \varphi_{e\_slave}) \cdot Q(m) \\ &= \int_{s_{min}}^{s_{max}} \gamma'(s) \exp(j2\pi\xi_m s) ds \end{aligned} \quad (5.117)$$

## Chapter 5. TomoSAR and differential TomoSAR algorithms

$$I_{flattening\_real}(m) \exp(j \cdot \varphi_{DEMerror} + j \cdot \varphi_{e\_master} - j \cdot \varphi_{e\_slave}) = p(\xi_m) \quad (5.118)$$

$$= \int_{s_{min}}^{s_{max}} \gamma'(s) \exp(j2\pi\xi_m s) ds$$

$$\varphi_{InSAR} = \varphi_{DEMerror} + \varphi_{e\_master} - \varphi_{e\_slave} \quad (5.119)$$

$$I_{flattening\_real}(m) \exp(j \cdot \varphi_{InSAR}) = p(\xi_m) \quad (5.120)$$

$$= \int_{s_{min}}^{s_{max}} \gamma'(s) \exp(j2\pi\xi_m s) ds$$

After this phase calibration, the data is ready for super-resolution reconstruction via Capon and compressive sensing (CS). However, the height reference is based on the strong scattering centre after INSAR calibration, so the real height reference cannot be known after this method. If geocoding is needed, control points are needed, or the result can be referenced to the DEM data after the DEM error estimation and DEM error compensation based on Equation (5.123).

$$I_{flattening\_real}(m) \exp(j \cdot \varphi_{InSAR}) \cdot \exp(-j \cdot \varphi_{DEMerror}) \quad (5.121)$$

$$= \int_{s_{min}}^{s_{max}} \gamma'(s) \cdot \exp(-j \cdot \varphi_{DEMerror}) \exp(j2\pi\xi_m s) ds$$

$$\gamma''(s) = \gamma'(s) \cdot \exp(-j \cdot \varphi_{DEMerror}) \quad (5.122)$$

$$I_{flattening\_real}(m) \exp(j \cdot (\varphi_{InSAR} - \varphi_{DEMerror})) \quad (5.123)$$

$$= \int_{s_{min}}^{s_{max}} \gamma''(s) \exp(j2\pi\xi_m s) ds$$

It is easy to see  $\varphi_{InSAR} - \varphi_{DEMerror} = \varphi_{e\_master} - \varphi_{e\_slave}$ , and  $\varphi_{e\_master} - \varphi_{e\_slave}$  is the difference of phase errors, which include atmospheric error (atmosphere and ionosphere), orbit error, deformation (linear and nonlinear) and noises. That is why this step is called phase calibration.

Besides, at the right part of Equation (5.123), the DEM error phase  $\exp(-j \cdot \varphi_{DEMerror})$  goes to  $\gamma'(s)$  and forms  $\gamma''(s)$ , shown in Equation (5.122) for all slave image. The DEM error phase is a phase and it cannot influence the magnitude of  $\gamma'(s)$ , which means that the magnitude of  $\gamma'(s)$  is the same as the magnitude of  $\gamma''(s)$ . The magnitude of  $\gamma''(s)$  is the inversion results of TomoSAR processing, therefore, InSAR with the DEM error phase method can be used for phase calibration. In this method, the accuracy of the DEM error estimation will influence the results of inversion according to Equation (5.123). After PS-InSAR or SBAS-InSAR, the DEM error is obtained. Then, the DEM error of the whole image can be obtained by interpolation.

Therefore, the DEM error is used to convert the reference from the unknown strong scattering centre to the DEM data.

## 5.4 SAR Tomography Three-dimensional High-resolution Imaging

For SAR tomography, it is desirable to have radar platforms fly closely along parallel trajectories at different altitudes. However, since the current single-antenna SAR system does not consider the application requirements of SAR tomography at the beginning of design before 2010 (although some SAR data, like TSX+TDX, have already been used in TomoSAR to obtain good results, it is not designed for TomoSAR application), the number of re-visit observations for the same target is small and the orbital intervals are not uniform. At this point, NSR only gets sparse synthetic aperture—a short synthetic aperture, few samples and a non-uniform sampling interval. Based on these principles, the SAR tomography 3D imaging algorithm is introduced in this section.

### 5.4.1 Sparse Aperture for 3D Imaging

After the phase error compensation, the multi-baseline observation data is

$$\gamma(s) = \sum_{m=1}^M \Delta \xi_m \mathbf{g}(\xi_m) \exp(-j2\pi \xi_m s) \quad (5.124)$$

where  $m = 1, 2, \dots, M$ .

If the vertical baseline has equal interval sampling ( $B_{\perp} = b_{\perp m} - b_{\perp 1}$ ) within the vertical baseline span, then

$$B_{\perp} = b_{\perp m} - b_{\perp 1} \quad (5.125)$$

$$b_{\perp m} = m \cdot \Delta b_{\perp} \quad (5.126)$$

where  $\Delta b_{\perp}$  is the vertical baseline sampling interval.

$$\Delta b_{\perp} = \frac{B_{\perp}}{M-1} = \frac{b_{\perp M} - b_{\perp 1}}{M-1} \quad (5.127)$$

Then the SLC signal is

$$\gamma(s) = \sum_{m=1}^M \mathbf{g}(\xi_m) \exp(-j2\pi \xi_m s) \quad (5.128)$$

## Chapter 5. TomoSAR and differential TomoSAR algorithms

In this, the elevation resolution (Zhu, 2011) of NSR is  $\rho_s$ , and according to the Nyquist theorem, the unambiguous image range in NSR direction is  $s_{amb}$  (Zhu, 2011) in the equation below.

$$\rho_s = \frac{\lambda r}{2B_{\perp}} \quad (5.129)$$

$$s_{amb} = \frac{\lambda r}{2\Delta b_{\perp}} \quad (5.130)$$

In the actual imaging, if the target span of NSR direction is less than the unambiguous image range, the system is oversampled and  $\gamma(s)$  can be reconstructed without ambiguity. If the target span of the NSR direction is greater than the unambiguous image range, at this time, it is under-sampled and the imaging results will have ambiguous targets (ghost targets). It should be noted that both (5.129) and (5.130) are obtained with uniform sampling. In practice, SAR tomographic observations are obtained from a radar platform at different times. At this point, due to orbital constraints, only sparse synthetic apertures are available in the NSR direction, and a small amount of sampled data is randomly distributed over a limited vertical baseline span. Since the condition of uniform sampling is implicit in (5.128),  $\gamma(s)$  becomes

$$\gamma(s) = \sum_{m=1}^M \Delta \xi_m g(\xi_m) \exp(-j2\pi \xi_m s) \quad (5.131)$$

If  $s_0$  is the real height position, the location of the aliased signal caused by ambiguity is at many positions, shown in Equation (5.132) below:

$$z \cdot s_{amb} + s_0, \quad z = \pm 1, \pm 2, \dots, \pm \infty \quad (5.132)$$

When the number of samples is large, the aliasing signal caused by randomly distributed non-uniform sampling will not show a significant impact on the real target; however, as the number of samples decreases, the amplitude of the aliasing signal will increase, and in severe cases, it will lead to false targets. However, tomographic SAR reconstruction methods, like numerous standard spectral estimation methods and the compressed sensing method, occurred to solve these problems, since TomoSAR only uses a small angular diversity and sparse aperture data. The most relevant spectral estimation algorithms, including adaptive beamforming, singular value decomposition (SVD), conventional beamforming (BF), nonlinear least squares (NLS), multiple signal classification (MUSIC) and multilook relax (M-RELAX) (Elsharkawy et al., 2018; Liu

## Chapter 5. TomoSAR and differential TomoSAR algorithms

and Li, 1998), are introduced for single polarisation TomoSAR in the following description (Zhu, 2011).

The characteristics of the above mentioned spectral estimation methods with application to TomoSAR are summarised in Table 5.1 regarding the computational cost, whether parametric or nonparametric, single-look or multi-look, estimation accuracy in case of multiple scatterers (in the presence of only single scatterers, all of the above-mentioned methods can give an accurate parameter estimation), elevation resolution and the risk of incorrect elevation estimates. In general, depending on the application, different methods are recommended, e.g. for resolving discrete scatterers with or without motion in an urban environment, high resolution SAR data is needed to observe the inherent scale of urban infrastructures, and hence single-look methods are recommended (Zhu, 2011). It is recommended to use SVD or M-RELAX for medium resolution applications (Zhu, 2011). For high resolution applications, NLS can provide excellent performance. However, the large computational cost renders it impractical (Zhu, 2011).

In our case, we have different land surface types such as ice, mountains, forests, rivers, bridges, buildings and dams. Thus, we need to find a suitable method for 3D TomoSAR imaging for the buildings, bridges and dams in this thesis. The potential of compressive sensing may solve the identified problems of TomoSAR imaging after reading many papers from the literature.

Table 5.1 Summary of the spectral estimation methods applied to TomoSAR (Zhu, 2011)

Method	Computational cost	Parametric	Multilook	Accuracy multiple scatterers	Elevation resolution	Risk of incorrect elevation estimation
BF (Zhu, 2011)	low	no	no	low	low	medium
SVD (Zhu, 2011)	low-medium	no	no	medium	low-medium	low
Capon (Zhu, 2011)	no	medium-high	yes	high	medium	medium
MUSIC (Zhu, 2011)	high	yes	yes	high	high	medium

## Chapter 5. TomoSAR and differential TomoSAR algorithms

Method	Computational cost	Parametric	Multilook	Accuracy multiple scatterers	Elevation resolution	Risk of incorrect elevation estimation
NLS (Zhu, 2011)	very high	yes	no	very high	very high	low
M-RELAX (Elsharkawy et al., 2018)	medium	yes	no	high	high	high

### 5.4.2 Basic Theory of Compressive Sensing

The well-known Shannon sampling theorem states that the signal must be sampled at least twice at its (mathematical) bandwidth for precise signal reconstruction (this is called Nyquist rate) (Albreem and Salleh, 2012). In applications, nearly all signal acquisition methods follow this principle. However, the sampling of some signals is not necessarily based on bandwidth, which can be represented by a model with a small number of sparse sampling (Starck et al., 2010; Albreem and Salleh, 2012). Compressive sensing theory completes the sampling scheme and it allows us to go beyond the Shannon limit to take advantage of the sparse property of the signal (Candès, 2006; Donoho, 2006a). It offers an aesthetic non-parametric realisation of a parametric estimator by assigning some pre-conditions to the signals and the sensing systems.

For an  $N \times 1$  unknown discrete signal  $\gamma$ , according to harmonic analysis theory, the signal  $\gamma$  can be expressed by the following orthogonal decomposition model,

$$\gamma = \sum_{n=1}^N a_n \psi_n = \Psi \mathbf{a} \quad (5.133)$$

where  $\psi_n, n = 1, 2, \dots, N$  is a set of the orthonormal basis,  $\Psi$  is a matrix composed of many basis functions, of which the matrix form is

$$\Psi = [\psi_1, \psi_2, \dots, \psi_N] \quad (5.134)$$

$a_n$  is a coefficient,  $a_n = \langle \gamma, \psi_n \rangle$ , and  $\mathbf{a}$  is an  $N \times 1$  dimensional vector representing a coefficient composition, and the matrix form is as follows:

$$\mathbf{a} = [a_1, a_2, \dots, a_N]^T \quad (5.135)$$

The basic idea of compressed sensing is to require the unknown signal  $\gamma$  to satisfy the sparsity (or compressibility). Thus, for the  $N \times 1$  dimensional signal  $\gamma$ , we call it sparsity (or compressibility), which means that there exists an  $N \times N$  dimensional



transformation matrix  $\Psi$  and the corresponding coefficient  $\mathbf{a}$ , for  $\gamma = \Psi \mathbf{a}$ , and the number of nonzero elements in  $\mathbf{a}$  is  $K$ , or the element in  $\mathbf{a}$  presents a power-law decay by a certain magnitude, the number of the element in  $\mathbf{a}$  significantly greater than zero is  $K$ , and  $K \ll N$  (Candès, 2006; Donoho, 2006a).

When signal  $\gamma$  satisfies sparsity,  $K$  is called the sparsity of signal  $\gamma$ , and  $\Psi$  is called sparse basis matrix. In compressive sensing theory, the observed value is not directly obtained by measuring the sparse signal  $\gamma$ . Instead, the signal  $\gamma$  is projected onto a set of low dimensional measurement vectors  $\phi_1, \phi_2, \dots, \phi_M$ ,  $M \ll N$  through non-correlated measurements on  $M \times 1$  dimensional observation vector  $\mathbf{g}$ .

$$\mathbf{g} = \Phi \gamma \quad (5.136)$$

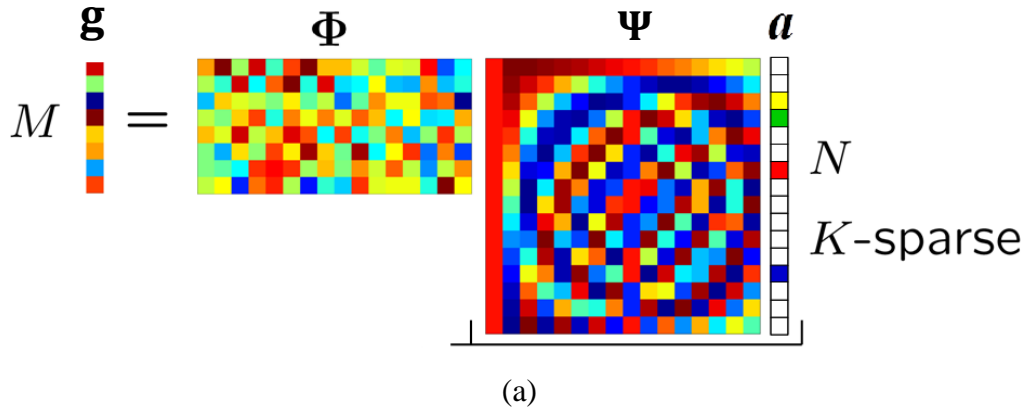
where  $\Phi$  is an  $M \times N$  dimensional matrix composed of measurement vectors, called a measurement matrix.

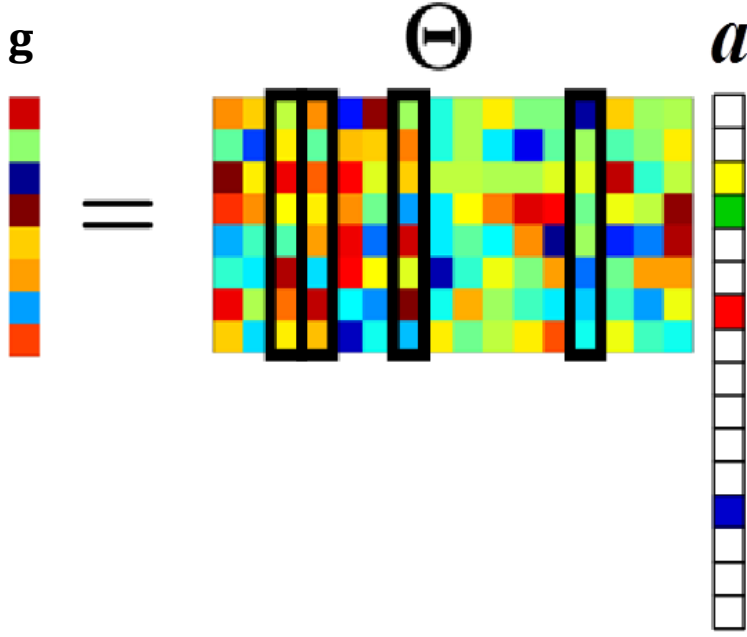
$$\Phi = [\phi_1, \phi_2, \dots, \phi_M]^T \quad (5.137)$$

Substitute Equation (5.133) into Equation (5.136), we get

$$\mathbf{g} = \Phi \gamma = \Phi \Psi \mathbf{a} = \Theta \mathbf{a} \quad (5.138)$$

where  $\Theta = \Phi \Psi = [\theta_1, \theta_2, \dots, \theta_m, \dots, \theta_M]^T$  is known as the sensing matrix (or compressive sensing information operator),  $\theta_m$  is a vector of  $N \times 1$  dimensions, called the sensing vector. The equation is shown in Figure 5.11.





(b)

Figure 5.11 Compressed sensing of the measurement process (Zhu, 2011): (a)  $\mathbf{g}$  is an  $M \times 1$  dimensional observation vector and the  $N \times 1$  dimension sparse coefficient vector  $\mathbf{a}$  is sparse with  $K = 4$ ; (b) Measurement process in terms of the matrix product  $\mathbf{\Theta} = \mathbf{\Phi\Psi}$  with the four columns corresponding to nonzero  $\mathbf{a}_i$  highlighted. The measurement vector  $\mathbf{g}$  is a linear combination of the four columns (sparse coefficient  $\mathbf{a}$  has 4-row non-zero elements, therefore only four columns of Matrix  $\mathbf{\Theta}$  work)

The CS theory tells us that in the absence of noise the exact solution to obtain the sparse coefficient  $\mathbf{a}$  is the one satisfying Equation (5.138) and employing the least number of coefficients, i.e. having the minimal L0 norm:

$$\hat{\mathbf{a}} = \arg \min_{\mathbf{a}} \|\mathbf{a}\|_0 \quad \text{subject to} \quad \mathbf{g} = \mathbf{\Theta}\mathbf{a} \quad (5.139)$$

The LP norm is

$$\text{LP} = \|\mathbf{a}\|_p = \sqrt[p]{\sum_{i=1}^n x_i^p} \quad (5.140)$$

where  $p = 0, 1, 2, \dots, n$ ;  $x = [x_1, x_2, \dots, x_n]$ ;  $x$  is a matrix. When  $p = 0$ , L0 means L0 norm. When  $p = 1$ , L1 means L1 norm.

If there is noise in the signal, then

$$\mathbf{g} = \mathbf{\Phi}\gamma + e = \mathbf{\Theta}\mathbf{a} + e \quad (5.141)$$

$e$  is Gaussian white noise and the variance is  $\sigma_e^2$ . In this case, the sparse reconstruction model under additive noise is

$$\hat{\mathbf{a}} = \arg \min_{\mathbf{a}} \|\mathbf{a}\|_0 \text{ subject to } \|\mathbf{g} - \mathbf{\Theta}\mathbf{a}\| \leq \sigma_e \quad (5.142)$$

After the sparse coefficient  $\mathbf{a} \approx \hat{\mathbf{a}}$  is obtained, the signal  $\gamma$  is reconstructed by the following equation

$$\gamma \approx \hat{\gamma} = \mathbf{\Psi}\hat{\mathbf{a}} \quad (5.143)$$

Theoretically speaking, this is the correct solution, but unfortunately, the L0 norm minimisation problem is NP-complete/hard (NP-hard problem is a problem that the complexity of the exhaustive search is exponential in  $n$  (for example  $n = 3.9\text{E}+47$ ), which is hard to solve). For  $M \gg O(K \log(N/K))$ , i.e. with  $\gamma$  sufficiently sparse, the L1 norm minimisation leads to probably the same result as the L0 norm minimisation (solving the L1 norm can also approximate the effect of the 0 norm, which means transforming the NP\_hard problem into a linear L1 norm programming problem for the simplification of the calculations) (Candès, 2006; Donoho, 2006a).

From the above discussion of the basic idea of compressive sensing, it is clear that the sparsity of a signal under a set of bases is the basic premise and standpoint of compressive sensing, which requires finding a suitable sparse basis for the signal characteristics. The sparse basis of a general signal seldom satisfies the condition that the coefficient has only  $K$  non-zero values, but the transformation coefficients can be satisfied with a higher probability by exponentially decaying to zero after being sorted. Therefore, a reasonable selection of sparse basis not only guarantees the high-precision signal reconstruction but it also helps to improve the speed of signal acquisition and reduce the storage and transmission of resources occupied by the signal. Now, the commonly used sparse bases are the Dirac basis, wavelet basis, chirplet basis and curvelet basis, and so on. In addition, the commonly used sparse reconstruction algorithms are the convex L1 minimum convex optimisation model (Least Absolute Shrinkage and Selection, second-order cone program, Basis Pursuit, interior-point, Fixed Point Continuation, Bregman iteration, Spectral Projected-Gradient and so on), the greedy algorithm (Orthogonal Matching Pursuit, Improved Matching Pursuit) and the minimum norm nonconvex optimization model, and so on (Candès, 2006; Donoho, 2006a; Muthukrishnan, 2005; Chen et al., 2001; Tibshirani, 1996; Mallat and Zhang, 1993; Needell and Tropp, 2009; Chartrand and Staneva, 2008; Candes et al., 2008). To make these methods work, besides the sparsity of the signal, CS relies on two principles: incoherence (incoherence between the measurement matrix  $\mathbf{\Phi}$  and the measurement basis  $\mathbf{\Psi}$ , if they have the items and mathematical expressions in Equation (5.134), (5.137) and

## Chapter 5. TomoSAR and differential TomoSAR algorithms

(5.138)), which pertains to the sensing modality (the sensing matrix  $\Theta$ , shown in (5.138)) (Candes et al., 2008), and restricted isometry property (RIP) which warrants sufficiently sparse reconstruction with noise (Zhu, 2011). The RIP requires

$$(1 - \delta_K)\|\mathbf{a}\|_2^2 \leq \|\Theta\mathbf{a}\|_2^2 \leq (1 + \delta_K)\|\mathbf{a}\|_2^2 \quad (5.144)$$

where  $\mathbf{a}$  is any  $N \times 1$  dimensional vector with  $K$  items of non-zero, if  $K$ -order constraint constant of the  $M \times N$  dimensional matrix  $\Theta$  is  $\delta_K \in (0,1)$ . The sparse reconstruction has RIP properties, which means that the  $K$ -restricted isometry constant  $\delta_K$  needs to satisfy Equation (5.144).

In addition,  $K + K' < M$ ,  $K$  and  $K'$  are defined as restricted orthogonality constants ( $\mathbf{a}$  and  $\mathbf{a}'$  are non-overlapping,  $\mathbf{a}'$  is a vector with sparsity  $K'$ ,  $\mathbf{a}$  is a vector with sparsity  $K$ ), and  $\theta_{K,K'}$  is defined as the minimum constant satisfying the following formula

$$|\langle \Theta\mathbf{a}, \Theta\mathbf{a}' \rangle| \leq \theta_{K,K'}\|\mathbf{a}\|_2\|\mathbf{a}'\|_2 \quad (5.145)$$

where  $\mathbf{a}'$  is a vector with sparsity  $K'$  and non-overlapping support set with  $\mathbf{a}$ . Based on the constraint isometric constant  $\delta_K$  and the orthogonal constraint constants  $\theta_{K,K'}$ , researchers proposed a variety of L1 norm reconfigurable conditions (Zhu, 2011; Candes et al., 2008) for the CS method.

The coherence between  $\Phi$  and  $\Psi$  is

$$\mu(\Phi, \Psi) = \sqrt{N} \max_{m,n} |\langle \phi_m, \psi_n \rangle| \quad (5.146)$$

$\phi_m$  is the row vector of the measurement matrix  $\Phi$ , and  $\psi_n$  is the column vector of the sparse basis matrix  $\Psi$ ,  $\mu(\Phi, \Psi) \in [1, N]$ .  $\Phi$  and  $\Psi$  are irrelevant. That is, the row vector that requires  $\Phi$  cannot be expressed sparsely by the column vector of  $\Psi$  nor can the column vector of  $\Psi$  be sparsely represented by the row vector of  $\Phi$ . When the sample number  $M$  satisfies the following conditions (Zhu, 2011; Candes et al., 2008; Xilong et al., 2012),

$$M = O(\mu^2(\Phi, \Psi) \cdot K \cdot \log N) \quad (5.147)$$

the sparse coefficient vector  $\mathbf{a}$  (shown in Equation (5.135)) can be solved by the minimum L1 norm problem. CS is mainly concerned with low coherence pairs, and the pairs ( $\Phi$  and  $\Psi$ ) are the Fourier matrix and identity matrix respectively, noiseless and wavelets basis, random matrices and any fixed basis (Zhu, 2011; Candes et al., 2008; Xilong et al., 2012).

### 5.4.3 An Improved Compressive Sensing Method

As SAR tomography is a semi-discrete problem ( $\gamma(s)$  is continuous), it is necessary to discretise  $\gamma(s)$  for actual processing so that it can be converted into a discrete problem for solution. Let  $\Delta s$  be the sampling interval of NSR direction (elevation  $s$ ) in the discretisation process,

$$\Delta s = \frac{\rho_s}{z} \quad (5.148)$$

where the Rayleigh resolution  $\rho_s = \frac{\lambda r}{2B_1}$ ,  $z$  is the upsampling factor,  $z > 1$ . In the sampling interval  $[S_{min}, S_{max}]$ , the total samples ( $N$ ) were obtained; this time, the SAR tomography model can be written in the following form.

$$\mathbf{g} \cong \Phi \gamma + e \quad (5.149)$$

where  $\mathbf{g}$  is an  $M \times 1$  dimensional observation vector,

$$\mathbf{g} = [\mathbf{g}(\xi_1), \mathbf{g}(\xi_2), \dots, \mathbf{g}(\xi_M)]^T \quad (5.150)$$

$\Phi$  is an  $M \times N$  dimensional matrix,

$$\Phi = [\phi_1, \phi_2, \dots, \phi_M]^T \quad (5.151)$$

$$\phi_M = [\exp(j2\pi\xi_m s_1), \exp(j2\pi\xi_m s_2), \dots, \exp(j2\pi\xi_m s_N)]^T \quad (5.152)$$

$\gamma$  is an  $N \times 1$  dimensional unknown signal vector, which is what we need to achieve at the end.

$$\gamma = [\gamma(s_1), \gamma(s_2), \dots, \gamma(s_N)]^T \quad (5.153)$$

$e$  is an  $M \times 1$  dimensional noise vector.

$$e = [e(\xi_1)e(\xi_2) \dots e(\xi_m)]^T \quad (5.154)$$

According to the model in Equation (5.149), SAR tomography essentially reconstructs the unknown signal  $\gamma$  from the measured data  $\mathbf{g}$ . Since the dimension of the measured data is much smaller than the dimension  $M \ll N$  of the unknown signal  $\gamma$ , according to the classical signal reconstruction theory, a direct solution of Equation (5.149) is a pathological problem (cannot be solved in the classical signal reconstruction theory as the number of the unknown parameters is larger than the number of measurements). There are usually only a few strong scatterers in the same azimuth-distance resolution unit (one pixel), that is,  $\gamma$  is sparse in the height field. In practice, there is some unavoidable clutter in addition to the main strong scatterers, whose intensities are far less than those of strong scatterers (Zhu, 2011; Candes et al., 2008; Xilong et al., 2012). Therefore, generally speaking,  $\gamma$  is compressible in the elevation region. In this case, the

## Chapter 5. TomoSAR and differential TomoSAR algorithms

sparse basis is the Dirac basis, sparse basis matrix  $\Psi = \mathbf{I}$ ,  $\mathbf{I}$  is  $N \times N$  dimension unit matrix,  $\gamma = \Psi \gamma = \gamma$ . In view of this, we can solve the problem of SAR tomography in the theoretical framework of compressive sensing.

The result is

$$\min_{\gamma} \|\gamma\|_1 \text{ subject to } \mathbf{g} = \Phi \gamma \quad (5.155)$$

For a given  $K$ , since  $\gamma$  is compressible in the elevation region, that is, the sparse basis matrix  $\Psi = \mathbf{I}$ ,  $\gamma = \Psi \gamma = \gamma$  quadratic relaxation can provide a good approximation of the sparsest solution. When noise is considered, the Equation (5.155) becomes

$$M = O(K \log N) \quad (5.156)$$

$$\min_{\gamma} \|\gamma\|_1 \text{ subject to } \|\mathbf{g} - \Phi \gamma\| \leq \sigma_e \quad (5.157)$$

where  $M$  is the smallest number of SLC data for CS method,  $O()$  is the time complexity function,  $\sigma_e$  is the standard deviation of the noise. If  $K$  is not known and measurement noise exists, Equation (5.155) can be approximated by

$$\hat{\gamma} = \arg \min_{\gamma} (\|\mathbf{g} - \Phi \gamma\|_2^2 + \lambda_k \|\gamma\|_1) \quad (5.158)$$

where  $\hat{\gamma} = \arg \min_{\gamma} ()$  means the optimum estimate of  $\gamma$ ,  $\hat{\gamma}$  is the best optimum estimate of  $\gamma$ , when  $\|\mathbf{g} - \Phi \gamma\|_2^2 + \lambda_k \|\gamma\|_1$  is the smallest; and  $\gamma \approx \hat{\gamma}$ ;  $\lambda_k$  is a Lagrange multiplier depending on the number of samples  $N$  (Chen et al., 2001), and the noise level  $\sigma_e$ . Equation (5.158) consists of an L2 norm residual and an L1 norm regularizer and Equation (5.158) can be interpreted as a Bayesian estimate with an exponential prior favouring sparse solution. By scaling down via the L1 and L2 norm minimisation method, model selection, parameter estimation and least-squares estimation, we are able to get all the results.

Now, various sparse reconstruction toolboxes are available for solving the L1 and L2 norm minimisation problem and input complex signal data, such as SparseLab, l1\_ls, YALL1, CVX, FPC\_AS, and l1-MAGIC. In this experiment, the CVX library is used as the library for coding for the special SAR data and my sparse reconstruction compressive sensing algorithm.

## 5.5 SAR Differential Tomography 4D Imaging

Based on the principles introduced in the previous section, the SAR differential tomography 4D imaging algorithm is introduced in this section.

### 5.5.1 D-TomoSAR Phase Error Compensation based on PS-InSAR

This sub-section introduces how to deal with the phase terms due to atmospheric disturbances (atmospheric, ionospheric influences can be split by different SAR frequencies, like the X band and L band), topographic deformation and other sources of errors in the SAR data.

#### 5.5.1.1 PS-InSAR based phase error compensation

Since the data used for SAR differential tomography is the same as the data used for SAR tomography, the phase terms in the data due to atmospheric disturbances and topographic deformation are also the same. The phase error compensation method based on the PS-InSAR intermediate output given previously is easy to extend to SAR differential tomography. However, it should be noted that the linear deformation phase in SAR tomography is part of the phase error, but this phase term is a valid source of information in SAR differential tomography. Only the nonlinear deformation phase is the phase error term for SAR differential tomography imaging. When considering the effects of various errors, the formula (Zhu, 2011; Candes et al., 2008; Xilong et al., 2012; Tebaldini and Guarnieri, 2010) for SAR differential tomography is written as

$$\begin{aligned} & \mathbf{g}(m, x, y) \\ &= \int_{s_{min}}^{s_{max}} \int_{v_{min}}^{v_{max}} f(s, v, x, y) \exp(j2\pi\xi_m s) \exp(j2\pi\eta_m v) \exp(j\varphi_e(m, s, v, x, y)) ds dv \\ & \quad m = 1, 2, \dots, M \end{aligned} \quad (5.159)$$

Among them,  $\varphi_e(m, s, v, x, y)$  is the phase error,  $\eta_m = -2t_m/\lambda$ . Since the phase error in the same azimuth-range resolution unit changes little along  $s$ , it can be considered that the phase error in the same resolution unit is a constant. At this point, the above formula is recorded as

$$\begin{aligned} & \mathbf{g}(m, x, y) \\ &= \int_{s_{min}}^{s_{max}} \int_{v_{min}}^{v_{max}} f(s, v, x, y) \exp(j2\pi\xi_m s) \exp(j2\pi\eta_m v) \exp(j\varphi_e(m, x, y)) ds dv \end{aligned}$$

## Chapter 5. TomoSAR and differential TomoSAR algorithms

$$m = 1.2.\dots, M \quad (5.160)$$

In contrast to SAR tomography, the phase error,  $\varphi_e(m, x, y)$ , in the above equation mainly includes the phase of the atmospheric effects and the nonlinear deformation.

$$\varphi_e(m, x, y) = \varphi_{atmo}(m, x, y) + \varphi_{nonl}(m, x, y) \quad (5.161)$$

If SAR tomography uses the same base image selected in PS-InSAR, the nonlinear deformation component is

$$\varphi_{nonl}(m, x, y) = -\phi_{nonl}(m, x, y) \quad (5.162)$$

Then, Equation (5.161) becomes

$$\varphi_e(m, x, y) = \varphi_{atmo}(m, x, y) - \phi_{nonl}(m, x, y) \quad (5.163)$$

Moreover, the observation data  $\mathbf{g}(m, x, y)$  is written as follows:

$$\begin{aligned} \mathbf{g}(m, x, y) &= \int_{s_{min}}^{s_{max}} \int_{v_{min}}^{v_{max}} \exp(j\varphi_{atmo}(D, x, y)) f(s, v, x, y) \exp(j2\pi\xi_m s) \exp(j2\pi\eta_m v) \\ &\quad \exp(j[\varphi_e(m, x, y) - \varphi_{atmo}(D, x, y)]) ds dv \\ &\quad m = 1.2.\dots, M \end{aligned} \quad (5.164)$$

where  $\varphi_{atmo}(D, x, y)$  is the atmospheric phase of the main image. Substituting Equation (5.163) into Equation (5.164), we get

$$\begin{aligned} \mathbf{g}(m, x, y) &= \int_{s_{min}}^{s_{max}} \int_{v_{min}}^{v_{max}} \exp(j\varphi_{atmo}(D, x, y)) f(s, v, x, y) \exp(j2\pi\xi_m s) \exp(j2\pi\eta_m v) \\ &\quad \exp(-j[\varphi_{atmo}(m, x, y) + \phi_{nonl}(m, x, y)]) ds dv \\ &\quad m = 1.2.\dots, M \end{aligned} \quad (5.165)$$

In differential tomography, we are mainly concerned with the magnitude information of  $f(s, v, x, y)$ , which is  $|f(s, v, x, y)|$ . After the above conversion, the phase error in differential tomography can be considered to be a negative value of the residual phase in PS-InSAR processing (based on Equation (5.163) and (5.165)). According to the previous analysis, the residual phase and its wrapped value have the following relationship:

$$\exp(jW[\varphi_{resi}(m, x, y)]) = \exp(j\varphi_{resi}(m, x, y)) \quad (5.166)$$

where  $\varphi_{resi}(m, x, y)$  is the residual phase,  $W[\varphi_{resi}(m, x, y)]$  is the wrapped phase value of the residual phase. Therefore, the effect of the phase error can be eliminated by multiplying the residual phase  $\exp(jW[\varphi_{resi}(m, x, y)])$  with  $\mathbf{g}(m, x, y)$ . Since PS-



InSAR retrieves only the residual phase values at the PS point, the processing needs to use the residual phase of many PS points in a small window and use the spatial smoothing to calculate the values at all pixels of the whole image.

**5.5.1.2 Improved phase error compensation algorithm (PS, SVD, PGA, weighted least squares and minimum entropy)**

In this section, we will extend the phase error compensation method of SAR tomography based on PS, SVD, PGA, weighted least squares and minimum entropy algorithm to SAR differential tomography for phase error compensation. Suppose there is a significant strong scatterer (PS) element at  $(x_0, y_0)$  within the target range, the element contains only a single strong scatterer of NSR height  $s_0$  and a deformation rate  $v_0$ , and the size of the strong scatterer is much smaller than the azimuth-range resolution of the size of the unit. At this time,  $f(s, v)$  can be defined as follows:

$$f(s, v) = A \exp(j\varphi) \delta(s - s_0, v - v_0) \quad (5.167)$$

where  $A$  is the amplitude of the complex scattering function and  $\varphi$  is the initial phase of the complex scattering function. Thus, the observed contamination data (with phase error) is:

$$\begin{aligned} \mathbf{g}(m) &= A \exp(j\varphi) \exp(j2\pi\xi_m s_0) \exp(j2\pi\eta_m v_0) \exp(j\varphi_e(m)) \\ m &= 1, 2, \dots, M \end{aligned} \quad (5.168)$$

Assuming the centres  $s_0$  (estimate the height  $s_0$  based on SVD) and  $v_0$  (set it as 0 at known (no deformation) locations or obtain it from PS-InSAR or static GPS) of the strong scattering elements are known (can be estimated or obtained, it should be noted that  $(s_0, v_0)$  is a reference in the phase calibration method at the PS point only for phase error estimation), the corresponding phase terms  $\exp(-j2\pi\xi_m s_0)$  and  $\exp(-j2\pi\eta_m v_0)$  are first removed from the observed data.

$$\begin{aligned} F(m) &= \exp(-j2\pi\xi_m s_0) \cdot \exp(-j2\pi\eta_m v_0) \cdot \mathbf{g}(m) \\ &= A \exp(j\varphi) \cdot \exp(j\varphi_e(m)) \\ m &= 1, 2, \dots, M \end{aligned} \quad (5.169)$$

Differentiating between the two adjacent observations after removing the linear phase, we get

$$\begin{aligned} F(m) - F(m-1) &= F(m) \cdot \left[ 1 - \frac{F(m-1)}{F(m)} \right] \\ &= F(m) \cdot \{1 - \exp(j[\varphi_e(m) - \varphi_e(m-1)])\} \\ m &= 2, 3, \dots, M \end{aligned} \quad (5.170)$$

## Chapter 5. TomoSAR and differential TomoSAR algorithms

If

$$\Delta F(m) = F(m) - F(m-1) \quad (5.171)$$

$$\Delta \varphi_e(m) = \varphi_e(m) - \varphi_e(m-1)$$

the Equation (5.170) will be

$$\begin{aligned} \Delta F(m) &= F(m) \cdot [1 - \exp(-j\Delta \varphi_e(m))] \\ m &= 2, 3, \dots, M \end{aligned} \quad (5.172)$$

Expanding  $\exp(-j\Delta \varphi_e(m))$  into the Taylor series mode and keeping the first order term

$$\exp(-j\Delta \varphi_e(m)) \approx 1 - j\Delta \varphi_e(m) \quad (5.173)$$

Equation (5.173) will be

$$\Delta F(m) \approx F(m) \cdot j\Delta \varphi_e(m) \quad m = 2, 3, \dots, M \quad (5.174)$$

and

$$\Delta \hat{\varphi}_e(m) = \Delta \varphi_e(m) \approx -j \frac{\Delta F(m)}{F(m)} \quad m = 2, 3, \dots, M \quad (5.175)$$

Since the phase error difference  $\Delta \varphi_e(m)$  is a real number, in order to not introduce an amplitude error, the real part on the right side of the above equation is extracted as the estimation of the phase error differential (in the equation, the Taylor approximation is used. This complex value is affected by the approximation of the differential calculation, the result is not necessarily a real number; sometimes it is a real number, sometimes it is not. According to the rationality of the phase error differential approximation formula, it can be predicted that the imaginary part of the estimated value is much smaller than the real part. Therefore, the real part is used in practical processing ).

$$\Delta \hat{\varphi}_e(m) \approx \text{Re} \left[ -j \frac{\Delta F(m)}{F(m)} \right] = \frac{\text{Im}[\Delta F(m) \cdot F^*(m)]}{|F(m)|^2} \quad m = 2, 3, \dots, M \quad (5.176)$$

The phase error  $\hat{\varphi}_e(m)$  is estimated by summing up the difference of the phase errors

$$\hat{\varphi}_e(m) = \begin{cases} 0, & m = 1 \\ \sum_{i=2}^m \Delta \hat{\varphi}_e(i), & m = 2, 3, \dots, M \end{cases} \quad (5.177)$$

Finally, we can eliminate the phase error

$$\begin{aligned} \mathbf{g}'(m, x, y) &= \exp(-j\hat{\varphi}_e(m)) \cdot \mathbf{g}(m, x, y) \\ &= \int_{s_{\min}}^{s_{\max}} \int_{v_{\min}}^{v_{\max}} f(s, v, x, y) \exp(j2\pi\xi_m s) \exp(j2\pi\eta_m v) ds dv \\ m &= 1, 2, \dots, M \end{aligned} \quad (5.178)$$

The minimum entropy method is executed to refine the phase errors. After the minimum entropy method, the refined estimated SAR phase error at each point  $(x, y)$  for

the whole image can be obtained and the SLC data is corrected using the phase error results. It can be seen from the above analysis that the difference between the phase error estimation in SAR differential tomography and the phase error estimation in SAR tomography is mainly due to the different phases of strong scatterer positions. Since SAR differential tomography is not only concerned about the NSR height but also the deformation rate, a strong scattering element exists in the  $s$ - $v$  two-dimensional plane and its corresponding phase is also related to the two-dimensional phase  $\exp(j2\pi\xi_m s_0)$  and  $\exp(j2\pi\eta_m v_0)$  of position  $s_0$  and  $v_0$ . In SAR tomography, the main concern is the NSR height, so the need to remove the linear phase term is only  $\exp(j2\pi\xi_m s_0)$ . The estimated phase error in D-TomoSAR is different from the estimated phase error (the linear deformation is included) in TomoSAR. In practice, as in the case of SAR tomography, the accuracy of phase error estimation needs to be improved by combining a number of PS points and combining PGA, SVD, weighted least squares and minimum entropy methods, discussed in the previous Section 5.4.3. Besides, for real processing, we select the special significant elements (PS points) according to the amplitude deviation index threshold like 0.20-0.30 (the threshold is usually used in the PS method of the majority of software, for example, within the StaMPS software). Since SAR differential tomography focuses on the relative height and relative deformation information of the target structure, the processing results are corrected based on a benchmark point (or a control point selected at the non-deformation point) where the height is set as 0, and the deformation is set as 0. Meanwhile, the deformation rate is in the line of sight direction and the height is converted to the vertical height (the NSR direction is corrected to the vertical height direction according to the incidence angle).

### 5.5.2 D-TomoSAR Imaging based on Compressive Sensing

SAR differential tomography is also a semi-discrete problem ( $f(s, v)$  is continuous), which needs to be solved by the discrete sampling of  $f(s, v)$  discretely in the actual processing ( $f(s, v) = A \exp(j\varphi)$ ,  $A$  is the amplitude at  $(s, v)$ ,  $\varphi$  is the phase at  $(s, v)$ ). Let  $\Delta s$  be the sampling interval of height  $s$  in the NSR direction and the sampling points as  $Q$ ; the sampling interval of deformation rate  $v$  be  $\Delta v$ , the sampling points be  $U$ ; the total sampling points  $N = Q * U$ . At this time, the SAR differential

## Chapter 5. TomoSAR and differential TomoSAR algorithms

tomography formula (Zhu, 2011; Candes et al., 2008; Xilong et al., 2012; Tebaldini and Guarnieri, 2010; Tebaldini, 2010) can be written as below.

$$\mathbf{g}(m) = \sum_{q=1}^Q \sum_{u=1}^U f(s_q, v_u) \exp(j2\pi\xi_m s_q) \exp(j2\pi\eta_m v_u) + e(m) \quad (5.179)$$

$$m = 1, 2, \dots, M$$

$$\mathbf{g} = \mathbf{\Phi} \cdot \mathbf{f} + \mathbf{e} \quad (5.180)$$

where  $e(m)$  is noise,  $\mathbf{g}$  is an  $M \times 1$  dimensional observation vector,  $\mathbf{f}$  is an  $N \times 1$  dimensional unknown signal vector,  $\mathbf{e}$  is an  $M \times 1$  dimensional noise vector,  $\mathbf{\Phi}$  is an  $M \times N$  dimensional measurement matrix.

$$\mathbf{g} = [\mathbf{g}(1) \ \mathbf{g}(2) \ \dots \ \mathbf{g}(M)]^T \quad (5.181)$$

$$\mathbf{f} = [f(s_1, v_1) \ \dots \ f(s_1, v_U) \ \dots \ f(s_Q, v_1) \ \dots \ f(s_Q, v_U)]^T \quad (5.182)$$

$$\mathbf{e} = [e(1) \ e(2) \ \dots \ e(M)]^T \quad (5.183)$$

$$\mathbf{\Phi} = [\phi_1 \ \phi_2 \ \dots \ \phi_M]^T \quad (5.184)$$

Moreover, an  $m^{th}$  row vector of a measurement matrix  $\mathbf{\Phi}$  is

$$\phi_m = \frac{1}{\sqrt{N}} (x_m \otimes y_m) \quad (5.185)$$

In the above equation, where the vector is normalised,  $\otimes$  is the Kronecker symbol, the standardisation here will not affect the final imaging effect because the normalised amplitude needs to be taken into account in the processing result.

The specific form of  $x_m$  and  $y_m$  is as follows.

$$x_m = [\exp(j2\pi\xi_m s_1) \ \exp(j2\pi\eta_m s_2) \ \dots \ (j2\pi\xi_m s_Q)]^T \quad (5.186)$$

$$y_m = [\exp(j2\pi\xi_m s v_1) \ \exp(j2\pi\eta_m v_2) \ \dots \ (j2\pi\xi_m v_U)]^T \quad (5.187)$$

If  $K$  is known, we can get  $f, A, \varphi, s$  and  $v$  (the equation is  $f(s, v) = A \exp(j\varphi)$ ) after many iteration estimations, according to the equations below.

$$\langle \phi_{m_1} \cdot \phi_{m_2} \rangle = \frac{1}{N} \langle x_{m_1} \otimes y_{m_1}, x_{m_2} \otimes y_{m_2} \rangle = 0 \quad (5.188)$$

$$m_1 \neq m_2 \in [1, M] \quad (5.189)$$

$$\min \|f\|_1 \text{ subject to } \|\mathbf{g} - \mathbf{\Phi}f\| \leq \sigma_e \quad (5.190)$$

$$\Gamma = [A \ \varphi \ s \ v]^T \quad (5.191)$$

The Cramér-Rao bound (CRB) (which is a lower bound on the variance of optimum unbiased estimators of a parameter) of each parameter ( $A, \varphi, s, v$ ) (Yang et al., 2016), shown below, can be used as the performance evaluation criteria for the estimated parameters (Zhu, 2011; Candes et al., 2008; Xilong et al., 2012; Tebaldini and Guarnieri,

2010; Tebaldini, 2010). These equations below show that the accuracy of the amplitude  $A$  is only determined by the number of sampling points and noise energy, but not by the two-dimensional sampling. The estimation accuracy of phase and height in SNR and deformation rate is not only related to the sampling points but it is also related to spatiotemporal correlation coefficient ( $\gamma_{b_{\perp}t}$ ) and signal-to-noise ratio (Zhu, 2011; Candes et al., 2008; Xilong et al., 2012; Tebaldini and Guarnieri, 2010; Tebaldini, 2010).

$$CRB_A = \frac{\sigma_e^2}{2M} \quad (5.192)$$

$$CRB_{\phi} = \frac{1}{2M \cdot SNR} \left\{ \frac{E(\xi^2)E(\eta^2) - [E(\xi\eta)]^2}{var(\xi) var(\eta) (1 - \gamma_{\xi\eta}^2)} \right\} \quad (5.193)$$

$$CRB_s = \frac{(\lambda r)^2}{32\pi^2 M \cdot SNR \cdot var(b_{\perp}) \cdot (1 - \gamma_{b_{\perp}t}^2)} \quad (5.194)$$

$$CRB_v = \frac{\lambda^2}{32\pi^2 M \cdot SNR \cdot var(t) \cdot (1 - \gamma_{b_{\perp}t}^2)} \quad (5.195)$$

where  $\sigma_e^2$  is the variances of the SLC signal, SNR is the signal-to-noise ratio,  $E()$  is the mean function,  $var()$  is the variance function,  $cov()$  is the covariance function, and  $M$  is the number of SLC data.

$$\gamma_{b_{\perp}t} = \frac{cov(b_{\perp}t)}{\sqrt{var(b_{\perp})}\sqrt{var(t)}} \quad (5.196)$$

$$\gamma_{\xi\eta} = \frac{cov(\xi\eta)}{\sqrt{var(\xi)}\sqrt{var(\eta)}} \quad (5.197)$$

Generally, the deformation always has linear or nonlinear terms, but in our D-TomoSAR experiment, only linear deformation is estimated. In practical data processing, the deformation retrieval can be achieved by using the compressed sensing method based on many available reconstruction toolboxes, like SparseLab, l1\_ls, YALL1, CVX, FPC\_AS, l1-MAGIC, and so on. In our D-TomoSAR compressive sensing experiment (Chapter 6), CVX is used for D-TomoSAR imaging.

## 5.6 Conclusions

In this chapter, most of the equations are derived from different theory books, theses and papers, they have been modified to use the same symbols and linked together

## Chapter 5. TomoSAR and differential TomoSAR algorithms

to show the mathematical derivation for the workflow of TomoSAR and D-TomoSAR imaging. These core equations (Equation (5.40), (5.41), (5.42), (5.43), (5.44), (5.45), (5.57), (5.58), (5.59), (5.66), (5.98), (5.99), (5.114), (5.120), (5.123), (5.115), (5.116), (5.119), and (5.178)) have been used in my practical data processing for TomoSAR and D-TomoSAR imaging ( I wrote my own code in MATLAB based on these equations and a sparse library called CVX). What is important is that the equations (Equation (5.114), (5.115), (5.116), (5.117), (5.118), (5.119), (5.120), (5.121), (5.122), (5.123)) have been derived by me to fulfil the mathematical derivation for the phase calibration of TomoSAR and D-TomoSAR imaging.

In this chapter, the principle of 3D SAR tomography imaging and four-dimensional differential tomography SAR imaging are first introduced. Next, the SAR tomography workflow and four-dimensional differential tomography workflow are presented. Then, the PS-InSAR, PGA and my phase error compensation algorithm based on PS, PGA, weighted least squares and minimum entropy (PS-SVD-PGA-LS-ME) are studied in detail. Thereafter, the sparse aperture for 3D imaging and the basic theory of compressive sensing is introduced. Moreover, my SAR tomography imaging algorithm and my differential tomography four-dimensional SAR imaging algorithm based on compressive sensing are studied with formula derivation and a programming workflow introduction. The new points of this chapter are phase calibration methods. The combined phase error compensation algorithm based on PS, SVD, PGA, weighted least squares and minimum entropy (PS-SVD-PGA-LS-ME) is proposed and studied with formula derivation. Meanwhile, the SAR interferometry phase (InSAR) calibration with the DEM error estimation (PS, SBAS and many other methods for DEM error estimation) and correction method (new point of this chapter) is also proposed and demonstrated in the mathematical formula derivation. In the next chapter, the experiment results, alongside the accuracy and performance of the 3D SAR tomography imaging and four-dimensional differential tomography SAR imaging methods are studied, analysed and discussed in detail.

# Chapter 6

## Application of TomoSAR to X-band

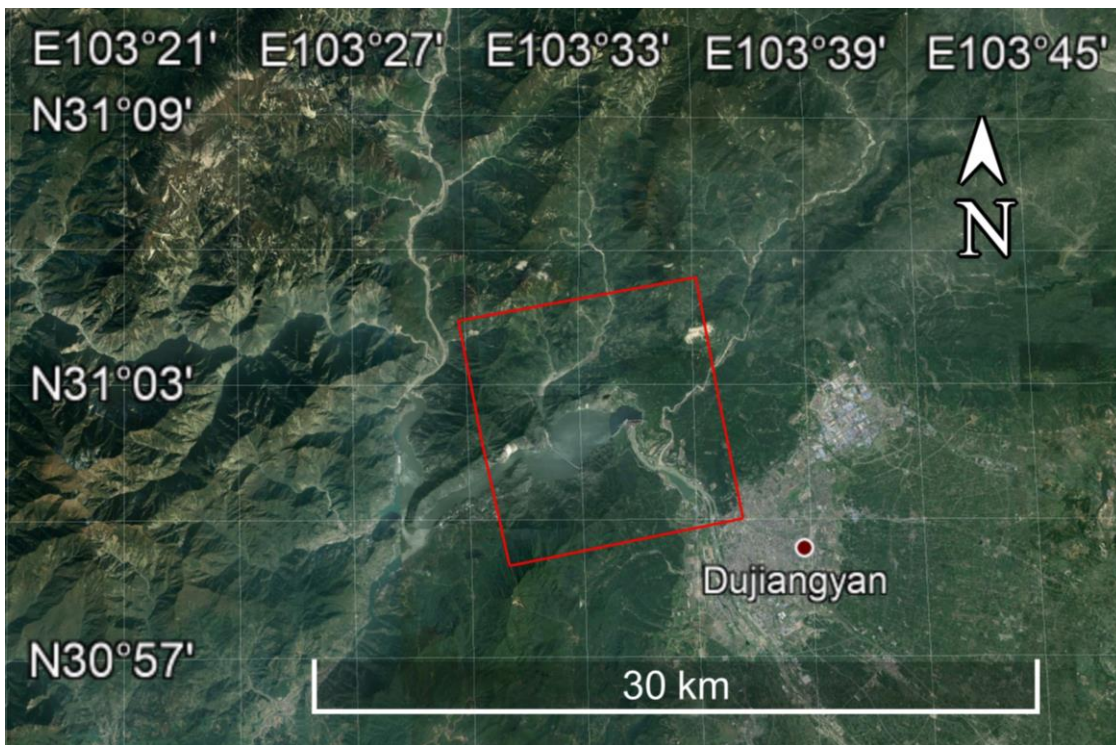
Based on the atmospheric and ionospheric correction algorithm study for TomoSAR imaging and the mathematical derivation for the workflow of TomoSAR and D-TomoSAR imaging introduced in previous chapters, the systematic 3D and 4D TomoSAR algorithm and methods are demonstrated, tested and analysed using COSMO-SkyMed X band data for the Zipingpu dam in Dujiangyan, Sichuan, China. This includes SAR co-registration, the orbit baseline estimation, DEM deramping, tropospheric phase distortion correction, the DEM error correction, phase calibration, the FFT reconstruction method, the Capon reconstruction method, the super-resolution reconstruction CS method and a LIDAR validation. This chapter proposed and tested an improved precise orbit, a registration offset rule and an interpolation method to estimate the pixel by pixel baseline. The baseline estimation results and TomoSAR processing results demonstrate the baseline estimation method works very well, which also fills in the gaps in the baseline estimation for 3D & 4D SAR tomography imaging (no papers have been published about this to date). The TanDEM 12 m high resolution data is introduced in deramping; PS-SVD-PGA-LE-ME phase calibration and InSAR phase calibration method with DEM phase error correction as proposed in Chapter 5, are tested in this chapter. The TomoSAR results in the dam area become better and better with the standard deviation quantification after the DEM deramping, tropospheric phase distortion correction, the DEM error correction and the phase calibration processing when it is conducted step by step. The super-resolution TomoSAR imaging based on the compressive sensing (CS) method is

## Chapter 6. Application of TomoSAR to X-band

simulated and tested on the Zipingpu dam in Dujiangyan, Sichuan, China. The results are shown and validated by the fieldwork Lidar data, which demonstrates that the CS method has high resolution reconstruction capabilities. Finally, the 4D TomoSAR algorithm and methods are tested and analysed using the COSMO-SkyMed X band data at Zipingpu dam, China for the purpose of deformation extraction.

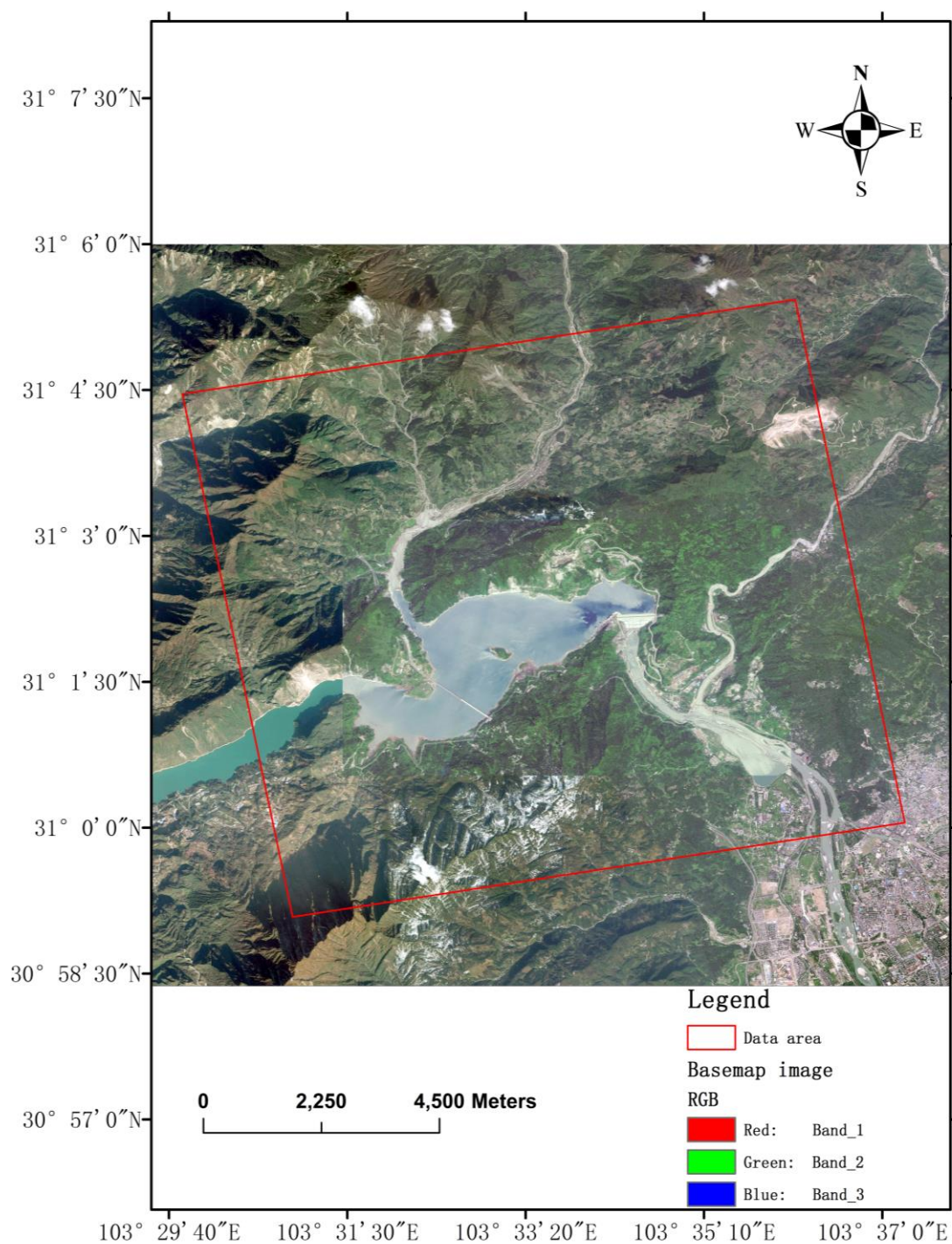
### 6.1 Test Sites and COSMO-SkyMed Spaceborne SAR

The test site is set in the densely vegetated mountainous rural areas at Zipingpu dam, Dujiangyan, Sichuan, China (shown in Figure 6.1). The small test subarea at Zipingpu dam for the TomoSAR imaging is shown in Figure 6.2. Construction on the dam began on 29-03-2001 and it was completed on 30-09-2005.



(a)





(b)

## Chapter 6. Application of TomoSAR to X-band

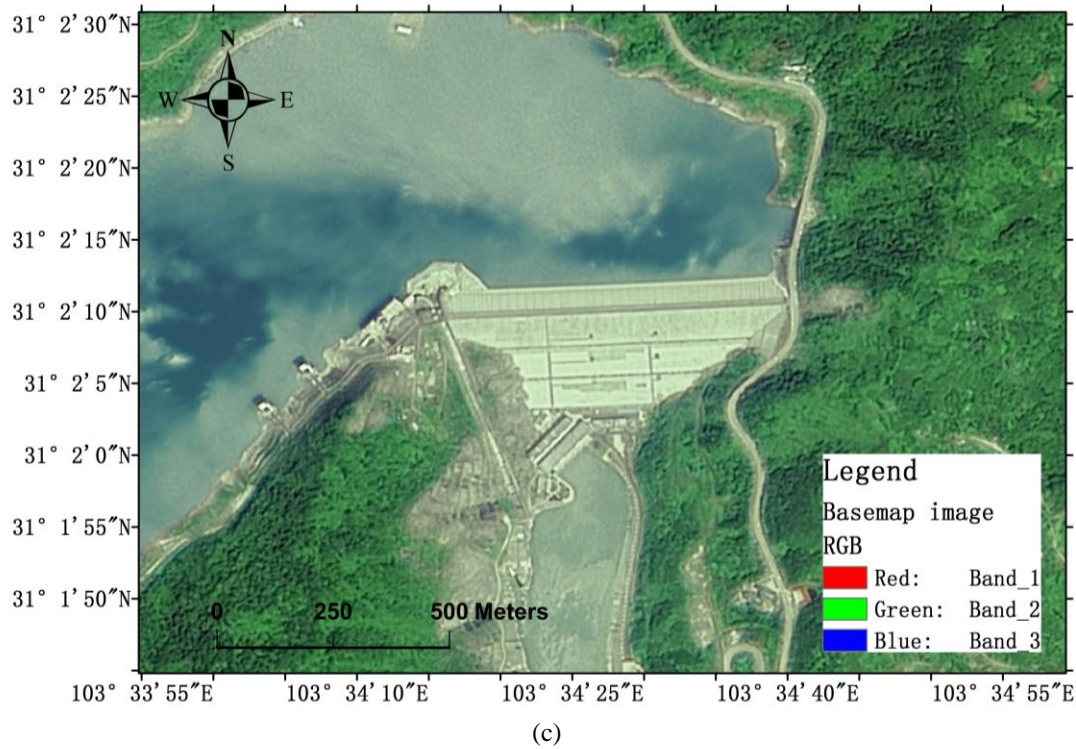


Figure 6.1 The test site in Sichuan China, the red area is the COSMO-SkyMed spotlight data stacks: (a) The test area in Google Earth map (image source: Landsat image/Copernicus); (b) The zoom-in test area map (image source: ArcGis online map); (c) The zoom-in map of Zipingpu dam (Source: Tianditu map, National Geomatics Center of China)

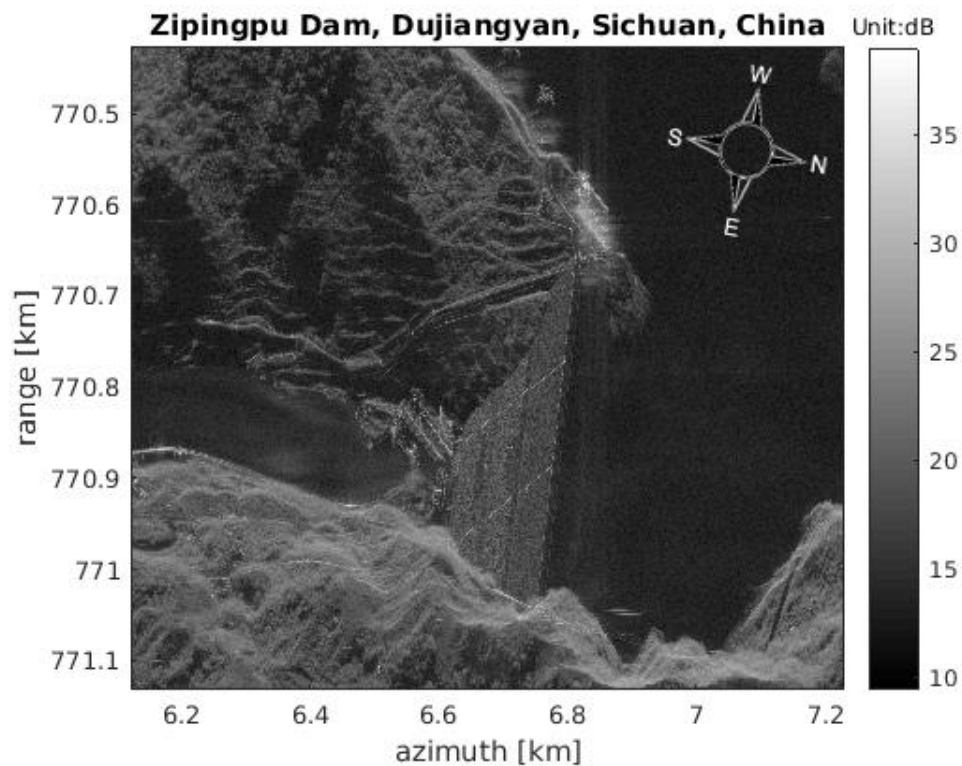


Figure 6.2 A small test subarea at Zipingpu dam in Dujiangyan, Sichuan, China (master image is from 25/07/2016), the colour of the figure is the average amplitude of all SAR SLC stacks, the unit is dB

Table 6.1 Ascending COSMO-SkyMed spotlight data stacks, the master image is 25/07/2016, shown in red font

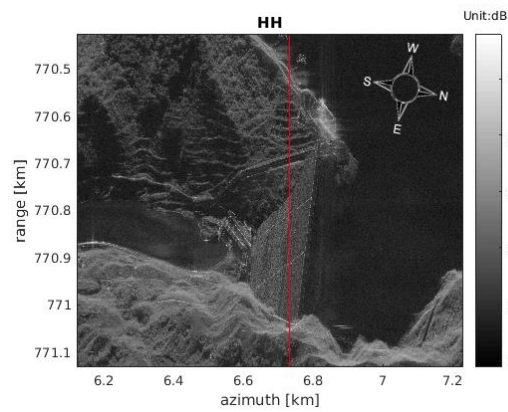
id	Incidence angle	time	Track type	Baseline (m)
1	37.66	03/06/2016	Ascending	-373.44
2	37.66	11/06/2016	Ascending	-289.25
3	37.66	19/06/2016	Ascending	743.28
4	37.66	23/06/2016	Ascending	920.38
5	37.66	05/07/2016	Ascending	-431.28
6	37.66	09/07/2016	Ascending	-629.15
7	37.66	25/07/2016	Ascending	0
8	37.66	06/08/2016	Ascending	820.31
9	37.66	10/08/2016	Ascending	203.46
10	37.66	22/08/2016	Ascending	-435.71
11	37.66	26/08/2016	Ascending	-140.25
12	37.66	07/09/2016	Ascending	186.17
13	37.66	11/09/2016	Ascending	611.54
14	37.66	23/09/2016	Ascending	-330.33

In 3D SAR imaging (SAR tomography) and 4D SAR imaging (differential SAR tomography) processing, 14 COSMO-SkyMed<sup>27</sup> X-band spotlight data stacks are used (the metadata of the ascending data stacks is shown in Table 6.1). According to the literature review, 3D SAR imaging (SAR tomography) and 4D SAR imaging methods have orbital, tropospheric and ionospheric phase distortion, temporal decorrelation scatterers, and possible height blurring and accuracy losses, particularly in densely vegetated mountainous rural areas. Therefore, it is necessary to correct the temporal decorrelation, an the orbital, tropospheric and ionospheric phase distortion (Feng and Muller, 2017), and it is also very important to account for absorbing some advantages of PS-InSAR (like orbital, tropospheric and ionospheric correction, DEM error estimation, deformation estimation) for 3D SAR imaging (SAR tomography), 4D SAR imaging and deformation information extraction.

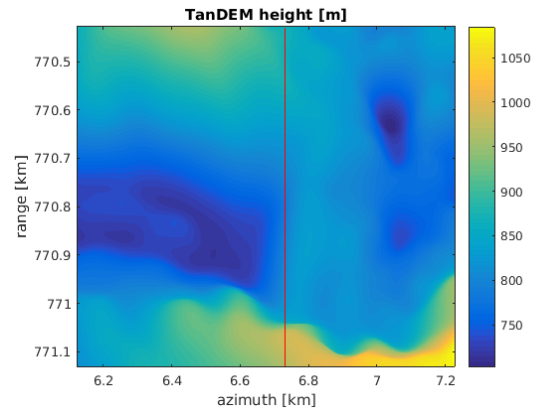
<sup>27</sup> The constellation of Small Satellites for Mediterranean basin Observation (COSMO-SkyMed) has four satellites, which is funded by the Italian Ministry of Defence (MoD) and the Italian Ministry of Research (MUR) and conceived by ASI (Agenzia Spaziale Italiana) in Italy.



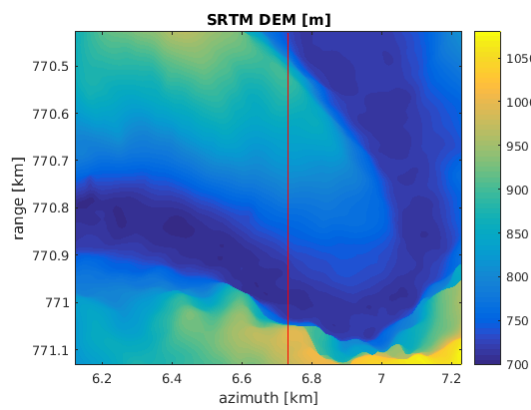
## Chapter 6. Application of TomoSAR to X-band



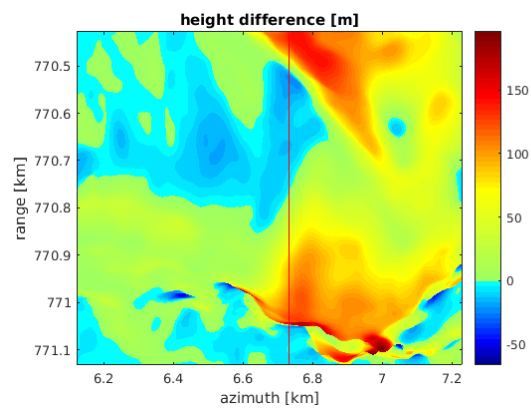
(a)



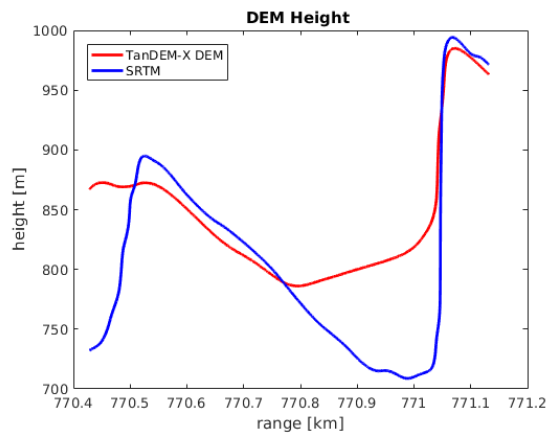
(b)



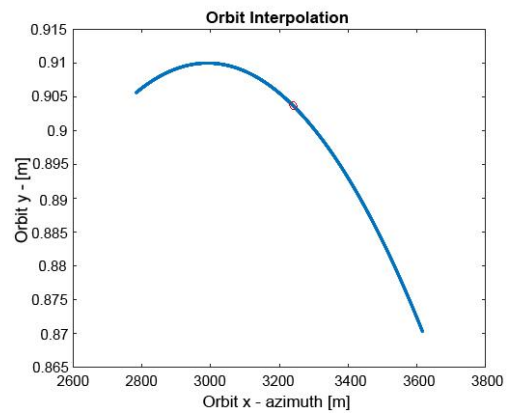
(c)



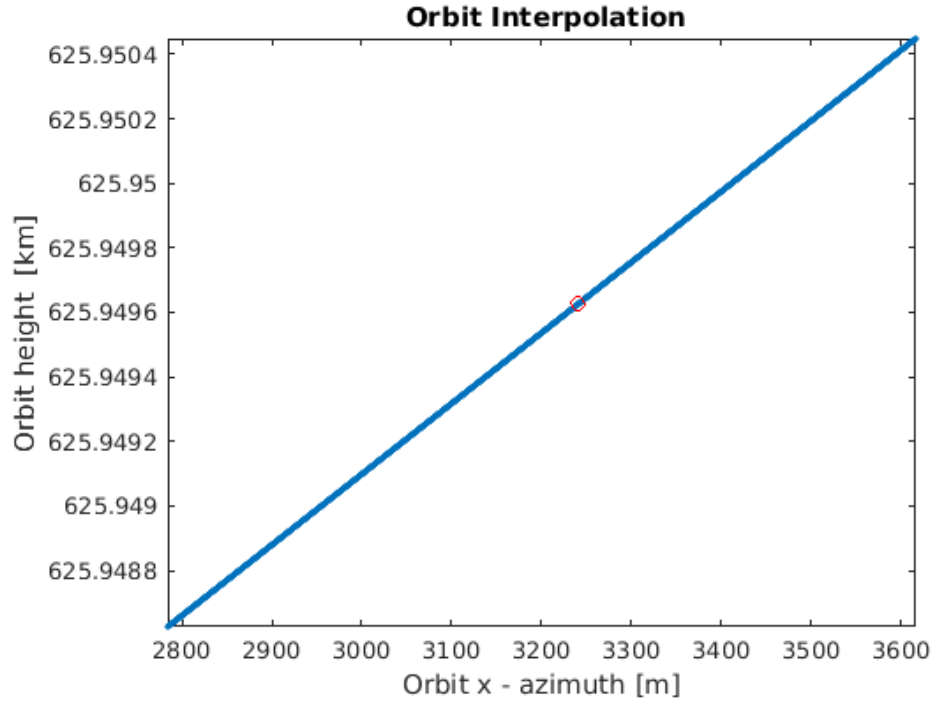
(d)



(e)



(f)



(g)

Figure 6.3 The position and information of Test-A area: (a) Azimuth test line on SAR image; (b) Azimuth test line on TanDEM-X DEM 12 m DEM, the dam is shown in the plot, as construction on the dam was completed on 30-09-2005, and TanDEM-X DEM was collected after 2010; (c) Azimuth test line on SRTM 30 m data, no dam is in SRTM, as SRTM was collected in 2000, but construction on the dam began on 20-03-2001; (d) The azimuth test line of the height difference between TanDEM-X DEM 12 m DEM and SRTM 30 m DEM; (e) The height of TanDEM-X DEM 12 m DEM and SRTM 30 m DEM at the azimuth test line in (d); (f) Azimuth test line orbit information (x-y plane) in the *SCH* coordinate system; (g) Azimuth test line orbit information (x-z plane) in the *SCH* coordinate system

An azimuth line is selected to test the TomoSAR algorithms in the subarea. We call it Test-A, whose information is shown in Figure 6.3 above. The dam is in the middle of this test line, the areas on two sides of the line are mountains with some sparse trees. The terrain height in this test area is from 700 to 1010 metres and the satellite orbit position of the test line is also shown in Figure 6.4 (e) and (f). The difference map between 30 m DEM and the TanDEM-X 12 m DEM, shown in Figure 6.3 (d), also indicates that the dam was built after 2000.

## 6.2 Co-registration

In TomoSAR processing, the shifts between master and slave images result from the change in radar acquisition geometry, which depends on the topography and slope.

## Chapter 6. Application of TomoSAR to X-band

Accurate (sub-pixel) image co-registration is required as the first essential processing step to improve the phase coherence. The conventional polynomial warp-based co-registration procedure becomes inaccurate when dealing with rough topography, long interferometric baselines and especially high-resolution SAR imagery (Nitti et al., 2011). In TomoSAR processing, a reference DEM is required to flatten the topographic phase (D. Ho Tong Minh et al., 2016), to compensate for the backscattered phase measurements and to geocode the TomoSAR products.

In this study, the quality improved TanDEM-X 12 m DEM data were obtained after the quality assessment and post-processing method conducted in Chapter 3 (Section 3.3). High-resolution DEM (like the TanDEM-X 12 m DEM) plays an important role in 3D TomoSAR imaging and 4D SAR differential tomography (Diff-TomoSAR) as the reference DEM, which is employed in the co-registration step of TomoSAR processing. First, all slave images are co-registered with the master image, and the DEM is transferred to the radar coordinates, then a simulated radar image in the radar coordinates is generated using the DEM and orbital data. Offset vectors are computed between simulated image and master SAR image with fine offsets estimated by matching methods, like “offsetprf” (default), “ampcor” or “Nstage” in the ISCE (Interferometric synthetic aperture radar Scientific Computing Environment) software. Although the river area is totally different in the simulated radar (compared Figure 6.4 to Figure 6.5), the image is masked first and split in different tiles. All tiles are matched separately and then a final shift (x, y) of the whole image is estimated by fitting the results of all tiles which will compensate for the river difference, layover and shadow issue. Finally, all radar images are co-registered with the master image; then eventually all data are well matched with DEM (although there are DEM errors existing, the DEM errors will be estimated and compensated in InSAR, PS-InSAR and compensated in TomoSAR processing through phase calibration). The DEM simulated radar image is shown in Figure 6.4 and the master image (20160725) is shown in Figure 6.5; the before co-registration slave image (20160603) is shown in Figure 6.6 and the after co-registration image (20160603) is shown in Figure 6.7. Moreover, the interferograms between the slave image (20160810) and the master image (20160725) are shown in Figure 6.8 and Figure 6.9, which has eliminated the DEM phase. The fringes can be clearly seen in the building, road and dam areas in these figures, while the fringes are not clear in the mountain tree areas as the coherence is very low, which is caused by foreshortening, shadows and the layover of SAR data in complex mountain tree areas.

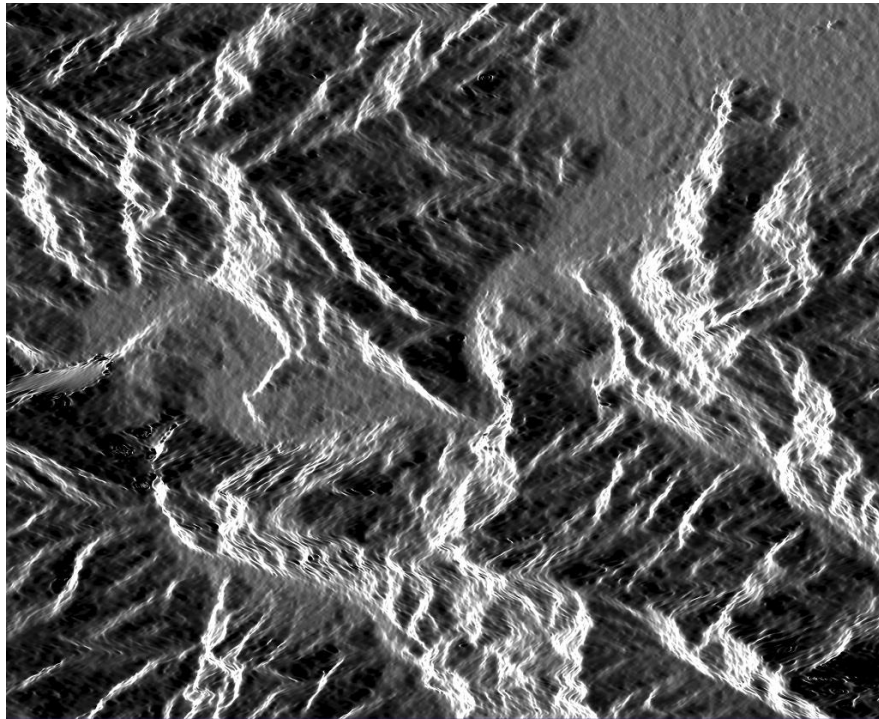


Figure 6.4 The DEM simulated radar image in radar coordinate system based on the 12 m TanDEM-X DEM data, the image is a simulated amplitude image

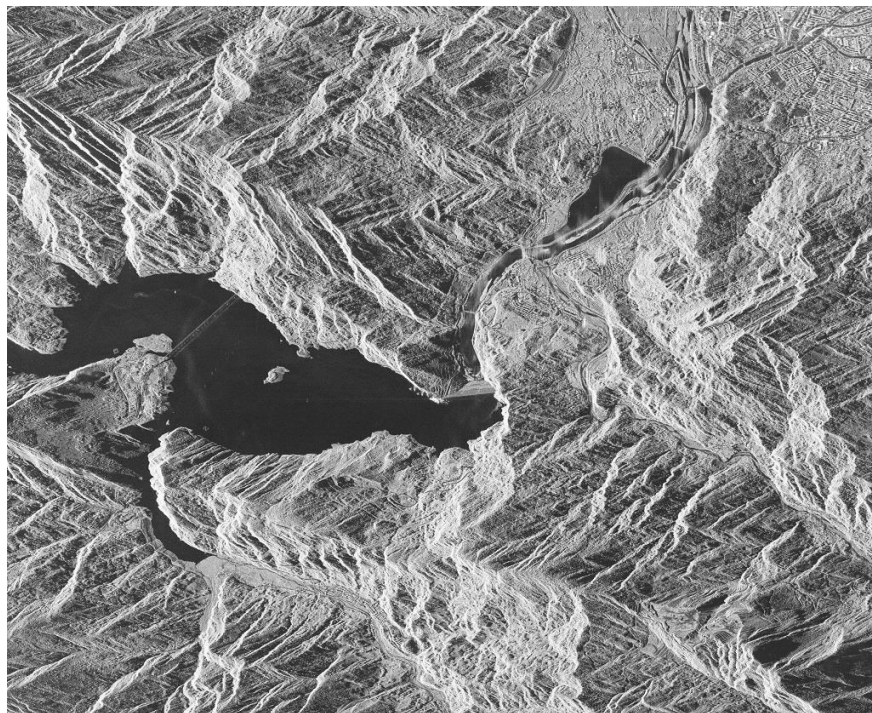


Figure 6.5 Master image (20160725) in the radar coordinate system, the image is the real amplitude image of the master SLC SAR data



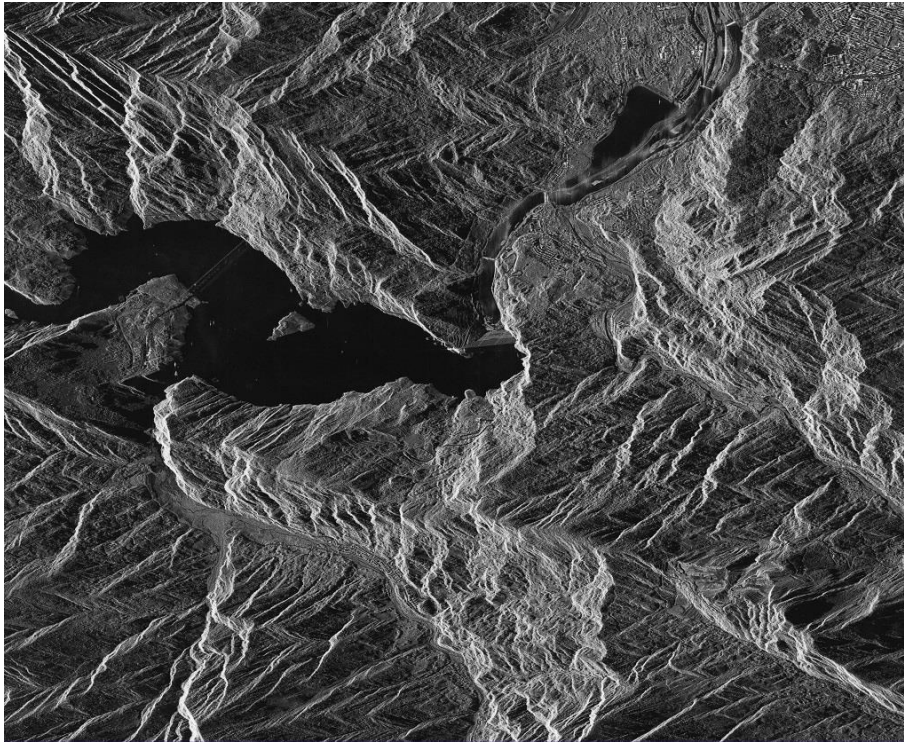


Figure 6.6 The slave image (20160603) before co-registration in the radar coordinate system, the image is the real amplitude image of the slave SLC SAR data

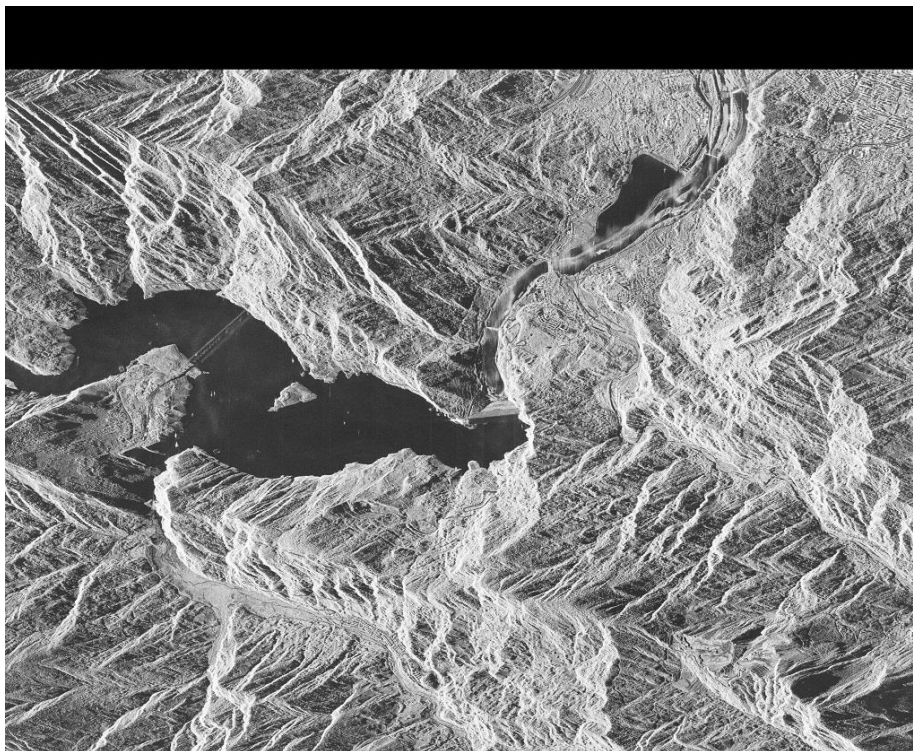


Figure 6.7 The slave image (20160603) after co-registration in the radar coordinate system, the image is a real amplitude image, the top black area in the figure shows the shift after co-registration



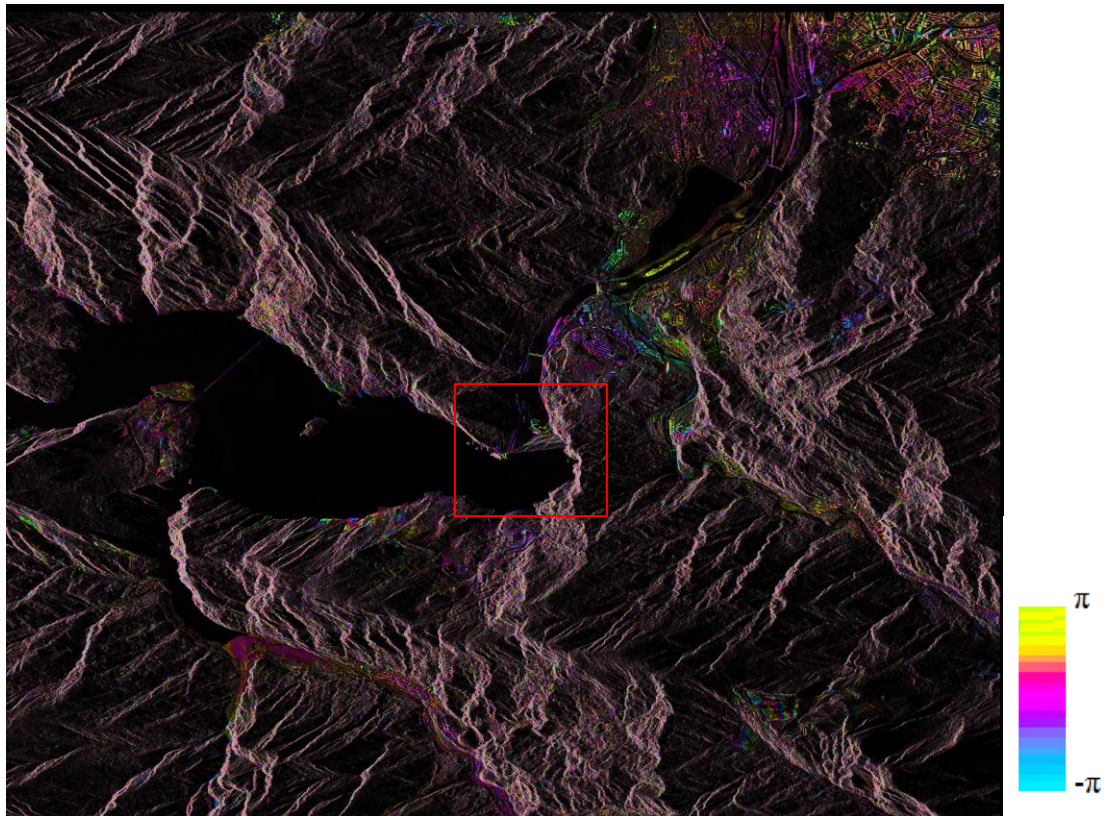


Figure 6.8 The interferogram between 20160810 and master 20160725 SLC after flattening and filtering in the radar coordinate system, the base map is the amplitude of the interferogram complex data; the phase is laid out on the base map. The fringes can be clearly seen in the bridge, building (top-right), road and dam areas in the figure, and the fringes of the dam area in the red rectangle box is shown in Figure 6.9 more clearly

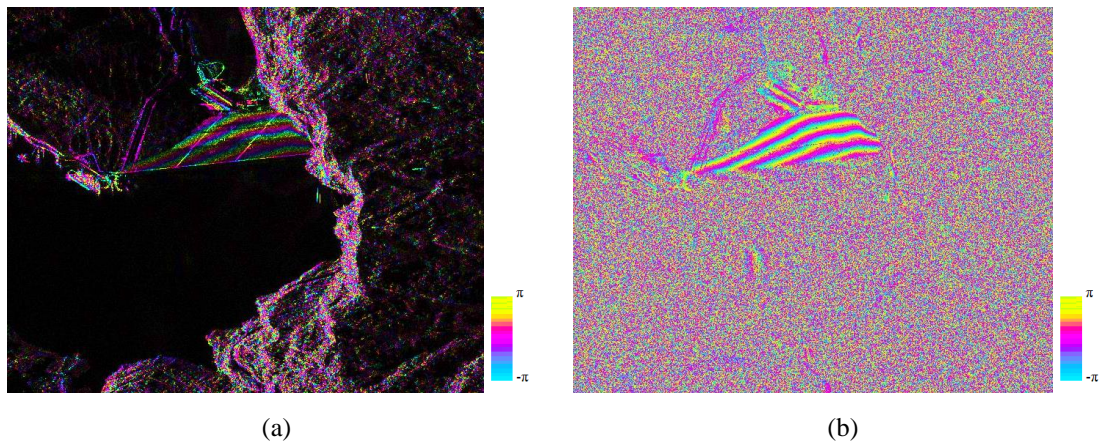


Figure 6.9 The zoom-in map of the interferogram (the red rectangle box area of Figure 6.8) between slave 20160810 SLC and master 20160725 SLC, the fringes are easily observed at the dam area: (a) The interferogram phase after flattening and filtering is laid out on the amplitude of the interferogram complex data; (b) The interferogram phase after flattening and filtering in the same area

### 6.3 Pixel-by-pixel Baseline estimation

In common InSAR, a single baseline is usually obtained, but in TomoSAR processing, a pixel by pixel baseline is needed. In Section 6.2, all SAR images are co-registered to the reference master SAR image with subpixel accuracy with the help of the external DEM (TDX-DEM 12 m). Using a precise orbit to estimate the orbit baseline is entirely dependent on the orbit accuracy; in our test area, a precise orbit is provided with the SLC data. Therefore, the improved precise orbit, registration rule (Section 6.2) and interpolation are used to estimate the baseline.

The geometry of the perpendicular baseline and the parallel baseline is shown in Figure 6.10. The perpendicular baseline is a scaling factor for the height ambiguity, while the parallel baseline, is, in fact, the actual path length difference. A large error in the perpendicular baseline decreases the SNR of the interferogram. As the basic range-Doppler approximation makes the orbit and baseline modules more robust, so that it can be used for both airborne and spaceborne data with post-estimation for baseline estimation. Based on this, the pixel-by-pixel baseline method is proposed. In the fine co-registration step, a pixel-by-pixel azimuth-range time for each pixel in the co-registered slave image can be obtained. Then, interpolating the orbit time is executed according to spatial distribution and the orbit is interpolated based on the new interpolated time to obtain the satellite position and velocity information based on the Hermite interpolation method in the Earth Centered Earth Fixed (ECEF) coordinate system (because the COSMO-SkyMed satellites use GPS, which uses the Earth Centred Earth Fixed (ECEF) coordinate system, for on-board orbital determination); meanwhile, the orbit vector was transferred to the *SCH* coordinate system (Zebker et al., 2010) (The *SCH* coordinate system aligns with the radar geometry, the *S* coordinate is along-track, *C* is the across-track ground coordinates and the *H* coordinate measures the height of the point above the surface; in addition, *x* is *S* coordinate, *y* is *C* coordinate and *z* is *H* coordinate. The zero point in the *SCH* coordinate system is the earth surface point projected by the satellite position of the first pixel of the SAR frame in the ECEF coordinate system. More specifically, the *x* and *y* value of the zero point value in the *SCH* coordinate system is the *x* and *y* position of the satellite position for the first pixel of the SAR frame in the ECEF coordinate system) for TomoSAR geocoding. The next step is using the range-Doppler equation to estimate pixel-by-pixel latitude, longitude, height for the reference/master

image and to figure out where the same latitude, longitude and height show up in the slave image. Then, the pixel-by-pixel baselines can be calculated by using satellite positions (the interpolated orbit information) and the pixel latitude, longitude and height. It can be seen from what is shown in Figure 6.11 (b) that the baseline is the same along the range pixels, but the parallel and perpendicular baselines change along the range pixels, as they depend on the look angle and the height of each pixel is different.

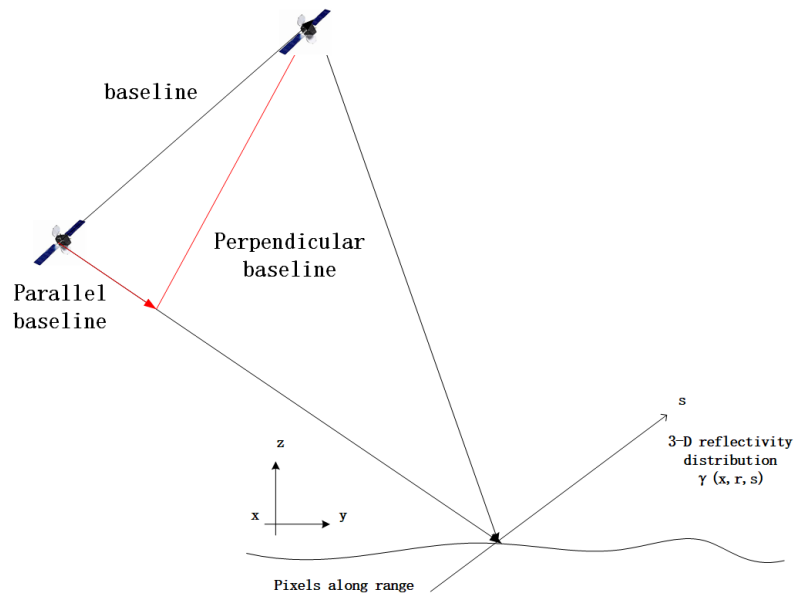


Figure 6.10 Typical geometry of InSAR and the baseline

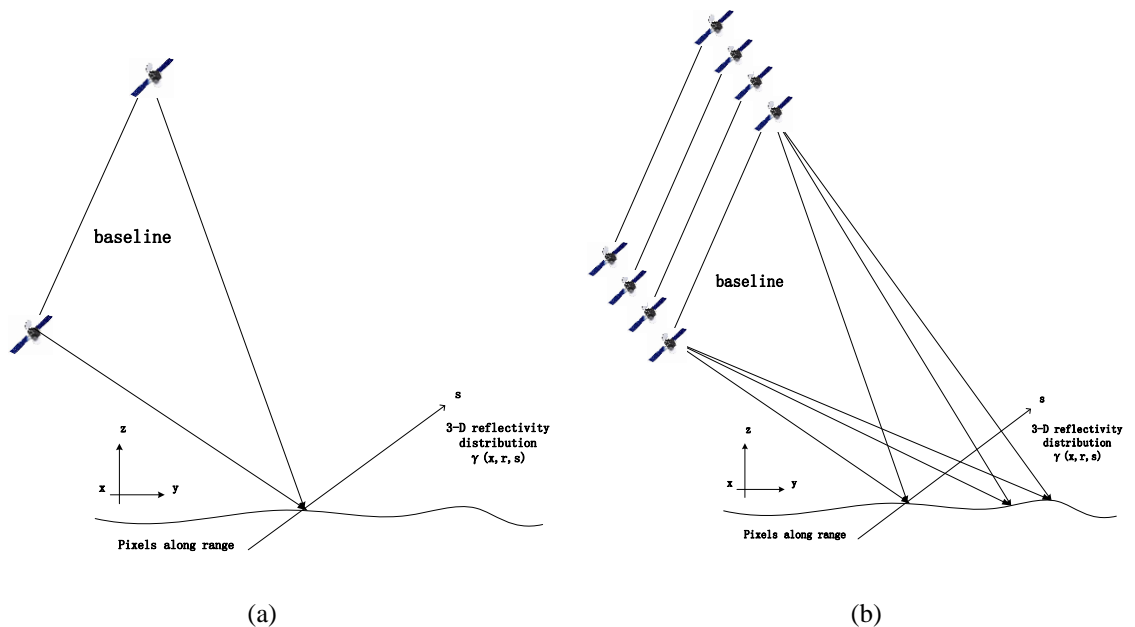


Figure 6.11 Pixel-by-pixel baselines estimation: (a) Single baseline; (b) Pixel by pixel baseline, each baseline can be decomposed into a perpendicular baseline and a parallel baseline

## Chapter 6. Application of TomoSAR to X-band

In our experiments, COSMO-SkyMed X band spotlight data stacks (the test area is shown in Figure 6.1 and the average amplitude of all SAR SLC stacks is shown in Figure 6.2) were used for the man-made infrastructure TomoSAR reconstruction. Meanwhile, one image of the SLC stacks was selected as the master image and other images (referred to as slave images) were registered to the master image. Moreover, interpolating orbits based on time is essential. In the case of the COSMO-SkyMed spotlight data experiment, the orbit time of the slave image after co-registration is a rectangle tile by rectangle tile along the azimuth, shown in Figure 6.12 (a). In the same tile, the time is the same along the azimuth in the same range pixels, shown in Table D. 1 and Figure 6.12 (a). Therefore, the orbit must be interpolated. The interpolated orbit result, which is smoother, especially along the azimuth direction, is shown in Table D. 2 and Figure 6.12 (b). The master (20160725) and the slave (20160603) orbit information of the SAR image are also shown in the *SCH* coordinate system in Figure 6.13.

After the orbit information is obtained, the baseline can be estimated using my pixel-by-pixel baseline method. The interpolated baselines (the absolute distance between the position of the two satellites) are shown in Figure 6.14 (a). The original and interpolated perpendicular baselines are shown in Figure 6.14 (b) and (c) individually. In Figure 6.14 (a) and (c), there are three line features along the azimuth direction; this is because the satellite does not fly in a straight line, as shown in Figure 6.13, which causes the baselines to vary. In more detail, in Figure 6.13 (c) and (d), the height increases when the satellites fly, while in the satellite's along and across-track direction, shown in Figure 6.13 (a) and (b), the master satellite and slave satellite manoeuvre differently. Figure 6.13 (g) and (h) are the zoom-in master and slave satellite orbit of the red rectangle box of Figure 6.13 (a) in the satellite's along and across-track directions. It can be seen that the baseline should decrease first and then increase, that is why there is the first line feature in Figure 6.14 (a) and (c). In the same way, Figure 6.13 (i) and (j) are the zoom in master and slave satellite orbit of the yellow rectangle box of Figure 6.13 (a) in the along and across direction, which will also cause the second line feature in Figure 6.14 (a) and (c) and the same pattern whereby the baseline first decreases and then increases. This pattern can also be seen in the red line in Figure 6.14 (a) and the baseline value of the red line does not change too much. The difference and the profile of the original and interpolated perpendicular baselines are shown in Figure 6.14 (d), (e) and (f) respectively. The maximum difference is 6.268 metres, the minimum difference is -0.129 metres, the mean difference is 3.81 metres and the standard deviation is 1.87 metres. In Figure 6.14 (e), the

blue line is the original perpendicular baseline, which jumps along the azimuth caused by the imprecise time, and the red line is our new interpolated perpendicular baseline, which is smoother.

In contrast to Figure 6.14 (a), there are other features along the range direction in Figure 6.14 (c) caused by the look angle along the range pixel. Because the parallel and perpendicular baselines depend on the look angle, shown in Figure 6.14 (b), this means that both of the baseline parameters depend on the relative position of a pixel in the interferogram geometry. In more detail, the parallel and perpendicular baselines are related to the orbital convergence and divergence, the geometric difference between near-range and far-range, and the contribution of the topography (Hanssen, 2001). The original and interpolated parallel baseline is shown in Figure 6.15 (a) and (b) separately. The differences and the profile of the original and interpolated parallel baseline are shown in Figure 6.15 (c), (d) and (e) respectively. The maximum difference is 0.04 millimetres, the minimum difference is -3.5 millimetres, the mean difference is -1.5 millimetres and the standard deviation is 0.9 millimetres. In Figure 6.15 (e), the parallel baselines are almost the same along the range pixel in the original and new parallel baseline. However, in Figure 6.15 (d), the blue line is the original parallel baselines which are not smooth along the azimuth caused by the imprecise time, and the new red line is smoother after our new interpolated method. All in all, the parallel baseline difference is very small; this is because the parallel baseline represents the basic master and slave path length difference, which relies on the slant range accuracy.

An orbit test is also executed using BioSAR (ESA BioSAR 2008 report) 2008 L band data<sup>28</sup> (the test line is shown in the red line in Figure 6.16 (a)) for 3D forest structure reconstruction. The test site is a forested area in the Vindeln municipality, situated in the province of Västerbotten in northern Sweden about 50 km northwest of Umeå. Almost all parts of the forests mapped by E-SAR are confined to the Krycklan River catchment, which covers 6700 ha in total. From the Tomogram results shown in Figure 6.16, it is clear to see that if the baseline is not good enough, the reconstruction results might not be accurate enough. In Figure 6.16 (b) and (c), compared to the pixel by pixel baseline, the single baseline causes results higher than the LIDAR truth at the left slant range (close to the aeroplane) and lower at the right slant range (far from the aeroplane), while LIDAR

---

<sup>28</sup> The original data were provided by ESA. The L band calibrated data were obtained from Stefano Tebaldini's group (Politecnico di Milano).

## Chapter 6. Application of TomoSAR to X-band

forest height is well matched with the reconstruction results based on the pixel by pixel baseline.

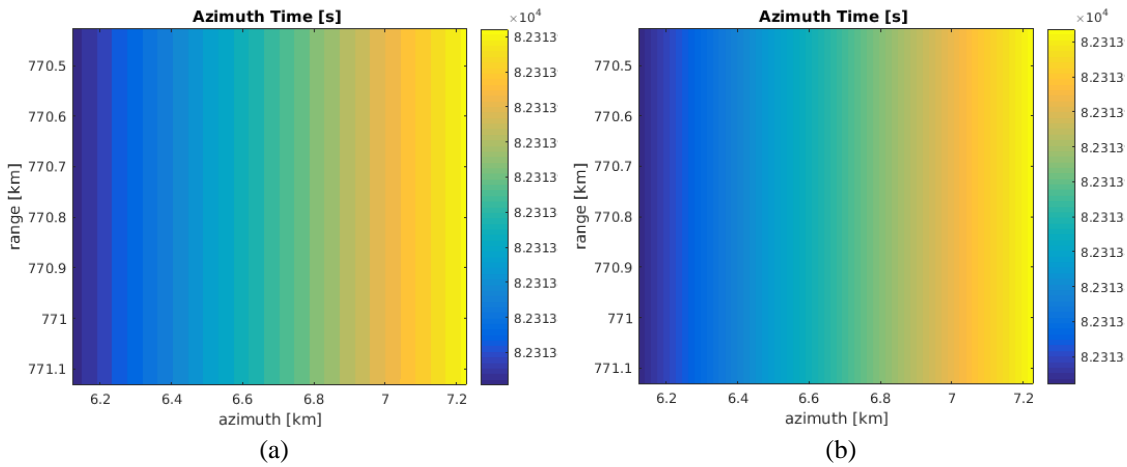
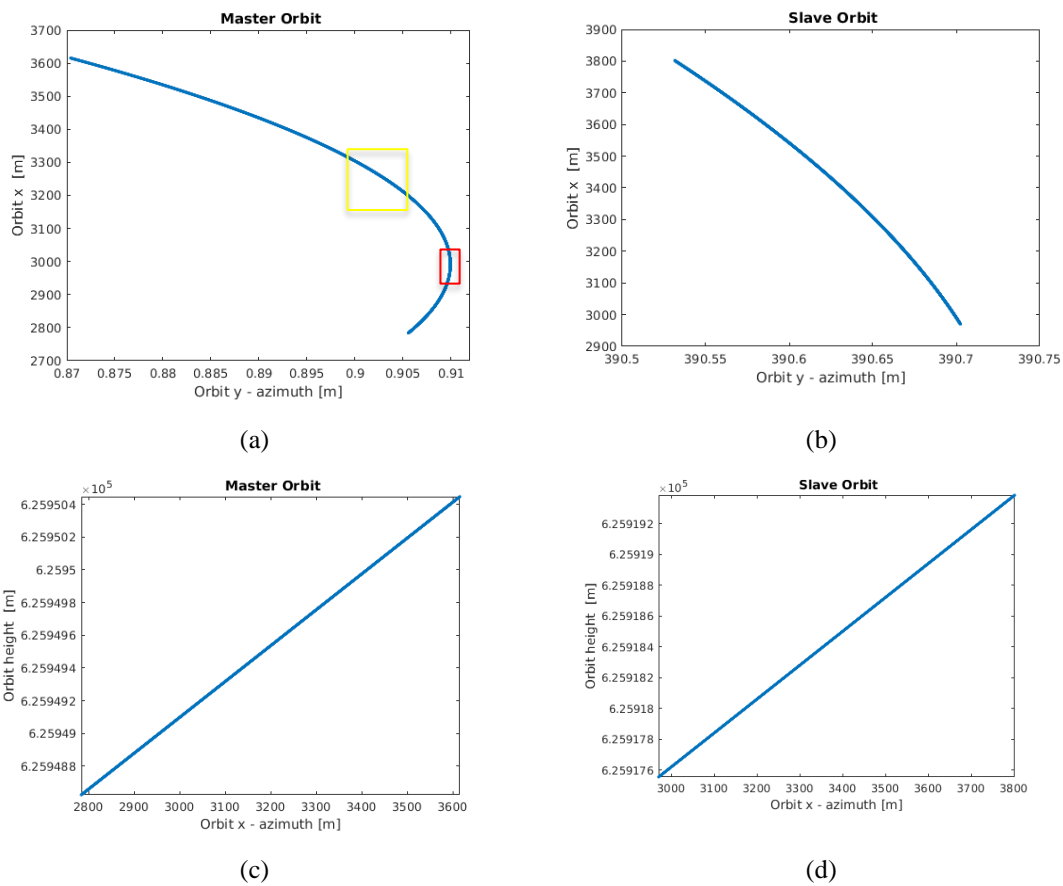


Figure 6.12 The original and interpolated time in each pixel: (a) The original time is the orbit time minus the reference time, which is 0 hour 0 minute 0 second of the SAR data acquisition day; (b) The new time after interpolation, the time has the same reference as in (a)





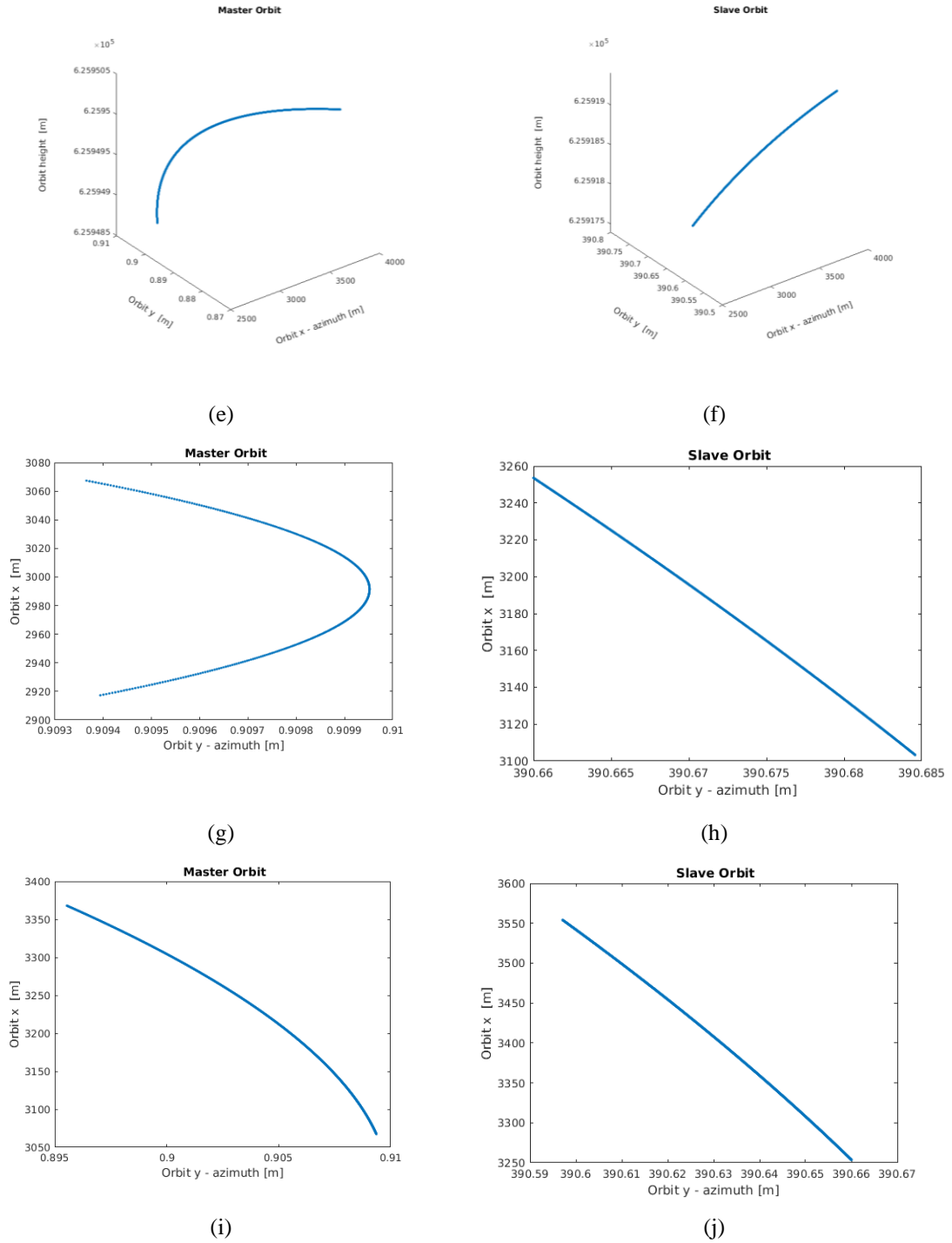
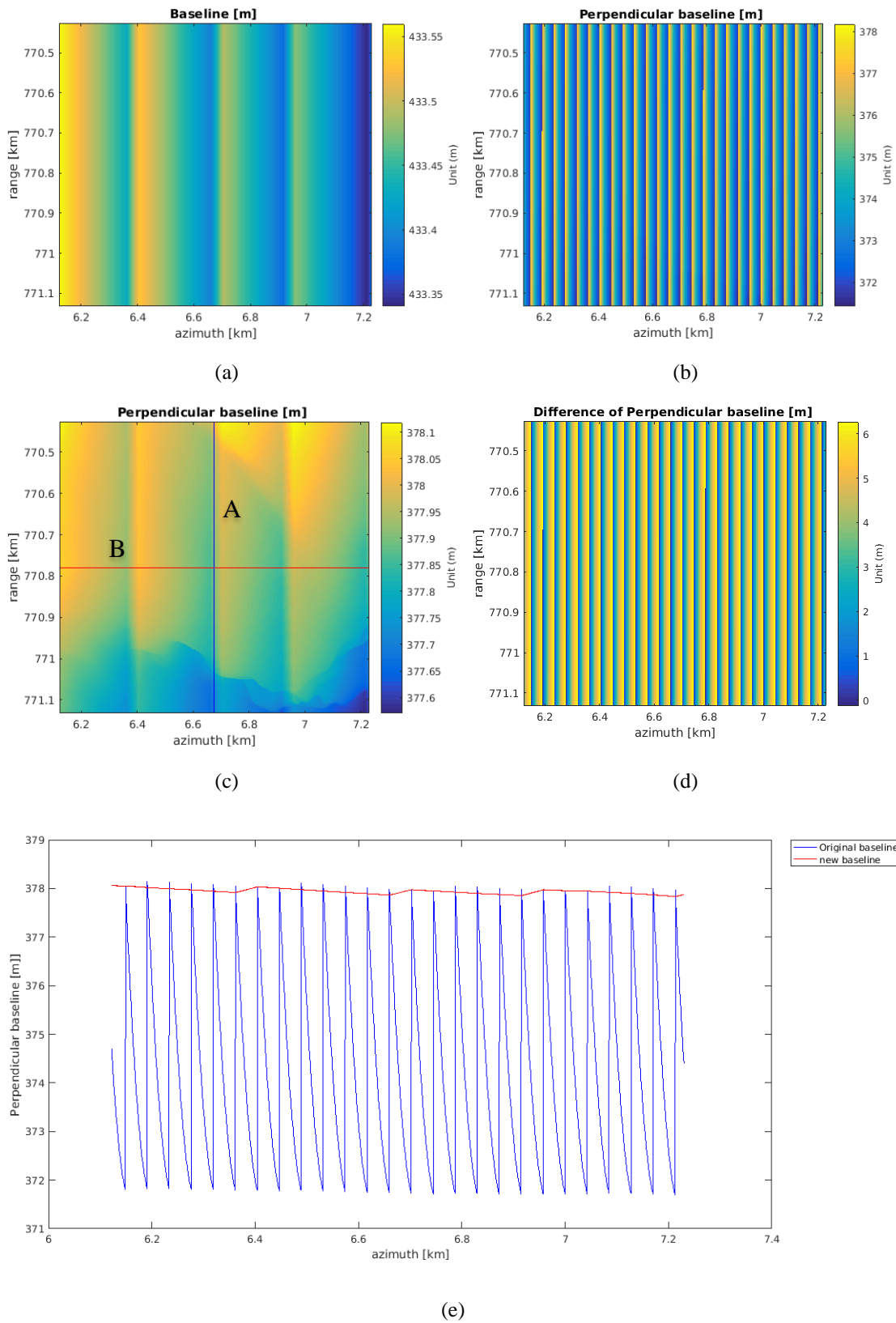
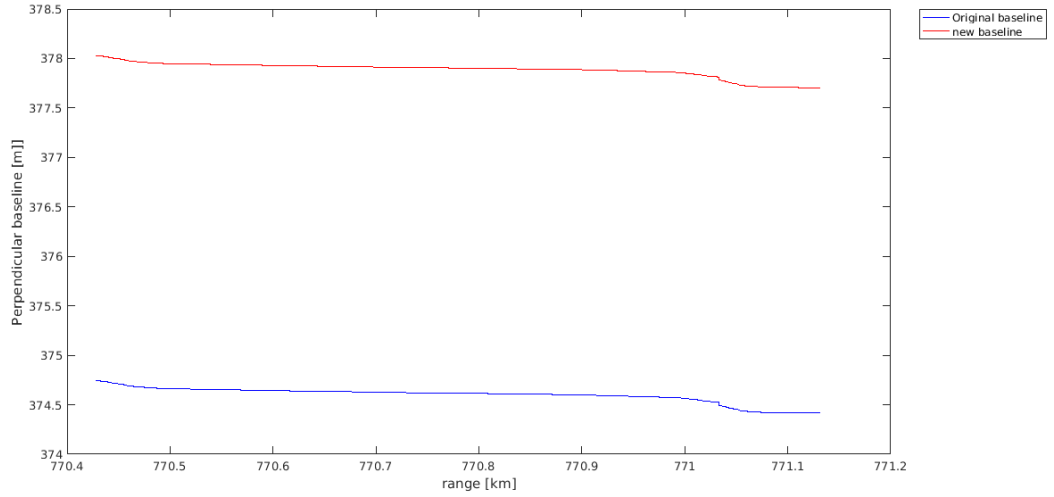


Figure 6.13 The interpolated orbits (x, y, z based on local *SCH* coordinate system, x means *S*, y means *C*, z means *H*) of the master (20160725) and slave (20160603) image (unit: metres): (a) Master orbit (20160630) position in the x-y plane; (b) Slave orbit position in the x-y plane; (c) Master orbit position in the x-z plane; (d) Slave orbit position in the x-z plane; (e) Master orbit position in the x-y-z plane; (f) Slave orbit position in the x-y-z plane; (g) The zoom in master satellite orbit of the red rectangle box of (a) in the satellite's along and across direction; (h) The zoom in slave satellite orbit of the red rectangle box of (a) in the satellite's along and across direction; (i) The zoom in master satellite orbit of the yellow rectangle box of (a) in the satellite's along and across direction; (j) The zoom in slave satellite orbit of the yellow rectangle box of (a) in the satellite's along and across direction

## Chapter 6. Application of TomoSAR to X-band

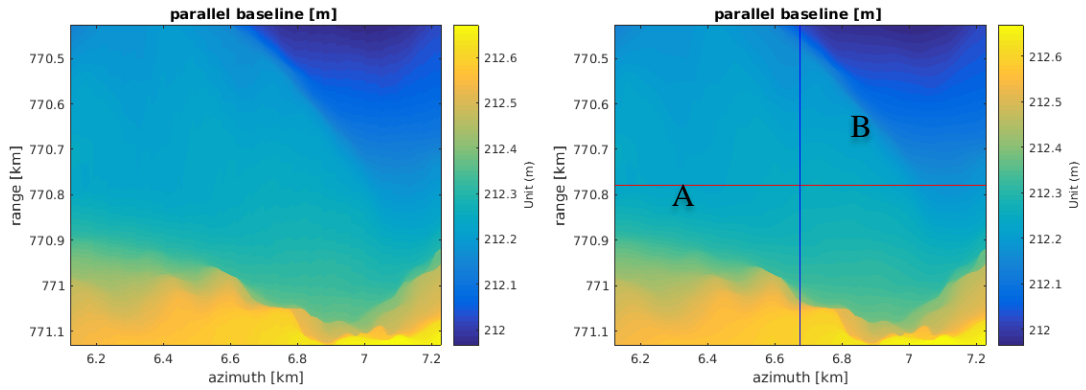






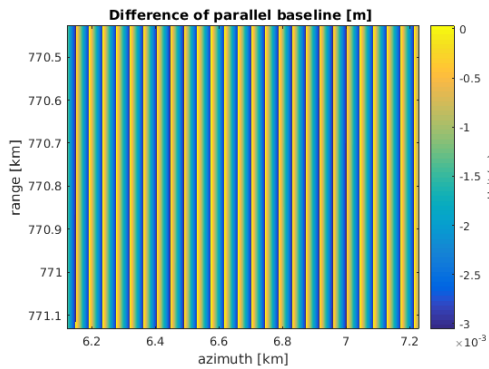
(f)

Figure 6.14 Perpendicular baseline estimation: (a) New baseline (the absolute distance between the position of two satellites) after interpolation; (b) Original perpendicular baseline; (c) New perpendicular baseline after interpolation; (d) The difference between the new baseline and the original baseline; (e) The profile of the new baseline and the original baseline of line B in figure (c); (f) The profile of the new baseline and the original baseline of line A in figure (c)



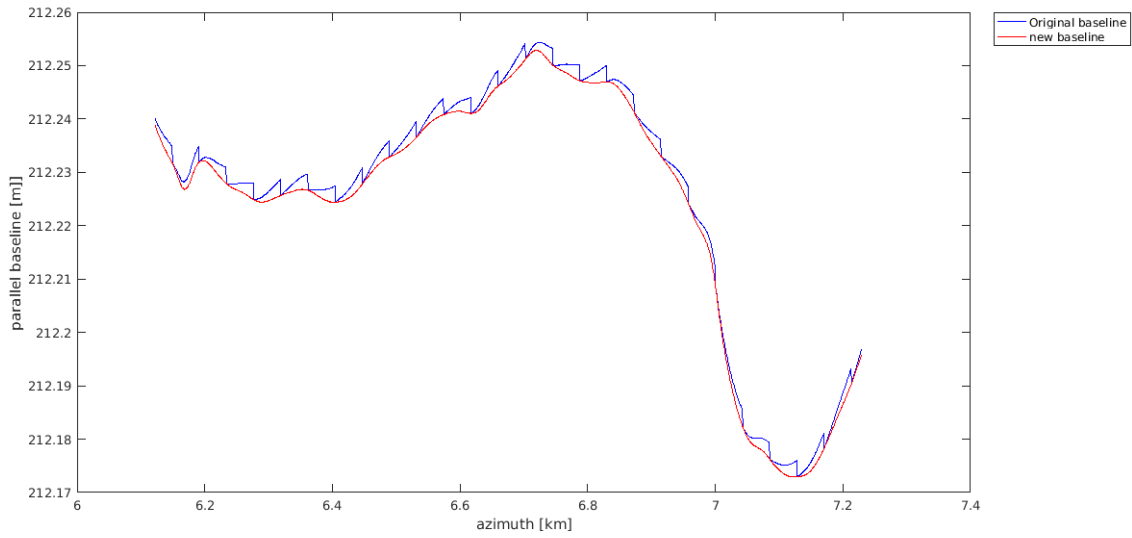
(a)

(b)

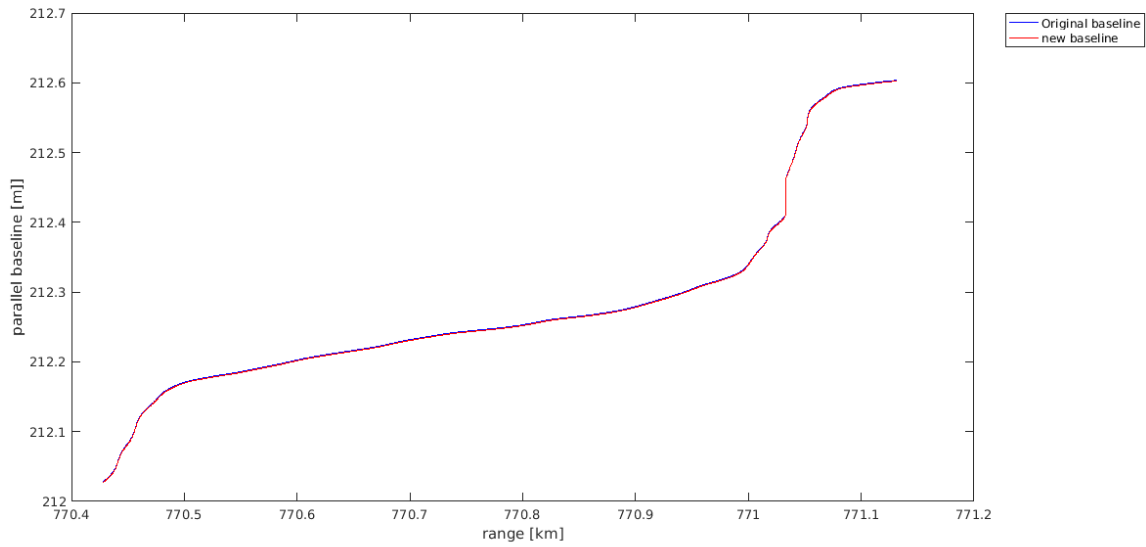


(c)

## Chapter 6. Application of TomoSAR to X-band

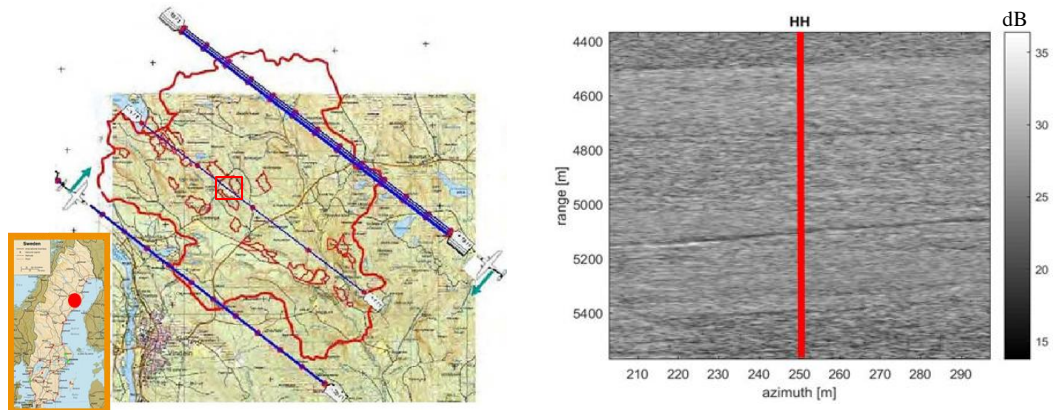


(d)

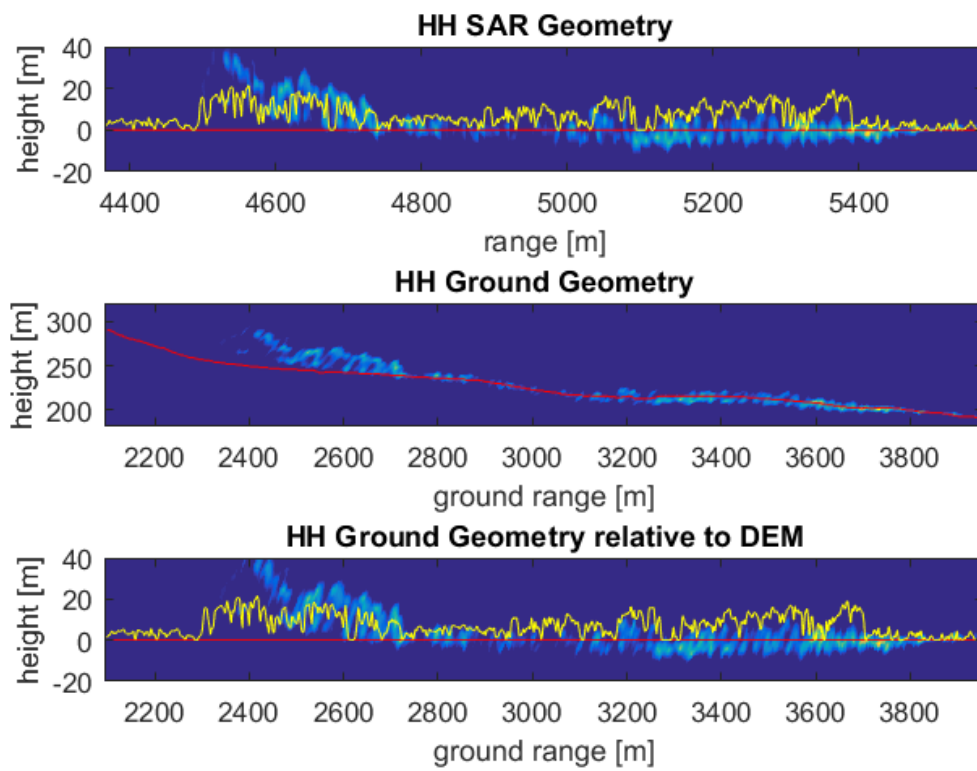


(e)

Figure 6.15 Parallel baseline estimation: (a) Original parallel baseline; (b) New parallel baseline after interpolation; (c) The difference between the new baseline and the original baseline; (d) The profile of the new baseline and the original baseline of line B in figure (b); (e) The profile of the new baseline and the original baseline of line A in figure (b)



(a)



(b)

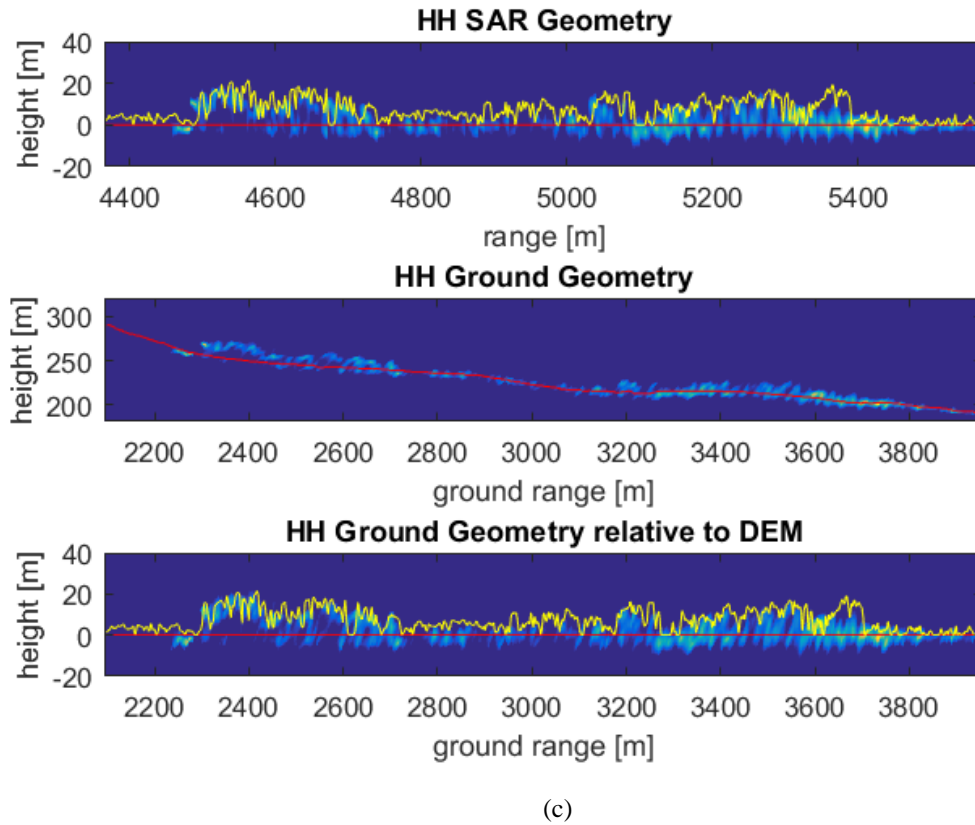


Figure 6.16 BioSAR 2008 L band data tomograms via the Capon method: (a) The BioSAR 2008 test site in Sweden and the L band SAR image (the grey colour of the figure is the average amplitude of all SAR SLC stacks, the unit is dB); (b) Tomograms via Capon (this is an adaptive beamforming Capon spectrum method (Capon, 1969)) based on common single baseline estimation, the red line is the DEM reference height and the yellow line is the LIDAR data; (c) Tomograms via Capon based on the pixel by pixel baselines, the red line is the DEM reference height and the yellow line is the LIDAR data

## 6.4 Deramping Results

As stated in the introduction in Chapter 5, in order to facilitate a high degree of focusing, it is necessary to correct the angular frequency in the NSR to the vicinity of zero frequency. This process is called deramping. The reference slant range used in the deramping can be the strong scattering centre distance of each image or the distance between the radar antenna phase centre of each image and a reference terrain (e.g. DEM). Although the removal of the slant range to the phase centre using the radar-recorded electromagnetic propagation delay is the most straightforward, we abandoned the direct deramping method based on the reference slant range because of the drawbacks introduced in Chapter 5. In this test, we used reference terrains - TanDEM 12 m data, which is directly used for deramping based on the Equation (5.41-5.45) in Chapter 5. In

this way, all TomoSAR height results are based on the TanDEM-X DEM 12 m surface. The TDX-DEM 12 m and SRTM 30 m are shown in Figure 6.3 (b) and (c) above. Work on the dam started on 29-03-2001 and it was completed on 30-09-2005, but the SRTM data were acquired in 2000. Therefore, the dam height difference is very clear in Figure 6.3 (d).

In this test, as SRTM 30 m cannot represent the real terrain for TomoSAR test, only the TanDEM-X DEM 12 m is used to correct the phase with the perpendicular baseline. Then, the FFT is used to test the azimuth line (Test-A) in the subarea of Zipingpu dam. The results are shown in Figure 6.17 (a) below; the colour, which is the inversion result, is the magnitude (intensity or amplitude) of the complex scattering coefficient  $\gamma(s)$  (see Section 5.1.1) along the height direction in the height-range plane, which is used to detect features along the height direction. It is easy to see, after using the TanDEM 12 m data, the stripe line (this line is the dam line, the stripe lines are caused by the ambiguity of the dam line, due to the perpendicular baseline sampling interval, shown in Equation (5.129) and (5.130) caused by the DEM and baseline) occurred in the dam area (at  $7.708$  to  $7.701 \times 10^5$  m in range). In addition, Capon is used to test the azimuth line (Test-A) in the subarea of the Zipingpu dam. The results are shown in Figure 6.17 (b) below; the colour, which is the inversion result, is also the magnitude (intensity or amplitude) of the complex scattering coefficient  $\gamma(s)$ , (see Section 5.1.1) along the height direction in the height-range plane, which is used to detect features along the height direction. The red line and its shape in the imaging result are used to represent the 3D structure in TomoSAR imaging in the height-range plane. Here, it represents the shape of the 3D terrain because the X-band signal has little penetration capability and this shape with the red line is the maximum position in the height direction; it usually shows the top of the 3D terrain. It is also easy to see, after using TanDEM 12 m data, that the tomogram is different in the dam area, and the dam area is almost flat (the standard deviation is 11.5 m, which is better than the standard deviation (24.5 m) of the tree area at  $7.7024$  to  $7.708 \times 10^5$  m in range) with some small bulges caused by DEM errors or other phase errors, which indicates the TanDEM-X DEM 12 m data can be directly used in the Capon TomoSAR method in the dam area.

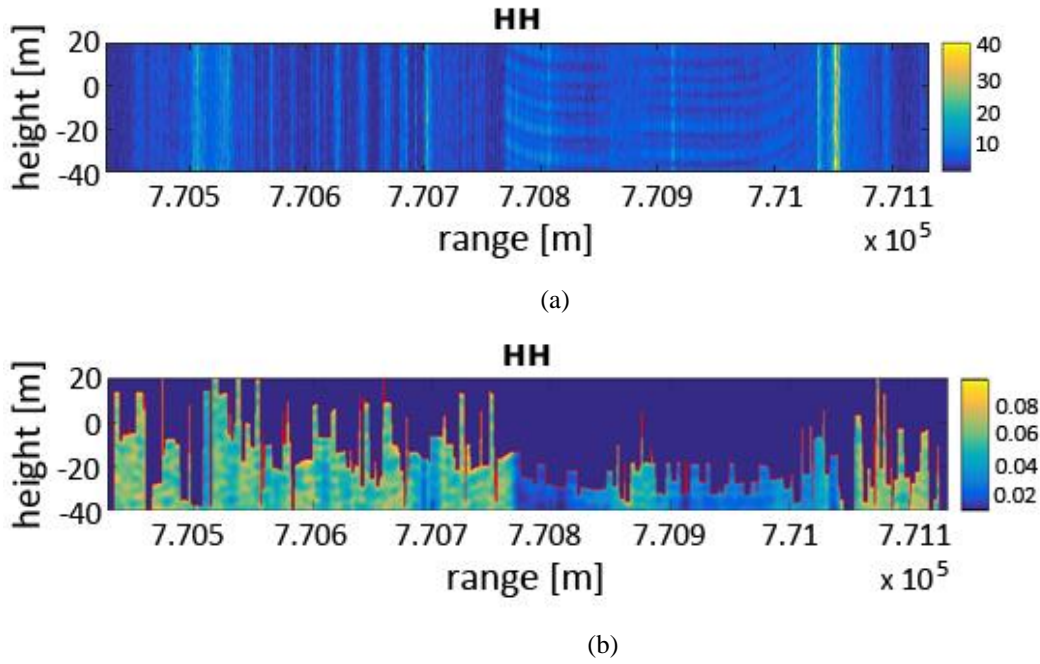


Figure 6.17 Tomograms results via FFT and Capon in Test-A after TanDEM-X DEM 12 m deramping: (a) Tomograms via FFT in Test-A, the colour is the magnitude (intensity or amplitude) of the complex scattering coefficient  $\gamma(s)$  along the height direction in the height-range plane; (b) Tomograms via Capon in Test-A, the colour is the normalization magnitude (intensity or amplitude) of the complex scattering coefficient  $\gamma(s)$  along the height direction in the height-range, the red top line represents the top of the 3D terrain from the Capon estimation results

## 6.5 Phase Calibration

Based on Chapter 4 and Chapter 5, the phase calibration methods are studied and tested in the Zipingpu dam Test-A area.

### 6.5.1 Atmospheric Correction and TomoSAR Results

In this test, atmospheric correction is applied to the phase calibration. The results are shown below. Based on Chapter 4 and Chapter 5, GACOS and ERA data were obtained to undertake atmosphere correction. Some data of GACOS and ERA atmospheric phase delay are shown in Figure 6.19 below. These figures show that the ERA data are related to the latest DEM and smoother, while the GACOS data use old SRTM data, which is not good enough and might cause errors (about 280-310 rad in phase delay errors, shown in Figure 6.19 (g)) in the dam area in the TomoSAR processing.

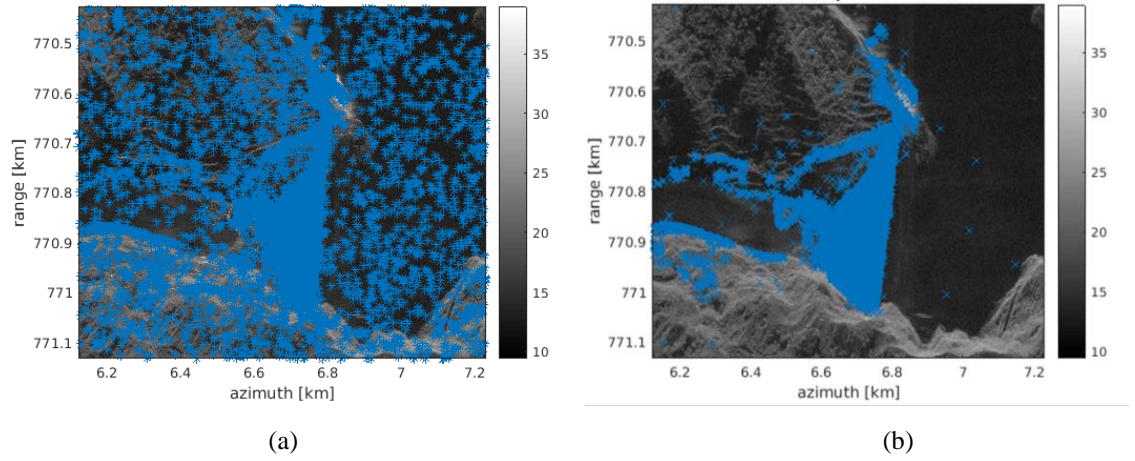
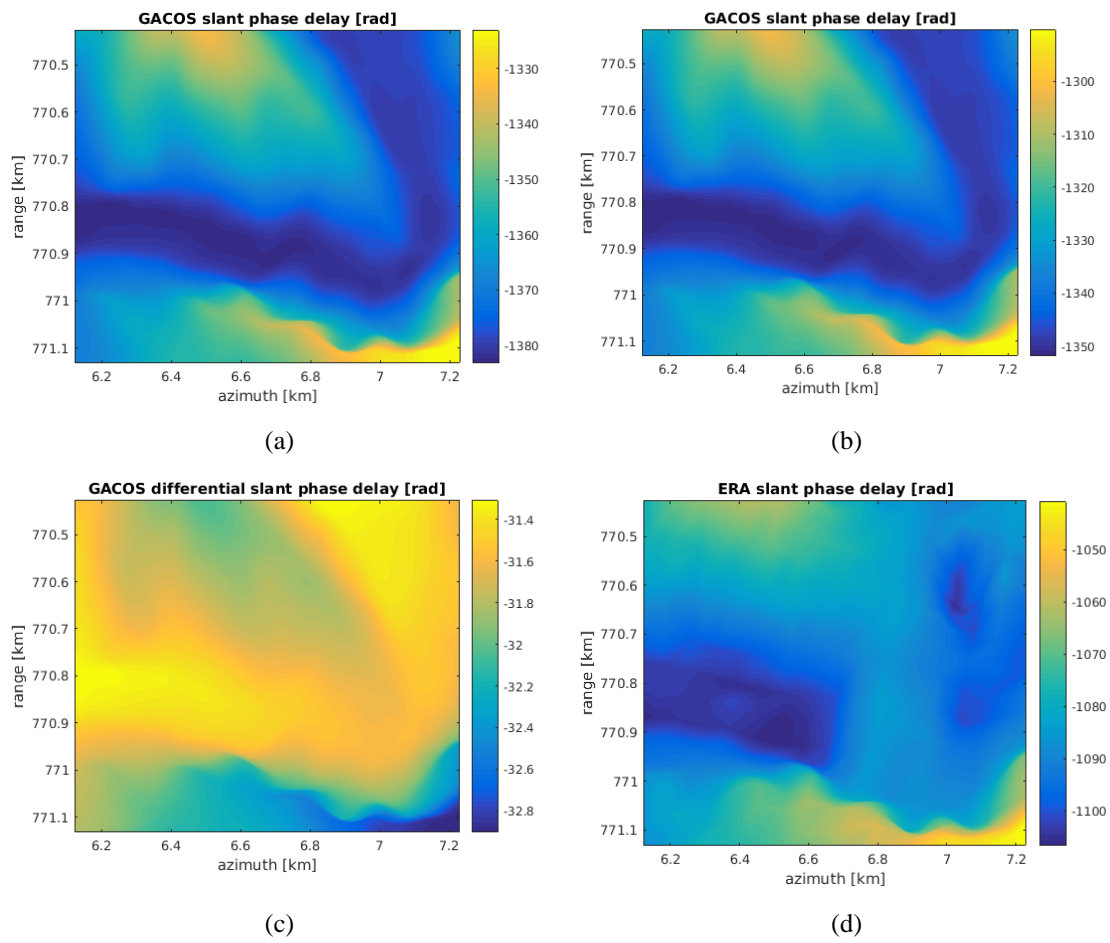


Figure 6.18 PS point for phase calibration: (a) Dispersion index  $\leq 0.4$ ; (b) Dispersion index  $\leq 0.2$





## Chapter 6. Application of TomoSAR to X-band

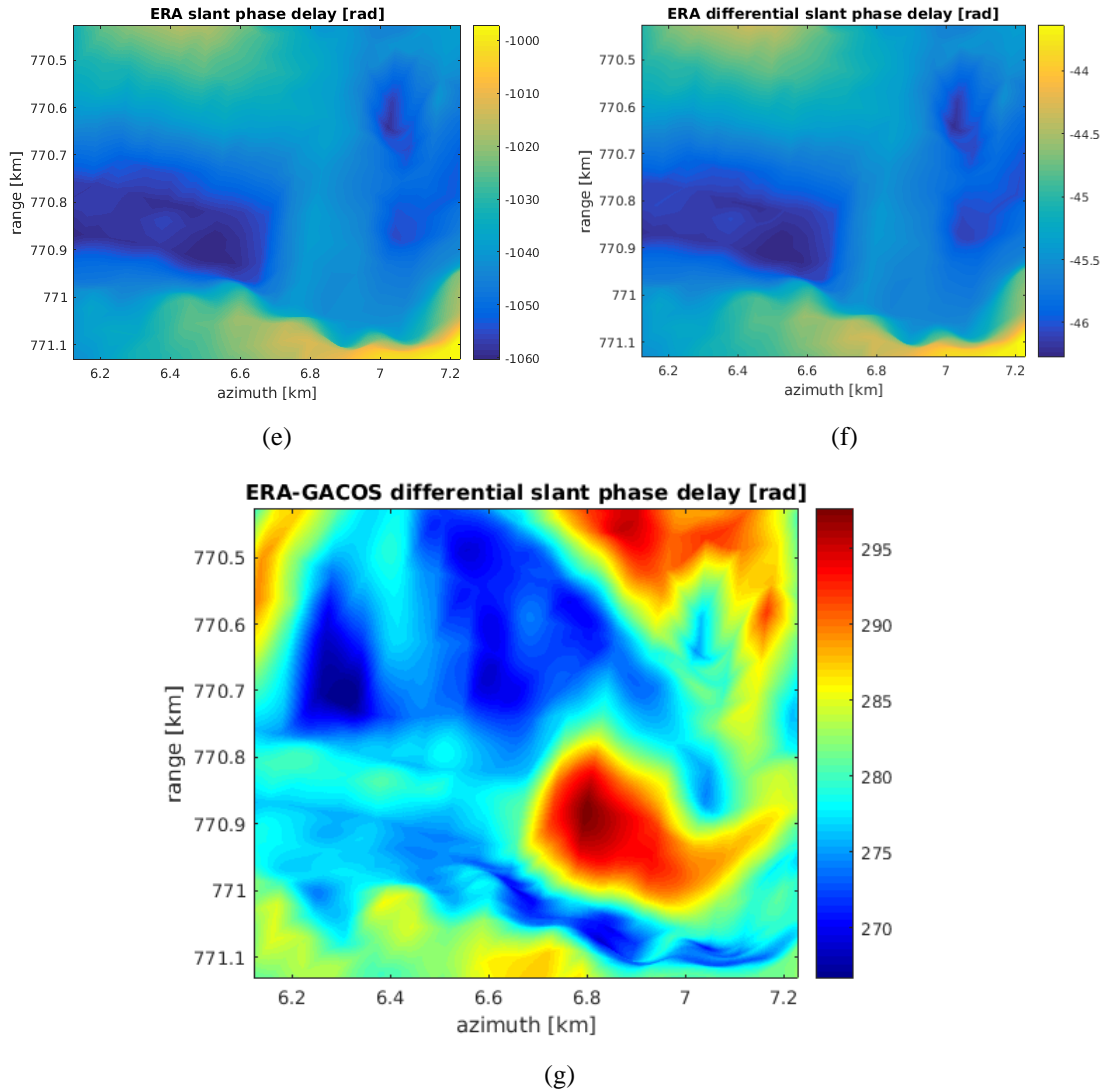


Figure 6.19 Comparison between the ERA and GACOS atmospheric phase delay: (a) GACOS atmospheric phase delay of 20160725; (b) GACOS atmospheric phase delay of 20160603; (c) GACOS differential atmospheric phase delay between 20160725 and 20160603; (d) ERA atmospheric phase delay of 20160725; (e) ERA atmospheric phase delay of 20160603; (f) The ERA differential atmospheric phase delay between 20160725 and 20160603; (g) The differential atmospheric phase delay between ERA and GACOS in 20160725

In the test, the ERA data were used in atmospheric correction after DEM deramping. The FFT result is shown in Figure 6.20 (a) below; the colour is also the magnitude (intensity or amplitude) of the complex scattering coefficient  $\gamma(s)$  along the height direction in the height-range plane. It is also easy to see, after using the TanDEM 12 m data and ERA data, the ambiguity stripe lines (dam line) caused by the DEM and baseline occur in the dam area. In addition, The Capon result is shown in Figure 6.20 (b) below; the colour is also the magnitude (intensity or amplitude) of the complex scattering coefficient  $\gamma(s)$  along the height direction in the height-range plane and the shape with



the red line is the maximum position in height direction, which is the top of the 3D terrain. Compared to Figure 6.17 (b), the dam area in Figure 6.20 (b) is more flat (the standard deviation is 8.72 m), which hints that the ERA data correction makes the result better. However, it still has some small bulges caused by DEM errors or other phase errors, which indicates that phase calibration (DEM errors and other phase errors) is needed.

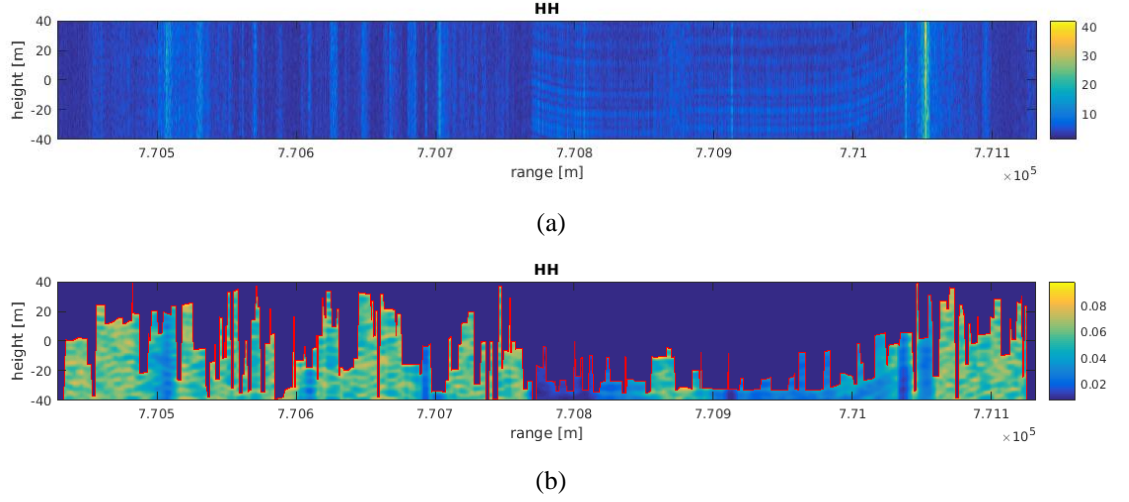


Figure 6.20 FFT and CAPON results: (a) Tomograms via FFT in Test-A, the colour is the magnitude (intensity or amplitude) of the complex scattering coefficient  $\gamma(s)$ ; (b) Tomograms via Capon in Test-A, the red line is the position of max scattering value, the colour is the normalization magnitude (intensity or amplitude) of the complex scattering coefficient  $\gamma(s)$

### 6.5.2 DEM Error Estimation for Phase Compensation

In Chapter 3, the DEM (SRTM 30 m or TanDEM 12 m) based co-registration is discussed. It is well known that, although the sub-pixel co-registration accuracy is achieved, and deramping is executed based on the DEM (SRTM 30 m or TanDEM 12 m), the DEM errors naturally exist because of the uncertainty of the DEM products (there is no true DEM data in the world). Therefore, the DEM error should be estimated and the DEM error compensation should be applied to TomoSAR processing.

As the DEM simulation phase is used, Equation (5.35) changes to Equation (6.2). The DEM phase error  $\varphi_{DEMerror}$  must be compensated for. Thus, TomoSAR processing should use the equations as below (all parameters are the same as in Chapter 5).

$$\varphi_m = -\frac{4\pi}{\lambda} [R - R_m(0)] = \varphi_{simu\_m} + \varphi_{DEMerror} \quad (6.1)$$

## Chapter 6. Application of TomoSAR to X-band

$$I_{flattening}(m) = p(\xi_m) = \exp(j \cdot \varphi_m) \cdot Q(m) \quad (6.2)$$

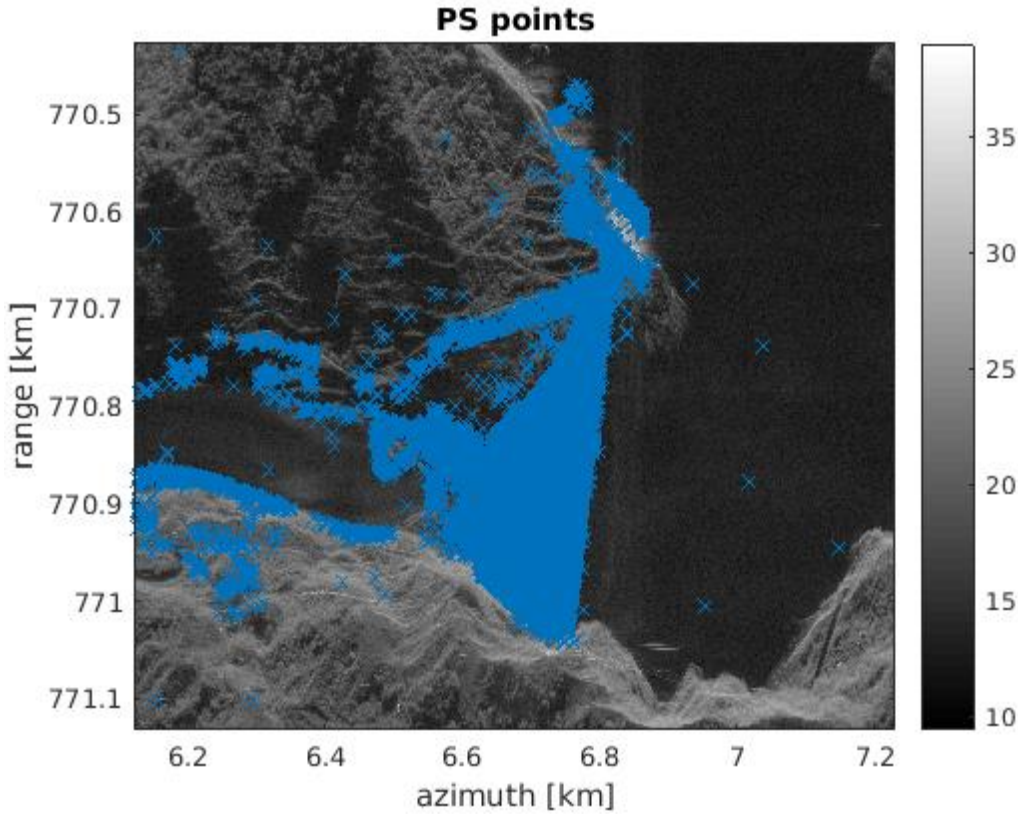
$$\begin{aligned} &= \exp(j \cdot \varphi_{simu\_m} + j \cdot \varphi_{DEMerror}) \cdot Q(m) \\ &= \int_{s_{min}}^{s_{max}} \exp\left(-j \frac{4\pi}{\lambda} R\right) \gamma(s) \exp(j2\pi\xi_m s) ds \end{aligned}$$

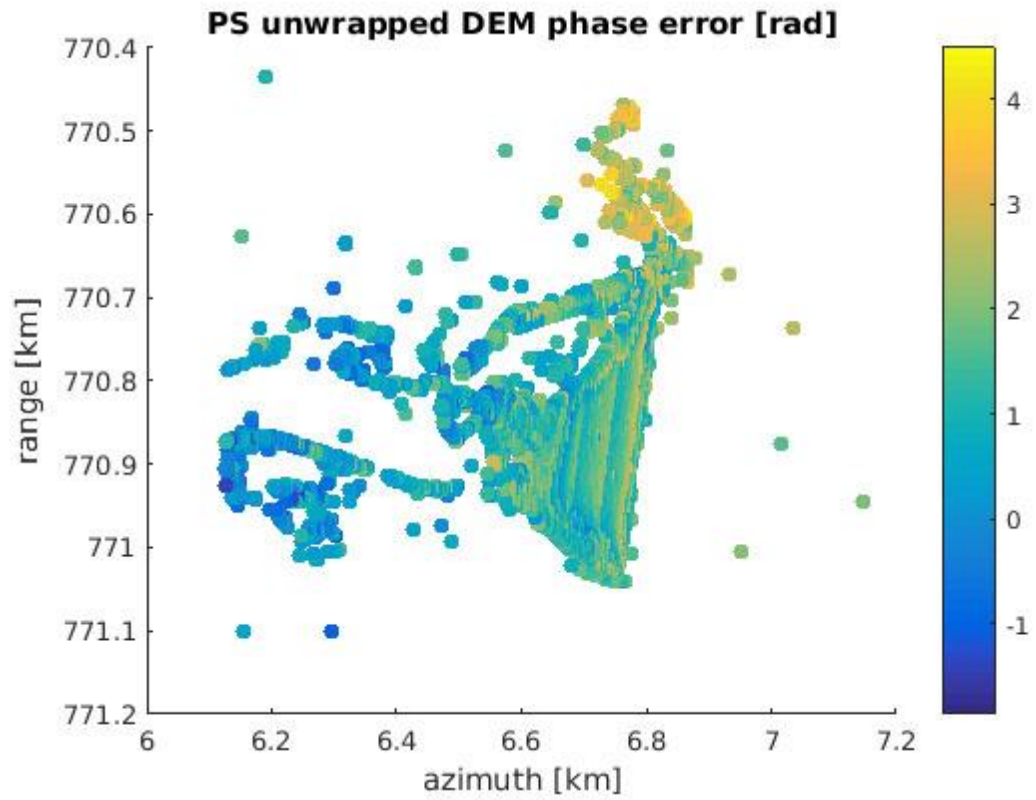
$$\gamma'(s) = \exp\left(-j \frac{4\pi}{\lambda} R\right) \gamma(s) \quad (6.3)$$

$$I_{flattening}(m) = p(\xi_m) = \int_{s_{min}}^{s_{max}} \gamma'(s) \exp(j2\pi\xi_m s) ds \quad (6.4)$$

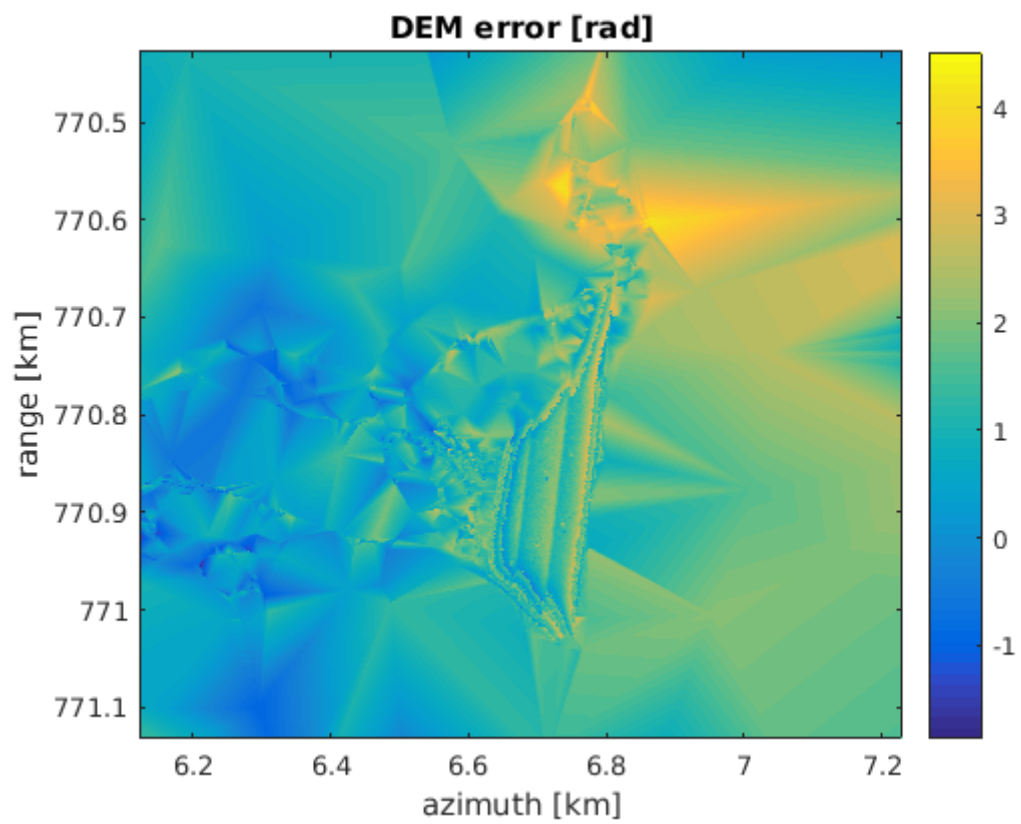
$$\xi_m = 2b_{\perp m}/\lambda r \quad (6.5)$$

In our test, the PS method is investigated. After PS-InSAR, the DEM errors of each PS point have been estimated. Then, the DEM error of the whole image can be obtained by interpolation. The DEM error map via PS-InSAR is shown in Figure 6.21 below. After the DEM errors are estimated, the phase of this DEM error will be compensated via simple phase addition and subtraction for TomoSAR processing.





(b)



(c)

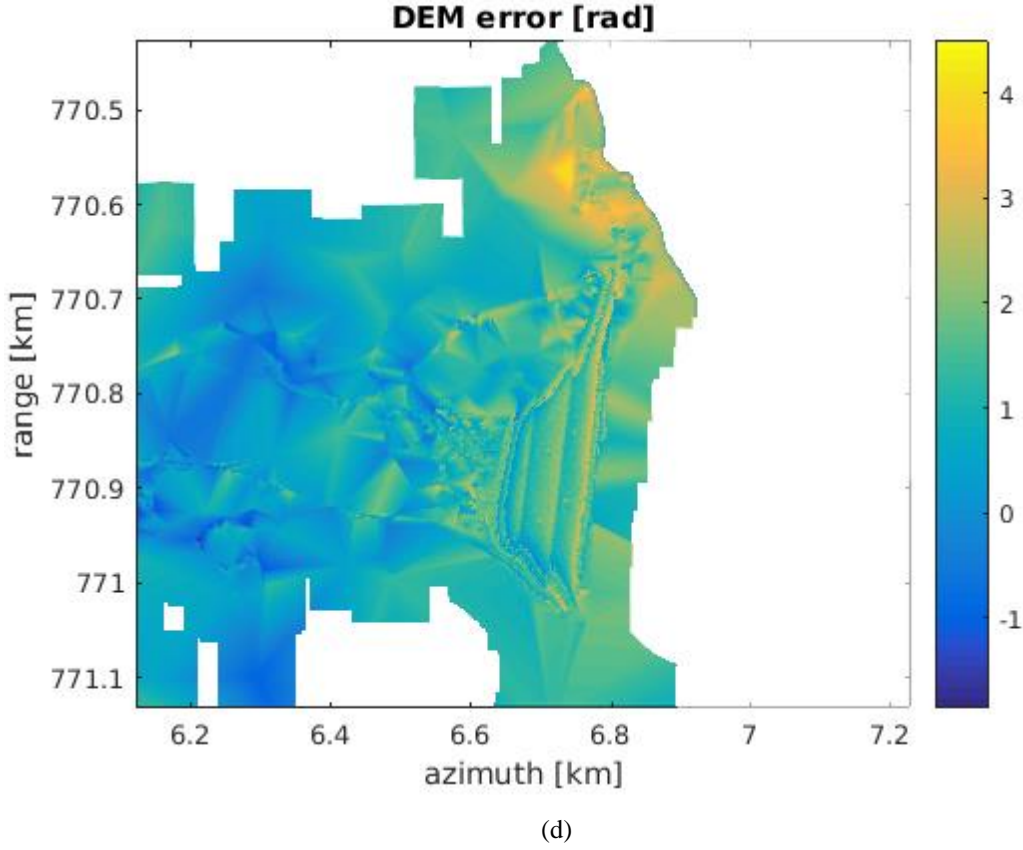


Figure 6.21 DEM error maps in the dam area, this plot (c) shows the DEM errors in each pixel of the test area: (a) The PS points using PS-InSAR in the test area; (b) The unwrapped phase of DEM error map at the PS points (20160603); (c) The unwrapped phase of DEM error map via PS-InSAR (20160603); (d) The unwrapped phase of the DEM error map via PS-InSAR (20160603), the river and no PS point in 100 m range are masked

### 6.5.3 PS-SVD-PGA-LS-ME Phase Calibration

As is well known, the SLC complex data have errors, which include an atmospheric error (atmosphere and ionosphere), orbit error, deformation (linear and nonlinear) and noise. The real complex data  $Q_{m\_real}$  can be written as an ideal complex data  $Q_{m\_ideal}$  plus all of the error phase  $\phi_e$ .

$$Q_{m\_real} = Q_{m\_ideal} \exp(j \cdot \phi_e) \quad (6.6)$$

After applying the above DEM error compensation and atmospheric correction, there are still errors and the residual error caused by the uncertainty of correction steps (atmosphere data) needs calibration. The  $I_{flattening}(m)$  in Equation (5.41) becomes  $I_{flattening\_ideal}(m)$ , while the  $I_{flattening\_real}(m)$  is the real flattening SLC data using external DEM and without atmospheric correction. In this way, the TomoSAR processing equations (Equation (5.41), (5.42), (5.43), (5.44) and (5.45)) become as below.

$$I_{flattening\_real}(m) = I_{flattening\_ideal}(m) \exp(j \cdot \phi_e) \quad (6.7)$$

$$\gamma'(s) = \exp\left(-j \frac{4\pi}{\lambda} r\right) \gamma(s) \quad (6.8)$$

$$p(\xi_m) = \int_{s_{min}}^{s_{max}} \gamma'(s) \exp(j2\pi\xi_m s) ds \quad (6.9)$$

$$I_{flattening\_ideal}(m) = I_{flattening\_real}(m) \exp(-j \cdot \phi_e) = p(\xi_m) \quad (6.10)$$

$$= \int_{s_{min}}^{s_{max}} \gamma'(s) \exp(j2\pi\xi_m s) ds$$

$$\xi_m = 2b_{\perp m}/\lambda r \quad (6.11)$$

Then, we used our new PS-SVD-PGA-LS-ME combined method to do the phase calibration. The data were split into tiles for processing. The PS points, shown in Figure 6.18, were selected first based on a dispersion index, which is the ratio of the amplitude standard deviation to the mean amplitude (Ferretti et al., 2001c) (in our test, we set a smaller dispersion index = 0.2 for robust estimation) and then the singular-value decomposition (SVD) method was used to estimate the phase scattering centre  $s_0$  (the PGA algorithm solves for a single strong scatterer at height 0 along the NSR direction, see Section 5.3.2. If the position of the strong scatterer is  $s_0$ , the linear phase  $2\pi\xi_m s_0$  should be removed first, see Equation (5.80)) of each PS point. Then, the phase of each point was corrected based on  $s_0$ . Moreover, the variance was calculated using the complex value of the SAR image and the least squares-PGA method was used to estimate the phase errors by using all of the PS points in each tile. Finally, the phase calibration was executed in each tile and the minimum entropy method was used to refine the estimated SAR phase error at each point  $(x, y)$  for the whole image.

## 6.6 Phase Calibration Results

### 6.6.1 DEM Error Compensation and Atmospheric Calibration

In this test, the DEM error compensation and ERA atmospheric correction are combined for the phase calibration. The FFT and Capon results are shown in Figure 6.22 below. Compared to the results in Figure 6.17 and Figure 6.20, the same dam area in the yellow box of Figure 6.22 is more flat (the standard deviation is 4.7 m) after correction, which indicates that the results are better and this correction works. The combined phase calibration method minimises all errors except for the noises (like thermal or other

## Chapter 6. Application of TomoSAR to X-band

residual noise). Therefore, it is ready for TomoSAR reconstruction with a noise nonsensitive algorithm.

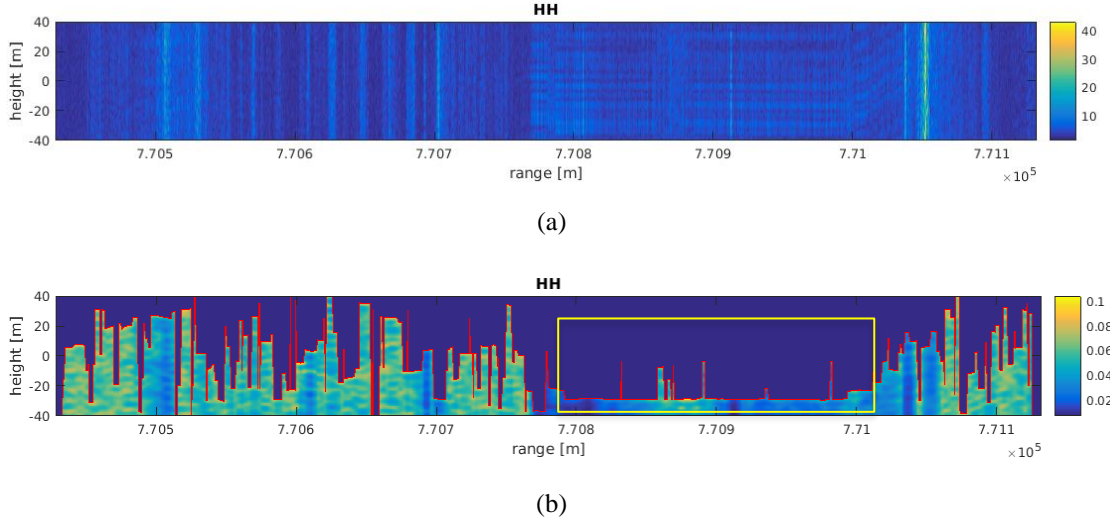
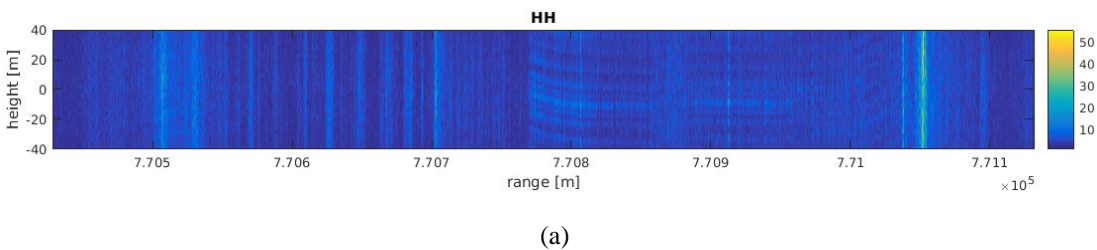


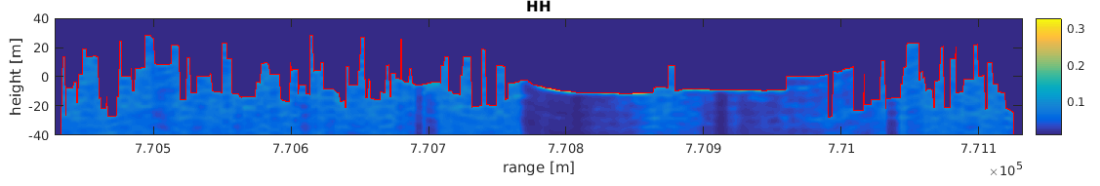
Figure 6.22 FFT and Capon results: (a) Tomograms via FFT in Test-A, the colour is the magnitude (intensity or amplitude) of the complex scattering coefficient  $\gamma(s)$ ; (b) Tomograms via Capon in Test-A, the dam area in the yellow box is very flat, the colour is the normalisation magnitude (intensity or amplitude) of the complex scattering coefficient  $\gamma(s)$

### 6.6.2 DEM Error, Atmospheric and PS-SVD-PGA-LS-ME Calibration

In this test, the DEM error compensation, atmospheric correction, PS-SVD-PGA, weighted least squares and minimum entropy (ME) (Pardini et al., 2014; Pardini et al., 2012) calibration are combined for the phase calibration. The results are shown in Figure 6.23 below. In contrast to the results in Figure 6.17, Figure 6.20 and Figure 6.22, the dam area in Figure 6.23 is more flat (the standard deviation is 4 m) after correction and it almost has no small bulge (one jump is shown, this is caused by the small feature of the dam, shown in the SAR image in Figure 6.2), which indicates that this correction works. Also, compared to Figure 6.22, the combined phase calibration method minimises all errors in Figure 6.23. Therefore, it is ready for TomoSAR reconstruction.







(b)

Figure 6.23 FFT and Capon results: (a) The tomograms via FFT in Test-A, the colour is the magnitude (intensity or amplitude) of the complex scattering coefficient  $\gamma(s)$ ; (b) The tomograms via Capon in Test-A, the colour is the normalisation magnitude (intensity or amplitude) of the complex scattering coefficient  $\gamma(s)$

### 6.6.3 SAR Interferometry Phase Calibration Reference to DEM

Another method to correct the phase error is using the SAR interferometry phase, which is detailed in Section 5.3.4. After InSAR phase calibration, the height reference is based on the strong scattering centre after InSAR calibration (InSAR height is at the strong scattering centre in the height direction), and the real height reference cannot be known after this method. If geocoding is needed, then control points are needed, or the result can be referenced to the DEM data after DEM error estimation and DEM error compensation. After PS-InSAR, the DEM error is obtained. Therefore, the DEM error is used to convert the unknown strong scattering centre to DEM data as the reference. After this phase calibration, the data are ready for super-resolution reconstruction via Capon and compressive sensing (CS).

In the Test-A area, the results are shown below the SAR interferometry phase (InSAR) and DEM phase error is used for phase calibration. A strong scattering line (InSAR strong scattering centre, it is the top of the 3D terrain for the X band because of its low penetration capability) is shown in the figures below, which indicates that the phase calibration method works. In the FFT results below, there are some ambiguity lines (repeat ghost targets), this repeat ghost line (shadow line) is caused by the ambiguity of the targets (the red line in Figure 6.24 (a) is the position of the potential detected targets for the X band SAR data) (see Equation (5.130)), the unambiguous image range), because the resolution of the FFT method is very low (see Equation (5.129)). Therefore, super-resolution methods, like compressive sensing (CS), are needed for TomoSAR imaging.

## Chapter 6. Application of TomoSAR to X-band

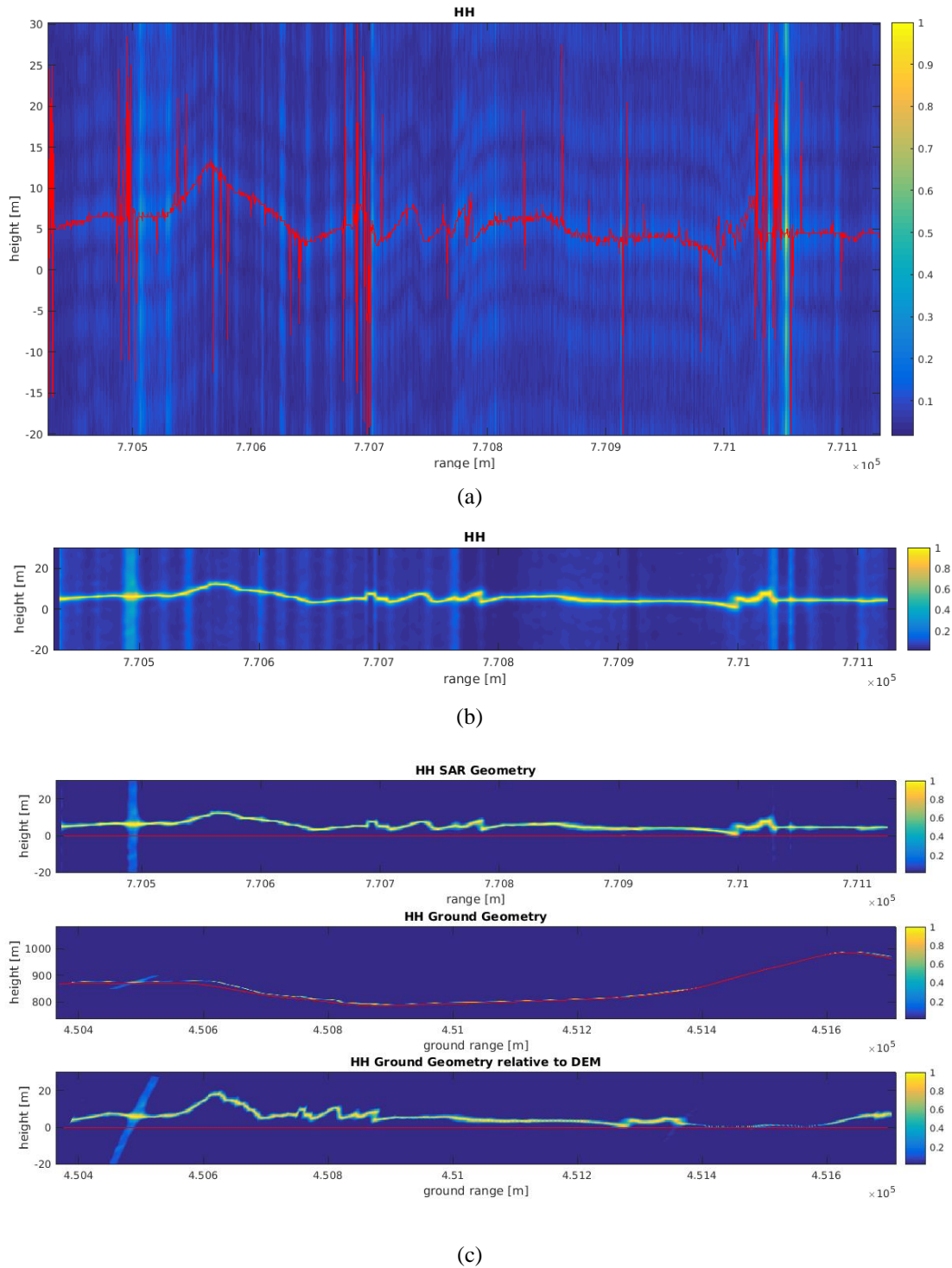


Figure 6.24 FFT and Capon results: (a) Tomograms via FFT in Test-A, the red line is the position of max scattering value, the colour is the normalisation magnitude (intensity or amplitude) of the complex scattering coefficient  $\gamma(s)$ ; (b) Tomograms via Capon in Test-A, the colour is the normalization magnitude (intensity or amplitude) of the complex scattering coefficient  $\gamma(s)$ ; (c) Geocoded tomograms via Capon in Test-A, the colour is the normalisation magnitude (intensity or amplitude) of the complex scattering coefficient  $\gamma(s)$



The Capon method is a mid-resolution reconstruction method (compared to CS used for high resolution sparse reconstruction) which aims to minimise spatial perturbations and sidelobes. In the Capon results, shown above, there are no ambiguity lines and the strong scattering centre line is clear, which indicates that the phase calibration method works. In addition, there is limited penetration in the tree area (at  $7.705\text{-}7.707 \times 105$  m in the range) because of the X band and it is a single line in the dam area because of the strong backscatters of the dam.

From these tests conducted in the mountainous tree areas with FFT and Capon (shown above), we conclude that the X band is not suitable for 3D tomographic forest mapping. Moreover, FFT and Capon can obtain inversion results with the X band data in the forest and dam areas, but it is usually at the top of the canopy. However, the X band can be used for the dam and building reconstruction.

## 6.7 TomoSAR Imaging Results

This section describes the spaceborne X-band data simulation test with the compressive sensing method first; then, a real test in Zipingpu dam Test-A area is studied using the compressive sensing method. After that, the test is executed in the Zipingpu dam area, and the TomoSAR results in the Zipingpu dam area using the compressive sensing method are shown. Finally, the fieldwork in Zipingpu dam for the validation of the TomoSAR results and discussion are presented.

### 6.7.1 Compressive Sensing (CS)

#### 6.7.1.1 *Simulation targets and tests with the CS method*

The simulation is executed based on the SAR tomography compressive sensing imaging algorithm introduced in Chapter 5. To check the CS algorithm for the COSMO-SkyMed 1-metre data, the simulation parameters are selected as almost the same as the COSMO-SkyMed X-band satellite. The simulation parameters are shown in Table 6.2 below. The centre radar frequency is 9.60 GHz for the X band; the pulse bandwidth determines the 1-metre range resolution and the measurements are set as 14. The acquisition geometry is shown in Figure 6.25; the orbital altitude is 619 km and the inclination angle is 37.77 degrees. The perpendicular baseline between the two satellites is selected from 200 to 400 metres (height ambiguity is 30-240 m based on Equation

## Chapter 6. Application of TomoSAR to X-band

(5.130)) randomly to simulate the real satellite baseline, shown in Figure 6.27. The topography and the two targets in the ground coordinate system are shown in Figure 6.26; the two simulation targets are at 15 m and 35 m in the vertical direction. The SLC data are simulated directly based on the range and complex reflectivity (the equation is shown in (5.21)), and the complex reflectivity has a random normal distribution value.

Table 6.2 Simulation parameters

Parameters	Value
Radar sensor	X-band
Radar frequency	9.60 GHz
Range resolution (Light velocity/2/ Bandwidth)	1 m
Pulse bandwidth	150 MHz
Orbital altitude	619 km
Number of flights (Measurements)	14
Inclination angle	37.77 degrees

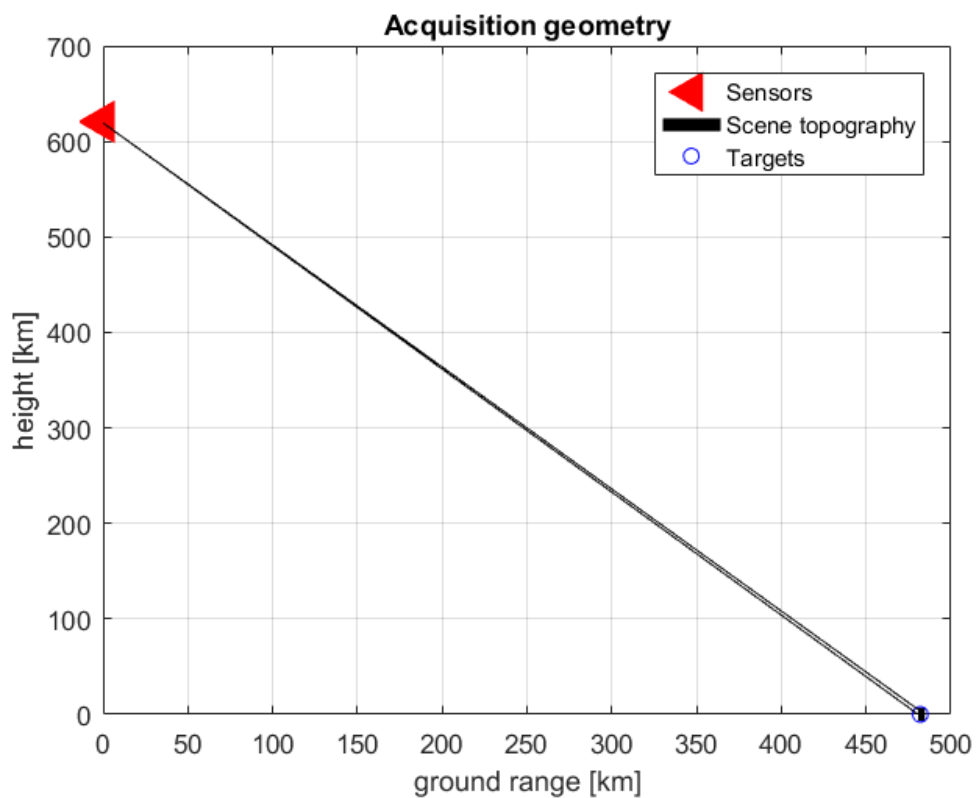


Figure 6.25 Acquisition geometry of the simulation

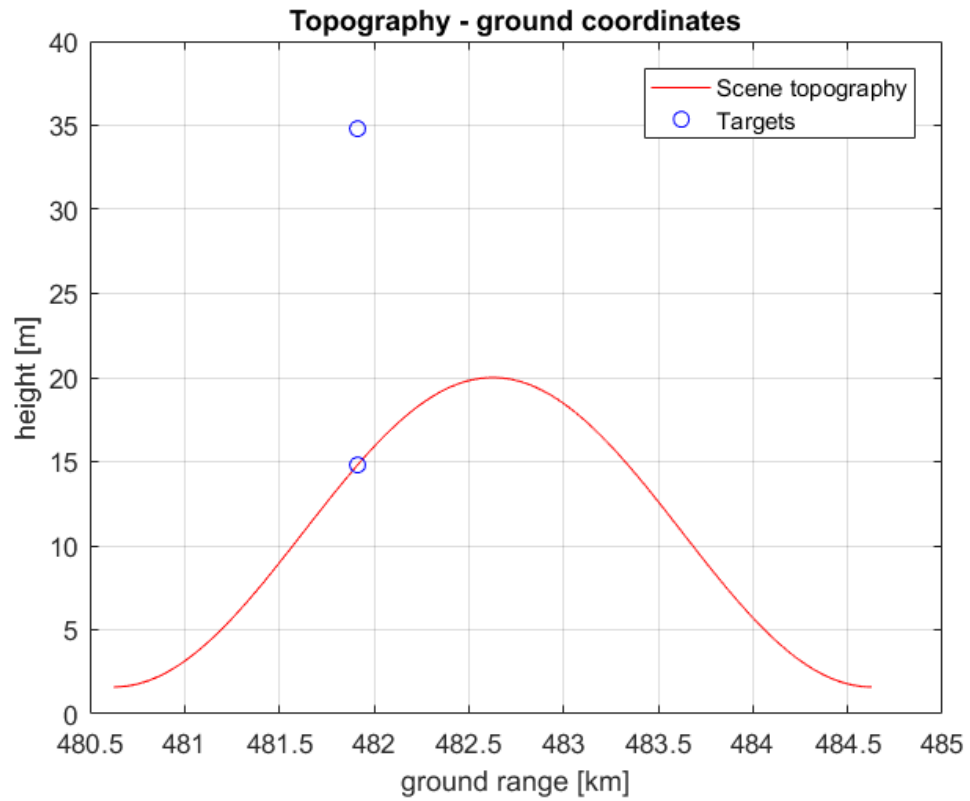


Figure 6.26 Topography and targets in the ground coordinate system, the simulation targets are at 15 m and 35 m in the vertical direction

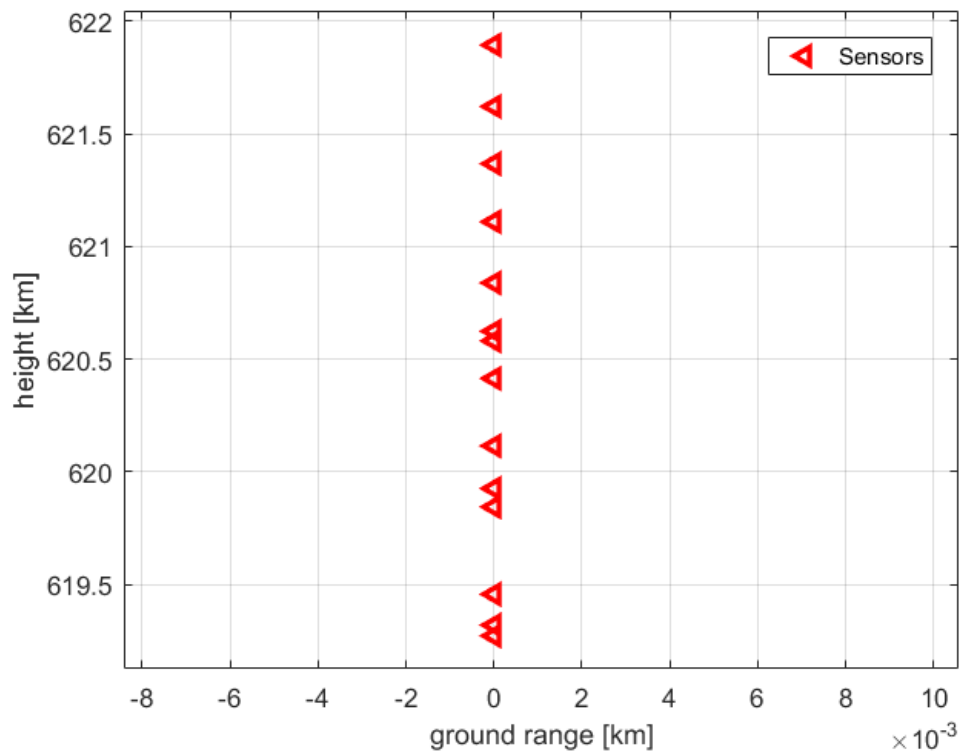


Figure 6.27 The position of the SAR sensors of the 14 measurements. The perpendicular baseline is 50-400 m (height ambiguity is 30-240 m)

## Chapter 6. Application of TomoSAR to X-band

The model used in SAR tomography compressive sensing imaging is based on Equation (5.136) and Equation (5.149) in Section 5.4.2 and 5.4.3. The simulated amplitude of the measured SAR SLC signal is shown in Figure 6.28 (a) and Figure 6.29 (a) below. After the CS method, we get inversion results that the two targets are at 0 m and 20 m, shown in Figure 6.28 (b) and Figure 6.29 (b). The simulation targets are set at 15 m and 35 m in the vertical direction (compared to Figure 6.26), but the topography is used for deramping based on Equation (5.41-5.45) in Chapter 5, which means that the inversion results are based on the topography as the reference. Therefore, the inversion results should be at 0 m and 20 m, which are right, as shown in Figure 6.28 (b) and Figure 6.29 (b).

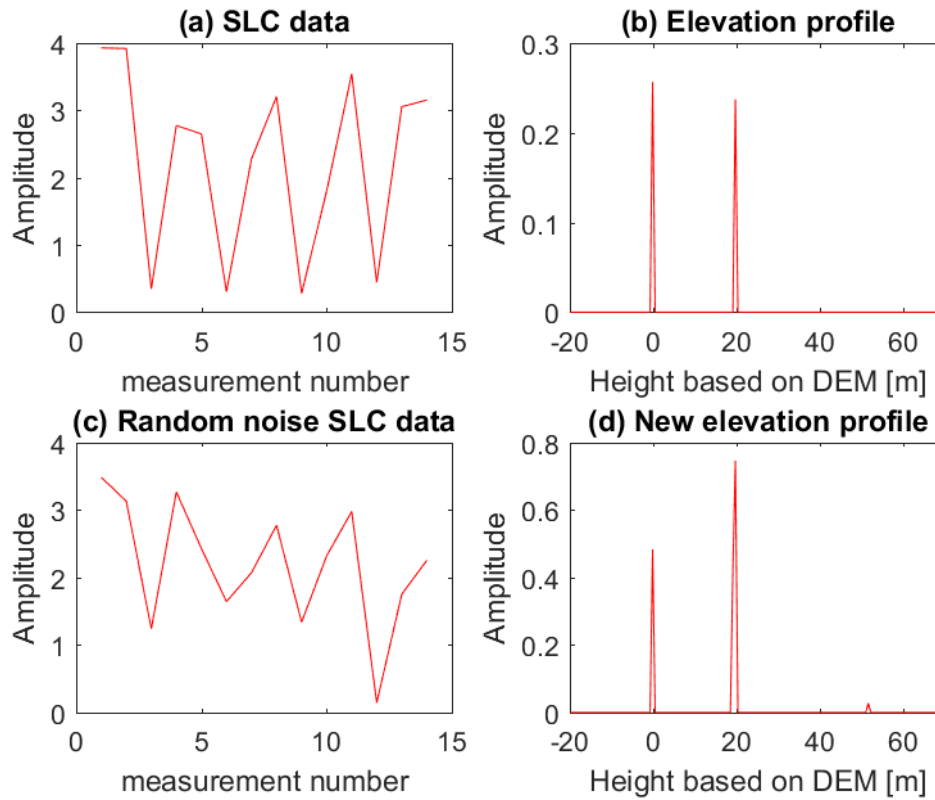


Figure 6.28 The SAR measurement signal with random noise and their CS inversion results

Then, the normally distributed random noise is added to the measurement signals, shown in Figure 6.28 (c). After the CS method, we get the inversion results, which are similar to the targets shown in Figure 6.28 (d). Compared to Figure 6.28 (b), the two targets are clearly shown in Figure 6.28 (d) and a false target occurs at the position of 50 m. However, it can be eliminated by post-processing. Moreover, a -3db (SNR) white

Gaussian noise is added to the measurement signals, shown in Figure 6.29 (c). After the CS method, we get the inversion results, which are also similar to the targets, shown in Figure 6.29 (d). Compared to Figure 6.29 (b), the two targets are clearly shown in Figure 6.29 (d), although the amplitude is different. After this, we need to use post-processing methods to refine and select the targets, such as the constant false alarm rate (CFAR) (Anitori et al., 2012; Bandiera et al., 2007) in radar. Actually, the post-processing method is an improved CFAR method for our application. First, the standard deviation of the amplitudes is calculated and the peaks of the amplitudes are found along the height direction; then, if the amplitudes of the peaks are larger than three times of the standard deviation, they are selected as targets. Thus, these simulations above demonstrate that the SAR tomography compressive sensing algorithm can be used for 3D imaging and reconstruction.

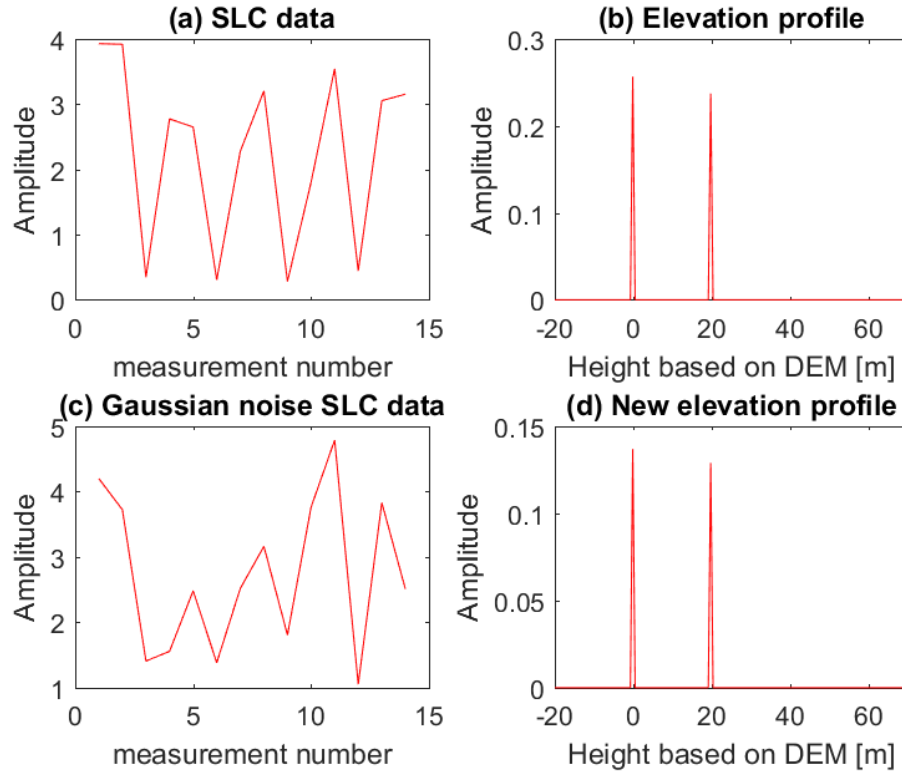


Figure 6.29 The SAR measurement signal with added white Gaussian noise and their CS inversion results

### 6.7.1.2 The real TOMOSAR test results in Test-A area

The results using our CS-TomoSAR and CFAR method of one pixel of the Test-A area after InSAR calibration and DEM referenced correction are shown in Figure 6.30 below, where the red curve line in the figure is the amplitude of the complex scattering

## Chapter 6. Application of TomoSAR to X-band

coefficient  $\gamma(s)$  along the height direction of this pixel. Based on the theory and equation in Chapter 5 and the simulation demonstration, the relatively high peaks (larger than three times of the standard deviation) are our targets. The noise can be easily seen along height direction in these results, so the improved CFAR method is needed to refine and select the targets

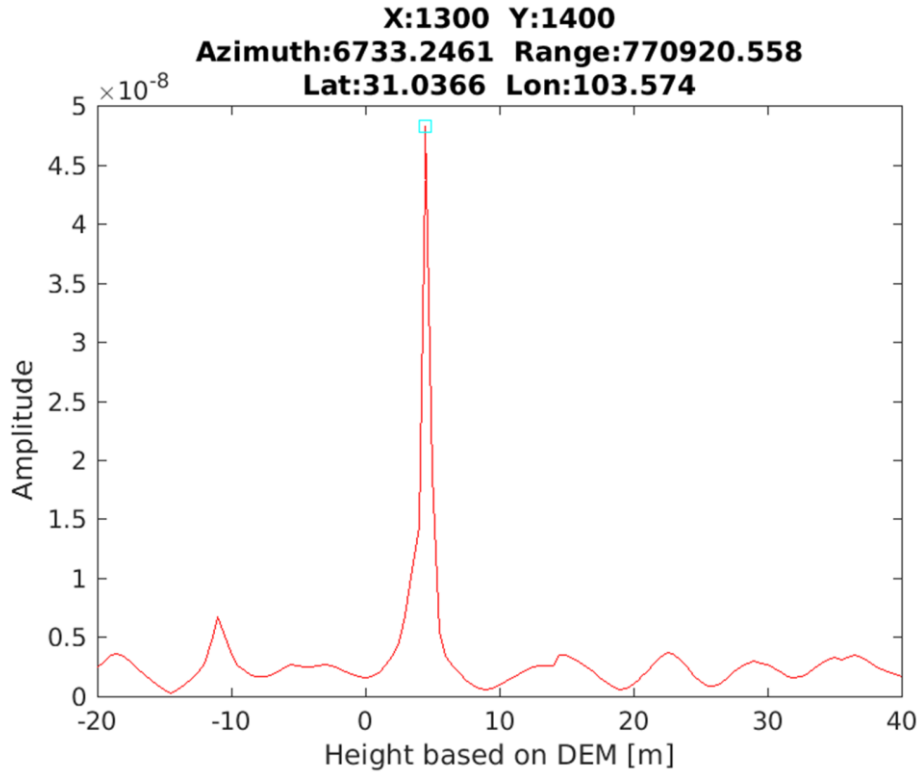


Figure 6.30 TomoSAR results of Test-A, the red curve line is the amplitude of the complex scattering coefficient  $\gamma(s)$  along the height direction, the highest peak is the detected targets in this pixel, the coordinates of this pixel are shown at the top of this figure

The results via CS of the Test-A area after DEM error compensation and atmospheric correction calibration (see Section 6.6.1) are shown in Figure 6.31 below. As the X band has little penetration capability, the results show high penetration capabilities, hinting that there are still some errors above the strong scattering line, which might be caused by phase error and noise.

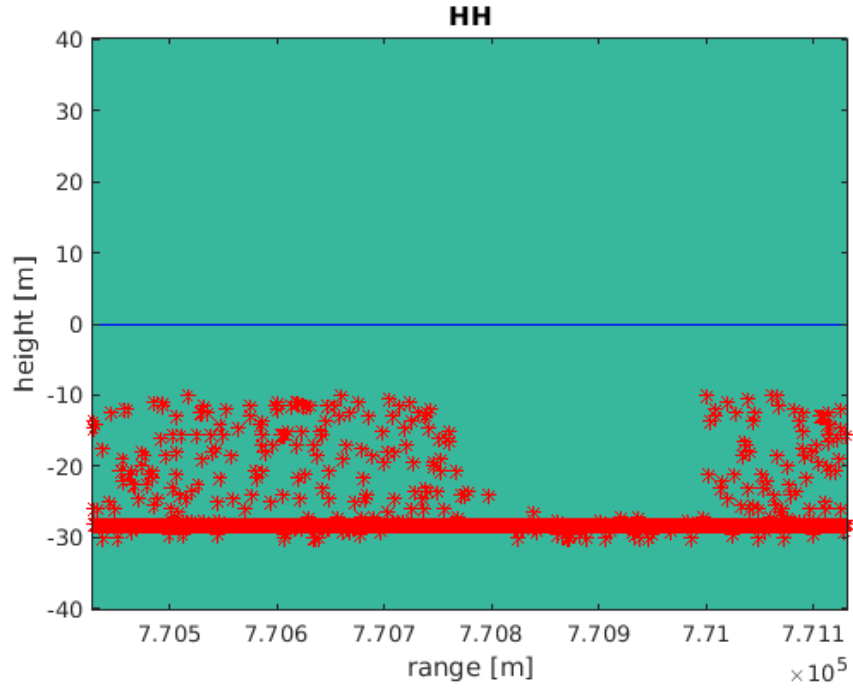


Figure 6.31 Tomograms via CS in Test-A after DEM error compensation and atmospheric correction calibration, the strong scattering line is the surface line, the dam area is clear at  $7.708$  to  $7.701 \times 10^5$  m in range, there are still some errors above the strong scattering line

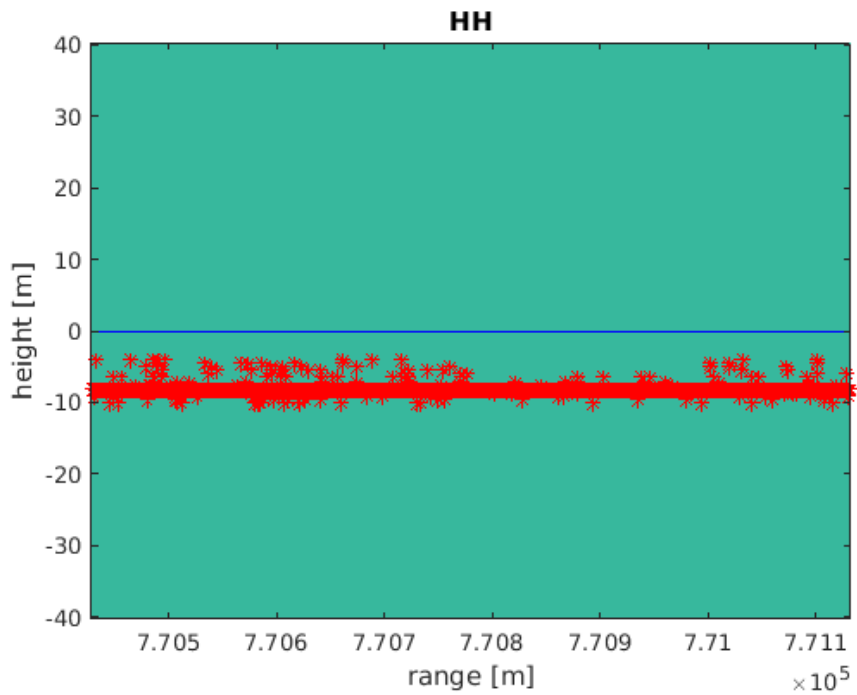


Figure 6.32 Tomograms via CS in Test-A after DEM error compensation, atmospheric correction, PS-SVD-PGA, weighted least squares and minimum entropy calibration, the strong scattering line is the surface line, the dam area is clear at  $7.708$  to  $7.701 \times 10^5$  m in range, there are still some errors above the strong scattering line

## Chapter 6. Application of TomoSAR to X-band

The results via the CS method of Test-A area after DEM error compensation, atmospheric correction, PS-SVD-PGA, weighted least squares and minimum entropy calibration (see Section 6.6.2) are shown in Figure 6.32 above. Compared to the results in Figure 6.31, the results in Figure 6.32 show that errors above the strong scattering line are minimised after my phase calibration method, which demonstrates that PS-SVD-PGA, weighted least squares and minimum entropy calibration method works. However, there are still errors caused by phase errors, which need to be eliminated by post-processing (check the strong scattering line and filter for the X band inversions). Also, the control points are needed for geocoding.

The results via CS and the improved CFAR method of the Test-A area after the InSAR phase calibration is shown in Figure 6.33 below. It is easy to see that a strong scattering line at 0 m (corresponding to the real strong scattering height position for X band, the position, which is the phase centre, cannot be known in this method) is shown in the figures below, and there are many targets around it. There is limited penetration in the tree area (at  $7.705\text{--}7.707 \times 10^5$  m in the range) and only one line can be seen here because the X band cannot penetrate the trees. Similarly, it is just one line in the dam area which is caused by the strong backscatters of the dam itself.

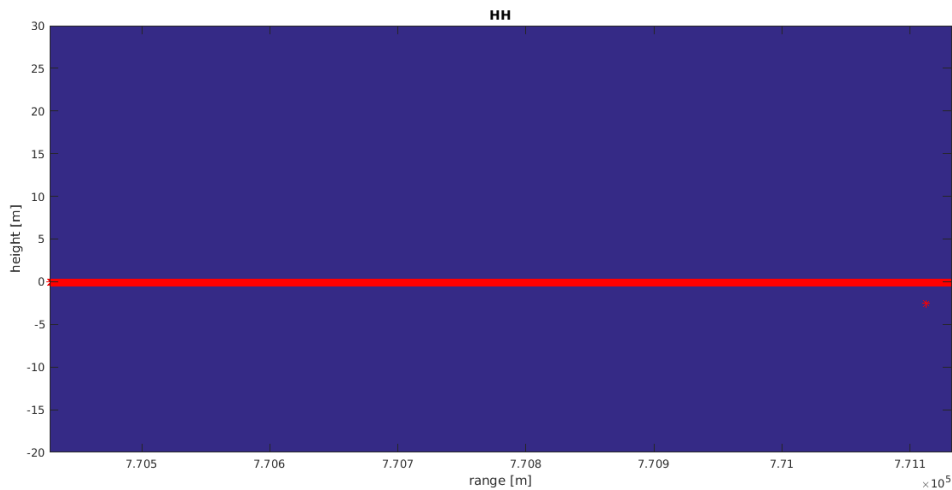


Figure 6.33 Tomograms via CS in Test-A after error elimination

The results (0.5 m resolution) via CS of Test-A area after InSAR phase calibration and DEM reference correction is shown in Figure 6.34 below. All results are referenced to DEM elevation, which can be used for geocoding. After CS imaging, the errors are filtered and the targets are selected by an improved CFAR method for our application. First, the standard deviation is calculated, and all peaks are found along the height



direction; then, if the amplitudes of the peaks are larger than three times of the standard deviation, they are selected as targets. Compared to the Capon method used above, the height resolution is improved, that is why compressive sensing (CS) is called a super-resolution reconstruction method for TomoSAR imaging. Moreover, the results show a strong scattering curve line and there are only a few targets around it, which indicates that the X band data could hardly penetrate the trees.

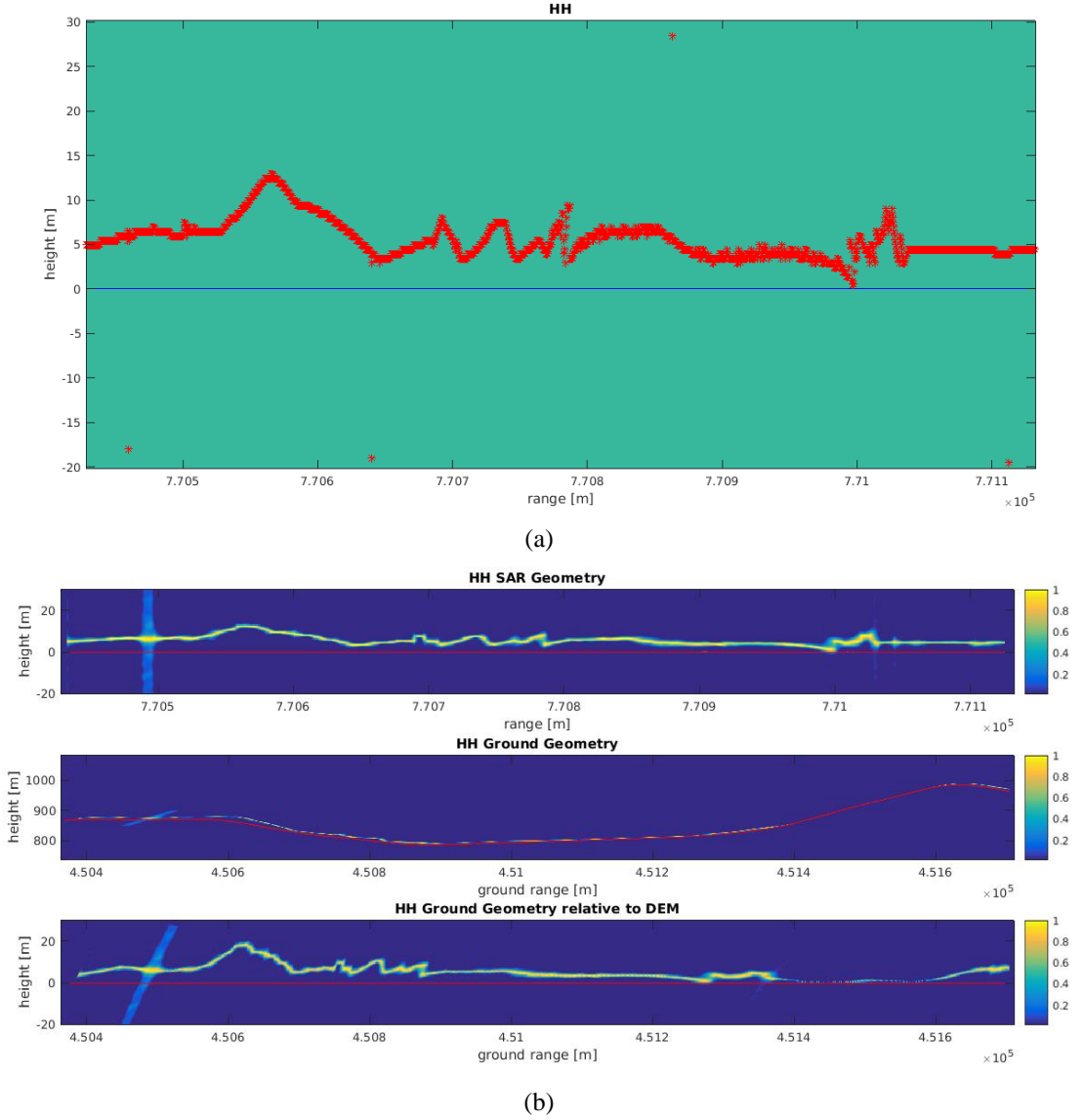
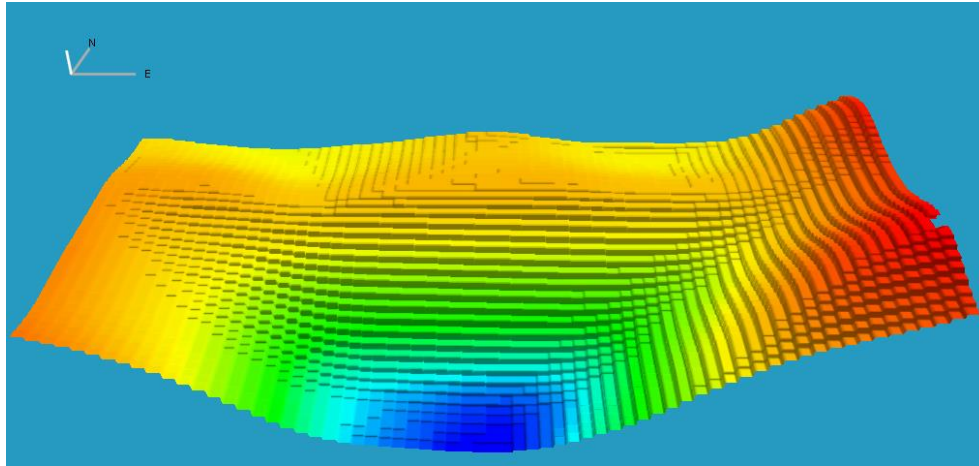
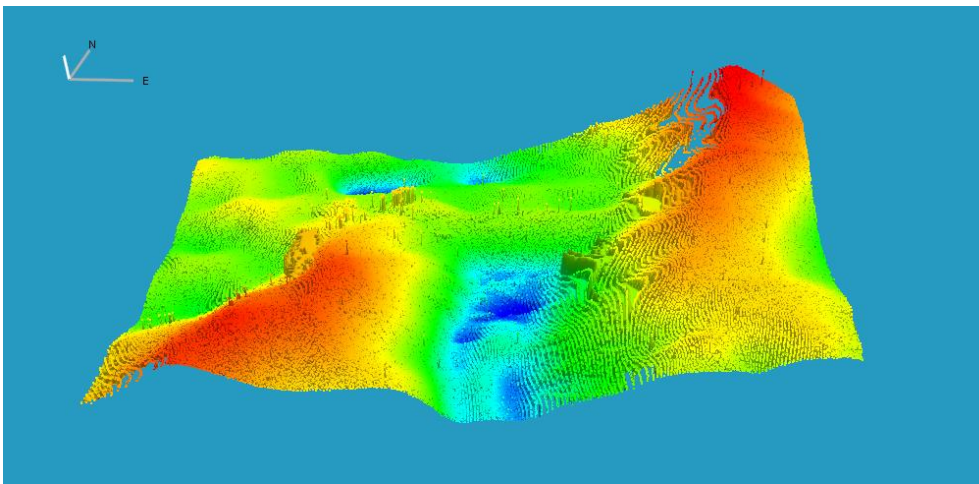


Figure 6.34 CS results in Test-A referenced to DEM elevation: (a) Tomograms via CS in Test-A after error elimination; (b) Geocoded tomograms via CS in Test-A after error elimination, the red line is the TanDEM-X DEM height value, the colour is the normalisation magnitude (intensity or amplitude) of the complex scattering coefficient  $\gamma(s)$

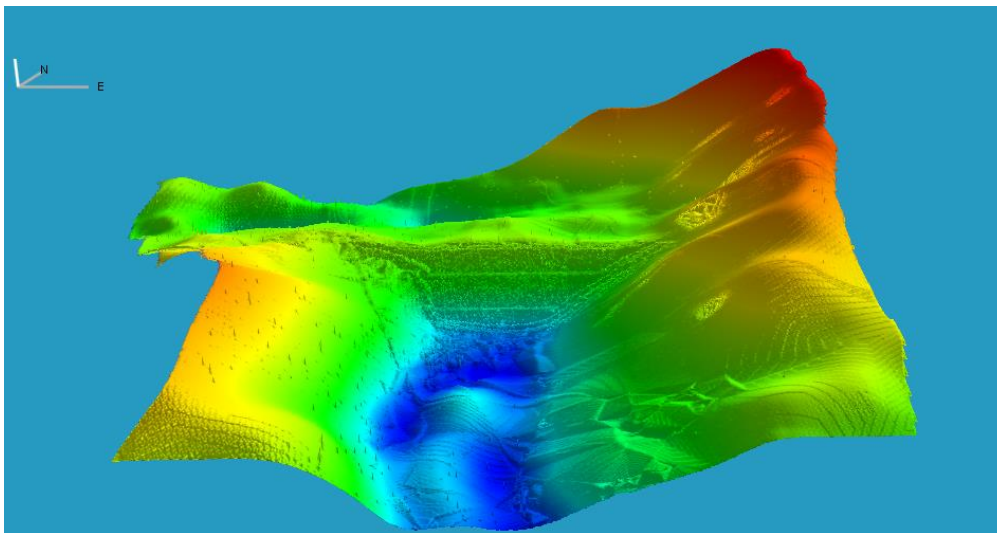
### 6.7.2 TomoSAR Results



(a)



(b)



(c)

Figure 6.35 TomoSAR results of the sub-test area at Zippingpu dam: (a) TanDEM-X 12 m DEM (12 m resolution) at Zippingpu dam; (b) TomoSAR imaging result of ALOS L band data (10 m resolution) at Zippingpu dam; (c) TomoSAR imaging result of COSMO-SkyMed spotlight data (1 m resolution) at Zippingpu dam

Finally, after geocoding (adding TanDEM-X 12 m DEM height), the TomoSAR results of the X-band COSMO-SkyMed spotlight data and ALOS L band data are obtained, as shown in Figure 6.35. Compared to the TanDEM-X 12 m DEM data in Figure 6.35 (a), the TomoSAR results in Figure 6.35 (b) and (c) have a better resolution. The ALOS L band 10 m TomoSAR results can get the top and bottom of the 3D structure in the tree area, shown in Figure 6.35 (b). However, in contrast to the ALOS L band 10 m TomoSAR results in Figure 6.35 (b), the 1 m TomoSAR imaging results of the COSMO-SkyMed spotlight data in Figure 6.35 (c) have better resolution results. It is easy to see that there are two line steps on the dam in the 1 m TomoSAR imaging results in Figure 6.35 (c), which can also be seen in LIDAR and the photos in Figure 6.36 (a), (b) and (c).

As the X band has little penetration capability and there is no penetration by the X band at all around the man-made dam, therefore, only one point of TomoSAR imaging result for each SAR pixel along the height direction in the dam area, which can be validated using LIDAR data. Besides, as the TomoSAR results are referenced to the TANDEM-X 12 m data (SAR interferometry phase (InSAR) calibration reference to DEM are used, see Section 6.6.3), the results already have absolute coordinates after geocoding (adding DEM height). If a high accuracy of position is needed, the LIDAR or other control data can be used as control points for geocoding.

### 6.7.3 Fieldwork in Zipingpu Dam for TomoSAR Result Validation

The fieldwork for the LIDAR data and related photos were collected at Zipingpu dam, Dujiangyan, China between 24-09-2017 and 29-09-2017. The ground-based V-Line 3D Terrestrial Laser Scanner (TLS) RIEGL VZ-1000 (shown in Figure 6.36 (d)), which uses a narrow infrared laser beam and a fast scanning mechanism (based on a fast rotating multi-facet polygonal mirror) with echo digitisation and online waveform processing, was used for the data acquisition. The photos of Zipingpu dam are shown in Figure 6.36 (a) and (b). The LIDAR data at Zipingpu dam, which is used for validation, is shown in Figure 6.36 (c).

Finally, the difference map between the X-band TomoSAR imaging results and the LIDAR data of fieldwork at the Zipingpu dam are shown in Table 6.3 and Figure 6.37. The map shows that the compressive sensing result has a good match with the LIDAR data after geocoding. In Figure 6.37, the maximum difference is 8.6 metres, the minimum

## Chapter 6. Application of TomoSAR to X-band

difference is -8.5 metres, the mean difference is 0.11 metres, the standard deviation is 2.81 metres and the RMSE is 2.82 metres. After the tree and mountain area mask, the maximum difference of the dam area is 5.3 metres, the minimum difference is -5.7 metres, the mean difference is 0.25 metres, the standard deviation is 1.04 metres (in dam area) and the RMSE is 1.07 metres. The compressive sensing result has a good match with LIDAR data after geocoding, which demonstrates that the compressive sensing method works very well for the retrieval in the dam area. Therefore, the TomoSAR imaging algorithm appears to work very well, and the high resolution 1m TomoSAR results in the dam area are very good for application as they match very well with the LIDAR data.

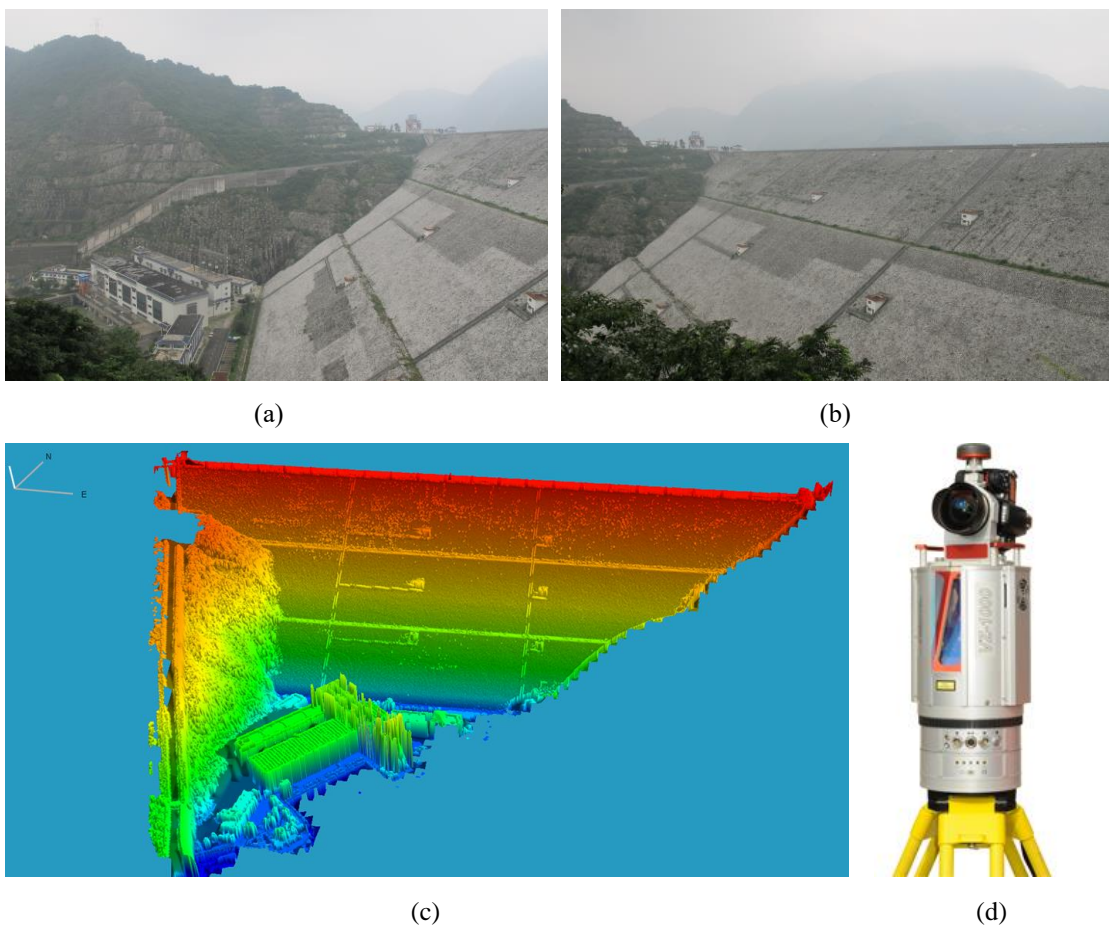


Figure 6.36 Fieldwork at Zipingpu dam in Dujiangyan Sichuan China, LIDAR point cloud of Zipingpu dam for validation is obtained via RIEGL VZ-1000: (a) Zipingpu dam in Dujiangyan; (b) Zipingpu dam in Dujiangyan; (c) LIDAR point cloud of Zipingpu dam; (d) RIEGL VZ-1000

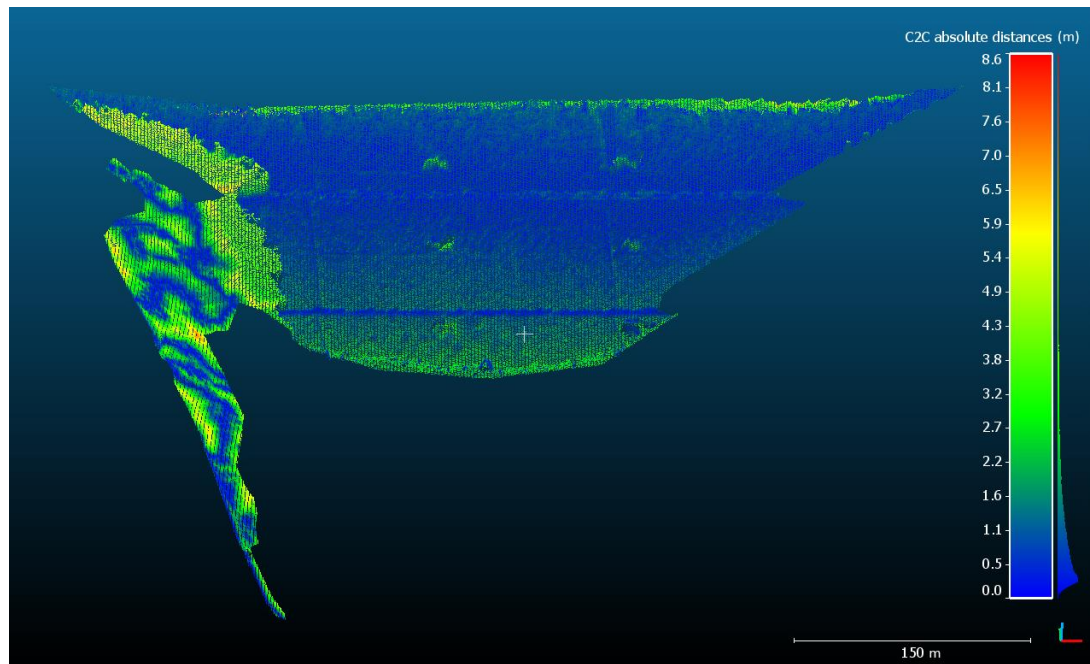


Figure 6.37 Difference map between the X-band TomoSAR imaging result and the LIDAR data of the fieldwork at Zipingpu dam, the difference is the absolute value (absolute distance) of the difference

Table 6.3 Ascending COSMO-SkyMed spotlight data stacks

Basic Stats	Area	Point number	Min (m)	Max (m)	Mean (m)	Stddev $\sigma$ (m)	RMSE (m)
TomoSAR-LIDAR	Dam and the mountain trees	75355	-8.5	8.6	0.11	2.81	2.82
TomoSAR-LIDAR	Dam	46878	-5.7	5.3	0.25	1.04	1.07

Finally, several lines (points of each line are stored in Google Earth KML (Keyhole Markup Language) format, the red colour points in the picture) of our TomoSAR results are shown in Google Earth (the speed is very slow when showing point cloud in Google Earth, so only several lines have been input into Google Earth for viewing).



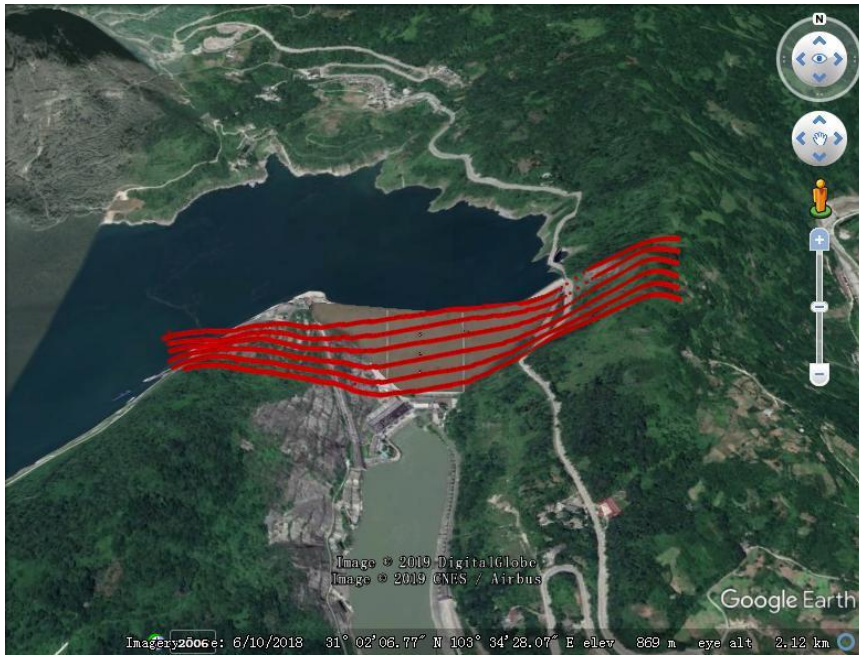


Figure 6.38 TomoSAR results shown in Google Earth, the TomoSAR results of the 6 azimuth lines in the test area are input into Google Earth for viewing

### 6.7.4 Discussion

All of the SAR SLC data must be first co-registered in the radar coordinate system to sub-pixel accuracy for the TomoSAR processing based on the master image orbit information and DEM. Using a precise orbit to estimate the orbit baseline is dependent on the orbit accuracy. Thus, if the precise orbit is not precise, orbit estimation and pre-processing (Feng et al., 2015) are needed to obtain a new accurate orbit. Moreover, based on our experiment, shown in Figure 6.12 and Figure 6.13, interpolating the orbit time according to the spatial distribution and orbit calculated from the interpolating orbit time to obtain the satellite position and velocity information based on the Hermite interpolation method are critical for the baseline estimation in order to overcome tile by tile problems and the low orbit resolution problem, which makes the baseline more reasonable, robust and smooth. From Figure 6.13, it is easy to see that the master and the slave orbit are slightly different, which causes the perpendicular baseline difference and makes the TomoSAR reconstruction work.

From Figure 6.14, the new perpendicular baseline is smoother than the original baseline. From Figure 6.14 (e) in the range direction, the perpendicular baseline has some sawtooth errors, while the new perpendicular is more reasonable after correction, which will improve the accuracy of the spatial frequency calculation for TomoSAR. In Figure

6.14 (f), there are about 3.5 metres differences in the azimuth direction, which means that the old original perpendicular baseline has systematic errors, which need to be corrected. From Figure 6.15 (d) and (e), the profile in azimuth is almost the same, and the profile of the parallel baseline along the range direction has a millimetre's level (almost the same) difference. The mean difference of the parallel baseline is -0.0015 metres, which means that the parallel baseline errors are tiny. Moreover, it also indicates that the SAR is good at range measure and good at DEM measure, as the parallel baseline is related to the DEM height phase and ellipsoid phase flattening (shown in Equation (5.37)).

The reference slant range used in the deramping processing can be the centre distance of each image or the distance between the radar antenna phase centre of each image and a reference terrain (e.g. known DEM data). It should be noted that there is no essential difference between these two methods; the only difference is the zero-point benchmark. In our experiment, coarse DEM (TanDEM-X 12 m) was used for deramping without introducing additional atmospheric phase errors using the radar transmission time delay and velocity in the accurate reference slant range calculation. However, it is well known that the DEM has elevation errors, which may also influence the TomoSAR results. Based on the phase shift, equations and previous experiments (Sun et al., 2011), the elevation error will only cause the overall translation of the three-dimensional target structure, and it will not affect its relative position and structure. Therefore, in the actual processing, only the DEM or control points are needed to perform overall correction of the result, and the external DEM is commonly used for TomoSAR deramping. For scenes with small relief, even ellipsoid models that are ameliorated according to the average elevation of the scene can be used. When using the InSAR phase calibration method with DEM error correction for TomoSAR, the accuracy of the DEM error estimation will influence the results of the inversion. Therefore, it is better to use high accuracy and high resolution DEM. However, the accuracy of the DEM error estimation in Man-made facility areas is usually very high, which can make phase calibration work very well.

From the BioSAR 2008 L band 3D SAR forest structure reconstruction experiment and the Tomogram results shown in Figure 6.16, it is clear to see that, if the baseline is not good enough, the reconstruction results might not be accurate. In Figure 6.16 (a) and (b), compared to pixel by pixel baseline, the single baseline causes the results to be higher than the LIDAR truth at the left slant range (close to the aeroplane) and lower at the right slant range (far from the aeroplane), while the LIDAR forest height is well matched with the reconstruction results based on the pixel by pixel baseline. Moreover,

## Chapter 6. Application of TomoSAR to X-band

in Figure 6.16 (b), the LIDAR forest height is not matched in SAR geometry (top picture), while it is well matched in ground geometry relative to DEM (bottom picture). From the results, shown in Figure 6.16 in the SAR geometry, the height direction is inclined to (not perpendicular to) the range direction. It is right that the results are a little bit inclined before geocoding because it is not transferred to the ground range in the ground geometry. Thus, it is right that the results are a little bit inclined before geocoding because it is not transferred to the elevation and ground range. In addition, the orbit vector based on the *SCH* coordinate system (Zebker et al., 2010), which is defined with respect to the projected ground track of the ideal satellite orbit for focusing, identifying the location of the image and motion-compensation, is commonly used and very important for TomoSAR geocoding.

Meanwhile, phase calibration is a critical step for TomoSAR imaging. In the Zipingpu dam test area, it is hard to obtain good compressive sensing results using the original baseline, while compressive sensing works very well after using the newly improved baseline with phase calibration. The compressive sensing results in the dam area have a good match with the LIDAR data. Although there are some differences except for the 0 metre difference, they are around 0.25 metres difference in average, which might be caused by other errors, like DEM uncertainty, orbital, tropospheric and ionospheric phase distortion and thermal noise.

### 6.8 D-TomoSAR based on Compressive Sensing Results

D-TomoSAR has the same steps as TomoSAR. The difference (see Section 5.5) is that, in the phase calibration step, we keep the deformation phase information in our PS-InSAR, PS-SVD-PGA-LS-ME method, and in D-TomoSAR, we also invert the velocity parameters. The inversion results can be displayed in the height-deformation velocity plane. Additionally, the improved CFAR method is a little bit different. In the improved CFAR, the standard deviation is calculated, and all peaks are found in height-deformation velocity plane; then, if the amplitude of the peaks is larger than three times of standard deviation, they are selected as targets. Finally, the velocity and height position are obtained.

In the sub-test area at Zipingpu dam, Dujiangyan, Sichuan, China, we used our CS-D-TomoSAR and CFAR method to get the results, shown in Figure 6.39. From Figure 6.39 (c), it is easy to detect two targets with the help of the height-velocity plane analysis



when the two targets are close enough. In addition, from Figure 6.39 (a) and (b), they are two close pixels, which has a contamination signal from each other, but they can also be clearly detected in the CS method. Moreover, the CS method is useful for high resolution D-TomoSAR inversion in man-made structures.

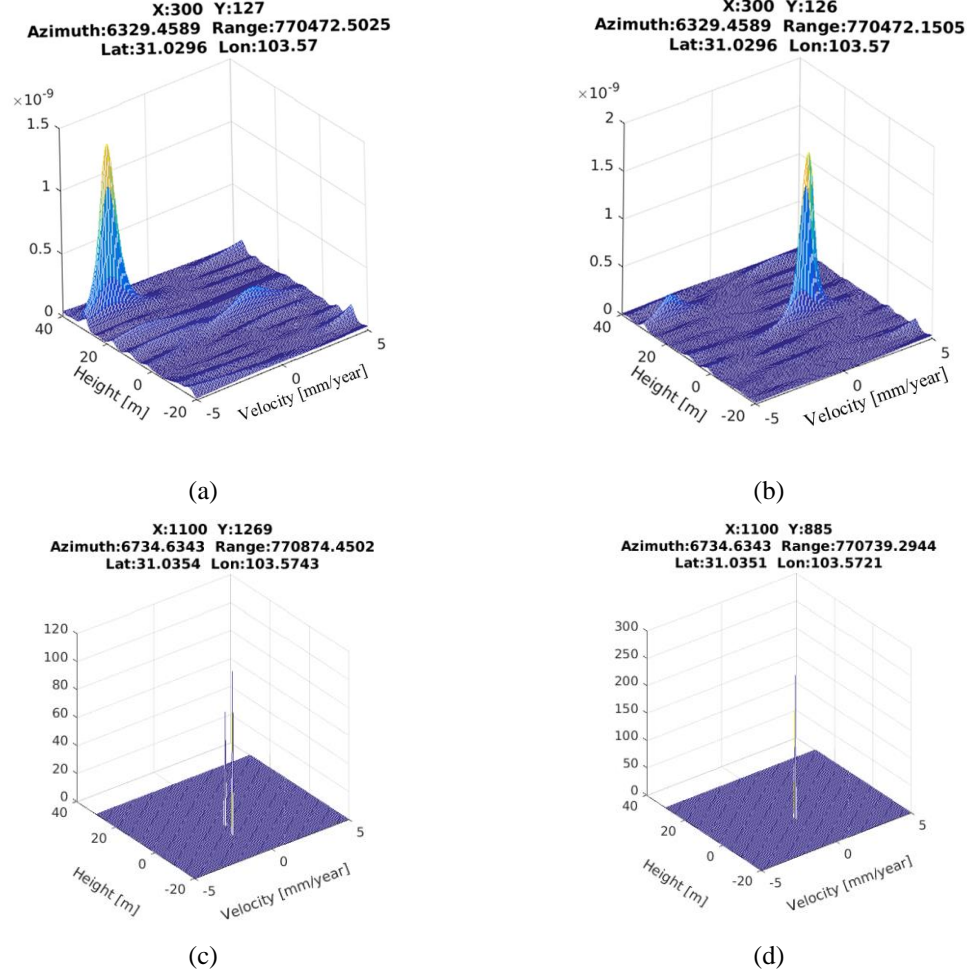


Figure 6.39 D-TomoSAR results in the sub-test area of Figure 6.2, the magnitude of  $f(s, v)$  is shown in the height-deformation velocity plane

Moreover, after using CS-D-TomoSAR and CFAR method, the D-TomoSAR results at the position of the PS points in the sub-test area of Figure 6.2 are shown in Figure 6.41. The velocities of the D-TomoSAR results are between -3 mm/year and 3 mm/year. After the PSInSAR processing and setting the zero velocity benchmark point at the no deformation area in the urban area (black star Figure 6.40), the deformation and mean velocity (shown in Figure 6.40) are obtained. Therefore, this means that the velocity map is used to validate the D-TomoSAR results, which are referenced by the same zero velocity benchmark point (black star Figure 6.40). The statistics and comparison between

## Chapter 6. Application of TomoSAR to X-band

the PS mean velocity and D-TomoSAR velocity are shown in Figure 6.42. From the statistics of the difference between the PS mean velocity and the D-TomoSAR velocity, the maximum difference in this dam area is 0.5 mm/year, the minimum difference is -0.41 mm/year, the mean difference is 0.03 mm/year and the standard deviation is 0.15 mm/year. Therefore, through this validation of the D-TomoSAR velocity and statistics of the difference, the D-TomoSAR results are nearly the same as the PS mean velocity results. Theoretically, the velocity should be the same and the difference should be 0 mm/year because the linear deformation phase information obtained by the PS-InSAR method is kept when doing the phase calibration. These differences might be caused by the D-tomoSAR estimation errors or other errors, such as DEM uncertainty, orbital, tropospheric and ionospheric phase distortion and thermal noise.

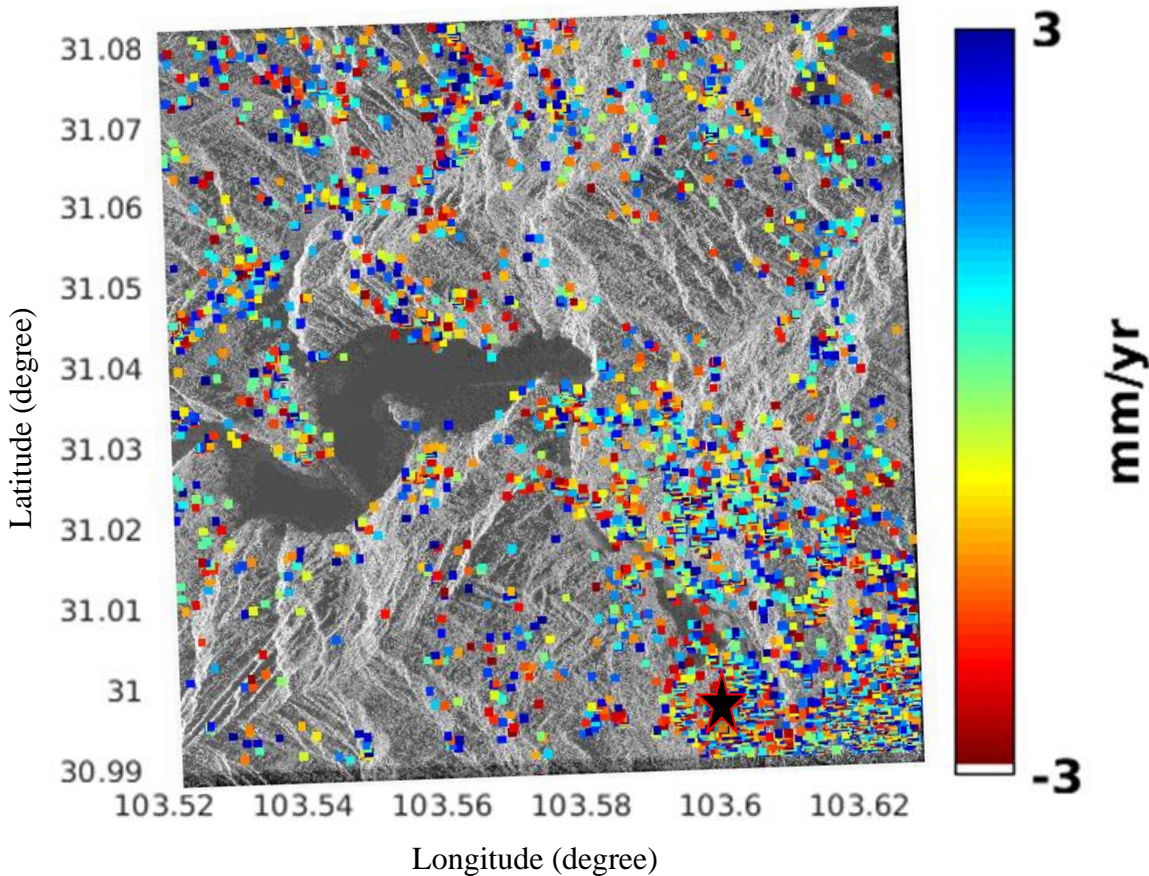
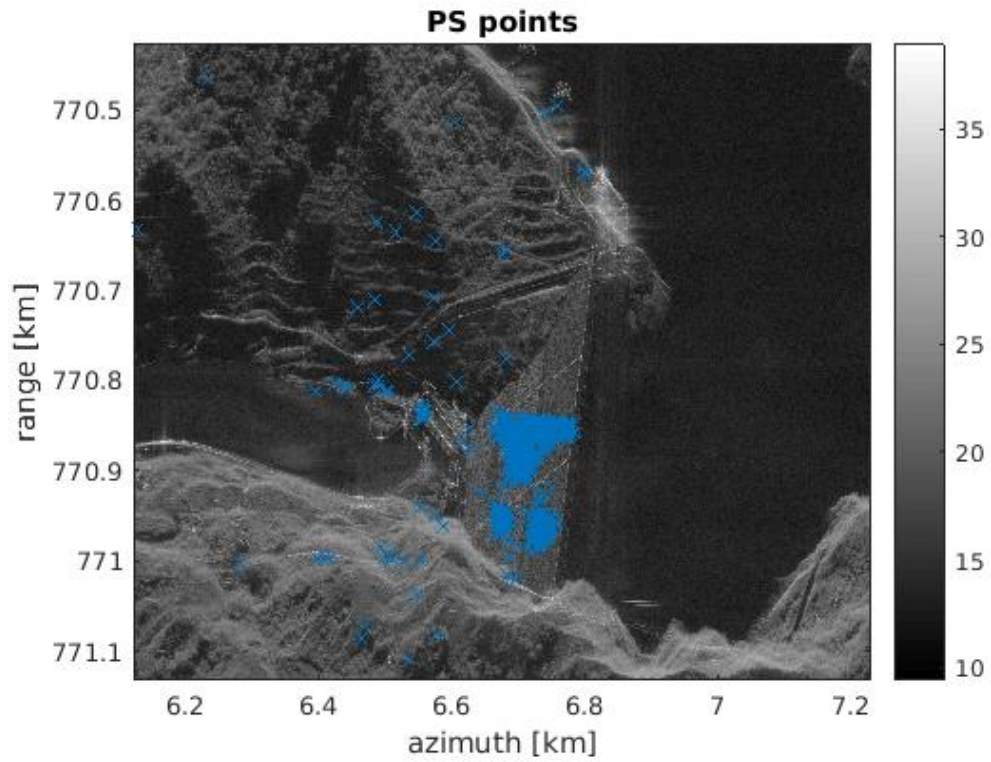
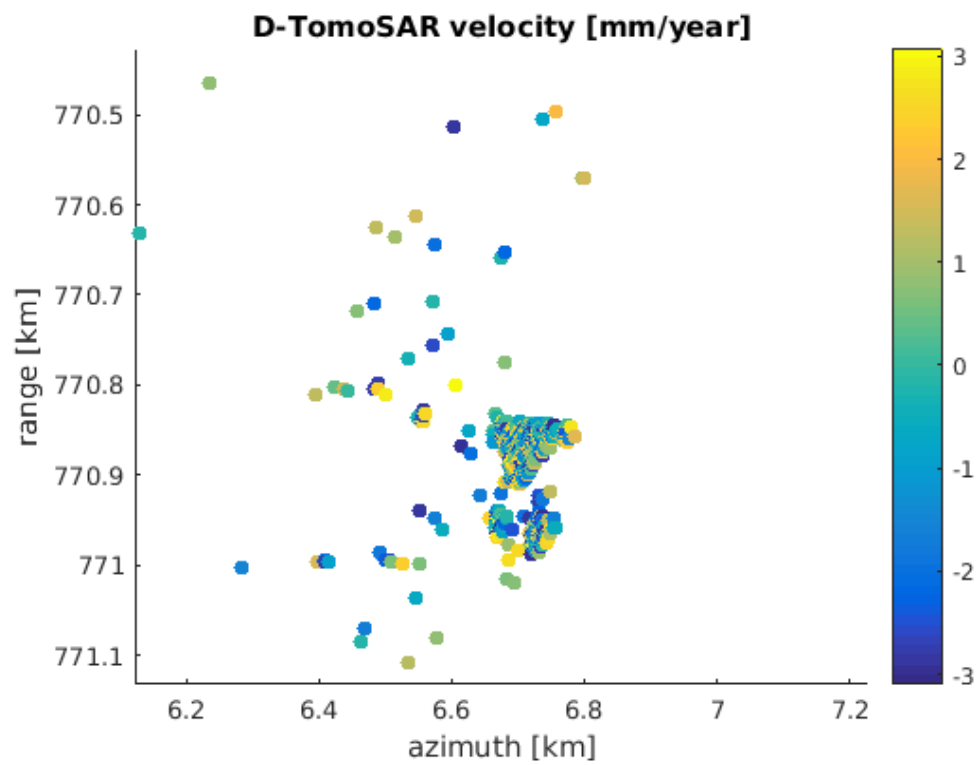


Figure 6.40 Mean velocity map of PS points in the COSMO-SkyMed spotlight SAR image area, the black star is the zero-velocity benchmark point



(a)



(b)

Figure 6.41 D-TomoSAR results at the position of the PS points in the sub-test area of Figure 6.2: (a) The position of PS points in D-TomoSAR test; (b) D-TomoSAR velocity

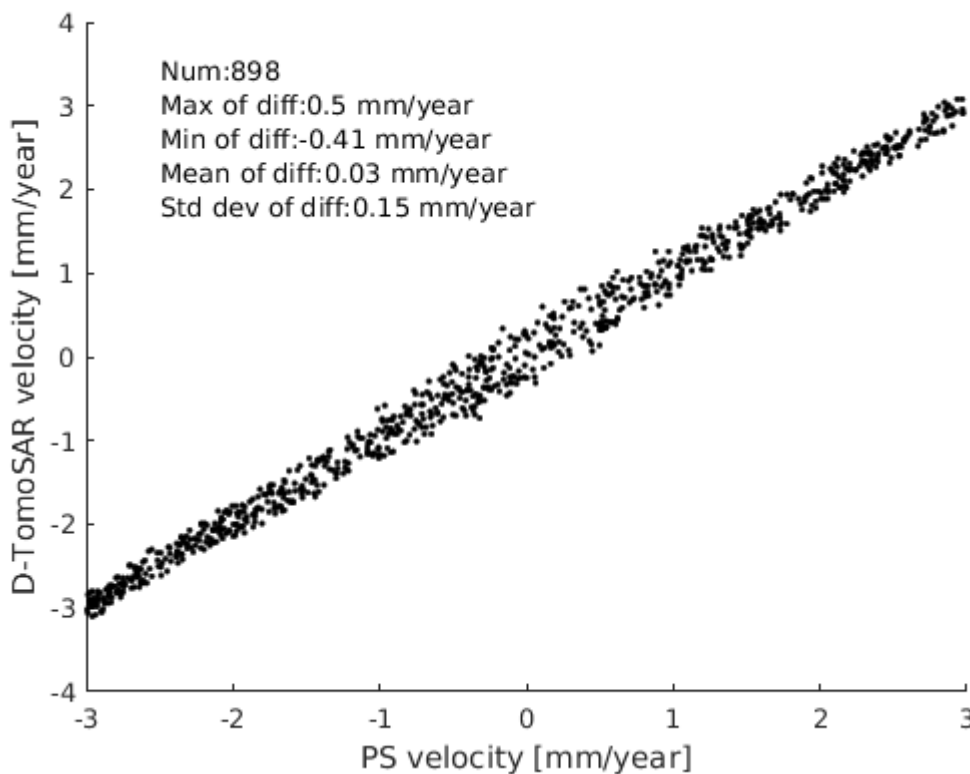


Figure 6.42 D-TomoSAR velocity results validation using PS velocity result in the sub-test area of Figure 6.2

## 6.9 Discussion on Limitations and Advantages of X-band

The results of the FFT, Capon and CS using COSMO-SkyMed X band spotlight data in the forest mountain area demonstrates that the X band has little penetration capability. The wavelength of the X band is 0.031 metres; it cannot penetrate the leaves of the forest. Therefore, it cannot be used for the forest structure reconstruction. However, it can get the top position of the canopy. The results of FFT, Capon and CS using the COSMO-SkyMed X band spotlight data in the dam area show that, with the super-resolution reconstruction CS method, the X band data have advantages to map the shape of the man-made structure (dam, buildings and manufactured facilities) with a high resolution and the X band can also map the top of the 3D terrain, which is best for high resolution DSM acquisition.

### 6.10 Conclusions

In this chapter, based on the theoretical study and mathematical derivation in previous chapters, the systematic TomoSAR algorithm and methods have been demonstrated, tested and analysed in various applications (urban building, bridge, dam, trees) to achieve better 3D & 4D tomographic SAR imaging results (for elevation and deformation extraction.) using the Cosmo X band data at Zipingpu dam, Dujiangyan, Sichuan, China.

In 3D and 4D SAR tomography, the baseline estimation is critical in the data processing. This chapter proposed an improved precise orbit, registration offset rule and interpolation method to estimate pixel by pixel baselines (novel contribution of this chapter). The baseline estimation results and TomoSAR processing results using the COSMO-SkyMed X band spotlight data at Zipingpu dam, China and the BioSAR 2008 L band data of the forest area at the Vindeln municipality, Umeå, Västerbotten in northern Sweden both demonstrate the precision and effectiveness of the baseline estimation method. Meanwhile, the removal of the slanted centre phase of the main image based on the parallel baseline and the DEM (TanDEM 12 m high resolution data) that establishes the spectral relationship (based on the perpendicular baseline) between the observed SAR images and estimated parameters, makes the 3D and 4D SAR tomographic reconstruction possible from multi-track SAR observations. The PS-SVD-PGA-LS-ME phase calibration method and the InSAR phase calibration method with the DEM phase error estimation and correction, as proposed in Chapter 5, are tested in this chapter. The TomoSAR results in the dam area become better and better with the standard deviation quantification after the DEM deramping, the tropospheric phase distortion correction, the DEM error correction and the phase calibration processing step by step. The phase calibration (InSAR phase calibration, tropospheric phase distortion correction, DEM error correction and phase error calibration) step is indispensable for TomoSAR imaging, which ultimately determines the accuracy of the inversion results.

The super-resolution TomoSAR imaging based on the compressive sensing method is simulated and tested at Zipingpu dam, Dujiangyan, Sichuan, China. The results are shown and validated by the fieldwork Lidar data, which demonstrates the CS method has high resolution reconstruction capabilities. In all of the tests, the FFT method shows some ambiguity in the height direction, while the Capon method has a better inversion to

## **Chapter 6. Application of TomoSAR to X-band**

avoid this ambiguity by minimising spatial perturbations and sidelobes and the Capon method might be better for ice and forest structure reconstruction because it can image continuous reflectivities. The CS algorithm is generally performed using SLC data (without multilook averaging for noise filtering), which is automatically performed in the stack dimension using a SAR model and a sparsity driven estimation technique used to characterise a minimal number ( $< 4$ ) of targets in the measured signal. Therefore, CS is well adapted to discrete scatterers or targets and 3D & 4D high resolution tomographic reconstruction. X band has little penetration capability and it cannot be used for forest structure reconstruction. However, it can be used for the retrieval of the top position of the canopy, the shape of man-made structures (dam, buildings and manufactured facilities) and the top surface of 3D terrain, which is best for high resolution DSM acquisition and target detection.

# Chapter 7

## Conclusions

In this chapter, the conclusions of this thesis are stated in the context of its aims, the overview of the research work, alongside potential study areas proposed for future work and the contributions made to the field by this work.

### 7.1 Thesis Overview

By using multi-baseline SAR data stacks, 3D SAR tomography (TomoSAR) (Reigber and Moreira, 2000; Fornaro et al., 2003; Nannini et al., 2008; Lombardini et al., 2013a) and 4D SAR differential tomography (Diff-TomoSAR) (Lombardini and Cai, 2012; Lombardini, 2005a; Xiang and Bamler, 2010; Lombardini and Pardini, 2012; Lombardini et al., 2013b; Tebaldini and Rocca, 2012; Huang et al., 2012) innovate the SAR interferometry, so that complex scenes which have multiple scatterers in a SAR pixel cell can be sensed (Feng and Muller, 2017). In addition to the 3D shape reconstruction, there are applications of deformation solution in complex urban and infrastructure areas (Fornaro et al., 2003; Lombardini et al., 2013a), and recent cryosphere ice investigations (Ferro-Famil et al., 2012), promising tomographic forest applications (Nannini et al., 2008; Lombardini and Cai, 2008; Pardini and Papathanassiou, 2011; Lombardini and Viviani, 2015), e.g. tree height estimation, biomass estimation, sub-canopy topographic imaging, and even search, rescue, tracking and surveillance under tree and forest (Lombardini and Viviani, 2015). However, these scenes are influenced by

## Chapter 7. Conclusions

DEM uncertainty and errors, the temporal decorrelation of scatterers, orbital, tropospheric and ionospheric phase distortion. Aiming to solve these problems in this thesis, the DEM generation by bistatic InSAR and photogrammetry are introduced first, then the automatic DEM quality validation is studied. In addition, the whole systematic method cycle for 3D and 4D TomoSAR imaging for the retrieval of height and deformation is explored, including problem formation, method development, and real SAR data tests.

### 7.1.1 DEM Validation

Similar to other geospatial data, DEM data also have random errors, systematic errors and blunders, which should be verified to “fit for applications”. In this thesis, DEM validation work focuses on an assessment of the accuracy of a TanDEM-X intermediate DEM (IDEM) and a TanDEM-X DEM (in comparison to KGPS, ICESat GLAS14 elevation data, “ground truth” from a national supplier - Bluesky and SRTM 1 and ASTER G-DEM) over the UK in order to extrapolate these results to the global area. GPS plus the DEM registration method is proposed to validate the absolute planimetric and vertical accuracy. Firstly, all DEM data are converted into the same coordinate system (OSGB36 & ODN), then, GPS points are selected, the height differences between the Bluesky data and the GPS points are calculated, and, where the differences are very large ( $> 60$  m), the GPS data are eliminated because of the errors in the GPS data. Afterwards, a suitable oversampling (three times) of the window size of the Bluesky DTM and the un-validated DEM data (template) is determined by taking the  $x$  and  $y$  coordinates of GPS as the central pixels. Next, a cross-correlation method is used to match the DEM in sub-pixel accuracy to find an accurate and correctly matched GPS planimetric coordinate in the un-validated DEM. Moreover, the RANSAC algorithm for outlier elimination is used to improve the DEM matching accuracy and  $x$  and  $y$  and the height  $z$  in the un-validated DEM are recorded. Finally, the absolute planimetric and vertical DEM accuracy are calculated using KGPS data  $(x, y, z)$  and matched points  $(x, y, z)$  in the un-validated DEM data. Through this research, the accuracy of TanDEM-X DEM and TanDEM-X IDEM in the UK is summarised: the accuracy of TanDEM-X IDEM against the kinematic GPS tracks in England & Wales is  $1.0 \pm 3.2$  m,  $0.8 \pm 5.6$  m in Scotland for 12 m,  $1.5 \pm 6.5$  m for 90 m and  $1.3 \pm 5.2$  m for 30 m in the UK; the accuracy of TanDEM-X DEM against the kinematic GPS tracks is  $0.08 \pm 6.7$  m for 90 m in the UK.



In addition, the quality of the DEM data is studied using a DEM co-registration method. First of all, the cross-correlation of the height histogram of two DEM heights and edge images derived from the two DEMs is used to estimate the vertical and horizontal shifts. Second, an initial matching matrix (coarse) is obtained by introducing sparse initial registration using a pyramidal method. Lastly, refined co-registration using the Iterative Closest Point (ICP) is utilised to get highly accurate matching matrices with the global optimisation of each tile by using Gaussian weights to obtain the final co-registration results. Extensive experiments were selected and executed in the UK using the TanDEM-X IDEM data and TanDEM-X DEM data. In the UK, before DEM co-registration, against the “ground truth” Bluesky DTM dataset, TanDEM-X IDEM has differences of  $1.2\pm4.4$  m in England and Wales and  $1.7\pm9.4$  m in Scotland for 12 m,  $2.1\pm17.5$  m for 30 m, and  $2.1\pm18.7$  m for 90 m; TanDEM-X DEM 90 m has differences of  $0.5\pm11.1$  m in the UK. After DEM co-registration, compared to Bluesky DTM, TanDEM-X IDEM has differences of  $0.4\pm2.3$  m for England & Wales  $0.5\pm4.2$  m at 12 m; corresponding values are  $0.1\pm3.9$  m at 30 m and  $0.01\pm4.5$  m at 90 m; the differences of TanDEM-X DEM 90 m are  $0.2\pm5.4$  m in the UK. Thus, DEM co-registration methods can address both horizontal and vertical offsets to minimise the systematic errors (shift or bias) for studying the DEM data quality.

Moreover, against the ICESat GLAS14 elevation data, the accuracy of TanDEM-X IDEM data is  $-0.03\pm3.7$  m in England and Wales, and  $0.4\pm5.3$  m in Scotland for 12 m,  $0.02\pm9.3$  m at 90 m and  $-0.07\pm6.6$  m for 30 m in the UK; the accuracy of TanDEM-X DEM 90 m data is  $0.2\pm10.1$  m in the UK. Moreover, 90% of the TanDEM-X DEM data (linear error at 90% confidence level) is lower than 18.4 m, while 90% of the TanDEM-X IDEM data (Linear error at 90% confidence level) is lower than 16.2 m (Feng and Muller, 2016). The results also show that the topographic parameters (slope, aspect and relief) have a strong impact on the vertical accuracy of the TanDEM-X IDEMs.

What’s more, in these validation work, both the standard deviation and RMSE of the DEM height difference reflect that the absolute vertical accuracy of the TanDEM-X IDEM product is better than the SRTM and ASTER GDEM product in a high and medium resolution (12 m, 30 m), while the vertical comparison accuracy of the TanDEM-X IDEM product to Bluesky DTM is worse (because of some errors) than the accuracy of the SRTM and ASTER GDEM product before the DEM co-registration and water mask. Compared to the TanDEM-X IDEM 90 m data, TanDEM-X DEM 90 m data, appears to have better accuracy after the DEM co-registration and water mask, which indicates the

## Chapter 7. Conclusions

TanDEM-X DEM data have been post-processed (with the bias, and so on) and generated by resampling from high resolution to 90 m resolution using angular degree grids rather than metric grids. After the DEM co-registration and the water mask, the vertical comparison accuracy of the IDEM product is better at 30 m than the SRTM and ASTER GDEM product. However, the vertical comparison accuracy of IDEM 90 m data compared to Bluesky DTM is still worse than the other data. Moreover, though TanDEM-X DEM 90 m and TanDEM-X IDEM 90 m are better than ASTER GDEM 90 m data, but they are still not better than the SRTM data (This might be because SRTM is edited data, while TanDEM-X IDEM and TanDEM-X DEM 90 m still have many errors). Therefore, it is necessary to improve the accuracy of TanDEM-X IDEM (12 m, 30 m and 90 m) and TanDEM-X DEM 90 m data in the future.

### 7.1.2 Atmospheric and Ionospheric Correction Algorithm

On many solar system planets and their satellites (moons), with magnetospheres and atmospheres, solar wind and EUV radiation create ions and electrons in the upper atmosphere as a plasma ionosphere, which dramatically decreases the accuracy of 3D and 4D tomographic SAR imaging. In this thesis, the principles of the atmospheric and ionospheric correction algorithm for TomoSAR 3D SAR tomography imaging are first introduced. Next, the PS method, the ERA-I model and the GACOS model for absolute and relative atmospheric phase correction are presented. Then, the ionospheric correction split spectrum algorithm for InSAR and differential TEC estimation are introduced, and two tests were studied in Tocopilla, Chile, whose results indicate that sometimes it is necessary to correct the large ionospheric phase delay for L-band InSAR processing. Finally, the new TomoSAR ionospheric correction algorithm method for TEC estimation by using IGS TEC data with split-spectrum differential TEC data and the least squares model is proposed and tested in San Francisco Bay, USA. The validation was executed last via IRI TEC data, which demonstrates that ionospheric correction is critical for TomoSAR imaging. Moreover, ionospheric tomography and ionospheric correction are both needed in radio astronomy and radar astronomy, and ionospheric tomography based on SAR imaging has very good prospects because it can more straightforwardly obtain surface information in three-dimensions across the globe when the SAR data are available at a high temporal resolution (like GEO SAR satellites, the small SAR satellite constellations, the Moon based SAR for Earth observation and so on).

### 7.1.3 Orbit Baseline Estimation for 3D & 4D TomoSAR Imaging

Baseline estimation is of great importance for 3D and 4D SAR tomography. A single baseline can be obtained in common InSAR, while a pixel-by-pixel baseline is necessary in TomoSAR processing. Firstly, to process TomoSAR and estimate baseline, it is needed to co-register all of the SAR SLC data. Based on the master image orbit information and the DEM in a radar coordinate system, the SAR amplitude image is simulated with the DEM heights. Then the master image, along with all other slave images, are matched to this simulated SAR image. In this way, all SAR images are co-registered with subpixel accuracy to the reference master SAR image with the help of an external DEM. As the basic range-Doppler model makes the orbit and baseline modules more robust so that they can be used for both airborne and spaceborne data with a post-estimation for any baseline. After the fine co-registration, each pixel in the co-registered slave image has a pixel-by-pixel azimuth-range time. Then, the Hermite interpolation method is used to get the position and velocity of the satellite by executing the interpolating orbital time based on the spatial distribution and orbit; TomoSAR geocoding is conducted by transferring the orbit vector to the *SCH* coordinate system. The pixel-by-pixel height, longitude and latitude of a reference/master image are estimated using the range-Doppler equation, and the same height, longitude and latitude are figured out in the slave image. Then the pixel-by-pixel baselines can be calculated by using satellite positions (interpolated orbits) and the pixel latitude, longitude and height. The removal of the slanted centre phase of the main image based on the parallel baseline and DEM establishes the ‘spectral’ (so that, FFT and many spectral estimation methods can be used in TomoSAR) relationship (based on the perpendicular baseline) between the observed SAR images and the estimated parameters, which makes the 3D and 4D SAR tomographic reconstruction possible from the multi-track SAR observations. This thesis proposes an interpolation method and an improved precise orbit and registration offset rule for the estimation of the baseline. The data were processed on Zipingpu dam, Sichuan, China using the Cosmo-SkyMed X band spotlight data and forest area at the Vindeln municipality, Umeå, Västerbotten in northern Sweden based on the BioSAR 2008 L band data. According to the TomoSAR processing results and the baseline estimation results, the proposed baseline estimation method has effectiveness.

### 7.1.4 TomoSAR and D-TomoSAR Algorithm and Experiments

3D SAR tomography (TomoSAR) and 4D SAR differential tomography (Diff-TomoSAR) exploit multi-baseline SAR data stacks to create an important new innovation in SAR Interferometry. This is in order to sense complex scenes with multiple scatterers mapped into the same SAR cell (pixel). For SAR tomography, the workflow ensures that all complex images are co-registered into SAR stacks. Then, the ionospheric and atmospheric correction is implemented. After that, it is necessary to conduct deramping and phase error compensation. Finally, the TomoSAR results can be obtained through height imaging and post-processing (improved CFAR). The step of D-TomoSAR is the same as that of TomoSAR, with the difference that D-TomoSAR estimates the deformation information. This thesis proposed a compressive sensing (CS) method with SAR interferometry phase (InSAR) calibration method with reference to DEM. Moreover, according to PS, SVD, PGA, weighted least squares and minimum entropy for TomoSAR and differential TomoSAR, a novel combined phase error calibration algorithm is proposed. In TomoSAR imaging, the PS-SVD-PGA, weighted least squares and minimum entropy phase calibration algorithm calibrates all errors, while for D-TomoSAR, the deformation phase information is kept in the PS-SVD-PGA weighted least squares and minimum entropy method in phase calibration, so that the velocity parameters in D-TomoSAR can be inverted, and the inversion results are displayed in the height-deformation velocity plane. Meanwhile, the systematic TomoSAR algorithm and methods have been established, demonstrated, tested and analysed in various applications (urban building, bridge, dams) to achieve better 3D and 4D D-tomographic SAR imaging results, which includes using Cosmo-Skymed X band data at Zipingpu dam in Dujiangyan, Sichuan, China and using ALOS L band data at San Francisco Bay (urban building and bridge), USA.

There is ambiguity in the height direction in the FFT method. The Capon method which has better inversion can minimise spatial perturbations and sidelobes, so that the ambiguity can be avoided. The Capon method might be better for forest structure reconstruction because it can image the continuous reflectivities in the forest canopies. The CS algorithm is generally performed using SLC stacks (without multilook averaging for noise filtering), which is automatically performed in the stack dimension using the SAR model and sparsity driven estimation technique to characterise a minimal number ( $< 4$ ) of targets in the measured signal. Therefore, CS is well adapted to discrete scatterers

or targets and therefore 3D and 4D high resolution tomographic reconstruction. The results demonstrate that the L band data are fit for the structure reconstruction of forests and manufacturing facilities (bridge, building, and so on), but the resolution is low. Because of the poor penetration capability, X band is not suitable for the reconstruction of the forest structure. However, it can retrieve the top surface of 3D terrain, the shape of the man-made structure (dam, buildings and manufactured facilities) and the top position of the canopy, which is applicable to target detection and high resolution DSM acquisition.

### 7.2 Contributions

The initial aims of this thesis were to assess uncertainties in the retrieval of topographic elevation (DEM, DSM, DTM) from different spaceborne sources (stereo-optical, LIDAR, InSAR, stereo-SAR, radar altimetric data). In addition, a new ionospheric & atmospheric correction and mapping method are studied and used for achieving better 3D & 4D tomographic SAR accuracy. Furthermore, with research on new 3D & 4D tomographic SAR imaging algorithm, a better systematic tomography SAR (TomoSAR) methods were built and tested in the densely vegetated mountainous rural areas of China, and urban building and bridge area in San Francisco Bay, USA.

Based on these aims and the research experiments, the contributions are made as follows:

1) A new DEM co-registration method with line feature validation (river network line, ridgeline, valley line, crater boundary feature and so on) is proposed and demonstrated to assist the study of the wide area DEM data quality. In the UK, before DEM co-registration, against Bluesky, TanDEM-X IDEM has differences of  $1.2\pm4.4$  m in England and Wales and  $1.7\pm9.4$  m in Scotland for 12 m,  $2.1\pm17.5$  m for 30 m, and  $2.1\pm18.7$  m for 90 m; against Bluesky, TanDEM-X DEM 90 m has differences of  $0.5\pm11.1$  m over the UK. After DEM co-registration, compared to Bluesky DTM, TanDEM-X IDEM has differences of  $0.4\pm2.3$  m for England & Wales  $0.5\pm4.2$  m at 12 m; corresponding values are  $0.1\pm3.9$  m at 30 m and  $0.01\pm4.5$  m at 90 m; against Bluesky, TanDEM-X DEM 90 m has differences of  $0.2\pm5.4$  m over the UK. This DEM co-registration method aligns two DEMs, which improves the quality of DEM vertical accuracy significantly and is suitable and helpful for DEM quality assessment. This

## Chapter 7. Conclusions

method can also be used for merging and fusing bathymetry topography (Seafloor) with World DEM to generate a future global DEM. This method can also be applied in finding the correct landing site and precise and safe planetary rover landing for future planetary missions.

2) A DEM validation method with absolute planimetric/vertical and vertical comparison accuracy assessment was studied and the quality of SRTM, ASTER GDEM TanDEM -X IDEM and TanDEM -X DEM data over the UK was assessed. The DEM validation method can be used in any DEM data quality assessment. Meanwhile, the UK DEM (especially TanDEM -X IDEM and TanDEM -X DEM) quality report and statistical analysis results will be useful for DEM users and DEM maker.

3) Earth magnetosphere and atmosphere, Solar wind and EUV radiation create ions and electrons in the upper atmosphere as plasma ionosphere, which dramatically decreases the accuracy of 3D & 4D tomographic SAR imaging. A new ionospheric correction and mapping method is proposed and developed to address these problems to improve the accuracy of 3D & 4D tomographic SAR imaging. Firstly, TEC calculation is executed for absolute TEC data inversion based on tile method, IGS TEC data, split-spectrum and an ionospheric model via least squares methods. Then the TEC can be used for ionosphere correction of 3D & 4D tomographic SAR imaging. This new method not only can address the SAR ionospheric accuracy degradation problem, it's high resolution TEC data can also be obtained after processing and can be used in many other fields, like communication, radio astronomy, TEC application in many other terrestrial planets and its satellites (moons), with the same earth-like environment, and so on.

4) A SAR tomography imaging algorithm and a differential tomography four-dimensional SAR imaging processing system based on compressive sensing are studied theoretically. Meanwhile, orbit baseline estimation for 3D & 4D TomoSAR imaging is also tested and studied. A pixel by pixel orbit baseline estimation method fills the research gaps of baseline estimation for 3D & 4D SAR tomography imaging. What's more, a new SAR interferometry phase (InSAR) calibration method reference to DEM with DEM error correction and a new phase error calibration and compensation algorithm based on PS, SVD, PGA, weighted least squares and minimum entropy are proposed and demonstrated to obtain better 3D & 4D tomographic SAR imaging results. Many experiments in this thesis demonstrate that these new methods are effective to compensate

phase errors for 3D & 4D tomographic SAR imaging, which is also potentially useful for the phase error calibration and compensation of future SAR missions.

5) A systematic TomoSAR algorithm and methods have been established, demonstrated, tested and analysed in various applications (urban building, bridge, dam) to achieve better 3D & 4D D-tomographic SAR imaging results, which include using Cosmo-SkyMed X band data in Zipingpu dam, Dujiangyan, Sichuan, China, and using ALOS L band data in San Francisco Bay (urban building and bridge). These experiments demonstrate that the systematic TomoSAR algorithm and methods are efficient and effective to obtain the 3D & 4D information and are also potentially useful for many future application and missions.

### 7.3 Publications

The following peer review publications (journal papers), conference publications & presentations and conference posters based on this study and research work in the UK are outlined here.

#### 7.3.1 Peer Review Publications

(1) Papers in draft

1. Feng, L., J. P. Muller. " Accuracy Assessment of 30 m SRTM and ASTER G-DEM with 12 m, 30 m, 90 m TanDEM-X IDEM and 90 m TanDEM-X DEM over the UK using a bare earth terrain model from aerial photogrammetry and kinematic GPS." Prepared to submit to ISPRS or PFG.
2. Feng, L., J. P. Muller. " Study on orbit baseline estimation for 3D & 4D TomoSAR imaging." Prepared to submit to Remote Sensing.
3. Feng, L., J. P. Muller. " Spaceborne multi-baseline SAR tomography using COSMO-SkyMed SAR at Zipingpu dam, Dujiangyan, Sichuan, China." Prepared to submit to Sensors.

(2) Papers in preparation

1. Comparison between radargrammetry & InSAR and tomography for DSM & subsurface DEM generation. In Prep.

## Chapter 7. Conclusions

2. *Study on ionospheric correction for TomoSAR. In Prep.*
3. *Generate and Fuse DEM based on radargrammetry (LRO mini-rf) and photogrammetry (LRO NAC) in the south pole of the Moon. In Prep.*

### 7.3.2 Conference Publications & Presentations

1. *Feng, L., J. P. Muller, Y. Li, and M. Li. "An Improved Baseline Estimation Method Using External DEMs in Different Terrain Areas." In ESA Special Publication, vol. 731, p. 42. 2015.*
2. *Feng, L., J. P. Muller. "ICESAT validation of TANDEM-X IDEM over the UK." ISPRS2016 Commission IV, WG IV/3. 2016*
3. *Feng, L., J. P. Muller. " Study on a DTM Co-registration Algorithm for Improving Rover Landing Positioning Accuracy." International Artificial Intelligence, Robotics and Automation in Space (i-SAIRAS 2018). 2018*

### 7.3.3 Conference Posters

1. "Flood Range Feature Extraction Algorithm for Large Areas Based on High Resolution DEMs" RSPSoc Wavelength Meeting in March 2015, Newcastle, UK.
2. "Accuracy Assessment of SRTM 1, ASTER G-DEM and TanDEM-X IDEM over the UK and its implications for China" Dragon3 Symposium in June 2015, Interlaken, Switzerland.
3. "Accuracy Assessment of TanDEM-X IDEM over the UK by using kinematic GPS" RSPSoc Wavelength Meeting in March 2016, MSSL, UK.
4. "Comparison between radargrammetry and tomography for DSM & subsurface DEM generation and deformation extraction in densely vegetated mountainous rural areas" POLinSAR Workshop and training, January 2017, Frascati, Rome, Italy.
5. "3D Point Cloud Reconstruction Using Tomography (3D tomographic SAR imaging) in Densely Vegetated Mountainous Rural Areas" ESA Fringe Workshop in June 2017, Helsinki, Finland.
6. "Radar Polar Region Research on Earth, Venus, Saturn, Jupiter and Their Moons" 3rd Beijing International Forum on Lunar and Deep-space Exploration, September 2017, Beijing, China.
7. "3D tomographic SAR imaging in densely vegetated mountainous rural areas in China



and Sweden" 2017 AGU Fall Meeting, 2017, New Orleans, Louisiana, USA

8. "Radar Polar Region Research on Earth, Venus, Saturn, Jupiter and Their Moons" 49th Lunar and Planetary Science Conference, 2018, Woodlands, Houston, TX, USA
9. "Study on Ionospheric Tomography and Ionospheric Correction in Radio Astronomy and Radar Astronomy" European Week of Astronomy and Space Science (EWASS 2018), 2018, Liverpool, UK.
10. "DEM generation and rover landing at the south pole of the Moon" European Planetary Science Congress 2018, 2018, Germany.

### 7.4 Future Work

In this thesis, many complex problems have been identified when applying DEM co-registration, DEM validation and spaceborne SAR tomography.

- (1) The matching accuracy, matching correct rates, processing speed and big data processing requirements for DEM co-registration.
- (2) The factors limiting the performance for TomoSAR and D-TomoSAR are:
  - 1) Atmosphere and ionosphere phase disturbances
  - 2) Temporal decorrelation
  - 3) Orbit baseline accuracy
  - 4) Phase calibration
  - 5) TomoSAR and D-TomoSAR method for special environment

Some of these problems for TomoSAR and D-TomoSAR cannot be easily addressed through data processing methods. Thus, my recommendations for future spaceborne SAR systems are:

- 1) Reduce the time interval of repeat-pass acquisitions with a preference for same orbit repeats such as the TerraSAR-X and Tandem-X.
- 2) Use lower frequencies for forest areas, like P-band.
- 3) Acquire data during dawn or dusk to reduce atmospheric & ionospheric effects.
- 4) Use other data for atmosphere and ionosphere correction, like GPS, atmosphere data, TEC, in-situ detector data, other satellite data and so on.

In TomoSAR and D-TomoSAR processing, advanced AI and cloud computing processing strategies, atmospheric and ionospheric models, data assimilation, new phase calibration methods, new TomoSAR and D-TomoSAR may be investigated in future.

## Chapter 7. Conclusions

New matching methods, AI and cloud computing for DEM co-registration, photogrammetry and radargrammetry should also be studied in the future. Specifically, the DEM co-registration algorithm with robotics techniques can also be tested and improved for future entry descent and landing mission's scenarios of other planets, some moons of the planets, some comets and some asteroids.

Besides, the application of TomoSAR and D-TomoSAR imaging in other fields may be studied. For example, it might be easier to obtain ice subsurface tomographic structure via LRO Mini-RF S-band data on the Moon's polar region, because of very weak magnetic fields (ionosphere) and negligible atmospheric influence. Thus, 3D SAR imaging (SAR tomography) and 4D SAR imaging methods in the north and south polar region on the Earth's Moon could be studied in the future.

What's more, ionospheric tomography and ionospheric correction are needed in radio astronomy and radar astronomy, and the ionospheric tomography based on SAR imaging has very good prospects because it can easily obtain surface information in three-dimensional across the global area. Thus, ionospheric tomography and ionospheric correction for radio astronomy and radar astronomy could also be investigated in future.

# Appendices

## A. KGPS tables

These statistical tables below are TanDEM-X IDEM data quality assessment results based on KGPS and Bluesky data, which shows the absolute planimetric and vertical accuracy of TanDEM-X IDEM data validated by KGPS and Bluesky in detail.

Table A. 1 12 m DEM difference statistics based on KGPS and Bluesky matching in England and Scotland (after eliminating GPS errors), unit: m.

DATA	REGION	Resolution	xMin	xMax	xMean	xStdev $\sigma$	xRMSE	yMin	yMax	yMean	yStdev $\sigma$	yRMSE	RMSE XY	hMin	hMax	hMean	hStdev $\sigma$	Height RMSE
IDEM	England	12 m	-6.0	6.0	-1.3	3.7	3.8	-6.0	6.0	0.8	3.6	3.7	5.4	-46.1	57.1	1.0	3.2	3.4
IDEM	Scotland	12 m	-6.0	6.0	-1.9	3.9	3.9	-6.0	6.0	-0.5	3.7	3.7	5.4	-26.6	38.9	0.8	5.6	5.6

Table A. 2 Difference statistics based on KGPS and Bluesky matching in England &amp; Wales (after eliminating GPS errors), unit: m.

DATA	REGION	Resolution	xMin	xMax	xMean	xStdev $\sigma$	xRMSE	yMin	yMax	yMean	yStdev $\sigma$	yRMSE	RMSE XY	hMin	hMax	hMean	hStdev $\sigma$	Height RMSE
IDEM	England & Wales	30 m	-15.0	15.0	-8.0	6.3	10.1	-15.0	15.0	0.3	9.5	9.5	13.9	-50.5	59.8	1.0	4.1	4.2
ASTER	England & Wales	30 m	-15.0	15.0	-4.4	9.0	10.1	-15.0	15.0	-1.8	10.0	9.9	14.1	-62.85	71.4	-2.0	10.8	11.0
SRTM	England & Wales	30 m	-15.0	15.0	-7.7	6.8	10.3	-15.0	15.0	2.8	9.4	9.8	14.2	-44.0	61.3	1.6	4.3	4.5

Table A. 3 Difference statistics based on KGPS and Bluesky matching in Scotland (after eliminating GPS errors), unit: m.

DATA	REGION	Resolution	xMin	xMax	xMean	xStdev $\sigma$	xRMSE	yMin	yMax	yMean	yStdev $\sigma$	yRMSE	RMSE XY	hMin	hMax	hMean	hStdev $\sigma$	Height RMSE
IDEM	Scotland	30 m	-15.0	15.0	-8.6	5.9	10.4	-15.0	15.0	0.9	9.1	9.2	13.9	-94.0	87.6	1.5	5.8	6.0
ASTER	Scotland	30 m	-15.0	15.0	-4.4	9.0	10.0	-15.0	15.0	1.0	9.9	10.0	14.1	-79.3	85.0	-3.0	11.6	11.9
SRTM	Scotland	30 m	-15.0	15.0	-8.6	5.4	10.2	-15.0	15.0	3.0	9.2	9.6	14.0	-43.4	60.7	1.9	5.6	6.0

Table A. 4 Difference statistics based on KGPS and Bluesky matching in the UK (after eliminating GPS errors), unit: m.

DATA	REGION	Resolution	xMin	xMax	xMean	xStdev $\sigma$	xRMSE	yMin	yMax	yMean	yStdev $\sigma$	yRMSE	RMSE XY	hMin	hMax	hMean	hStdev $\sigma$	Height RMSE
IDEM	UK	30 m	-15.0	15.0	-5.7	8.0	9.8	-15.0	15.0	1.3	9.3	9.4	13.6	-94.0	88.0	1.3	5.2	5.3
ASTER	UK	30 m	-15.0	15.0	-4.4	6.5	7.8	-15.0	15.0	3.4	7.1	8.0	11.1	-79.8	85.7	-1.6	11.5	11.7
SRTM	UK	30 m	-15.0	15.0	-6.4	7.4	9.7	-15.0	15.0	3.3	9.0	9.6	13.6	-43.4	64.6	1.7	5.2	5.4

Table A. 5 Difference statistics based on KGPS and Bluesky matching in England & Wales (after eliminating GPS errors), unit: m.

DATA	REGION	Resolution	xMin	xMax	xMean	xStdev $\sigma$	xRMSE	yMin	yMax	yMean	yStdev $\sigma$	yRMSE	RMSE XY	hMin	hMax	hMean	hStdev $\sigma$	Height RMSE
IDEM	England & Wales	90 m	-45.0	32.4	-20.6	17.3	27.0	-45.0	45.0	-17.4	20.8	27.1	38.2	-50.8	78.0	1.3	5.4	5.6
ASTER	England & Wales	90 m	-45.0	30.4	-21.6	16.7	27.3	-45.0	44.9	-8.7	23.4	25.0	37.0	-83.7	71.0	-1.2	11.3	11.3
SRTM	England & Wales	90 m	-45.0	37.0	-21.0	16.0	26.3	- 42.289	45.0	11.6	19.0	22.2	34.5	-48.0	64.0	1.5	4.3	4.6

Table A. 6 Difference statistics based on KGPS and Bluesky matching in Scotland (after eliminating GPS errors), unit: m.

DATA	REGION	Resolution	xMin	xMax	xMean	xStdev $\sigma$	xRMSE	yMin	yMax	yMean	yStdev $\sigma$	yRMSE	RMSE XY	hMin	hMax	hMean	hStdev $\sigma$	Height RMSE
IDEM	Scotland	90 m	-45.0	21.0	-21.9	15.2	26.7	-45.0	45.0	1.5	22.8	22.9	35.1	-51.2	78.0	1.5	7.7	7.8
ASTER	Scotland	90 m	-45.0	24.7	-22.9	16.2	28.1	-45.0	45.0	-3.5	23.4	23.6	36.7	-76.9	93.0	-2.2	12.4	12.6
SRTM	Scotland	90 m	-45.0	25.4	-28.5	10.8	30.5	-45.0	45.0	4.4	16.0	16.6	34.7	-44.5	67.8	1.9	6.1	6.4

Table A. 7 Difference statistics based on KGPS and Bluesky matching in the UK (after eliminating GPS errors), unit: m.

DATA	REGION	Resolution	xMin	xMax	xMean	xStdev $\sigma$	xRMSE	yMin	yMax	yMean	yStdev $\sigma$	yRMSE	RMSE XY	hMin	hMax	hMean	hStdev $\sigma$	Height RMSE
IDEM	UK	90 m	-45.0	40.3	-16.2	19.1	25.0	-45.0	45.0	-11.6	23.8	26.4	36.4	-51.2	78.0	1.5	6.5	6.6
TanDEM	UK	90 m	-45.0	45.0	7.2	17.3	18.8	-21.7	33.1	0.3	21.9	22.5	29.4	-68.6	105.5	0.08	6.7	6.7
ASTER	UK	90 m	-45.0	45.0	-4.2	18.6	19.0	-45.0	45.0	-4.0	18.1	18.6	26.6	-75.8	110.2	-1.7	11.7	11.8
SRTM	UK	90 m	-45.0	4.05	-18.4	18.8	26.3	-45.0	45.0	11.8	19.9	23.1	35.0	-50.0	61.3	1.7	5.1	5.4

## B. Tables of the accuracy of DEM products

These tables below are the inter-comparison RMSE accuracy results and the accuracy of DEM products compared to Bluesky DTM data over UK before and after DEM co-registration.

### **(1) 12 m DEM products**

Table B. 1 DEM products (12 m) control point data RMSE statistics in England

DEM Product	Absolute Horizontal RMSE (m)	Absolute Vertical RMSE (m)	Control point data	Matching status	Relative Vertical RMSE (m)	Relative Control point data
TanDEM-X IDEM	5.4	3.4	KGPS	before	3.7	Bluesky
				after	1.9	Bluesky

Table B. 2 DEM products (12 m) accuracy (90% means 1.6\* RMSE) in England

DEM Product	Independent Pixel Spacing	Absolute Horizontal Accuracy (90% Confidence level) (m)	Absolute Vertical Accuracy, (90% Confidence level) (m)	Matching status	Relative Vertical Accuracy (90%) (m)	Coverage
TanDEM-X IDEM	12 m	$\leq 8.6$	$\leq 5.4$	before	$\leq 6.0$	England
				after	$\leq 3.1$	England

Table B. 3 DEM products (12 m) RMSE statistics in Scotland

DEM Product	Absolute Horizontal RMSE (m)	Absolute Vertical RMSE (m)	Control point data	Matching status	Relative Vertical RMSE (m)	Relative Control point data
TanDEM-X IDEM	5.4	5.6	KGPS	before	9.3	Bluesky
				after	4.1	Bluesky

Table B. 4 DEM products (12 m) accuracy (90% means 1.6\* RMSE) in Scotland

DEM Product	Independent Pixel Spacing	Absolute Horizontal Accuracy (90% Confidence level) (m)	Absolute Vertical Accuracy, (90% Confidence level) (m)	Matching status	Relative Vertical Accuracy (90%) (m)	Coverage
TanDEM-X IDEM	12 m	≤ 8.5	≤ 9.0	before	≤ 14.8	Scotland
				after	≤ 6.6	Scotland

**(2) 30 m DEM products**

Table B. 5 DEM products (30 m) RMSE statistics in WALES and England

DEM Product	Absolute Horizontal RMSE (m)	Absolute Vertical RMSE (m)	Control point data	Relative Vertical RMSE (m)	Relative Control point data
TanDEM-X IDEM	13.9	4.2	KGPS	6.8	Bluesky
SRTM 1	14.2	4.5	KGPS	5.9	Bluesky
ASTER G-DEM	14.1	11.0	KGPS	8.4	Bluesky



Table B. 6 DEM products (30 m) accuracy (90% means 1.6\* RMSE) in WALES and England

<b>DEM Product</b>	<b>Independent Pixel Spacing</b>	<b>Absolute Horizontal Accuracy (90% Confidence level) (m)</b>	<b>Absolute Vertical Accuracy, (90% Confidence level) (m)</b>	<b>Relative Vertical Accuracy (90%) (m)</b>	<b>Coverage</b>
<b>TanDEM-X IDEM</b>	30 m	$\leq 22.2$	$\leq 6.7$	$\leq 10.9$	WALES and England
<b>SRTM 1</b>	30 m	$\leq 22.7$	$\leq 7.3$	$\leq 9.4$	WALES and England
<b>ASTER G-DEM</b>	30 m	$\leq 22.6$	$\leq 17.6$	$\leq 13.4$	WALES and England

Table B. 7 DEM products (30 m) RMSE statistics in Scotland

<b>DEM Product</b>	<b>Absolute Horizontal RMSE (m)</b>	<b>Absolute Vertical RMSE (m)</b>	<b>Control point data</b>	<b>Relative Vertical RMSE (m)</b>	<b>Relative Control point data</b>
<b>TanDEM-X IDEM</b>	13.9	6.0	KGPS	20.0	Bluesky
<b>SRTM 1</b>	14.0	6.0	KGPS	10.5	Bluesky
<b>ASTER G-DEM</b>	14.1	11.9	KGPS	17.6	Bluesky

Table B. 8 DEM products (30 m) accuracy (90% means 1.6\* RMSE) in Scotland

<b>DEM Product</b>	<b>Independent Pixel Spacing</b>	<b>Absolute Horizontal Accuracy (90% Confidence level) (m)</b>	<b>Absolute Vertical Accuracy, (90% Confidence level) (m)</b>	<b>Relative Vertical Accuracy (90%) (m)</b>	<b>Coverage</b>
<b>TanDEM-X IDEM</b>	30 m	$\leq 22.2$	$\leq 9.6$	$\leq 31.9$	Scotland

<b>DEM Product</b>	<b>Independent Pixel Spacing</b>	<b>Absolute Horizontal Accuracy (90% Confidence level) (m)</b>	<b>Absolute Vertical Accuracy, (90% Confidence level) (m)</b>	<b>Relative Vertical Accuracy (90%) (m)</b>	<b>Coverage</b>
<b>SRTM 1</b>	30 m	$\leq 22.5$	$\leq 9.5$	$\leq 16.8$	Scotland
<b>ASTER G-DEM</b>	30 m	$\leq 22.6$	$\leq 19.1$	$\leq 28.1$	Scotland

Table B. 9 DEM products (30 m) RMSE statistics in UK

<b>DEM Product</b>	<b>Absolute Horizontal RMSE (m)</b>	<b>Absolute Vertical RMSE (m)</b>	<b>Control point data</b>	<b>Matching status</b>	<b>Relative Vertical RMSE (m)</b>	<b>Relative Control point data</b>
<b>TanDEM-X IDEM</b>	13.6	5.3	KGPS	before	14.8	Bluesky
				after	3.7	Bluesky
<b>SRTM 1</b>	13.6	5.4	KGPS	before	7.1	Bluesky
				after	4.1	Bluesky
<b>ASTER G-DEM</b>	11.1	11.7	KGPS	before	12.2	Bluesky
				after	4.5	Bluesky

Table B. 10 DEM products (30 m) accuracy (90% means 1.6\* RMSE) in UK

<b>DEM Product</b>	<b>Independent Pixel Spacing</b>	<b>Absolute Horizontal Accuracy (90% Confidence level) (m)</b>	<b>Absolute Vertical Accuracy, (90% Confidence level) (m)</b>	<b>Matching status</b>	<b>Relative Vertical Accuracy (90%) (m)</b>	<b>Coverage</b>
<b>TanDEM-X IDEM</b>	30 m	$\leq 21.8$	$\leq 8.5$	before	$\leq 23.7$	UK
				after	$\leq 6.0$	UK
<b>SRTM 1</b>	30 m	$\leq 21.8$	$\leq 8.7$	before	$\leq 11.3$	UK
				after	$\leq 6.6$	UK
<b>ASTER G-DEM</b>	30 m	$\leq 17.8$	$\leq 18.6$	before	$\leq 19.5$	UK
				after	$\leq 7.2$	UK

**(3) 90 m DEM products**

Table B. 11 DEM products (90 m) RMSE statistics in WALES and England

<b>DEM Product</b>	<b>Absolute Horizontal RMSE (m)</b>	<b>Absolute Vertical RMSE (m)</b>	<b>Control point data</b>	<b>Relative Vertical RMSE (m)</b>	<b>Relative Control point data</b>
<b>TanDEM-X IDEM</b>	38.2	5.6	KGPS	8.3	Bluesky
<b>SRTM 1</b>	34.5	4.6	KGPS	5.5	Bluesky
<b>ASTER G-DEM</b>	37.0	11.3	KGPS	11.5	Bluesky

Table B. 12 DEM products (90 m) accuracy (90% means 1.6\* RMSE) in WALES and England

<b>DEM Product</b>	<b>Independent Pixel Spacing</b>	<b>Absolute Horizontal Accuracy (90% Confidence level) (m)</b>	<b>Absolute Vertical Accuracy, (90% Confidence level) (m)</b>	<b>Relative Vertical Accuracy (90%) (m)</b>	<b>Coverage</b>
<b>TanDEM-X IDEM</b>	90 m	$\leq 61.2$	$\leq 9.0$	$\leq 13.3$	WALES and England
<b>SRTM 1</b>	90 m	$\leq 55.2$	$\leq 7.3$	$\leq 8.8$	WALES and England
<b>ASTER G-DEM</b>	90 m	$\leq 59.2$	$\leq 18.1$	$\leq 18.4$	WALES and England

Table B. 13 DEM products (90 m) RMSE statistics in Scotland

<b>DEM Product</b>	<b>Absolute Horizontal RMSE (m)</b>	<b>Absolute Vertical RMSE (m)</b>	<b>Control point data</b>	<b>Relative Vertical RMSE (m)</b>	<b>Relative Control point data</b>
<b>TanDEM-X IDEM</b>	35.1	7.8	KGPS	23.3	Bluesky
<b>SRTM 1</b>	34.7	6.4	KGPS	13.0	Bluesky
<b>ASTER G-DEM</b>	36.7	12.6	KGPS	19.2	Bluesky

Table B. 14 DEM products (90 m) accuracy (90% means 1.6\* RMSE) in Scotland

<b>DEM Product</b>	<b>Independent Pixel Spacing</b>	<b>Absolute Horizontal Accuracy (90% Confidence level) (m)</b>	<b>Absolute Vertical Accuracy, (90% Confidence level) (m)</b>	<b>Relative Vertical Accuracy (90%) (m)</b>	<b>Coverage</b>
<b>TanDEM-X IDEM</b>	90 m	$\leq 56.2$	$\leq 12.5$	$\leq 37.2$	Scotland

<b>DEM Product</b>	<b>Independent Pixel Spacing</b>	<b>Absolute Horizontal Accuracy (90% Confidence level) (m)</b>	<b>Absolute Vertical Accuracy, (90% Confidence level) (m)</b>	<b>Relative Vertical Accuracy (90%) (m)</b>	<b>Coverage</b>
<b>SRTM 1</b>	90 m	$\leq 55.5$	$\leq 10.2$	$\leq 20.8$	Scotland
<b>ASTER G-DEM</b>	90 m	$\leq 58.7$	$\leq 20.1$	$\leq 30.8$	Scotland

Table B. 15 DEM products (90 m) RMSE statistics in UK

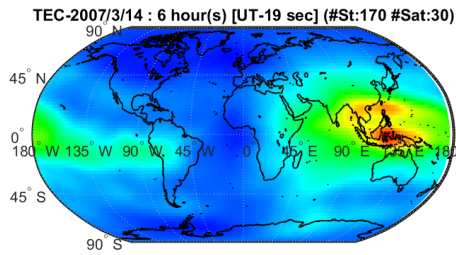
<b>DEM Product</b>	<b>Absolute Horizontal RMSE (m)</b>	<b>Absolute Vertical RMSE (m)</b>	<b>Control point data</b>	<b>Matching status</b>	<b>Relative Vertical RMSE (m)</b>	<b>Relative Control point data</b>
<b>TanDEM-X IDEM</b>	36.4	6.6	KGPS	before	18.2	Bluesky
				after	4.4	Bluesky
<b>TanDEM-X DEM</b>	29.4	6.7	KGPS	before	11	Bluesky
				after	5.2	Bluesky
<b>SRTM 1</b>	35.0	5.4	KGPS	before	9.4	Bluesky
				after	4.0	Bluesky
<b>ASTER G-DEM</b>	26.6	11.8	KGPS	before	14.8	Bluesky
				after	4.5	Bluesky

Table B. 16 DEM products (90 m) accuracy (90% means 1.6\* RMSE) in UK

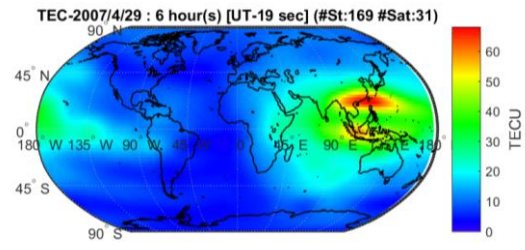
<b>DEM Product</b>	<b>Independent Pixel Spacing</b>	<b>Absolute Horizontal Accuracy (90% Confidence level) (m)</b>	<b>Absolute Vertical Accuracy, (90% Confidence level) (m)</b>	<b>Matching status</b>	<b>Relative Vertical Accuracy (90%) (m)</b>	<b>Cover age</b>
<b>TanDEM-X IDEM</b>	90 m	$\leq 58.2$	$\leq 10.6$	before	$\leq 29.1$	UK
				after	$\leq 7.1$	UK
<b>TanDEM-X DEM</b>	90 m	$\leq 47.0$	$\leq 10.7$	before	$\leq 17.6$	UK
				after	$\leq 8.4$	UK
<b>SRTM 1</b>	90 m	$\leq 56.0$	$\leq 8.6$	before	$\leq 15.0$	UK
				after	$\leq 6.4$	UK
<b>ASTER G-DEM</b>	90 m	$\leq 42.5$	$\leq 18.8$	before	$\leq 23.7$	UK
				after	$\leq 7.2$	UK

## C. The Global TEC map from IGS

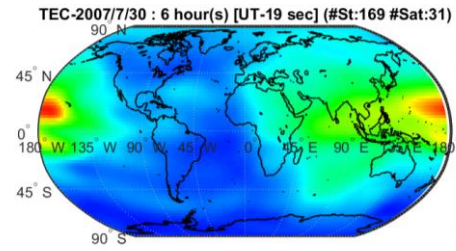
These figures are the global TEC map of the closest time of the ALOS SAR measurement time from International GPS Service Centre (IGS) (19 s means the difference between UT (TAI) and GPS time, St is station number used, Sat is satellite number used for generating the TEC data).



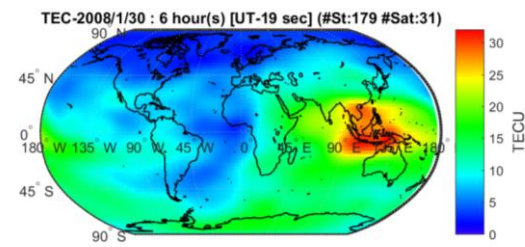
(a)



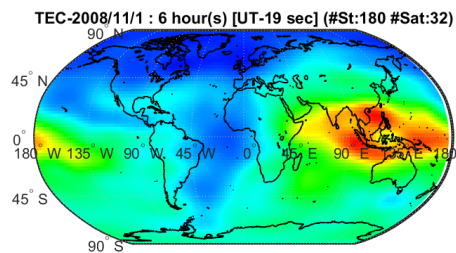
(b)



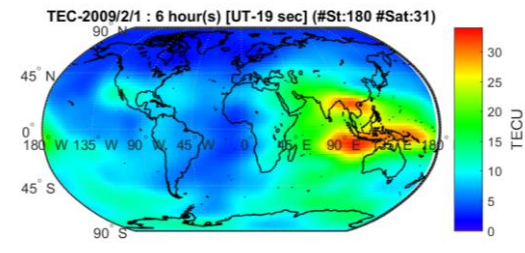
(c)



(d)



(e)



(f)

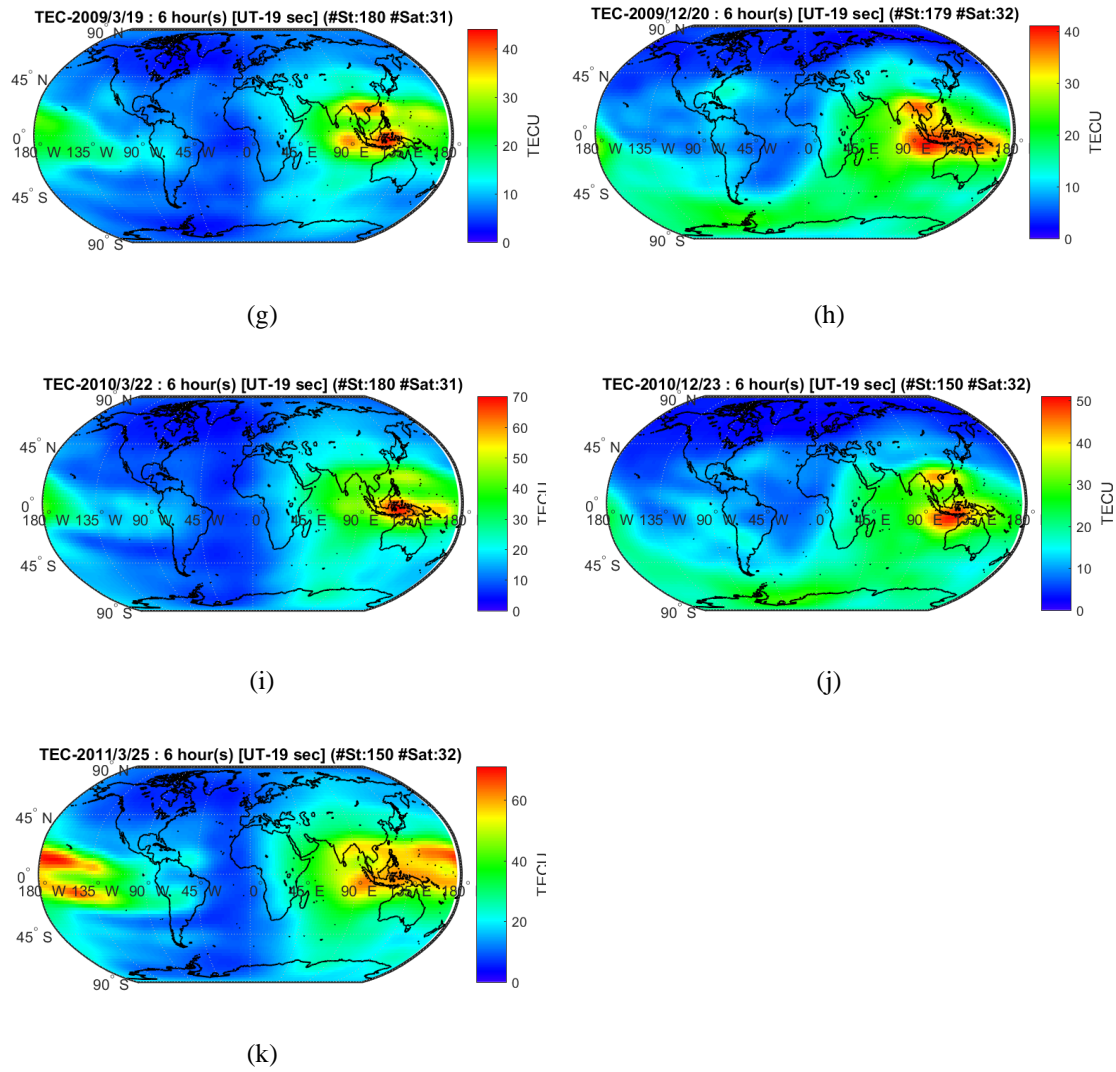


Figure C. 1 The global TEC map of the closest time of the ALOS SAR measurement time from International GPS Service Centre (IGS)



## D. The original and new interpolated orbits

Table D. 1 The original orbit information based on time in the azimuth direction in the first range pixel, the text is orbit time (unit: seconds), x, y, z (unit: metres). The original orbit information is based on time (Time, x, y, z in *SCH* coordinate system, the time is based on the reference time, which is the start time of the first pixel of the SAR frame)

<b>Id</b>	<b>Time (s)</b>	<b>x (m)</b>	<b>y (m)</b>	<b>z (m)</b>
30	0.558387	2958.930	390.704	625917.531
31	0.558387	2958.930	390.704	625917.531
32	0.558387	2958.930	390.704	625917.531
33	0.558387	2958.930	390.704	625917.531
34	0.558387	2958.930	390.704	625917.531
35	0.558387	2958.930	390.704	625917.531
36	0.558387	2958.930	390.704	625917.531
37	0.558387	2958.930	390.704	625917.531
38	0.558387	2958.930	390.704	625917.531
39	0.558387	2958.930	390.704	625917.531
40	0.558387	2958.930	390.704	625917.531
41	0.558387	2958.930	390.704	625917.531
42	0.558387	2958.930	390.704	625917.531
43	0.558387	2958.930	390.704	625917.531
44	0.558387	2958.930	390.704	625917.531
45	0.558387	2958.930	390.704	625917.531
46	0.558387	2958.930	390.704	625917.531
47	0.558387	2958.930	390.704	625917.531
48	0.558387	2958.930	390.704	625917.531
49	0.558387	2958.930	390.704	625917.531
50	0.558387	2958.930	390.704	625917.531
51	0.566199	2990.882	390.700	625917.601
52	0.566199	2990.882	390.700	625917.601
53	0.566199	2990.882	390.700	625917.601
54	0.566199	2990.882	390.700	625917.601
55	0.566199	2990.882	390.700	625917.601
56	0.566199	2990.882	390.700	625917.601
57	0.566199	2990.882	390.700	625917.601
58	0.566199	2990.882	390.700	625917.601
59	0.566199	2990.882	390.700	625917.601

<b>Id</b>	<b>Time (s)</b>	<b>x (m)</b>	<b>y (m)</b>	<b>z (m)</b>
60	0.566199	2990.882	390.700	625917.601
61	0.566199	2990.882	390.700	625917.601
62	0.566199	2990.882	390.700	625917.601
63	0.566199	2990.882	390.700	625917.601
64	0.566199	2990.882	390.700	625917.601
65	0.566199	2990.882	390.700	625917.601
66	0.566199	2990.882	390.700	625917.601
67	0.566199	2990.882	390.700	625917.601
68	0.566199	2990.882	390.700	625917.601

Table D. 2 The new interpolated orbits based on time in the azimuth direction in the first range pixel, the text is orbit time (unit: seconds), x, y, z (unit: metres). The new orbit information is based on time after interpolation (Time, x, y, z in *SCH* coordinate system, the reference time is the start time of the first pixel of the SAR frame)

<b>Id</b>	<b>Time (s)</b>	<b>x (m)</b>	<b>y (m)</b>	<b>z (m)</b>
30	0.564069	2982.170	390.701	625917.582
31	0.56417	2982.583	390.701	625917.583
32	0.564272	2983.000	390.701	625917.584
33	0.564373	2983.413	390.701	625917.585
34	0.564475	2983.830	390.701	625917.586
35	0.564576	2984.244	390.701	625917.587
36	0.564678	2984.661	390.701	625917.588
37	0.564779	2985.074	390.701	625917.589
38	0.564881	2985.491	390.701	625917.590
39	0.564982	2985.904	390.701	625917.590
40	0.565083	2986.317	390.701	625917.591
41	0.565185	2986.734	390.700	625917.592
42	0.565286	2987.148	390.700	625917.593
43	0.565388	2987.565	390.700	625917.594
44	0.565489	2987.978	390.700	625917.595
45	0.565591	2988.395	390.700	625917.596
46	0.565692	2988.808	390.700	625917.597
47	0.565794	2989.225	390.700	625917.598
48	0.565895	2989.639	390.700	625917.599
49	0.565997	2990.056	390.700	625917.600
50	0.566098	2990.469	390.700	625917.600
51	0.566199	2990.882	390.700	625917.601
52	0.566301	2991.299	390.700	625917.602
53	0.566402	2991.712	390.700	625917.603
54	0.566504	2992.129	390.700	625917.604
55	0.566605	2992.542	390.700	625917.605
56	0.566707	2992.960	390.700	625917.606
57	0.566808	2993.373	390.700	625917.607

<b>Id</b>	<b>Time (s)</b>	<b>x (m)</b>	<b>y (m)</b>	<b>z (m)</b>
58	0.56691	2993.790	390.700	625917.608
59	0.567011	2994.203	390.700	625917.609
60	0.567113	2994.620	390.699	625917.610
61	0.567214	2995.033	390.699	625917.610
62	0.567316	2995.451	390.699	625917.611
63	0.567417	2995.864	390.699	625917.612
64	0.567518	2996.277	390.699	625917.613
65	0.56762	2996.694	390.699	625917.614
66	0.567721	2997.107	390.699	625917.615
67	0.567823	2997.524	390.699	625917.616
68	0.567924	2997.937	390.699	625917.617

This page is intentionally left blank.

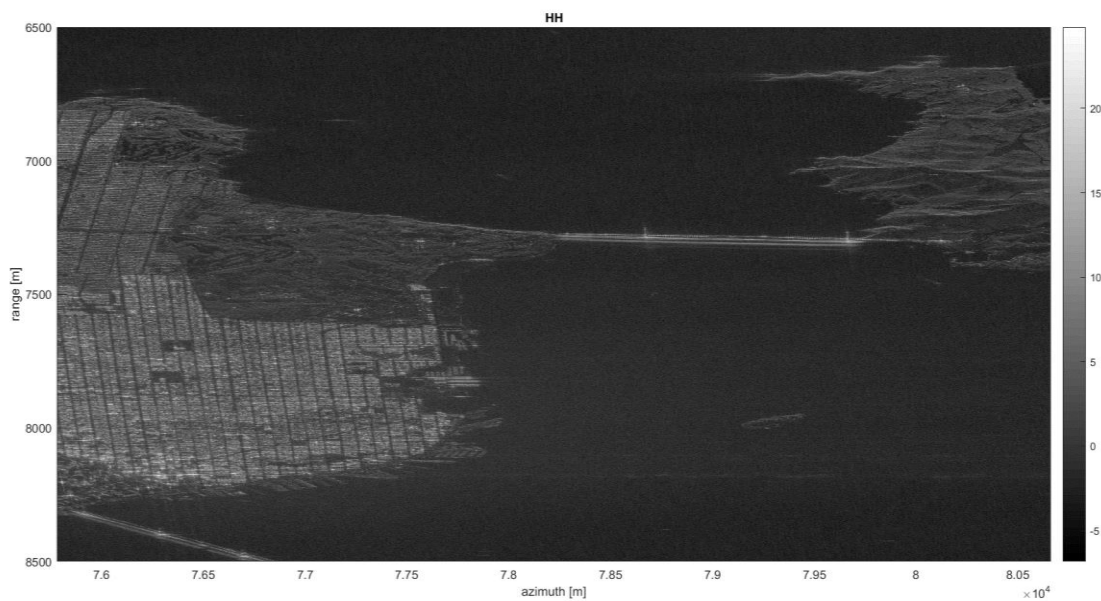
## **E. The Application of TOMOSAR to ALOS L Band over San Francisco**

### **1.1 Test Sites, the ALOS Data and the LIDAR Data**

The test site is selected at the famous SAR test site in San Francisco Bay, USA. SAR image of 20090201 is the master image for InSAR and TomoSAR. The Advanced Land Observing Satellite one (ALOS-1) data were downloaded from the Alaska Satellite Facility (ASF-Team, 2010) for our TomoSAR test and ionospheric research. 11 ALOS-1 ascending data stacks are used, and the metadata of the ascending data stacks are shown in Table E. 1. The incidence angle is about 24.0 degrees, the time is from 14/03/2007 to 25/03/2011, and the baseline is from -647 metres to 4778 metres. The small test area SAR image is shown in Figure E. 1 (a). The LIDAR Points are obtained from the LIDAR Point Cloud (LPC) projects collected by USGS with LAS format (geo-referenced x, y, z coordinates) (Witt III, 2015; Heidemann, 2012; Stoker et al., 2016; Arundel et al., 2015). The coordinates system is (x and y) is the North American Datum of 1983 (NAD 83), and the vertical datum for orthometric heights (z) is the North American Vertical Datum of 1988 (NAVD 88). Firstly, the geoid (Geoid12b) model is used to convert the orthometric heights to the ellipsoid heights, and the data are transformed into WGS84 geodetic coordinate system (latitude and longitude). Then, the DEM (bare earth, 1 m resolution, or DTM) and DSM (1 m resolution with buildings and bridges) data are extracted from the data. The LIDAR DEM data are fused with SRTM 30 m data (shown in Figure E. 1 (b).) to obtain the final fused DEM (shown in Figure E. 1 (d)), which is used as terrain data for deramping in 3D TomoSAR imaging. Meanwhile, the LIDAR DSM data (shown in Figure E. 1 (c).) are used to validate the 3D TomoSAR imaging results at the last step. The difference map between the LIDAR DSM data and the final fused DEM data is shown in Figure E. 1 (e), where buildings and bridges are clearly seen.

Table E. 1 ALOS data metadata, master image is on 01/02/2009, shown in red font

id	Incidence angle	time	Track type	Baseline (m)
1	24.0	14/03/2007	Ascending	1497
2	24.0	29/04/2007	Ascending	1990
3	24.0	30/07/2007	Ascending	1947
4	24.0	30/01/2008	Ascending	3246
5	24.0	01/11/2008	Ascending	-647
6	24.0	01/02/2009	Ascending	0
7	24.0	19/03/2009	Ascending	473
8	24.0	20/12/2009	Ascending	1734
9	24.0	22/03/2010	Ascending	2688
10	24.0	23/12/2010	Ascending	3719
11	24.0	25/03/2011	Ascending	4778



(a)

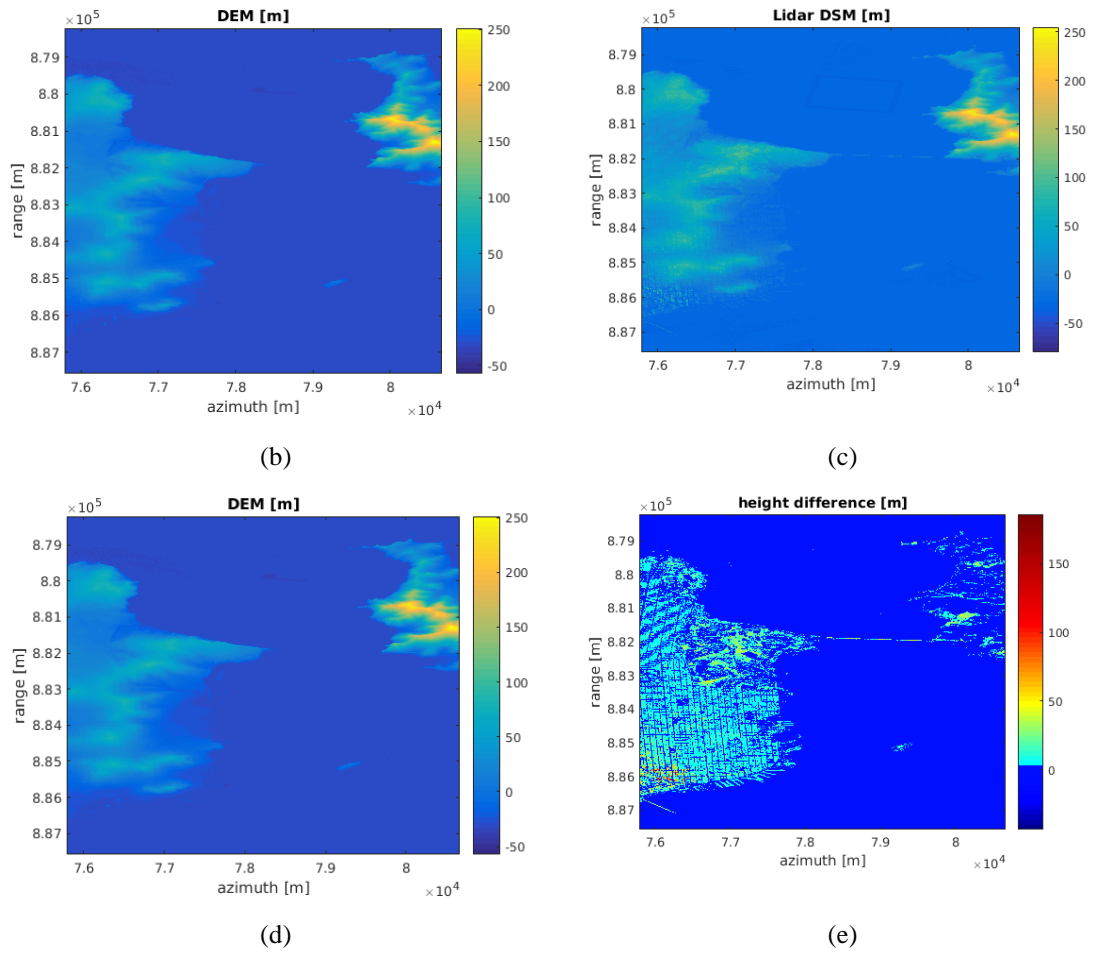
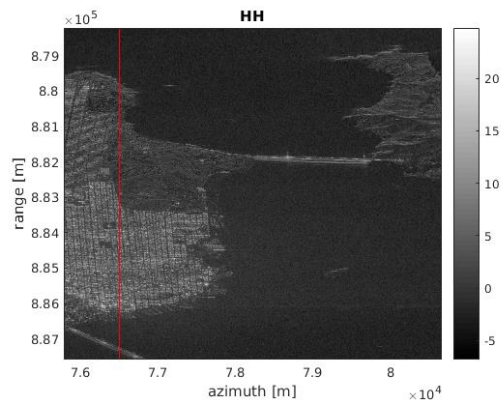
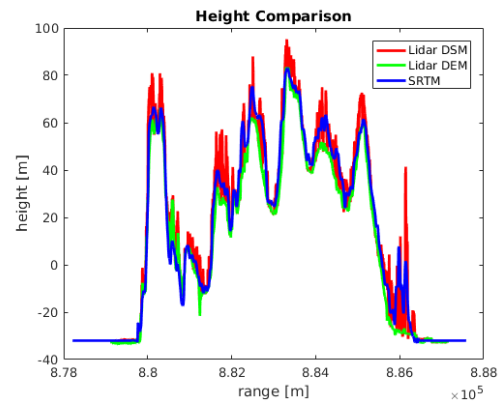


Figure E. 1 The small test area in San Francisco Bay, USA: (a) SAR image; (b) 30 m SRTM data; (c) 1 m LIDAR DSM data; (d) Final fused DEM data (5 m); (e) Difference map between (c) and (d)

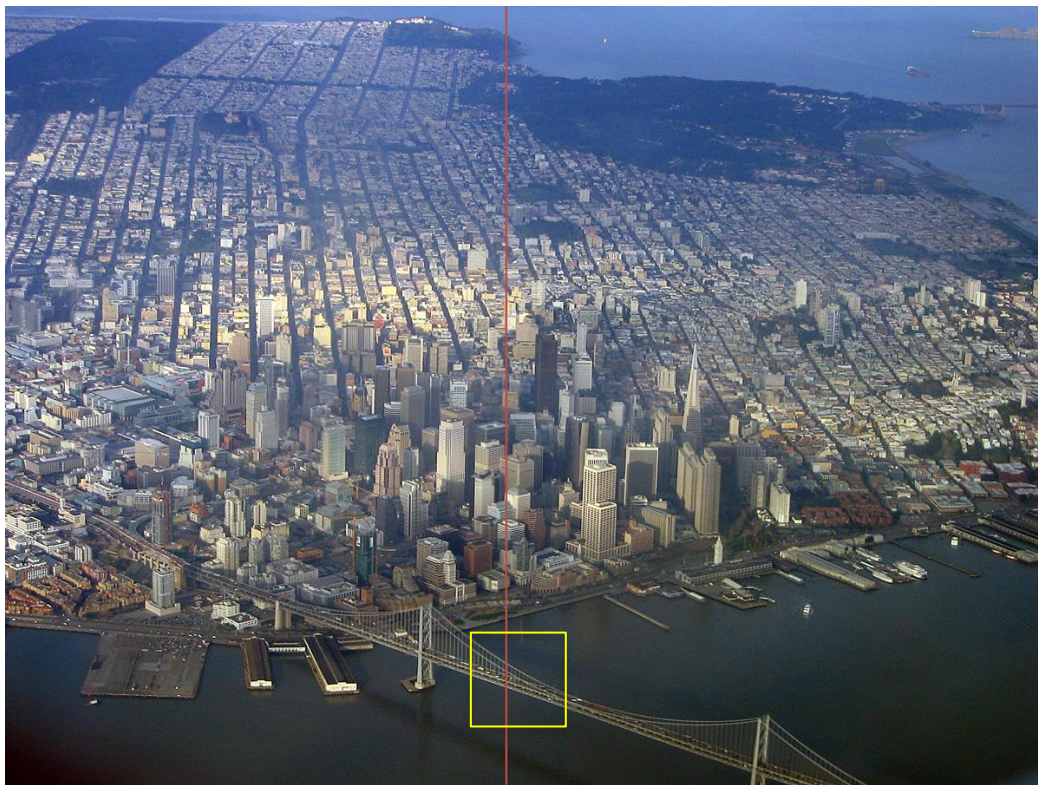
Two sub-test lines are selected to test the TomoSAR algorithms. We call them Test-A and Test-B. The information of these two test lines is shown in Figure E. 2 and Figure E. 3 below.



(a)



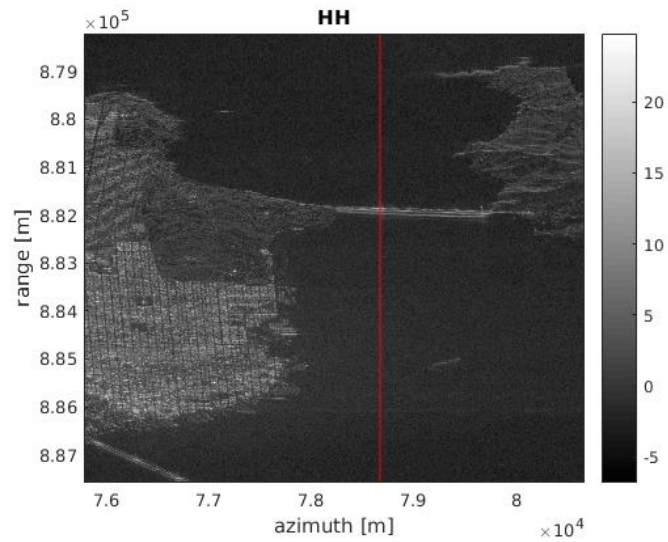
(b)



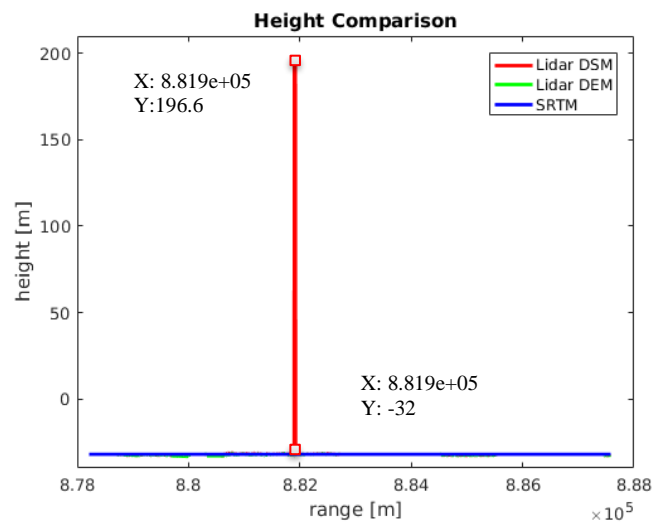
(c)

Figure E. 2 The position and information of Test-A area : (a) Azimuth test line on SAR image; (b) Height comparison at the azimuth test line; (c) The test line (red) on the image of the building area of San Francisco Bay, USA, Copyright © 2007 FreeLargePhotos.com





(a)



(b)



(c)

Figure E. 3 The position and information of Test-B area : (a) Azimuth test line on SAR image; (b) Height comparison at the azimuth test line; (c) The test line (yellow) on the image of the Golden Gate Bridge of San Francisco Bay, USA , Copyright 2002 Strength in Perspective

The ALOS-1 (a 4-ton weight satellite) was developed by the Japan Aerospace Exploration Agency (JAXA) and launched on January 24th, 2006, which has contributed to the fields of mapping, disaster monitoring, land coverage observation, and resource surveying. ALOS-1 has three sensors: the Panchromatic Remote-sensing Instrument for Stereo Mapping (PRISM), the Phased Array Type L-band Synthetic Aperture Radar (PALSAR) and the Advanced Visible and Near Infrared Radiometer type 2 (AVNIR-2).

Table E. 2 Characteristics of ALOS PALSAR sensor

Parameter Name	Value
Orbit Direction	Ascending
Altitude	706 km
Radar wavelength	23.61 cm
PRF	1915.709 Hz
Incidence Angle	24.0
Swath Width	12.44 km
Azimuth Resolution	4.45 m
Range Resolution	9.52 m
Temporal Baseline	46 days

## 1.2 Compressive Sensing Results

### 1.2.1 Data Preparation

The InSAR interferogram (show in Figure E. 4 (b)) is obtained by ISCE software, then the split spectrum differential data, which will be used in TEC estimation and TomoSAR, are obtained by split spectrum method (Section 4.2.2), shown in Figure E. 4 (a). The split spectrum differential data are used for ionospheric correction for InSAR, and the corrected result is shown in Figure E. 4 (c). Compared to the InSAR interferogram (some fringes are shown in Figure E. 4 (a)) before ionospheric correction, there is no deformation (no fringes) after ionospheric correction in the InSAR interferogram, shown in Figure E. 4 (c). Then, TEC calculation was executed for absolute TEC data inversion based on the IGS TEC data, split-spectrum and the temporal variance ionospheric model via least squares method (Section 4.2.4 in Chapter 4). After using the least squares method, the absolute TEC of the master SLC date in the test area is obtained, and then other slave

absolute TEC data can be obtained by adding the split spectrum differential data. These TEC data are used in ionospheric calibration; the steps and results are shown in the section below.

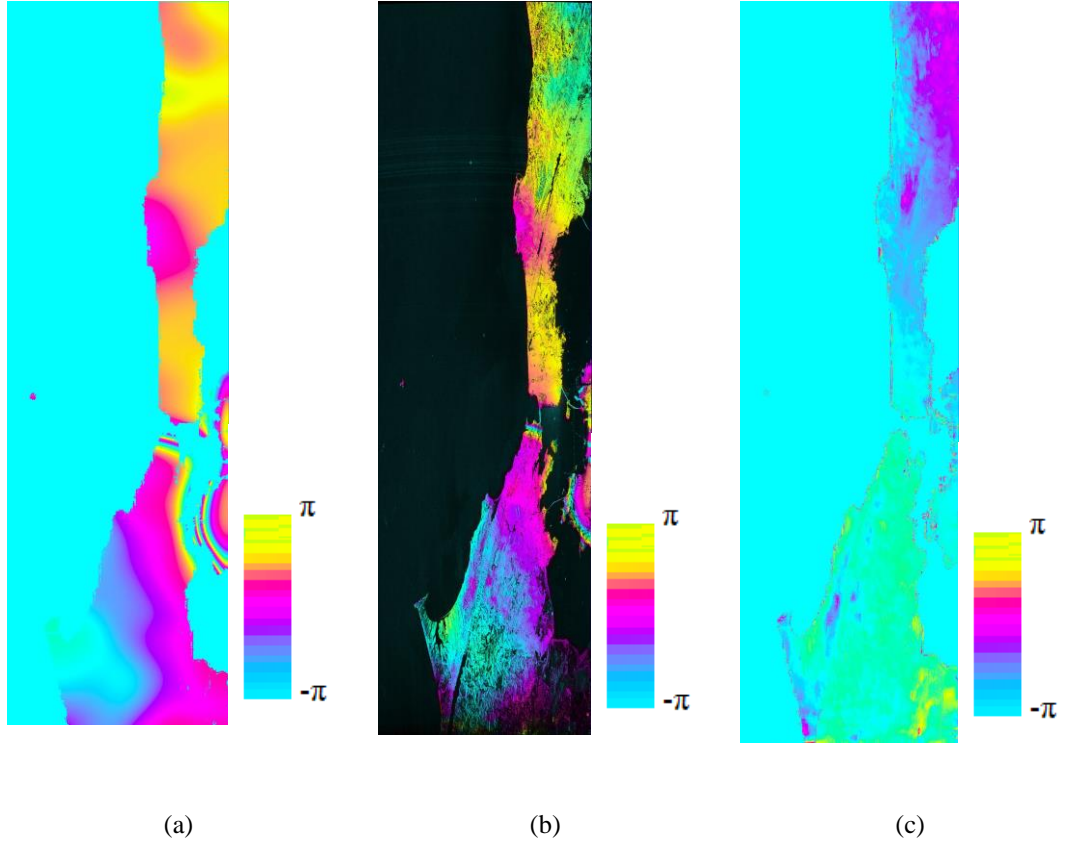


Figure E. 4 Ionospheric correction via split spectrum: (a) Ionosphere differential phase (20090319-20090201) via split spectrum; (b) 20090319-20090201 unwrapped interferogram before ionospheric correction; (c) 20090319-20090201 unwrapped interferogram after ionospheric correction

### 1.2.2 Results before Ionospheric Calibration

In the Test-A area, DEM deramping, ERA tropospheric correction, PS-SVD-PGA, weighted least squares and minimum entropy calibration (PS-SVD-PGA-LS-ME) are combined for phase calibration. As DEM deramping is the basic step and executed for TomoSAR, the height reference is the final fused DEM. Then, a test is studied via FFT and Capon method after these calibrations; the results are shown below. The colour in these results is also the magnitude (intensity or amplitude) of the complex scattering coefficient  $\gamma(s)$  along height direction in the height-range plane.

A strong scattering line around 0 m (the ground surface) and the strong scattering line (the top of the building at  $8.83-8.86 \times 10^5$  m in the range,) is around the LIDAR DSM are shown in Figure E. 5 and Figure E. 6 below. However, it is easy to see from these

results that there are still some errors (targets are randomly distributed in Figure E. 6 and the red jump line in Figure E. 5 (a) and (b)), which needs ionospheric calibration, like using our split spectrum ionospheric phase distortion correction method.

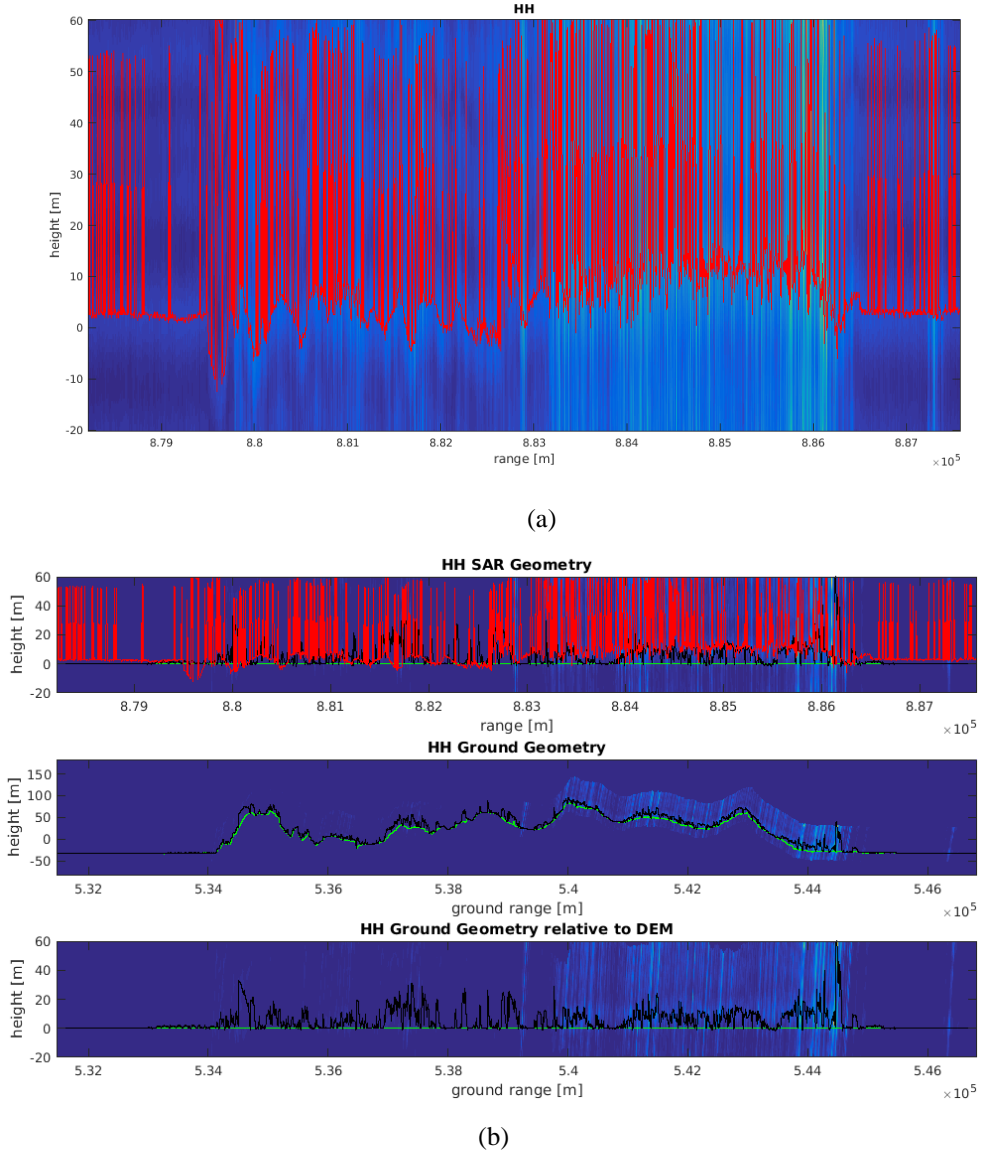


Figure E. 5 TomoSAR results via FFT in Test-A area before ionospheric calibration: (a) Tomograms via FFT in Test-A, the red jump line is the position of max scattering value, the colour is the magnitude of the complex scattering coefficient  $\gamma(s)$ ; (b) Geocoded tomograms via FFT in Test-A, the colour is the magnitude of the complex scattering coefficient  $\gamma(s)$ , the red line is the position of max scattering value, the green line is the fused DEM, and the black line is the LIDAR DSM

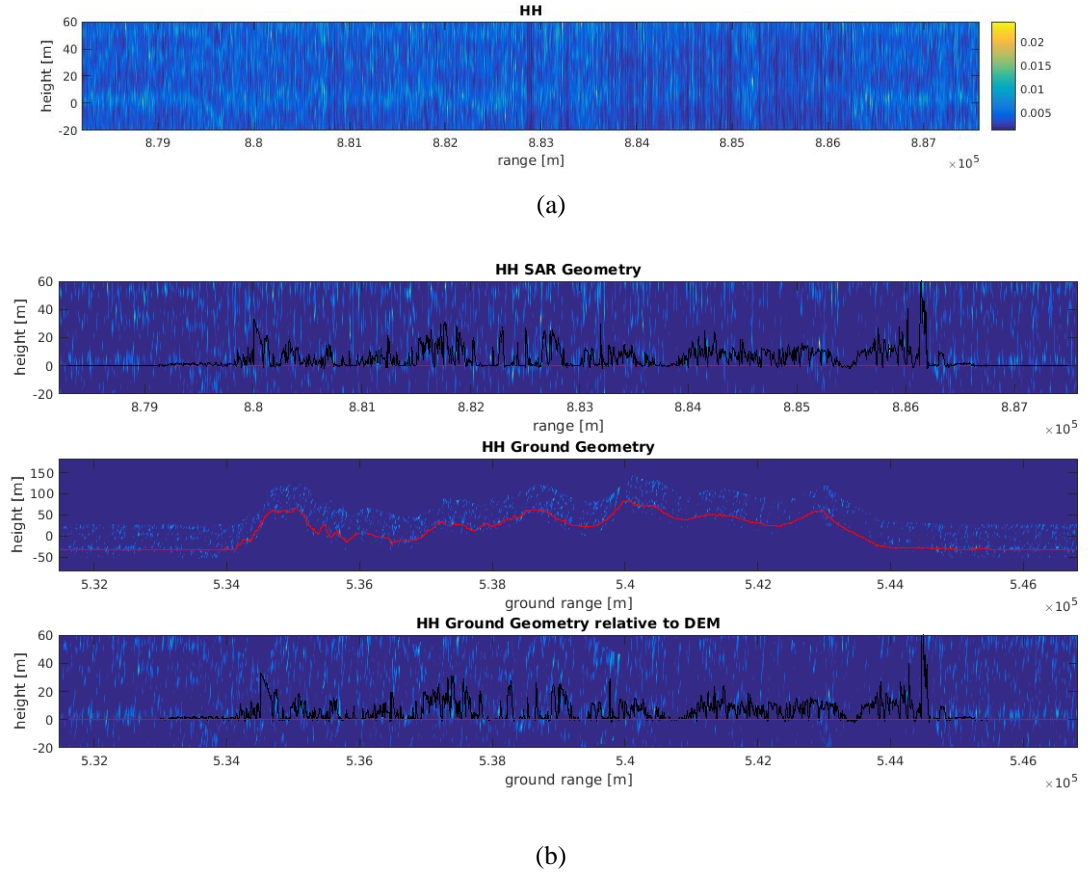


Figure E. 6 TomoSAR results via Capon in Test-A area before ionospheric calibration: (a) Tomograms via Capon in Test-A before magnitude filtering of scattering coefficient, the colour is the magnitude of the complex scattering coefficient  $\gamma(s)$ ; (b) Geocoded tomograms via Capon in Test-A after magnitude filtering of scattering coefficient (noise filter), the colour is the magnitude of the complex scattering coefficient  $\gamma(s)$ , the red line is the fused DEM, and the black line is the LIDAR DSM

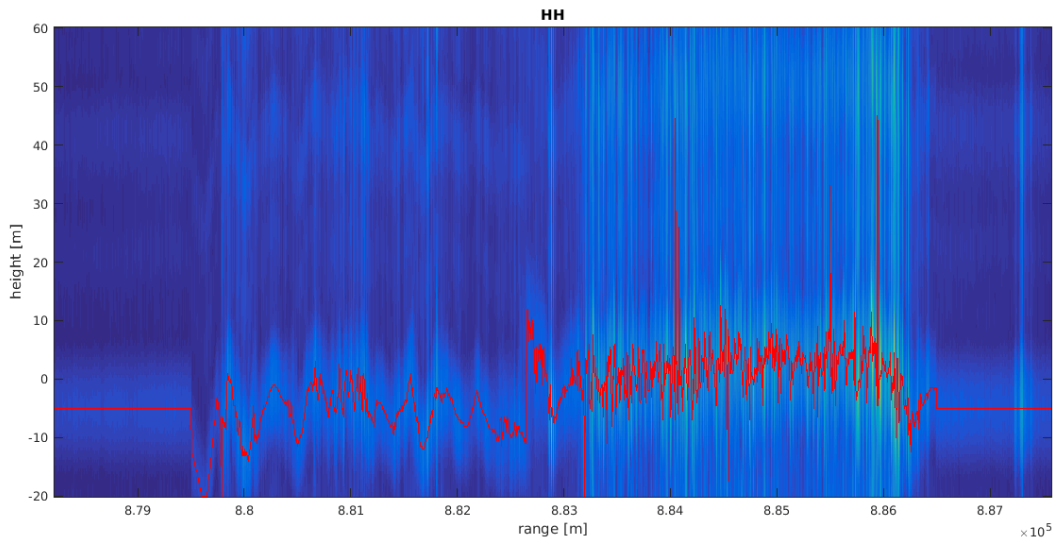
### 1.2.3 Results after Ionospheric Calibration

In the Test-A area, our split spectrum ionospheric phase distortion correction method is combined with DEM deramping, ERA tropospheric correction, PS-SVD-PGA, weighted least squares and minimum entropy calibration (PS-SVD-PGA-LS-ME) for phase calibration first. Then, a test is studied via FFT and Capon method after these calibrations; the results are shown below.

Compared the results (in Figure E. 7 (a) and (b)) after ionospheric correction to the results before ionospheric correction (in Figure E. 5 (a) and (b)), there is no big jump when seeing the red line in Figure E. 7 (a) and (b), which indicates our ionospheric phase calibration method works.

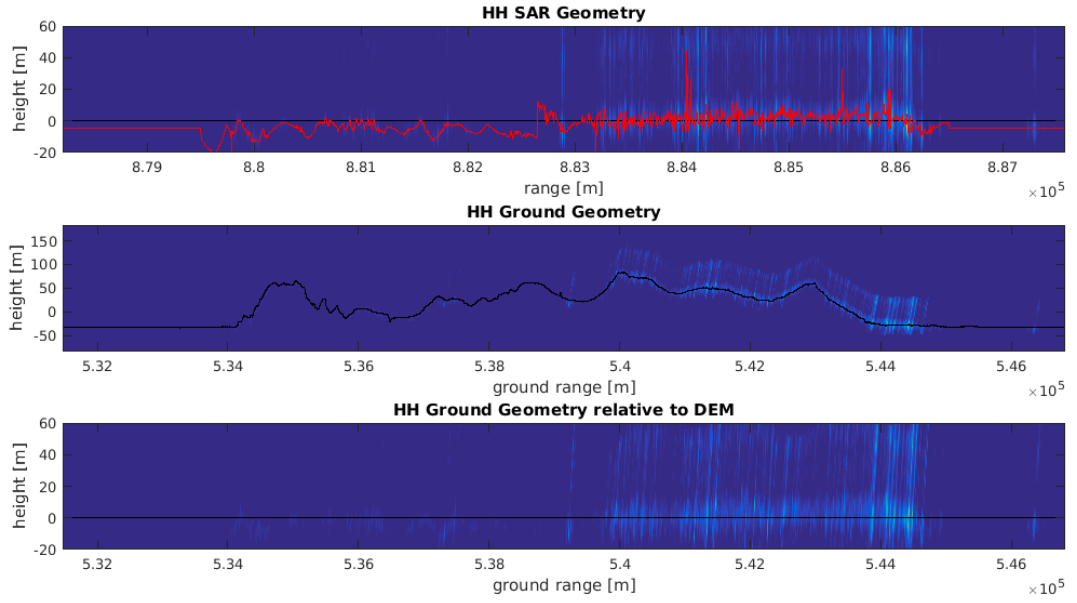
A strong scattering line around - 6 m is shown in Figure E. 7 and Figure E. 8 (all results of FFT and Capon) below. Compared to the LIDAR DSM (in Figure E. 8) and the

InSAR calibration results (a strong scattering line around 0 m in Figure E. 9 and Figure E. 11), the structure is the same, but a group shift occurs. This might be caused by the errors and uncertainties in the split spectrum results (absolute TEC results), but it does not influence the TomoSAR structure. This shift can be corrected by the control point in TomoSAR processing. Therefore, it is ready for TomoSAR reconstruction after all these calibrations (ERA tropospheric, split spectrum ionospheric phase distortion correction and other errors). In the TomoSAR reconstruction results, shown in Figure E. 7 and Figure E. 8, of the urban building area in Test-A, there are strong scatterers at the top and the bottom (at  $8.83\text{--}8.86 \times 10^5$  m in the range). Moreover, some high buildings (compared to LIDAR data) are shown in the FFT and Capon results of this test area in Figure E. 7 and Figure E. 8.



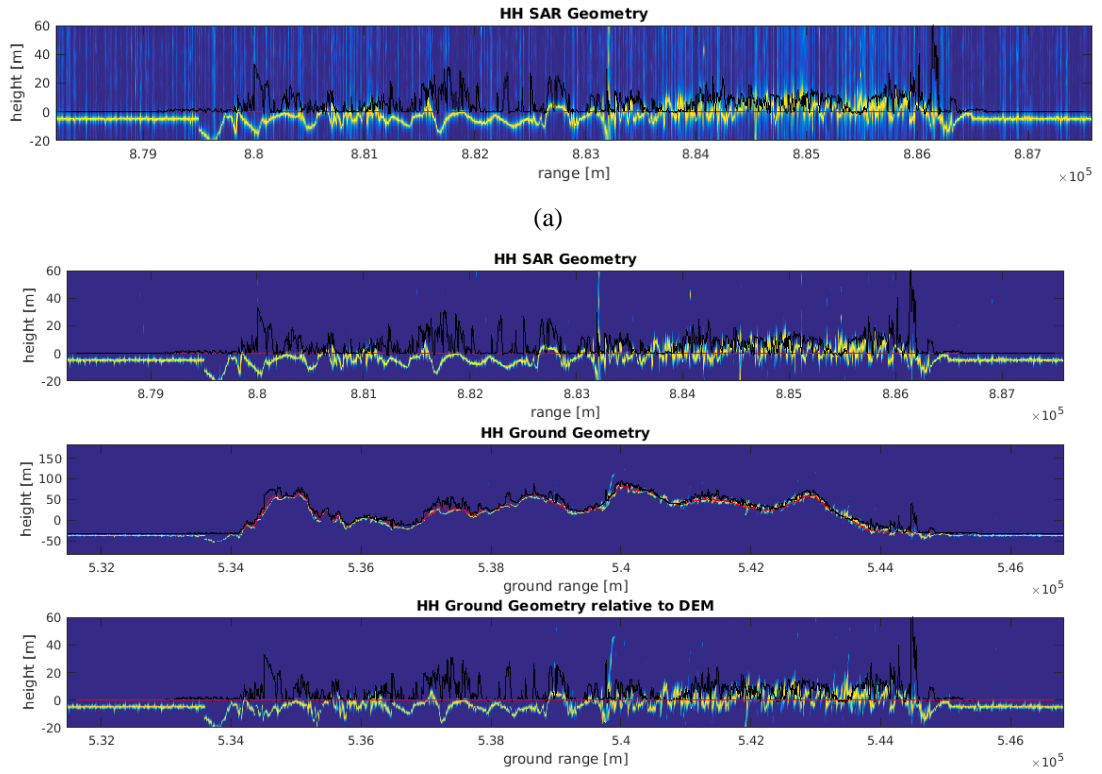
(a)





(b)

Figure E. 7 TomoSAR results via FFT in Test-A area after ionospheric calibration: (a) Tomograms via FFT in Test-A, the red line is the position of max scattering value; (b) Geocoded tomograms via FFT in Test-A, the red line is the position of max scattering value, the colour is the magnitude of the complex scattering coefficient  $\gamma(s)$ , and the black line is the fused DEM



(b)

Figure E. 8 TomoSAR results via Capon in Test-A area after ionospheric calibration: (a) Tomograms via Capon in Test-A (before filter), the colour is the magnitude of the complex scattering coefficient  $\gamma(s)$ , the

red line is the fused DEM, and the black line is the LIDAR DSM; (b) Geocoded tomograms via Capon in Test-A (after noise filter), the colour is the magnitude of the complex scattering coefficient  $\gamma(s)$ , the red line is the fused DEM, and the black line is the LIDAR DSM

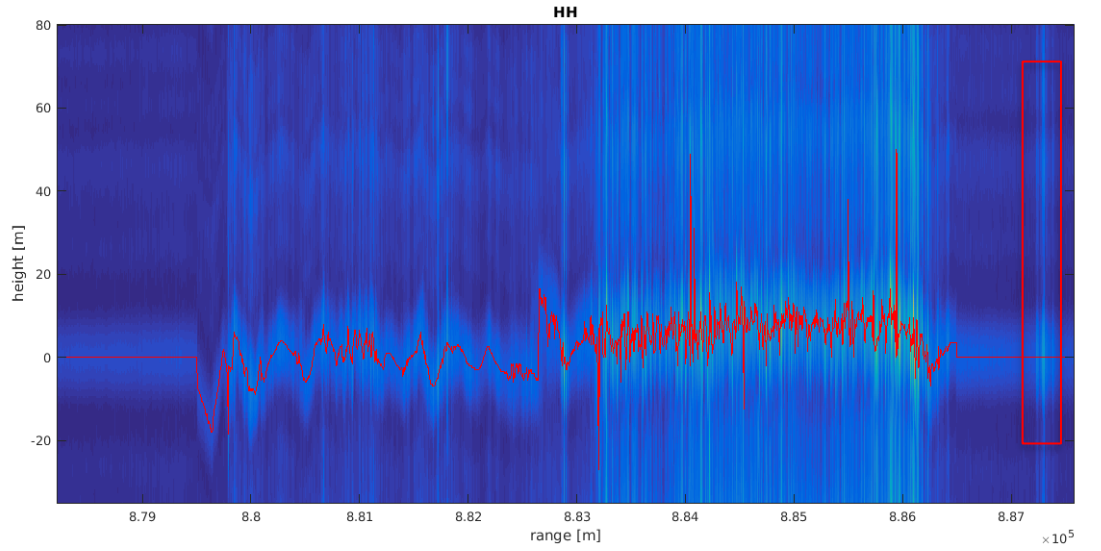
## 1.2.4 Results after InSAR Phase Calibration

Then, the test is studied via FFT, Capon and CS method after phase calibration (InSAR calibration, including ERA tropospheric, split spectrum ionospheric phase distortion correction, DEM error correction and other errors correction) in Test-A and Test-B area.

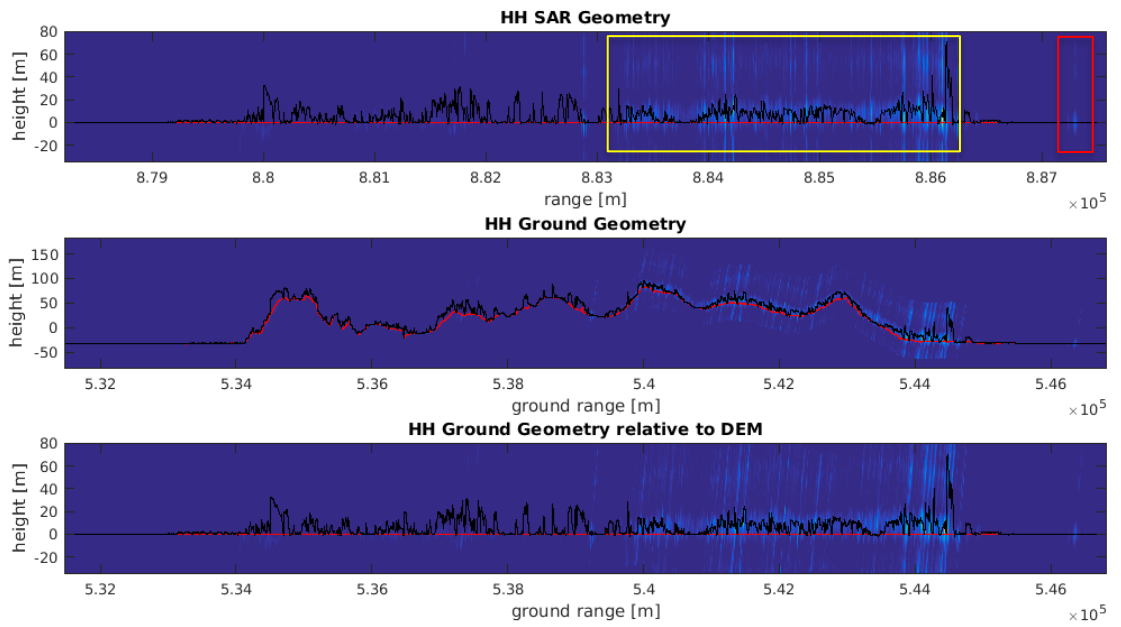
### 1.2.4.1 FFT results

A strong scattering line (the max magnitude of the complex scattering coefficient  $\gamma(s)$ ) at 0 m are shown in the figures below, which indicates the phase calibration works. In FFT results, there are still some ambiguity lines, but this ambiguity does not influence greatly after filtering. In the urban building area in Test-A (shown in Figure E. 9), there are strong scatterers at the top and the bottom (at  $8.83\text{--}8.86 \times 10^5$  m in the range). In addition, the bridge (shown in the yellow box of Figure E. 2 (c)) is shown in the FFT results (in the red box) in Figure E. 9 (a) and (b), which does not match the LIDAR DSM. This is because there is no LIDAR data (Figure E. 1 (c)) of this bridge here. Moreover, in Test-B, the top and the bottom of the cable support tower of the bridge (also see the yellow line in Figure E. 3 (c)) is easy to be seen from the results below and the highest point of the cable support tower is about 230 m (at  $8.82 \times 10^5$  m along the range direction). Besides, two layers (the top of the buildings around the black line and the bottom of the buildings around the red line) are clearly shown in the yellow box in Figure E. 9 (b) below, in which one is the roof reflectors, and the other is the ground-wall double bounce reflectors.



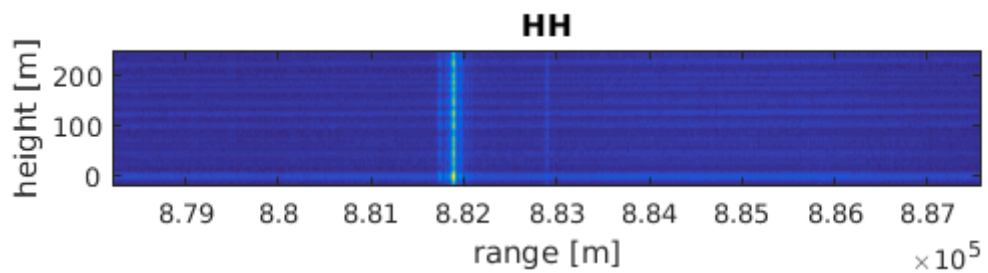


(a)



(b)

Figure E. 9 TomoSAR results referenced to SRTM via FFT in Test-A area: (a) Tomograms via FFT in Test-A, the red line is the position of max scattering value, the colour is the magnitude of the complex scattering coefficient  $\gamma(s)$ ; (b) Geocoded tomograms via FFT in Test-A, the colour is the magnitude of the complex scattering coefficient  $\gamma(s)$ , the red line is the fused DEM, and the black line is the LIDAR



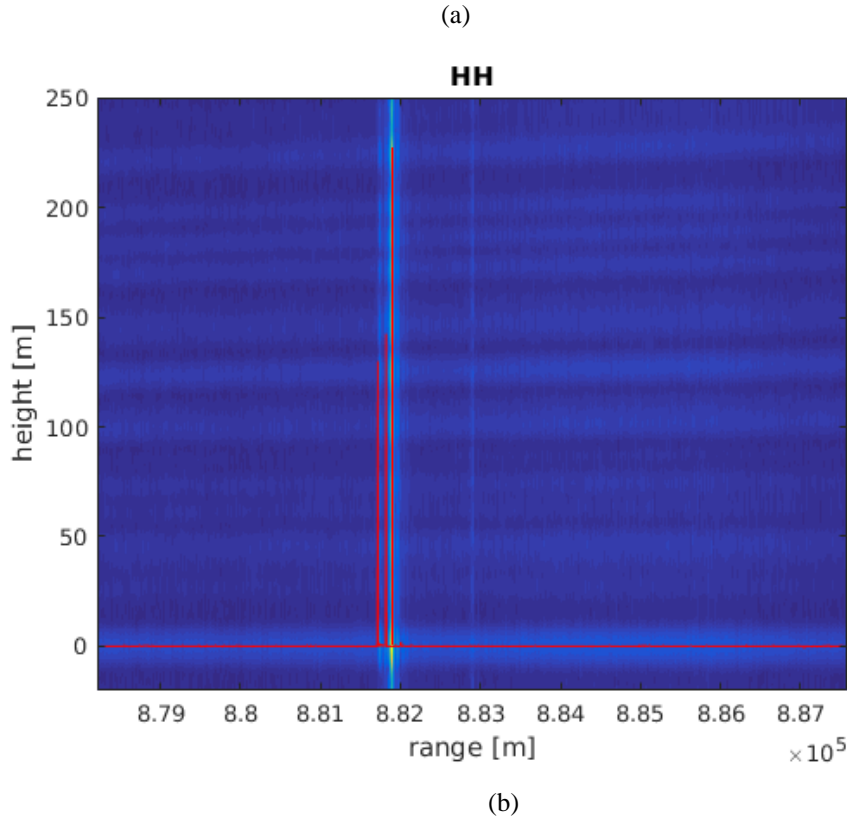
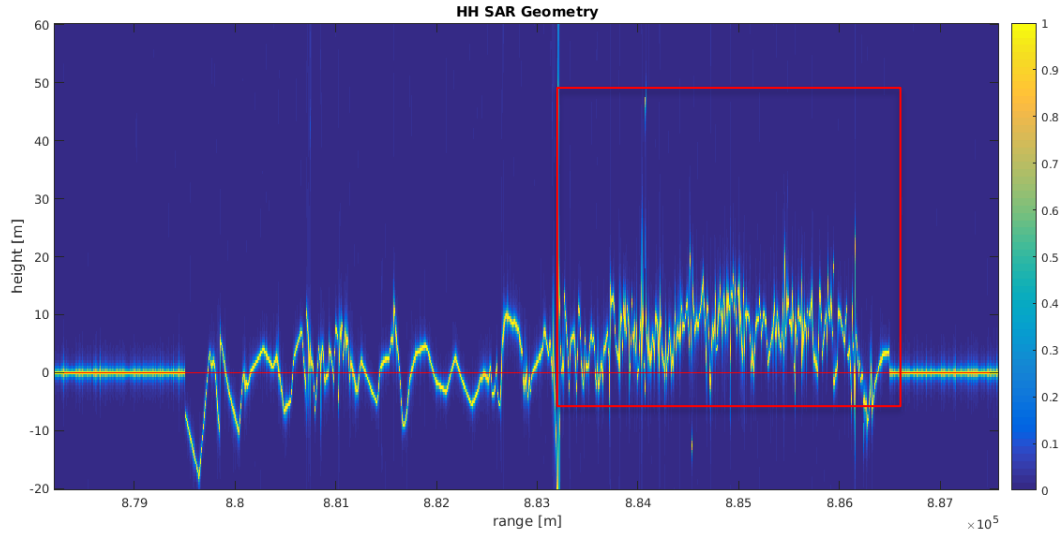


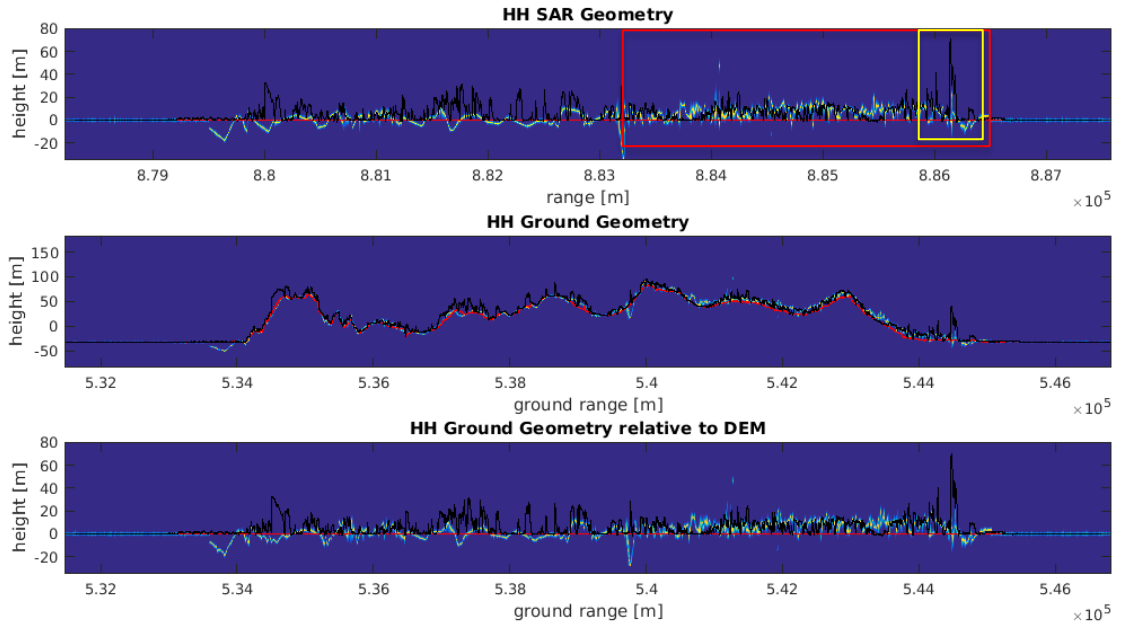
Figure E. 10 TomoSAR results via FFT in Test-B area: (a) Tomograms via FFT in Test-B; (b) Tomograms via FFT in Test-B, the red line is the position of max scattering value

#### 1.2.4.2 Capon results

A strong scatter line (the max magnitude of the complex scattering coefficient  $\gamma(s)$ ) at 0 m are also shown in the Capon results below, which indicates the phase calibration works. In the urban building area in Test-A, two layers (the top of the buildings around the black line and the bottom of the buildings around the red line shown in Figure E. 11 (b)) are shown in the red box in Figure E. 11 (a) and (b), where the top is the roof reflectors and the bottom is a strong ground-wall double bounce reflection (at  $8.83\text{-}8.86 \times 10^5$  m in the range); besides, some high buildings (shown in yellow box of Figure E. 11 (b)) are detected in this area in the Capon results (these high buildings can also be seen in the yellow line in (c) of Figure E. 2). Moreover, in Test-B, the top and the bottom of the cable support tower of the bridge (also see the yellow line in (c) of Figure E. 3) is easy to be seen in the results below and the highest point of the cable support tower is about 230 m (at  $8.82 \times 10^5$  m along the range direction). Compared to FFT results, the Capon results have more clear targets in Test-A and Test-B by minimising the ambiguity.

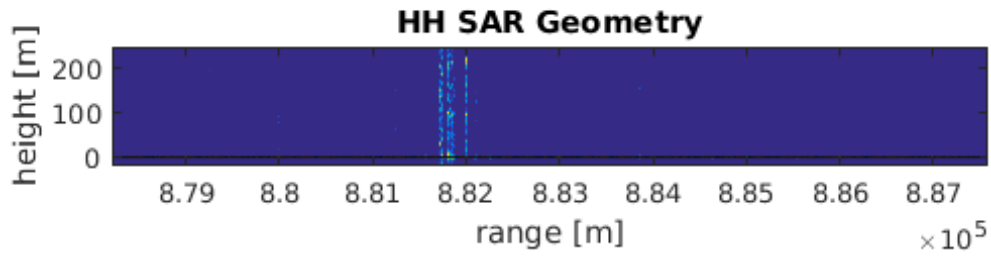


(a)

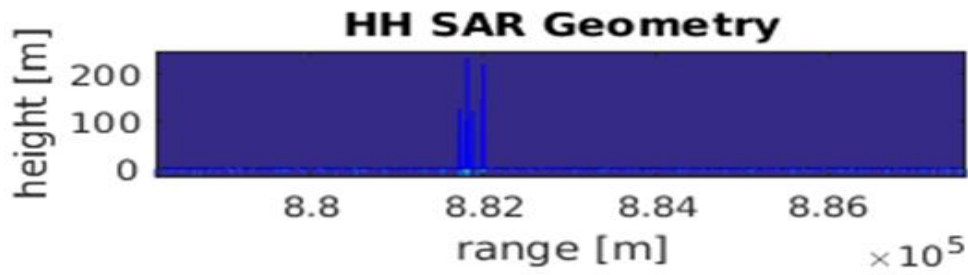


(b)

Figure E. 11 TomoSAR results referenced to SRTM via FFT in Test-A area: (a) Tomograms via Capon in Test-A (after noise filtering), the colour is the magnitude of the complex scattering coefficient  $\gamma(s)$ , the red line is the fused DEM; (b) Geocoded tomograms via Capon in Test-A (after magnitude noise filtering), the colour is the magnitude of the complex scattering coefficient  $\gamma(s)$ , the red line is the fused DEM, and the black line is the LIDAR DSM



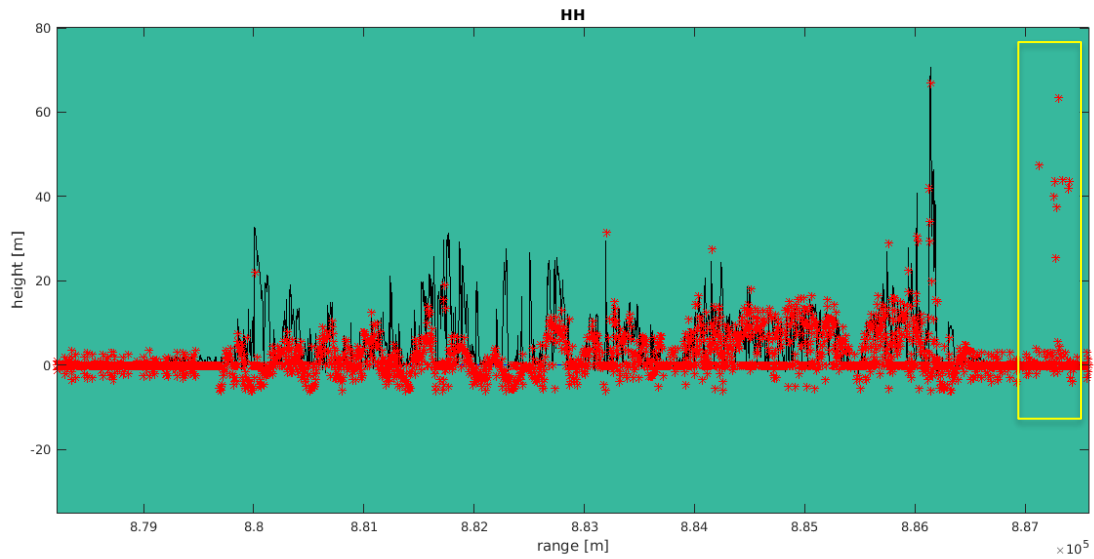
(a)



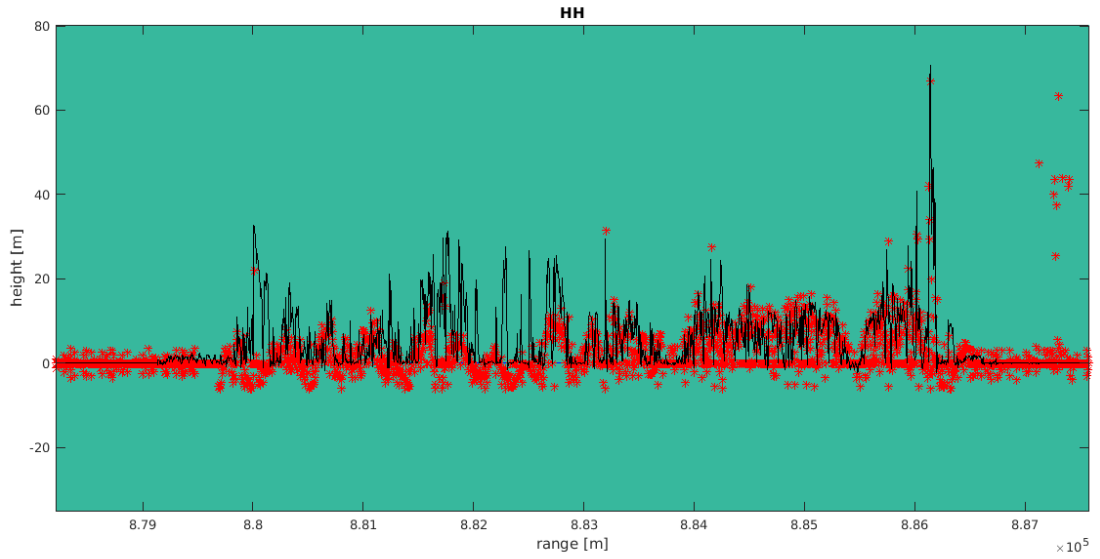
(b)

Figure E. 12 TomoSAR results via Capon in Test-B area: (a) Tomograms via Capon in Test-B; (b) Tomograms via Capon in Test-B, the blue line is the position of max scattering value

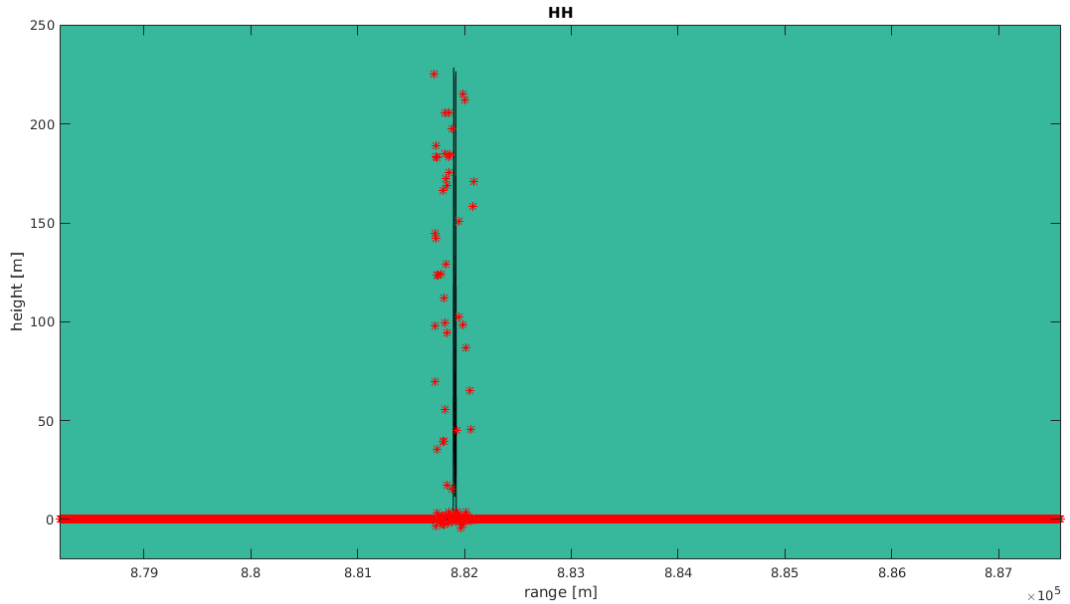
#### 1.2.4.3 CS method results



(a)



(b)



(c)

Figure E. 13 TomoSAR results via CS in Test-A and Test-B area: (a) CS result (red star) in Test-A, the black line in the background is LIDAR DSM for validation; (b) CS result (red star) in Test-A, the black line in the foreground is LIDAR DSM for validation; (c) CS result (red star) in Test-B, the black line is LIDAR DSM for validation

A strong scattering line at 0 m is also shown in the CS results above, which indicates the phase calibration works. In urban building area in Test-A (Figure E. 13 (a) and (b)), there are strong scattering signals at the top and the bottom (the top of the buildings and the bottom of the buildings at  $8.83\text{-}8.86 \times 10^5$  m in the range), and some

high buildings are detected in this area in CS results. Also, the bridge scattering at the right side is also detected ( $8.875 \times 10^5$  m at the range).

Moreover, in Test-B, the top and the bottom of the cable support tower of the bridge (also see the yellow line in Figure E. 3 (c)) is easy to be seen in the results above ( $8.82 \times 10^5$  m at the range). In Test-A and Test-B, compared to FFT and Capon method, the CS method has higher resolution.

## 1.3 Assessment and Discussion

The processed LIDAR DSM data (the processing workflow is introduced in 0) are used for the validation of the results in this test area. In Figure E. 13 (a) and (b), the LIDAR DSM is well matched with CS results referenced to the fused DEM, and that the highest building matched with LIDAR DSM in Test-A is about 70 metres (the highest position of the blackline at the right side in Figure E. 13 (a)) is also detected in the CS method. The bridge (shown in the yellow box of Figure E. 2 (c)) shown in the CS results (yellow box of Figure E. 13 (a)) in Figure E. 13 (a) and (b) does not match the LIDAR DSM. This is because there is no LIDAR data (Figure E. 1 (c)) of this bridge here, but the CS method detected the height around 65 m in Test-A. Therefore, these results demonstrate that the CS algorithm works very well in our test.

For the Golden gate bridge test, the LIDAR DSM is also well matched with CS results, shown in Figure E. 13 (c). The height of the cable support tower in the design is 227.4 metres (Wikipedia, 2008) and the top of the tower is 230 metres measured from the river surface in Figure E. 14 (Wikipedia, 2008). The height in LIDAR DSM is 228.6 metres ( $196.6 - (-32) = 228.6$ ), shown in Figure E. 3 (b) and Figure E. 13 (c) (the black line). In addition, the reference of the CS results is the maximum scattering in the height direction, which is the river surface. Our CS result (shown in Figure E. 13 (c)) of the height for the tower is 228 metres, which is almost the same height as the design in Figure E. 14 and the LIDAR DSM. Therefore, it implies that the CS results of the cable support tower are comparable and reasonable. Compared to the LIDAR DSM, the FFT and Capon methods also work very well for 3D TomoSAR imaging. However, compared to FFT and Capon method, the CS method has a higher resolution for the 3D structure reconstruction in height direction and CS algorithm is generally performed using SLC data (without multilooking averaging for noise filtering), which is automatically performed in the stack dimension using SAR model and sparsity driven estimation

technique to characterise a minimal number ( $< 4$ ) of targets in the measured signal. Therefore, L band data can be used to map the structure of the man-made structure ((bridge, buildings and manufactured facilities)).

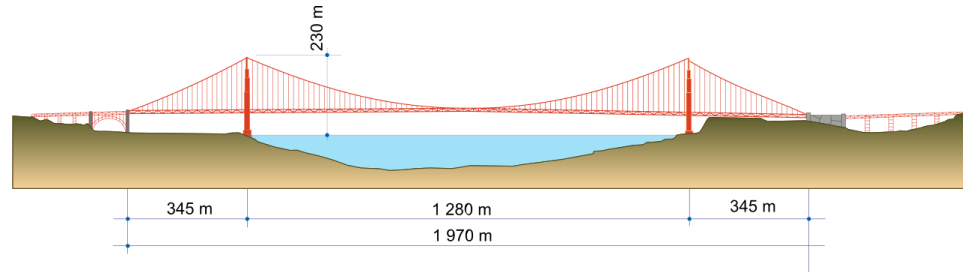


Figure E. 14 The height, depth, and length of the Golden gate bridge (Wikipedia, 2008)

## 1.4 Conclusions

After baseline estimation, phase calibration (before and after ionospheric phase distortion correction, tropospheric correction, DEM error correction and errors elimination) is studied in Test-A and Test-B experiments at San Francisco Bay, USA. The experiments indicate that phase calibration (the orbital, tropospheric, ionospheric phase distortion correction, and the DEM error correction) step is indispensable for TomoSAR imaging, which ultimately influences the inversion results. Moreover, the FFT and Capon method are studied and tested in Test-A and Test-B experiments, the results show that the resolution of the FFT method is very low and has an ambiguity in the height direction (sidelobe blurring effect); and the Capon method is a mid-resolution reconstruction method, which aims to minimise spatial perturbations and sidelobes. In addition, the super-resolution reconstruction CS method is studied and validated, which demonstrates L band data with the CS method is fit for the reconstruction of manufacture facilities (bridge) and buildings in the urban area.

This page is intentionally left blank.



## References

- Aarons, J. 1982. Global morphology of ionospheric scintillations. *Proceedings of the IEEE*, 70, 360-378.
- Aguilera, E., Nannini, M. & Andreas, R. Wavelet-based compressed sensing for polarimetric sar tomography. Proceedings of ESA POLinSAR Workshop, 2013. 1-5.
- Ahuja, S. & Waslander, S. L. 3d scan registration using curvelet features. Computer and Robot Vision (CRV), 2014 Canadian Conference on, 2014. IEEE, 77-83.
- Akbarimehr, M., Motagh, M. & Haghshenas-Haghighi, M. 2013. Slope stability assessment of the sarcheshmeh landslide, northeast iran, investigated using insar and gps observations. *Remote Sensing*, 5, 3681-3700.
- Albreem, M. A. & Salleh, M. Lattice sphere multiuser detection via compressive sensing. Communications (APCC), 2012 18th Asia-Pacific Conference on, 2012. IEEE, 423-426.
- Álvarez, O., Gimenez, M., Braitenberg, C. & Folguera, A. 2012. Goc satellite derived gravity and gravity gradient corrected for topographic effect in the south central andes region. *Geophysical Journal International*, 190, 941-959.
- André, S. L., André, T. C., Watters, T. R. & Robinson, M. S. 2008. Application of an adaptive least squares correlation algorithm for stereo matching planetary image data. *Journal of Geophysical Research: Planets*, 113.
- Anitori, L., Otten, M., Van Rossum, W., Maleki, A. & Baraniuk, R. Compressive cfar radar detection. Radar Conference (RADAR), 2012 IEEE, 2012. IEEE, 0320-0325.
- Antennas, I. & Committee, P. S. W. P. S. 1977. *Ieee standard definitions of terms for radio wave propagation*, IEEE.
- Anthony, W. Y., Krainak, M. A., Harding, D. J., Abshire, J. B., Sun, X., Valett, S., Cavanaugh, J. & Ramos-Izquierdo, L. Spaceborne laser instruments for high-

- resolution mapping. *Solid State Lasers XIX: Technology and Devices*, 2010. International Society for Optics and Photonics, 757802.
- Argyriou, N. & Teeuw, R. 2013. Srtm-based geomorphometrics for detecting neotectonic deformation: A cost-effective alternative to insar in vegetated regions? *First International Conference on Remote Sensing and Geoinformation of the Environment (Rscy2013)*, 8795.
- Arundel, S., Phillips, L., Lowe, A., Bobinmyer, J., Mantey, K., Dunn, C., Constance, E. & Usery, E. 2015. Preparing the national map for the 3d elevation program—products, process and research. *Cartography and Geographic Information Science*, 42, 40-53.
- ASF-Team. 2010. *Alaska satellite facility* [Online]. Available: <https://www.asf.alaska.edu/sar-data/palsar/> [Accessed 28/01 2018].
- Baby, H. B., Gole, P. & Lavergnat, J. 1988. A model for the tropospheric excess path length of radio waves from surface meteorological measurements. *Radio science*, 23, 1023-1038.
- Bamler, R. 1992. A comparison of range-doppler and wavenumber domain sar focusing algorithms. *Geoscience and Remote Sensing, IEEE Transactions on*, 30, 706-713.
- Bamler, R., Eineder, M., Adam, N., Zhu, X. & Gernhardt, S. 2009. Interferometric potential of high resolution spaceborne sar. *Photogrammetrie-Fernerkundung-Geoinformation*, 2009, 407-419.
- Bamler, R. & Hanssen, R. 1997. Decorrelation induced by interpolation errors in insar processing. *Igarss '97 - 1997 International Geoscience and Remote Sensing Symposium, Proceedings Vols I-Iv*, 1710-1712.
- Bamler, R. & Hartl, P. 1998. Synthetic aperture radar interferometry. *Inverse problems*, 14, R1.
- Bandiera, F., De Maio, A. & Ricci, G. 2007. Adaptive cfar radar detection with conic rejection. *IEEE Transactions on Signal Processing*, 55, 2533-2541.
- Bejar Pizarro, M., Carrizo, D., Socquet, A. & Armijo, R. Asperities, barriers and transition zone in the north chile seismic gap: State of the art after the 2007 mw 7.7 tocopilla earthquake inferred by gps and insar data. *ESA Special Publication*, 2010.

- Bekaert, D., Hooper, A. & Wright, T. 2015. A spatially variable power law tropospheric correction technique for insar data. *Journal of Geophysical Research: Solid Earth*, 120, 1345-1356.
- Belcher, D. 2008. Theoretical limits on sar imposed by the ionosphere. *Radar, Sonar & Navigation, IET*, 2, 435-448.
- Belcher, D. P. & Cannon, P. S. 2014. Amplitude scintillation effects on sar. *IET Radar, Sonar & Navigation*, 8, 658-666.
- Béniguel, Y. 2011. Gism global ionospheric scintillation model, technical manual. IEEA, September.
- Benson, R. F. 2010. Four decades of space-borne radio sounding.
- Benson, T. 1999. Fundamentals of applied electromagnetics. *International Journal of Electrical Engineering Education*, 36, 83.
- Berardino, P., Fornaro, G., Lanari, R. & Sansosti, E. 2002. A new algorithm for surface deformation monitoring based on small baseline differential sar interferograms. *IEEE transactions on geoscience and remote sensing*, 40, 2375-2383.
- Berry, P., Garlick, J. D. & Smith, R. G. 2007. Near-global validation of the srtm dem using satellite radar altimetry. *Remote Sensing of Environment*.
- Besl, P. J. & McKay, N. D. 1992. A method for registration of 3-d shapes. *IEEE Transactions on pattern analysis and machine intelligence*, 14, 239-256.
- Bhang, K. J., Schwartz, F. W. & Braun, A. 2007. Verification of the vertical error in c-band srtm dem using icesat and landsat-7, otter tail county, mn. *Geoscience and Remote Sensing, IEEE Transactions on*, 45, 36-44.
- Bilitza, D., Altadill, D., Truhlik, V., Shubin, V., Galkin, I., Reinisch, B. & Huang, X. 2017. International reference ionosphere 2016: From ionospheric climate to real-time weather predictions. *Space Weather*, 15, 418-429.
- Bilitza, D., Brown, S. A., Wang, M. Y., Souza, J. R. & Roddy, P. A. 2012. Measurements and iri model predictions during the recent solar minimum. *Journal of Atmospheric and Solar-Terrestrial Physics*, 86, 99-106.
- Bluesky. 2018. *Products / lidar & height data* [Online]. Available: <https://www.blueskymapshop.com/products/height-data> [Accessed 2018.05.30 2018].
- Bock, Y. & Williams, S. 1997. Integrated satellite interferometry in southern california. *Eos, Transactions American Geophysical Union*, 78, 293-300.

- Böer, J., Gonzalez, C., ChristopherWecklich, B., DanielSchulze, M. & Bachmann, M. Performance assessment of the final tandem-x dem. Living Planet Symposium, 2016. 81.
- Bondarenko, Y., Medvedev, Y., Vavilov, D. & Marshalov, D. Radar observations of near-earth asteroids using the quasar vlbi network telescopes. European Planetary Science Congress, 2017.
- Borde, A., Guth, A. H. & Vilenkin, A. 2003. Inflationary spacetimes are incomplete in past directions. *Physical review letters*, 90, 151301.
- Bracewell, R. 2003. *Fourier analysis and imaging*, Springer Science & Business Media.
- Bradley, B. A., Sakimoto, S. E., Frey, H. & Zimbelman, J. R. 2002. Medusae fossae formation: New perspectives from mars global surveyor. *Journal of Geophysical Research: Planets (1991–2012)*, 107, 2-1-2-17.
- Breit, H. & Bamler, R. 1998. An insar processor for on-board performance monitoring of the srtm/x-sar interferometer. *Igarss '98 - 1998 International Geoscience and Remote Sensing Symposium, Proceedings Vols 1-5*, 1904-1907.
- Brenner, A. C., DiMarzio, J. P. & Zwally, H. J. 2007. Precision and accuracy of satellite radar and laser altimeter data over the continental ice sheets. *IEEE Transactions on Geoscience and Remote Sensing*, 45, 321-331.
- Brown, D. G. & Bara, T. J. 1994. *Recognition and reduction of systematic-error in elevation and derivative surfaces from 7-1/2-minute dems*.
- Brown, L. G. 1992. A survey of image registration techniques. *ACM computing surveys (CSUR)*, 24, 325-376.
- Buckley, S., Rossen, P. & Persaud, P. 2000. Roi\_pac documentation-repeat orbit interferometry package. *JET Propulsion Lab., Pasadena, CA*.
- Budden, K. G. 1988. *The propagation of radio waves: The theory of radio waves of low power in the ionosphere and magnetosphere*, Cambridge University Press.
- Budden, K. G. 2009. Radio waves in the ionosphere. *Radio Waves in the Ionosphere*, by KG Budden, Cambridge, UK: Cambridge University Press, 2009.
- Budge, M. C. & German, S. R. 2015. *Basic radar analysis*, Artech House.
- Budillon, A., Johnsy, A. C. & Schirinzi, G. 2017. A fast support detector for superresolution localization of multiple scatterers in sar tomography. *IEEE Journal of Selected Topics in Applied Earth Observations and Remote Sensing*.

- Cahill, J. T., Bussey, D. B. J., Patterson, G. W., Turner, F. S., Lopez, N. R., Raney, R., Neish, C. & Team, M.-R. Global mini-rf s-band cpr and m-chi decomposition observations of the moon. 43rd Lunar and Planetary Science Conference, 2012.
- Cahill, J. T., Thomson, B., Patterson, G. W., Bussey, D. B. J., Neish, C. D., Lopez, N. R., Turner, F. S., Aldridge, T., McAdam, M. & Meyer, H. 2014. The miniature radio frequency instrument's (mini-rf) global observations of earth's moon. *Icarus*, 243, 173-190.
- Cai, Z., Zheng, C., Tang, Z. & Qi, D. 2010. Lunar digital elevation model and elevation distribution model based on chang'e-1 lam data. *Science China Technological Sciences*, 53, 2558-2568.
- Candès, E. J. Compressive sampling. Proceedings of the international congress of mathematicians, 2006. Madrid, Spain, 1433-1452.
- Candes, E. J., Wakin, M. B. & Boyd, S. P. 2008. Enhancing sparsity by reweighted  $\ell_1$  minimization. *Journal of Fourier analysis and applications*, 14, 877-905.
- Capon, J. 1969. High-resolution frequency-wavenumber spectrum analysis. *Proceedings of the IEEE*, 57, 1408-1418.
- Carabajal, C. C. & Harding, D. J. 2005. Icesat validation of srtm c - band digital elevation models. *Geophysical research letters*, 32.
- CARTER, J. R. 1992. The effect of data precision on the calculation of slope and aspect using gridded dems. *Cartographica: The International Journal for Geographic Information and Geovisualization*, 29, 22-34.
- Carter, L. M., Campbell, B. A., Neish, C. D., Nolan, M. C., Patterson, G. W., Jensen, J. R. & Bussey, D. B. J. 2017. A comparison of radar polarimetry data of the moon from the lro mini-rf instrument and earth-based systems. *IEEE Transactions on Geoscience and Remote Sensing*, 55, 1915-1927.
- Caruso, V. Standards for digital elevation models. American Society for Photogrammetry and Remote Sensing (ASPRS) and American Congress on Surveying and Mapping (ACSM) annual convention proceedings, 1987a. 159-166.
- Caruso, V. 1987b. *Standards for digital elevation models*.
- Chapin, E., Chan, S. F., Chapman, B. D., Chen, C. W., Martin, J. M., Michel, T. R., Muellerschoen, R. J., Pi, X. & Rosen, P. A. Impact of the ionosphere on an l-band space based radar. Radar, 2006 IEEE Conference on, 2006. IEEE, 8 pp.

- Chartrand, R. & Staneva, V. 2008. Restricted isometry properties and nonconvex compressive sensing. *Inverse Problems*, 24, 035020.
- Chen, A. C. 2013. L-band insar estimates of greenland ice sheet accumulation rates. Stanford University.
- Chen, C. W. & Zebker, H. A. 2000. Network approaches to two-dimensional phase unwrapping: Intractability and two new algorithms. *JOSA A*, 17, 401-414.
- Chen, C. W. & Zebker, H. A. 2001. Two-dimensional phase unwrapping with use of statistical models for cost functions in nonlinear optimization. *JOSA A*, 18, 338-351.
- Chen, C. W. & Zebker, H. A. 2002. Phase unwrapping for large sar interferograms: Statistical segmentation and generalized network models. *Geoscience and Remote Sensing, IEEE Transactions on*, 40, 1709-1719.
- Chen, H. & Kasilingam, D. Super-resolution processing for polarimetric synthetic aperture radar tomography. Radar Conference, 2007 IEEE, 2007. IEEE, 618-623.
- Chen, J. Y. & Zebker, H. A. 2012. Ionospheric artifacts in simultaneous l-band insar and gps observations. *Ieee Transactions on Geoscience and Remote Sensing*, 50, 1227-1239.
- Chen, S. S., Donoho, D. L. & Saunders, M. A. 2001. Atomic decomposition by basis pursuit. *SIAM review*, 43, 129-159.
- Chen, Y. 2008. Bundle adjustment of mars hirise orbiter stereo images based on the rigorous sensor model. *change*, 2, 2.
- Cheney, M. 2001. Tomography problems arising in synthetic aperture radar. *Contemporary Mathematics*, 278, 15-28.
- Chengalur, J. N. 2017. Book review: Interferometry and synthesis in radio astronomy. *Journal of Astronomical Instrumentation*.
- Chin, G., Brylow, S., Foote, M., Garvin, J., Kasper, J., Keller, J., Litvak, M., Mitrofanov, I., Paige, D. & Raney, K. 2007. Lunar reconnaissance orbiter overview: Theáinstrument suite and mission. *Space Science Reviews*, 129, 391-419.
- Collin, R. E. 2007. *Foundations for microwave engineering*, John Wiley & Sons.
- Comblet, F., Khenchaf, A., Baussard, A. & Pellen, F. 2006. Bistatic synthetic aperture radar imaging: Theory, simulations, and validations. *Antennas and Propagation, IEEE Transactions on*, 54, 3529-3540.

- Costa, M. G., Pinho, M. D. & Fernandes, D. 2015. Curvelet-based compressive sensing for insar raw data. *Image and Signal Processing for Remote Sensing Xxi*, 9643.
- Costantini, M. 1998. A novel phase unwrapping method based on network programming. *Geoscience and Remote Sensing, IEEE Transactions on*, 36, 813-821.
- CRCSI. 2015. *Satellite and airborne sar sensor specifications* [Online]. Available: <http://www.crcsi.com.au/assets/Uploads/Files/Adjunct-Reference-1-SAR-Sensor-Specifications-FINAL.pdf> [Accessed 1 September 2015].
- Crosetto, M. & Aragues, F. 1999. Radargrammetry and sar interferometry for dem generation: Validation and data fusion, ceos'99 sar workshop, esa-cnes toulouse, 26-29. October.
- Curlander, J. C. 1982. Location of spaceborne sar imagery. *Ieee Transactions on Geoscience and Remote Sensing*, GE-20, 359-364.
- Danielson, J. J. & Gesch, D. B. 2011a. *Global multi-resolution terrain elevation data 2010*.
- Danielson, J. J. & Gesch, D. B. 2011b. Global multi-resolution terrain elevation data 2010 (gmted2010). US Geological Survey.
- Davis, J., Herring, T., Shapiro, I., Rogers, A. & Elgered, G. 1985. Geodesy by radio interferometry: Effects of atmospheric modeling errors on estimates of baseline length. *Radio science*, 20, 1593-1607.
- De Zotti, G., Bonato, M. & Cai, Z.-Y. 2018. Star formation across cosmic time with radio surveys. The promise of the ska. *arXiv preprint arXiv:1802.06561*.
- Denker, H. 2005. Evaluation of srtm3 and gtopo30 terrain data in germany. *Gravity, geoid and space missions*. Springer.
- DHI, G. 2014. Eu-dem statistical validation. EEA, DHI: DHI GRAS • c/o Geocenter Denmark.
- Di, L., Schlesinger, B. & Kobler, B. 2000. Us fgdc content standard for digital geospatial metadata: Extensions for remote sensing metadata. *International archives of photogrammetry and remote sensing*, 33, 78-81.
- Ding, X. L., Li, Z. W., Zhu, J. J., Feng, G. C. & Long, J. P. 2008. Atmospheric effects on insar measurements and their mitigation. *Sensors*, 8, 5426-U1.
- Djachkova, M., Litvak, M., Mitrofanov, I. & Sanin, A. 2017. Selection of luna-25 landing sites in the south polar region of the moon. *Solar System Research*, 51, 185-195.

- Donoho, D. L. 2006a. Compressed sensing. *IEEE Transactions on information theory*, 52, 1289-1306.
- Donoho, D. L. 2006b. Compressed sensing. *Information Theory, IEEE Transactions on*, 52, 1289-1306.
- Dowman, I., Chugani, K. & Kitmitto, K. 2000a. Planimetric quality assurance of the landmap mosaic: Methods and results. ... *Annual Conference of* ....
- Dowman, I., Chugani, K., Kitmitto, K., Muller, J.-P. & Walker, A. Planimetric quality assurance of the landmap mosaic: Methods and results. 26th Annual Conference of the Remote Sensing Society, RSS, University of Leicester, 2000b. 12-14.
- Eckert, S., Kellenberger, T. & Itten, K. 2005. Accuracy assessment of automatically derived digital elevation models from aster data in mountainous terrain. *International Journal of Remote Sensing*, 26, 1943-1957.
- Eichel, P. & Jakowatz, C. 1989. Phase-gradient algorithm as an optimal estimator of the phase derivative. *Optics letters*, 14, 1101-1103.
- Elachi, C. 1988. Spaceborne radar remote sensing: Applications and techniques. *New York, IEEE Press, 1988, 285 p.*
- Elphic, R., Eke, V., Teodoro, L., Lawrence, D. & Bussey, D. 2007. Models of the distribution and abundance of hydrogen at the lunar south pole. *Geophysical Research Letters*, 34.
- Elsharkawy, R., Hindy, M., Sebak, A.-R., Saleeb, A. & El-Rabaie, E.-S. M. 2018. Gain optimization for millimeter wave reflectarray antennas based on a phase gradient approach. *International Journal of Speech Technology*, 1-8.
- Elvidge, S. 2014. On the use of multi-model ensemble techniques for ionospheric and thermospheric characterisation. University of Birmingham.
- Enßle, F., Heinzl, J. & Koch, B. 2014. Accuracy of vegetation height and terrain elevation derived from icesat/glas in forested areas. ... *Journal of Applied Earth Observation and* ....
- Evans, J. 1974. Some post-war developments in ground-based radiowave sounding of the ionosphere. *Journal of Atmospheric and Terrestrial Physics*, 36, 2183-2234.
- Evans, J. V. & Hagfors, T. 1968. Radar astronomy. *New York: McGraw-Hill, 1968, edited by Evans, John V.; Hagfors, Tor.*
- Fabian, E., Johannes, H. & Barbara, K. 2000. Evaluating height differences between global digital surface models and icesat heights at footprint geolocation.



- Fang, W. & Xiang, L. 2010. Development of bi-/multi-static synthetic aperture radar [j]. *Electronics Optics & Control*, 4, 015.
- Farr, T. G., Rosen, P. A., Caro, E., Crippen, R., Duren, R., Hensley, S., Kobrick, M., Paller, M., Rodriguez, E., Roth, L., Seal, D., Shaffer, S., Shimada, J., Umland, J., Werner, M., Oskin, M., Burbank, D. & Alsdorf, D. 2007. The shuttle radar topography mission. *Reviews of Geophysics*, 45, RG2004.
- Fattahi, H., Simons, M. & Agram, P. 2017. Insar time-series estimation of the ionospheric phase delay: An extension of the split range-spectrum technique. *IEEE Transactions on Geoscience and Remote Sensing*, 55, 5984-5996.
- Fell, P. & Tanenbaum, M. 2002. Comparison of national vertical and chart datums with wgs 84 (egm96) geoid. *Oceans 2002 Conference and Exhibition.:* IEEE.
- Feltens, J. & Schaer, S. Igs products for the ionosphere. Proceedings of the 1998 IGS Analysis Center Workshop Darmstadt, Germany, 1998.
- Feng, L. & Muller, J.-P. 2016. Icesat validation of tandem-x i-dems over the uk. *International Archives of the Photogrammetry, Remote Sensing & Spatial Information Sciences*, 41.
- Feng, L. & Muller, J. 3d point cloud reconstruction using tomography (3d tomographic sar imaging) in densely vegetated mountainous rural areas. ESA Fringe 2017, 2017 Helsinki, Finland.
- Feng, L., Muller, J., Li, Y. & Li, M. An improved baseline estimation method using external dems in different terrain areas. FRINGE 2015, 2015.
- Ferreti, A., Prati, C. & Rocca, F. 2000. Nonlinear subsidence rate estimation using permanent scatterers in differential sar interferometry. *IEEE Transactions on Geoscience and Remote Sensing*, 38, 2202-2212.
- Ferretti, A., Fumagalli, A., Novali, F., Prati, C., Rocca, F. & Rucci, A. 2011. A new algorithm for processing interferometric data-stacks: Squeesar. *Geoscience and Remote Sensing, IEEE Transactions on*, 49, 3460-3470.
- Ferretti, A., Monti-Guarnieri, A., Prati, C., Rocca, F. & Massonet, D. 2007a. *Insar principles-guidelines for sar interferometry processing and interpretation*.
- Ferretti, A., Prati, C. & Rocca, F. Analysis of permanent scatterers in sar interferometry. Geoscience and Remote Sensing Symposium, 2000. Proceedings. IGARSS 2000. IEEE 2000 International, 2000. IEEE, 761-763.

- Ferretti, A., Prati, C. & Rocca, F. 2001a. Multibaseline phase unwrapping for insar topography estimation. *Nuovo Cimento Della Societa Italiana Di Fisica C-Geophysics and Space Physics*, 24, 159-176.
- Ferretti, A., Prati, C. & Rocca, F. 2001b. Permanent scatterers in sar interferometry. *Geoscience and Remote Sensing, IEEE Transactions on*, 39, 8-20.
- Ferretti, A., Prati, C. & Rocca, F. 2001c. Permanent scatterers in sar interferometry. *IEEE Transactions on geoscience and remote sensing*, 39, 8-20.
- Ferretti, A., Savio, G., Barzaghi, R., Borghi, A., Musazzi, S., Novali, F., Prati, C. & Rocca, F. 2007b. Submillimeter accuracy of insar time series: Experimental validation. *Ieee Transactions on Geoscience and Remote Sensing*, 45, 1142-1153.
- Ferro-Famil, L., Leconte, C., Boutet, F., Phan, X.-V., Gay, M. & Durand, Y. Posar: A vhr tomographic gb-sar system application to snow cover 3-d imaging at x and ku bands. *Radar Conference (EuRAD), 2012 9th European, 2012. IEEE*, 130-133.
- Fischler, M. A. & Bolles, R. C. 1981. Random sample consensus: A paradigm for model fitting with applications to image analysis and automated cartography. *Communications of the ACM*, 24, 381-395.
- Fitch, J. P. 2012. *Synthetic aperture radar*, Springer Science & Business Media.
- Fitzpatrick, P. 2009. *Advanced calculus*, American Mathematical Soc.
- Fornaro, G., Franceschetti, G. & Lanari, R. 1996a. Interferometric sar phase unwrapping using green's formulation. *Geoscience and Remote Sensing, IEEE Transactions on*, 34, 720-727.
- Fornaro, G., Franceschetti, G., Lanari, R. & Sansosti, E. 1996b. Robust phase-unwrapping techniques: A comparison. *JOSA A*, 13, 2355-2366.
- Fornaro, G., Lombardini, F. & Serafino, F. 2005. Three-dimensional multipass sar focusing: Experiments with long-term spaceborne data. *IEEE Transactions on Geoscience and Remote Sensing*, 43, 702-714.
- Fornaro, G., Pauciuolo, A., Reale, D. & Verde, S. 2014. Multilook sar tomography for 3-d reconstruction and monitoring of single structures applied to cosmo-skymed data. *IEEE Journal of Selected Topics in Applied Earth Observations and Remote Sensing*, 7, 2776-2785.

- Fornaro, G., Reale, D. & Serafino, F. 2009. Four-dimensional sar imaging for height estimation and monitoring of single and double scatterers. *Geoscience and Remote Sensing, IEEE Transactions on*, 47, 224-237.
- Fornaro, G. & Serafino, F. Spaceborne 3d sar tomography: Experiments with ers data. *Geoscience and Remote Sensing Symposium*, 2004. IGARSS'04. Proceedings. 2004 IEEE International, 2004. IEEE, 1240-1243.
- Fornaro, G., Serafino, F. & Reale, D. 2010. 4-d sar imaging: The case study of rome. *IEEE Geoscience and Remote Sensing Letters*, 7, 236-240.
- Fornaro, G., Serafino, F. & Soldovieri, F. 2003. Three-dimensional focusing with multipass sar data. *IEEE Transactions on Geoscience and Remote Sensing*, 41, 507-517.
- Freeman, A. 1992. Sar calibration: An overview. *Ieee Transactions on Geoscience and Remote Sensing*, 30, 1107-1121.
- Freeman, A. 2004. Calibration of linearly polarized polarimetric sar data subject to faraday rotation. *Geoscience and Remote Sensing, IEEE Transactions on*, 42, 1617-1624.
- Fritz, T., Breit, H., Rossi, C., Balss, U., Lachaise, M. & Duque, S. Interferometric processing and products of the tandem-x mission. 2012 IEEE International Geoscience and Remote Sensing Symposium, 2012. IEEE, 1904-1907.
- Fuhrmann, T., Cuenca, M. C., Knopfler, A., van Leijen, F. J., Mayer, M., Westerhaus, M., Hanssen, R. F. & Heck, B. 2015. Estimation of small surface displacements in the upper rhine graben area from a combined analysis of ps-insar, levelling and gnss data. *Geophysical Journal International*, 203, 614-631.
- Fujisada, H., Bailey, G. B., Kelly, G. G., Hara, S. & Abrams, M. J. 2005. Aster dem performance. *Geoscience and Remote Sensing, IEEE Transactions on*, 43, 2707-2714.
- Fujisada, H., Urai, M. & Iwasaki, A. 2012. Technical methodology for aster global dem. *Geoscience and Remote ....*
- Gabriel, A. K. & Goldstein, R. M. 1988. Crossed orbit interferometry - theory and experimental results from sir-b. *International Journal of Remote Sensing*, 9, 857-872.
- Gabriel, A. K., Goldstein, R. M. & Zebker, H. A. 1989. Mapping small elevation changes over large areas: Differential radar interferometry. *Journal of Geophysical Research: Solid Earth*, 94, 9183-9191.

- Gao, Y., Wang, K. & Liu, X. 2012. Exploitation of srtm dem in insar data processing and its application to phase unwrapping. *Journal of Electromagnetic Waves and Applications*, 26, 1788-1797.
- Gay, M. & Ferro-Famil, L. Penetration depth of synthetic aperture radar signals in ice and snow: An analytical approach. Workshop Remote Sensing and Modeling of Surface Properties., 2016.
- Ge, D. Q., Wang, Y., Zhang, L. & Guo, X. F. 2009. Using permanent scatterer insar to detect land subsidence and ground fissures: A case study in xi'an city. *2009 Ieee International Geoscience and Remote Sensing Symposium, Vols 1-5*, 616-619.
- Gesch, D., Oimoen, M., Danielson, J. & Meyer, D. 2016. Validation of the aster global digital elevation model version 3 over the conterminous united states. *The International Archives of Photogrammetry, Remote Sensing and Spatial Information Sciences*, 41, 143.
- Gesch, D. B. 1994. Topographic data requirements for eos global change research. *Work*.
- Ghiglia, D. C. & Romero, L. A. 1994. Robust two-dimensional weighted and unweighted phase unwrapping that uses fast transforms and iterative methods. *JOSA A*, 11, 107-117.
- Gilman, M. & Tsynkov, S. 2015. A mathematical model for sar imaging beyond the first born approximation. *SIAM Journal on Imaging Sciences*, 8, 186-225.
- Gocho, M., Yamada, H., Arii, M., Sato, R., Yamaguchi, Y. & Kojima, S. Verification of simple calibration method for multi-baseline sar tomography. *Antennas and Propagation (ISAP), 2016 International Symposium on*, 2016. IEEE, 312-313.
- Goldstein, R., ZEBKER, H. & WERNER, C. 1988. Satellite radar interferometry- two-dimensional phase unwrapping. *Radio science*, 23, 713-720.
- Goldstein, R. M., Engelhardt, H., Kamb, B. & Frolich, R. M. 1993. Satellite radar interferometry for monitoring ice sheet motion: Application to an antarctic ice stream. *SCIENCE-NEW YORK THEN WASHINGTON-*, 262, 1525-1525.
- Gomba, G., Eineder, M., Parizzi, A. & Bamler, R. High-resolution estimation of ionospheric phase screens through semi-focusing processing. *Geoscience and Remote Sensing Symposium (IGARSS), 2014 IEEE International*, 2014. IEEE, 17-20.

- Gomba, G., González, F. R. & De Zan, F. 2017. Ionospheric phase screen compensation for the sentinel-1 tops and alos-2 scansar modes. *IEEE Transactions on Geoscience and Remote Sensing*, 55, 223-235.
- Gomba, G., Parizzi, A., De Zan, F., Eineder, M. & Bamler, R. 2016. Toward operational compensation of ionospheric effects in sar interferograms: The split-spectrum method. *IEEE Transactions on Geoscience and Remote Sensing*, 54, 1446-1461.
- Goncalves, J. A. & Oliveira, A. M. 2004. Accuracy analysis of dems derived from aster imagery. *International Archives of Photogrammetry* ....
- Gong, W., Meyer, F., Webley, P. W., Morton, D. & Liu, S. 2010. Performance analysis of atmospheric correction in insar data based on the weather research and forecasting model (wrf). *2010 Ieee International Geoscience and Remote Sensing Symposium*, 2900-2903.
- Gong, W. Y., Meyer, F. J., Liu, S. Z. & Hanssen, R. F. 2015. Temporal filtering of insar data using statistical parameters from nwp models. *Ieee Transactions on Geoscience and Remote Sensing*, 53, 4033-4044.
- González, C. & Bräutigam, B. 2015. Relative height accuracy estimation method for insar-based dems. *IEEE Journal of Selected Topics in Applied Earth Observations and Remote Sensing*, 8, 5352-5360.
- Gonzalez, J. H., Bachmann, M., Böer, J., Fiedler, H., Krieger, G. & Zink, M. 2009. Tandem-x mission and dem accuracy. *Proceedings of wave propagation in communication, microwaves systems and navigation, WFMN*.
- Goodman, J. M. 2006. *Space weather & telecommunications*, Springer Science & Business Media.
- Graham, L. C. 1974. Synthetic interferometer radar for topographic mapping. *Proceedings of the IEEE*, 62, 763-768.
- Gray, A. L., Mattar, K. E. & Sofko, G. 2000. Influence of ionospheric electron density fluctuations on satellite radar interferometry. *Geophysical Research Letters*, 27, 1451-1454.
- Green, B. 2002. Canny edge detection tutorial. *Retrieved: March, 6, 2005*.
- Greenwalt, C. R. & Shultz, M. E. 1962. Principles of error theory and cartographic applications. DTIC Document.
- Greisen, E. W. 2003. Aips, the vla, and the vlba. *Information handling in astronomy-historical vistas*. Springer.

- Grossmann, A. 1988. Wavelet transforms and edge detection. *Stochastic processes in physics and engineering*. Springer.
- Gruen, A. & Akca, D. 2005. Least squares 3d surface and curve matching. *ISPRS Journal of Photogrammetry and Remote Sensing*, 59, 151-174.
- GSFC, N. 2012. *International reference ionosphere* [Online]. Available: <https://iri.gsfc.nasa.gov/> [Accessed 10 Nov 2017].
- Gwinner, K., Jaumann, R., Hauber, E., Hoffmann, H., Heipke, C., Oberst, J., Neukum, G., Ansan, V., Bostelmann, J. & Dumke, A. 2016. The high resolution stereo camera (hrsc) of mars express and its approach to science analysis and mapping for mars and its satellites. *Planetary and Space Science*, 126, 93-138.
- Hagfors, T. & Evans, J. 1968. Radar studies of the moon. *Radar Astronomy*, 219, 273.
- Haklay, M. 2010. How good is volunteered geographical information? A comparative study of openstreetmap and ordnance survey datasets. *Environment and planning B: Planning and design*, 37, 682-703.
- Hanssen, R. F. 2001. *Radar interferometry: Data interpretation and error analysis*, Springer Science & Business Media.
- Hayakawa, M. 2007. Vlf/lf radio sounding of ionospheric perturbations associated with earthquakes. *Sensors*, 7, 1141-1158.
- Heidemann, H. K. 2012. Lidar base specification. US Geological Survey.
- Helm, V., Humbert, A. & Miller, H. 2014. Elevation and elevation change of greenland and antarctica derived from cryosat-2. *The Cryosphere*, 8, 1539-1559.
- Herrera, G., Tomás, R., López-Sánchez, J. M., Delgado, J., Mallorqui, J., Duque, S. & Mulas, J. 2007. Advanced dinsar analysis on mining areas: La union case study (murcia, se spain). *Engineering Geology*, 90, 148-159.
- Hirano, A., Welch, R. & Lang, H. 2003. Mapping from aster stereo image data: Dem validation and accuracy assessment. *ISPRS Journal of Photogrammetry and Remote Sensing*, 57, 356-370.
- Hofton, M., Dubayah, R., Blair, J. B. & Rabine, D. 2006. Validation of srtm elevations over vegetated and non-vegetated terrain using medium footprint lidar. *Photogrammetric Engineering & Remote Sensing*, 72, 279-285.
- Holzner, J., Suchandt, S., Eineder, M., Breit, H. & Adam, N. Co-registration-geometrical analysis and verification for sar interferometry under srtm data conditions. Geoscience and Remote Sensing Symposium, 2001. IGARSS'01. IEEE 2001 International, 2001. IEEE, 393-395.

- Homer, J., Longstaff, I., She, Z. & Gray, D. 2002. High resolution 3-d imaging via multi-pass sar. *IEE Proceedings-Radar, Sonar and Navigation*, 149, 45-50.
- Hooper, A., Segall, P. & Zebker, H. 2007. Persistent scatterer interferometric synthetic aperture radar for crustal deformation analysis, with application to volcán alcedo, galápagos. *Journal of Geophysical Research: Solid Earth*, 112.
- Hooper, A., Zebker, H., Segall, P. & Kampes, B. 2004. A new method for measuring deformation on volcanoes and other natural terrains using insar persistent scatterers. *Geophysical research letters*, 31.
- Horsley, S., Artoni, M. & La Rocca, G. 2015. Spatial kramers–kronig relations and the reflection of waves. *Nature Photonics*, 9, 436.
- Hosford, S., Baghdadi, N., Bourguine, B., Daniels, P. & King, C. Fusion of airborne laser altimeter and radarsat data for dem generation. Geoscience and Remote Sensing Symposium, 2003. IGARSS'03. Proceedings. 2003 IEEE International, 2003. IEEE, 806-808.
- Hu, C., Tian, Y., Dong, X., Wang, R. & Long, T. 2017. Computerized ionospheric tomography based on geosynchronous sar. *Journal of Geophysical Research: Space Physics*, 122, 2686-2705.
- Huang, Y., Ferro-Famil, L. & Reigber, A. 2012. Under-foliage object imaging using sar tomography and polarimetric spectral estimators. *IEEE transactions on geoscience and remote sensing*, 50, 2213-2225.
- Huang, Y., Ferro-Famil, L. & Reigber, A. Under-foliage target detection using multi-baseline l-band polinsar data. Radar Symposium (IRS), 2013 14th International, 2013. IEEE, 449-454.
- Hunsucker, R. D. 2013. *Radio techniques for probing the terrestrial ionosphere*, Springer Science & Business Media.
- Hunsucker, R. D. & Hargreaves, J. K. 2002. The high-latitude ionosphere and its effects on radio propagation. *The High-Latitude Ionosphere and its Effects on Radio Propagation, by RD Hunsucker and JK Hargreaves, pp. 638. ISBN 0521330831. Cambridge, UK: Cambridge University Press, December 2002., 638.*
- Hunter, G. J. & Goodchild, M. F. 1997. Modeling the uncertainty of slope and aspect estimates derived from spatial databases. *Geographical Analysis*, 29, 35-49.
- Iliffe, J. 2000. *Datums and map projections for remote sensing, gis, and surveying*, Whittles Publishing.

- Iliffe, J., Ziebart, M., Cross, P., Forsberg, R., Strykowski, G. & Tscherning, C. C. 2003. Osgm02: A new model for converting gps-derived heights to local height datums in great britain and ireland. *Survey Review*, 37, 276-293.
- Ince, E. S. & Pagiatakis, S. D. 2017. Goce gradiometer measurements response to ionospheric dynamics. *Journal of Geophysical Research: Space Physics*.
- Jackson, H. D. & Woode, A. 1992. Development of the ers-1 active radar calibration unit. *Microwave Theory and Techniques, IEEE Transactions on*, 40, 1063-1069.
- Jakowatz, C. V. & Thompson, P. 1995. A new look at spotlight mode synthetic aperture radar as tomography: Imaging 3-d targets. *IEEE transactions on image processing*, 4, 699-703.
- Jakowatz, C. V. & Wahl, D. E. 1993. Eigenvector method for maximum-likelihood estimation of phase errors in synthetic-aperture-radar imagery. *JOSA A*, 10, 2539-2546.
- Ji, H. J. M. F. H. 2012. Wei (national key laboratory of microwave imaging technology, institute of electronics, chinese academy of sciences, beijing 100190, china); current situation and development trend of inflight antenna pattern measurement techniques of spaceborne sar [j]. *Journal of Radars*, 3.
- Jolivet, R., Agram, P. S., Lin, N. N. Y., Simons, M., Doin, M. P., Peltzer, G. & Li, Z. H. 2014. Improving insar geodesy using global atmospheric models. *Journal of Geophysical Research-Solid Earth*, 119, 2324-2341.
- Jones, J., Brown, P., Ellis, K., Webster, A., Campbell-Brown, M., Krzemenski, Z. & Weryk, R. 2005. The canadian meteor orbit radar: System overview and preliminary results. *Planetary and Space Science*, 53, 413-421.
- Jones, R. M. & Stephenson, J. J. 1975. A versatile three-dimensional ray tracing computer program for radio waves in the ionosphere. *NASA STI/Recon Technical Report N*, 76.
- Just, D. & Bamler, R. 1994. Phase statistics of interferograms with applications to synthetic aperture radar. *Appl Opt*, 33, 4361-8.
- Kanade, T. & Okutomi, M. 1994. A stereo matching algorithm with an adaptive window: Theory and experiment. *IEEE Transactions on Pattern Analysis and Machine Intelligence*, 16, 920-932.
- Kellermann, K., Lister, M., Homan, D., Vermeulen, R., Cohen, M., Ros, E., Kadler, M., Zensus, J. & Kovalev, Y. 2004. Sub-milliarcsecond imaging of quasars and



- active galactic nuclei. Iii. Kinematics of parsec-scale radio jets. *The Astrophysical Journal*, 609, 539.
- Kelley, K. & Quinn, P. 2017. A radio astronomy search for cold dark matter axions. *The Astrophysical Journal Letters*, 845, L4.
- Kelley, M. C. 2009. *The earth's ionosphere: Plasma physics and electrodynamics*, Academic press.
- Ketelaar, V. 2009. Satellite radar interferometry, remote sensing and digital image processing.
- Kim, J. S. 2013. Development of ionosphere estimation techniques for the correction of sar data. ETH Zurich.
- Kim, J. S. & Papathanassiou, K. Sar observation of ionosphere using range/azimuth sub-bands. EUSAR 2014; 10th European Conference on Synthetic Aperture Radar; Proceedings of, 2014. VDE, 1-4.
- Kimura, H. 2009. Calibration of polarimetric pulsar imagery affected by faraday rotation using polarization orientation. *Geoscience and Remote Sensing, IEEE Transactions on*, 47, 3943-3950.
- Kirk, R., Howington - Kraus, E., Rosiek, M., Anderson, J., Archinal, B., Becker, K., Cook, D., Galuszka, D., Geissler, P. & Hare, T. 2008. Ultrahigh resolution topographic mapping of mars with mro hirise stereo images: Meter - scale slopes of candidate phoenix landing sites. *Journal of Geophysical Research: Planets*, 113.
- Komatsu, E. & Spergel, D. N. The cosmic microwave background bispectrum as a test of the physics of inflation and probe of the astrophysics of the low-redshift universe. The Ninth Marcel Grossmann Meeting: On Recent Developments in Theoretical and Experimental General Relativity, Gravitation and Relativistic Field Theories (In 3 Volumes), 2002. World Scientific, 2009-2010.
- Kramer, M., Stairs, I. H., Manchester, R., McLaughlin, M., Lyne, A., Ferdman, R., Burgay, M., Lorimer, D., Possenti, A. & D'Amico, N. 2006. Tests of general relativity from timing the double pulsar. *Science*, 314, 97-102.
- Kraus, J. D. 1966. Radio astronomy. *New York: McGraw-Hill*, 1966.
- Kraus, J. D., Tiuri, M., Räsänen, A. V. & Carr, T. D. 1986. *Radio astronomy*, Cygnus-Quasar Books Powell, Ohio.

- Krieger, G., Fiedler, H., Hajnsek, I., Eineder, M., Werner, M. & Moreira, A. Tandem-x: Mission concept and performance analysis. *IEEE International Geoscience and Remote Sensing Symposium*, 2005a. 4890-4893.
- Krieger, G., Moreira, A., Fiedler, H., Hajnsek, I., Werner, M., Younis, M. & Zink, M. 2007. Tandem-x: A satellite formation for high-resolution sar interferometry. *IEEE Transactions on Geoscience and Remote Sensing*, 45, 3317-3341.
- Krieger, G., Moreira, A., Hajnsek, I., Werner, M., Fiedler, H. & Settelmeier, E. The tandem-x mission proposal. *ISPRS Hannover Workshop*, 2005b.
- Kumar, P., Rani, M., Bisht, P., Yadav, M., Sharma, M., Prawasi, R. & Hooda, R. 2011. An overview of synthetic aperture radar and its applications. *NY SCI. J.*, 4, 6, 6.
- Kumar, S., Tan, E. L., Razul, S. G., See, C. M. S. & Siingh, D. 2014. Validation of the iri-2012 model with gps-based ground observation over a low-latitude singapore station. *Earth, Planets and Space*, 66, 17.
- Kundu, M. R. 1965. Solar radio astronomy. *New York: Interscience Publication*, 1965.
- Kuzuoka, S., Ferretti, A. & Novali, F. 2013. An advanced insar algorithm for surface deformation monitoring: Squeesar (tm). *Conference Proceedings of 2013 Asia-Pacific Conference on Synthetic Aperture Radar (Apsar)*, 336-337.
- Labroue, S., Boy, F., Picot, N., Urvoy, M. & Ablain, M. 2012. First quality assessment of the cryosat-2 altimetric system over ocean. *Advances in Space Research*, 50, 1030-1045.
- Lancashire, D. 1987. Ers-1 ami calibration and characterisation plan'. *Marconi Space Systems Report, ER-PL-MSS-AM-0008*.
- Landmap, T. 2014. *Landmap: Elevation earth observation collection*. Nerc earth observation data centre [Online]. Available: <http://catalogue.ceda.ac.uk/uuid/f5d48fb0372be25b737f92976e386f53> [Accessed].
- Lawrence, K. J., Benner, L. A., Brozovic, M., Ostro, S. J., Jao, J. S., Giorgini, J. D., Slade, M. A., Jurgens, R. F., Nolan, M. C. & Howell, E. S. 2018. Arecibo and goldstone radar images of near-earth asteroid (469896) 2005 wc1. *Icarus*, 300, 12-20.
- Lawrence, R., Little, C. G. & Chivers, H. 1964. A survey of ionospheric effects upon earth-space radio propagation. *Proceedings of the IEEE*, 52, 4-27.
- Lazarov, A. D. & Kostadinov, T. P. 2013. *Bistatic sar/gisar/fisar geometry, signal models and imaging algorithms*, John Wiley & Sons.

- Lee, J.-S. & Pottier, E. 2009. *Polarimetric radar imaging: From basics to applications*, CRC press.
- Levanon, N. 1988. Radar principles. *New York, Wiley-Interscience, 1988, 320 p.*, 1.
- Li, J., Chen, J., Wang, P. & Loffeld, O. 2018. A coarse-to-fine autofocus approach for very high-resolution airborne stripmap sar imagery. *IEEE Transactions on Geoscience and Remote Sensing*.
- Li, N. & Wu, J. 2018. Research on methods of high coherent target extraction in urban area based on psinsar technology. *International Archives of the Photogrammetry, Remote Sensing & Spatial Information Sciences*, 42.
- Li, P., Shi, C., Li, Z., Muller, J.-P., Drummond, J., Li, X., Li, T., Li, Y. & Liu, J. 2013. Evaluation of aster gdem using gps benchmarks and srtm in china. *International Journal of Remote Sensing*, 34, 1744-1771.
- Li, Z. 2005. Correction of atmospheric water vapour effects on repeat-pass sar interferometry using gps, modis and meris data. University of London.
- Li, Z. & Bethel, J. 2008. Image coregistration in sar interferometry. *The International Archives of the Photogrammetry, Remote Sensing and Spatial Information Sciences*, 37, 433-438.
- Li, Z., Ding, X., Chen, W., Liu, G., Shea, Y. & Emerson, N. 2008. Comparative study of tropospheric empirical model for hong kong region. *Surv. Rev*, 40, 328-341.
- Li, Z. H., Fielding, E. J., Cross, P. & Preusker, R. 2009. Advanced insar atmospheric correction: Meris/modis combination and stacked water vapour models. *International Journal of Remote Sensing*, 30, 3343-3363.
- Li, Z. H., Muller, J. P., Cross, P. & Fielding, E. J. 2005. Interferometric synthetic aperture radar (insar) atmospheric correction: Gps, moderate resolution imaging spectroradiometer (modis), and insar integration. *Journal of Geophysical Research-Solid Earth*, 110.
- Li, Z. T. & Bethel, J. 2007. Dem alignment and registration in interferometric sar processing and evaluation. *2007 IEEE International Geoscience and Remote Sensing Symposium*. IEEE.
- Liao, M., Wang, Y., Lu, I., Li, D., Fang, Z. & Wei, Z. Result evaluation of coherent target model product with long-term insar data set in shanghai. *Fringe 2005 Workshop*, 2006.
- Lieu, D. & Sorby, S. 2008. *Visualization, modeling, and graphics for engineering design*, Cengage Learning.

- Lin, S.-Y., Muller, J.-P., Mills, J. P. & Miller, P. E. 2010. An assessment of surface matching for the automated co-registration of mola, hrsc and hirise dtms. *Earth and Planetary Science Letters*, 294, 520-533.
- Liu, J., Kuga, Y., Ishimaru, A., Pi, X. & Freeman, A. 2003. Ionospheric effects on sar imaging: A numerical study. *Geoscience and Remote Sensing, IEEE Transactions on*, 41, 939-947.
- Liu, X., Ma, H. & Sun, W. 2006. Study on the geolocation algorithm of space-borne sar image. *Advances in machine vision, image processing, and pattern analysis*. Springer.
- Liu, Z.-S. & Li, J. 1998. Implementation of the relax algorithm. *IEEE Transactions on aerospace and electronic systems*, 34, 657-664.
- Liu, Z., Skone, S., Gao, Y. & Komjathy, A. 2005. Ionospheric modeling using gps data. *GPS Solutions*, 9, 63-66.
- Lombardini, F. 2005a. Differential tomography: A new framework for sar interferometry. *IEEE Transactions on Geoscience and Remote Sensing*, 43, 37-44.
- Lombardini, F. 2005b. Differential tomography: A new framework for sar interferometry. *Geoscience and Remote Sensing, IEEE Transactions on*, 43, 37-44.
- Lombardini, F. Full-resolution adaptive differential tomography. *Geoscience and Remote Sensing Symposium, 2009 IEEE International, IGARSS 2009, 2009. IEEE*, III-176-III-179.
- Lombardini, F. & Cai, F. 3d tomographic and differential tomographic response to partially coherent scenes. *Geoscience and Remote Sensing Symposium, 2008. IGARSS 2008. IEEE International, 2008. IEEE*, II-457-II-460.
- Lombardini, F. & Cai, F. Evolutions of diff-tomo for sensing subcanopy deformations and height-varying temporal coherence. *Fringe 2011, 2012*. 43.
- Lombardini, F. & Cai, F. 2014. Temporal decorrelation-robust sar tomography. *IEEE Transactions on Geoscience and Remote Sensing*, 52, 5412-5421.
- Lombardini, F., Cai, F. & Pasculli, D. 2013a. Spaceborne 3-d sar tomography for analyzing garbled urban scenarios: Single-look superresolution advances and experiments. *IEEE Journal of Selected Topics in Applied Earth Observations and Remote Sensing*, 6, 960-968.

- Lombardini, F. & Gini, F. Multiple reflectivities estimation for multibaseline insar imaging of layover extended sources. Radar Conference, 2003. Proceedings of the International, 2003. IEEE, 257-263.
- Lombardini, F., Montanari, M. & Gini, F. 2003. Reflectivity estimation for multibaseline interferometric radar imaging of layover extended sources. *IEEE Transactions on Signal Processing*, 51, 1508-1519.
- Lombardini, F. & Pardini, M. 2012. Superresolution differential tomography: Experiments on identification of multiple scatterers in spaceborne sar data. *IEEE Transactions on Geoscience and Remote Sensing*, 50, 1117-1129.
- Lombardini, F. & Viviani, F. 4d characterization of short-and long-term height-varying decorrelated forest sar backscattering. Geoscience and Remote Sensing Symposium (IGARSS), 2015 IEEE International, 2015. IEEE, 1547-1550.
- Lombardini, F., Viviani, F., Cai, F. & Dini, F. Forest temporal decorrelation: 3d analyses and processing in the diff-tomo framework. Geoscience and Remote Sensing Symposium (IGARSS), 2013 IEEE International, 2013b. IEEE, 1202-1205.
- Lord, R. & Inggs, M. 1999. Efficient rfi suppression in sar using lms adaptive filter integrated with range/doppler algorithm. *Electronics Letters*, 35, 629-630.
- Lu, Z. & Dzurisin, D. 2014. Insar imaging of aleutian volcanoes. *Insar imaging of aleutian volcanoes*. Springer.
- Luckman, A. & Grey, W. 2003. Urban building height variance from multibaseline ers coherence. *IEEE transactions on geoscience and remote sensing*, 41, 2022-2025.
- Madanayake, A., Randeny, T., Udayanga, N., Sengupta, A., Jones, G., Wijenayake, C. & Bruton, L. T. 2017. Applications of rf aperture-array spatially-bandpass 2-d iir filters in sub-nyquist spectrum sensing, wideband doppler radar and radio astronomy beamforming. *Multidimensional Systems and Signal Processing*, 28, 1523-1548.
- Mahafza, B. R. 2005. *Radar systems analysis and design using matlab second edition*, Chapman and Hall/CRC.
- Mahapatra, P. S., Samiei-Esfahany, S. & Hanssen, R. F. 2015. Geodetic network design for insar. *Ieee Transactions on Geoscience and Remote Sensing*, 53, 3669-3680.
- Mallat, S. G. & Zhang, Z. 1993. Matching pursuits with time-frequency dictionaries. *IEEE Transactions on signal processing*, 41, 3397-3415.

- Mandt, K. E., Greathouse, T. K., Retherford, K. D., Gladstone, G. R., Jordan, A. P., Lemelin, M., Koeber, S. D., Bowman-Cisneros, E., Patterson, G. W. & Robinson, M. 2016. Lro-lamp detection of geologically young craters within lunar permanently shaded regions. *Icarus*, 273, 114-120.
- Mannucci, A., Wilson, B., Yuan, D., Ho, C., Lindqwister, U. & Runge, T. 1998. A global mapping technique for gps - derived ionospheric total electron content measurements. *Radio science*, 33, 565-582.
- Martin, B. R. & Irvine, J. 1983. Assessing basic research: Some partial indicators of scientific progress in radio astronomy. *Research policy*, 12, 61-90.
- Martín del Campo, G., Shkvarko, Y., Reigber, A. & Nannini, M. 2018. Tomosar imaging for the study of forested areas: A virtual adaptive beamforming approach. *Remote Sensing*, 10, 1822.
- Massonnet, D., Rossi, M. & Adragna, F. 1994. Radar interferometric mapping of deformation in the year after the landers earthquake. *Nature*, 369, 227-230.
- Massonnet, D., Rossi, M., Carmona, C., Adragna, F., Peltzer, G., Feigl, K. & Rabaute, T. 1993. The displacement field of the landers earthquake mapped by radar interferometry. *Nature*, 364, 138-142.
- Massonnet, D. & Souyris, J.-C. 2008. *Imaging with synthetic aperture radar*, CRC Press.
- Mattson, S., Boyd, A., Kirk, R., Cook, D. & Howington-Kraus, E. Hijack: Correcting spacecraft jitter in hirise images of mars. Proceedings of the 2009 European Planetary Science Congress, Potsdam, Germany, 2009.
- Maune, D. F. 2007. *Digital elevation model technologies and applications: The dem users manual*, Asprs
- Maxwell, J. C. 1861. Xxv. On physical lines of force: Part i.—the theory of molecular vortices applied to magnetic phenomena. *The London, Edinburgh, and Dublin Philosophical Magazine and Journal of Science*, 21, 161-175.
- Maxwell, J. C. 1864. *A dynamical theory of the electromagnetic field*, The Society.
- Maxwell, J. C. 1873. *A treatise on electricity and magnetism*, two volumes. Oxford.
- Mayhew, S. 2015. *A dictionary of geography*, Oxford University Press, USA.
- McCormack, H., Thomas, A. & Solomon, I. 2011. The capabilities and limitations of satellite insar and terrestrial radar interferometry.

- McKerracher, J., Sequeira, H., Raney, R., Schulze, R., Bussey, D., Butler, B. & Neish, C. Mini-rf calibration, a unique approach to on-orbit synthetic aperture radar system calibration. Pl. The 41st Lunar and Planetary Science Conference, Woodlands, TX, USA, 2010. 2352-2353.
- Meadows, P. 1992. Ers-1. Sar. Raw replica pulse analysis'. *GEC-Marconi Research Centre Report*.
- Melbourne, W., Davis, E., Duncan, C., Hajj, G., Hardy, K., Kursinski, E., Meehan, T., Young, L. & Yunck, T. 1994. The application of spaceborne gps to atmospheric limb sounding and global change monitoring.
- Mercer, J. B. Sar technologies for topographic mapping. In D. Fritsch and D. Hobbie,(Eds.), *Photogrammetric Week*, 1995. Citeseer.
- Meyer, F. J. & Nicoll, J. The impact of the ionosphere on interferometric sar processing. *Geoscience and Remote Sensing Symposium*, 2008. IGARSS 2008. IEEE International, 2008a. IEEE, II-391-II-394.
- Meyer, F. J. & Nicoll, J. B. 2008b. Prediction, detection, and correction of faraday rotation in full-polarimetric l-band sar data. *Geoscience and Remote Sensing, IEEE Transactions on*, 46, 3076-3086.
- Miliareisis, G. C. & Argialas, D. 1999. Segmentation of physiographic features from the global digital elevation model/gtopo30. *Computers & Geosciences*, 25, 715-728.
- Min, R., Hu, Y., Pi, Y. & Cao, Z. 2012. Sar tomography imaging using sparse bayesian learning. *IEICE transactions on communications*, 95, 354-357.
- Minh, D. H. T., Le Toan, T., Rocca, F., Tebaldini, S., Villard, L., Réjou-Méchain, M., Phillips, O. L., Feldpausch, T. R., Dubois-Fernandez, P. & Scipal, K. 2016. Sar tomography for the retrieval of forest biomass and height: Cross-validation at two tropical forest sites in french guiana. *Remote Sensing of Environment*, 175, 138-147.
- Minh, D. H. T., Tebaldini, S., Rocca, F., Le Toan, T., Villard, L. & Dubois-Fernandez, P. C. 2015. Capabilities of biomass tomography for investigating tropical forests. *IEEE Transactions on Geoscience and Remote Sensing*, 53, 965-975.
- Mitchell, J., Lawrence, S., Robinson, M., Speyerer, E. & Denevi, B. 2017. Searching for water ice at the lunar north pole using high-resolution images and radar.
- Mora, O., Mallorqui, J. J. & Broquetas, A. 2003. Linear and nonlinear terrain deformation maps from a reduced set of interferometric sar images. *IEEE Transactions on Geoscience and Remote Sensing*, 41, 2243-2253.

- Moreira, A., Krieger, G., Hajnsek, I., Hounam, D., Werner, M., Riegger, S. & Settelmeier, E. Tandem-x: A terrasars-x add-on satellite for single-pass sar interferometry. Geoscience and Remote Sensing Symposium, 2004. IGARSS'04. Proceedings. 2004 IEEE International, 2004. IEEE, 1000-1003.
- Morrison, K. & Bennett, J. 2014. Tomographic profiling—a technique for multi-incidence-angle retrieval of the vertical sar backscattering profiles of biogeophysical targets. *IEEE Transactions on Geoscience and Remote Sensing*, 52, 1350-1355.
- Motagh, M., Schurr, B., Anderssohn, J., Cailleau, B., Walter, T. R., Wang, R. & Villotte, J.-P. 2010. Subduction earthquake deformation associated with 14 november 2007, mw 7.8 tocopilla earthquake in chile: Results from insar and aftershocks. *Tectonophysics*, 490, 60-68.
- Muller, J.-P., Morley, J., Walker, A., Kitmitto, K., Mitchell, K., Chugani, K., Smith, A., Barnes, J., Keenan, R. & Cross, P. 2001. The landmap project for the automated creation and validation of multiresolution orthorectified satellite image products and a 1" dem of the british isles from ers tandem sar interferometry.
- Muthukrishnan, S. 2005. Data streams: Algorithms and applications. *Foundations and Trends® in Theoretical Computer Science*, 1, 117-236.
- Nannini, M. & Scheiber, R. A time domain beamforming algorithm for sar tomography. Proc. EUSAR, 2006. 1-4.
- Nannini, M. & Scheiber, R. Height dependent motion compensation and coregistration for airborne sar tomography. Geoscience and Remote Sensing Symposium, 2007. IGARSS 2007. IEEE International, 2007. IEEE, 5041-5044.
- Nannini, M., Scheiber, R. & Horn, R. Imaging of targets beneath foliage with sar tomography. Synthetic Aperture Radar (EUSAR), 2008 7th European Conference on, 2008. VDE, 1-4.
- Nannini, M., Scheiber, R., Horn, R. & Moreira, A. 2012. First 3-d reconstructions of targets hidden beneath foliage by means of polarimetric sar tomography. *IEEE Geoscience and Remote Sensing Letters*, 9, 60-64.
- Nannini, M., Scheiber, R. & Moreira, A. 2009. Estimation of the minimum number of tracks for sar tomography. *IEEE Transactions on Geoscience and Remote Sensing*, 47, 531-543.



- NASA. 2015. *Earth's upper atmosphere* [Online]. Available: [https://www.nasa.gov/mission\\_pages/sunearth/science/mos-upper-atmosphere.html](https://www.nasa.gov/mission_pages/sunearth/science/mos-upper-atmosphere.html) [Accessed 10 Feb 2018].
- NASA. 2016. *Solar storm and space weather - frequently asked questions* [Online]. Available: [https://www.nasa.gov/mission\\_pages/sunearth/spaceweather/index.html](https://www.nasa.gov/mission_pages/sunearth/spaceweather/index.html) [Accessed 10 Feb 2017].
- NASA. 2017. *Mini-rf: Using radar to search the darkness* [Online]. Available: <https://lunar.gsfc.nasa.gov/lessonkit/Mini-RF-Using%20Radar%20to%20Search%20the%20Darkness.pdf> [Accessed 10 Sep 2017].
- NASA, I. T. 2010. *Icesat: Glas instrument* [Online]. [Accessed 1 October 2015].
- Nava, B., Coisson, P. & Radicella, S. 2008. A new version of the nequick ionosphere electron density model. *Journal of Atmospheric and Solar-Terrestrial Physics*, 70, 1856-1862.
- Needell, D. & Tropp, J. A. 2009. Cosamp: Iterative signal recovery from incomplete and inaccurate samples. *Applied and computational harmonic analysis*, 26, 301-321.
- Neo, Y. L., Wong, F. H. & Cumming, I. G. 2008. Processing of azimuth-invariant bistatic sar data using the range doppler algorithm. *Geoscience and Remote Sensing, IEEE Transactions on*, 46, 14-21.
- Newburgh, L., Bandura, K., Bucher, M., Chang, T.-C., Chiang, H., Cliche, J., Davé, R., Dobbs, M., Clarkson, C. & Ganga, K. Hirax: A probe of dark energy and radio transients. *Ground-based and Airborne Telescopes VI*, 2016. International Society for Optics and Photonics, 99065X.
- Nezlin, D. V., Kostylev, V., Blyakhman, A. B., Ryndyk, A. G. & Myakinkov, A. 2007. *Bistatic radar: Principles and practice*. England: Wiley.
- Nitti, D. O., Hanssen, R. F., Refice, A., Bovenga, F. & Nutricato, R. 2011. Impact of dem-assisted coregistration on high-resolution sar interferometry. *IEEE Transactions on Geoscience and Remote Sensing*, 49, 1127-1143.
- Nozette, S., Spudis, P., Bussey, B., Jensen, R., Raney, K., Winters, H., Lichtenberg, C. L., Marinelli, W., Crusan, J. & Gates, M. 2010. The lunar reconnaissance orbiter miniature radio frequency (mini-rf) technology demonstration. *Space Science Reviews*, 150, 285-302.

- OGC 1999. The opengis abstract specification-topic 7: The earth imagery case.
- Oliver, C. & Quegan, S. 2004. *Understanding synthetic aperture radar images*, SciTech Publishing.
- Ordnance-Survey. 2015. *A guide to coordinate systems in great britain* [Online].  
Available: <https://www.bnhs.co.uk/focuson/grabagridref/html/OSGB.pdf>  
[Accessed 6 Jan 2015].
- Ostro, S. J. 1993. Planetary radar astronomy. *Reviews of Modern Physics*, 65, 1235.
- Ostro, S. J., Hudson, R. S., Benner, L. A., Giorgini, J. D., Magri, C., Margot, J.-L. & Nolan, M. C. 2002. Asteroid radar astronomy. *Asteroids III*, 151-168.
- Otto, G. P. & Chau, T. K. 1989. "Region-growing" algorithm for matching of terrain images. *Image and vision computing*, 7, 83-94.
- Ouzounov, D., Pulinets, S., Romanov, A., Romanov, A., Tsybulya, K., Davidenko, D., Kafatos, M. & Taylor, P. 2011. Atmosphere-ionosphere response to the m9 tohoku earthquake revealed by multi-instrument space-borne and ground observations: Preliminary results. *Earthquake Science*, 24, 557-564.
- Paillou, P. & Gelautz, M. 1999. Relief reconstruction from sar stereo pairs: The "optimal gradient" matching method. *IEEE transactions on Geoscience and Remote Sensing*, 37, 2099-2107.
- Pardini, M., Bianco, V. & Papathanassiou, K. 2014. Phase calibration of multi-baseline pol-insar data stacks. *DLR Interner Bericht*.
- Pardini, M. & Papathanassiou, K. Robust estimation of the vertical structure of forest with coherence tomography. Proceedings of ESA POLinSAR Workshop, 2011. ESA.
- Pardini, M. & Papathanassiou, K. A two-step phase calibration method for tomographic applications with airborne sar data. EUSAR 2014; 10th European Conference on Synthetic Aperture Radar; Proceedings of, 2014. VDE, 1-4.
- Pardini, M., Papathanassiou, K., Bianco, V. & Iodice, A. Phase calibration of multibaseline sar data based on a minimum entropy criterion. Geoscience and Remote Sensing Symposium (IGARSS), 2012 IEEE International, 2012. IEEE, 5198-5201.
- Parker, A. L. 2016. *Insar observations of ground deformation: Application to the cascades volcanic arc*, Springer.

- Parker, W. V. 2018. *Discover the benefits of radar imaging*. [Online]. Available: <https://ejournal.com/print/articles/discover-the-benefits-of-radar-imaging> [Accessed 10 June 2018].
- Paskevich, V. 2005. Srtm30plus-na\_pctshade. Tif-srtm30plus color-encoded shaded relief image of north america (approximately 1km)-geotiff image.
- Pasquali, P., Prati, C., Rocca, F., Seymour, M., Fortuny, J., Ohlmer, E. & Sieber, A. A 3-d sar experiment with emsl data. Geoscience and Remote Sensing Symposium, 1995. IGARSS'95.'Quantitative Remote Sensing for Science and Applications', International, 1995. IEEE, 784-786.
- Patterson, G., Raney, R., Cahill, J., Bussey, D. & Team, M.-R. Characterization of lunar crater ejecta deposits using m-chi decompositions of mini-rf radar data. European Planetary Science Congress 2012, 2012. 731.
- Patterson, G., Stickle, A., Turner, F., Jensen, J., Bussey, D., Spudis, P., Espiritu, R., Schulze, R., Yocky, D. & Wahl, D. 2017. Bistatic radar observations of the moon using mini-rf on Iro and the arecibo observatory. *Icarus*, 283, 2-19.
- Pauciullo, A., De Maio, A., Perna, S., Reale, D. & Fornaro, G. 2014. Detection of partially coherent scatterers in multidimensional sar tomography: A theoretical study. *IEEE Transactions on Geoscience and Remote Sensing*, 52, 7534-7548.
- Pauciullo, A., Reale, D., De Maio, A. & Fornaro, G. 2012. Detection of double scatterers in sar tomography. *IEEE Transactions on Geoscience and Remote Sensing*, 50, 3567-3586.
- Pfeifle, R. & Seidel, H.-P. 1996. Scattered data approximation with triangular b-splines. Wiesbaden: Vieweg+Teubner Verlag.
- Pi, X., Freeman, A., Chapman, B., Rosen, P. & Li, Z. 2011. Imaging ionospheric inhomogeneities using spaceborne synthetic aperture radar. *Journal of Geophysical Research: Space Physics*, 116.
- Pi, X., Mannucci, A., Lindqwister, U. & Ho, C. 1997. Monitoring of global ionospheric irregularities using the worldwide gps network. *Geophysical Research Letters*, 24, 2283-2286.
- Piau, P. Performances of the 3d-sar imagery. Geoscience and Remote Sensing Symposium, 1994. IGARSS'94. Surface and Atmospheric Remote Sensing: Technologies, Data Analysis and Interpretation., International, 1994. IEEE, 2267-2271.

- Pike, R. J. 2002. A bibliography of terrain modeling (geomorphometry), the quantitative representation of topography. *USGS Open file report*.
- Pinel, V., Hooper, A., De la Cruz-Reyna, S., Reyes-Davila, G., Doin, M. & Bascou, P. 2011. The challenging retrieval of the displacement field from insar data for andesitic stratovolcanoes: Case study of popocatepetl and colima volcano, mexico. *Journal of Volcanology and Geothermal Research*, 200, 49-61.
- Poli, D. & Caravaggi, I. 2012. Digital surface modelling and 3d information extraction from spaceborne very high resolution stereo pairs. *JRC Scientific and Technical Reports, Ispra*.
- Ponomarenko, P., St-Maurice, J., Waters, C., Gillies, R. & Koustov, A. Refractive index effects on the scatter volume location and doppler velocity estimates of ionospheric hf backscatter echoes. *Annales geophysicae: atmospheres, hydrospheres and space sciences*, 2009. 4207.
- Priyadarshi, S. 2015. A review of ionospheric scintillation models. *Surveys in geophysics*, 36, 295-324.
- Purcell, E. M. & Morin, D. J. 2013. *Electricity and magnetism*, Cambridge University Press.
- Puysségur, B., Michel, R. & Avouac, J. P. 2007. Tropospheric phase delay in interferometric synthetic aperture radar estimated from meteorological model and multispectral imagery. *Journal of Geophysical Research: Solid Earth*, 112.
- Qin, Y., Perissin, D. & Lei, L. Insar x-band atmospheric water vapor analysis and comparison in hong kong. *Geoscience and Remote Sensing Symposium (IGARSS)*, 2013 IEEE International, 2013. IEEE, 125-128.
- Quegan, S. 2017. *Biomass: First steps from selection to reality* [Online]. Available: <https://slideplayer.com/slide/3397572/> [Accessed 10 October 2016].
- Reale, D., Fornaro, G., Paucullo, A., Zhu, X. & Bamler, R. 2011. Tomographic imaging and monitoring of buildings with very high resolution sar data. *IEEE Geoscience and remote sensing letters*, 8, 661-665.
- Redfearn, J. 1948. Transverse mercator formulae. *Empire Survey Review*, 9, 318-322.
- Reigber, A. & Moreira, A. 2000. First demonstration of airborne sar tomography using multibaseline l-band data. *IEEE Transactions on Geoscience and Remote Sensing*, 38, 2142-2152.

- Reigber, A., Neumann, M., Guillaso, S., Sauer, S. & Ferro-Famil, L. Evaluating polinsar parameter estimation using tomographic imaging results. Radar Conference, 2005. EURAD 2005. European, 2005. IEEE, 189-192.
- Ren Kun, P. V., and Shi Xiangquan 2003. Comparison of satellite baseline estimation methods for interferometry applications. *Geoscience and Remote Sensing Symposium IGARSS '03*. Toulouse, France.
- Reuter, H., Nelson, A., Strobl, P. & Mehl, W. 2009. A first assessment of aster gdem tiles for absolute accuracy, relative accuracy and terrain parameters. ... *and Remote Sensing*.
- Richards, M. A. 2005. *Fundamentals of radar signal processing*, Tata McGraw-Hill Education.
- Rignot, E. J. 2000. Effect of faraday rotation on l-band interferometric and polarimetric synthetic-aperture radar data. *Geoscience and Remote Sensing, IEEE Transactions on*, 38, 383-390.
- Rincon, R. F., Ranson, K. J., Agueh, T. E. F. & Carter, L. M. 2019. Spaceborne synthetic aperture radar system and method. Google Patents.
- Rodriguez, E., Morris, C., Belz, J., Chapin, E., Martin, J., Daffer, W. & Hensley, S. 2005. An assessment of the srtm topographic products. *Technical Report JPL D-31639*.
- Rodriguez, E., Morris, C. S. & Belz, J. E. 2006. A global assessment of the srtm performance. *Photogrammetric Engineering & Remote Sensing*, 72, 249-260.
- Rogers, A. & Ingalls, R. 1969. Venus: Mapping the surface reflectivity by radar interferometry. *Science*, 165, 797-799.
- Rogers, J. R. & Hopler, M. D. 1988. Conversion of group refractive index to phase refractive index. *JOSA A*, 5, 1595-1600.
- Rohlfs, K. & Wilson, T. L. 2013. *Tools of radio astronomy*, Springer Science & Business Media.
- Rose, R. 1982. *Understanding the united kingdom: The territorial dimension in government*, Longman Publishing Group.
- Rosen, P. A., Hensley, S. & Chen, C. Measurement and mitigation of the ionosphere in l-band interferometric sar data. Radar Conference, 2010 IEEE, 2010. IEEE, 1459-1463.
- Rovelli, C. 2017. Planck stars: New sources in radio and gamma astronomy? *arXiv preprint arXiv:1708.01789*.

- Rusu, R. B. & Cousins, S. 3d is here: Point cloud library (pcl). Robotics and automation (ICRA), 2011 IEEE International Conference on, 2011. IEEE, 1-4.
- Saatchi, S., Ulander, L., Williams, M., Quegan, S., LeToan, T., Shugart, H. & Chave, J. 2012. Forest biomass and the science of inventory from space. *Nature Climate Change*, 2, 826.
- Sandwell, D., Garcia, E., Soofi, K., Wessel, P., Chandler, M. & Smith, W. H. 2013. Toward 1-mgal accuracy in global marine gravity from cryosat-2, envisat, and jason-1. *The Leading Edge*, 32, 892-899.
- Sanin, A., Mitrofanov, I., Litvak, M., Malakhov, A., Boynton, W., Chin, G., Droege, G., Evans, L., Garvin, J. & Golovin, D. 2012. Testing lunar permanently shadowed regions for water ice: Lend results from lro. *Journal of Geophysical Research: Planets*, 117.
- Sardon, E., Rius, A. & Zarraoa, N. 1994. Estimation of the transmitter and receiver differential biases and the ionospheric total electron content from global positioning system observations. *Radio science*, 29, 577-586.
- Satimagingcorp. 2015. *About digital elevation models* [Online]. Available: <http://www.satimagingcorp.com/> [Accessed 1 September 2015].
- Schaer, S., Gurtner, W. & Feltens, J. Ionex: The ionosphere map exchange format version 1. Proceedings of the IGS AC workshop, Darmstadt, Germany, 1998.
- Scheiber, R. & Moreira, A. 2000. Coregistration of interferometric sar images using spectral diversity. *Geoscience and Remote Sensing, IEEE Transactions on*, 38, 2179-2191.
- Scheiber, R., Reigber, A., Ulbricht, A., Papathanassiou, K., Horn, R., Buckreuss, S. & Moreira, A. Overview of interferometric data acquisition and processing modes of the experimental airborne sar system of dlr. Geoscience and Remote Sensing Symposium, 1999. IGARSS'99 Proceedings. IEEE 1999 International, 1999. IEEE, 35-37.
- Schultz, H., Riseman, E. M., Stolle, F. R. & Woo, D.-M. Error detection and dem fusion using self-consistency. Computer Vision, 1999. The Proceedings of the Seventh IEEE International Conference on, 1999. IEEE, 1174-1181.
- Schurr, B., Asch, G., Rosenau, M., Oncken, O., Barrientos, S., Salazar, P. & Vilotte, J. 2012. The 2007 m7. 7 tocopilla northern chile earthquake sequence—along and across strike rupture segmentation and the role of mejillones peninsula. *Journal of Geophysical Research*, 117, B05305.

- Schutz, B., Zwally, H., Shuman, C., Hancock, D. & DiMarzio, J. 2005. Overview of the icesat mission. *Geophysical Research Letters*, 32.
- Schwerdt, M., Bräutigam, B., Bachmann, M., Döring, B., Schrank, D. & Gonzalez, J. H. 2010. Final terrasar-x calibration results based on novel efficient methods. *Geoscience and Remote Sensing, IEEE Transactions on*, 48, 677-689.
- Secan, J. 2007. Wbmod ionospheric scintillation model-an abbreviated user's guide (version 15). *Northwest Research Associates, Inc., Tucson, AZ*.
- Secan, J., Fremouw, E. & Robins, R. 1987. A review of recent improvements to the wbmod ionospheric scintillation model. *Effect of the Ionosphere on Communication, Navigation and Surveillance Systems*, edited by J Goodman (US Govt Printing Office, Springfield, Va., USA), 607-618.
- Shaft, P. 1974. On the relationship between scintillation index and rician fading. *IEEE Transactions on Communications*, 22, 731-732.
- Sharp, G. C., Lee, S. W. & Wehe, D. K. 2002. Icp registration using invariant features. *IEEE Transactions on Pattern Analysis and Machine Intelligence*, 24, 90-102.
- Sharp, R. D., Johnson, R. & Shelley, E. 1977. Observation of an ionospheric acceleration mechanism producing energetic (kev) ions primarily normal to the geomagnetic field direction. *Journal of Geophysical Research*, 82, 3324-3328.
- Shih, P. T. Y. 2014. Evaluating information loss of srtm dem data with different grid. *Journal of Surveying Engineering*, 140.
- Shim, J., Kuznetsova, M., Rastätter, L., Bilitza, D., Butala, M., Codrescu, M., Emery, B., Foster, B., Fuller-Rowell, T. & Huba, J. 2012. Cedar electrodynamics thermosphere ionosphere (eti) challenge for systematic assessment of ionosphere/thermosphere models: Electron density, neutral density, nmf2, and hmf2 using space based observations. *Space Weather*, 10, 1-16.
- Shin, D. & Muller, J.-P. 2012. Progressively weighted affine adaptive correlation matching for quasi-dense 3d reconstruction. *Pattern Recognition*, 45, 3795-3809.
- Simpson, R. A. 1997. Electromagnetic radiation electromagnetic radiation. *Encyclopedia of planetary science*. Springer.
- Singh, S. & Datar, A. 2013. Edge detection techniques using hough transform. *International Journal of Emerging Technology and Advanced Engineering*, 3, 333-337.

- Slater, J. A., Garvey, G., Johnston, C., Haase, J., Heady, B., Kroenung, G. & Little, J. 2006. The srtm data “finishing” process and products. *Photogrammetric Engineering & Remote Sensing*, 72, 237-247.
- Smith, E. K. & Weintraub, S. 1953. The constants in the equation for atmospheric refractive index at radio frequencies. *Proceedings of the IRE*, 41, 1035-1037.
- Smolicic, V., Padovani, P., Delhaize, J., Prandoni, I., Seymour, N., Jarvis, M., Afonso, J., Magliocchetti, M., Huynh, M. & Vaccari, M. 2015. Exploring agn activity over cosmic time with the ska. *arXiv preprint arXiv:1501.04820*.
- Solberg, S., Astrup, R. & Weydahl, D. J. 2013. Detection of forest clear-cuts with shuttle radar topography mission (srtm) and tandem-x insar data. *Remote Sensing*, 5, 5449-5462.
- Soumekh, M. 1999. *Synthetic aperture radar signal processing*, New York: Wiley.
- Spudis, P., Bussey, D., Baloga, S., Cahill, J., Glaze, L., Patterson, G., Raney, R., Thompson, T., Thomson, B. & Ustinov, E. 2013. Evidence for water ice on the moon: Results for anomalous polar craters from the lro mini - rf imaging radar. *Journal of Geophysical Research: Planets*, 118, 2016-2029.
- Starck, J.-L., Murtagh, F. & Fadili, J. M. 2010. *Sparse image and signal processing: Wavelets, curvelets, morphological diversity*, Cambridge university press.
- Stebler, O., Brodbeck, R., Pasquali, P. & Nuesch, D. Multibaseline pol-insar experiment for the estimation of the scattering processes and their spatial distribution within vegetation layers. Geoscience and Remote Sensing Symposium, 2000. Proceedings. IGARSS 2000. IEEE 2000 International, 2000. IEEE, 132-134.
- Stebler, O., Meier, E. & Nuesch, D. Multi-baseline airborne pol-insar measurements for the estimation of scattering processes within vegetation media. Geoscience and Remote Sensing Symposium, 2001. IGARSS'01. IEEE 2001 International, 2001. IEEE, 3172-3174.
- Stebler, O., Meier, E. & Nuesch, D. Forward and inverse modelling of multi-baseline l-band pol-insar e-sar data. Geoscience and Remote Sensing Symposium, 2002. IGARSS'02. 2002 IEEE International, 2002. IEEE, 823-825.
- Stiglitz, M. R. & Resnick, L. 1989. Radar principles for the non-specialist. *Microwave Journal*, 32, 174-175.



- Stoker, J., Abdullah, Q., Nayegandhi, A. & Winehouse, J. 2016. Evaluation of single photon and geiger mode lidar for the 3d elevation program. *Remote Sensing*, 8, 767.
- Strozzi, T., Kouraev, A., Wiesmann, A., Wegmüller, U., Sharov, A. & Werner, C. 2008. Estimation of arctic glacier motion with satellite l-band sar data. *Remote Sensing of Environment*, 112, 636-645.
- Sun, L. & Muller, J.-P. 2016. Evaluation of the use of sub-pixel offset tracking techniques to monitor landslides in densely vegetated steeply sloped areas. *Remote Sensing*, 8, 659.
- Sun, X.-L., YU, A.-x., DU, H.-d., DONG, Z. & LIANG, D.-n. 2011. Sar tomography based on simulated interferometric phase. *Journal of National University of Defense Technology*, 33, 105-110.
- Sutinjo, A. T., Ung, D., Colegate, T. M., Wayth, R. B., Hall, P. J. & de Lera Acedo, E. 2017. Revisiting hybrid interferometry with low-frequency radio astronomy arrays. *IEEE Transactions on Antennas and Propagation*.
- Tachikawa, T., Kaku, M., Iwasaki, A., Gesch, D. & Oimoen, M. 2011. *Aster global digital elevation model version 2—summary of validation results*.
- Tantianuparp, P., Balz, T., Wang, T., Jiang, H., Zhang, L. & Liao, M. Analyzing the topographic influence for the ps-insar processing in the three gorges region. Geoscience and Remote Sensing Symposium (IGARSS), 2012 IEEE International, 2012. IEEE, 3843-3846.
- Tao, Y., Muller, J.-P., Sidiropoulos, P., Xiong, S.-T., Putri, A., Walter, S., Veitch-Michaelis, J. & Yershov, V. 2018. Massive stereo-based dtm production for mars on cloud computers. *Planetary and Space Science*, 154, 30-58.
- Tao, Y. & Muller, J. Performance of global 3d model retrievals of the martian surface using the ucl casp-go system on ctx stereo images on linux clusters and microsoft azure® cloud computing platforms. High-Performance Computing in Geoscience and Remote Sensing VIII, 2018. International Society for Optics and Photonics, 1079207.
- Team, A. V. 2009. *Aster global dem validation summary report*.
- Tebaldini, S. An algebraic approach to ground-volume decomposition from multi-baseline polinsar data. Geoscience and Remote Sensing Symposium, 2009 IEEE International, IGARSS 2009, 2009a. IEEE, III-967-III-970.

- Tebaldini, S. 2009b. Algebraic synthesis of forest scenarios from multibaseline polinsar data. *IEEE Transactions on Geoscience and Remote Sensing*, 47, 4132-4142.
- Tebaldini, S. 2010. *Multibaseline sar imaging: Models and algorithms*, VDM Verlag.
- Tebaldini, S. & Guarnieri, A. M. 2010. On the role of phase stability in sar multibaseline applications. *IEEE Transactions on Geoscience and Remote Sensing*, 48, 2953-2966.
- Tebaldini, S., Nagler, T., Rott, H. & Heilig, A. L-band 3d imaging of an alpine glacier: Results from the alptomosar campaign. Geoscience and Remote Sensing Symposium (IGARSS), 2015 IEEE International, 2015. IEEE, 5212-5215.
- Tebaldini, S. & Rocca, F. 2012. Multibaseline polarimetric sar tomography of a boreal forest at p-and l-bands. *IEEE Transactions on Geoscience and Remote Sensing*, 50, 232-246.
- Tebaldini, S., Rocca, F., d'Alessandro, M. M. & Ferro-Famil, L. 2016. Phase calibration of airborne tomographic sar data via phase center double localization. *IEEE Transactions on Geoscience and Remote Sensing*, 54, 1775-1792.
- Thayer, G. D. 1974. An improved equation for the radio refractive index of air. *Radio Science*, 9, 803-807.
- Theiler, P. W., Wegner, J. D. & Schindler, K. 2014. Keypoint-based 4-points congruent sets—automated marker-less registration of laser scans. *ISPRS journal of photogrammetry and remote sensing*, 96, 149-163.
- Thompson, A. R., Moran, J. M. & Swenson, G. W. 1986. *Interferometry and synthesis in radio astronomy*, Springer.
- Thompson, D. G., Bates, J. S. & Arnold, D. V. Extending the phase gradient autofocus algorithm for low-altitude stripmap mode sar. Radar Conference, 1999. The Record of the 1999 IEEE, 1999. IEEE, 36-40.
- Thomson, B., Bussey, D., Neish, C., Cahill, J., Heggy, E., Kirk, R., Patterson, G., Raney, R., Spudis, P. & Thompson, T. 2012. An upper limit for ice in shackleton crater as revealed by lro mini - rf orbital radar. *Geophysical Research Letters*, 39.
- Thorne, K. S. 1967. Primordial element formation, primordial magnetic fields, and the isotropy of the universe. *The Astrophysical Journal*, 148, 51.
- Thrift, N. & Walling, D. 2000. Geography in the united kingdom 1996–2000. *Geographical journal*, 166, 96-124.

- Tibshirani, R. 1996. Regression shrinkage and selection via the lasso. *Journal of the Royal Statistical Society. Series B (Methodological)*, 267-288.
- Titov, D., Barabash, S., Bruzzone, L., Dougherty, M., Erd, C., Fletcher, L., Gare, P., Gladstone, R., Grasset, O. & Gurvits, L. Juice: Complementarity of the payload in addressing the mission science objectives. EGU General Assembly Conference Abstracts, 2014.
- Tomas, R., Herrera, G., Lopez-Sanchez, J., Vicente, F., Cuenca, A. & Mallorquí, J. 2010. Study of the land subsidence in orihuela city (se Spain) using psi data: Distribution, evolution and correlation with conditioning and triggering factors. *Engineering Geology*, 115, 105-121.
- Tonggang, Z., Minyi, C., Xinghua, W. & Guoqing, Z. Fully automatic dem deformation detection without control points using differential model based on lzd algorithm. Geoscience and Remote Sensing Symposium, 2005. IGARSS'05. Proceedings. 2005 IEEE International, 2005. IEEE, 3982-3985.
- Torson, J. M. Application of graphical interaction to the analysis of radio astronomy data. ACM SIGGRAPH Computer Graphics, 1980. ACM, 140-146.
- Trisakti, B. & Carolita, I. 2010. Comparison result of dem generated from aster stereo data and srtm. *International Journal of Remote Sensing and Earth Sciences (IJReSES)*, 4.
- Ulaby, F. T., Long, D. G., Blackwell, W. J., Elachi, C., Fung, A. K., Ruf, C., Sarabandi, K., Zebker, H. A. & Van Zyl, J. 2014. *Microwave radar and radiometric remote sensing*, University of Michigan Press Ann Arbor.
- Ulander, L. M., Fröling, P.-O., Gustavsson, A., Murdin, D. & Stenström, G. Fast factorized back-projection for bistatic sar processing. Synthetic Aperture Radar (EUSAR), 2010 8th European Conference on, 2010. VDE, 1-4.
- Usai, S., Sansosti, E., Berardino, P., Lanari, R., Fornaro, G., Tesauro, M. & Lundgren, P. 2000. Modelling terrain deformations at the phlegrean fields with insar. *Igarss 2000: Ieee 2000 International Geoscience and Remote Sensing Symposium, Vol I - Vi, Proceedings*, 2245-2247.
- Verma, A. K., Margot, J.-L. & Greenberg, A. H. 2017. Prospects of dynamical determination of general relativity parameter  $\beta$  and solar quadrupole moment with asteroid radar astronomy. *The Astrophysical Journal*, 845, 166.

- Vincent, O. R. & Folorunso, O. A descriptive algorithm for sobel image edge detection. Proceedings of Informing Science & IT Education Conference (InSITE), 2009. Informing Science Institute California, 97-107.
- Vondrak, R., Keller, J., Chin, G. & Garvin, J. 2010a. Lunar reconnaissance orbiter (lro): Observations for lunar exploration and science. *Space science reviews*, 150, 7-22.
- Vondrak, R., Keller, J. & Russell, C. 2010b. The design of the lunar exploration neutron detector (lend) experiment is presented, which was optimized to address several of the primary measurement requirements of nasa's lunar reconnaissance orbiter (lro): High spatial resolution hydrogen mapping of the moon's upper-most surface, identification of putative deposits of appreciable near-surface water ice in the moon's polar cold traps, and characterization.
- Wadge, G., Webley, P., James, I., Bingley, R., Dodson, A., Waugh, S., Veneboer, T., Puglisi, G., Mattia, M. & Baker, D. 2002. Atmospheric models, gps and insar measurements of the tropospheric water vapour field over mount etna. *Geophysical Research Letters*, 29.
- Wahl, D. E., Eichel, P., Ghiglia, D. & Jakowatz, C. 1994. Phase gradient autofocus-a robust tool for high resolution sar phase correction. *IEEE Transactions on Aerospace and Electronic Systems*, 30, 827-835.
- Walters, R., Elliott, J., Li, Z. & Parsons, B. 2013. Rapid strain accumulation on the ashkabad fault (turkmenistan) from atmosphere - corrected insar. *Journal of Geophysical Research: Solid Earth*, 118, 3674-3690.
- Walters, R., Parsons, B. & Wright, T. 2014. Constraining crustal velocity fields with insar for eastern turkey: Limits to the block - like behavior of eastern anatolia. *Journal of Geophysical Research: Solid Earth*, 119, 5215-5234.
- Wang, B., Chen, S., Yi, H. & Mao, L. Subsidence monitoring by permanent scatterers in insar: A case study of yancheng city in jiangsu. *Multimedia Technology (ICMT)*, 2010 International Conference on, 2010. IEEE, 1-6.
- Wang, J., Liu, S., Shen, Y. & Zhu, Z. 2018. Low-power single-ended sar adc using symmetrical dac switching for image sensors with passive cds and pga technique. *IEEE Transactions on Circuits and Systems I: Regular Papers*, 65.
- Wang, r. x. 2006. Three linear ccd image satellite photography measuring principle. *Beijing Surveying and Mapping Press*.

- Wang, X., Cheng, X., Gong, P., Huang, H., Li, Z. & Li, X. 2011. Earth science applications of icesat/glas: A review. *International Journal of Remote Sensing*, 32, 8837-8864.
- Wang, Y. & Zhu, X. X. Insar forensics: Tracing insar scatterers in high resolution optical image. Proc. FRINGE WORKSHOP, 2015. 1-8.
- Wang, Y., Zhu, X. X. & Bamler, R. 2014. An efficient tomographic inversion approach for urban mapping using meter resolution sar image stacks. *IEEE Geoscience and Remote Sensing Letters*, 11, 1250-1254.
- Wasnik, M. D. 2014. Image stitching using matlab. *International Journal of Innovative Technology and Exploring Engineering (IJITEE) Volume-3*.
- Wechsler, S. P. 1999. Digital elevation model (dem) uncertainty: Evaluation and effect on topographic parameters. *ESRI User Conference*.
- Wechsler, S. P. 2007. Uncertainties associated with digital elevation models for hydrologic applications: A review. *Hydrology and Earth System Sciences*, 11, 1481-1500.
- Wegmuller, U., Werner, C., Strozzi, T. & Wiesmann, A. 2006. Ionospheric electron concentration effects on sar and insar. *2006 Ieee International Geoscience and Remote Sensing Symposium, Vols 1-8*, 3731-3734.
- Werninghaus, R. Terrasar-x mission. Remote Sensing, 2004. International Society for Optics and Photonics, 9-16.
- Wessel, B., Gruber, A., González, J. H., Bachmann, M. & Wendleder, A. Tandem-x: Dem calibration concept. Geoscience and Remote Sensing Symposium, 2008. IGARSS 2008. IEEE International, 2008a. IEEE, III-111-III-114.
- Wessel, B., Huber, M., Wohlfart, C., Marschalk, U., Kosmann, D. & Roth, A. 2018. Accuracy assessment of the global tandem-x digital elevation model with gps data. *ISPRS Journal of Photogrammetry and Remote Sensing*, 139, 171-182.
- Wessel, B., Marschalk, U., Gruber, A., Huber, M., Hahmann, T., Roth, A. & Habermeyer, M. Design of the dem mosaicking and calibration processor for tandem-x. 7th European Conference on Synthetic Aperture Radar, 2008b. VDE, 1-4.
- Whitney, H. E. & Malik, C. 1968. A proposed index for measuring ionospheric scintillation. AIR FORCE CAMBRIDGE RESEARCH LABS HANSCOM AFB MA.

- Wikipedia. 2016a. *Digital elevation model* [Online]. Available:  
[https://en.wikipedia.org/wiki/Digital\\_elevation\\_model](https://en.wikipedia.org/wiki/Digital_elevation_model) [Accessed 10 Jan 2016].
- Wikipedia. 2016b. *Electromagnetic spectrum* [Online]. Available:  
[https://en.wikipedia.org/wiki/Electromagnetic\\_spectrum](https://en.wikipedia.org/wiki/Electromagnetic_spectrum) [Accessed 20 Jan 2016].
- Wikipedia, T. o. 2008. *Golden gate bridge* [Online]. Available:  
[https://en.wikipedia.org/wiki/Golden\\_Gate\\_Bridge](https://en.wikipedia.org/wiki/Golden_Gate_Bridge) [Accessed 30/05 2018].
- Wild, S. 2017. Ghana telescope ready for action. NATURE PUBLISHING GROUP  
 MACMILLAN BUILDING, 4 CRINAN ST, LONDON N1 9XW, ENGLAND.
- Williams, S., Bock, Y. & Fang, P. 1998. Integrated satellite interferometry:  
 Tropospheric noise, gps estimates and implications for interferometric synthetic  
 aperture radar products. *Journal of Geophysical Research: Solid Earth* (1978–  
 2012), 103, 27051-27067.
- Witt III, E. C. 2015. Geospatial resources for the geology community: The usgs national  
 map. *The Journal of Geology*, 123, 283-294.
- Wong, F., Stevens, D. & Cumming, I. Phase-preserving processing of scansar data with  
 a modified range doppler algorithm. *Geoscience and Remote Sensing*, 1997.  
 IGARSS'97. Remote Sensing-A Scientific Vision for Sustainable Development.,  
 1997 IEEE International, 1997. IEEE, 725-727.
- Wong, F. H., Cumming, I. G. & Neo, Y. L. 2008. Focusing bistatic sar data using the  
 nonlinear chirp scaling algorithm. *Geoscience and Remote Sensing, IEEE  
 Transactions on*, 46, 2493-2505.
- Wortham, C. B. 2014. Vector deformation time-series from spaceborne motion  
 compensation insar processors. Stanford University.
- Wright, P., Quegan, S., Wheadon, N. S. & Hall, C. D. 2003. Faraday rotation effects on  
 l-band spaceborne sar data. *Geoscience and Remote Sensing, IEEE Transactions  
 on*, 41, 2735-2744.
- Xiang, Z. X. & Bamler, R. Compressive sensing for high resolution differential sar  
 tomography-the sl1mmer algorithm. *Geoscience and Remote Sensing  
 Symposium (IGARSS)*, 2010 IEEE International, 2010. IEEE, 17-20.
- XiaoFan, L., Muller, J. P., Chen, F. & YongHong, Z. 2011. Measuring displacement  
 field from terrasar-x amplitude images by subpixel correlation: An application to  
 the landslide in shuping, three gorges area. *Acta Petrologica Sinica*, 27, 3843-  
 3850.

- Xilong, S., Anxi, Y., Zhen, D. & Diannong, L. 2012. Three-dimensional sar focusing via compressive sensing: The case study of angel stadium. *IEEE Geoscience and Remote Sensing Letters*, 9, 759-763.
- Xilong, S., Zheng, D., Anxi, Y. & Diannong, L. Super-resolution sar tomographic imaging using envisat-asar data. Synthetic Aperture Radar (AP SAR), 2011 3rd International Asia-Pacific Conference on, 2011. IEEE, 1-4.
- Xiong, S., Zeng, Q., Jiao, J., Gao, S. & Zhang, X. Improvement of ps-insar atmospheric phase estimation by using wrf model. Geoscience and Remote Sensing Symposium (IGARSS), 2014 IEEE International, 2014. IEEE, 2225-2228.
- Xu, C., Wei, M., Griffiths, S., Mercer, B. & Abdoullaev, R. Hybrid dem generation and evaluation from spaceborne radargrammetric and optical stereoscopic dems. Proc. of Canadian Geomatics Conference, 2010. Citeseer.
- Xu, T., Ren, L. & Gao, R. 2017. Earth gravity field solution with combining champ and grace data. *Geodesy and Geodynamics*.
- Xu, W. & Cumming, I. 1999. A region-growing algorithm for insar phase unwrapping. *Geoscience and Remote Sensing, IEEE Transactions on*, 37, 124-134.
- Xuedong, Z., Daqing, G., Weiyu, M., Ling, Z., Yan, W. & Xiaofang, G. Study the land subsidence along jinghu highway (beijing-hebei) using ps-insar technique. Geoscience and Remote Sensing Symposium (IGARSS), 2011 IEEE International, 2011. IEEE, 1608-1611.
- Yamazaki, D., O'Loughlin, F., Trigg, M. A., Miller, Z. F., Pavelsky, T. M. & Bates, P. D. 2014. Development of the global width database for large rivers. *Water Resources Research*, 50, 3467-3480.
- Yang, B., Xu, H., You, Y. & Xie, X. The hybrid cramér-rao bounds on elevation in compressive sensing sar tomography. Compressed Sensing Theory and its Applications to Radar, Sonar and Remote Sensing (CoSeRa), 2016 4th International Workshop on, 2016. IEEE, 128-132.
- Ye, W., Yeo, T. S. & Bao, Z. 1999. Weighted least-squares estimation of phase errors for sar/isar autofocus. *IEEE Transactions on Geoscience and Remote Sensing*, 37, 2487-2494.
- Yeh, K. C. & Liu, C.-H. 1982. Radio wave scintillations in the ionosphere. *Proceedings of the IEEE*, 70, 324-360.
- Yong, Y., Chao, W., Hong, Z., Zhi, L. & Xin, G. 2002. A phase unwrapping method based on minimum cost flows method in irregular network. *Igarss 2002: Ieee*

*International Geoscience and Remote Sensing Symposium and 24th Canadian Symposium on Remote Sensing, Vols I-Vi, Proceedings*, 1726-1728.

- Yoo, J.-C. & Han, T. H. 2009. Fast normalized cross-correlation. *Circuits, systems and signal processing*, 28, 819.
- Young, I., Sanina, E. & Babanin, A. 2017. Calibration and cross validation of a global wind and wave database of altimeter, radiometer, and scatterometer measurements. *Journal of Atmospheric and Oceanic Technology*, 34, 1285-1306.
- Yu, A., Jiang, T., Guo, W., Jiang, G., Wei, X. & Zhang, Y. 2017a. Bias compensation for rational function model based on total least squares. *The Photogrammetric Record*, 32, 48-60.
- Yu, C., Li, Z. & Penna, N. T. 2018. Interferometric synthetic aperture radar atmospheric correction using a gps-based iterative tropospheric decomposition model. *Remote Sensing of Environment*, 204, 109-121.
- Yu, C., Penna, N. T. & Li, Z. 2017b. Generation of real - time mode high - resolution water vapor fields from gps observations. *Journal of Geophysical Research: Atmospheres*, 122, 2008-2025.
- Yu, J. H., Li, X., Ge, L. & Chang, H.-C. Radargrammetry and interferometry sar for dem generation. 15th Australasian Remote Sensing & Photogrammetry Conf. Alice Springs, Australia, 2010. Citeseer, 1212-1223.
- Yuan, Y., Zhu, P., Zhao, N., Xiao, L., Garnero, E., Xiao, Z., Zhao, J. & Qiao, L. 2017. The 3 - d geological model around chang'e - 3 landing site based on lunar penetrating radar channel 1 data. *Geophysical Research Letters*, 44, 6553-6561.
- Zahzam, N., Bidel, Y., Bresson, A., Huynh, P.-A., Liorzou, F., Lebat, V., Foulon, B. & Christophe, B. Hybrid atom electrostatic system for satellite geodesy. EGU General Assembly Conference Abstracts, 2017. 14958.
- Zappa, E. & Busca, G. 2008. Comparison of eight unwrapping algorithms applied to fourier-transform profilometry. *Optics and Lasers in Engineering*, 46, 106-116.
- Zebker, H. A., Hensley, S., Shanker, P. & Wortham, C. 2010. Geodetically accurate insar data processor. *IEEE Transactions on Geoscience and Remote Sensing*, 48, 4309-4321.
- Zebker, H. A., Rosen, P. A., Goldstein, R. M., Gabriel, A. & Werner, C. L. 1994. On the derivation of coseismic displacement fields using differential radar



- interferometry: The landers earthquake. *Journal of Geophysical Research: Solid Earth*, 99, 19617-19634.
- Zebker, H. A., Rosen, P. A. & Hensley, S. 1997. Atmospheric effects in interferometric synthetic aperture radar surface deformation and topographic maps. *Journal of Geophysical Research: Solid Earth (1978–2012)*, 102, 7547-7563.
- Zhang, L., Ding, X. & Lu, Z. 2011. Ground settlement monitoring based on temporarily coherent points between two sar acquisitions. *ISPRS Journal of Photogrammetry and Remote Sensing*, 66, 146-152.
- Zhang, Z. 2000. A flexible new technique for camera calibration. *IEEE Transactions on pattern analysis and machine intelligence*, 22.
- Zhang, Z., Xing, M., Ding, J. & Bao, Z. 2007. Focusing parallel bistatic sar data using the analytic transfer function in the wavenumber domain. *Geoscience and Remote Sensing, IEEE Transactions on*, 45, 3633-3645.
- Zhao, F., Huang, Q. & Gao, W. Image matching by normalized cross-correlation. *Acoustics, Speech and Signal Processing*, 2006. ICASSP 2006 Proceedings. 2006 IEEE International Conference on, 2006. IEEE, II-II.
- Zheng, Y.-q., Wang, H. & Wang, Y.-f. 2009. Selection and design of optical systems for spaceborne hyperspectral imagers [j]. *Optics and Precision Engineering*, 11, 004.
- Zhu, X. 2011. Very high resolution tomographic sar inversion for urban infrastructure monitoring—a sparse and nonlinear tour. Technische Universität München.
- Zhu, X. X. & Bamler, R. Compressive sensing for high resolution differential sar tomography-the sl1mmer algorithm. *Geoscience and Remote Sensing Symposium (IGARSS)*, 2010 IEEE International, 2010a. IEEE, 17-20.
- Zhu, X. X. & Bamler, R. 2010b. Tomographic sar inversion by l1 norm regularization—the compressive sensing approach. *IEEE Transactions on Geoscience and Remote Sensing*, 48, 3839-3846.
- Zhu, X. X. & Bamler, R. 2010c. Very high resolution spaceborne sar tomography in urban environment. *IEEE Transactions on Geoscience and Remote Sensing*, 48, 4296-4308.
- Zhu, X. X. & Bamler, R. Tomographic sar inversion from mixed repeat-and single-pass data stacks—the terrasars-x/tandem-x case. In: *Proceedings of XXII ISPRS Congress*, Melbourne, Australia, 2012.

- Zhu, X. X. & Bamler, R. 2014. Superresolving sar tomography for multidimensional imaging of urban areas: Compressive sensing-based tomosar inversion. *IEEE Signal Processing Magazine*, 31, 51-58.
- Zink, M., Bachmann, M., Brautigam, B., Fritz, T., Hajnsek, I., Moreira, A., Wessel, B. & Krieger, G. 2014. Tandem-x: The new global dem takes shape. *IEEE Geoscience and Remote Sensing Magazine*, 2, 8-23.
- Zink, M., Krieger, G., Fiedler, H., Hajnsek, I. & Moreira, A. The tandem-x mission concept. Synthetic Aperture Radar (EUSAR), 2008 7th European Conference on, 2008. VDE, 1-4.
- Zisk, S. H. 1972. A new, earth-based radar technique for the measurement of lunar topography. *The moon*.
- Zitova, B. & Flusser, J. 2003. Image registration methods: A survey. *Image and vision computing*, 21, 977-1000.
- Zwally, H., Schutz, B., Abdalati, W., Abshire, J., Bentley, C., Brenner, A., Bufton, J., Dezio, J., Hancock, D. & Harding, D. 2002. Icesat's laser measurements of polar ice, atmosphere, ocean, and land. *Journal of Geodynamics*, 34, 405-445.